

**FLUIDS ENGINEERING DIVISION**

Editor  
**J. KATZ (2008)**

Assistant to the Editor  
**L. MURPHY (2008)**

Associate Editors  
**M. J. ANDREWS (2009)**  
**S. BALACHANDAR (2008)**  
**A. BESKOK (2008)**  
**K. S. BREUER (2006)**  
**G. L. CHAHINE (2006)**  
**D. DRIKAKIS (2008)**  
**P. A. DURBIN (2008)**  
**S. GOGENINI (2006)**  
**A. GOTO (2007)**  
**F. F. GRINSTEIN (2006)**  
**T. J. HEINDEL (2007)**  
**H. JOHARI (2009)**  
**J. KOMPENHANS (2009)**  
**JINKOOK LEE (2006)**  
**Y. T. LEE (2007)**  
**J. A. LIBURDY (2007)**  
**P. LIGRANI (2008)**  
**T. J. O'HERN (2008)**  
**U. PIOMELLI (2007)**  
**S. ROY (2007)**  
**D. SIGINER (2008)**  
**Y. TSUJIMOTO (2006)**  
**S. P. VANKA (2007)**  
**Y. ZHOU (2008)**

**PUBLICATIONS COMMITTEE**  
Chair, **B. RAVANI**

**OFFICERS OF THE ASME**  
President, **T. E. SHOUP**  
Executive Director, **V. R. CARTER**  
Treasurer, **T. D. PESTORIUS**

**PUBLISHING STAFF**  
Managing Director, Publishing  
**P. DI VIETRO**  
Manager, Journals  
**C. MCATEER**  
Production Assistant  
**M. ANDINO**

**TECHNICAL PAPERS**

- 893 Characteristics of Fuel Droplets Discharged From a Compensated Fuel/Ballast Tank**  
Jerry W. Shan, Paisan Atsavapranee, Peter A. Chang, Wesley M. Wilson, and Stephan Verosto
- 903 Predictions of Charge Drift in a Concept Electro sprayed DISI Engine**  
Geraldo C. S. Nhumairo and A. Paul Watkins
- 913 Surfactant Effects on the Free Surface Thermal Structure and Subsurface Flow in a Wind-Wave Tunnel**  
Supathorn Phongikaroon and K. Peter Judd
- 921 Hybrid Particle/Grid Method for Predicting Motion of Micro- and Macrofree Surfaces**  
Eiji Ishii, Toru Ishikawa, and Yoshiyuki Tanabe
- 931 Hydrofoil Drag Reduction by Partial Cavitation**  
Eduard Amromin, Jim Kopriva, Roger E. A. Arndt, and Martin Wosnik
- 937 Unsteady Flow Structure and Global Variables in a Centrifugal Pump**  
José González and Carlos Santolaria
- 947 Numerical Study of Unsteady Flows in a Scroll Compressor**  
M. M. Cui
- 956 Numerical Study of Active Flow Control for a Transitional Highly Loaded Low-Pressure Turbine**  
Donald P. Rizzetta and Miguel R. Visbal
- 968 The Instability of Shear Thinning and Shear Thickening Spiralling Liquid Jets: Linear Theory**  
J. Uddin, S. P. Decent, and M. J. Simmons
- 976 Transpiration Induced Shock Boundary-Layer Interactions**  
B. Wasistho
- 987 Measurement of Permeability and Slip Coefficient of Porous Tubes**  
N. M. Brown and F. C. Lai
- 993 Pressure-Driven Flows of Bingham Plastics Over a Square Cavity**  
Evan Mitsoulis, S. Marangoudakis, M. Spyratos, Th. Zisis, and Nikolaos A. Malamataris
- 1004 Air Flow Through Compressed and Uncompressed Aluminum Foam: Measurements and Correlations**  
Nihad Dukhan, Rubén Picón-Feliciano, and Ángel R. Álvarez-Hernández
- 1013 Effects of Curvature and Convective Heat Transfer in Curved Square Duct Flows**  
R. N. Mondal, Y. Kaga, T. Hyakutake, and S. Yanase
- 1023 Numerical Simulation of Two-Dimensional Laminar Incompressible Wall Jet Flow Under Backward-Facing Step**  
P. Rajesh Kanna and Manab Kumar Das
- 1036 Pressure Drop of Fully-Developed, Laminar Flow in Microchannels of Arbitrary Cross-Section**  
M. Bahrami, M. M. Yovanovich, and J. R. Culham

(Contents continued on inside back cover)

This journal is printed on acid-free paper, which exceeds the ANSI Z39.48-1992 specification for permanence of paper and library materials. ©<sup>TM</sup>  
85% recycled content, including 10% post-consumer fibers.

Transactions of the ASME, Journal of Fluids Engineering (ISSN 0098-2202) is published bimonthly (Jan., Mar., May, July, Sept., Nov.) by The American Society of Mechanical Engineers, Three Park Avenue, New York, NY 10016. Periodicals postage paid at New York, NY and additional mailing offices.

POSTMASTER: Send address changes to Transactions of the ASME, Journal of Fluids Engineering, c/o THE AMERICAN SOCIETY OF MECHANICAL ENGINEERS, 22 Law Drive, Box 2300, Fairfield, NJ 07007-2300.

CHANGES OF ADDRESS must be received at Society headquarters seven weeks before they are to be effective. Please send old label and new address.

STATEMENT from By-Laws. The Society shall not be responsible for statements or opinions advanced in papers or printed in its publications (B7.1, Par. 3).

COPYRIGHT © 2006 by the American Society of Mechanical Engineers. Authorization to photocopy material for internal or personal use under those circumstances not falling within the fair use provisions of the Copyright Act, contact the Copyright Clearance Center (CCC), 222 Rosewood Drive, Danvers, MA 01923, tel: 978-750-8400, www.copyright.com. Request for special permission or bulk copying should be addressed to Reprints/Permission Department, Canadian Goods & Services Tax Registration #126148048.

- 1045 Design of a Low-Turbulence, Low-Pressure Wind-Tunnel for Micro-Aerodynamics  
Michael J. Martin, Kevin J. Scavazze, Iain D. Boyd, and Luis P. Bernal
- 1053 Design Optimization of Micro Synthetic Jet Actuator for Flow Separation Control  
Oktay Baysal, Mehti Köklü, and Nurhak Erbaş
- 1063 Resistance and Fluctuating Pressures of a Large Elbow in High Reynolds Numbers  
Tadashi Shiraishi, Hisato Watakabe, Hiromi Sago, Mamoru Konomura, Akira Yamaguchi, and Tadashi Fujii
- 1074 A Computational Study of Torque and Forces Due to Compressible Flow on a Butterfly Valve Disk in Mid-stroke Position  
Zachary Leutwyler and Charles Dalton
- 1083 RANS Simulations of a Simplified Tractor/Trailer Geometry  
Christopher J. Roy, Jeffrey Payne, and Mary McWherter-Payne
- 1090 Experimental Study of the Flow in a Simulated Hard Disk Drive  
Charlotte Barbier, Joseph A. C. Humphrey, and Eric Maslen
- 1101 Onset of Vortex Shedding in a Periodic Array of Circular Cylinders  
L. Zhang and S. Balachandar
- 1106 Detection of Partial Blockages in a Branched Piping System by the Frequency Response Method  
Pranab K. Mohapatra, M. Hanif Chaudhry, Ahmed Kassem, and Jamaluddin Moloo

## TECHNICAL BRIEFS

- 1115 The Classical Plane Couette-Poiseuille Flow With Variable Fluid Properties  
Asterios Pantokratoras
- 1122 Moderately and Widely Spaced Circular Cylinders in Crossflow and a Universal Wake Number  
D. Sumner and A. J. Schenstead
- 1126 3-D Simulation of Dividing Flows in 90 deg Rectangular Closed Conduits  
A. S. Ramamurthy, Junying Qu, Diep Vo, and Chao Zhai

## ANNOUNCEMENT

- 1130 2007 Fluids Engineering Award

The ASME Journal of Fluids Engineering is abstracted and indexed in the following:

*Applied Science & Technology Index, Chemical Abstracts, Chemical Engineering and Biotechnology Abstracts (Electronic equivalent of Process and Chemical Engineering), Civil Engineering Abstracts, Computer & Information Systems Abstracts, Corrosion Abstracts, Current Contents, Ei EncompassLit, Electronics & Communications Abstracts, Engineered Materials Abstracts, Engineering Index, Environmental Engineering Abstracts, Environmental Science and Pollution Management, Excerpta Medica, Fluidex, Index to Scientific Reviews, INSPEC, International Building Services Abstracts, Mechanical & Transportation Engineering Abstracts, Mechanical Engineering Abstracts, METADEX (The electronic equivalent of Metals Abstracts and Alloys Index), Petroleum Abstracts, Process and Chemical Engineering, Referativnyi Zhurnal, Science Citation Index, SciSearch (The electronic equivalent of Science Citation Index), Shock and Vibration Digest, Solid State and Superconductivity Abstracts, Theoretical Chemical Engineering*

# Characteristics of Fuel Droplets Discharged From a Compensated Fuel/Ballast Tank

Jerry W. Shan<sup>1</sup>  
Paisan Atsavapranee  
Peter A. Chang  
Wesley M. Wilson  
Stephan Verosto

Naval Surface Warfare Center,  
Carderock Division,  
West Bethesda, MD 20817

*Fuel droplets, formed by the interaction of fuel plumes with a water/fuel interface, can be discharged during the refueling of water-filled compensated fuel/ballast tanks. Motivated by increasingly stringent environmental regulations, a study was initiated to understand the physical mechanisms involved in the formation and transport of fuel droplets by complex immiscible flows inside a model tank. In particular, optical measurements were made of the size distribution of fuel droplets in water discharged from a three-bay model of a compensated fuel/ballast tank. The volumetric fuel concentration of discharge from the tank was inferred from measurements of droplet size and number. Flow visualizations inside the model were coupled to optical measurements of fuel droplets at the tank outlet to show that the presence of fuel in the discharged water was correlated to the formation of fuel plumes within the water-filled tank. The size distribution of fuel droplets at the tank exit is found to differ from the size distribution reported for the generation zone (near the fuel plumes) inside the tank. Thus, the advection of fuel droplets from the generation zone to the tank outlet is shown to affect the characteristics of discharged fuel droplets. The transport process specifically prevents large-diameter droplets from reaching the tank exit. Buoyancy tends to cause larger fuel droplets generated within the tank to rise and separate out of the flow before they can be discharged. The buoyancy time,  $\tau_b(D)$ , relative to the characteristic advection time,  $\tau_a$ , of fuel droplets is a key parameter in predicting the fate of fuel droplets. The influence of buoyancy on the size distribution of discharged droplets was found to be modeled reasonably well by a Butterworth filter that depends on the ratio of timescales  $\tau_a/\tau_b(D)$ . This model, which relates the size distribution of discharged droplets to generated droplets, is found to produce the correct qualitative behavior that larger fuel droplets are discharged when the fuel plumes move closer to the tank exit, i.e., for decreasing advection time  $\tau_a$ . [DOI: 10.1115/1.2234780]*

## 1 Introduction

The generation of droplets by the motion of two immiscible fluids occurs in situations as diverse as the liquid emulsions used for dispersed-phase reactions in chemical engineering operations [1], and the oil-in-water emulsions of common salad dressings. An oil-in-water dispersion of interest for environmental reasons is the diesel fuel discharged in droplet form during the refueling of compensated fuel tanks on naval vessels. Compensated fuel/ballast systems are used by the U.S. Navy in the DD-963, CG 47, DDG 51, LHA 1 classes, and more recently in the LHD 7, to maintain uniform trim and draft. In such ships, when oil is consumed from the fuel tank, it is replaced by water to compensate for the change in ballast. During refueling of a water-filled tank, the inflowing diesel fuel can be entrained into the water in the form of fuel droplets, potentially causing the concentration of fuel oil in the discharged water to exceed environmental regulations. For this reason, there has been considerable recent interest in the Navy in studying and modeling the flows which generate and transport immiscible droplets.

Several basic flow phenomena have been identified and studied for their contribution to the fuel droplets in the discharged water. Friedman and Katz [2] investigated a vertical water jet impinging on a fuel/water interface. Their work was motivated by the vertical jet of water which can impinge on a residual fuel layer at the

top of the tank at the onset of refueling of a compensated fuel/ballast tank. Different flow regimes were identified as a function of interface Richardson number

$$Ri_i \equiv D_p \frac{(\rho - \rho_f)g}{\rho U_p^2} \quad (1)$$

based on the pipe diameter,  $D_p$ ; jet exit velocity,  $U_p$ ; water density,  $\rho$ ; fuel density,  $\rho_f$ ; and the gravitational acceleration,  $g$ . As the Richardson number decreased, increasing numbers of fuel and water droplets were formed as the jet deformed and ultimately penetrated the fuel/water interface. Fuel-droplet size distributions exhibited a polydisperse log-normal size distribution [3]. Wu and Katz [4] also investigated the entrainment of fuel droplets due to shear at a statically stable fuel/water interface. Their experiments showed that roll up of the immiscible shear layer led to mixing and droplet formation above a threshold shear rate (Weber number) at low  $Ri$ .

A third mechanism for fuel-droplet production is the fuel plume that forms inside the tank. As fuel spills through the manhole connecting each bay of the tank, a positively buoyant jet of fuel is formed inside the seawater-filled tank, as seen in Fig. 1. Impingement of the fuel plume on the fuel/water interface produces numerous droplets. This plume was identified and studied in earlier experiments by Chang et al. [5,6]. Their measurements in a half-scale, two-bay model of a portion of the fuel/ballast tank showed that the size distribution for the fuel droplets was log-normal in the generation zone close to the buoyant plume.

This paper describes experiments conducted on a three-bay model of a portion of the compensated fuel/ballast tank. The experiments sought to characterize the fuel droplets in the discharged seawater from the tank, and to identify their primary

<sup>1</sup>Present address: Department of Mechanical and Aerospace Engineering, Rutgers—The State University of New Jersey, Piscataway, NJ 08854.

Contributed by the Fluids Engineering Division of ASME for publication in the JOURNAL OF FLUIDS ENGINEERING. Manuscript received December 12, 2002; final manuscript received March 9, 2006. Review conducted by Joseph Katz.

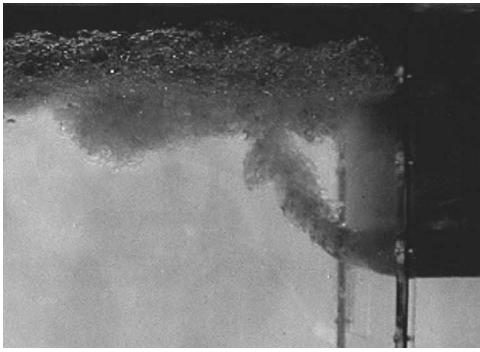


Fig. 1 Plume of fuel in water

source. Optical measurements are made of the number and size of fuel droplets advected by water to the outlet of the tank during refueling. The fuel concentration of the overboard discharge is computed from the droplets. Simultaneous flow visualization inside the fuel tank allowed the fuel discharge to be correlated to the presence of specific flow events. The size distributions of fuel droplets at the outlet and in the production zone are compared, and the influence of the advective transport process on the droplet characteristics is assessed. A model is proposed which relates the size distribution of the discharged droplets to the production distribution of the droplets.

## 2 Experimental Facility and Instrumentation

A three-bay model of a portion of a compensated fuel/ballast tank was constructed for the experiment. The tank consisted of three divided bays, connected by manholes cut into the dividing plates (Fig. 2). The tank was constructed of clear acrylic and had overall interior dimensions of 2.30 m × 0.559 m × 0.281 m. Two-in. (5.08 cm) diameter inlet and outlet pipes carried the fuel and discharge water. For the purposes of this paper, the inlet bay is labeled Bay 1, and the exit bay is labeled Bay 3, as shown in Fig. 2. The tank was initially filled with fresh water for each test. Fuel is pumped in through the inlet pipe in Bay 1, filling the top of that

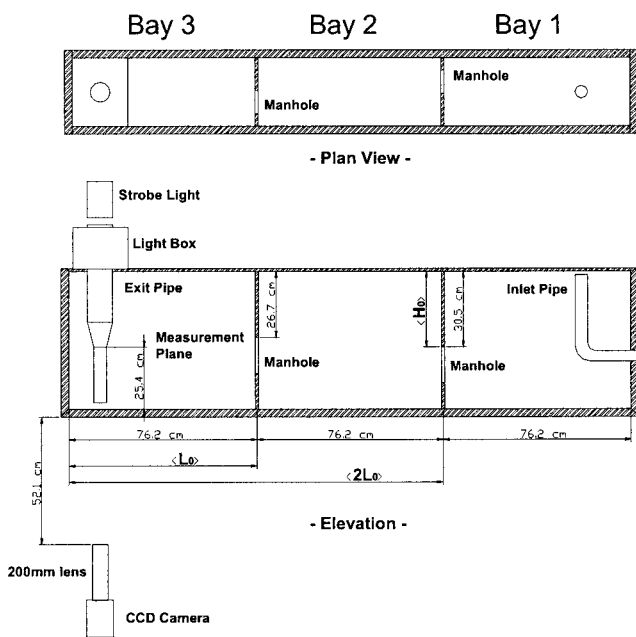


Fig. 2 Experimental facility and optical arrangement. Imaging arrangement shown is for low-resolution measurements; camera is closer to tank for high-resolution measurements.

bay until fuel spills over through the manhole into Bay 2. The top of Bay 2 fills with fuel until fuel spills over into the Bay 3. The experiment ends when the level of fuel in Bay 3 reaches the level of the outlet pipe and bulk fuel discharge begins. The diesel fuel has specific gravity of 0.84 and kinematic viscosity of  $2.7 \times 10^{-6} \text{ m}^2/\text{s}$ , while the fresh water has a density of  $1.0 \times 10^3 \text{ kg/m}^3$  and kinematic viscosity of  $1.0 \times 10^{-6} \text{ m}^2/\text{s}$ .

The Reynolds number and the Richardson number (alternatively, the Froude number) characterize the plume spilling from the manhole. The ratio of potential energy to the kinetic energy of the mean flow in the manhole is

$$Ri \equiv \frac{(\rho - \rho_f)gH_0}{\rho U_m^2} \approx \frac{(\rho - \rho_f)gH_0}{\rho(\dot{Q}/A_m)^2} \quad (2)$$

based on the mean flow speed in the manhole,  $U_m$ ; the volume flow rate,  $\dot{Q}$ ; the manhole area,  $A_m$ ; and the distance from the manhole to the top of the tank,  $H_0$  (Fig. 2). The fluid densities and the distance  $H_0$  in the model tank are the same as in the full-scale compensated fuel/ballast tank. Thus, in order to match Richardson numbers, the mean flow rate  $U_m = \dot{Q}/A$  must be matched between model- and full-scale tanks. For these experiments, a full-scale flow rate of  $\dot{Q} = 25 \text{ l/s}$  was chosen as representative of in-port refueling procedures (full-scale flow rates typically range from 8.2 l/s to over 63 l/s, depending on operating conditions). The model-scale flow rate was limited by the available pumps to 1/17th the flow rate of the full-scale tank, i.e.,  $\dot{Q} = 1.48 \text{ l/s}$ . Thus, to ensure comparable Richardson numbers to the full-scale case, the area,  $A_m$ , of the model-scale manhole was chosen to be 1/16th that of the full-scale manhole. The model-scale manhole, which had dimensions of 14.6 cm × 9.53 cm, matched the full-scale manhole in all other aspects of the geometry. The model and full-scale Richardson numbers are  $Ri \approx 42$ , based Eq. (2).

The Reynolds number based on the mean flow through the manhole is

$$Re \equiv \frac{U_m A_m^{1/2}}{\nu_f} \approx \frac{\dot{Q} A_m^{1/2}}{A_m \nu_f} \quad (3)$$

where  $A_m^{1/2}$  is a length scale based on the area of the manhole and  $\nu_f$  is the kinematic viscosity of fuel. The Reynolds number of the mean flow in the experiment,  $Re \approx 5 \times 10^3$ , is one quarter of the Reynolds number of the full-scale case. Alternatively, the jet Reynolds number,  $Re_j \equiv u_j \delta_j / \nu_f$  is approximately  $6 \times 10^3$  for the conditions of the experiment, based on the measured jet thickness,  $\delta_j \approx 5 \text{ cm}$ , and the inferred jet speed,  $u_j \approx \dot{Q} / \delta_j W_m \approx 0.3 \text{ m/s}$ , where  $W_m$  is the manhole width. Measurements indicate that the Reynolds number of the experiment is sufficiently high that turbulence transition can be expected to occur within several jet thicknesses of the manhole [7]. This was verified in the flow visualizations shown in Figs. 3 and 4. Data on turbulent mixing in a shear layer, jets, and other flows suggest that a mixing transition to fully developed turbulence occurs for  $Re > 10^4$ , or  $Re_{Taylor} > 100$  [8]. However, for liquid-phase jets, the mixing transition is more gradual than for gas-phase jets, and only a weak dependence on Reynolds numbers is documented. For example, in axisymmetric, turbulent jets, the scalar variance depends on Reynolds number in power-law fashion with an exponent of  $-0.647$  [8]. Because transition distance and measures of mixing such as scalar variance depend weakly on Reynolds numbers for liquid-phase jets, greater priority was placed on matching Richardson number than Reynolds number. The present experiments are believed to be reasonably representative of the full-scale flow because the Froude (or equivalently Richardson number) is exactly matched and the Reynolds number of the experiment is the same order of magnitude as that of the full-scale case.

For each experiment, a digital camera recorded backlit images of the cross section of exit pipe, while a video camera simulta-

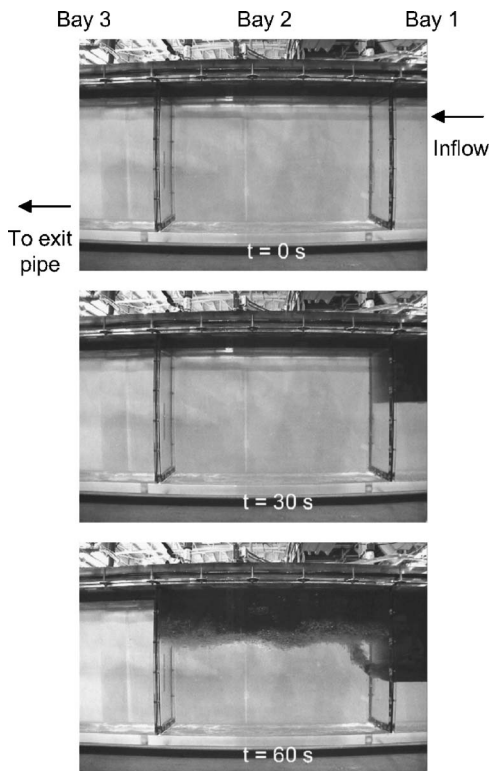


**Fig. 3** Flow visualization of refueling of compensated fuel/ballast tank. First fuel plume forms in Bay 2 at  $t \approx 35$  s.

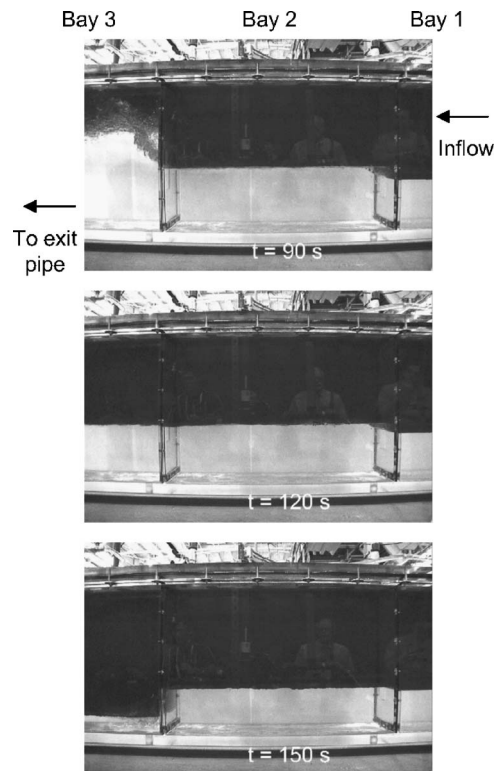


**Fig. 4** Flow visualization. Second fuel plume forms in Bay 3 at  $t \approx 70$  s.

neously recorded flow visualization inside the fuel tank. Optical data were taken for eight runs at the same inflow rate,  $\dot{Q} = 1.48$  l/s. In half of the runs, the digital camera imaged the entire cross section of the exit pipe for low-resolution images, while in the other half of the runs, the camera imaged a much smaller portion of the exit pipe for magnified, high-resolution images. Data from both the low-resolution and high-resolution images were processed and combined using a procedure described below.

### 2.1 Silhouette Photography and Droplet Identification.

Fuel droplets in the overboard discharge were imaged and characterized with silhouette photography in a measurement plane inside the exit pipe (Fig. 2). A digital camera (Kodak ES 4.0) using a 200 mm focal-length macrolens (Nikon Micro-Nikkor) recorded images of  $(2048 \times 2048)$ -pixel resolution at 15 frames/s for the entire duration, approximately 150 s, of each run. The low-resolution images had a field of view of  $50.8 \text{ mm} \times 50.8 \text{ mm}$  covering the entire cross section of the effluent pipe, yielding a pixel resolution of  $2.48 \times 10^{-2} \text{ mm/pixel}$ . The high-resolution images had a field of view covering a square,  $7.6 \text{ mm} \times 7.6 \text{ mm}$  portion of the effluent pipe, resulting in a pixel resolution of  $3.7 \times 10^{-3} \text{ mm/pixel}$ . For each of four high-resolution tests, the field of view was shifted so that the images covered a representative sample of the entire effluent pipe. A strobe light (Genrad) illuminated a diffuser plate to provide back illumination for fuel droplets in the outlet pipe. The stroboscope was used so that its short pulse duration,  $1\text{--}2 \mu\text{s}$ , would eliminate smearing from the motion of the droplets. In order to provide a uniformly illuminated background, the diffuser needed to be larger than the pipe diameter at the measurement plane. This was the reason for the expansion in exit-pipe diameter from 5.08 to 10.2 cm downstream of the measurement plane (Fig. 2).

An automated software program, written within the Matrox Inspector environment, was used to identify, count, and size the fuel droplets. A Sobel edge-detection filter was applied to the raw image, followed by a threshold operation. The combination of edge-

detection filtering and thresholding discarded the out-of-focus droplets outside of the measurement plane. After filtering and image segmentation, automated droplet analysis was used to identify and size the fuel droplets. A morphology filter was used to remove objects having a compactness ratio,  $R_c \equiv L_p^2/4\pi A > 2$ , or an elongation ratio,  $R_e \equiv \text{length}/\text{breadth} > 2$ , where  $L_p$  is the perimeter and  $A$  is the area. Circular objects have compactness and elongation values of unity. This morphology filtering was used to reject impurities, such as tiny fibers, in the water while retaining nearly spherical droplets. For the conditions of the experiment, the droplets are expected to be nearly spherical [9,10], as was also verified from the images. Once identified, the fuel droplets are sized from their silhouetted area

$$D \approx \left( \frac{4A}{\pi} \right)^{1/2} \quad (4)$$

where  $A$  is the measured silhouette area. A similar image analysis procedure was used by Kulenovic et al. to characterize gas-phase droplets in boiling liquid propane [11].

An example of the droplet identification procedure is shown in Fig. 5. A magnified portion of a typical backilluminated image of the exit pipe is shown, and the Sobel-filtered image is also shown. In-focus droplets are identified, while out-of-focus droplets outside of the measurement plane are discarded. A calibration procedure, described in the follow section, was used to determine the depth-of-field of the measurement plane. The minimum resolvable diameter of the fuel droplets was determined by the contrast between fuel and water. Fuel droplets below 0.10 mm had too low contrast to be reliably identified with the back illumination and imaging arrangement. Also, the water and fuel were filtered but it was not possible to completely remove small particles, which could be confused with fuel droplets of very small diameter. For these reasons, it was judged that the minimum diameter of fuel droplets that could be reliably identified was 0.10 mm. The cross-over between the high- and low-resolution images was set at a

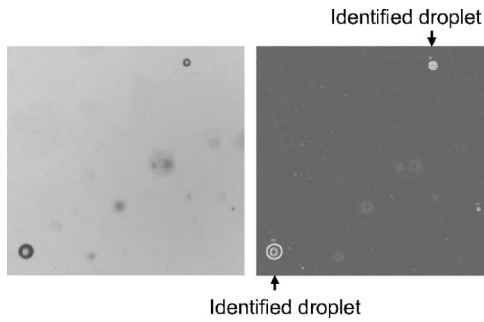


**Fig. 5 Sample of droplet-identification process. Left: Magnified view of typical image. Right: Identified droplets in Sobel-filtered image.**

droplet diameter of 0.18 mm. With these criteria and the analysis procedure described above, a total of  $4.7 \times 10^4$  droplets were identified and measured from the low-resolution images of four separate runs. A total of 380 droplets were measured in the high-resolution images from four distinct runs.

The volumetric fuel concentration was computed from the measured number and size of fuel droplets in the discharge pipe as

$$C(t) \equiv \frac{V_f}{V_t} = \frac{4\pi/3 \sum_{D,LR} (D/2)^3 N(D,t)}{(hA_t)_{LR}} + \frac{4\pi/3 \sum_{D,HR} (D/2)^3 N(D,t)}{(hA_t)_{HR}} \quad (5)$$

where subscripts LR and HR refer to the low-resolution and high-resolution images, respectively.  $V_f$  is the total volume occupied by fuel droplets,  $V_t$  is the total volume of the measurement plane,  $h$  is the image's depth-of-field,  $A$  is the area covered by the image, and  $N(D,t)$  is the measured number of droplets of diameter  $D$ .

**2.2 Depth-of-Field Calibration and Error Analysis.** In order to determine the measurement volume with accuracy, a depth-of-field calibration was conducted to measure the thickness of the measurement plane. The calibration was conducted with a tank and imaging apparatus, shown in Fig. 6, that replicated the optics

and field of view of the three-bay tank. The top and bottom of the tank are of the same material and thickness as the top of the light box and the bottom of the three-bay tank, respectively. The height of the calibration tank and the optical pathlength from the camera to the measurement plane was also identical to the distances in the three-bay tank. A thin glass plate was mounted on a vertical arm and stage (Newport), which allowed precise vertical travel. With the glass plate at the image plane of the camera, oil droplets were injected underneath the plate to serve as calibration targets (Fig. 6). The images, taken with the glass plate at different vertical positions in increments of 0.25 mm, were processed with the same automated droplet identification procedure described previously. The depth of field was measured as the distance between the two planes of critical focus, where out-of-focus droplets were no longer identified by the image analysis procedure. For the low-resolution images, the depth of field was measured to be  $7.3 \pm 0.13$  mm. The depth of field for the high-resolution images was measured to be  $1.0 \pm 0.13$  mm.

The uncertainty in the droplet size measurement arises from the perspective error across the thickness of the measurement volume, the pixelation of the droplet, and optical distortion. The error caused by the focal depth is the depth of field divided by the working distance. For the low-resolution images, the depth of field was 7.3 mm and the working distance was 0.81 m. Therefore, the perspective error was 1% of the droplet diameter. The perspective error of the high-resolution images is also 1%. The uncertainty due to pixelation of the droplet is estimated at one pixel. The error due to optical distortion is estimated to be 1% [12]. The largest droplets measured by the low-resolution images were 1.5 mm in diameter, while the largest droplets measured in the high-resolution images were 0.18 mm in diameter. Assuming the uncertainties are independent, the total uncertainty in droplet diameter is estimated to be 0.03 mm for the low-resolution images, and 0.005 mm for the high-resolution images.

The uncertainty in volumetric concentration is

$$U_C^2 = \left(\frac{\partial C}{\partial V_f}\right)^2 U_{V_f}^2 + \left(\frac{\partial C}{\partial V_t}\right)^2 U_{V_t}^2 = \left(\frac{1}{V_t}\right)^2 U_{V_f}^2 + \left(\frac{V_f}{V_t^2}\right)^2 U_{V_t}^2 \quad (6)$$

where  $U_{V_f}$  and  $U_{V_t}$  are the uncertainties in the volume of fuel droplets, and the total volume of the measurement plane, respectively. The uncertainty in  $V_t$  is in turn

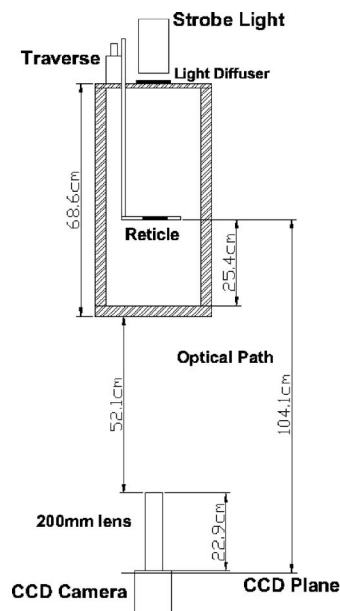


**Fig. 6 Depth-of-field calibration apparatus and sample image**

$$U_{V_t}^2 = \left( \frac{\partial V_t}{\partial h} \right)^2 U_h^2 = A_i^2 U_h^2 \quad (7)$$

where  $A_i$  is the cross-sectional area of the image, and  $U_h$  is the uncertainty in the depth of field. The uncertainty in the total measurement volume is

$$U_{V_t}^2 = \left( \frac{\partial V_t}{\partial D} \right)^2 U_D^2 + \left( \frac{\partial V_t}{\partial N} \right)^2 U_N^2 = \left( \sum \frac{1}{2} \pi N D^2 \right)^2 U_D^2 + \left( \sum \frac{1}{6} \pi D^3 \right)^2 U_N^2 \quad (8)$$

where  $U_D$  is the uncertainty in the droplet diameter and  $U_N$  is the uncertainty in the droplet count for each bin of the size histogram. Equations (6)–(8) hold for both low-resolution and high-resolution images. The uncertainty in droplet diameter is 0.03 mm and 0.005 mm for low-resolution and high-resolution images, respectively, and the uncertainty in the depth of field is 0.13 mm. Estimating that 95% of all droplets are identified and counted, the total uncertainty in measured fuel concentration is  $7.8 \times 10^{-6}$ , or 10% of the peak concentration.

### 3 Experimental Results

**3.1 Flow Visualization.** The basic mechanisms of fuel-water mixing, droplet formation, and droplet transport to the exit pipe are seen from flow visualizations of the refueling tests. The flow visualizations can be correlated with quantitative measurements of droplet distribution and fuel concentration in the exit pipe. Figures 3 and 4 show a sequence of digital video images taken from the side of the tank during a refueling experiment. The images span the time from the beginning of refueling to the onset of bulk fuel discharge. Ballast water initially filling the tank is clear, while the diesel fuel that is pumped in appears dark. The experiment begins with fuel being pumped through the inlet pipe into the top of Bay 1 (the rightmost bay in the image). Fuel fills the top of Bay 1 and displaces water into Bay 2. The fuel/water interface in Bay 1 is statically stable, and does not generate any visible droplets. Water displaced by the entering fuel flows right-to-left through the manholes in the partitions between the bays and is discharged from the exit pipe at the bottom of Bay 3 (the left-most bay in the image).

Fuel begins to be displaced from the Bay 1 into the Bay 2 at  $t \approx 35$  s. As the fuel passes through the manhole dividing the two bays, it rises under the effect of buoyancy, creating a fuel plume. The plume is turbulent and interacts with the fuel/water interface to produce numerous droplets and a fuel/water emulsion layer in the second bay. The plume in Bay 2 ends at  $t \approx 70$  s as the fuel levels in Bay 1 and Bay 2 equalize. At the same time, a new plume forms in Bay 3 as fuel spills through the manhole from Bay 2. This second, and final, plume ends at  $t \approx 105$  s. The test ends with bulk fuel discharge, when the fuel in the third bay is drawn directly into the outlet pipe. This occurs at  $t = 137$  s, when vortices form at the exit pipe and draw fuel directly into the effluent.

The time-varying fuel concentration, incorporating data from four low-resolution and four high-resolution refueling tests, is shown in Fig. 7. The concentration in the exit pipe is nearly zero for the first 35 s, as only water is displaced by the entering fuel. At  $t \approx 35$  s, when the first plume forms, a brief jump in fuel concentration is seen. The likely cause for this is that the plume forming in Bay 2 causes a pressure disturbance which dislodges residual fuel droplets coating the inside surfaces of the tank. Notice that a similar brief spike occurs near  $t \approx 0$ , when the flow is initiated. Apart from the two brief disturbances, the fuel concentration in the discharged water is nearly zero until  $t \approx 60$  s. Around then, droplets formed by the plume in Bay 1 begin to reach the exit pipe in Bay 3. At  $t \approx 70$ , a second plume forms in Bay 2, at nearly the same time that fuel droplets generated by the first plume begin to arrive at the exit pipe. The second plume, which is much closer to the exit pipe in the third bay, ultimately contributes

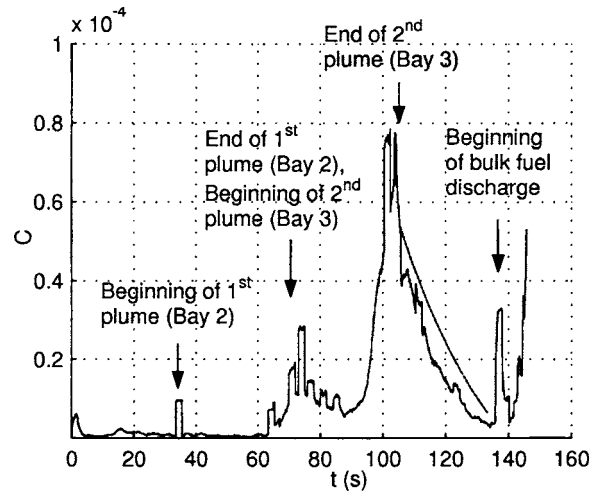


**Fig. 7 Volumetric fuel concentration in discharge from experimental tank during refueling. Exponential decay  $C(t) \propto e^{-0.03 \text{ s}^{-1}(t-105 \text{ s})}$  shown in dashed line for comparison.**

more to the overall discharged fuel concentration than the first plume. However, in the time interval  $80 \text{ s} \leq t \leq 90 \text{ s}$ , the discharged fuel concentration temporarily decreases because the majority of droplets from the first plume have already been discharged (peak around  $t = 75$  s) and the droplets from the second plume have not yet reached the exit pipe, which is located at the bottom of the other end of Bay 3.

The second plume contributes to the overall discharged fuel concentration beginning around  $t = 90$  s, reaching a peak around  $t \approx 105$  s. The fuel concentration in the effluent decays exponentially after the plumes end and production of new droplets has presumably stopped. For the decay rate, an exponential of the form  $C(t) \propto e^{-0.03 \text{ s}^{-1}(t-t_0)}$ , is shown in Fig. 7, with  $t_0 = 105$  s. The decay rate is consistent with the rate  $\dot{Q}/V$  predicted for dilution of a tank, where the remaining water volume in Bay 3 at  $t = t_0$  is used for  $V$ . More specifically, from the flow visualizations, the remaining water volume in Bay 3 at  $t_0 = 105$  s is approximately half of the total volume of the bay, or  $1/2 \times 28 \text{ cm} \times 56 \text{ cm} \times 76 \text{ cm} = 6.0 \times 10^4 \text{ cm}^3$ . Thus, the predicted dilution rate, using  $\dot{Q} = 1.48 \text{ l/s} = 1480 \text{ cm}^3/\text{s}$  and  $V = 6.0 \times 10^4 \text{ cm}^3$ , is  $\dot{Q}/V = 0.025 \text{ s}^{-1}$ , which compares well with the fitted value of  $0.03 \text{ s}^{-1}$  shown in Fig. 7.

The correlation between the measured fuel concentration at the exit and the presence the fuel plumes in the tank suggests that the greatest contribution to the discharged fuel concentration comes from the plumes rather than the horizontal, stably fuel layer that is also present in the tank. The fuel concentration of the effluent water rises, with some time lag, as the plumes form, and drops sharply when the plumes diminish in strength. The proximity of the buoyant jet to the outlet pipe also influences the fuel concentration in the discharged water. Higher fuel concentrations are seen in the effluent when the buoyant jet occurs the same bay as the exit pipe. In other words, although the plumes in Bay 2 and Bay 3 are comparable in strength and thus are expected to have the same production of droplets, they have different contributions to the discharged fuel concentration. This suggests that the advection of droplets is important to the fuel concentration of the effluent water discharged during refueling. The size distribution of the discharged fuel droplets also depends on the transport process, as will be seen in the next section.

**3.2 Distribution of Droplets.** The size of each fuel droplet discharged through the effluent pipe during refueling is measured from the image data, as described in Sec. 2. Figure 8 shows the

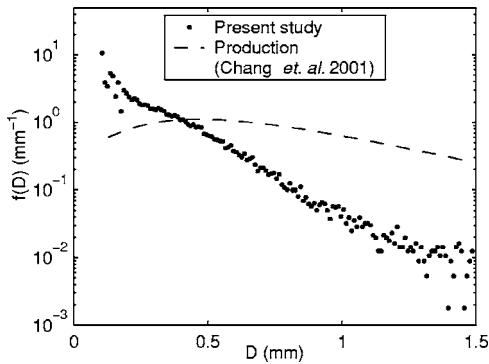


**Fig. 8 Measured distribution of droplet sizes for fuel droplets discharged from tank. Log-normal production distribution (for droplets in generation zone) shown for comparison.**

measured probability distribution,  $f(D)$ , of droplet diameter,  $D$ . The size distribution of fuel droplets is computed by averaging the size histograms for eight separate refueling tests, and normalizing the averaged histogram so that the definite integral is the probability that the droplet diameter lies between the limits of integration

$$\Pr\{D_1 \leq D < D_2\} = \int_{D_1}^{D_2} f(D)dD = F(D_2) - F(D_1) \quad (9)$$

The cumulative distribution,  $F(D_i)$ , in the above expression thus represents the probability that  $D \leq D_i$ . As seen in Fig. 8, the probability distribution of size is strongly biased toward small droplets. Droplets of diameter  $D=0.2$  mm are two orders of magnitude more likely to be found in the effluent water than droplets of diameter  $D=1$  mm. The distribution increases up to the finest resolved scale (0.1 mm) of this experiment. An explanation for this observation will be discussed in Sec. 3.3.

The bias towards small fuel droplet diameter reaching the exit pipe is also apparent in the cumulative distribution shown in Fig. 9. The cumulative distribution,  $F(D)$ , defined as

$$F(D) = \int_0^D f(D)dD \quad (10)$$

represents the proportion of droplets with diameter less than  $D$ . The vast majority of the fuel droplets are small; 90% of the droplets in the discharged water are less than 0.58 mm in diameter, and 99% are less than 1 mm in diameter.

The monotonically decreasing size distribution in the effluent pipe contrasts with previously measured production distributions close to the droplet generation zone. In two similar experiments

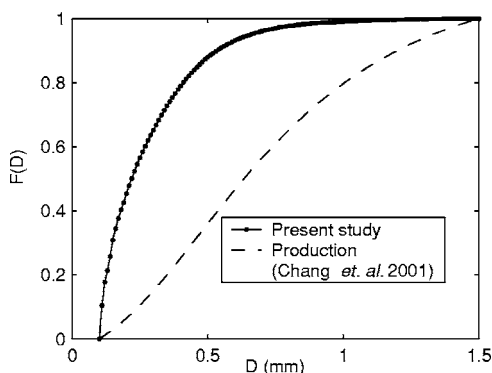


**Fig. 9 Cumulative size distribution of fuel droplets discharged from the fuel tank, compared to cumulative distribution for droplets in generation zone**

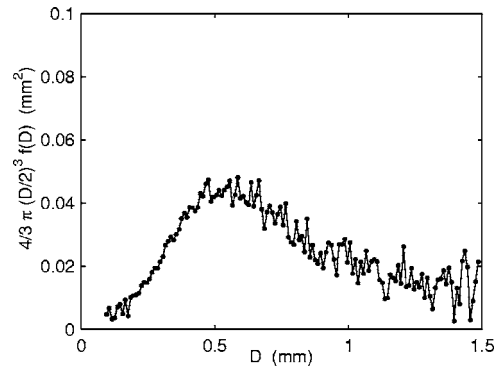


**Fig. 10 Contribution of droplets of varying size to the fuel concentration of effluent water**

by Friedman et al. [3] and Chang et al. [5], log-normal size distributions were reported for fuel droplets generated by impingement on an immiscible fuel/water interface. In particular, the experiments of Chang et al. [5] match the Richardson number and Reynolds number of the present experiment. Using a similar silhouette photography technique, Chang et al. [5] made measurements of the production size distribution close to the fuel plumes in a half-scale, two-bay model of a portion of a compensated fuel/ballast tank. They reported a log-normal distribution of droplet sizes in the generation zone, i.e.

$$f_{\text{gen}}(D) = \frac{1}{D\sigma(2\pi)^{1/2}} \exp\left\{-\frac{1}{2\sigma^2}[\ln(D) - \ln(\mu)]^2\right\} \quad (11)$$

where  $\mu$  and  $\sigma$  are the mean droplet diameter and standard deviation, respectively. Chang et al. [5] found the production distribution to be well characterized by a log-normal distribution with  $\mu=0.8$  mm and  $\sigma=0.5$  mm (Fig. 8) for the same Reynolds numbers and Froude numbers as those of the current experiment. As seen in Fig. 8, the size distribution of fuel droplets discharged from the three-bay model in this study is significantly different from the reported size distribution near the generation zone, although the production distribution is presumably the same. This difference in size distribution again suggests that the advective transport process plays an important role in determining the characteristics of the droplets that are carried to the exit pipe. A model for the transport of buoyant droplets which seeks to explain this difference will be discussed in Sec. 3.3.

Although the small droplets occur with the greatest probability, their contribution to the overall fuel concentration in the effluent water is relatively small. Figure 10 shows the relative importance of droplets of differing sizes to the total volume of fuel discharged. The most important fuel droplets in terms of the overall fuel concentration in the effluent water are between 0.3 and 1 mm in diameter. Droplets less than 0.3 mm in diameter, although they occur in large numbers, make only a minimal contribution to the fuel concentration.

As each bay of the tank is filled, and the buoyant flow events move progressively closer to the exit pipe, the size distribution of discharged droplets changes with the decreasing advection time. A shorter advection time should enable larger droplets, which would otherwise rise out of the flow and merge with the stable fuel layer at the top tank, to reach the exit pipe. Thus, one would expect to find progressively larger fuel droplets in the discharged effluent as the filling process continues. Evidence for this may be seen in Fig. 11, which shows the size distribution of discharged fuel droplets over two 35 s time intervals. During the first time interval, 35 s  $< t < 70$  s, the droplets are generated by a plume in Bay 2 (the middle bay), while the droplets of the second time interval, 70 s  $< t < 105$  s, are generated by a plume in Bay 3 (the final bay). The measured size distribution indeed shows a higher probability of finding large droplets for the later time interval as compared to the



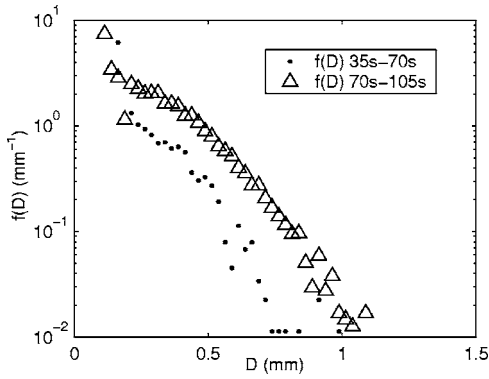


Fig. 11 Increasing droplet size in discharge water over time

earlier interval. The mean droplet diameters for  $35 \text{ s} < t < 70 \text{ s}$  and  $70 \text{ s} < t < 105 \text{ s}$  are 0.31 mm and 0.38 mm, respectively. One can appreciate, at least qualitatively, that as the generation zone moves closer to the tank exit, the advection time for droplets generated by the jet decreases and there is a greater likelihood that larger, more-buoyant fuel droplets will be discharged. The roles of buoyancy and advective transport in determining the characteristics of the discharged fuel droplets are discussed further in the following section.

**3.3 Influence of Transport on Discharged Droplets.** The difference in fuel-droplet size distribution between the exit pipe and the generation zone (near the fuel plumes) suggests that the advective-transport process plays an important role in determining the characteristics of the fuel droplets that are eventually discharged. Advection of immiscible droplets toward the outlet by the mean flow competes with buoyancy which causes large fuel droplets to rise and merge with the statically stable fuel layer. One may define two characteristic times associated with the buoyant droplets:  $\tau_\nu$ , the momentum (viscous) relaxation time, and  $\tau_b$ , the buoyancy time required for a droplet to rise and merge with the stable fuel layer (e.g., Ref. [13]). The relaxation and buoyant times for droplets of various diameters can be compared to  $\tau_a$ , the time required for a droplet traveling at the mean-flow speed to advect from the generation zone to the outlet. The ratios of  $\tau_\nu$  and  $\tau_b$  to  $\tau_a$  reflect the relative influence of drag and buoyancy on the droplets that are ultimately discharged.

An estimate of the mean flow speeds inside the tank is made by noting that fuel droplets reach the exit pipe two bay lengths away from the first fuel plume in approximately 40 s (Fig. 7). Based on the advection time and distance, an empirical estimate can be made of the flow speed. With this mean flow speed and the measured diameter of fuel droplets in the model fuel/ballast tank, the Reynolds number  $\text{Re} \equiv UD/\nu$  of the droplets is of order 1–10. For a clean (uncontaminated by surfactants) and spherical droplet at low Reynolds numbers, the drag would be

$$F_{\text{drag,droplet}} = 4\pi\mu U(D/2) \left( \frac{\mu + \frac{3}{2}\mu_f}{\mu + \mu_f} \right) \quad (12)$$

where  $D$  is the diameter,  $U$  is the relative speed,  $\mu_f$  is the viscosity of the fluid in the droplet, and  $\mu$  is the viscosity of the fluid outside [9,14]. If even slight impurities are present in the fluids, however, surface-tension gradients in the skin of the droplets inhibit the flow in the droplet. The drag of the contaminated droplet is higher than that of the clean droplet and approaches the drag of a solid sphere [10,15]. White [16] suggests the following curve-fit formula for laminar-flow drag about a solid sphere

$$F_{\text{drag,sphere}} = \frac{1}{8}\pi\rho U^2 D^2 \left( \frac{24}{\text{Re}} + \frac{6}{1 + \text{Re}^{1/2}} + 0.4 \right) \quad (13)$$

which fits experimental data to within 10% for  $0 < \text{Re} < 2 \times 10^5$ . Because the full-scale case of refueling the compensated fuel/ballast tank in a Navy vessel is certainly contaminated by surfactants, no special effort was made to avoid surfactant contamination in the experiment. Thus, Eq. (13) is used to estimate the drag of fuel droplets in the model tank.

In the absence of gravity, the equation of motion for the droplet,  $m dU/dt = F_{\text{drag}}$ , may be written using  $m = 4/3\rho_f\pi(D/2)^3$  as

$$\frac{dU}{dt} = \frac{U}{\tau_\nu} \quad (14)$$

where the momentum relaxation time,  $\tau_\nu$ , is defined as

$$\tau_\nu(D) \equiv \frac{\frac{4\pi}{3}\rho_f(D/2)^3 U}{F_{\text{drag}}} \quad (15)$$

where  $\rho_f$  is the density of the fuel inside the droplet and Eq. (13) is used for the drag of the droplet. The momentum relaxation time is the characteristic time required for the droplet to reach equilibrium, or “catch-up,” with the mean flow. The relaxation time for 1-mm-diameter fuel droplets is 0.016 s, and decreases rapidly (approximately as the square of diameter) for smaller droplets.

In comparison, the advection times are much larger. An estimate of the advection time can be made by noting the lag time between the formation of the fuel plume and the arrival of fuel droplets at the exit pipe. For the first plume, the time interval from the beginning of the fuel plume to the peak of the fuel concentration in the discharge is  $\tau_{a,\text{far}} \approx 40 \text{ s}$  (Fig. 7). For the second plume,  $\tau_{a,\text{near}} \approx 30 \text{ s}$ . In either case, the fuel droplets relax to the mean flow velocity nearly instantaneously relative to the time it takes them to be advected to the discharge pipe, i.e.,  $\tau_\nu/\tau_a \ll 1$  for the fuel droplets generated in the tank. Thus, the fuel droplets can be assumed to be moving with the flow, with the exception of buoyancy-induced rising, and possible effects of turbulent velocity fluctuations.

The buoyancy time,  $\tau_b$ , is the characteristic time for a droplet to rise and merge with the stable fuel layer at the top of the tank. Equating the net buoyancy force to the drag (Eq. (13)), the terminal speed,  $U_t$ , of a spherical droplet moving freely under gravity at small Reynolds number can be found implicitly from

$$F_{\text{drag}}(U_t) = \frac{1}{8}\pi\rho U_t^2 D^2 \left( \frac{24}{\text{Re}} + \frac{6}{1 + \text{Re}^{1/2}} + 0.4 \right) = \frac{4}{3}\pi \left( \frac{D}{2} \right)^3 (\rho - \rho_f)g \quad (16)$$

where  $\text{Re} = U_t D/\nu$ . Taking the depth of the manhole top in the fuel tank,  $H_0$ , to be the characteristic length, the buoyancy time of a droplet of diameter  $D$  is defined as

$$\tau_b(D) \equiv \frac{H_0}{U_t} \quad (17)$$

The buoyancy time may be viewed as an order-of-magnitude estimate for the time required for a fuel droplet to rise out of the flow.

The buoyancy time, which is  $\tau_b \approx 9.4 \text{ s}$  for 1-mm-diameter droplets and  $\tau_b \approx 350 \text{ s}$  for 0.1-mm-diameter droplets, rapidly increases for smaller droplets. Table 1 summarizes the characteristic times  $\tau_a$  and  $\tau_b$  for droplets of various sizes for the flow conditions of this experiment. As seen in the table, smaller fuel droplets tend to remain longer in the flow, while larger droplets have a tendency to rise quickly to the top of the tank. A key parameter in determining whether a droplet of a given size is likely to be discharged is the buoyancy time relative to the advection time,  $\tau_b/\tau_a$

**Table 1 Characteristic Reynolds numbers and time scales for fuel droplets of varying diameter  $D$**

$D$ (mm)	Re	$\tau_r(D)$ (s)	$\tau_b(D)$ (s)	$\tau_{a,\text{far}}$ (s)	$\tau_{a,\text{near}}$ (s)
0.10	3.8	0.00034	350	$\approx 40$	$\approx 30$
0.20	7.6	0.0011	95	$\approx 40$	$\approx 30$
0.50	19	0.0053	22	$\approx 40$	$\approx 30$
1.00	38	0.016	9.4	$\approx 40$	$\approx 30$

(cf. Stokes number). For an advection distance  $L$ , one can estimate a critical diameter,  $D^*$ , such that the fuel droplets have a buoyancy time equal to the advection time, i.e.

$$D^* \equiv D \Big|_{\tau_b = \tau_a} \quad (18)$$

For the advection time from the first plume, the critical diameter  $D^* \approx 0.33$  mm. For the second plume, which occurs closer to the outlet, the critical diameter is larger,  $D^* \approx 0.40$  mm.

The critical diameter may be viewed as an order-of-magnitude estimate of the diameter for which fuel droplets of diameter  $D \gg D^*$  are unlikely to be discharged. The critical diameter decreases with longer advection distances, as droplets have more time to rise to the top of the tank. The transport process, in which advection competes with buoyancy, in effect selects smaller droplets generated by the buoyant jets to be transported to the outlet and discharged. Experimental evidence for this is seen from the measured cumulative distribution (Fig. 9), in which approximately 80% of the discharged fuel droplets are less than  $D^* \approx 0.40$  mm in diameter. In fact, the predicted reduction in critical diameter from 0.40 to 0.33 mm agrees reasonably well with the measured reduction in mean droplet diameter from over the course of the refueling experiment from 0.38 to 0.31 mm.

It should be noted that turbulence within the tank can also influence the effective buoyancy times. For example, Friedman and Katz report that for high turbulence levels, where the root-mean-square (RMS) fluctuations were on the order of 10 cm/s and exceeded the terminal speed in quiescent flow, the mean droplet rise speed in isotropic turbulence can vary significantly from the rise speed in quiescent flow [17]. The difference in rise speeds between large and small droplets decreases at high turbulence levels. However, the qualitative behavior is consistent: smaller droplets still rise more slowly than larger droplets. As will be discussed later, the effect of turbulence in the flow can be incorporated into a model of droplet-size selection.

The size distribution of droplets at the outlet may be expected to depend on the distribution of the droplets generated by the buoyant flow events, and the advective and buoyancy time scales, i.e.,  $f(D) = \Phi(f_{\text{gen}}, t_a, t_b(D))$ . From dimensional considerations, it is reasonable to suppose that the distribution of droplets discharged from the tank depends on the ratio of advective and buoyancy time scales

$$\frac{f(D)}{f_{\text{gen}}(D)} \propto g\left(\frac{\tau_b(D)}{\tau_a}\right) \quad (19)$$

where  $\tau_a$  is either 30 s or 40 s, depending on whether the plume is in the middle or final bay. The undetermined function  $g$  represents the probability that a droplet of radius  $a$ , generated some distance from the exit of the tank, will be discharged. It should have several properties: the behavior of  $g$  should reflect the experimental observation that smaller droplets are more likely to be discharged, i.e.,  $g(D)$  should be monotonically decreasing with droplet radius,  $a$ . Also,  $g$  should incorporate the observation that larger droplets are discharged when the generation zone moves closer to the tank exit, i.e.,  $g(D)$  should broaden as the generation zone moves closer to the outlet.

One possible form for  $g$  is

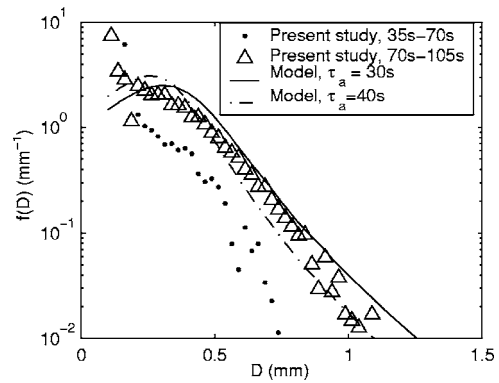


**Fig. 12 Comparison of modeled and measured size distribution of discharged droplets for differing distances from generation zone to tank exit**

$$g(D) = \frac{1}{1 + (c_1 \tau_a / \tau_b(D))^{2N}} \quad (20)$$

where  $c_1$  and  $N$  are constants. Although not the only possible functional form for  $g$ , Eq. (20) satisfies the constraint that  $g$  pass small spatial sizes. The form of  $g$  in Eq. (20) also satisfies the experimental observation that larger droplets are discharged as the distance from the generation zone to the outlet increases, i.e., as  $\tau_a$  increases. A possible formulation for the size distribution of droplets at the exit is then given by

$$f(D) \propto f_{\text{gen}}(D)g(D) = f_{\text{gen}}(D) \frac{1}{1 + (c_1 \tau_a / \tau_b(D))^{2N}} \quad (21)$$

where  $\tau_a$  depends on the distance from the buoyant jet to the outlet,  $f_{\text{gen}}$  is the size distribution of generated droplets, and  $c_1$  and  $N$  are constants which may depend on the precise geometry of the tank, and the turbulence levels in the tank.

The experiments of Friedman and Katz indicate that the effective rise velocity of fuel droplets can increase with decreasing droplet size at high turbulence levels, which could reduce the bias toward small droplets. This may be accommodated by allowing the parameters  $c_1$  and  $N$  to vary with droplet size. In the present experiments, measurements were not made of the turbulent fluctuations of the flow inside the tank. Thus, we make use of the lowest-order approximation that  $c_1$  and  $N$  are constants.

Figure 12 shows the modeled and measured distributions of fuel droplets at the exit pipe of the tank for two different advection times  $\tau_a$ . The advection time  $\tau_a = 40$  s represents the case when the generation zone (the fuel plume) is in the middle bay, while  $\tau_a = 30$  s represents the case when the plume is in the final bay. The modeled distribution uses fitted parameters of  $N=2$  and  $c_1=0.8$ . A log-normal distribution is used for the size distribution,  $f_{\text{gen}}(D)$ , of fuel droplets in the generation zone, as reported by several investigators, including Friedman et al. and Chang et al. [3,5]. The values chosen for mean diameter and standard deviation in  $f_{\text{gen}}(D)$  are those reported by Chang et al., whose experimental flow conditions matched those of the present experiment. Although not a perfect fit, the model for  $f(D)$  shown Fig. 12 characterizes the size distribution of discharged droplets better than the lognormal (production) model. Moreover, Eq. (21) modeling the discharge size distribution has the qualitatively correct behavior that larger droplets are discharged as the advection time decreases (i.e., as the plume moves from the middle bay to the final bay).

The function  $g$  in Eq. (20) has the form of an  $N$ th-order Butterworth filter

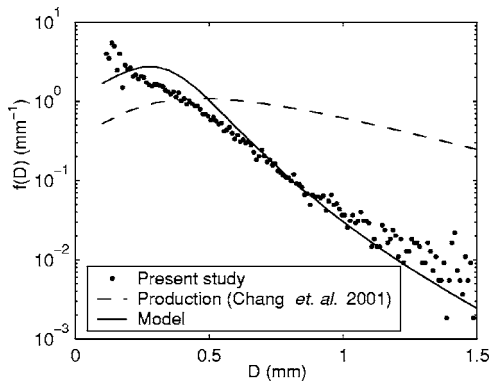


**Fig. 13 Comparison of modeled and measured size distribution of discharged droplets. The log-normal distribution of droplets in the generation zone (close to the fuel plume) is shown with a dotted line.**

$$g = \frac{1}{1 + (\Omega/\Omega_c)^{2N}} \quad (22)$$

with frequency

$$\Omega = 1/\tau_b \quad (23)$$

and cutoff frequency,  $\Omega_c$

$$\Omega_c = 1/c_1 \tau_a \quad (24)$$

Viewed in this light, the transport process (specifically, the competition between advection and buoyancy) acts as a filter which passes small fuel droplets while blocking larger ones.

The droplets that are discharged over the entire experiment include droplets that are generated by two plumes, one occurring in the middle bay (Bay 2) and another in the final bay (Bay 3). Both plumes are similar, and the characteristics of the fuel droplets generated by each buoyant jet can also be expected to be similar (Fig. 3). However, the characteristic advection times  $\tau_a$  from the generation zone to the outlet pipe are different between the two plumes. Larger droplets are more likely to be discharged when the plume closer to the exit pipe and the advection time is shorter. To account for this, the size distribution of fuel droplets for the entire test is modeled by summing the two modeled size distribution for  $\tau_{a,near}=30$  s and  $\tau_{a,far}=40$  s, i.e.

$$f(D) \propto f_{gen}(D)[g_{near}(D) + g_{far}(D)] \propto f_{gen}(D) \times \left[ \frac{1}{1 + (c_1 \tau_{a,near}/\tau_b(D))^{2N}} + \frac{1}{1 + (c_1 \tau_{a,far}/\tau_b(D))^{2N}} \right] \quad (25)$$

As before, a lognormal distribution, with the experimental parameters reported by Chang et al. [5], is used for  $f_{gen}$ , the size distribution of droplets generated by the plumes.

Figure 13 shows the modeled size distribution of the fuel droplets discharged over duration of the test. The modeled size distribution is compared with the measured size distribution. Also shown is the log-normal distribution of droplet sizes reported by Chang et al. for the generation zone, i.e., in the vicinity of the fuel plumes [5]. As seen from the figure, the model for  $f(D)$  of Eq. (25), which incorporates the effects of buoyancy and advection, fits the experimental size distribution of droplets significantly better than the generation-zone distribution  $f_{gen}(D)$ .

The cumulative distribution,  $F(D_i)$ , representing the probability that  $D \leq D_i$ , is computed from the modeled distribution in Eq. (26) and shown in Fig. 14. Also shown for comparison are the cumulative size distribution measured in the present experiment, and the cumulative size distribution reported by Chang et al. for the generation zone [5]. The cumulative distribution computed from

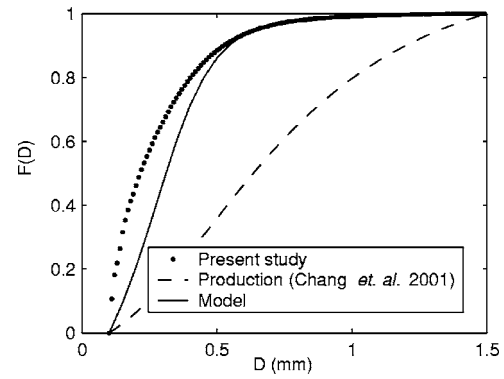


**Fig. 14 Comparison of modeled and measured cumulative size distribution of discharged droplets. The log-normal distribution of droplets in the generation zone (close to the buoyant jet) is shown with a dotted line.**

the model of Eq. (20) matches the measured cumulative distribution reasonably well. The fit to the data is again better than the cumulative distribution associated with the log-normal distribution of fuel droplet sizes reported for the generation zone. The transport process, modeled by the function  $g(D)$  (Eq. (20)), acts to reduce the number of large-diameter droplets that reach the tank outlet.

In both the size distribution and the cumulative distribution, a difference is seen between the modeled and the measured distributions for very small droplets. The model predicts a peak in the size distribution at  $D \approx 0.3$  mm, and a decrease in the number of droplets below that size. However, the number of small droplets is found experimentally to increase nearly monotonically with decreasing droplet size. A possible explanation for this difference is based on the earlier observations of Chang et al. that larger “droplets” can break into smaller ones [5]. Figure 15 shows a close-up of the generation zone (in the vicinity of the plume). Within that generation zone, one can see droplets of fuel, as well as droplets of water enclosed in a skin of oil. The latter are seen to break as their skins thin over time (Fig. 15). Thus, in the time it takes for the oil-skin balloons to be advected to the tank exit, they can break to form small fuel droplets. The opposite situation, of oil droplets merging to form larger droplets, happens with much less frequency due to the very low fuel concentrations (less than  $10^{-4}$  by volume) of the experiments. Thus, a possible explanation for the relative abundance of small droplets in the effluent is that oil-skin balloons generated by the plumes are converted to much smaller oil droplets during the advection process to the tank exit.

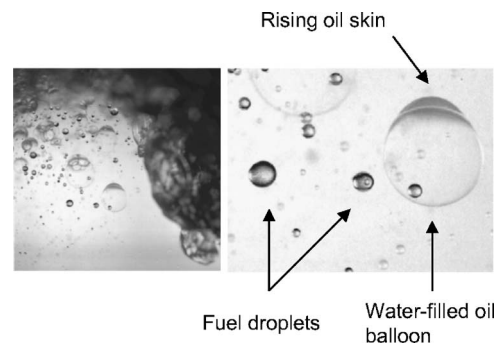


**Fig. 15 Left: View of droplet generation zone (in the vicinity of the fuel plume). Right: Close-up of fuel droplets and oil-skin balloons formed by plume (adapted from Chang et al. (see Ref. [5])).**

## 4 Conclusions

Oil droplets discharged during refueling of a model of a portion of a compensated fuel/ballast tank have been characterized and related to buoyant flow events within the tank. In particular, the fuel concentration of overboard discharge is shown to be correlated to the formation of fuel plumes within the tank. The volumetric fuel concentration in discharge from the tank is minimal before the development of the plumes, increases as each jet forms, and declines as the plumes ends. The size distribution of fuel droplets in the effluent water is different from the distribution of droplets within the tank near the generation zone (in the vicinity of the plumes). The size distribution of discharged fuel droplets is strongly biased toward small droplets, and is monotonically decreasing with droplet diameter, over the resolved size range.

Buoyancy, which tends to cause fuel droplets to rise and separate out of the water layer, is shown to be an important factor in determining the characteristics of the droplets that are discharged. The characteristic buoyancy time,  $\tau_b$ , relative to the characteristic advection time,  $\tau_a$ , is found to be a key parameter in predicting the fate of fuel droplets. A function is introduced which relates the size distribution of droplets in the generation zone to the size distribution in the effluent. This function models the effect of the transport process as a low-pass filter in the parameter  $\tau_a/\tau_b$ . Small droplets, for which  $\tau_a < \tau_b$ , are easily transported to the tank exit, while large droplets, for which  $\tau_a > \tau_b$ , are less likely to be discharged. The model is shown to fit the measured size distribution of discharged fuel droplets reasonably well, and also accounts for the observed increase in discharged droplet size over time, as the generation zone moves closer to the exit.

## Acknowledgment

The authors wish to thank Larry Tomlinson, Thomas O'Connell, John McGinn, and Kevin Burns for their support of these experiments. The authors would also like to thank Si-Wook Kim and William Lee for their help with the droplet-analysis software.

## Nomenclature

$A$	= droplet silhouette area
$A_i$	= total area of image
$A_m$	= manhole area
$C$	= volumetric fuel concentration
$D_p$	= pipe diameter
$D$	= droplet diameter
$D^*$	= critical diameter such that $\tau_b = \tau_b$
$f$	= droplet-size probability distribution at exit
$f_{\text{gen}}$	= droplet-size probability distribution in generation zone
$F$	= cumulative distribution
$F_{\text{drag}}$	= drag force
$g$	= gravitational acceleration
$h$	= depth of measurement volume
$H_0$	= vertical distance from top of manhole to top of tank
$L_p$	= perimeter of droplet
$N$	= measured number of droplets
$\dot{Q}$	= volume flow rate
$R_c$	= compactness ratio
$R_e$	= elongation ratio

$Re$	= Reynolds number
$Ri$	= Richardson number
$U$	= uncertainty
$U_p$	= mean pipe-exit speed
$U_m$	= mean flow speed in manhole
$U_t$	= terminal speed of buoyant spherical droplet
$V_f$	= total volume of fuel droplets
$V_t$	= total volume of measurement "plane"
$W_m$	= manhole width
$\delta_j$	= jet thickness at manhole
$\rho$	= water density
$\rho_f$	= fuel density
$\mu$	= viscosity
$\sigma$	= standard deviation
$\tau_a$	= advection time
$\tau_b$	= buoyancy time
$\tau_v$	= momentum relaxation time
$\nu_f$	= kinematic viscosity of fuel
$\Omega$	= frequency
$\Omega_c$	= cutoff frequency

## References

- [1] Sathyagal, A. N., Ramkrishna, D., and Narsimhan, G., 1996, "Droplet Breakage in Stirred Dispersions. Breakage Functions From Experimental Drop-Size Distributions," *Chem. Eng. Sci.*, **51**, pp. 1377–1391.
- [2] Friedman, P. D., and Katz, J., 1999, "The Flow and Mixing Mechanisms Caused by the Impingement of an Immiscible Interface With a Vertical Jet," *Phys. Fluids*, **11**, pp. 2598–2606.
- [3] Friedman, P. D., Winthrop, A. L., and Katz, J., 2001, "Droplet Formation and Size Distributions From an Immiscible Interface Impinged With a Vertical Negatively Buoyant Jet," *Atomization Sprays* **11**, pp. 269–290.
- [4] Wu, X., and Katz, J., 1999, "On the Flow Structures and Mixing Phenomenon in a Fuel/Water Stratified Shear Flow," *Proc. ASME/JSME Joint Fluids Engineering Conference*, San Diego, CA, July 18–23.
- [5] Chang, P. A., Atsavaprane, P., McGinn, J., and Hwang, W., 2001, "Buoyant Flow Event Experiments in a Half-Scale, Two-Bay Model of a Compensated Fuel/Ballast Tank," Hydro. Dir. Tech. Report NSWCCD-50-TR-2001/032, Nav. Surf. War. Cnt., Carderock Div., May.
- [6] Atsavaprane, P., Verosto, S., and Shan, J. W., 2003, "Experimental Techniques to Determine Oil-in-Water Concentrations During Compensated Fuel Ballast Refueling Tests," *Proc. ASME/SNAME Marine Env. Eng. Tech. Symp (MEETS)*.
- [7] Chen, C. J., and Rodi, W., 1980, *Vertical Turbulent Buoyant Jets*, Pergamon Press, Oxford.
- [8] Dimotakis, P. E., 2000, "The Mixing Transition in Turbulence," *J. Fluid Mech.*, **409**, pp. 69–98.
- [9] Batchelor, G. K., 1967, *An Introduction to Fluid Dynamics*, Cambridge University Press, Cambridge.
- [10] Clift, R., Grace, J. R., and Weber, M. E., 1978, *Bubbles, Drops, and Particles*, Academic Press, New York.
- [11] Kulenovic, R., Mertz, R., and Groll, M., 2002, "High Speed Flow Visualization of Pool Boiling From Structured Tubular Heat Transfer Surfaces," *Exp. Therm. Fluid Sci.*, **25**, pp. 547–555.
- [12] Atsavaprane, P., Chang, P. A., Wilson, W., and Verosto, S., 2002, "Effluent Fuel Concentration Measurements in a Half-Scale, Three-Bay Compensated Fuel/Ballast Tank," Hydro. Dir. Tech. Report NSWCCD-50-TR-2002/021, Nav. Surf. War. Cnt., Carderock Div., April.
- [13] Martínez-Bazán, C., and Lasheras, J. C., 2001, "Turbulent Dispersion of Bubbles in a Plane, Free Shear Layer," *Exp. Therm. Fluid Sci.*, **25**, pp. 437–445.
- [14] Acheson, D. J., 1990, *Elementary Fluid Dynamics*, Oxford Univ. Press, Oxford.
- [15] Takagi, S., and Matsumoto, Y., 2000, "Contaminant Effect on the Motion of a Rising Bubble," *Proc. ASME Fluids Engineering Division Summer Meeting*, Boston, MA, July 11–15.
- [16] White, F. M., 1991, *Viscous Fluid Flow*, McGraw-Hill, New York.
- [17] Friedman, P. D., and Katz, J., 2001, "Dispersion of Fuel Droplets in Isotropic Turbulence," 4th Int. Conf. Multiphase Flow, New Orleans, LA, May 27–April 1.

# Predictions of Charge Drift in a Concept Electro sprayed DISI Engine

Geraldo C. S. Nhumaió  
e-mail: geraldo.nhumaió@talk21.com

A. Paul Watkins

School of Mechanical, Aerospace  
and Civil Engineering,  
University of Manchester,  
Sackville Street, P.O.Box 88,  
Manchester, M60 1QD, UK

*Limited to nonvaporizing spray cases, this work discusses the transport of charged droplets within a cylinder of a motored axisymmetric model electro sprayed direct injection spark ignition (eDISI) engine with electrified walls. The concept engine investigated here is assumed to operate with an electrostatic atomizer previously studied for application in fuel burners [Yule et al., 1994, Fuel, 74(7), pp. 1094–1103]. A split/multiple injection strategy is employed in which three pulses of 5 mg each are made at crank angles of 80, 150 and 300 deg ATDC of the intake, which fall within the intervals for stable combustion of either early or late injection modes of operation of DISI engines [Jackson et al., 1997, SAE Paper No. 970543]. The direct Simulation Monte Carlo (DSMC) approach embodied in an in-house CFD research code is used to simulate the discrete phase flow with the electrical charge distribution for different instants within the computational cells being computed by simple addition of the droplet charges residing in particular cells at particular instants of time. It is shown in the half engine cycle investigated that the use of charged sprays in eDISI engines may help to reduce the in-cylinder wall-wetting phenomenon. In addition, pockets of highest electrical charge are found to populate the region near the spark plug by 345 deg CA, which may be a path for improved combustion efficiency. [DOI: 10.1115/1.2243299]*

*Keywords: electro sprays, electrohydrodynamics, DISI engines, GDI engines, model engines, engine computer simulations, gasoline split injection, gasoline multiple injection*

## 1 Introduction

**1.1 Electro sprays as a Well-Established Technology.** Electro sprays, or sprays from electrostatic atomizers/nebulizers, are used in a variety of engineering fields, a few of which are nonimpacting (laser and ink-jet) printing, paint, crop and liquid metal spraying, rocket propulsion, meteorological studies/experiments, mass spectrometry, and pollution research. Most often, electrostatic spraying is a field driven process in which low energy consumption atomizers (e.g., Fig. 1) are used to produce equi-sized droplets [1]. Great energy reductions are further achieved with assistance of air/gas blast technology. A desirable objective in electro spraying technology is to utilize electrostatic forces on charged droplets to control trajectories (dispersion, drift, and/or penetration).

The history of electro sprays can be traced back to 1600 when William Gilbert [2] reported experiments on interacting electric fields with liquids. Until the 1960s, considerable research and developments were mostly carried out with use of semi-conducting liquids (liquids with resistivities in the range  $10^4$  to  $10^6 \Omega\text{m}$ , e.g., solvents in electro spray mass spectrometry).

**1.2 Motivation for Hydrocarbon Electro sprays in DISI Engine Technology.** A promising technology for improved management and combustion of hydrocarbon sprays has been proposed over the decades post-1960s due to the growing importance of electrohydrodynamics (EHD) in insulating liquids (liquids having resistivities in the range  $10^{12}$  to  $10^{16} \Omega\text{m}$ ). Charge injection hydrocarbon atomizers (Fig. 1(b)) have been demonstrated to provide sprays at a wide range of flow rates and arbitrary and selectable droplet sizes [3–5]. In [3], a burner using an electrostatic method to produce and control hydrocarbon fuel sprays was in-

vestigated. In [4], a set of differences between the spray characteristics of an actual diesel engine injector and those of an electrostatic atomizer were discussed with considerable advantages placed into the latter injection strategy given the compactness of the atomizer and the capability of this to produce monodispersed droplet size distribution. An air assisted electrostatic atomizer for gas turbine applications was presented in [5] where a unimodal spray distribution with droplet SMD reduced by 50% relative to an ordinary electrostatic atomizer was demonstrated.

The controllability of charged sprays influenced by externally applied electric fields poses another advantage. Presented in Ref. [6] are the experimental and numerical investigations of charged sprays discharging into open atmospheres; this work was extended to accommodate earthed plates near the spray [7], electric sources introduced into the flow domain, and the effects of sibling charge [8]. Latter, a confined flow with electrically passive moving boundaries and circular orifice inlet valve was also discussed [9].

All the results reflected in the aforementioned representative studies are encouraging for an extension within the context of DISI engine cylinders; hence the present work seeks to evaluate the effects of charge on the distribution of spray in order to reduce the DISI engines in-cylinder wall wetting, which has been a problematic issue as far as the future (e.g., 2004–2008) emissions legislations are concerned.

## 2 Mathematical Model

The present study adds the effects of electrostatics into the commonly known equations governing the two-phase flow in reciprocating engines. Hence, space in this paper will be devoted to briefly outline the application of non-relativistic quasi-static approximations of Maxwell's electromagnetic equations as well as the related constitutive equations. The latter equations are idealized models of material behavior [10] but in them lies the key to many and varied means of fluid-electrical field interaction.

Contributed by the Fluids Engineering Division of ASME for publication in the JOURNAL OF FLUIDS ENGINEERING. Manuscript received September 29, 2005; final manuscript received January 31, 2006. Assoc. Editor: Theodore Heindel.

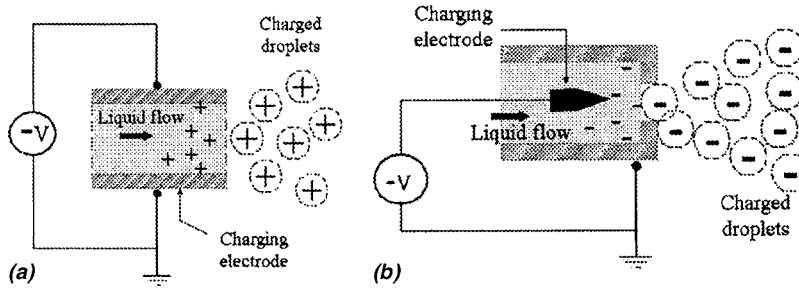


**Fig. 1** Illustration of charge induction (left) and charge injection (right) techniques used for semi-conducting liquids and insulators, respectively. (a) Charge induction technique: used in fluids with resistivities in the range  $10^4$  to  $10^6 \Omega\text{m}$ , e.g. agricultural, coat and paint spraying and xerocopy, laser and ink jet printing. The polarity of charged droplets is opposite to that of the charging field. (b) Charge injection technique: used in fluids with resistivities in the range  $10^{12}$  to  $10^{16} \Omega\text{m}$ , e.g. hydrocarbon fuels. The polarity of charged droplets is the same as that of the charging field. Negative (electron emission) potential is favored over positive potential (field ionization), since it requires field intensities lower by a factor of  $\sim 10$  to inject the same amount of charge [1].

The following three equations are of particular importance in order to couple the electricity and the hydrodynamics:

$$q_s = 2.780 \times 10^{-9} d \quad (1)$$

$$\nabla(\epsilon E) = q_v \quad (2)$$

$$\tau_{ij}^e = \epsilon E_i E_j - \frac{1}{2} \delta_{ij} (1-b) E_k E_k \quad (3)$$

where  $q_s$  denotes the minimum specific charge of a given class of droplets with diameter  $d$  [11–13],  $q_v$  is the cell charge density, which, once the droplet locations are known, is computed by simple addition of the droplet charges residing in particular cells at particular instants of time,  $\epsilon$  is the space permittivity,  $E = -\nabla V$  is the electric field with  $V$  standing for voltage,  $\tau_{ij}^e$  is the Maxwell stress tensor,  $\delta_{ij}$  is the Kronecker delta, and  $b = (\rho/\epsilon)(\partial\epsilon/\partial\rho)\Theta$  is the electrostriction parameter at ambient temperature  $\Theta$ . The coefficient  $2.78 \times 10^{-9}$  of Eq. (1) is the result of the model hypothesis that places a maximum entropy to the Rayleigh maximum specific charge of an individual droplet, which is defined as  $q_s = 6(\epsilon_0 \sigma_T)^{1/2} / \rho_d r^{3/2}$ , where  $\sigma_T$  is the surface tension,  $\epsilon_0$  is the permittivity of vacuum, and  $\rho_d$  is the mass density of droplets with radius  $r$ .

**2.1 Charge Transfer Relation.** The charge transfer equation of form (1) has been preferred in order to minimize the elaborate considerations required when dealing with the general form of the constitutive equation for the electrical current density, which, most often, defines the charge transfer mechanism as a function of ionic drift, charge convection, charge diffusion, and residual conductivity [10].

**2.2 Electric Energy Equation.** When solving for either the liquid or gas phases, one needs the electric forces whose derivation results from the solution of Eq. (2), the electric energy equation. Given the electric field distribution, the liquid phase momentum equation is then defined as

$$\frac{du_d}{dt} = (F_D + S_{\text{grid}}) + F_Q + F_I \quad (4)$$

where  $F_D$ ,  $F_I$ , and  $F_Q$  denote drag, image, and electrostatic forces acting on a spherical droplet and  $S_{\text{grid}}$  is a coordinate induced term, which depends on the coordinate system used. ( $F_D + S_{\text{grid}}$ ) is detailed in [14]. Given the DDM model employed for the discrete phase,  $F_Q$  is taken as the Kelvin force density with polarization dependent on mass density alone and defined by [15]

$$F_Q = q_s E + P \cdot \nabla E \quad (5)$$

where  $P = nq_s d$  is the polarization density with  $n$  standing for drop number density and  $d$  the vector distance.

In the present work  $F_I$  is a negative force when two dielectrics (i.e., space and dielectric walls) are in interaction. As explained in [16], for a point charge  $q$  near a dielectric boundary (Fig. 2), two image charges are required to describe the field and potentials in two dielectrics. One image,  $q'$ , is at the same image position,  $P'$ , as for a conductor. A second image charge  $q''$  is located opposite  $q'$  at location  $P$  and together with the original charge  $q$  in the first dielectric. After some derivations on the basis that the expressions for electric potential in medium 1,  $V_1(x, y, z)$ , and in medium 2,  $V_2(x, y, z)$ , yield the same potential at the boundary  $x=0$ , then Eqs. (6) are obtained.

$$q' = \frac{\epsilon - \epsilon^*}{\epsilon + \epsilon^*} q \quad \text{and} \quad q'' = \frac{2\epsilon^*}{\epsilon + \epsilon^*} q \quad (6)$$

It may be seen that if  $\epsilon < \epsilon^*$ , the image charge  $q'$  is opposite in sign to the original charge,  $q$ , which must therefore be attracted

**Table 1** Typical dielectric constants [17]

Material	Dielectric constant
Vacuum and most gases	1
Insulating oils	2.2
Polystyrene	2.5
Polymethyl methacrylate	3.4
Polyplexiglas	3.4
Porcelain	7
Water	80
Barium titanite	1200

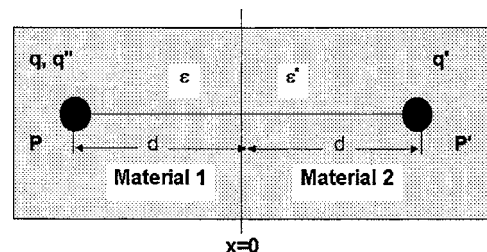


**Fig. 2** Image charges at the interface between two dielectrics [16]

**Table 2 Engine operating conditions**

Engine		Injection system	
Bore	80 mm	Number of holes	1
Stroke	94 mm	Hole diameter	250 $\mu\text{m}$
TDC clearance	37 mm	Mean injection velocity	98 m/s
Compression ratio	4.9	Start of injection	80, 150, and 300 deg ATDC of intake
Speed	2500 rpm		
Piston temperature	370 K	Mass of fuel injected ( $3 \times 5$ mg/pulse)	15 mg
Head surface temperature	360 K	Initial spray cone angle	15 deg
Cylinder liner temperature	360 K	Initial droplet Sauter mean diameter	15 $\mu\text{m}$
		Initial droplet size distribution	Rosin/Rammler

towards the interface as in the case of conducting surface. However, the force of attraction is reduced in the ratio  $(\epsilon - \epsilon^*)/(\epsilon + \epsilon^*)$ . Interestingly, if  $\epsilon > \epsilon^*$ , the charge  $q$  experiences a force repelling it from the interface because the image charge now has the same polarity as  $q$ . The Coulomb's law is then applied to the two image charges  $q'$  and  $q''$ , i.e.,

$$F_I = -\frac{q' \cdot q''}{4\pi\epsilon r^2} \quad (7)$$

where  $r$  is the vector distance between the two charges ( $r=2d$  in Fig. 2) and  $\epsilon$  and  $\epsilon^*$  are the permittivities of media 1 and 2, which are properties that may be ascribed to any substances with the vacuum as the reference dielectric, i.e.,

$$\epsilon = \epsilon_r \epsilon_0 \quad \text{and} \quad \epsilon^* = \epsilon_r^* \epsilon_0 \quad (8)$$

The permittivity of free space  $\epsilon_0$  has the value  $\sim 8.854 \times 10^{-12}$  F/m whereas the relative permittivity  $\epsilon_r$  has the value 2.2 for the present case of insulating oils [17]. As for the dielectric constant  $\epsilon_r^*$ , a value of 2 has been assumed to represent material still to be selected/identified. Some typical values of  $\epsilon_r$  are given in Table 1.

Most gases have dielectric constants close to the vacuum, whereas most liquid and solid insulators are in the range of 2.5 to 8. Conducting liquids can be much higher, with water among the highest of the liquids at 80. Nominal values for solids can be quite high, but, since many solids also display nonlinear material relations, the equivalent linear parameter (dielectric constant) may not be valid in a particular application [17].

**2.3 Maxwell Stress Tensor.** Equation (3) is the electrical part of the Maxwell electromagnetic stress, which leads to three distinct electrical body forces: the coulombic, dielectrophoretic, and electrostrictive forces [11].

Coupling between electricity and the carrier phase is such that the divergence of the stress tensor within the control volume leads to an explicit form of linear momentum balance comprising both viscous and electrical contributions, i.e.,  $\tau_{ij} = \tau_{ij}^e + \tau_{ij}^h$  with  $\tau_{ij}^h = -p\delta_{ij} + \eta(\partial U_i/\partial x_j + \partial U_j/\partial x_i)$ . Substituting this tensor in the momentum conservation equations of the continuum phase one obtains the Navier-Stokes equation that together with the incompressibility<sup>1</sup> conditions gives [11]

$$\rho \frac{DU}{Dt} = -\nabla p^* + \eta \nabla^2 U + q_v E - \frac{1}{2} E^2 \nabla \epsilon \quad (9)$$

where  $\eta$  is the dynamic viscosity and  $p^* = p - (1/2)\rho(\partial \epsilon/\partial \rho)\Theta E^2$  is the modified pressure with the subscript  $\Theta$  denoting local temperature.

Following the details in Ref. [18], various simplifications have been introduced for the solution of these and correlated relations; otherwise, additional constitutive and/or conservation equations

would be required for the electrically related properties, an example being the permittivity [15]. The breakup, coalescence, and heat and mass transfer mechanisms were not accounted for given the need to conserve the drop charges throughout the droplet lifetime. In the absence of appropriate models for charged sprays as evaluated in the present study, the drop-wall interactions model of Park and Watkins [19], devised for uncharged sprays, has been implemented. In this model, the impinging droplets with Weber number below 80 are considered as inelastically reflected back in the axial direction with velocities given by

$$(v_a/v_b)^2 = 1 - 0.95 \cos^2 \beta \quad (10)$$

where  $v_a$  and  $v_b$  are the velocities of the drops after and before impaction, respectively, and  $\beta$  is the angle between the approaching drops and the normal to the surface. Droplet with Weber numbers higher than 80 are assumed to spread out and reside in the air within the computational wall thickness; indeed they are forced out from the wall in order to create the wall spray.

### 3 Engine Operating, Initial and Boundary Conditions

Table 2 summarizes the engine operating conditions for which the computations were carried out. The availability of experimental data only allowed the examination of a plain orifice electrostatic atomizer that produces a full cone spray. This kind of spray is also employed by Toyota in its D-4 DISI engine [20,21] and it has proved to vaporize without risk of plug carbon fouling.

The experimental research involving electrostatic atomization of hydrocarbon fuels using plain orifice atomizers [6], which preceded the present investigations, suggested a bimodal distribution with size ranges falling outside the desirable values for DISI engines, i.e., the SMD and DV90 of less than 25 and 40  $\mu\text{m}$ , respectively. Injection of two different size ranges as required by a bimodal distribution would need some delicate considerations (mathematical and physical assumptions) in the modeling, and this has not been done. Instead a fine spray obtained by charge induction<sup>2</sup> [22], as shown in Fig. 3, is used on the basis of future improved atomizer design.

Briefly, the boundary conditions for the liquid and gas phases are shown in Fig. 4. These comprise an annular air inlet, axis of symmetry, injector orifice, and walls (with wall functions being used to solve for the turbulence energy and its dissipation). The electrical boundary conditions are also depicted in Fig. 4 where, after the injection has elapsed, the injector orifice is assumed to consist of the same voltage as that of the cylinder roof, i.e.,  $-0.05$  kV. The values of  $-1$  kV at the piston surface,  $-0.1$  kV at the cylinder liner, and  $-0.05$  kV at the cylinder roof were computationally found to cause sufficient droplet repulsion from the walls [18]. Negative (electron emission) potential of  $-12$  kV at the injector orifice was taken from previous works [3]. Although

<sup>1</sup>The flow is of compressed turbulence type where the effects of compression enter the dissipation of turbulence kinetic energy equation through the source term.

<sup>2</sup>Charge induction is used to charge(semi) conducting liquids. In the present case of hydrocarbons the technique used is charge injection, in which the charging electrode is embedded into the fluid.

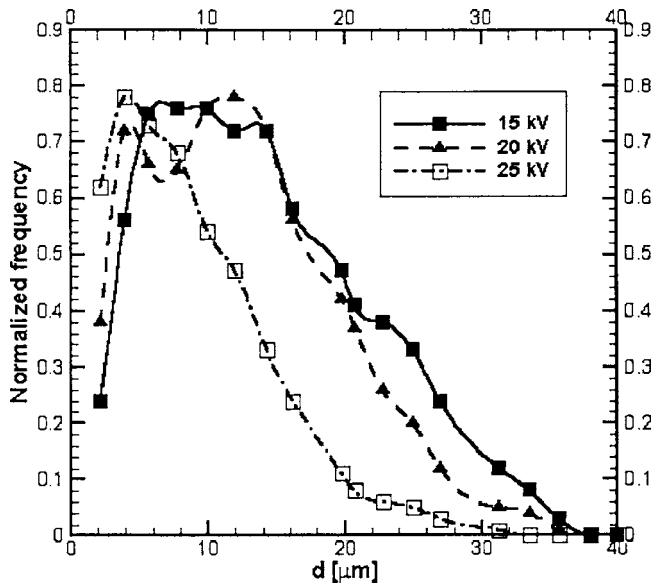


Fig. 3 Droplet frequency distributions derived from charge induction [22]

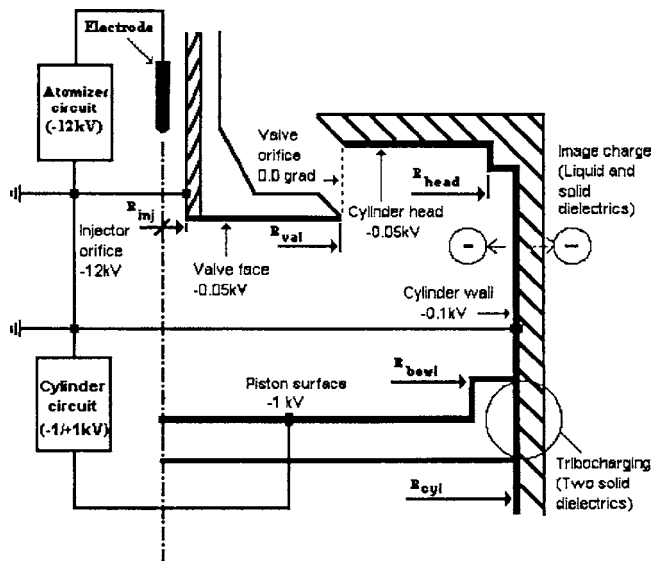


Fig. 4 Simplified geometry of the investigated concept eDISI engine

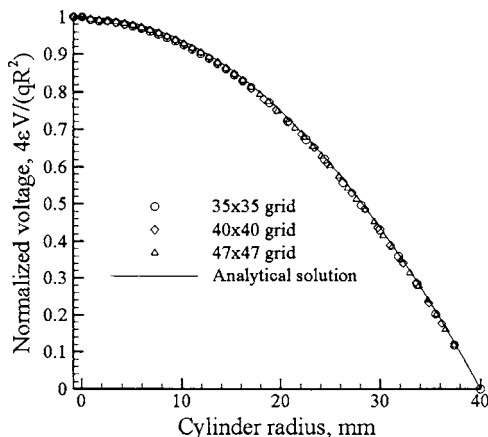


Fig. 5 Tested cases for grid calibration

this value may be seen as equivalent to that of spark jump, the currents involved in the fuel system of the present work are relatively insignificant; the current carried away by the liquid (spray current) is of order  $1.5 \mu\text{A}$  [3] and the current passed through the liquid to the nozzle body (leakage current) is also of order  $1.5 \mu\text{A}$  [3]. From this, it may follow that the spray induced in-cylinder current is negligible. Tribocharging is not modeled due to its complexity throughout the engine cycle as it may cause unpredictable polarity changes, depending on factors such as the interacting surfaces, relative velocities, and temperatures involved, to mention a few [15].

As shown in Fig. 4, the simulations are carried out using an axisymmetric engine configuration with moving valve and piston, which cause the computational domain to expand and contract as the engine cycle develops. While accommodating expanding and compressing grids, the in-house CFD research code implemented here tracks the discrete phase using the discrete droplet model.

#### 4 Grid Refinement Tests

Grid refinement tests were carried out using grids of  $25 \times 25$ ,  $30 \times 30$ ,  $35 \times 35$ ,  $40 \times 40$ ,  $47 \times 47$ , and  $60 \times 60$ , but only the  $35 \times 35$ ,  $40 \times 40$ , and  $47 \times 47$  grids are reported here, as shown in Fig. 5, since other grid densities were characterized by numerical instabilities leading to the code crashing when all the engine and electrostatic parameters were reactivated. Grids coarser than  $35 \times 35$  were only problematic with early injection while those in the range above  $47 \times 47$  failed in both cases of early and late injections. Although the  $35 \times 35$  grid also gave sensible results, its coarseness caused numerical instabilities in some test cases of high injection velocity. The  $47 \times 47$  and  $40 \times 40$  grids allowed the code to run under all the conditions investigated. The relatively larger CPU time associated with the  $47 \times 47$  grid favored the  $40 \times 40$  grid option, whose configurations for two cases of piston position are illustrated in Fig. 6.

#### 5 Numerical Validation

An EPISO (engine pressure with splitting of operators) code, whose grid expands and compresses in harmony with the piston and valve motions [14], was set to cope with the DISI engine working principles, and the electrostatic effects [6] were then incorporated into this code. The liquid and the gas phases were handled through the discrete droplet model and the general transport equations, respectively.

The novelty of the in-cylinder atomization principle envisaged in this study posed the need to simplify the real internal combustion engine processes down to some particular cases that could allow model validation. Hence the validation with experimental results required stopping the piston motion and elimination of the wall boundary corresponding to the cylinder roof [18].

The data used for CFD droplet introduction is shown in Fig. 7. Here, a dynamic similarity between nozzles of 500 and 250  $\mu\text{m}$  orifice diameters was used to reconstruct data of reference [23], which reports that a bimodal spray distribution is generated at sufficient levels of charge injection. Droplets with diameters typically 1/10 of the orifice diameter are produced in small numbers while larger droplets of diameters comparable to the diameter of the orifice generally contain most of the spray volume. Negligibly small counts are recorded in between these two droplet size populations.

Shown in Fig. 8 are the measured [23] and computed axial and radial velocity profiles for a spray discharged by a 250  $\mu\text{m}$  atomizer orifice diameter into a free bounded domain of 150 mm length by 75 mm diameter, with flow rate and specific charge of  $1.67 \text{ cm}^3/\text{s}$  and  $-1.80 \text{ C}/\text{m}^3$ , respectively.

In general, Fig. 8 shows a relatively improved collocation in the case of radial velocity profiles (column on the right). As for the axial velocity profiles (column on the left), pronounced divergence between experiments and CFD appears to occur at axial



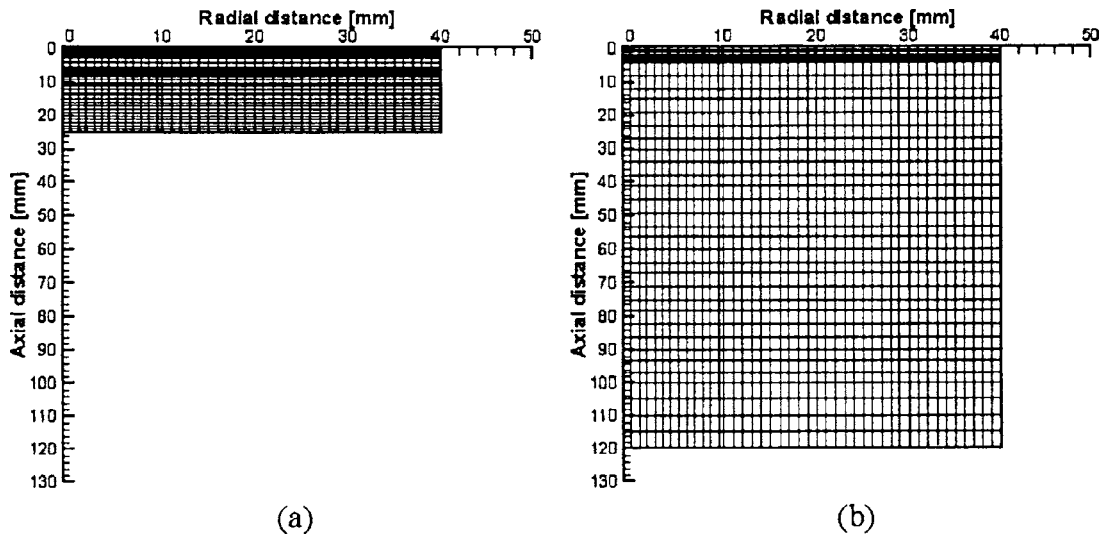


Fig. 6 Computational grid used in the study with the piston near the TDC (a) and BDC (b), respectively

levels closer to the nozzle orifice. Various reasons contribute for the discrepancies shown here, the primary to mention being that the random sampling of droplet sizes in a bi-modal spray distribution of Fig. 8 requires principles of physics beyond the scope of the present study.

In addition to the physics of bi-modal distribution, the continuity and momentum equations implemented in the injection cell (the flow driving element within the present system, which is made up of constant pressure boundaries at this particular section of the report) were those of uncharged sprays, which do not account for the effects of electrostatics, i.e., no gas acceleration due to charge has been imposed in either axial and radial directions of the injection cell. Indeed, one would expect the uncharged spray theory to lead to pronounced droplet axial acceleration, which, in turn, would cause overpredictions of axial velocity profiles as observable at axial positions  $x=60, 90,$  and  $120$  mm. The improved collocation of axial velocity profiles shown at level  $150$  mm may be due to the spray being dilute enough at this location so that the flow characteristics are mostly determined by the gas dynamics.

Although of less significance, another contributing factor for the discrepancies is the cylindrical coordinate system used in the computations, which defines singularities at the cylinder axis with

consequent use of solid body angular momentum equations in order to calculate the flow parameters at the first radial grid line.

In general, and on the face of difficulties associated with experimental facilities at present, the comparisons of the axial and radial velocity profiles are encouraging for the extension of the code to other simulation conditions (e.g., the engine conditions as envisaged in the present study).

## 6 Results and Discussion

Reported in [18] are various parametric studies from which only a selected portion of the investigations is presented as outlined below.

### 6.1 Effects of Reverse Gas Flow on Wall Impinging Droplets.

The effects of the reverse gas flow on wall impinging droplets were examined using pulse 1, which impinged on the piston surface in the uncharged spray case. It should be noted here that technical limitations only allowed the use of the wall impaction model of Park and Watkins [19], which can hardly mimic the actual flow conditions of the DISI engine open valve injection mode. For the purposes of the present study and in order to minimize the number of variables intervening within the process, the results of the model implementation are simply presented in terms of the ratio between the impacting droplets and those residing and leaving the piston surface before the inlet valve closure.

Depicted in Fig. 9 is that, by  $4$  ms after the first few droplets of the leading edge hit the piston surface, the cumulative number of the impinging droplets reaches a maximum of about  $480$  these, representing  $25\%$  of the  $1851$  injected droplet parcels within this single pulse. The reflected droplet parcels (droplets with  $We < 80$ ) represent nearly  $1/3$  of the impinging droplets while those sliding on the piston surface are relatively higher (nearly  $2/3$  of the totally impinging droplets). The significant proportion of droplets residing on the piston surface suggests that the reverse gas flow alone does not suffice to prevent wall wetting.

### 6.2 Effects of Charge on Flow Development.

Figure 10 depicts the flow development of the uncharged (left) and charged (right) spray cases. Here, large circles denote droplets with diameters larger than the SMD at particular control stations, while the smaller droplets are represented by smaller circles.

In the station  $90$  deg CA, which depicts one of the earliest stages of the gas induction through the centrally located valve, the uncharged spray shows a relatively higher spray penetration and reduced radial expansion than the charged case. This is to be expected given the Coulombic repulsions between the charged

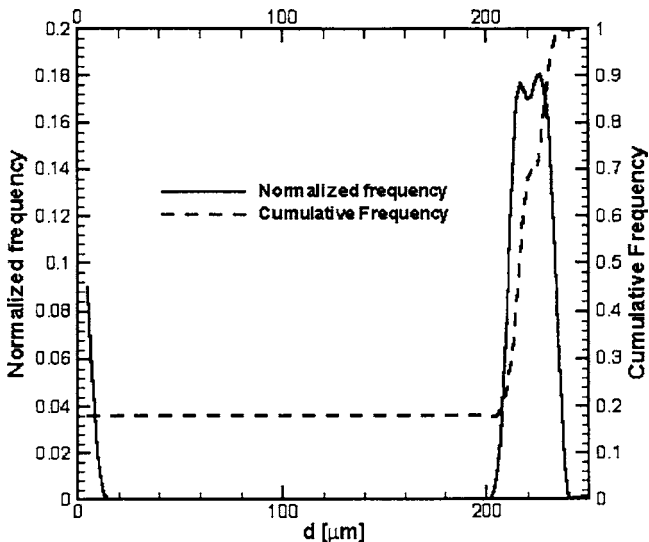


Fig. 7 Distribution of the injected spray for numerical validation

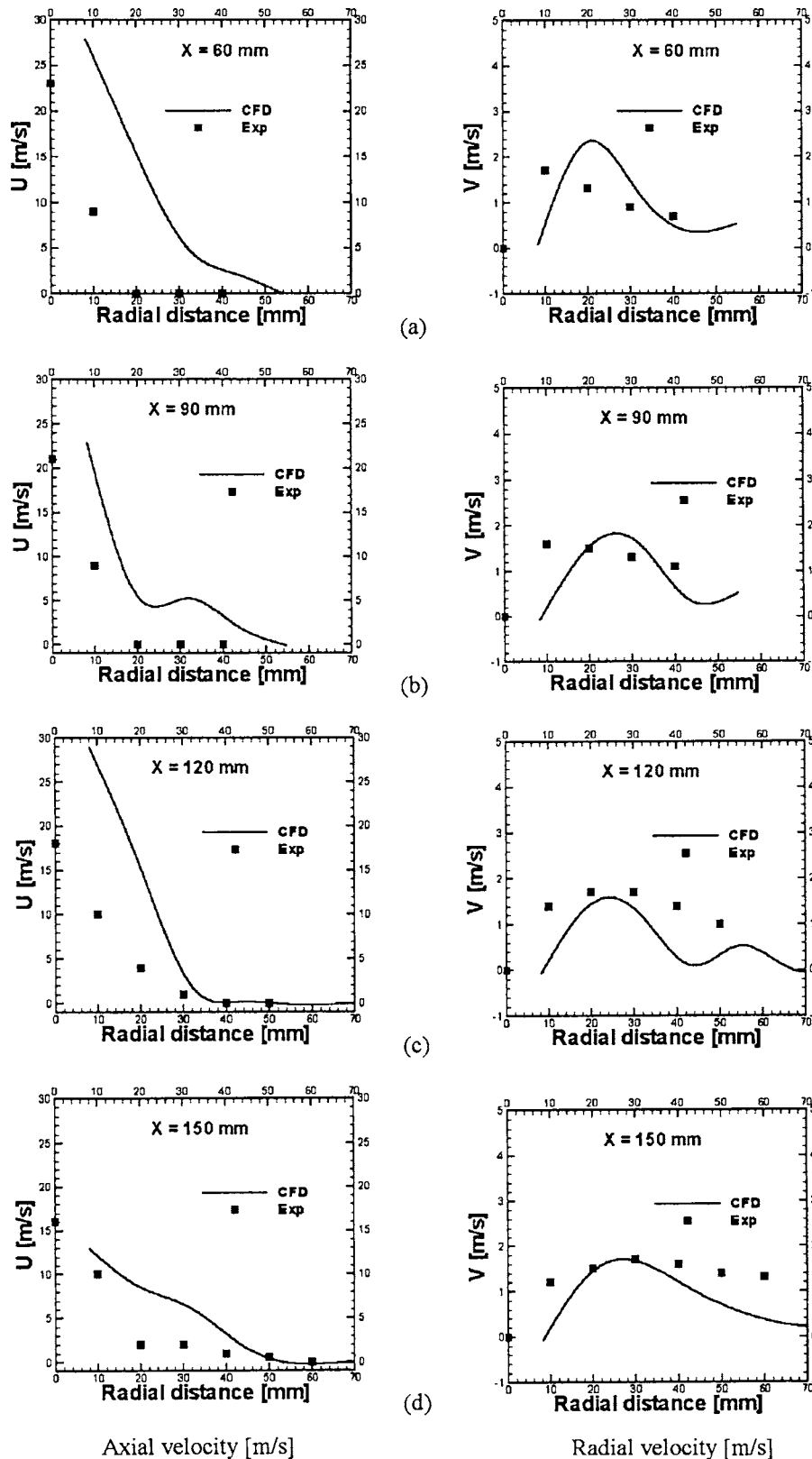
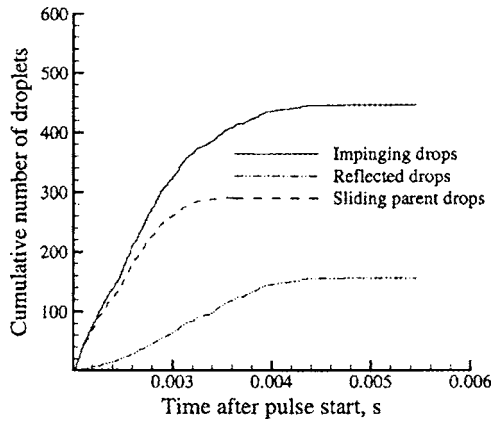


Fig. 8 PDA measured [23] and computed  $U$  and  $V$  velocity profiles for  $1.67 \text{ cm}^3/\text{s}$  and  $-1.80 \text{ C}/\text{m}^3$  using a  $250 \mu\text{m}$  diameter atomizer orifice

droplets promoting radial dispersion in detriment of the axial displacement. Hence, the charged spray easily fills the region of the recirculation flow adjacent to the valve face.

Shown in stations (b) through to (f) is a (relatively poor) wall wetting development of the uncharged spray. Given that the ma-

jority of the droplets tend to creep near the in-cylinder wall shear layers throughout the flow development, considerable liquid ends up permanently squished in the cylinder liner-cylinder roof intersection, a fact that is not attractive in the emissions point of view. On the other hand, most of the droplets injected in pulse 3 tend to



**Fig. 9 Cumulative number of piston-impinging droplet parcels of an uncharged spray during the intake stroke**

form a thick film and reside on the piston surface by the spark time, which is another negative effect in engine in-cylinder flows, where a rich mixture is expected near the spark plug by the spark time.

In general, the charged spray that develops in a domain confined within walls charged with the same polarity as that of the charged spray disperses wider in response to the effects of the inter-droplet and droplet-wall Coulomb forces.

It appears from the stations (c) through to (f) that the increasing pressure of the trapped gas favors the effectiveness of the droplet-wall Coulomb forces. Pronounced effects are shown at station (f) where the piston repulsion forces cause intense droplet reverse flow, soon after the injection of the third pulse, with no droplets appearing to populate the squish region in the intersection cylinder liner-cylinder roof up until the spark time (i.e., control station 345 deg CA). Also observable in Fig. 10(f) is that, in addition to the minimized in-cylinder wall wetting, a rich mixture may be achieved near the spark location by the spark time. Obviously, improved geometries (e.g., use of pent roof and bowl in piston) would infer additional improvements to the currently investigated system.

**6.3 Charge Drift and Its Effects on In-Cylinder Liquid Films.** As far as the charge drift is concerned, Fig. 11 illustrates that a maximum charge at the range of  $-215 \mu\text{C}$  occurs near the corner between the cylinder axis and the piston surface by the spark time. This occurrence derives from the fact that, by this time, the piston repulsion field combined with the high gas pressure causes the droplets of the third pulse to densely populate this location.

The station 157 deg CA elucidates that the incoming flow from the valve sweeps the droplets to a position located halfway of the cylinder liner where they build a small pocket of  $-2 \mu\text{C}$  of charge. In the following period (190, 225, and 290 deg CA), and in harmony with increasing drop concentration in this area, the charge builds up to values as high as  $-4 \mu\text{C}$ , thus increasing the repulsive (Coulomb) forces near the boundaries. Just for reference, it should be remembered here that the force exerted by a point charge of  $-1 \mu\text{C}$  on a point charge of equal magnitude located 10 mm away in air ( $\epsilon \sim 1$ ) is of order 90 N [11]. In the present case where the charges involved are of order  $-4$  and  $-215 \mu\text{C}$  while the distances are far below 10 mm, the forces are of order of thousands of N. This is why the repulsion forces near the walls subsequently cause detachment of the pocket as soon as the effects of reverse flow are counterbalanced by the increasing gas pressure. By 315 deg CA, the pocket is gradually pushed inside the computational domain in harmony with the motion of droplets.

The study of liquid phase films was carried out only when implementing the wall impaction model of [19] on the piston sur-

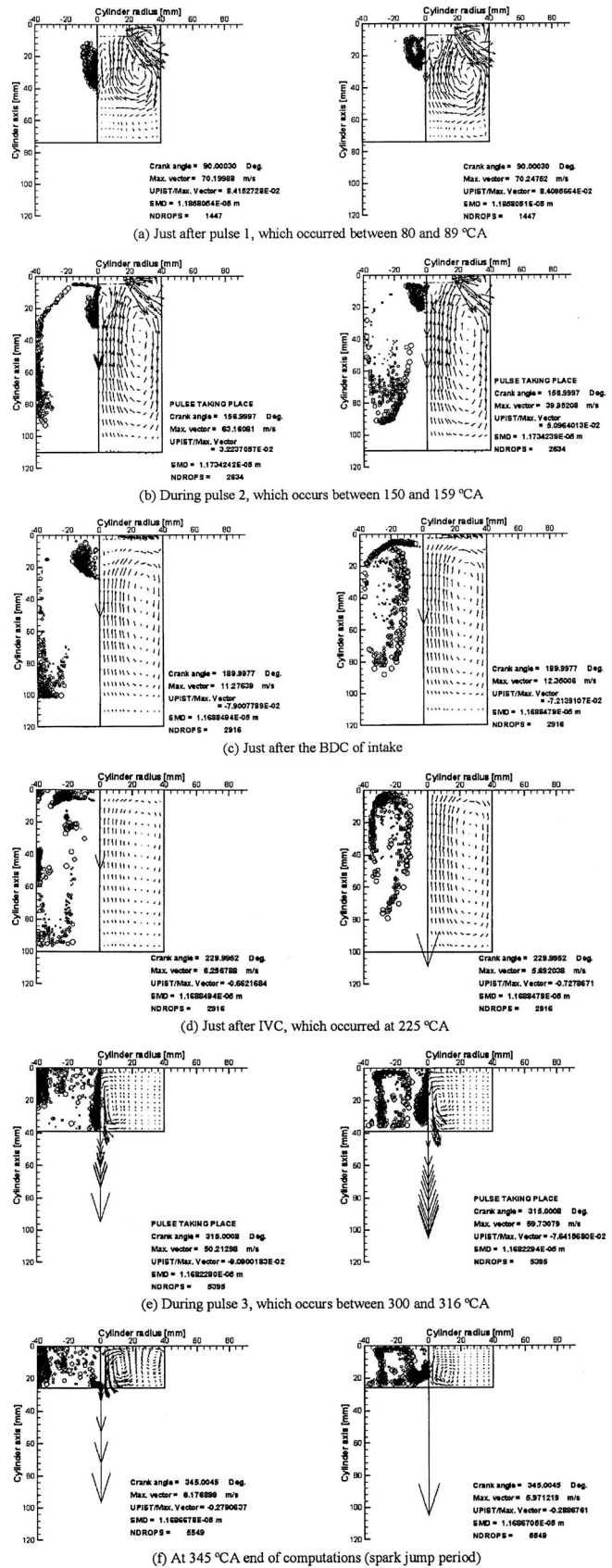


**Fig. 10 Droplet locations and gas velocity vectors of uncharged (left) and charged (right) cases at different stations of the flow development**

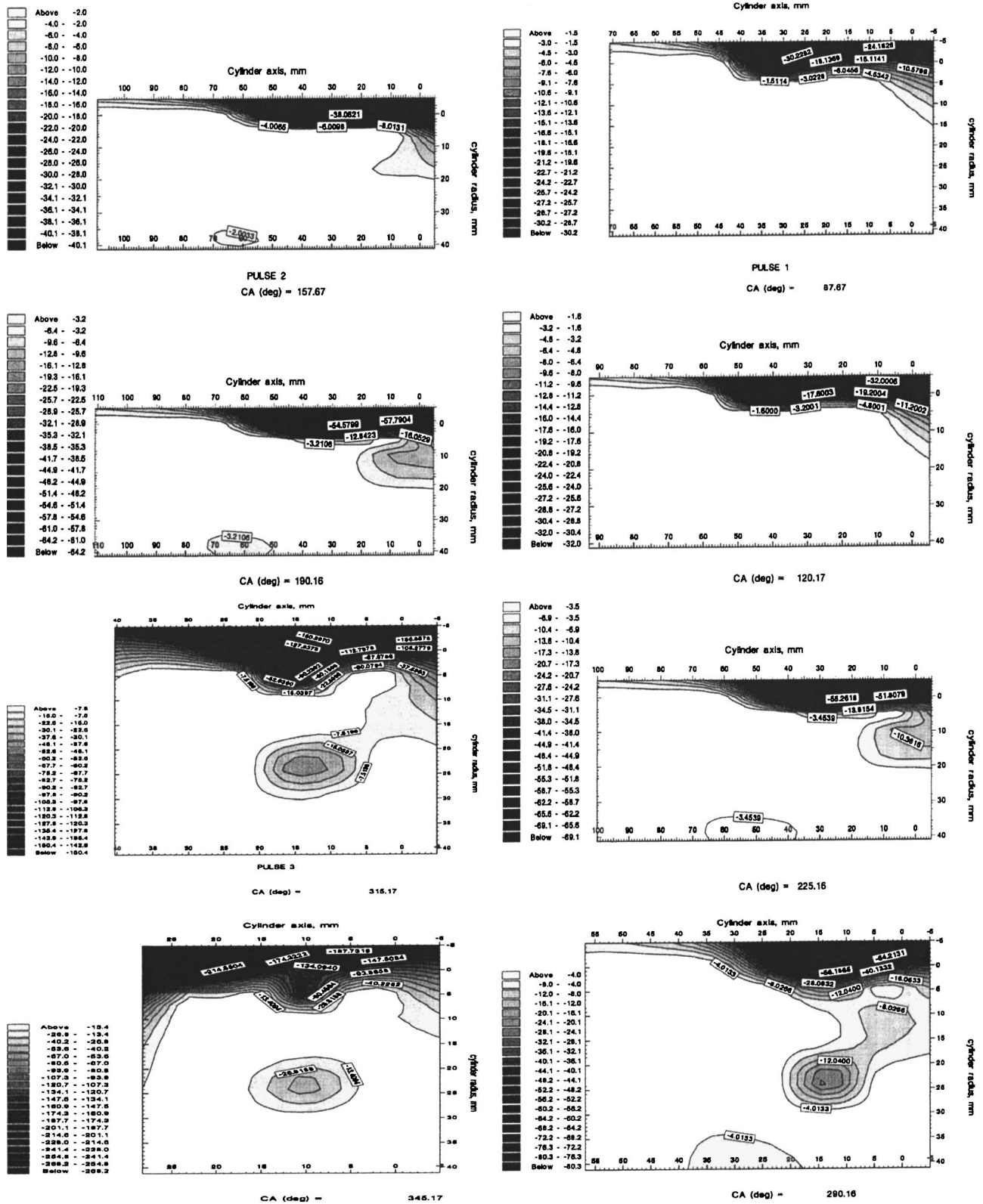


Fig. 11 Charge distribution (in  $\mu\text{C}$ ) as function of time

face. The film thickness was derived from the collectives of independent and noncoalescing droplets that resided in different computational cells while creeping along the piston surface [24].

Shown in Fig. 12 is the film thickness opposite the piston surface for both the uncharged and charged spray cases 2 ms after the third pulse. Here, while the piston repulsion forces in the charged

spray case decrease the mean value of the film thickness of the uncharged spray case to  $\sim 40\%$ , the inter-droplet Coulomb repulsion forces cause the creeping fluid to spread wider ( $\sim 15\%$ ) relative to the baseline uncharged spray. Indeed, the redistribution of liquid phase into larger surface area is a path for improved droplet evaporation rates.

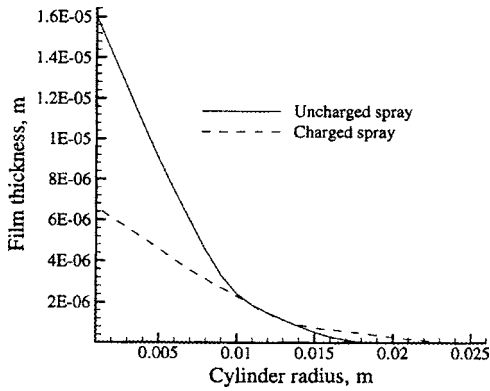


Fig. 12 Film thickness on the piston surface 2 ms after the third pulse of uncharged and charged sprays

Figures 13(a) and 13(b) illustrate the number of impinging droplets as a function of the applied voltages on the cylinder roof and liner, respectively. Observable here are the pronounced impingements on the cylinder liner for any of the cases of the implemented boundary voltages. To reason the higher impingement rate on the cylinder liner one would distinguish between the phenomena before and after the inlet valve closure as follows. Before the inlet valve closure at 225 deg CA, the induced air causes strong acceleration to droplets moving near the valve perimeter (Figs. 10(b) and 10(c)) with the consequence being the inertia forces of the swept droplets outweighing the cylinder liner repulsive forces. After the inlet valve closure, there is preservation of two pockets of stagnant flow, which were formed near the cylinder roof at

earlier stages of air induction (Fig. 10(a)). These pockets act as a baffle to droplets approaching the cylinder roof, hence helping the effectiveness of the repulsion forces on this wall boundary.

The interdroplet and droplet-piston surface Coulomb forces arising from each spray event cause instantaneous increase of impingements on both walls.

Summarized in Table 3 are the effects of the boundary electric fields. As shown in most of the cells of the last row, the cumulative values of the liquid phase concentration on the walls are well below 1% of the totally injected liquid. Hence, it may be assumed that only a moderate impingement rate will be obtained if the wall voltage is at least  $-50$  and  $-100$  V on the cylinder roof and liner. For the cylinder liner, which is (hypothetically) rubbed by the piston rings, these values appear to be sensible [18]. Emphasis should be made here that the impinging droplet parcels were merely counted without investigation of the effects of the droplet masses on wall impaction.

#### 6.4 Charged Spray With Electrically Passive Boundaries.

Figure 14 reports a charged spray that develops in an environment characterized by neutral wall boundaries. In the sense of the present study, neutral (or passive) wall boundaries apply when the Dirichlet (prescribed) electric boundary conditions are replaced by the condition of no electric flux across the walls. Of particular interest in this figure is the intensive cylinder roof impingement, which is undesirable in the context of DISI engine technology. About 127 parcels of droplet parcels were found to leave the cylinder in the back flow period (period between the BDC and the IVC). This number of lost parcels is 21 times greater than that found in the case of charged spray with electrified boundaries (six droplet parcels) and represents, on the other hand, 47% of the uncharged spray case (272 droplets).

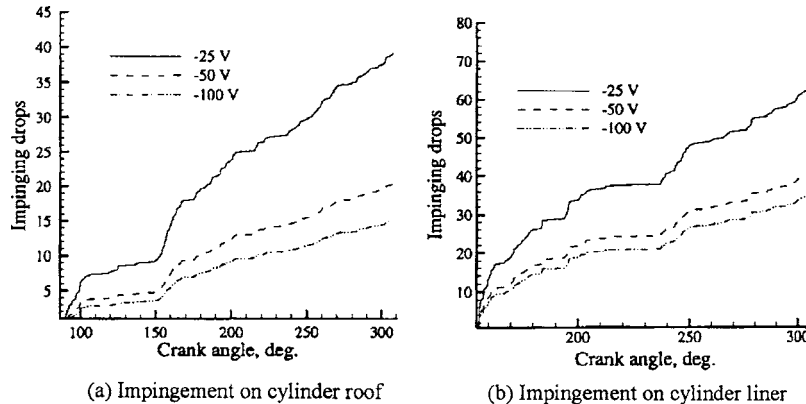


Fig. 13 Cumulative number of impinging drop parcels from a charged spray subjected to various electrical boundary conditions

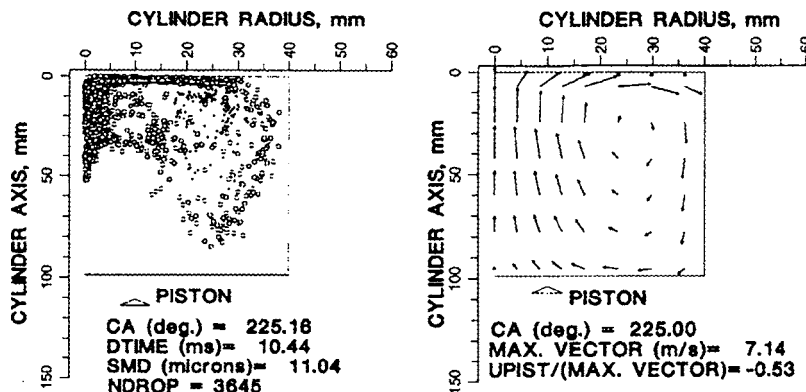


Fig. 14 Droplet locations and gas velocity vectors for a charged spray with neutral boundaries at the station 225 deg CA

**Table 3 Summary of the effects of the boundary voltages**

Case	Cumulative number of impinging droplets					
	Cylinder liner			Cylinder roof		
Uncharged	426 (7.25% of the injected droplets)			187 (3.18% of the injected droplets)		
Charged	-25 V case	-50 V case	-100 V case	-25 V case	-50 V case	-100 V case
	62	41	33	39	18	15
% relative to uncharged	14.6	9.6	7.7	20.8	9.6	8.0
% relative to injected drops <sup>a</sup>	1.06	0.70	0.56	0.66	0.31	0.26

<sup>a</sup>The number of injected droplets per cycle was 5873 from which nearly 4.6% (272 parcels) and 0.1% (6 parcels) were lost in the back flow period for the uncharged and charged sprays, respectively. Relative percentages are overpredicted since a given parcel of droplets may impinge more than once on a given in-cylinder surface.

**7 Conclusions**

The transport of charge within the cylinder of a motored axisymmetric model eDISI engine with electrified walls was investigated. In the lack of adequate experimental data, the wall impaction model of Park and Watkins [19], developed for uncharged sprays, was implemented to examine the levels of liquid phase accumulation near the wall boundaries for which different electric potentials were applied. Observed in the study is that the Coulomb forces are effective in reducing the spray impingement and promoting the redirection of the spray towards the spark location where the mixture must be rich by the spark time. By reducing the wall impacting droplets while promoting those freely flying, a path is open for an improved overall spray evaporation rate given the higher gas temperatures (relative to the temperatures of in-cylinder surfaces) at the late stages of the compression stroke. Also observed in the study are pockets with highest charge concentrate near the centerline by the spark time, which may be an additional path for improved evaporation rates and combustion efficiency [3,25].

**Nomenclature**

- DTIME = elapsed time after first spray pulse, s
- DV90 = droplet diameter corresponding to 90% volume distribution,  $\mu\text{m}$
- $d$  = droplet diameter,  $\mu\text{m}$
- $E$  = electric field ( $=-\nabla V$ ), V/m
- $P$  = pressure, Pa
- $q_v$  = computational cell volume charge,  $\text{C}/\text{m}^3$
- SMD = Sauter mean diameter (Same as  $D_{32}$ ),  $\mu\text{m}$
- $U$  = velocity component, m/s
- $V$  = applied voltage, V
- $\beta$  = angle between the approaching drops and the normal to the surface, deg
- $\epsilon$  = relative permittivity of space
- $\eta$  = dynamic viscosity,  $\text{kg}/\text{s}\cdot\text{m}$
- $\rho$  = mass density,  $\text{kg}/\text{m}^3$

**Acronyms**

- BDC = bottom dead center
- CA = crank angle
- DISI = direct injection spark ignition engine
- DSMC = direct simulation Monte Carlo
- eDISI = electrosprayed direct injection spark ignition
- EHD = electrohydrodynamics
- IVC = inlet valve closure
- NDROP = number of droplets at different time instants

**Subscripts**

- $a$  = after
- $b$  = before
- $d$  = discrete phase
- $D$  = drag
- $l$  = image
- $Q$  = charge

$\Theta$  = temperature

**References**

- [1] Balchandran, W., 1998, "The Present and the Future Trends in Electrostatic Atomisation of Liquids," 12th UMIST Short Course on Atomizer and Spray Technology, Manchester, UK.
- [2] Gilbert, W., 1600, *De Magnete*, 1958 reprint, Dover, New York.
- [3] Yule, A. J., Shrimpton, J. S., Watkins, A. P., Balachandran, W., and Hu, D., 1994, "Electrostatically Atomised Hydrocarbon Sprays," *Fuel*, **74**(7), pp. 1094-1103.
- [4] Kelly, A. J., 1988, "The Electrostatic Atomization of Hydrocarbons," *ASME J. Eng. Gas Turbines Power*, **110**(3), pp. 361-368.
- [5] Balachandran, W., Machowski, W., Halimic, M., Morgan, L., Gray, C., and Wilson, C., 1999, "Development of an Electrostatic Nozzle for Gas Turbine Applications," *Proc. ILASS-Europe '99 Conf.*, Toulouse, France, July 5-7.
- [6] Shrimpton, J. S., 1995, "Electrostatic Atomisation and Combustion of Hydrocarbon Oils," Ph.D. thesis, UMIST, Manchester, UK.
- [7] Shrimpton, J. S., Yule, A. J., Watkins, A. P., and Balachandran, W., 1996, "Effect of an External Electric Field on a Dielectric Charged Drop," *Proc. 1996 ILASS-Europe Conference*, Lund, Sweden.
- [8] Shrimpton, J. S., Watkins, A. P., and Yule, A. J., 1996, "Modelling of Charged Hydrocarbon Sprays Including Drop Break-Up," in *ECCOMAS-96*, Wiley, New York.
- [9] Shrimpton, J. S., 2000, "Characteristics of Unsteady State Sprays," *Proc. 8th ICLASS Conference*, Pasadena, CA.
- [10] Richardson, A. T., 1995, "Electrohydrodynamics: An Interdisciplinary Subject Come of Age," 9th Int. Conf. on Electrostatics, York.
- [11] Chang, J. S., Crowley, J. M., and Kelly, A. J., 1995, *Handbook of Electrostatic Processes*, Marcel Dekker, New York.
- [12] Kelly, A. J., 1984, "Low Charge Density Electrostatic Atomisation," *IEEE Trans. Ind. Appl.*, Vol. **IA-20**(2), pp. 267-273.
- [13] Kelly, A. J., 1982, "The Electrostatic Atomization of Hydrocarbons," 2nd International Conference on Liquid Atomization and Spray Systems, Madison, WI.
- [14] Watkins, A. P., 1989, *Computer Simulation of Fluid Flow, Heat and Mass Transfer and Combustion in Reciprocating Engines*, N. C. Markatos, ed., Hemisphere, Washington, DC, pp. 193-237.
- [15] Melcher, J. R., 1981, *Continuum Electromechanics*, MIT, Cambridge, MA.
- [16] Taylor, D. M., and Secker, P. E., 1994, *Industrial Electrostatics - Fundamentals and Measurements*, Research Studies, Tauton, UK.
- [17] Crowley, J. M., 1986, *Fundamentals of Applied Electrostatics*, Wiley, New York.
- [18] Nhumaiio, G. C. S., 2000, "Application of Electrostatically Charged Sprays in Gasoline Direct Injection Engines Using Plain Orifice Atomizers," Ph.D. thesis, UMIST, Manchester, UK.
- [19] Park, K., and Watkins, A. P., 1996, "Assessment and Application of a New Spray Wall Impaction Model," *Proc. of Inst. of Mech. Eng. Conf. on Computers in Reciprocating and Gas Turbines*, C499/004/96, London, pp. 1-10.
- [20] Tomada, T., Sasaki, S., Sawada, D., Saito, A., and Sami, H., 1997, "Development of Direct Injection Gasoline Engine - Study of Stratified Mixture Formation," SAE Technical Paper No. 970539.
- [21] Zhao, F. Q., Lai, M. C., and Harrington, D. L., 1999, "Automotive Spark-Ignited Direct-Injection Gasoline Engines," *Prog. Energy Combust. Sci.*, **25**, pp. 437-562.
- [22] Grace, J. M., 1993, "Droplet Motion and Control in an Electrohydrodynamic Fine Spray," Ph.D. thesis, University of Notre Dame, Notre Dame, IN.
- [23] Shrimpton, J. S., Yule, A. J., and Watkins, A. P., 1996, "Spray Visualisation and Phase Doppler Anemometry Measurements of Charged Hydrocarbon Sprays," *Proc. 8th Int. Symp. on Application of Laser Techniques to Fluid Mechanics*, Lisbon.
- [24] Nhumaiio, G. C. S., and Watkins, A. P., 2005, "Simulation of Electrostatics in Model DISI Engine In-Cylinder Flows," *IMEchE Int. J. Engine Res.*, **6**, pp. 527-546.
- [25] Jackson, N. S., Stokes, J., Whitaker, P. A., and Lake, T. H., 1997, "Stratified and Homogeneous Charge Operation for the Direct Injection Gasoline Engine-High Power With Low Fuel Consumption and Emissions," SAE Technical Paper No. 970543.

# Surfactant Effects on the Free Surface Thermal Structure and Subsurface Flow in a Wind-Wave Tunnel

Supathorn Phongikaroon<sup>1</sup>  
e-mail: supathorn.phongikaroon@inl.gov

K. Peter Judd<sup>2</sup>

Coastal and Ocean Remote Sensing Division,  
Naval Research Laboratory,  
Washington, DC 20375

*In this study, the dynamic effects of surfactant (oleyl alcohol) on the surface temperature and the near surface velocity field of a wind driven free surface are investigated. Different surfactant concentrations and wind speeds were examined to elucidate the flow physics. The water surface was imaged with an infrared (IR) detector and the subsurface flow was interrogated utilizing digital particle image velocimetry (DPIV). The IR imagery reveals the presence of a Reynolds ridge that demarcates the boundary between clean (hot) fluid and contaminated (cold) fluid. The clean region was found to be composed of laminae structures known as fishscales. A "wake region" which is an intermediate temperature region resulting from mixing of the near surface fluid layers develops behind the ridge. Experimental results from infrared imagery indicate that the fishscales in the clean region become elongated and narrowed as the wind speed increases. In addition, the results reveal that higher wind speed is required to form a Reynolds ridge in the presence of higher surfactant concentration. The plots of the surface temperature probability density functions reveal that these thermal structures undergo the same evaporative process while the increase in wind speed enhances this process. DPIV results reveal that the growth of a subsurface boundary layer for the contaminated case is more pronounced than that for the clean case. [DOI: 10.1115/1.2234781]*

## 1 Introduction

It has been known that surface-active materials or surfactants are naturally present in bodies of water. It diffuses to the free surface forming a thin layer that is known to change the boundary condition at the interface and influence wave motions [1–3]. When a contaminated film on a flowing stream is trapped against a barrier, it is compressed and a no-slip boundary condition is impressed on the underlying flow field. As a result, the adjacent subsurface flow forms a viscous boundary layer. This causes a slight elevation in the free surface forming a demarcation line separating the clean and contaminated regions. This structure is known as the "Reynolds ridge."

The interest of an oil slick or a thin film of oil on a free surface can be traced back to the work of Franklin [4]. Later, Reynolds [5] reported a similar discovery and proved that the surface tension gradient was the physical mechanism behind the ridge's formation. He demonstrated the equivalence between the case of spreading of an oil slick on a clean water surface to that of a thin stationary film met by an oncoming flow. Since that time, many independent studies [6–12] of the effect of surfactant on the formation of the Reynolds ridge have been reported.

Satterly and Mill [6] and Satterly and Turnbull [7] studied different geometrical formations of the ridge on a free surface. Their study indicated that surface tension gradient, film thickness, stream velocity, and area variation were potential factors that could affect the formation. Later, Hall [8] reported the observation of lines on the surface of moving water near footbridges and sluices and discussed these aforementioned factors. In 1968,

Sellin [9] conducted an experiment on this natural phenomenon by measuring an elevation profile perpendicular to the water surface using a reflected light Schlieren system showing the leading edge of the contaminated free surface region.

McCutchen [2] proposed the first description of the physical mechanisms associated with the formation of a Reynolds ridge and used simple relations from the laminar boundary layer theory and the balancing of surface shear stress with the surface tension gradient to formulate a relation for the surface pressure. Following McCutchen's work, Harper and Dixon [10] developed a theoretic model based on the steady, two dimensional viscous boundary layer equations to describe the relation between surface slope and the underlying flow. The results were compared to Sellin's experimental data and revealed that the surface slope relied on the subsurface flow velocities.

Scott [11] extended Sellin's work utilizing a laser-beam deflection technique. Measurements were made with different water flow velocities and results compared to Harper and Dixon's theoretical model and found to be within an agreeable range. Warncke and co-workers [12] simultaneously measured the slope near the ridge using a displacement of collimated light technique and the planar velocity field in the neighborhood of the ridge using digital particle image velocimetry (DPIV). Vorticity contours near the surface and boundary layer profiles at different downstream distances were reported. They concluded that the obtained profiles were similar to those that occurred near a flat plate with a pressure gradient.

The studies described above are principally devoted to the investigation of the hydrodynamical behavior in the neighborhood of a Reynolds ridge. In fact, there is little understanding of the interaction between the subsurface hydrodynamics and temperature field in the vicinity of a Reynolds ridge. In addition, previous studies have focused on the case in which a surfactant film is compressed against a barrier by a subsurface current forming a Reynolds ridge.

<sup>1</sup>Present address: Idaho National Laboratory, P.O. Box 1625, Idaho Falls, ID 83403.

<sup>2</sup>Present address: Mechanical Engineering, Clemson University, Clemson, SC 29634.

Contributed by the Fluids Engineering Division of ASME for publication in the JOURNAL OF FLUIDS ENGINEERING. Manuscript received July 15, 2004; final manuscript received February 2, 2006. Review conducted by Joseph Katz.

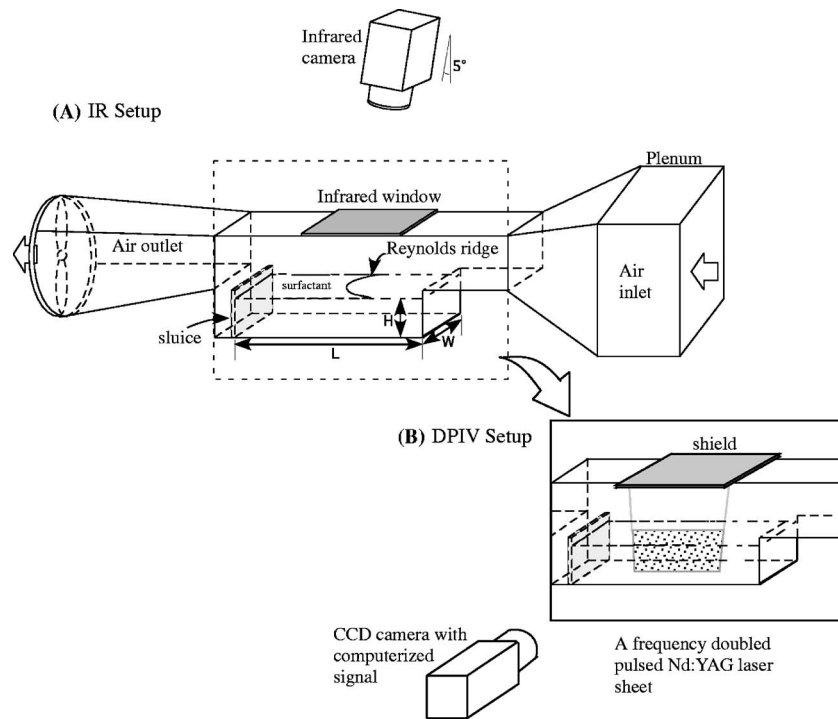


**Fig. 1** The wind-wave tunnel facility, the tunnel dimensions are  $L=35$  cm,  $W=10.4$  cm, and  $H=8.9$  cm: (a) IR camera setup; and (b) DPIV camera and beam orientation

In the present work, we investigate the more complex scenario in which clean and contaminated free surfaces are subjected to a wind shear. We believe that this situation is more closely related to what occurs in nature; surfactant patches or surface slicks are formed on free surfaces due to the compression of surfactant material by a wind [13–15]. Our goal is to document the surface temperature field characteristics about the ridge and compare with the measured subsurface velocity field for various surface conditions. We feel that the results from this experimental work would shed light on some of the fundamental effects wind stress has on surface flow stability as well as heat, mass and momentum transport. This information may prove useful in the study of flows on the ocean surface especially wind/wave interaction, generation and possibly energy dissipation of wind generated waves.

## 2 Experimental Setup and Methods

A small Plexiglas water tank ( $35\text{ cm} \times 10.4\text{ cm} \times 10.4\text{ cm}$ ) was constructed and fitted to a wind tunnel section (TSI model 8390), as shown in Fig. 1. The mean wind speed through the tunnel section was obtained via a commercial pressure transducer (MKS Baratron 223B) connected to a pitot tube. A barrier was attached near the end of the tank to hold the water and to act as a spillway. The tank was filled through the bottom with doubly distilled water (Barnstead FISTREEM™ II GlassStill) and was permitted to overflow for half an hour prior to each experimental run in order to reduce the presence of natural surfactant. This would be referred to as the “clean case.” Before acquiring data, the liquid level was adjusted to the height of 8.9 cm.

There is no forced convection on the water side of the interface. The motion of the liquid was solely generated by the wind shear applied to the interface from the air side. Therefore, heat transfer across the air-water interface was due to evaporative cooling and to the difference between the bulk air flow in the tunnel and water temperature.

For the “contaminated case,” the cleaning process is the same as described above. However, an insoluble surfactant, oleyl alcohol (Sigma Aldrich,  $\rho=0.85\text{ g/cm}^3$ ), was deposited carefully on the water surface with a microsyringe. The reason for using this surfactant is because it does not impede the evaporation process [16]. A stock solution was prepared by diluting oleyl alcohol in 99% heptane (Sigma Aldrich). Here, the heptane was permitted to evaporate leaving an oleyl alcohol monolayer. Although several surfactant concentrations were examined for this study, similar features were observed for each of the different concentrations. Therefore, only one surfactant concentration level ( $c=0.08\text{ }\mu\text{g/cm}^2$ ) is presented.

Imagery of the free surface flow for the “clean” and “contaminated” surface cases was captured using an infrared (IR) detector (Indigo charge coupled device (CCD) camera having a  $320 \times 256$  array with a resolution of  $\pm 0.02\text{ K}$ ) operating at a sampling rate of 30 Hz. The images were recorded looking down through a silicone IR window ( $20.3\text{ cm} \times 13.0\text{ cm} \times 0.64\text{ cm}$ ) which allowed the transmission of radiation in the  $3\text{--}5\text{ }\mu\text{m}$  wavelength range. The optical depth (the depth below which a negligible amount of radiation can escape from the surface) of the water in this band width is approximately  $20\text{ }\mu\text{m}$ . Image sequences were captured using a personal computer (PC) based video data acquisition system (National Instruments). The image data was post processed using *ImageJ*, an image analysis package available from the NIH.

Immediately following the acquisition of the IR images, for each experimental run, DPIV was performed to capture the subsurface velocity field. Particle images were captured with a  $1\text{ k} \times 1\text{ k}$  CCD Kodak Megaplug ES 1.0 cross correlation camera. The region of interest was  $6.4\text{ cm} \times 19.5\text{ cm}$  and located approximately 1 mm below the free surface (see Fig. 1(b)). The flow was illuminated with a frequency doubled pulsed Nd:Yttrium–aluminum–garnet laser (532 nm). The flow was seeded with



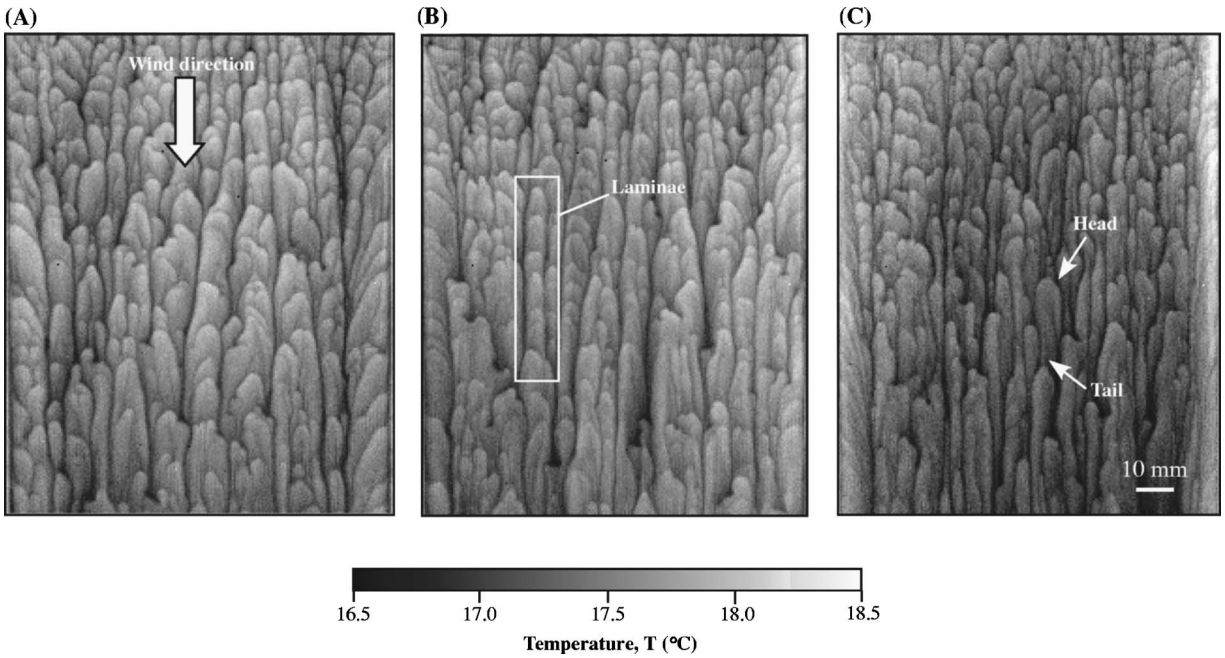


Fig. 2 IR images of the free surface flow at a wind speed of (a) 5.1, (b) 6.7, and (c) 8.1 m/s. The image is 10.4 cm  $\times$  12.8 cm.

neutrally buoyant silver coated polystyrene particles with mean diameter of 10  $\mu$ m. Laser and camera were synchronized by a PC based data acquisition system. Velocity vectors and statistics were computed from particle image pairs using *FlowManager*, a commercial software analysis package. A rectangular interrogation window with a length of 32 pixels and a height of 16 pixels with 50% window overlap was used to obtain the velocity field. This particular window selection was chosen to resolve the boundary layer in the vertical direction. The uncertainty of the velocities was estimated to be below 5%. The details of the technique can be found in Willert and Gharib [17] and Volino and Smith [18].

### 3 Results and Discussion

**3.1 Infrared Imagery.** Figures 2(a)–2(c) are representative IR images of the free surface flow at three different wind speeds for a clean surface. Each image is an instantaneous realization of

the surface thermal structure present at each of the respective wind speeds. The top of each image is 6.1 cm downstream from the leading edge of the channel. Wind direction is from top to bottom as shown in Fig. 2(a) and the mean wind speeds are 5.1, 6.7, and 8.14 m/s. The tunnel inlet temperature and relative humidity were  $24 \pm 3^\circ\text{C}$  and  $22\% \pm 4\%$ , respectively. The bulk water temperature at the start of the experiment was  $20 \pm 0.5^\circ\text{C}$ .

A scale is given to show the relation between the image gray scale and corresponding temperature levels of the surface layer. The calibration technique can be found in Saylor et al. [16]. Here, warmer fluid is represented by the lighter regions and the cooler fluid by the darker areas. Typically, the temperature variation between these dark and light regions is about 1–2 $^\circ\text{C}$ . It can be observed that the images are composed of an array of streamwise oriented laminae as highlighted in Fig. 2(b). The laminae, also called *fishscales* [19], occur when rising buoyant thermal plumes

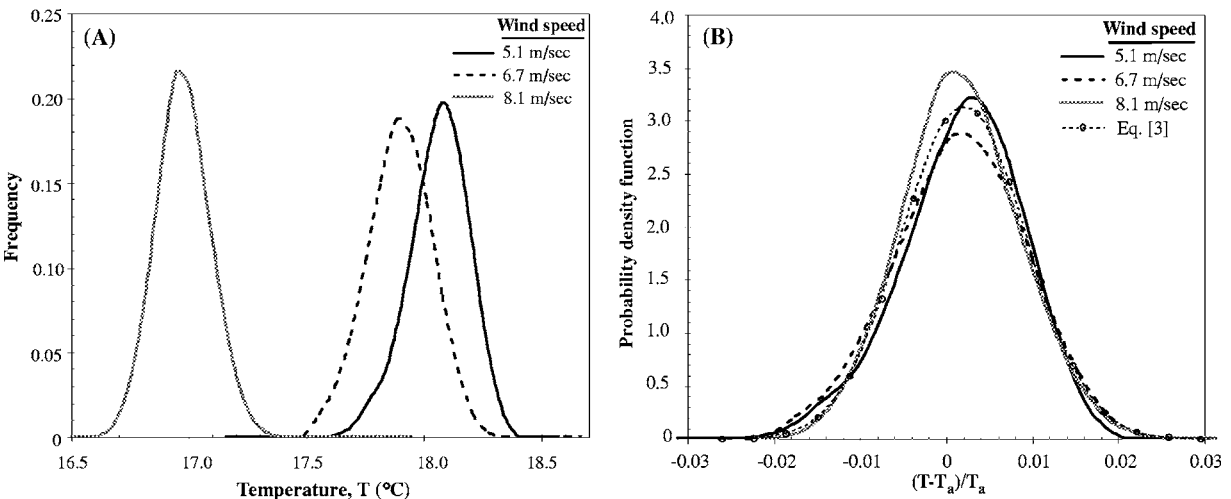


Fig. 3 Plots of (a) temperature pdf and (b) normalized temperature pdf for the extracted IR image at different wind speeds

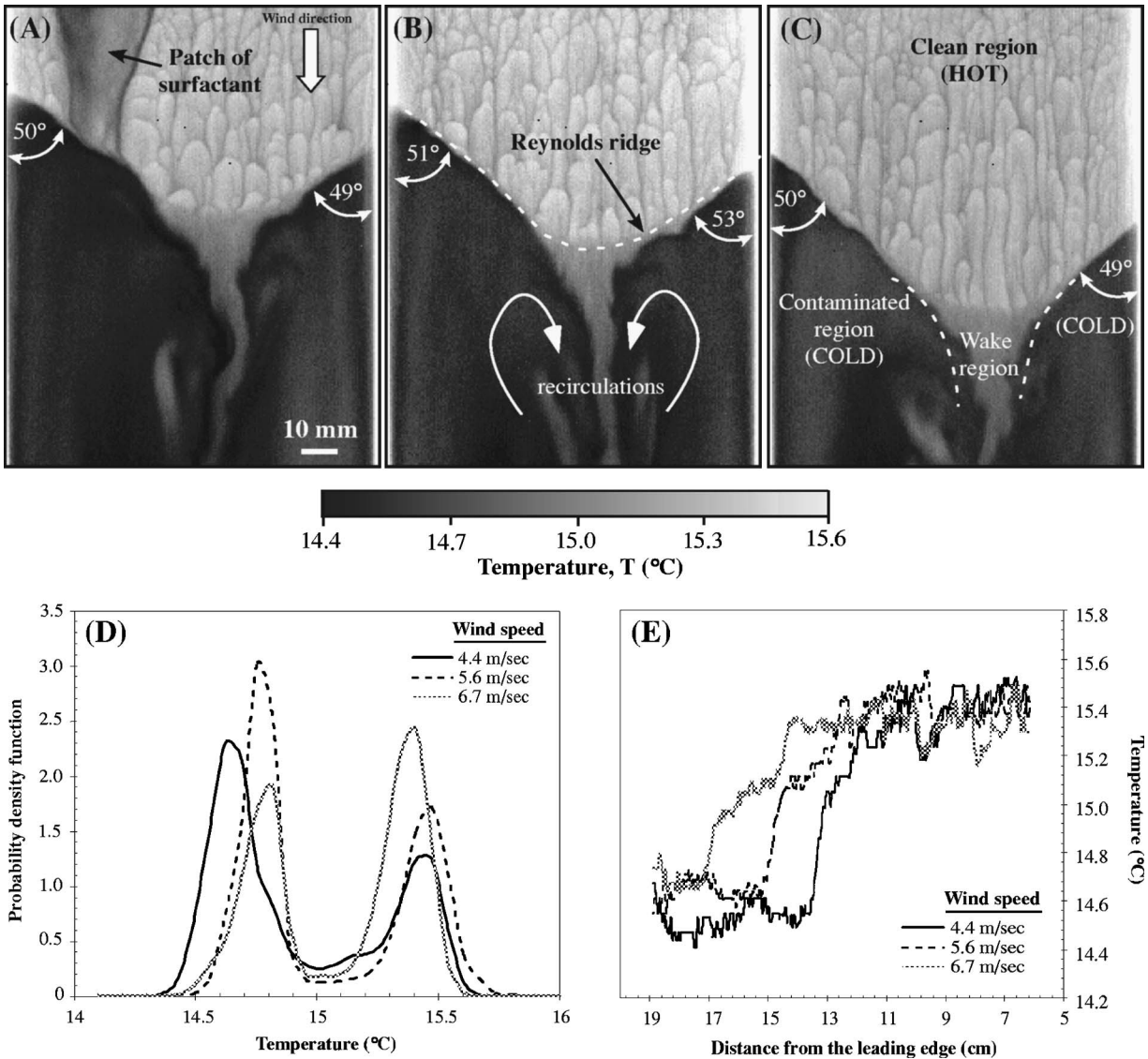


Fig. 4 IR images of the contaminated free surface at a wind speed of (a) 4.4, (b) 5.5, and (c) 6.7 m/s; (d) plots of the temperature pdfs; (e) extracted temperature profiles taken through the center of the IR image (vertical line section)

in the bulk are sheared by the wind on the free surface. The laminae are composed of a head-to-tail structure as indicated in the Fig. 2(c). As the wind speed increases, the fishscales become elongated and narrowed.

From this IR imagery, it can be hypothesized that evaporation and forced convection from the air side are the two dominant mechanisms that cause the appearance of these thermal structures. To shed light on this hypothesis, the statistical distribution of the temperature fields is computed. Figure 3(a), displaying the temperature distribution frequency, illustrates that as the wind speed increases, the average surface temperature decreases. The probability density functions for these three conditions are plotted and shown in Fig. 3(b). The normal distribution function is one of the most widely used distribution functions in engineering applications. It represents the distribution of a variety of observed data well and has the following form:

$$f(T) = A \exp\left(-\frac{1}{2C^2}(T-B)^2\right) \quad (1)$$

where  $A$  is the coefficient,  $B$  is the mean, and  $C$  is the standard deviation. For this study,  $B$  is the mean temperature and is defined as

$$B = \int_0^{T_{\max}} Tf(T)dT = \frac{\sum_{i=1}^N n_i T_i}{\sum_{i=1}^N n_i} \quad (2)$$

where  $n_i$  is the number of occurrences of temperature  $T_i$  and  $N$  is the total number of intervals or temperatures. A plot of  $f(T)$  versus  $T$  reveals a symmetrical bell-shaped curve about the value of  $T = B$  where the maximum value of the function occurs. The standard deviation,  $C$ , is a controlling parameter in the structure of the distribution; the curve becomes narrower and more concentrated about  $B$  for a small value of  $C$  and vice versa. For any value of  $C$ , the area under the bell-shaped curve from  $T=0$  to  $T=\infty$  is 1.0.

Here, the temperature distribution of the clean case at different wind speeds, normalized with the average free surface temperature  $T_a$  can be expressed as follows:

$$f\left(\frac{T-T_a}{T_a}\right) = (3.1 \pm 0.21) \exp\left(-\frac{1}{2(0.0073 \pm 0.00056)^2} \times \left(\left(\frac{T-T_a}{T_a}\right) - (0.0021 \pm 0.00012)\right)^2\right) \quad (3)$$

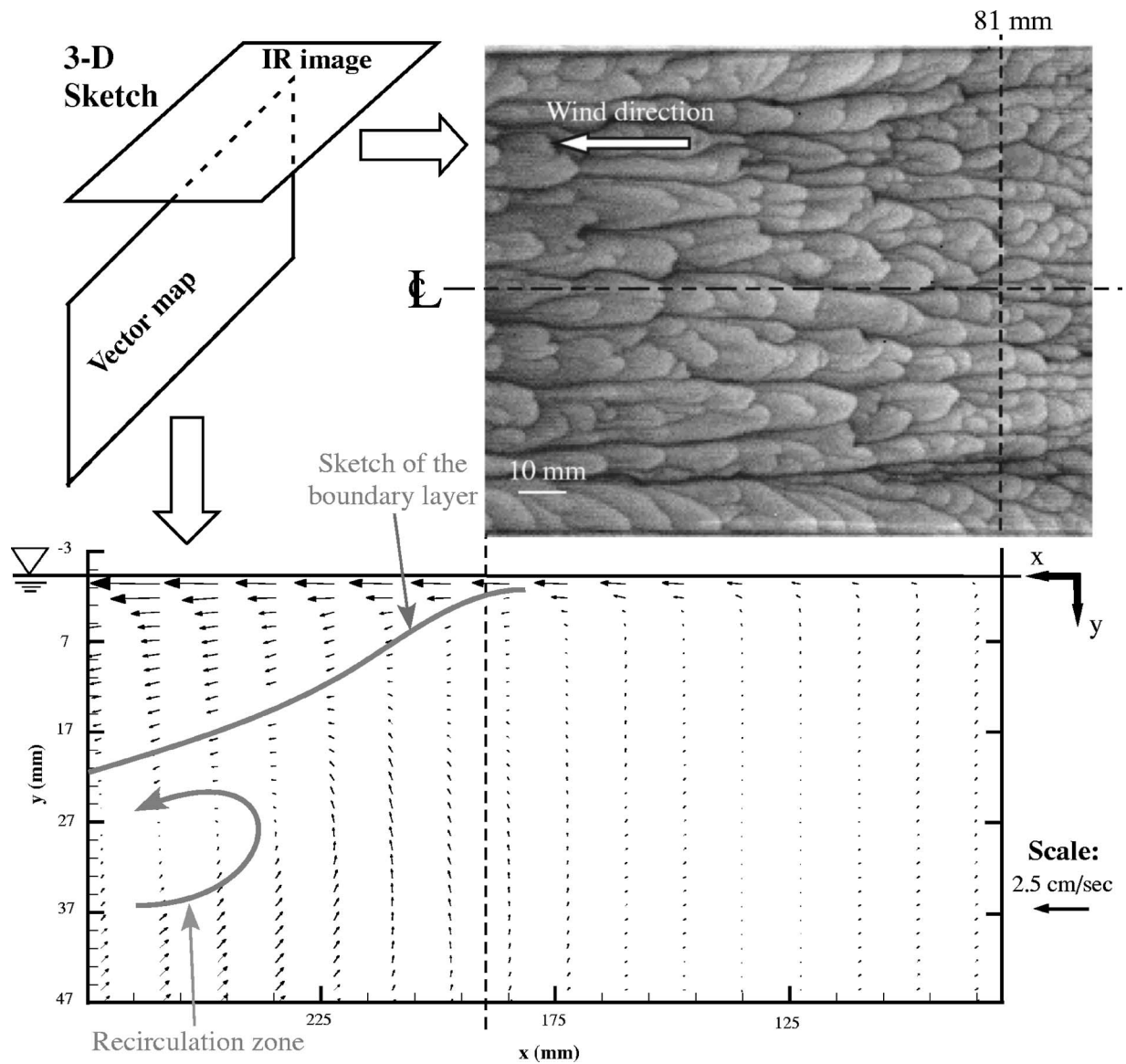


**Fig. 5** Velocity vector plot for the clean case at the wind speed of 5.1 m/s with a corresponding IR image. Dashed lines show the common region of the IR image and the DPIV velocity field.

The values in Eq. (3) were obtained from the best-fit curve through the experimental data sets. Figure 3(b) shows Eq. (3) superimposed on the resulting data points. This figure illustrates that the shape at each wind speed remains similar suggesting that the thermal structures undergo the same evaporative process while the increase in wind speed enhances this process.

Figures 4(a)–4(c) are IR images of the contaminated case for the wind speeds 4.4, 5.5, and 6.7 m/s, respectively. As mentioned above, the concentration of oleyl alcohol on the free surface before introducing the wind was  $0.08 \mu\text{g}/\text{cm}^2$ . It is important to point out that similar characteristics can be observed for higher surfactant concentration, that is fishscales in the clean region and a D-shape Reynolds ridge. However, higher wind speeds were required to form the Reynolds ridge as the amount of surfactant concentration was increased. The wind direction is from top to bottom. The images in Figs. 4(a)–4(c) are representative of a highly turbulent flow that has reached a statistically steady state (stationary flow). An evolution to steady state of the wind driven Reynolds ridge can be found in Phongikaroon et al. [20]. Experimental observations suggest that the position of the ridge can be maintained indefinitely as long as the applied wind shear and sur-

factant concentration remain constant. From observing several sequences of the IR imagery, the advection of hot and cold fluid plume structures can be detected and provide a clear sense of the surface flow pattern.

Figure 4(c) reveals three distinct regions of the surface flow; for clarity, nomenclature for most of the flow structures is present in this figure. The first region, located upstream of the ridge, is the clean or hot region. The second region, located downstream of the ridge where the surfactant has accumulated, is the contaminated or cold region. The association between these two regions has been experimentally shown by Saylor et al. [16] and later confirmed numerically by Handler et al. [21]. As mentioned earlier, oleyl alcohol does not interfere with the evaporation process at the free surface; however, the surfactant region appears cooler because it is damping out the hot thermal plumes that would reach the free surface. The intermediate region or “wake region,” appeared downstream of the ridge and situated in a valley between the two recirculation zones in the contaminated regions. It appears that the fishscales in the clean region move downstream and rapidly subduct beneath the ridge. The diameters of these recirculation regions are approximately 2.5 cm and are composed of a hot core

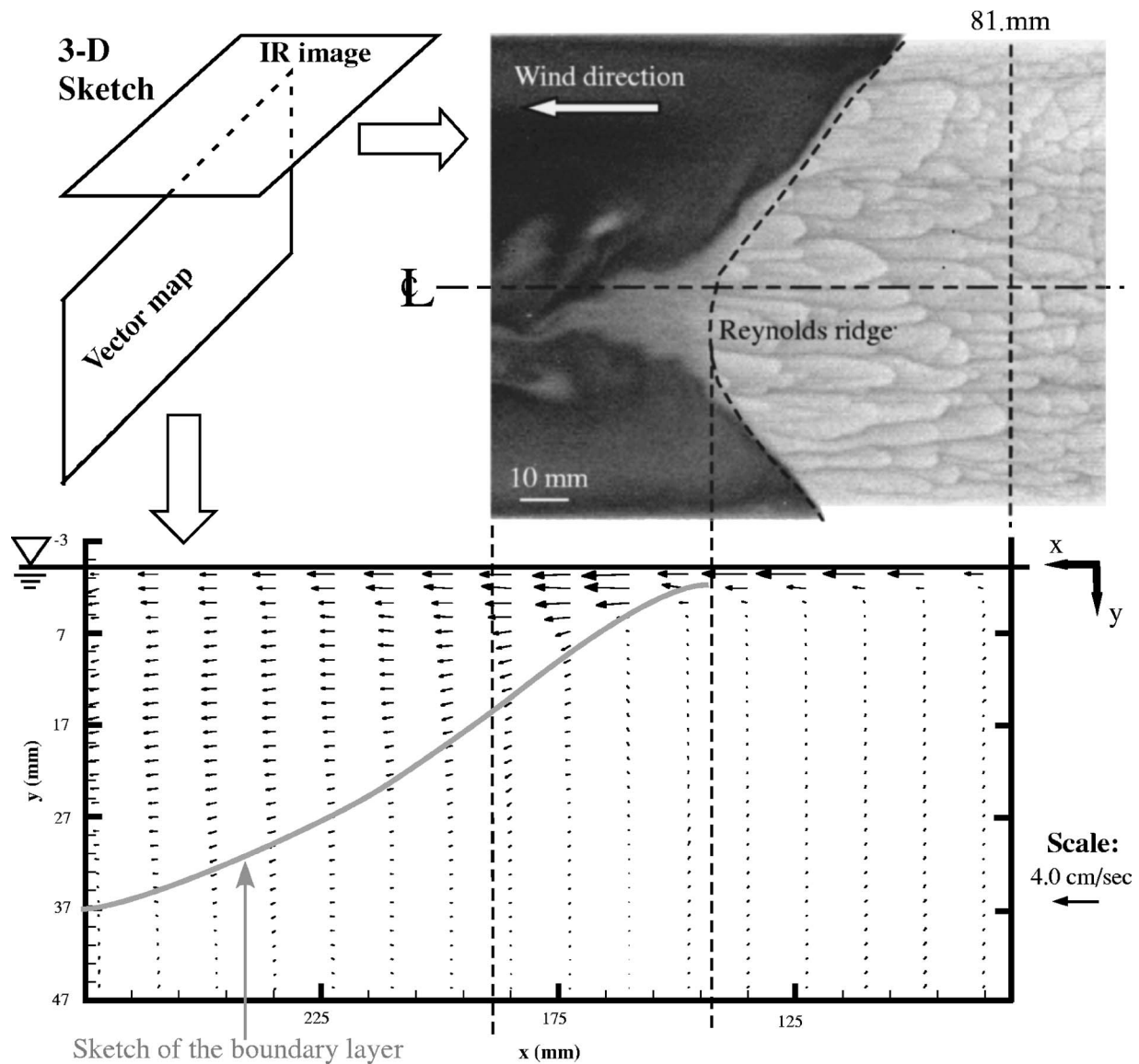


**Fig. 6 Streamwise velocity profiles at various downstream distances for the contaminated case. Dashed lines show both the common region and the location of the Reynolds ridge (occurs at about 144 mm downstream of the leading edge of the channel).**

with cold band. Here, the eddy on the left hand side of the image rotates clockwise while that on the right hand side rotates counterclockwise. They rotate faster and become tighter (e.g., at the high wind speed of 6.7 m/s, the diameter is reduced to 2 cm) as the wind speed increases.

It is interesting to note that the angle formed by the ridge with the tank walls for all contaminated cases is independent of wind speed and is approximately 50 deg (see Fig. 4). As the wind speed increases, it can be clearly seen that the position of the ridge shifts further downstream because the flow is more energetic and is able to further compress the surfactant film against the sluice. The temperature distributions over the entire IR images for the free surface for all mentioned wind speeds are shown in Fig. 4(d). As expected, the temperature distributions are bimodal in nature: this corresponds to the (1) the lower temperature peak for the contaminated region and (2) the higher temperature peak for the clean region. The temperature over the IR images in the clean region of the free surface flow decreases as the wind speed increases exhibiting the similar trend as observed earlier in Fig. 3(a). In addition, the surface temperature extracted along the centerline of each IR image is shown in Fig. 4(e).

**3.2 DPIV Results.** The plane of interrogation for the velocity field and area imaged with the IR detector are defined in Fig. 5. The planes are perpendicular to one another with the planar velocity measured along the centerline of the channel. A 3D schematic image is given in the figure to provide the full visualization of these representative data sets. Figure 5 is a representative mean velocity field calculated from the DPIV data (300 realizations of the flow) at the low wind speed condition of 5.1 m/s for the clean case. The right edge of the velocity vector plot is 8.1 cm from the leading edge of the channel. A dashed line is drawn across the DPIV vector plot to locate this position on the given IR image. Another dashed line is drawn to show the downstream end of the IR image on the DPIV vector map. For presentation purposes, velocity vectors are shown every third point in the  $x$  direction and every point in the  $y$  direction. The vector map reveals a monotonic increase in speed at the free surface and growth in the boundary layer (BL) along the channel length. This is a typical characteristic of free surface flows with clean surfaces. The BL thickness is approximately 21 mm (as indicated in Fig. 5). The edge of the boundary layer is determined where the velocity drops to 10% of

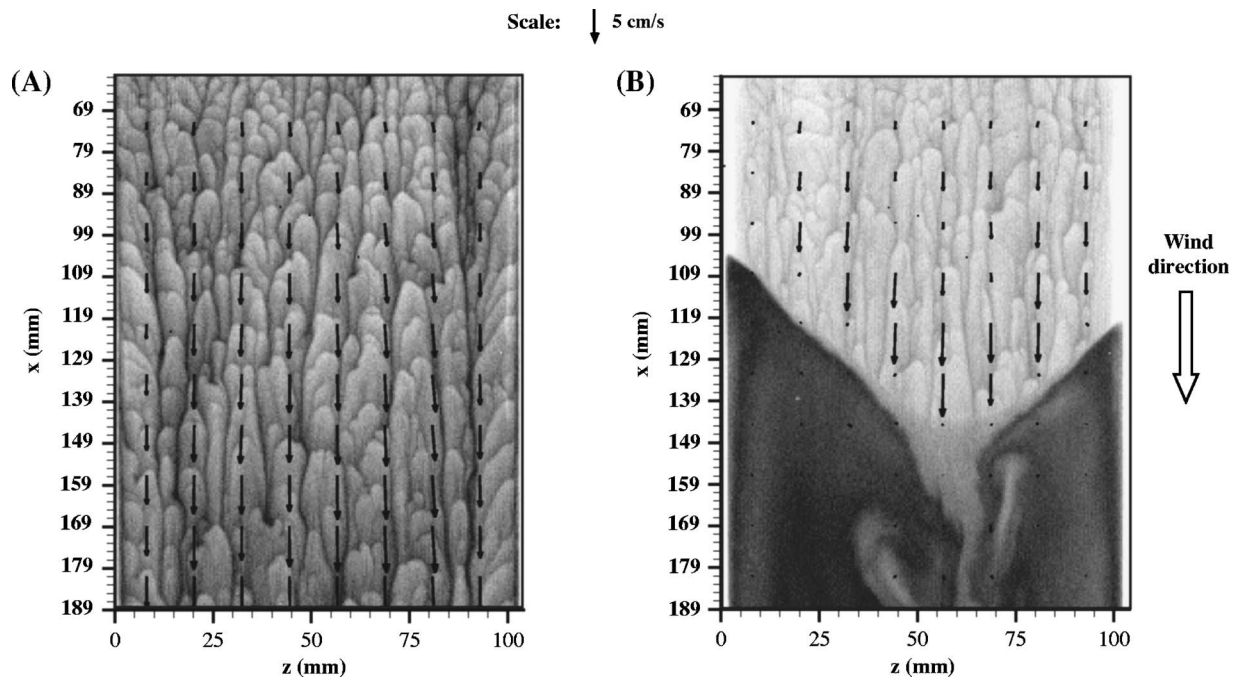


**Fig. 7 Surface velocity vector maps superimposed on IR images for: (a) clean surface at a wind speed of 5.1 m/s, and (b) contaminated case at a wind speed of 6.7 m/s**

its surface value.

The velocity field data at the wind speed of 6.7 m/s was selected for the discussion of the contaminated case. The result is shown in Fig. 6 and displayed similarly as that in the clean case. Dashed lines are used to demark the three common regions shared by the IR image and the DPIV velocity vectors: (1) the upstream point from the leading edge, (2) the location of the Reynolds ridge (at 144 mm in the  $x$  direction), and (3) the downstream section. The near surface velocity is seen to decrease as it approaches the Reynolds ridge, dropping from 5.4 to 3.8 cm/s. The vector plot, as shown in Fig. 6, displays the growth of the boundary layer beneath the surfactant film. In this case, there is a favorable pressure gradient in the BL region that overcomes the recirculation zone and pushing it deeper into the bulk (not shown). Here, the BL thickness is approximately 37 mm. Furthermore, the near surface velocity behind the ridge slowly decreases because of the compressed surfactant film. This similar feature was also observed and reported by Warncke et al. [12] in the case of the formation of a Reynolds ridge with a surface current and contaminated interface.

#### 4 Discussion

Past research efforts have relied primarily on techniques associated with quantifying the hydrodynamics of the flow, i.e., direct visualization [2], slope detection [9,11], and simultaneous measurements of surface slope and subsurface velocity field [12] to locate the Reynolds ridge. The use of thermal imaging provides a simplified approach to detecting the Reynolds ridge.

In this work, the laminae in the clean region of each IR image can be used to determine the free surface drift velocity. Handler et al. [19] have demonstrated a relationship between the laminae and the characteristic cross-stream length scale ( $\lambda$ ). Here,  $\lambda$  is defined as  $\lambda = 100\nu/u^*$  where  $\nu$  is the water kinematic viscosity ( $\nu = \mu/\rho$  where  $\mu$  and  $\rho$  are water viscosity and density, respectively) and  $u^*$  is the friction velocity in water. For all of our experimental cases,  $u^*$  was estimated to be in range of 1–2 cm/s, which is approximately 0.2% of the wind speed. In addition, the wind shear ( $\tau$ ), which is defined as  $\tau = (u^*)^2\rho$ , was estimated to be in the range of 0.1–0.3 N/m<sup>2</sup>. From this perspective, these fishscale structures

can be used to determine the surface drift velocity by tracking the downstream displacement of these thermal patterns using a cross-correlation technique. The result of the drift velocity vector is displayed in Fig. 7. The information provided by IR surface thermal structures, such as the surface drift velocity, can be used to “fill in” the gap in reliable velocity data; this is a straightforward technique for providing planar velocities. The result indicates the existence of the transition region closer to the leading edge of the channel. The drift velocity in the fully developed region is estimated to be about 2% of the applied wind speed. Hence, the friction velocity in water is approximately 10% of the drift velocity in this study.

Phongikaroon et al. [20] and Judd et al. [22] have provided simplified versions of the stress balance given in Warncke and Gharib [23]. The balance in the vicinity of the Reynolds ridge is between the external wind shear, the Marangoni stress from the surface tension ( $\sigma$ ) gradient, and the shear stress in the water at the interface. In this study, the shear viscosities of the surfactant film can be neglected [24]; therefore, the interfacial stress term describing the rheological effects at the interface is disregarded. The equation after coordinate transformation can be written as follows:

$$\tau + \partial\sigma/\partial x = -\mu(\partial U/\partial y) \quad (4)$$

where  $x$  is the streamwise coordinate with a positive sign pointing downstream and  $y$  is the vertical coordinate with a positive sign pointing from the water surface into the water column (as shown in Figs. 5 and 6). In the clean case, the surface tension gradient can be omitted, and  $\tau$  is simply balanced by  $-\mu(\partial U/\partial y)$ . It is important to point out that since  $\partial U/\partial y$  is negative,  $-\mu(\partial U/\partial y)$  becomes positive and balances with  $\tau$ , which is positive in this specified coordinate system. In the vicinity of the Reynolds ridge, the term  $\partial\sigma/\partial x$  is negative. This implies that there is an abrupt change in  $\partial U/\partial y$  near the water interface. In fact, from Eq. (4), it is possible that the velocity gradient term could be reduced to almost zero in the close vicinity of the Reynolds ridge itself.

The results of temperature pdfs reveal that the variations in temperature at the free surface exist from both evaporative and forced convective (wind) processes. By extracting self-similarity,

it can be observed that these thermal structures undergo the same evaporative process and that the wind only enhances this condition. Other existing issues involve the physics of angle formation by the ridge with the channel wall and the recirculation regions. It is felt that any predictive model attempting to simulate more realistic flow scenarios involving air/water interactions must account for the observed phenomena. Thus, such experiments may serve as simple benchmark cases that can be used to validate simulations.

### Acknowledgment

This work is supported by the National Research Council (NRC) Postdoctoral Fellowship through the Naval Research Laboratory and the Office of Naval Research. The authors thank Professor K. A. Flack at the U.S. Naval Academy for lending us the wind tunnel and Dr. R. A. Handler and Dr. G. B. Smith for contributing important suggestions.

### References

- [1] Davies, J. T., and Rideal, E. K., 1963, *Interfacial Phenomena*, Academic Press, New York, Chap. 7.
- [2] McCutchen, C. W., 1970, "Surface Films Compacted by Moving Water: Demarcation Lines Reveal Film Edges," *Science*, **170**, pp. 61–64.
- [3] Davies, J. T., 1972, "Turbulence Phenomena at Free Surfaces," *AIChE J.*, **18**(1), pp. 169–1973.
- [4] Franklin, B., Brownrigg, W., and Farish, 1774, "Of the Stilling of Waves by means of Oil. Extracted from Sundry Letters between Benjamin Franklin, LL. D. F. R. S. William Brownrigg, M. D. F. R. S., and the Reverend Mr. Farish," *Philos. Trans. R. Soc. London*, **64**, pp. 445–460.
- [5] Reynolds, O., 1900, *Papers on Mechanical and Physical Subjects, by Osborne Reynolds Reprinted from Various Transactions and Journals. Vol. 1*, Cambridge University Press, Cambridge, pp. 411–412.
- [6] Satterly, J., and Mills, W. J. P., 1927, "The Ripple in Front of an Ascending Liquid Surface," *Trans. R. Soc. Canada*, **3**, pp. 277–297.
- [7] Satterly, J., and Turnbull, R., 1929, "The Ridge at the Junction of Clean and Contaminated Liquid Surfaces," *Trans. R. Soc. Canada*, **23**, pp. 95–118.
- [8] Hall, R. O., 1936, "Lines on the Surface of Moving Water," *Nature (London)*, **138**, pp. 466.
- [9] Sellin, R. H. J., 1968, "Existence of a Surface Tension Discontinuity at a Liquid Free Surface," *Nature (London)*, **217**, pp. 536–538.
- [10] Harper, J. F., and Dixon, J. N., 1974, "The Leading Edge of a Surface Film on Contaminated Flowing Water," *Proc. Fifth Australasian Conference on Hydraulics and Fluid Mechanics*, University of Canterbury, Christchurch, New Zealand, pp. 499–505.
- [11] Scott, J. C., 1982, "Flow Beneath a Stagnant Film on Water: the Reynolds Ridge," *J. Fluid Mech.*, **116**, pp. 283–296.
- [12] Warncke, A., Gharib, M., and Roesger, T., 1996, "Flow Measurements Near a Reynolds Ridge," *ASME J. Fluids Eng.*, **118**, pp. 621–624.
- [13] Woodcock, A. H., 1941, "Surface Cooling and Streaming in Shallow Fresh and Salt Water," *J. Mater. Res.*, **4**(2), pp. 153–161.
- [14] Scott, J. C., 1972, "The Influence of Surface-Active Contamination on the Initiation of Wind Waves," *J. Fluid Mech.*, **56**(3), pp. 591–606.
- [15] Romano, J. C., 1996, "Sea-Surface Slick Occurrence in the Open Sea (Mediterranean, Red Sea, Indian Ocean) in Relation to Wind Speed," *Deep-Sea Res.*, Part I, **43**(4), pp. 411–423.
- [16] Saylor, J. R., Smith, G. B., and Flack, K. A., 2000, "The Effect of a Surfactant Monolayer on the Temperature Field of a Water Surface Undergoing Evaporation," *Int. J. Heat Mass Transfer*, **43**, pp. 3073–3086.
- [17] Willert, C. E., and Gharib, M., 1991, "Digital Particle Image Velocimetry," *Exp. Fluids*, **10**, pp. 181–183.
- [18] Volino, R. J., and Smith, G. B., 1999, "Use of Simultaneous IR Temperature Measurements and DPIV to Investigate Thermal Plumes in a Thick Layer Cooled From Above," *Exp. Fluids*, **27**, pp. 70–78.
- [19] Handler, R. A., Smith, G. B., and Leighton, R. I., 2001, "The Thermal Structure of an Air-Water Interface at Low Wind Speeds," *Tellus, Ser. A*, **53A**, pp. 233–244.
- [20] Phongikaroon, S., Judd, K. P., Smith, G. B., and Handler, R. A., 2004, "The Thermal Structure of a Wind-Driven Reynolds Ridge," *Exp. Fluids*, **37**, pp. 153–158.
- [21] Handler, R. A., Leighton, R. I., Smith, G. B., and Nagaosa, R., 2003, "Surfactant Effects on Passive Scalar Transport in a Fully Developed Turbulent Flow," *Int. J. Heat Mass Transfer*, **46**, pp. 2219–2238.
- [22] Judd, K. P., Phongikaroon, S., Smith, G. B., and Handler, R. A., 2005, "Thermal Structure of Clean and Contaminated Free-Surfaces Subjected to an Impinging Gas Jet," *Exp. Fluids*, **38**, pp. 99–111.
- [23] Warncke, A., and Gharib, M., 2000, "Experimental Study of the Wake Behind a Surface-Piercing Cylinder for a Clean and Contaminated Free Surface," *J. Fluid Mech.*, **402**, pp. 109–136.
- [24] Vogel, M. J., and Hirs, A. H., 2002, "Concentration Measurements Downstream of an Insoluble Monolayer Front," *J. Fluid Mech.*, **472**, pp. 283–305.

# Hybrid Particle/Grid Method for Predicting Motion of Micro- and Macrofree Surfaces

Eiji Ishii

Mechanical Engineering Research Laboratory,  
Hitachi, Ltd.,  
832-2, Horiguchi, Hitachinaka,  
Ibaraki 312-0034, Japan  
e-mail: eishii.ishii.pk@hitachi.com

Toru Ishikawa

Yoshiyuki Tanabe

Automotive Systems,  
Hitachi, Ltd.,  
2520 Takaba, Hitachinaka,  
Ibaraki 312-8503, Japan

*We developed a method of hybrid particle/cubic interpolated propagation (CIP) to predict the motion of micro- and macrofree surfaces within gas-liquid flows. Microfree surfaces (smaller than the grid sizes) were simulated with the particle method, and macrofree surfaces (larger than the grid sizes) were simulated with the grid method (CIP is a kind of grid method). With the hybrid, velocities given by the advection part of the particle method were combined with those given by the advection part of CIP. Furthermore, the particles used with the particle method were assigned near the macrofree surfaces by using the volume fraction of liquid that was calculated with CIP. The method we developed was used to predict the collapse of a liquid column. Namely, it was simultaneously able to predict both large deformation in the liquid column and its fragmentation, and the predicted configurations for the liquid column agreed well with the experimentally measured ones. It was also used to predict the behavior of liquid films at the outlet of a fuel injector used for automobile engines. The particle method in the simulation was mainly used for liquid films in the air region and the grid method was used for the other regions to shorten the computational time. The predicted profile of the liquid film was very sharp in the air region where the liquid film became thinner than the grid sizes; there was no loss of liquid film with numerical diffusion.*

[DOI: 10.1115/1.2234784]

## Introduction

Fine atomization of the liquid jet from the fuel injector in automobile engines lowers engine emissions and improves fuel efficiency. Breakup behaviors of liquid films into droplets near the injector outlet are strongly related to this atomization. However, it is difficult to simultaneously simulate microlevel free surfaces like droplets and macrolevel free surfaces like liquid films, because the computational grid scales used in computational fluid dynamics limit the minimum scale of the free surfaces. The behavior of liquid films at the injector outlet have mainly been simulated with the Eulerian method. However, it causes a loss of liquid film with numerical diffusion, and it requires a long time for computation in terms of practical engineering because meshes finer than the thickness of liquid films must be used. There have been examples that have simulated the breakup of the liquid jet; however, most of these, e.g., Pan and Suga [1] and Tanguy et al. [2,3], have been done with simple nozzle shapes. From the aspect of practical engineering, simulations to achieve more complex nozzle shapes are needed to design injectors that can provide fine atomization.

Numerous methods have been proposed to solve the free surface problems between a gas and a liquid, and these can be grouped into two categories, i.e., Eulerian or Lagrangian methods. The Eulerian methods can be further classified into two types of numerical approaches. The first is based on the front tracking method where Unverdi and Tryggvason [4] explicitly represented free surfaces through connected marker points. The advantage of their approach was that it reduced the number of nodes representing the front and avoided introducing numerical diffusion, which smooths out the free surface. The second approach is the front capturing method where the front of the free surface is directly captured on regular, fixed grids that cover both liquid and gas

domains. For example, Harlow and Welch's marker-and-cell method [5] uses marker particles to identify each fluid. Hirt and Nichols' volume of fluid (VOF) method [6] is widely used, and the free surface is defined as the change in the volume fraction of liquid. Sussman et al.'s level set method [7] uses the level set function to determine the location of the free surface. A reinitialization of the level set function is required to maintain the characteristics of the distance function near the free surface.

Lagrangian methods are suitable for moving boundary problems because they permit free surfaces to be precisely followed to the boundaries and they allow surface boundary conditions to be easily applied (see Ref. [8]). Enright et al.'s hybrid particle level set [9] is another Lagrangian method; it combines the best properties of the level set method and the marker particle Lagrangian scheme. It randomly places a set of marker particles near the free surface and allows them to passively advect with the flow; this obtains a subgrid scale accuracy near the free surface with the level set method. Evans and Harlow's particle-in-cell (PIC) [10], Brackbill and Ruppel's fluid-implicit-particle [11], and Tanaka's cubic interpolation with volume/area coordinate (CIVA)-particle method [12] also use a number of marker particles to describe the spatial distributions of the free surface. PIC uses a number of particles to describe the spatial distributions of variables within a cell, and the particles are used to calculate the convection terms.

Yabe and Aoki's method of cubic interpolated propagation (CIP) [13] is similar to PIC. CIP calculates the advection equations by interpolating the spatial distributions of variables within an upper-wind cell by using a cubic-polynomial function; the advection equation is calculated in third order precision, and a sharp profile of the free surface is obtained. The governing equations, except for the advection terms, are discretized using the finite-difference method.

The Lagrangian particle methods use particles that move as a fully Lagrangian description. Gingold and Monaghan's smooth particle hydrodynamic method [14] is grid-free; the spatial derivatives are derived from using the kernel function of distances among particles. Koshizuka et al.'s moving particle semi-implicit (MPS) method [15] was developed to analyze incompressible

Contributed by the Fluids Engineering Division of ASME for publication in the JOURNAL OF FLUIDS ENGINEERING. Manuscript received December 19, 2004; final manuscript received February 28, 2006. Review conducted by Joseph Katz. Paper presented at the 2004 ASME Heat Transfer/Fluids Engineering Summer Conference (HT-FED2004), July 11–15, 2004, Charlotte, NC.

flows using particle motions without the need for grids. The free surfaces are recognized according to the decrease in the particle number density. Governing equations are transformed to interactions among particles. The particles then move as a fully Lagrangian description in the advection step; this avoids introducing the loss of free surfaces with numerical diffusion. The nonadvection equations are explicitly solved, while Poisson's equation of pressure is implicitly solved.

In calculating the liquid jet from fuel injectors for automobile engines, the main difficulty in using the front capturing methods is that when the liquid film at the outlet of the injector becomes too thin to be adequately resolved on the grid, the level set method and CIP lose mass while VOF forms "blobby" filaments that locally enforce mass conservation. We developed a hybrid method that combines MPS and CIP to predict the motion of both micro- and macrofree surfaces. We used MPS to predict the motion of microfree surfaces (smaller than grid sizes), and CIP to predict the motion of macrofree surfaces (larger than grid sizes). Furthermore, to fit the complex boundaries of flow passes within injectors, we used a CIP code that was combined with the finite-volume method using unstructured grid spaces [16]. Velocities given by the advection part of MPS were combined with those given by the advection part of CIP with the hybrid method. Furthermore, the particles for MPS were assigned near the macrofree surfaces by using the volume fraction of liquid that was calculated with CIP.

We used the new method to predict fragmentation in a liquid column. That is, it was used to predict both large deformation in the liquid column and its fragmentation simultaneously, and the predicted configurations for the water column agreed well with measurements done by Koshizuka et al. [15]. It was also applied to simulating a liquid jet from a fuel injector for automobile engines. We only focused on the flow field near the injector outlet, and tried to simulate the motions of liquid films by using groups of particles in MPS. The particle method in the simulation was mainly used for the liquid films in the air region and the grid method was used for the other regions to shorten the computational time. The predicted profile for the liquid film was very sharp in the air region where the liquid film became thinner than the grid sizes; there was no loss of liquid film with numerical diffusion.

## Formulation

**MPS Method.** MPS was developed by Koshizuka et al. [15] to analyze incompressible flows based on particle motion. Particle interaction models are prepared corresponding to differential operators. Governing equations are transformed to interactions among particles. Grids are not necessary. The particles move as a fully Lagrangian description. Incompressibility is implicitly incorporated in the algorithm by solving Poisson's equation of pressure, while other terms are explicitly calculated.

Mass and momentum conservation equations for incompressible flow are written as

$$\frac{D\rho}{Dt} = 0 \quad \text{and} \quad (1)$$

$$\rho \frac{D\vec{u}}{Dt} = -\nabla p + \mu \nabla^2 \vec{u} + \rho \vec{g} \quad (2)$$

where the left sides of Eqs. (1) and (2) indicate Lagrangian differentiation including convection terms. The mass conservation equation is represented by the density being constant. Since fully Lagrangian description is employed in MPS, the convection terms are not explicitly considered. First, the viscous and gravitation terms are explicitly calculated and the Laplacian operator is written as

$$(\nabla^2 \phi)_i = \frac{2d}{\lambda n_0} \sum_{j \neq i} (\phi_j - \phi_i) w(|r_j - r_i|) \quad (3)$$

where  $\phi_i$  and  $r_i$  are the scalar quantity and coordinates of particle  $i$ , respectively,  $d$  is the number of spatial dimensions, and  $n_0$  is the particle number density. All the interactions are limited among the neighboring particles within a weight function. The  $w$  in Eq. (3) is the weight function that defines particle interactions and is written as

$$w(r_{ij}) = \begin{cases} \frac{r_e}{r_{ij}} - 1 & (r_{ij} \leq r_e) \\ 0 & (r_{ij} > r_e) \end{cases} \quad (4)$$

where  $r_{ij}$  is the distance between two particles, and  $r_e$  is the radius of the interaction area between them. Particle number density  $n_i$  and parameter  $\lambda$  are defined as

$$n_i = \sum_{j \neq i} w(|r_j - r_i|) \quad \text{and} \quad (5)$$

$$\lambda = \frac{\sum_{j \neq i} |r_j - r_i|^2 w(|r_j - r_i|)}{\sum_{j \neq i} w(|r_j - r_i|)} \quad (6)$$

After the source terms are calculated, the motion of particles is calculated using a fully Lagrangian description. The continuity equation requires the particle number density to be constant, i.e.,  $n_i = n_0$ , and the Poisson equation of pressure is solved with a source term representing deviations in the particle number density from  $n_0$

$$\langle \nabla^2 p \rangle_i = \frac{\rho}{\Delta t^2} \frac{n_i - n_0}{n_0} \quad (7)$$

Finally, the velocities are modified with the new time pressure

$$\delta u = -\frac{\Delta t}{\rho} \nabla p \quad (8)$$

where the pressure gradient is defined by

$$(\nabla p)_i = \frac{d}{n_0} \sum_{j \neq i} \left[ \frac{p_j - p_i}{|r_j - r_i|^2} (r_j - r_i) w(|r_j - r_i|) \right] \quad (9)$$

The particle coordinates are also modified with new velocities.

**CIP Method.** The governing equations for fluid flow are written as

$$\frac{\partial f}{\partial t} + u_j f_{,j} = g \quad (10)$$

where  $f$  is a vector of dependent variables and  $g$  is a vector of source terms. Equation (10) is a nonconservative form of the convection terms, but CIP ensures good conservation [13]. Vectors  $f$  and  $g$  are given as

$$f = \begin{pmatrix} F \\ \rho \\ u_i \\ p \end{pmatrix} \quad g = \begin{pmatrix} 0 \\ -\rho u_{j,j} \\ -\frac{1}{\rho} p_{,i} + \frac{1}{\rho} \tau_{ij,j} \\ -\rho C_s^2 u_{j,j} \end{pmatrix} \quad (11)$$

where  $F$  is a tangent function of the volume fraction of liquid  $\theta_{\text{CIP}}$ ,  $\rho$  is density, and  $u_i$  is a velocity component. Here,  $p$  is pressure and  $C_s$  in the pressure equation is the speed of sound. With CIP,  $F$  is transformed into  $\theta_{\text{CIP}}$



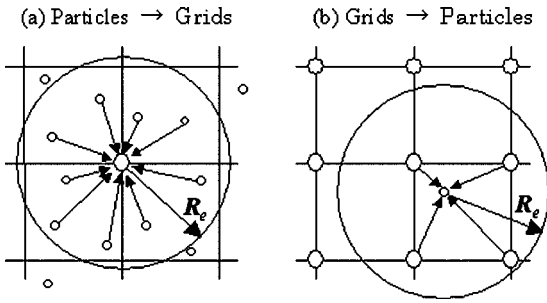


Fig. 1 Interpolation between particle coordinates and grid coordinates

$$\theta_{CIP} = \frac{\arctan(F)}{0.99\pi} + 0.5 \quad (12)$$

Note that  $\theta_{CIP}$  is limited to being close to 0 or 1 ( $\theta_{CIP}=0$  in gas;  $\theta_{CIP}=1$  in liquid) because of the tangent function. The density, viscosity, and speed of sound in the gas-liquid flow are given as

$$\rho = \rho_l \theta_{CIP} + \rho_g (1 - \theta_{CIP}) \quad (13)$$

$$\mu = \mu_l \theta_{CIP} + \mu_g (1 - \theta_{CIP}) \quad \text{and} \quad (14)$$

$$C_s = C_{sl} \theta_{CIP} + C_{sg} (1 - \theta_{CIP}) \quad (15)$$

Here, subscripts *l* and *g* mean liquid and gas. The CIP method can be used for both compressible and incompressible flow (Eq. (15) is used to change the speed of sound in gas or liquid), and Eq. (11) is solved through a procedure that is almost the same as an incompressible solver [13]. Furthermore, the compressibility of the gas region in this study was so weak that Eq. (11) was solved as an almost incompressible flow with the CIP method. Equation (10) is split into advection and nonadvection equations using a time-splitting procedure

$$\frac{\partial f}{\partial t} + u_j f_{,j} = 0 \quad \text{and} \quad (16)$$

$$\frac{\partial f}{\partial t} = g \quad (17)$$

The advection (Eq. (16)) is solved first, followed by the nonadvection equation. Yabe et al. [13] proposed a method of solving Eq. (16) by interpolating spatial distributions of variables within a cell by using a cubic-polynomial function, i.e., third order precision for solving the advection equation (16). Nonadvection (Eq. (17)) is solved after solving Eq. (16) using the fractional-step method [17]. To fit the complex boundary of flow pass within injectors, we used the finite-volume method using unstructured

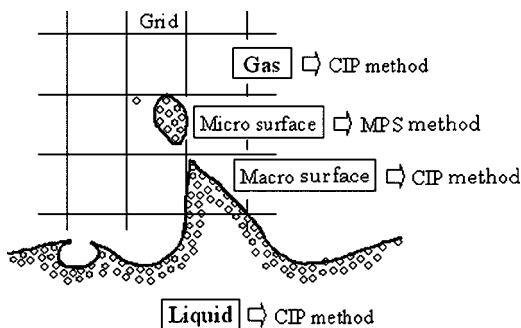


Fig. 2 Assignment of CIP and MPS method to predict free surfaces in gas-liquid flows

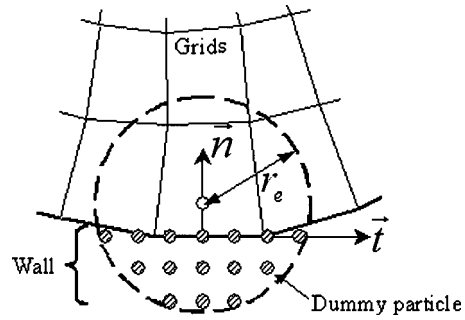


Fig. 3 Boundary condition of MPS at wall

grid spaces [16], where variables were located in the center of each cell.

**Hybrid Particle/CIP Method.** We combined velocities given by the advection part of the MPS method with those given by the advection part of CIP, and the velocities were interpolated in terms of the particle coordinates and grid coordinates. Figure 1(a) shows the interpolation from particle coordinates to grid coordinates, and the interpolation function is written as

$$\tilde{u}_{(MPS)} = \frac{\sum_{i \neq j} \tilde{u}_{(MPS)} W(R_{ij})}{\sum_{i \neq j} W(R_{ij})} \quad (18)$$

where  $\tilde{u}_{MPS}$  is velocity given in terms of particle coordinates, which is given by the advection part of the MPS method, and

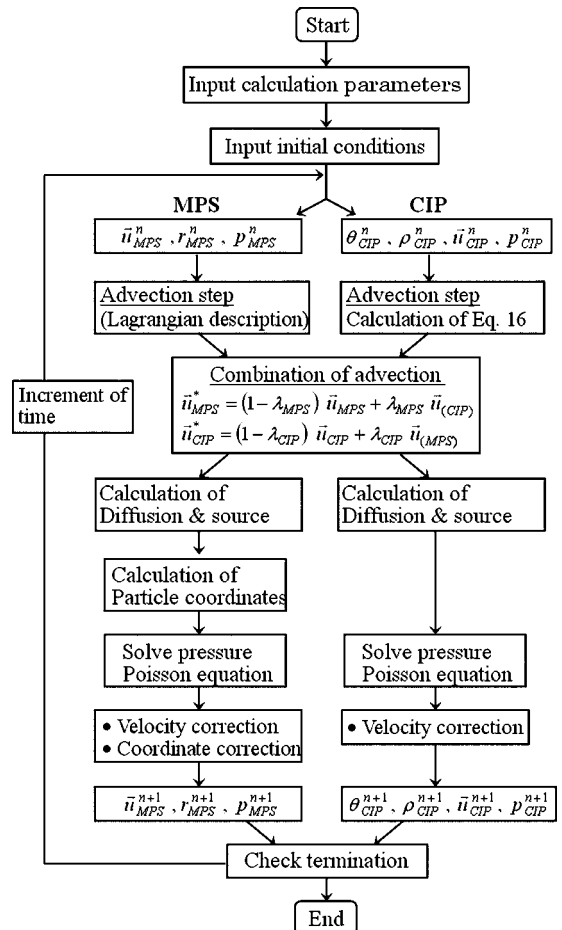


Fig. 4 Calculation algorithm for present method

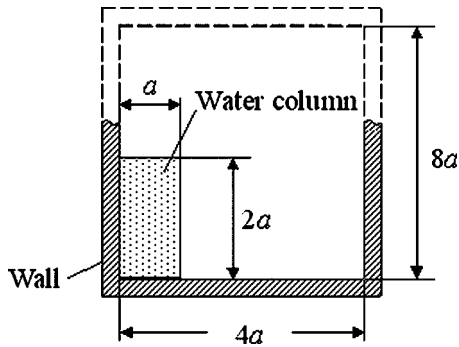


Fig. 5 Geometry for collapse of water column

$\vec{u}_{(MPS)}$  is velocity interpolated in terms of grid coordinates. Furthermore,  $R_{ij}$  is the distance between a particle and a grid. Weight function  $W(R_{ij})$  in Eq. (18), which has the same formulation as that with the MPS method, is written as

$$W(R_{ij}) = \begin{cases} \frac{R_e}{R_{ij}} - 1 & (R_{ij} \leq R_e) \\ 0 & (R_{ij} > R_e) \end{cases} \quad (19)$$

where  $R_e$  is defined as a larger value than the grid sizes. Figure 1(b) shows interpolation from grid coordinates to particle coordinates. The interpolation function is written as

$$\vec{u}_{(CIP)} = \frac{\sum_{i \neq j} \vec{u}_{CIP} W(R_{ij})}{\sum_{i \neq j} W(R_{ij})} \quad (20)$$

where  $\vec{u}_{CIP}$  is velocity given in terms of grid coordinates, which is given by the advection part of CIP, and  $\vec{u}_{(CIP)}$  is velocity interpolated in terms of particle coordinates.

Velocity  $\vec{u}_{MPS}$  given by the advection part of the MPS method is combined with velocity  $\vec{u}_{(CIP)}$  given in Eq. (20) and is then modified as follows:

$$\vec{u}_{MPS}^* = (1 - \lambda_{MPS}) \vec{u}_{MPS} + \lambda_{MPS} \vec{u}_{(CIP)} \quad (21)$$

Here,  $\lambda_{MPS}$  is written as

$$\lambda_{MPS} = \begin{cases} 0 \leftarrow \text{gas} & (\theta_{(CIP)} < \theta_{\min}) \\ (\theta_{(CIP)} - \theta_{\min}) / (\theta_{\max} - \theta_{\min}) & (\theta_{\min} \leq \theta_{(CIP)} \leq \theta_{\max}) \\ 1 \leftarrow \text{liquid} & (\theta_{(CIP)} > \theta_{\max}) \end{cases} \quad (22)$$

where  $\lambda_{MPS}$  changes from 0 to 1 between gas and liquid regions. Furthermore,  $\theta_{(CIP)}$  is the volume fraction of liquid given by the particle coordinates and is calculated by

$$\theta_{(CIP)} = \frac{\sum_{i \neq j} \theta_{CIP} W(R_{ij})}{\sum_{i \neq j} W(R_{ij})} \quad (23)$$

Here,  $\theta_{CIP}$  is the volume fraction of liquid calculated using CIP in terms of the grid coordinates, and  $\theta_{\min}$  and  $\theta_{\max}$  were, respectively, set to 0.2 and 0.8 in this study. Equation (21) shows that modified velocity  $\vec{u}_{MPS}^*$  is equal to velocity  $\vec{u}_{(MPS)}$  when a particle is in the gas region ( $\lambda_{MPS}=0$ ). However, modified velocity  $\vec{u}_{MPS}^*$  is equal to velocity  $\vec{u}_{(CIP)}$  when a particle is in the liquid region

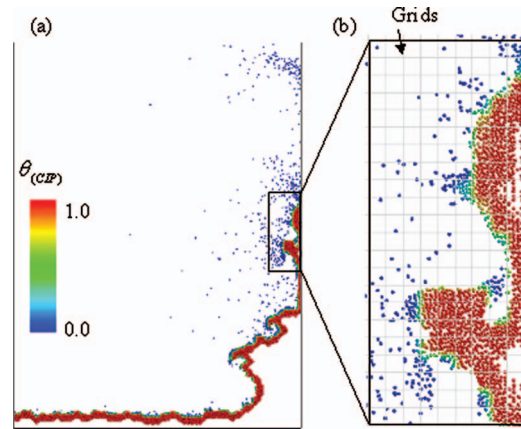


Fig. 7 Distribution of volume fraction of liquid  $\theta_{(CIP)}$  in terms of particle coordinates at 0.7 s

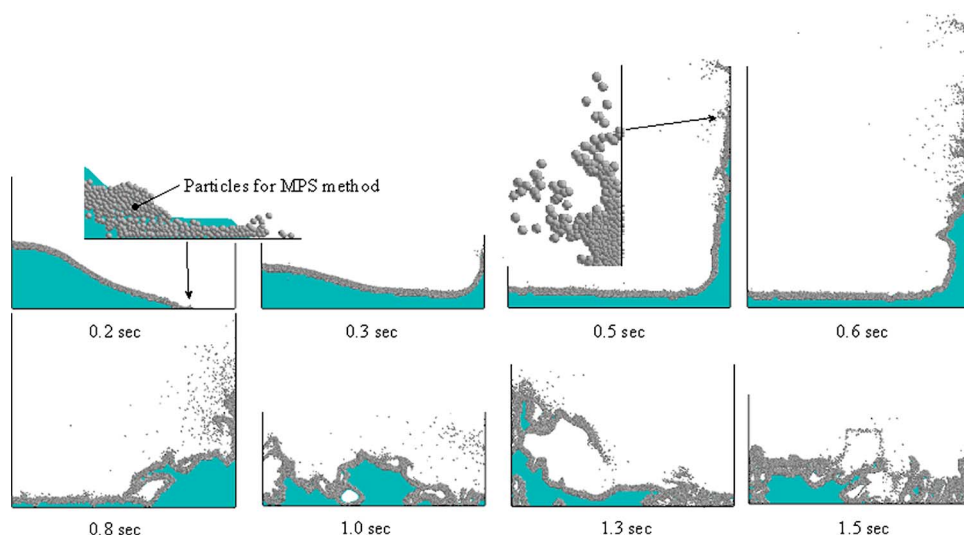
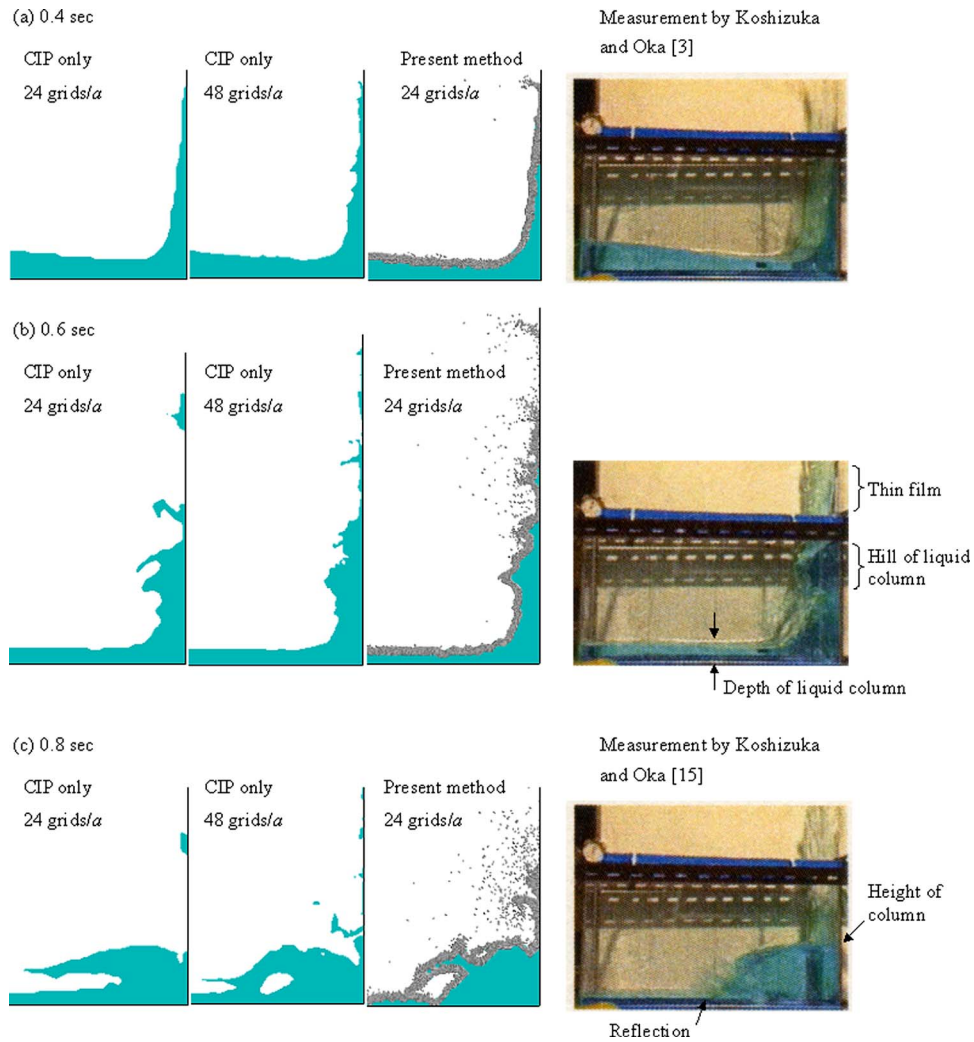


Fig. 6 Collapse of water column. Twenty-four grids are assigned per width  $a$ , and 120 particles are initially assigned per width  $a$  near free surface of water column.



**Fig. 8** Grid/number-of-density sensitivity study. Estimation of recovered scale with MPS by comparing cases using CIP with 24 and 48 grids per width  $a$  for water column: (a) 0.4, (b) 0.6, and (c) 0.8 s.

( $\lambda_{MPS}=1$ ).

With CIP, velocity  $\vec{u}_{CIP}$  given by the advection part is combined with velocity  $\vec{u}_{(MPS)}$  given in Eq. (18), and is then modified as follows:

$$\vec{u}_{CIP}^* = (1 - \lambda_{CIP})\vec{u}_{CIP} + \lambda_{CIP}\vec{u}_{(MPS)} \quad (24)$$

Here,  $\lambda_{CIP}$  is written as

$$\lambda_{CIP} = (1 - \alpha)\beta \quad (25)$$

where

$$\alpha = \begin{cases} 0 \leftarrow \text{gas} & (\theta_{CIP} < \theta_{min}) \\ (\theta_{CIP} - \theta_{min}) / (\theta_{max} - \theta_{min}) & (\theta_{min} \leq \theta_{CIP} \leq \theta_{max}) \\ 1 \leftarrow \text{liquid} & (\theta_{CIP} > \theta_{max}) \end{cases} \quad (26)$$

and

$$\beta = \frac{\sum_{i \neq j} W(R_{ij})}{N_0} \quad (27)$$

Here,  $N_0$  in Eq. (27) is particle number density in liquid, and then  $\beta$  changes from 0 to 1. Furthermore  $\theta_{min}$  and  $\theta_{max}$  in Eq. (26) were set to 0.2 and 0.8, respectively. Equation (24) shows that modified velocity  $\vec{u}_{CIP}^*$  is equal to velocity  $\vec{u}_{CIP}$  when a grid is in the gas

region and particle density is 0 ( $\alpha=0$ ,  $\beta=0$ , then  $\lambda_{CIP}=0$ ). However, modified velocity  $\vec{u}_{CIP}^*$  is equal to velocity  $\vec{u}_{(MPS)}$  when a grid is in the gas region and particle density is 1 ( $\alpha=0$ ,  $\beta=1$ , then  $\lambda_{CIP}=1$ ). Furthermore, when a grid is in the liquid region ( $\beta=0$ , then  $\lambda_{CIP}=0$ ), modified velocity  $\vec{u}_{CIP}^*$  is equal to velocity  $\vec{u}_{CIP}$ . Figure 2 shows how the MPS method and CIP are assigned according to Eqs. (21) and (24) to calculate the motion of free surfaces. The motion of macrofree surfaces that are larger than the grid sizes are mainly solved with CIP, and the motion of microfree surfaces that are smaller than the grid sizes are mainly solved with the MPS method. Flow fields except those on free surfaces are solved with CIP. In the numerical grid coupling laws in Eqs. (21) and (24), control parameters that affect the numerical results are  $\theta_{min}$  and  $\theta_{max}$ ; the ranges of  $\theta_{min}$  and  $\theta_{max}$  are  $0 \leq \theta_{min} < \theta_{max} \leq 1$ . As the range between  $\theta_{min}$  and  $\theta_{max}$  is a transition region between MPS and CIP, if we select a large range, numerical stability is improved; however, the interface of the free surface is smoothed out more (less fragmented). Furthermore, the surface tension effect is not used in the numerical model. A way to include the effect is to integrate Brackbill's continuum surface force (CSF) model [18] into MPS as it has been integrated into the grid method, i.e., surface force is integrated into the momentum equation, Eq. (2), in the form of a volume force. The characteristic function in the CSF model can be defined through particle distri-

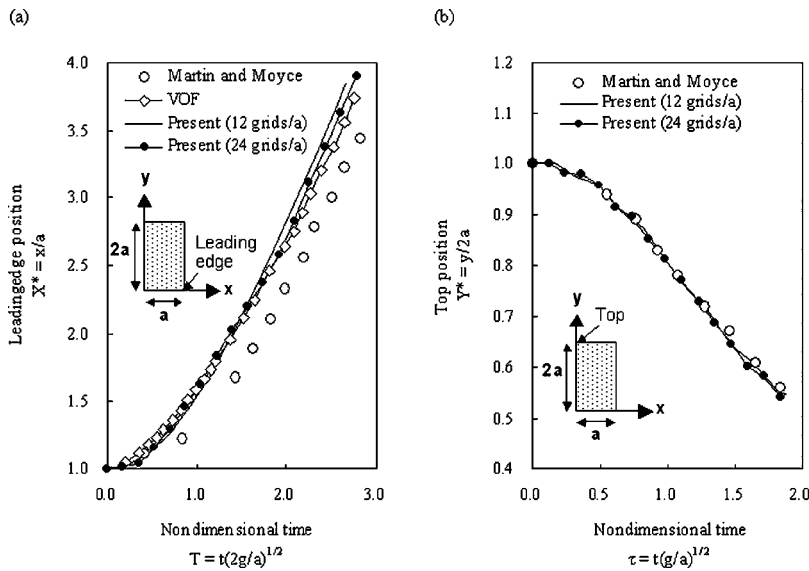


Fig. 9 Motion of leading edge and top of water column

bution; the characteristic function is 0 at the particle coordinates near the free surfaces and 1 at the other particle coordinates.

Figure 3 shows the wall-boundary condition used with the MPS method in a two-dimensional space. Here,  $\vec{n}$  is a normal vector,  $\vec{t}$  is a tangential vector, and  $r_e$  is the radius of the interaction area of particles. Dummy particles are generated at the wall when a particle approaches it, so the wall particles that are normally used with the MPS method have been neglected to reduce their numbers.

Figure 4 shows the standard algorithm used with the present method. The advection equation for CIP is solved by interpolating the spatial distributions of variables within a cell with a cubic-polynomial function. Velocities in the advection part of the MPS method and CIP are combined in each time step, i.e., the velocities in the terms of both particle and grid coordinates are modified by Eqs. (21) and (24). We next calculate the diffusion and source terms, and particle coordinates are calculated with the MPS method. After that, the pressure Poisson equations for both methods are solved and new time pressures are obtained. Finally, we obtain new time velocities for both methods with the pressure gradient, modifying the new time coordinates of the particles. This algorithm is basically semi-implicit time marching, which has been widely used with the grid method.

## Results and Discussion

**Application to Collapse of Water Column.** We applied our present method to the collapse of a water column. Figure 5 out-

lines the geometry for the collapse of a water column; it has the same dimensions as those in the experiment done by Koshizuka et al. [15]. The water column is located on the left vertical wall, and the initial width of the column is  $a$  and its height is  $2a$ , where  $a$  is 146 mm. The computational domain is  $4a \times 8a$ , where all boundaries are defined as walls.

Figure 6 shows the predicted configuration for a collapsing water column with the present method. In the calculation, 24 grids are assigned per width  $a$ , and 120 particles are initially assigned per width  $a$  within a range of three meshes from the free surface. The figure shows that the particles are only assigned near the free surface, predicting fragmentation of the water column. At 0.2 s, the right side of the water column slides to the right. At 0.3 s, the collapsing water runs into the right vertical wall and rises. The rising water forms a thin film along the vertical wall, and stops rising at 0.5 s, while the film continues to fragment. The film falls due to gravity at 0.6 s. At 0.8 s, the left side of the falling water hits the water at the bottom wall, and splashes toward the left vertical wall at 1.0 s. After that, the water column returns to the right vertical wall at 1.3 and 1.5 s.

Figure 7(a) shows the distribution in the volume fraction of liquid  $\theta_{(CIP)}$  calculated with Eq. (23) (blue area:  $\theta_{(CIP)}=0$ , red:  $\theta_{(CIP)}=1$ ) in terms of the particle coordinates, where Fig. 7(b) is an enlarged portion of Fig. 7(a). According to Eq. (21), motion on the macrofree surfaces (larger than grid sizes) are mainly calculated with CIP, and their fragmentation (smaller than grid sizes) is done with the MPS method.

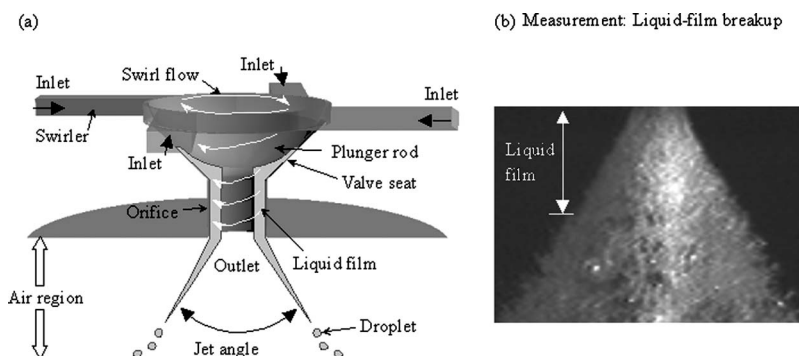


Fig. 10 Geometry for swirl fuel injector

Figure 8 shows a study done on grid/number-of-density sensitivity. We ran cases using CIP with 24 and 48 grids per width  $a$  for the water column, and we estimated the unresolved scale that was simulated with 24-grid resolution. We then checked the recovered scale with MPS with the present method. The figure also has measurements done by Koshizuka and Oka [15] to verify the configuration of the water column. At 0.4 s, the water film at the top of the column along the vertical wall, which was simulated with 24-grid resolution, is less dense with numerical diffusion than that simulated with 48-grid resolution. The loss of water film at the top of the column recovers with particles of MPS with the present method. The profile of the water column simulated with the present method agrees well with measurement. At 0.6 s, the thin water film falling down the vertical wall is more compact with 24-grid resolution than that with 48-grid resolution. Although the loss of thin water film on the wall recovers with the present method, it is more fragmented than that achieved with measurements because surface tension was neglected in the calculation. The predicted configuration for the water column agrees well with the measurements, e.g., for the profile of the hill of the water column and the depth of the water column. However, simulation cannot predict the frothy spray behavior just outside the liquid layer at the base of the hill on the vertical wall. At 0.8 s, the falling water on the left side of the column hits the water at the bottom and it is deflected to the upper left in the measurements. The contact made by the falling water is not simulated with 24-grid resolution and the present method simulates this. The predicted height of the water column on the right also agrees well with the measurements. We found that the particle motion simulated with MPS with the present method assisted the motion of macroscale free surfaces simulated with CIP. We also found that the particle motion with MPS formed on the foundation of macroscale free surfaces simulated with CIP, e.g., the deflection at the left of the water column was not simulated, which was mainly caused by the lack of grid resolution with CIP.

Figure 9 plots the predicted development of the leading edge and the top position of the column over time. Figure 9(a) plots the leading-edge position, and Fig. 9(b) plots the top position. The axes are nondimensional scales;  $T$  is the nondimensional time for the leading edge, and  $\tau$  is that for the top. Parameter  $X^*$  is the position of the leading edge at time  $T$ , and  $Y^*$  is that of the top at time  $\tau$ . We ran cases using the present method with 12 and 24

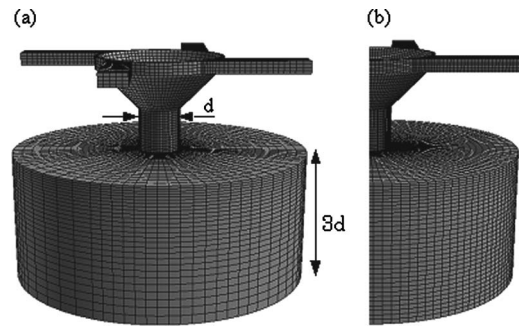


Fig. 11 Computational grids: (a) 102,884 elements and (b) 209,428 elements (half size)

grids per width  $a$  for the water column. The leading edge position simulated with 12 grids per width  $a$  moved faster than that simulated with 24 grids. This was due to the grid resolution with CIP. The results simulated with the present method were also compared with a case using the VOF method [6] and with measurements done by Martin and Moyce [19]. We found that the leading-edge position in Fig. 9(a) moved faster than that in the measurements, but the top position in Fig. 9(b) agreed well with Martin and Moyce's measurements. In Fig. 9(a), the leading-edge position simulated with VOF [6] also moved faster than the measurements. This was due to the friction between the fluid and the lower wall, which caused a rounded leading edge. The leading-edge position simulated with the present method with 24-grid resolution agreed well with that simulated with VOF until  $T = 2.0$ . However, it moved a little faster than that simulated with VOF after  $T = 2.0$ . There is a diffusion effect of the micro-macrocoupling in the MPS interface tracking that affect the accuracy of the numerical solutions. This is a necessary future work concerning MPS and artificial diffusion in the interface.

**Application to Fuel Injector.** We also applied the present method to the breakup of liquid films within the fuel injector used in direct-injection gasoline engines. Figure 10 outlines the geometry of a swirl fuel injector and the measurement for liquid-film breakup. The fuel enters the four inlets of the swirler, forming a

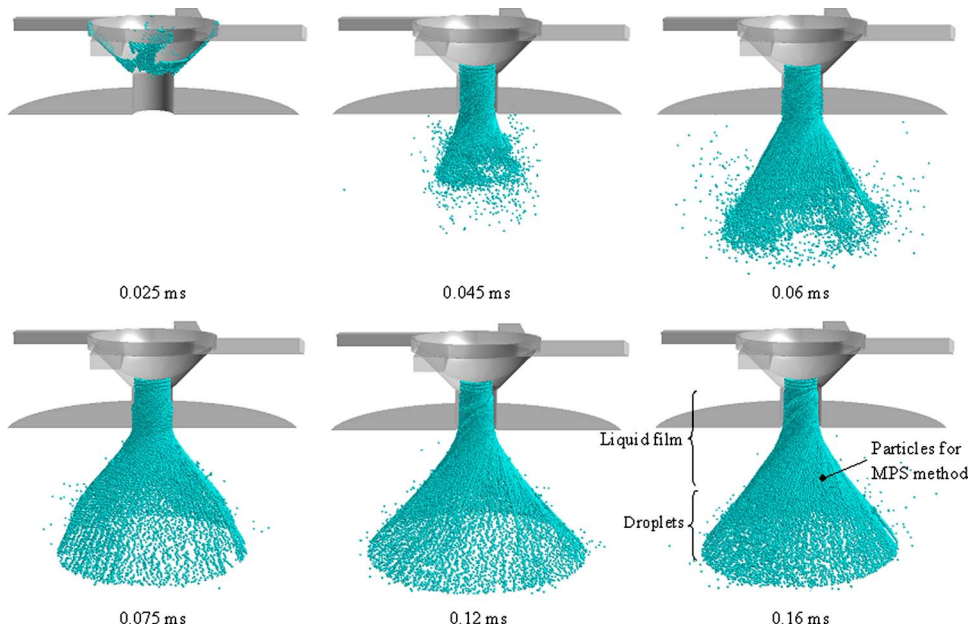
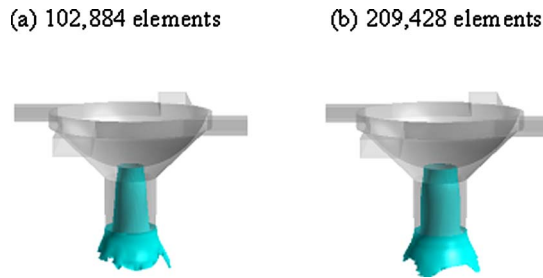


Fig. 12 Configurations for liquid films in swirl fuel injector used in automobile engines



**Fig. 13 Configurations for liquid films at 0.16 ms simulated with the VOF method**

swirled flow. Then, centrifugal force caused by the motion of the swirled flow forms a liquid film on the fuel on the inside wall of the orifice. After that, the liquid film leaves, enters the air region at the outlet of the orifice, then breaks up into droplets. Figure 11 is a computational grid; the air region is at the outlet of the orifice. We used two computational grids of 102,884 elements or 209,428 elements to study the grid resolution. Figure 11 shows half the original grids for the 209,428 elements. The densities for air and fuel in the calculation were 1.2 and 684 kg/m<sup>3</sup>, and their viscosities were  $1.81 \times 10^{-5}$  Pa s and  $4.88E-4$  Pa s. The fuel pressure at the inlet was 7.1 MPa and the pressure in the air region was 0.1 MPa.

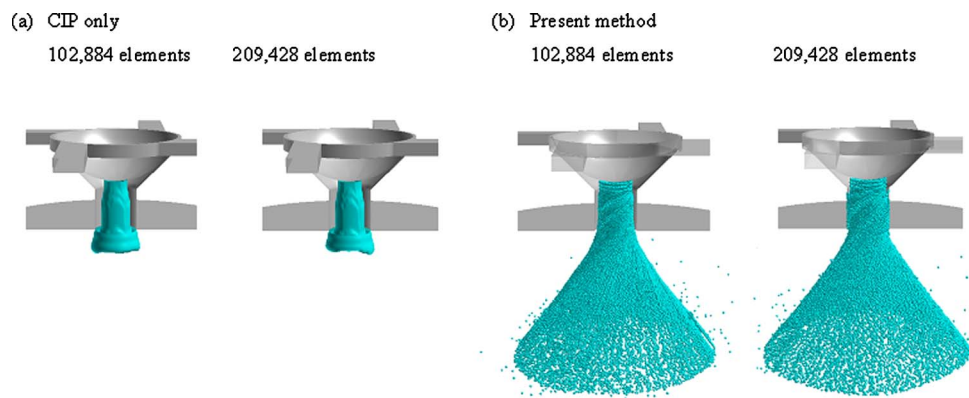
Figure 12 shows the configurations for the liquid films calculated using a grid of the 102,884 elements from 0 to 0.16 ms. The computational time was about 15 h with a 2.5 GHz, Pentium 4 processor. The light blue area indicates the number of particles used with the MPS method, which was about 30,000. As the particles have been assigned near the free surfaces of the liquid film, the configuration for the liquid film can be recognized according to the particle distributions. At 0.025 ms, the fuel is between the plunger rod and valve seat. At 0.045 ms, a liquid column is injected from the orifice. At this time, there is no liquid film on the inside wall of the orifice because of the weak swirl flow. After 0.06 ms, the jet angle gradually increases in proportion to the increasing swirl flow within the orifice. Finally, the liquid jet reaches a steady state at 0.16 ms. We find that liquid film is formed at the outlet of the orifice and the tip of the liquid film breaks up; the macroscopic behavior of the liquid-film-like jet angle agrees well with that in the experimental results in Fig. 10. However, the tip of the liquid film completely fragments into the particles, because the present method does not take the surface-tension effect into account. To predict microstructures like the breakup length and size of droplets, the surface-tension effect has been taken into consideration in the particle motion for MPS. A

way to include the effect is to integrate Brackbill's CSF model [18] into MPS as it has been integrated into the grid method, i.e., surface force is integrated into the momentum equation, Eq. (2), in the form of a volume force. It should also be noted that liquid films and droplets mean a group of particles in the present method, and the distribution of individual particles, whose particle number density defined by Eq. (5) is zero, makes no sense.

Figure 13 shows configurations for liquid films at 0.16 ms, which were simulated with the VOF method with the 102,884 and 209,428 elements. Isosurfaces are shown, where the volume fraction of the liquid is 0.5. Liquid film is formed on the inside wall of the orifice, and a cavity of air is generated at the center of the orifice; the size of the cavity simulated with the 102,884 elements is smaller than that simulated with the 209,428 elements. The liquid film enters the air region at the outlet of the orifice, and soon vanishes with numerical diffusion in both cases with the 102,884 and 209,428 elements. We need a huge number of grids in the air region to simulate the liquid film.

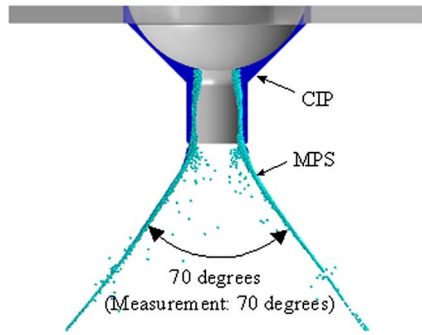
Figure 14 shows a study of grid/number-of-density sensitivity with configurations for liquid film at 0.16 ms. We ran cases using CIP with the 102,884 and 209,428 elements, and we estimated the unresolved scale that was simulated with 102,884 elements. We then checked the recovered scale with MPS using the present method. There is a case simulated with the 209,428 elements to verify our study of grid resolution with the present method. Isosurfaces are shown in Fig. 14(a), where the volume fraction of liquid is 0.5. Liquid film is formed on the inside wall of the orifice. The liquid film enters the air region at the outlet of the orifice, and soon vanishes with numerical diffusion in both cases with the 102,884 and 209,428 elements. Although this trend is the same as that simulated with VOF, the size of the liquid films at the outlet of the orifice are smaller than that simulated with VOF because the tangent function in Eq. (12) used with CIP limits the volume fraction of the liquid close to 0 or 1; only liquid films larger than the grid-sizes in the air region are shown. With VOF, there are more regions where the volume fraction of the liquid is between 0 and 1 than with CIP. We find from Fig. 14(b) that the loss of liquid film in the air region recovers with the present method, and there are few differences in the configurations for simulations with the 102,884 and 209,428 elements. However, no ligaments generated from the liquid film can be seen in Fig. 10(b) because surface tension was neglected in the calculation.

Figure 15 outlines the configuration for a liquid film in the cutting plane along the injector axis. We found that liquid film was formed on the inside wall of the orifice, and entered the air region. The tip of the liquid film then broke up into droplets. The dark-blue area represents liquid film predicted with CIP, and the light-blue area is liquid film predicted with the MPS method. We found that CIP could mainly be used within the flow pass of the injector,



**Fig. 14 Grid/number-of-density sensitivity study. Estimation of recovered scale with MPS by comparing cases using CIP with 102,884 and 209,428 elements: (a) CIP only and (b) present method.**

(a) 102,884 elements



(b) 209,428 elements

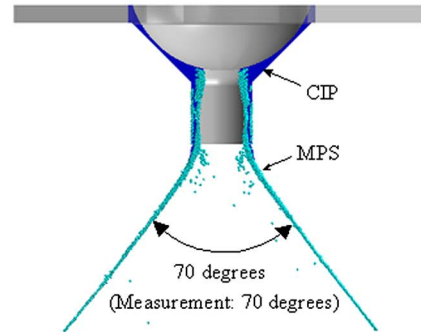


Fig. 15 Configuration for liquid film in cutting plane along injector axis

and MPS could be used for simulating liquid film in the air region. We also found that the present method was able to simulate liquid films that were thinner than the grid sizes. It was difficult to verify the thickness of liquid film because of various difficulties with the measurements. However, we could compare the jet angle predicted using the present method with the measurements. The jet angle agreed well with a measurement of 70 degrees in both cases with the 102,884 and 209,428 elements.

## Conclusion

We developed a hybrid particle/CIP method to predict the motion of micro- and macrofree surfaces within gas-liquid flows, which combined particle and grid methods (CIP itself is a kind of grid method). With the hybrid, the particle method was used to simulate microfree surfaces and the grid method was then used to simulate macrofree surfaces. Furthermore, the velocities given by the advection part of the particle method were combined with those given by the advection part of CIP. We used our new method to predict fragmentation in a liquid column and it could simultaneously predict both large deformation in the liquid column and its fragmentation. We also used it to predict the breakup of liquid films within the fuel injectors used in automobile engines. The particle method in the simulation was mainly used for liquid films in the air region and the grid method was used for the other regions to shorten the computational time. The predicted profile of the liquid film was very sharp in the air region where the liquid film became thinner than the grid sizes.

## Acknowledgment

The authors would like to thank Professor Koshizuka of the University of Tokyo for providing the images of a collapsing water column.

## Nomenclature

$C_s$	= speed of sound
$d$	= number of spatial dimensions
$f$	= vector of dependent variables
$F$	= tangent function of volume fraction of liquid
$g$	= source terms or acceleration of gravity
$n_0$	= particle number density
$N_0$	= particle number density used in Eq. (27)
$p$	= pressure
$r_e$	= radius of interaction area
$R_e$	= radius of interpolation area
$r_{ij}$	= distance between two particles
$R_{ij}$	= distance between particle and grid
$t$	= time
$T$	= nondimensional time for leading edge of water column

$u$	= velocity
$\vec{u}_{CIP}$	= velocity (calculated with CIP method) given in terms of grid coordinates
$\vec{u}_{(CIP)}$	= velocity (calculated with CIP method) interpolated in terms of particle coordinates
$\vec{u}_{MPS}$	= velocity (calculated with MPS method) given in terms of particle coordinates
$\vec{u}_{(MPS)}$	= velocity (calculated with MPS method) interpolated in terms of grid coordinates
$w$	= weight function used with MPS method
$W$	= weight function used in interpolation between particle coordinates and grid coordinates
$X^*$	= position of leading edge of water column at time $T$
$Y^*$	= position of top of a water column at time $\tau$
$\mu$	= viscosity
$\theta_{CIP}$	= volume fraction of liquid given by CIP method
$\theta_{(CIP)}$	= volume fraction of liquid given by particle coordinates
$\rho$	= density
$\tau_{ij}$	= viscous stress
$\tau$	= non-dimensional time for top of water column
$\phi$	= scalar quantity

## References

- [1] Pan, Y., and Suga, K., 2004, "Direct Simulation of Water Jet Into Air," 5th International Conference on Multiphase Flow, ICMF'04, Paper No. 377.
- [2] Tanguy, S., Ménard, T., Berlemont, A., Estivalezes, J. L., and Couderc, F., 2004, "Developpement D'une Methode Level Set Pour Le Suivi D'interfaces et Applications," Advances in the Modeling Methodologies of Two-phase flows, Lyons, France, Paper No. 13.
- [3] Tanguy, S., and Berlemont, A., 2005, "Application of a Level Set Method for Simulation of Droplet Collisions," Int. J. Multiphase Flow, **31**, pp. 1015–1035.
- [4] Unverdi, S. O., and Tryggvason, G., 1992, "A Front-Tracking Method for Viscous, Incompressible, Multi-Fluid Flows," J. Comput. Phys., **100**, pp. 25–37.
- [5] Harlow, F. H., and Welch, J. E., 1965, "Numerical Calculation of Time-Dependent Viscous Incompressible Flow of Fluid With Free Surface," Phys. Fluids, **8**, pp. 2182–2189.
- [6] Hirt, C. W., and Nichols, B. D., 1981, "Volume of Fluid (VOF) Method for the Dynamics of Free Boundaries," J. Comput. Phys., **39**, pp. 201–225.
- [7] Sussman, M., Smereka, P., and Osher, S., 1994, "A Level Set Approach for Computing Solutions to Incompressible Two-Phase Flow," J. Comput. Phys., **114**, pp. 146–159.
- [8] Floryan, J. M., and Rasmussen, H., 1989, "Numerical Method for Viscous Flows With Moving Boundaries," Appl. Mech. Rev., **42**(12), pp. 323–341.
- [9] Enright, D., Fedkiw, R., Ferziger, J., and Mitchell, I., 2002, "A Hybrid Particle Level Set Method for Improved Interface Capturing," J. Comput. Phys., **183**, pp. 83–116.
- [10] Evans, M. W., and Harlow, F. H., 1964, "The Particle-in-Cell Method for Hydrodynamics Calculations," Los Alamos Scientific Laboratory Report No. LA-2139.
- [11] Brackbill, J. U., and Ruppel, H. M., 1986, "FLIP: A Method for Adaptively Zoned, Particle-in-Cell Calculations of Fluid Flows in Two Dimensions," J.

Comput. Phys., **65**, pp. 314–343.

- [12] Tanaka, N., 1999, “Development of a Highly Accurate Interpolation Method for Mesh-free Flow Simulations 1. Integration of Gridless, Particle and CIP Methods,” *Int. J. Numer. Methods Fluids*, **30**, pp. 957–976.
- [13] Yabe, T., and Aoki, T., 1996, “A Dream to Solve Dynamics of All Materials Together,” *International Conference on High-Performance Computing in Automotive Design, Engineering, and Manufacturing*, Paris, France, Oct. 7–10, pp. 2105–2108.
- [14] Gingold, R. A., and Monaghan, J. J., 1982, “Kernel Estimates as a Basis for General Particle Methods in Hydrodynamics,” *J. Comput. Phys.*, **46**, pp. 429–453.
- [15] Koshizuka, S., and Oka, Y., 1996, “Moving-Particle Semi-Implicit Method for Fragmentation of Incompressible Fluid,” *Nucl. Sci. Eng.*, **123**, pp. 421–434.
- [16] Ishii, E., Kameya, H., Watanabe, A., and Urashin, M., 2002, “Calculation of Two-Phase Flows in an Oil Separator by Using a Cubic Interpolated Propagation Code on Unstructured Grid Spaces,” *Proceedings of ASME FEDSM2002-31229*.
- [17] Yanenko, N. N., 1971, *The Method of Fractional Steps*, Springer-Verlag, Berlin.
- [18] Brackbill, J. U., and Zemach, C., 1992, “A Continuum Method for Modeling Surface Tension,” *J. Comput. Phys.*, **100**, pp. 335–354.
- [19] Martin, J. C., and Moyce, W. J., 1952, “An Experimental Study of the Collapse of Liquid Columns on a Rigid Horizontal Plane,” *Philos. Trans. R. Soc. London*, **244**, pp. 312–324.



# Hydrofoil Drag Reduction by Partial Cavitation

**Eduard Amromin**  
Mechmath LLC,  
Prior Lake, MN 55372

**Jim Kopriva**

**Roger E. A. Arndt**

**Martin Wosnik**

Saint Anthony Falls Laboratory,  
University of Minnesota,  
Minneapolis, MN 55414

*Partial cavitation reduces hydrofoil friction, but a drag penalty associated with unsteady cavity dynamics usually occurs. With the aid of inviscid theory a design procedure is developed to suppress cavity oscillations. It is demonstrated that it is possible to suppress these oscillations in some range of lift coefficient and cavitation number. A candidate hydrofoil, denoted as OK-2003, was designed by modification of the suction side of a conventional NACA-0015 hydrofoil to provide stable drag reduction by partial cavitation. Validation of the design concept with water tunnel experiments has shown that the partial cavitation on the suction side of the hydrofoil OK-2003 does lead to drag reduction and a significant increase in the lift to drag ratio within a certain range of cavitation number and within a three-degree range of angle of attack. Within this operating regime, fluctuations of lift and drag decrease down to levels inherent to cavitation-free flow. The favorable characteristics of the OK-2003 are compared with the characteristics of the NACA-0015 under cavitating conditions. [DOI: 10.1115/1.2234787]*

## 1 Introduction

Drag reduction by cavitation is usually associated with supercavitation that occurs at a very high speed/low cavitation number. Operating in a cavity reduces the wetted surface and hence reduces friction. However, there is a drag penalty associated with creating a cavity. This penalty usually offsets any possible friction reduction, as follows from data described in [1]. Nevertheless, there has been a successful experience in drag reduction utilizing partial cavitation, which does not cover the trailing part of the body completely (reported for ships with specially designed bottoms by Ivanov [2] and Latorre [3]). A possibility of such drag reduction is associated with the suppression of cavity pulsation by adjusting the pressure gradient in the reattachment region via special design of the bodies. This procedure addresses the need for hydrofoil drag reduction where conventional foils suffer a drag increase due to cavitation.

The theory of ideal cavitation (as defined by Birkhoff [4]), suggests a possibility of hydrofoil drag reduction by partial cavitation. The authors have developed a design procedure in the framework of a model of ideal cavitation that has been earlier employed in other design problems for cavitating hydrofoils [5–7]. As is usual in engineering, the design employs some known hydrofoil as an initial approach. In this case it was the NACA-0015. The designed OK-2003 hydrofoil exhibited a drag reduction by partial cavitation, and this result was recently reported at a conference [8].

A detailed experimental study validated the desired features of the design concept in the range of cavitation number and angle of attack where drag reduction takes place. These features include a sharp lift increase and a very low level of drag and lift fluctuations.

This paper describes the unusual characteristics of the novel hydrofoil OK-2003 in comparison with the traditional hydrofoil NACA-0015. The main points of the design algorithm are also discussed.

## 2 General Design Concept

The objective of the design is a hydrofoil that has no cavitation-induced drag within a given range of cavitation number and lift

coefficient. This requires the variation of several pairs of auxiliary parameters {cavity lengths, angles of attack} to find the combination that will fit the given requirements.

The presented design of low-drag partially cavitating hydrofoils is based on determination of a cavity shape on a hydrofoil in ideal incompressible fluid. After the fluid velocity potential is defined, the cavity shape must be found from the solution of a boundary value problem for the Laplace equation:

$$\Delta\Phi = 0 \quad (1)$$

The boundary conditions include the normal velocity requirement

$$\left. \frac{\partial\Phi}{\partial N} \right|_S = 0 \quad (2)$$

the definition of incoming flow

$$\text{grad } \Phi|_{x \rightarrow -\infty} = \{1, \sin(\alpha)\} \quad (3)$$

and the pressure constancy condition for the surface of the cavity

$$(\text{grad } \Phi)^2|_{S^*} = 1 + \sigma \quad (4)$$

Here the surface  $S$  includes  $S^*$  (the cavity surface defined by an arc of constant pressure and of a fixed length) and the hydrofoil wetted surfaces. A fictitious boundary in the tail of cavity is also included in  $S$  (as shown in Fig. 1). This term was first suggested by Birkhoff and Zarantonelo [9] for part of a boundary of closed cavities, where the pressure is not constant in steady flows.

The applied scheme of cavity closure is similar to that employed by Kinnas et al. [10]; it is a generalization of the Riabouchinsky scheme. There is a drag associated with the cavity closure. This drag will go to zero if cavity closure is achieved by a smooth reattachment to the afterbody of the designed foil. This requires that the afterbody is tangent to the cavity at the point of reattachment, as shown in Fig. 2 for the design condition. Out of this condition, a fictitious body and associated drag will be inherent to the designed hydrofoil.

A condition for lift determination must be added to Eqs. (1)–(4). Traditionally, the Kutta-Joukovskii condition is employed for this aim. The following formula describes the velocity behavior in the vicinity of hydrofoil's trailing edge:

$$U(x) \sim (C-x)^\Theta \left[ \frac{C^*}{(C-x)} + 1 + \dots \right] \quad (5)$$

This formula is deduced by analyzing a conformal mapping of the trailing edge vicinity into a circle. Here  $\Theta = \beta/(2\pi - \beta)$ , the origin

Contributed by the Fluids Engineering Division of ASME for publication in the JOURNAL OF FLUIDS ENGINEERING. Manuscript received February 28, 2005; final manuscript received February 7, 2006. Review conducted by Joseph Katz.

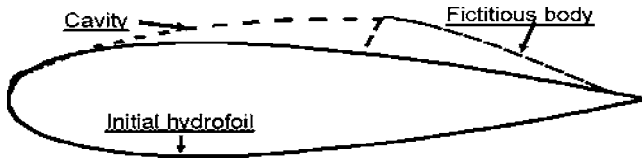


Fig. 1 Schematic of cavitating flow

coincides with the hydrofoil leading edge. The coefficient  $C^*$  must be zero to satisfy the Kutta-Joukovskii condition.

There are different applicable numerical techniques to solve the nonlinear boundary value problem (1)–(5) for arbitrary hydrofoils (developed by Ullman [11], Pelone et al. [12], and others). The technique applied here was recently described by Amromin [13].

The problem solution provides both the hydrofoil shape and the pressure distribution over its contour at the angle of attack that corresponds to the design condition. As shown in Fig. 3, the pressure coefficient is  $C_p = C_p^* = -\sigma$  over approximately 75% of the suction side of the foil. It will result in a fiction drag reduction on the order of the reduction in wetted surface. The boundary between the cavity and the fluid is a constant-pressure surface. For a selected pair  $\{l, a\}$ , there is a unique surface shape and cavitation number  $\sigma$ . Another boundary of the cavity is the surface of the designed hydrofoil itself. One may join two points on  $S^*$  by any new arc that will be located within the basic contour. One can generate many such contours from the basic contour and the drag-free hydrofoil would not be unique for the certain basic contour. All that is necessary is that there is adequate space between the cavity and the hydrofoil surface. The cavity cannot be infinitely thin due to capillarity effects and the cavity should be stable to small perturbations of the angle of attack. In addition, the contour of designed hydrofoil must be inside of the contour of the initial hydrofoil with the cavity. Thus, there is no uniqueness in this part of the design algorithm.

The principles of the design procedure are illustrated with the OK-2003 hydrofoil developed on the basis of the NACA-0015 hydrofoil (studied by Arndt et al. [14,15]). The shape of this hydrofoil is shown in Fig. 4. The pressure sides of the OK-2003 and

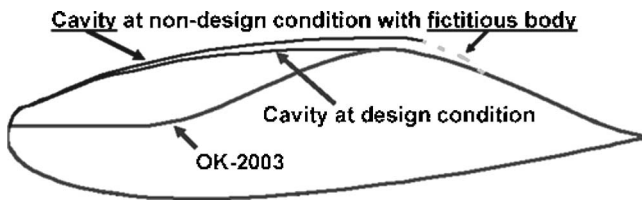


Fig. 2 Computed cavities on the developed hydrofoil OK-2003. The fictitious body of the initial NACA-0015 hydrofoil at design conditions is transformed into the afterbody of the hydrofoil OK-2003.

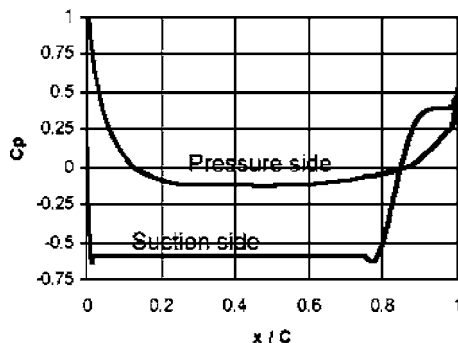


Fig. 3 Pressure distribution over a basic contour

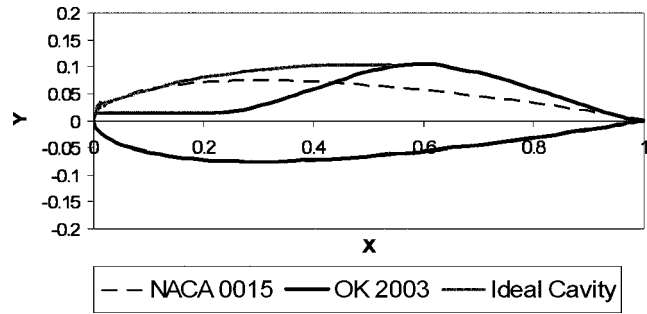


Fig. 4 Contours of the designed hydrofoil OK-2003 (solid line), the initial hydrofoil NACA-0015 (dashed line), and the basic contour (transparent line) that is a solution of Eqs. (1)–(5) for the initial hydrofoil

NACA-0015 completely coincide and are located along the bottom in Fig. 4. This provides a favorable basis for comparison between the new and traditional hydrofoils. The OK-2003 is designed for partial cavitating conditions where the cavity reattaches at the 60% point along the chord. This *ideal cavity* can also be compared with the computed cavity shape in Fig. 4. The defined geometric zero angle of attack used experimentally is located along the  $x$  axis.

There are some details concerning the shape of the foil at cavity detachment. If the detachment point is placed slightly downstream from the position described by the Brillouin-Villat condition, one will obtain a pressure minimum upstream of it (Gurevich [16] provides a mathematical proof with the employment of Lavrentiev variation principle). A similar technique was previously used in ship hull drag reduction by partial cavitation [2]. The role of such minimum is to stabilize the leading edge of the cavity.

The second point must be located upstream of the fictitious contour. A pressure minimum is also necessary there to “lock” the cavity length near a stable position. As a result, the pressure distribution over the designed hydrofoils under cavitation-free conditions has two minima (i.e., the inviscid pressure distribution has two minima, as shown in Fig. 5).

### 3 Experimental Setup

The experimental validation of the design procedure was carried out in the Saint Anthony Falls Laboratory (SAFL) water tunnel. This water tunnel has a  $0.19 \times 0.19$  m square cross-section allowing for a hydrofoil span of 0.19 m. The hydrofoil chord length used in this tunnel is 0.081 m. This chord length was selected to minimize any bias due to the combined effects of blockage and Reynolds number. The Reynolds numbers tested ranged between  $6.5 \times 10^5$  to  $8 \times 10^5$  based on free-stream test speeds of 8–10 m/s.

The foils were mounted on a specially designed force balance that allowed for ventilation and adjustable lift and drag sensitivity.

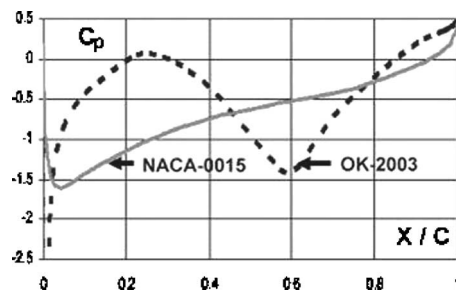


Fig. 5 Comparison of pressure distributions over the suction side of the designed OK-2003 hydrofoil and the initial NACA-0015 hydrofoil computed for an ideal fluid

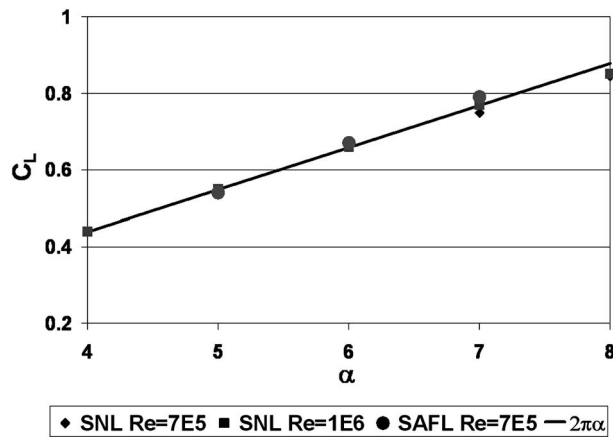


Fig. 6 Comparison of lift and coefficient recorded at SAFL and at the Sandia National Laboratories (SNL)

The adjustable sensitivity is obtained by exchanging loading elements. The accuracy of the force balance for lift and drag was established to be 3% and 3.5%, respectively, based on full-scale measurements of 900 N lift and 100 N drag.<sup>1</sup> All lift and drag data were recorded at a minimum of 2000 samples per second over a time interval of 2 s. This allowed for accurate statistical and frequency analysis.

Figures 6 and 7 give direct comparison between measurements made at SAFL to Sandia National Laboratories (SNL) at Reynolds numbers of  $7 \times 10^5$  and  $10^6$  [17]. The SAFL data were collected at a Reynolds number of approximately  $7 \times 10^5$ . No corrections to the SAFL data were made to account for tare forces due to the hydrofoil mounting plugs interacting with the flow, any pressure differential effect on the seal, and tip clearance effects. All these corrections will have a negligible effect on the lift measurements. However, these corrections would be more significant for drag measurements. This can be seen in Fig. 7 where the data varies slightly from the SNL.

To facilitate observations of cavitation on the suction side, the OK-2003 hydrofoil was mounted at a negative angle of attack to permit viewing through the bottom window. This is shown in Fig. 8. To avoid confusion the minus signs have been deleted from the presentation angle of attack.

Measurements of lift and drag were supplemented with high-speed video (HSV) observation of cavity dynamics. This made it possible to obtain data on oscillations of cavity length and shape.

#### 4 Measurements of Lift and Drag

As widely employed in engineering, the hydrofoil design is optimized for a selected value of lift coefficient. The theoretical variation of  $C_L(\alpha)$  is substantially different from that measured due to the combined effects of Reynolds number and flow blockage. The optimal range of angle of attack determined experimentally was 5–7 deg for the OK-2003. Since there was a consistent amount of data and video available for both the NACA-0015 and OK-2003 hydrofoils at an angle of attack of 7 deg, the majority of the comparisons are made at this angle.

Although the lift values for NACA and OK are quite different under noncavitating conditions, they become equal with a decrease in cavitation number to a value corresponding to ideal reattachment of the sheet cavity on the OK-2003 foil. This is shown

<sup>1</sup>One issue with the current force balance was sealing. During the study two different seals were tested. This issue affected the ability to compare drag data from different versions of the balance due to a different drag offset with each seal due to pressure differential effects. The drag accuracy is based on the worst-case scenario between the two seals used. This error is found to be much less by limiting comparisons to within data sets associated with each version of the balance.

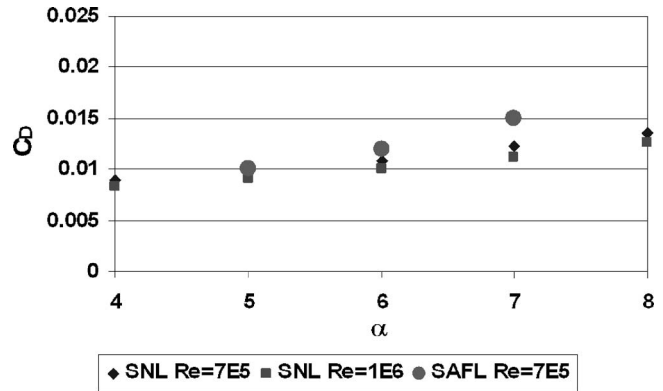


Fig. 7 Comparison of drag coefficient recorded at SAFL and at the Sandia National Laboratories

in Fig. 9 where their lift is to be equal for  $\sigma < 1.1$  at  $\alpha = 7$  deg. This confirms the relevance of comparing the two hydrofoils. This figure also gives a direct comparison of drag data. Note that the more streamlined NACA foil outperforms the OK foil with a blunt afterbody in noncavitating flow. As cavitation number is lowered, the drag of the OK-2003 foil decreases and becomes lower than the increasing drag of the NACA-0015 foil. As manifested by experimental data in Figs. 10 and 11,  $\alpha = 5$ –6 deg appears to be the optimal angle of attack for the hydrofoil OK-2003. Over a range of cavitation number its drag is considerably lower than the drag of a NACA-0015 foil. At lower cavitation numbers, the drag of the OK-2003 foil increases until the drag of the two foils coincide.

The region of best performance of the OK-2003 foil corresponds to an ideal cavity length under partial cavitating conditions with ideal cavity reattachment. The maximum lift and minimum

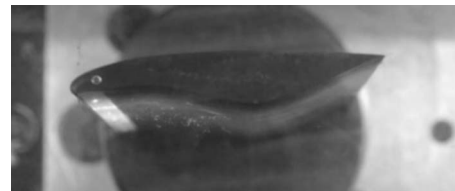


Fig. 8 View of OK-2003 in the SAFL water tunnel

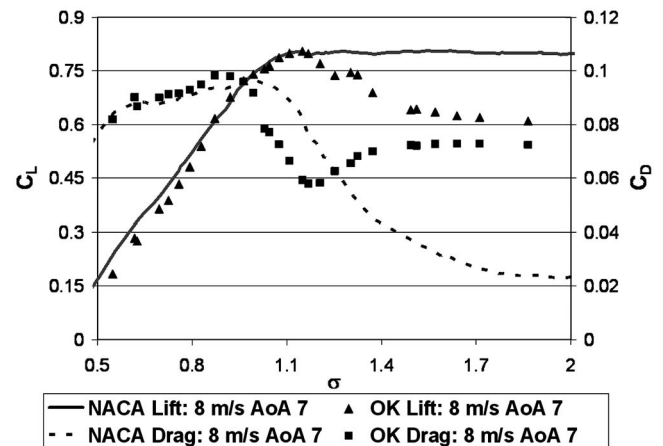


Fig. 9 Coefficient of lift and drag versus cavitation number for OK-2003 and NACA-0015 at the same free-stream speed

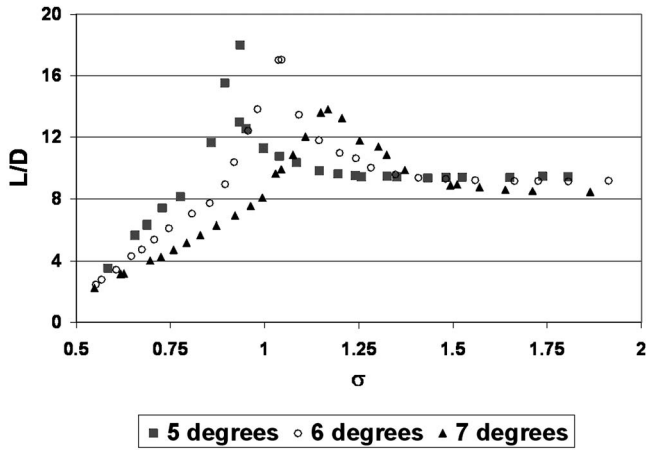


Fig. 10 Lift to drag ratio of OK-2003 for different angles of attack

drag all coincide at the same value of  $\sigma$ . Further substantiation of the design procedure is given in Sec. 6 where HSV will be discussed.

Different trends for the two hydrofoils become evident by normalizing the drag data to their noncavitating values. As shown in Fig. 12, the effects of cavitation on the drag behavior are entirely different for the OK-2003 and NACA-0015 hydrofoils.

The drag coefficient of the conventional NACA-0015 hydrofoil increases steadily with the onset of cavitation and approaches a

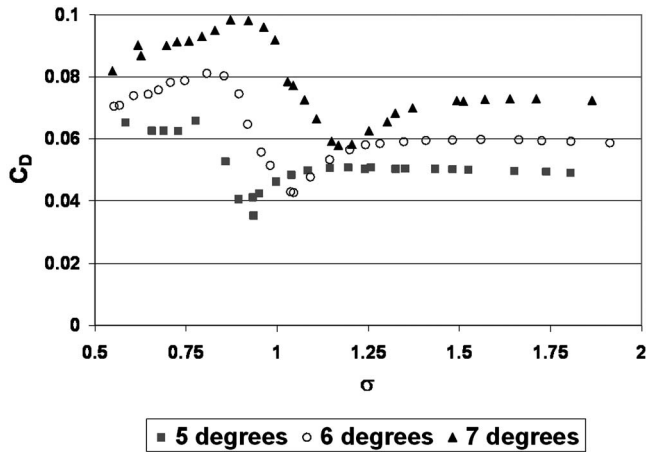


Fig. 11 Effect of angle of attack on the drag of OK-2003

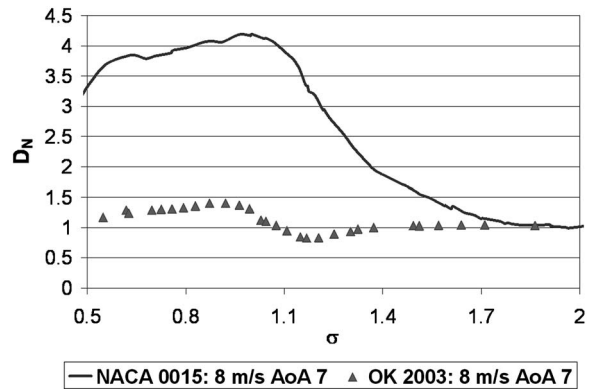


Fig. 12 Comparison of normalized drag of hydrofoils OK-2003 and NACA-0015

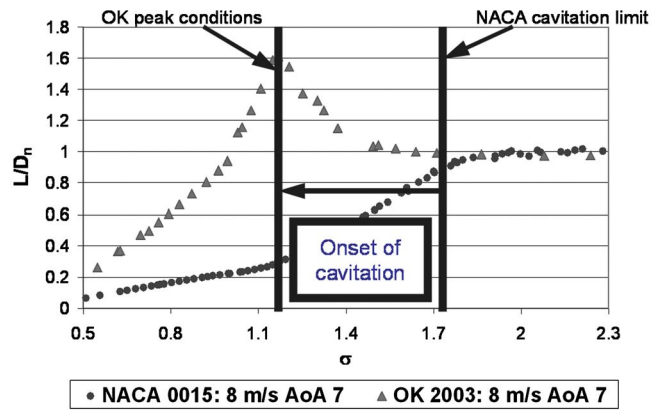


Fig. 13 Comparison of normalized lift to drag ratio for the NACA-0015 and OK-2003. All data is normalized to it respective non-cavitating condition. Thick vertical lines separate a range where partial cavitation inflicts an opposite performance response.

maximum in the regime of partial cavitation. For the OK-2003 foil, the drag first decreases with the onset of cavitation until the cavity length surpasses the length for ideal reattachment. Thereafter an increase in drag finally occurs. The minimal drag corresponding to a value of  $\sigma$  depends on  $\alpha$ . Comparison of the normalized lift to drag ratio for the two foils is shown in Fig. 13. The data are normalized to emphasize the different impact that cavitation has on the efficiency of two kinds of hydrofoils.

At the water tunnel test conditions (Reynolds number around  $7 \times 10^5$ ), the cavitation-free drag of OK is much higher than expected. This may be due to laminar separation that is numerically predicted for the test Reynolds numbers. Because of very stable cavities over the OK-2003 hydrofoil, the boundary layer downstream of cavity reattachment may be laminar at a local Reynolds number smaller than  $10^6$ , as it takes place for boundary layers with low pressure gradient over cavitation-free hydrofoils (as shown by Bourgoyne et al. [18], the laminar-turbulent transition can take place at  $Re \gg 10^7$ ). A lower drag coefficient is expected for full-scale flows ( $Re > 10^7$ ). Nevertheless, the absolute values of lift to drag ratio of the OK are 50% greater than that of the NACA foil over a certain range of cavitation number for an angle of attack of 7 deg. As much as a 100% increase was found for an angle of attack of 6 deg as shown in Fig. 14.

The 50% increase of lift to drag ratio was measured in a narrow range of  $\sigma$ . Hydrofoils are usually designed for a fixed load. Consequently, the attendant increase of lift to drag ratio effectively results in a decrease in drag.

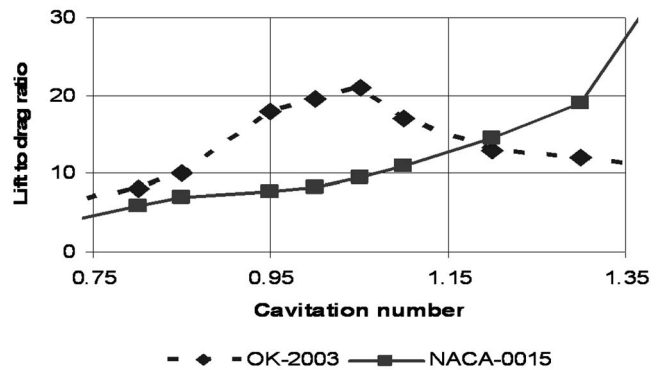


Fig. 14 Comparison of lift to drag ratios of the hydrofoil OK-2003 at  $\alpha=6$  deg and NACA-0015

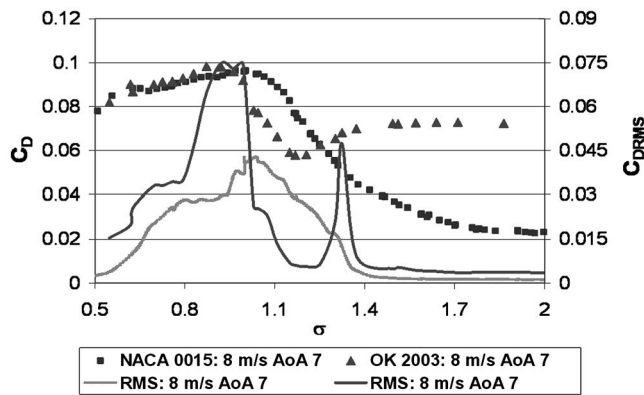


Fig. 15 Correlation between average and fluctuating (rms) drag coefficient for the NACA-0015 and OK-2003.  $C_{DRMS}$  is scale along the right while  $C_D$  is scaled on the left.

## 5 Measurements of Fluctuations

A unique feature of the new hydrofoil design is abnormally lower drag and lift fluctuation levels. As shown in Fig. 15, the OK-2003 has no significant fluctuation of drag or lift in range of  $\sigma$  corresponding to ideal reattachment or minimum drag. Moreover, for the minimum-drag cavities, the fluctuation level drops down to the level inherent to cavitation-free flow.

As shown in Fig. 16, the lift fluctuation for peak-lift cavities is also suppressed. In fact, partial cavities appeared to be too calm for the use of ordinary assumptions for boundary layer transition

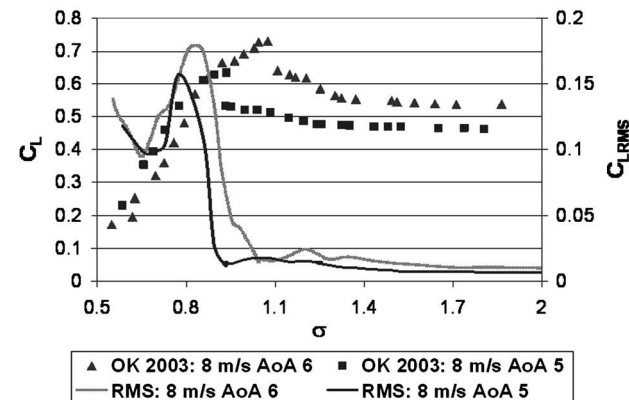
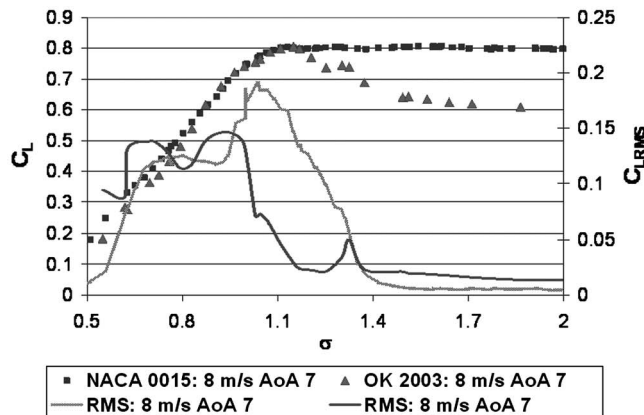


Fig. 16 Correlation between average and fluctuating (rms) lift coefficient for NACA-0015 and OK-2003. The top plot features  $\alpha=7$  deg, the bottom plot features  $\alpha=5$  deg and  $\alpha=6$  deg.

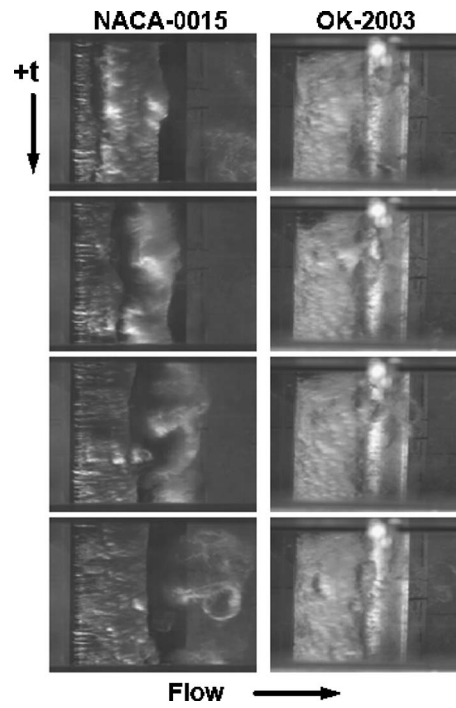


Fig. 17 Comparison in the variation in cavity length on the NACA-0015 and the OK-2003 based one shedding cycle at peak conditions. NACA-0015 left ( $U=7.65$  m/s,  $\alpha=8$  deg,  $\sigma=1.3$ ,  $\sigma/2\alpha=4.66$ ) and OK-2003 right ( $U=8$  m/s,  $\alpha=7$  deg,  $\sigma=1.14$ ,  $\sigma/2\alpha=4.67$ ). Note the stable reattachment on the OK 2003 while the NACA-0015 foil experiences large fluctuations in cavity length.

after reattachment. It is necessary to emphasize that such abnormal behavior of the cavitating OK-2003 hydrofoil takes place only in the regime of partial cavitation near  $\sigma$  that corresponds to ideal cavity reattachment. The following cavity growth due to a decrease of cavitation number leads to a periodic shedding cavity similar to the NACA-0015 shedding. At these low cavitation numbers the OK-2003 has lost all benefits of its design.

## 6 Visual Comparison

Measurements of lift and drag were supplemented with high speed video (HSV) of cavity dynamics. The video was recorded at 2000 fps, which is more than adequate to visualize cavity pulsation for both the OK-2003 and NACA-0015. This made it possible to observe oscillations of cavity length shown in Fig. 17 and the transparency of wake behind the hydrofoil OK-2003 as shown in Fig. 18.

The stationary images taken from the HSV for the OK-2003 represents the peak operating conditions at a free-stream speed of 8 m/s and an angle of attack of 7 deg. Each image is taken at 5 ms intervals for both the NACA-0015 (left) and OK-2003

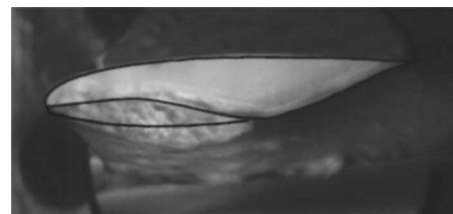


Fig. 18 Sideview of a low-drag cavity for the OK-2003 hydrofoil. The foil's profile and the cavity shape with ideal reattachment from computation are superimposed onto the HSV.

(right). HSV was not recorded for the exact same free-stream speed and angle of attack for the NACA-0015 hydrofoil but at slightly different conditions of  $U=7.65$  m/s and  $\alpha=8$  deg. Similar cavity characteristics can easily be found by matching  $\sigma/2\alpha$  [16]. Therefore  $\sigma/2\alpha$  was matched for the comparison shown in Fig. 17.

In the vicinity of ideal cavity closure on the OK-2003, the two hydrofoils demonstrate very different cavity dynamics. The NACA foil's cavity length shows a wide variation in one shedding cycle as has been previously observed. On the other hand, the cavity patterns on the OK are quite stable (Figs. 17 and 18). This is due to the fact that the cavity length,  $l$ , is fixed by the shape of the hydrofoil's suction side surface. The relatively uniform spanwise cavity and transparent wake coupled with low amplitude cavity oscillations are implicit proof of cavity stability. There was no observed cloud cavitation of OK-2003 in the studied ranges of  $\sigma$  and  $\alpha$ .

## 7 Conclusions

The developed OK-2003 hydrofoil exhibits an unusual drag reduction and lift increase with the growth of partial cavities within a significant range of cavitation number and within a 3 deg range of angle of attack. It is important to emphasize that the effective drag reduction is associated with an increase of lift coefficient, hence a substantial increase in the lift to drag ratio. Since the load of a hydrofoil is usually fixed, this corresponds to a substantial decrease in drag. The OK-2003 hydrofoil also exhibits an unusual decrease of fluctuation levels within the same ranges of cavitation number and angle of attack. Drag and lift fluctuations are reduced to cavitation-free levels.

The experiments validated the effectiveness of a design procedure based on ideal cavitation theory for developing drag reduction schemes. Currently ventilation is being studied as a means to maintain the ideal cavity length over a range of operating speed and depth of submergence. In addition, consideration of 3D effects, scale effects and stability of low-drag partial cavities under periodical excitation will be included in future work as the necessary steps to engineering applications.

## Acknowledgment

The authors are indebted to the Defense Advanced Research Projects Agency for support of this study.

## Nomenclature

$C$	= hydrofoil chord
$C_D$	= drag coefficient
$C_L$	= lift coefficient
$C_{DRMS}$	= rms drag coefficient
$C_{LRMS}$	= rms lift coefficient
$C_p$	= dimensionless pressure coefficient
$D$	= drag
$H$	= thickness of cavity or fictitious body
$l$	= cavity length

$L$	= lift
$N$	= normal to $S$
$P_C$	= pressure within cavity
$P_\infty$	= unperturbed pressure
$Re$	= Reynolds number
$S$	= boundary of inviscid flow
$S^*$	= the cavity surface
$U$	= velocity in inviscid flow related to $U_\infty$
$U_\infty$	= free stream speed
$\alpha$	= angle of the attack
$\beta$	= trailing edge corner
$\delta_C$	= hydrofoil camber
$\delta_T$	= hydrofoil thickness
$\sigma$	= $2(P_\infty - P_C)/(\rho U_\infty^2)$ -cavitation number
$\rho$	= water density
$\Phi$	= velocity potential

## References

- [1] Knapp, R. T., Daily, J. W., and Hammit, F. G., 1970, *Cavitation*, McGraw-Hill, New York.
- [2] Ivanov, A. N., and Kalyzhny, V. G., 1996, "The Perspectives of Applications of Ventilated Cavities on Naval Combat Ships," Intl. Conf. on 300th Ann. of Russian Navy, St. Petersburg, A2, pp. 41–46.
- [3] Latorre, R., 1971, "Ship Hull Drag Reduction Using Bottom Air Injection," *Ocean Eng.*, **24**, pp. 161–175.
- [4] Birkhoff, G., 1971, "Mathematical Analysis of Cavitation," IUTAM Symposium, Leningrad.
- [5] Shen, Y. T., and Eppler, R. 1981, "Wing Section for Hydrofoils," *J. Ship Res.*, **35**, pp. 191–200.
- [6] Jessup, S. D., and Wang, H.-C. 1997, "Propeller Design and Evaluation for a High Speed Patrol Boat Incorporating Iterative Analysis with Panel Method." SNAME Propeller/Shafting'97 Symp., Virginia Beach, VA.
- [7] Cox, B. D., Kimball, R. W., and Scherer, O. 1997, "Hydrofoil Sections with Thick Trailing Edges." SNAME Propeller/Shafting'97 Symp., Virginia-Beach.
- [8] Amromin, E. L., Hansberger, J., Arndt, R. E. A., Wang, H., and Wosnik, M. 2003, "Investigation of a low-drag partially cavitating hydrofoil," Cav-2003 Symposium.
- [9] Birkhoff, G., and Zarantonelo, E. 1957, *Jets, Wakes and Cavities*, Academic, New York.
- [10] Kinnas, S. A., and Fine, N. E. 1993, "A numerical nonlinear analysis of the flow around two-and three-dimensional partially cavitating hydrofoil," *J. Fluid Mech.*, **254**, pp. 151–181.
- [11] Ullman, J. S. 1987, "The surface singularity method applied to partially cavitating hydrofoils," *J. Ship Res.*, **31**, pp. 107–124.
- [12] Pelone, C., and Rowe, A. 1988, "Effect of separation on partial cavitation," *ASME J. Fluids Eng.*, **110**, pp. 182–189.
- [13] Amromin, E. L. 2002, "Scale Effect of Cavitation Inception on a 2D Eppler Hydrofoil," *ASME J. Fluids Eng.*, **124**, pp. 186–193.
- [14] Arndt, R. E. A., Song, C. C. S., Kjeldsen, M., He, J., and Keller, A. 2001, "Instability of Partial Cavitation: A Numerical/Experimental Approach," *Proceedings Twenty-Third Symposium on Naval Hydrodynamics*, Office of Naval Research, Naval Studies Board, National Research Council, National Academies Press.
- [15] Kjeldsen, M., Arndt, R. E. A., and Effertz, M., 2000, "Spectral Characteristics of Sheet/Cloud Cavitation," *ASME J. Fluids Eng.*, **122**(3), pp. 481–487.
- [16] Gurevich, M. I. 1970, *Theory of Jets in Ideal Fluids*, Academic, New York.
- [17] Sheldahl, R. E., and Klimas, P. C. 1981, "Aerodynamic Characteristics of Seven Airfoil Sections Through 180 Degrees Angle of Attack for Use in Aerodynamic Analysis of Vertical Axis Wind Turbines," Report SAND80-2114, Sandia National Laboratories, Albuquerque, NM.
- [18] Bourgoyne, D. A., Hamel, J. M., Ceccio, S. L., and Dowling, D. R. 2003, "Time-Averaged Flow Over a Hydrofoil at High Reynolds Number," *J. Fluid Mech.*, **496**, pp. 365–404.

# Unsteady Flow Structure and Global Variables in a Centrifugal Pump

**José González**  
e-mail: [aviados@uniovi.es](mailto:aviados@uniovi.es)

**Carlos Santolaria**

Área de Mecánica de Fluidos,  
Universidad de Oviedo,  
Campus de Viesques,  
33271 Gijón (Asturias), Spain

*A relationship between the global variables and the dynamic flow structure numerically obtained for a low specific speed centrifugal pump is presented in this paper. A previously developed unsteady flow model is used to correlate the dynamic field with the flow characteristics inside the impeller and volute of a single-stage commercial pump. Actually, the viscous incompressible Navier-Stokes equations are solved within a 3D unsteady flow model. A sliding mesh technique is applied to take into account the impeller-volute interaction. After the numerical model has been successfully compared with the experimental data for the unsteady pressure fluctuations pattern in the volute shroud, a new step is proposed in order to correlate the observed effects with the flow structure inside the pump. In particular, the torque as a function of the relative position of the impeller blades is related to the blades loading, and the secondary flow in the volute is related to the different pressure patterns numerically obtained. Local flow analysis and qualitative study of the helicity in different volute sections is performed. The main goal of the study presented is the successful correlation of local and global parameters for the flow in a centrifugal pump. The pressure forces seem to be the main driven mechanism to establish the flow features both in the impeller and volute, for a wide range of operating conditions. [DOI: 10.1115/1.2234782]*

## Introduction

The complexity of any study of the flow in a turbomachine is obvious and has led to much of the research work over recent decades [1]. Referring to pumps, many studies have been carried out, but even nowadays some flow events are still under study and far from being fully understood [2–4]. Moreover, the present trends towards smaller (more compact) units and more loaded blades complicate the issue and produce new and unexpected patterns.

Nowadays, pump technology constitutes a major research field among cutting-edge technological companies. Some authors [3,5] have classified the various efforts into different categories, namely hydraulics (losses and static performance), cavitation (modern solutions and modifications to prevent the appearance of this effect), vibrations (dynamic effects of the flow), and machine arrangement (shaft and bearing configurations). Nevertheless, only during the last decades, have the modern designs tried to take into account unsteady or dynamic effects, which were impossible to determine and ignored by the classical design procedures [4,6].

When a dynamic study is proposed, difficulties arise in two areas: geometrical variables, which are quite complex, and the flow varying from its regular or symmetrical state. Sometimes both difficulties interact, producing an extremely distorted flow pattern [3]. The pressure fluctuations interact with the volute casing or even with the circuit and give rise to dynamic effects (mainly unsteady forces) over the mechanical parts, which are one of the most important sources of vibration and hydraulic noise (see Ref. [7] for a general review and see Refs. [8,9] for more particular studies).

For centrifugal pumps, several experimental data, starting with the historical articles [10,11] and including more recent ones, in which extremely advanced measuring techniques [12–14] or even visualization techniques are employed [9,15,16], have been presented in previous studies. All this knowledge is now available

and the databases constructed from these works constitute a very rich seed for the new advances; as for example, [14] have measured the unsteady pressure field inside the impeller of a centrifugal pump using piezoresistive pressure transducers and a telemetry system. They measured pressure pulses amplitude and found that they were particularly high at the trailing edge of the blades, on their pressure sides, and reached even 35% of the pump head at off-design conditions.

On the other hand, the application of numerical procedures to this industry has provided a very valuable tool [17,4]. For example, today it is possible to predict the performance curve and static pressure distributions with amazing accuracy, in the very early design stages. Such information accelerates the whole design cycle and produces an enormous time and money saving in the final product [5]. The evolution of numerical flow studies has also undergone a tremendous development in recent years (see Ref. [18] for general applications and see Refs. [19,20] for a more particular research on pumps). Many flow aspects have been numerically analyzed and, for example, [20] reports an adequate and accurate performance description for an axial or mixed-flow pump using coarse CFD models.

One specific turbomachinery feature that constitutes the driving mechanism for the dynamic effects on a centrifugal pump is the so-called rotor stator interaction. Although the impeller blades are equally spaced, nonaxis symmetry appears due to the geometrical restriction that the volute tongue causes on the flow leaving the impeller [21–23]. Different possibilities for the numerical study of the rotor-stator interaction in a centrifugal pump have been considered and widely reported [24–26]. Ranging from a separate calculation in impeller and volute to the full unsteady models, some other possibilities like the mixing plane or the frozen rotor computations have shown their advantages and drawbacks. The main conclusion from those models is the need for a fully unsteady calculation with relative motion of the impeller if the dynamic effects are to be taken into account. Reference [24] showed results of a numerical simulation using the sliding mesh technique. Although they found some problems in the comparison of their results with the experiments, they pointed out the profits of

Contributed by the Fluids Engineering Division of ASME for publication in the JOURNAL OF FLUIDS ENGINEERING. Manuscript received May 11, 2004; final manuscript received February 24, 2006. Assoc. Editor: Jinkook Lee.

**Table 1 Main characteristics of the centrifugal pump**

$D_2 = 200$ mm	Impeller outlet diameter.
$b_2 = 16.9$ mm	Impeller outlet width.
$\beta_2 = 29^\circ$	Outlet blade angle.
$\omega = 169.65$ rad/s	Rotational speed.
$f_{BP} = 189$ Hz	Blade passing frequency.
$Q_N = 0.015$ m <sup>3</sup> /s	Nominal flow rate.
$H_N = 12.88$ m	Head at nominal flow rate.
$\omega_s = 0.52$	Specific speed.

the method and foresaw the implementation of this method in the numerical solutions to handle the particularities of the turbomachinery flows.

In this work a numerical fully unsteady model, already discussed and validated [27,28] is used as analysis tool. From those previous studies, it has been noted how the two main contributions to the fluctuations obtained at the blade passing frequency are the flow structure exiting from the impeller and the tongue effect itself. The effects of the first one represent the jet-wake structure at all the angular positions. The second one corresponds to the effect felt in any point due to any blade facing the volute tongue. From the different flow rates investigated, both effects have been compared and highest influence is found at the blade passing frequency. Those effects have been also numerically captured.

In the frame of the numerical model described, a detailed flow study inside the impeller and volute of a single stage centrifugal pump is shown here. In particular, a relationship between the unsteady pressure patterns in the volute of a centrifugal pump and the different instantaneous flow fields obtained is researched using a CFD technique, which includes the sliding mesh technique with a fully unsteady calculation. Some flow patterns are often very difficult or impossible to measure directly and cover a wide range of very important unsteady aspects, such as: torque pulsations in the impeller shaft for different flow rates in function of the impeller relative position; incidence at the leading edge of the blades with different flow conditions; and secondary flows generated in the volute due to the radial gap change between the impeller and the tongue. An example of these secondary flow patterns is also thoroughly investigated.

In order to ensure the correctness of the numerical results, it is always desirable to have as many experimental data as possible. In this work, an intensive series of laboratory measurements is carried out at positions where the accessibility of the pump's geometry allowed doing so. Particularly, the pressure pulsations on the shroud side are measured for different circumferential locations and several flow rates.

### Pump Facility and Measurements Chain

A hydraulic facility designed according to International Standards [29] is used for the experiments. The water is pumped from and returned to a 100 m<sup>3</sup> reservoir. The radial flow pump has a single axial suction duct and a vaneless volute casing. It is a backward curved blade commercial pump, with the main characteristics shown in Table 1. The flow rate uncertainties are calculated and found to be always less than 2.5%, with a confidence level of 95%. The head and efficiency uncertainties are kept below 3% and 4%, respectively, within the same confidence level.

On the volute shroud, 36 pressure taps are located, one every 10 deg, in a circumference just behind the impeller exit. Miniature fast-response piezoelectric pressure transducers Kistler-601 are placed in these taps. The transducers are connected to a charge amplifier, which produces a pressure measurement with an esti-

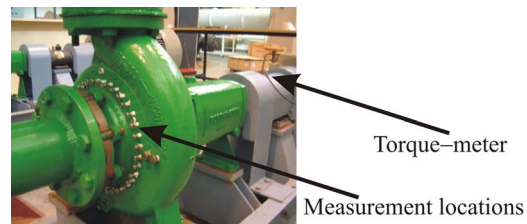


**Fig. 1 General view of the pump. The transducers were placed on the shroud side.**

mated combined uncertainty of less than  $\pm 1.5\%$ . An optic device pointing at the pump shaft gives the triggering signal to start all the measurements at the same impeller position. The resulting pressure signals, as well as the signal from the tachometer are digitized and stored in a personal computer equipped with a multichannel analog-to-digital conversion card. After the signals are recorded, spectral analysis (using a fast Fourier transform with Hanning window) is performed. The positioning of the pressure taps on the shroud side of the pump is shown in Fig. 1. A more detailed description of such arrangement together with the uncertainties calculation was described in Ref. [30].

A FAST Technology torquemeter is also available for the experiments. The torque range is 0–175 N m and the combined uncertainty of this torquemeter and the amplification system (cables, display, and amplifier) is kept for the particular values of the experiments under  $\pm 0.2\%$ .

### Numerical Model

**Geometry, Grid, and Flow Solver.** The discretization of the geometry is done keeping the balance between calculation time (details included in section numerical solution control) and the accuracy order of the simulation of the flow structure. Special care is taken in the near tongue region by carrying out a detailed study of flow vectors and stagnation point placement. Structured hexahedral cells are generated to define the inlet and outlet zones (more than 34,500 cells and around 45,000 cells, respectively) while unstructured tetrahedral cells are used to define the impeller and volute (almost 163,000 cells and 90,000 cells, respectively). A final grid with around 335,000 cells defines the whole geometry. In the volute, a mesh refinement zone is defined for a region near the tongue. Once the geometry is defined, the model is ready to be simulated. The grid generated for both the volute and the impeller is shown in Fig. 2, stressing these particular features.

The numerical model, which is implemented on a commercial code (FLUENT), solves the fully 3D incompressible Navier-Stokes equations, by including the centrifugal force source in the impeller and the unsteady terms. Turbulence is simulated with the standard  $k-\epsilon$  model. For such calculations, wall functions, based on the logarithmic law, have been used. The time dependent term scheme is second order, implicit. The pressure-velocity coupling are calculated through the SIMPLEC algorithm. Second order, upwind discretizations have been used for convection terms and central difference schemes for diffusion terms. Although grid size is not adequate for a full investigation of local boundary layer variables, global values are well captured and the details of the flow near the tongue and blade wakes do follow the usual trends found in the bibliography [13,23].

**Boundary Conditions.** The modeled boundary conditions are those considered most physically meaningful for turbomachinery flow simulations and those which give a flow solution neither limited nor restricted by them (for any flow rate): Particularly, total pressure at the inlet and a pressure drop proportional to the kinetic energy at the outlet. The flow rate is changed by modifying the constant for that pressure drop at the outlet, which simulates the closure of a valve. These boundary conditions avoid the defi-



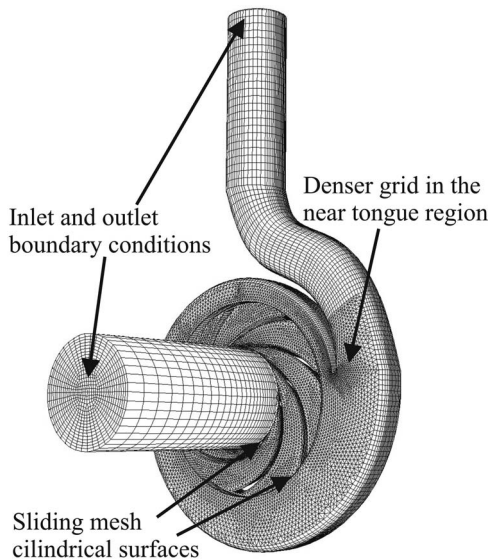


Fig. 2 Sketch of the pump unstructured mesh and its main features

inition of a uniform and constant velocity profile at the inlet or outlet, which, in general, would not be so realistic. Also, the no-slip condition with a logarithmic law for the boundary layers has been imposed over the impeller blades and sidewalls, the volute casing and the inlet and outlet pipe walls.

At the inlet and exit pipes, there is an unavoidable effect on the final flow solution as a result of the boundary conditions. A reasonable length must be added to the real machine geometry to avoid this effect as much as possible and to better simulate the pumping circuit influence. As can be observed in Fig. 2, an important effort has been devoted to overcome this problem.

**Unsteady Solution Characteristics.** A cluster with twelve Athlon-K7 (500 MHz) nodes is used for the calculations. The time step used in the unsteady calculation has been set to  $2.94 \times 10^{-4}$  s in order to have enough time resolution for the dynamic analysis; Courant number is kept below 2, which assures very good time accuracy and numerical stability. The impeller grid rotation is related to this time step and also to the rotational speed of the pump ( $\omega=169.65$  rad/s). Therefore, a complete revolution is performed each 126 steps. This is done in order to keep the frequency resolution well above the blade passing frequency and its basic harmonics.

The number of iterations has been adjusted to reduce the residuals to below an acceptable value at each time step. In particular, the ratio between the sum of the residuals and the sum of the fluxes for a given variable in all the cells is reduced to the value of  $10^{-5}$  (five orders of magnitude). Initializing the unsteady calculation with the steady solution, more than five impeller revolutions are necessary to achieve a fully periodic unsteady solution convergence. The whole procedure (rotor frozen solution and unsteady calculation) takes one week with the available CPU, for each of the operating points analyzed.

The grid size dependence is studied through intensive tests. Several grid spacings are considered in successive refinements. First of all, a 2D model had been developed, where preliminary tests pointed out the limitations of this strong simplification and other relevant features. In particular, the grid spacing near the volute tongue had been observed as a main parameter. When a 3D model was first developed [28], this feature still influenced the whole flow solution. For the 3D model, many grid dependence tests had been carried out and more conclusions obtained. Mainly, a clear inlet and outlet boundary conditions were found to be the origin of difficulties, not only the kind of boundary conditions, but

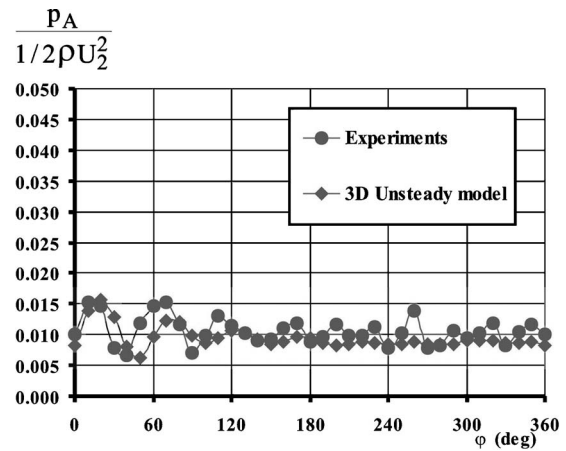


Fig. 3 Comparison of the pressure fluctuations at the  $f_{BP}$  for  $Q=Q_N$ . Tongue at  $\varphi=0$  deg.

also the relative position of these conditions to the impeller. Starting from that first 3D model, an increase of the inlet and exit pipe lengths is achieved in order to preserve the solution from the imposed boundary conditions. With this 3D final model, some full machine tests are carried out. Different meshes are considered up to 700,000 cells. The overall performance of the pump is kept the same for the definitive grids, even with less than a half of the cells finally used for the computations (the variations observed in flow rate, head and efficiency remained below very reasonable values, always less than 1.2%). Although the static values can vary within that range, more detailed flow patterns, especially near the walls, are observed with increasing cell numbers. The numerical accuracy for the pressure fluctuations is estimated to be 0.001 times the dynamic pressure (non-dimensional values, that is the pressure amplitude divided by  $1/2\rho U_2^2$ ).

The time step used to obtain the present results is also checked by repeating the numerical calculations with a half of its value ( $1.47 \times 10^{-4}$  s, that is 252 steps for each complete revolution of the impeller) and, therefore, doubling the frequency accuracy. The differences in the pressure fluctuations found are two orders of magnitude below the estimated numerical accuracy. During the numerical study, the guidelines proposed by the classical theories on numerical accuracy where followed; a summary is given by [31].

### Experimental and Numerical Dynamic Results

Before the unsteady calculations were made, a comparison for both the numerical and experimental performance curves for the tested pump was carried out. The results in static variables (head, flow rate, momentum, efficiency), taking into account that the numerical model does not consider the disk friction losses and mechanical losses at the bearings, match very well with the experimental measurements [28]. Moreover, the static pressure distributions around the impeller are also well predicted with respect to the measured values and are intensively compared [32].

Referring to the dynamic pressure fields inside the volute for different flow rates, one possible comparison is with the pressure values at the shroud of the pump. An example of that comparison is shown in Figs. 3 and 4, where nondimensional values of pressure fluctuations at the blade passing frequency,  $p_A$  divided by  $1/2\rho U_2^2$ , are compared for the numerical and experimental results. Although some differences were found and discussed, very good agreement for all flow rates has been also obtained (see Ref. [32] for a full flow rate range comparison).

Basically, there will be five numerical variables considered. First, a summary of the pressure fluctuations at the blade passing frequency observed as function of the axial position are presented

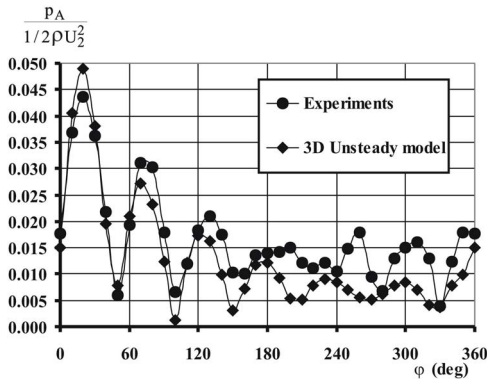


Fig. 4 Comparison of the pressure fluctuations at the  $f_{BP}$  for  $Q = 1.5 Q_N$ . Tongue at  $\varphi = 0$  deg

(the core of this study was already published, [28]) and then, the pressure distributions, the torque instantaneous evolution, the velocity fields and the helicity in radial planes will be considered.

### Global Flow Variables

The global frame of the study is settled by considering the comparison between the average measured torque and the numerical model prediction. The instantaneous torque evolution is only available in with the numerical results. The pressure fluctuations at different axial planes are then analyzed.

**Instantaneous Total Torque in the Impeller.** First of all, the torque in the pump shaft is analyzed to establish the global effect on the pump shaft induced by the flow. With this goal in mind, different instantaneous torque values are numerically obtained. The equivalent experimental values are not available as only average torque is captured with the measuring devices used in this research. The relationship between torque and pressure patterns should be straightforward if one considers that the former is the main effect of the local distinct values of the latter between pressure and suction side of the blades.

Figure 5 shows the total torque in function of time for the three flow rates considered. The average torque during a blade passing period for each flow rate is considered in order to obtain non-dimensional values. Maximum variation is found for the lower flow rate, while for the nominal flow rate an almost constant torque is obtained, independently of the blade positions. On the other hand, an opposite evolution of the total torque is found for the higher and lower flow rates. For the shown period, the former reaches its minimum whereas the latter has its maximum (at an instant be-

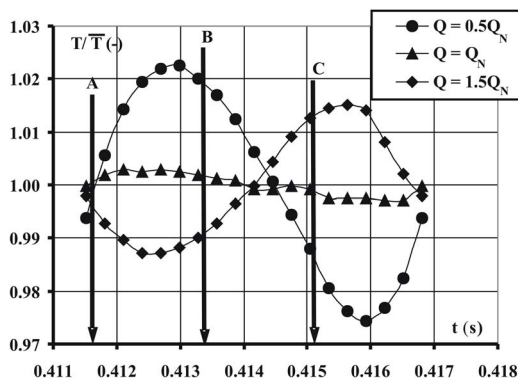


Fig. 5 Instantaneous torque in the impeller (numerical values). A representation of the three time instants (A, B, and C) considered along the present study is shown.

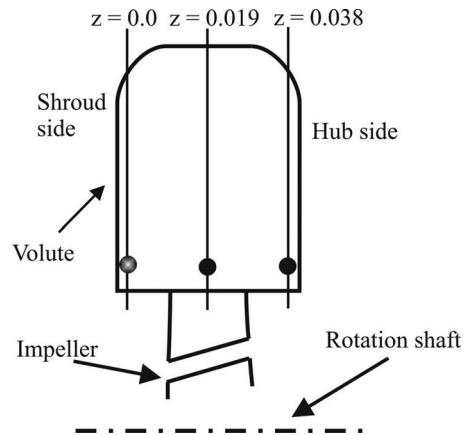


Fig. 6 Different axial planes considered in the numerical study

tween 0.412 and 0.413 s).

In conclusion, a good correlation is found for the two sets of variables considered (pressure distribution and torque are clearly related). Global variable trends (total torque) follow the expected relative evolution from the observed pressure field and, therefore, agree with the local flow numerically obtained. As far as the torque evolution has been compared with experimental data and good agreement was found, the afore-mentioned conclusion stresses the fact that the pressure forces are considerably more relevant than any other effect (viscous or momentum changes, among others, which are included in the global variable) for this kind of centrifugal pump.

The torque evolution cannot be obtained experimentally on an unsteady basis, but the average value for the different flow rates studied is compared. The result of this comparison gives a non-dimensional difference of 0.05 for the nominal flow rate, 0.1 for the higher flow rate and 0.07 for the lower flow rate, with higher values measured in the experimental setup. These values can be easily plotted in Fig. 5, but the experimental uncertainty (depending on the flow rate) must also be considered. In any case and because of the simplifications introduced by the model, there is a slight underestimation of the torque needed for all the whole flow rate range.

**Pressure Fluctuations at Different Axial Planes.** As a second and different approach to be considered, the pressure fluctuations at the blade passing frequency are analyzed. Such a study is carried out in order to obtain information on the secondary flow patterns and possible influence on the axial evolution of these pressure fluctuations. As stated in the previous section, the pressure fluctuating patterns have been already studied and compared with experimental data in previous works [32]. The stress here is placed on the axial evolution of this variable.

Three different axial planes are considered in the present analysis of the pressure fluctuations (see the scheme in Fig. 6), one near the hub, another close to the shroud and a central one (in the three planes, the circumferential points considered are placed on a section just beyond the impeller exit, as shown in Fig. 6). The plane with the experimental data available is distinguished by a different representation. For all flow rates, a parallel behavior is found (Figs. 7–9). In particular, it is clear that there are similar values for the fluctuations in both side planes (shroud and hub) and a higher value for the central plane. All the differences in the fluctuations obtained for the three axial planes studied are the result of the flow pattern in the volute entrance, where the strong diffusion of the flow (due to increase of the normal section) causes a very complex secondary flow, similar to the results reported by [33]. The general trend on the pressure differences indicates lower differences between different axial planes for increasing flow rate. In particular, the value of the fluctuations in the central plane double

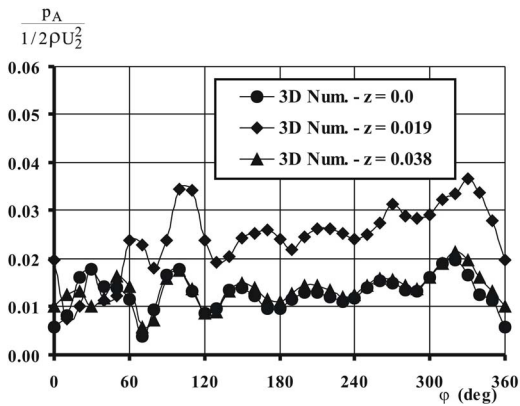


Fig. 7 Nondimensional pressure fluctuation at the  $f_{BP}$  for three axial positions at the volute. The tongue is at  $\varphi=0$  deg and  $Q=0.5 Q_N$ .

the equivalent values in the sidewalls, at least for  $120 \text{ deg} < \varphi < 360 \text{ deg}$ , as can be observed in Fig. 7. For high flow rates (Figs. 8 and 9), these differences are lower (maximum about 20% of the local value in all the angular positions). For the nominal flow rate (Fig. 8) the differences remains more constant for the different angular positions than for the off-design conditions (Figs. 7 and 9). At this point, it must be kept in mind that these pressure fluctuations are filtered at the blade passing frequency, and therefore the effect of other peak values are not considered.

Then, when operating far from the nominal flow rate, the pump creates a strong difference in the pressure fluctuations around the volute for the three different axial planes considered. This results in an increase of pressure fluctuations in the centre-plane. In particular, the greatest differences between these three planes arise at the lower flow rate considered ( $0.5 Q_N$ ). This behavior will be considered when observing a local flow variable, namely the helicity.

### Flow Study Using the Numerical Model

A numerical simulation as a means of studying the flow inside a pump has wider possibilities than experiments. For example, results corresponding to the flow structure can be captured without specific and expensive arrangements both in the impeller or inside the volute discharge. The latter is very interesting not only for the prediction of the losses during the pressure recovery (diffusion) process for which the volute is designed but also to characterize the secondary flow pattern inside a pump [34].

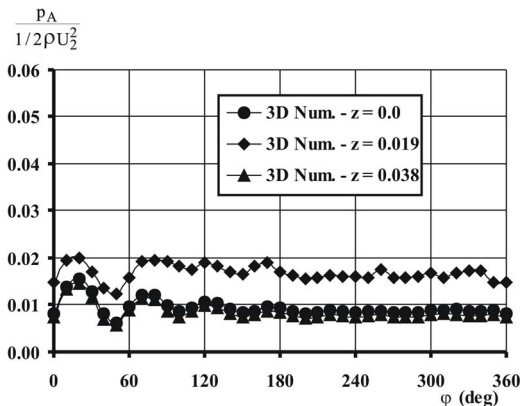


Fig. 8 Nondimensional pressure fluctuation at the  $f_{BP}$  for three axial positions at the volute. The tongue is at  $\varphi=0$  deg and  $Q=Q_N$ .

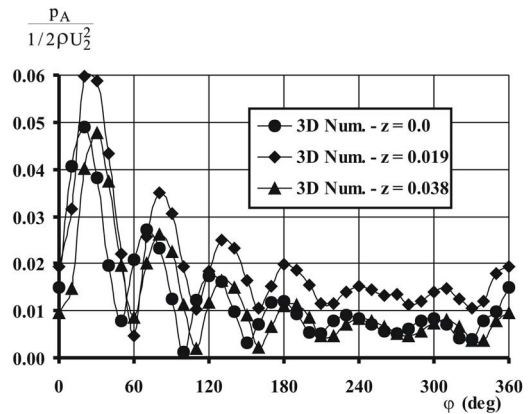
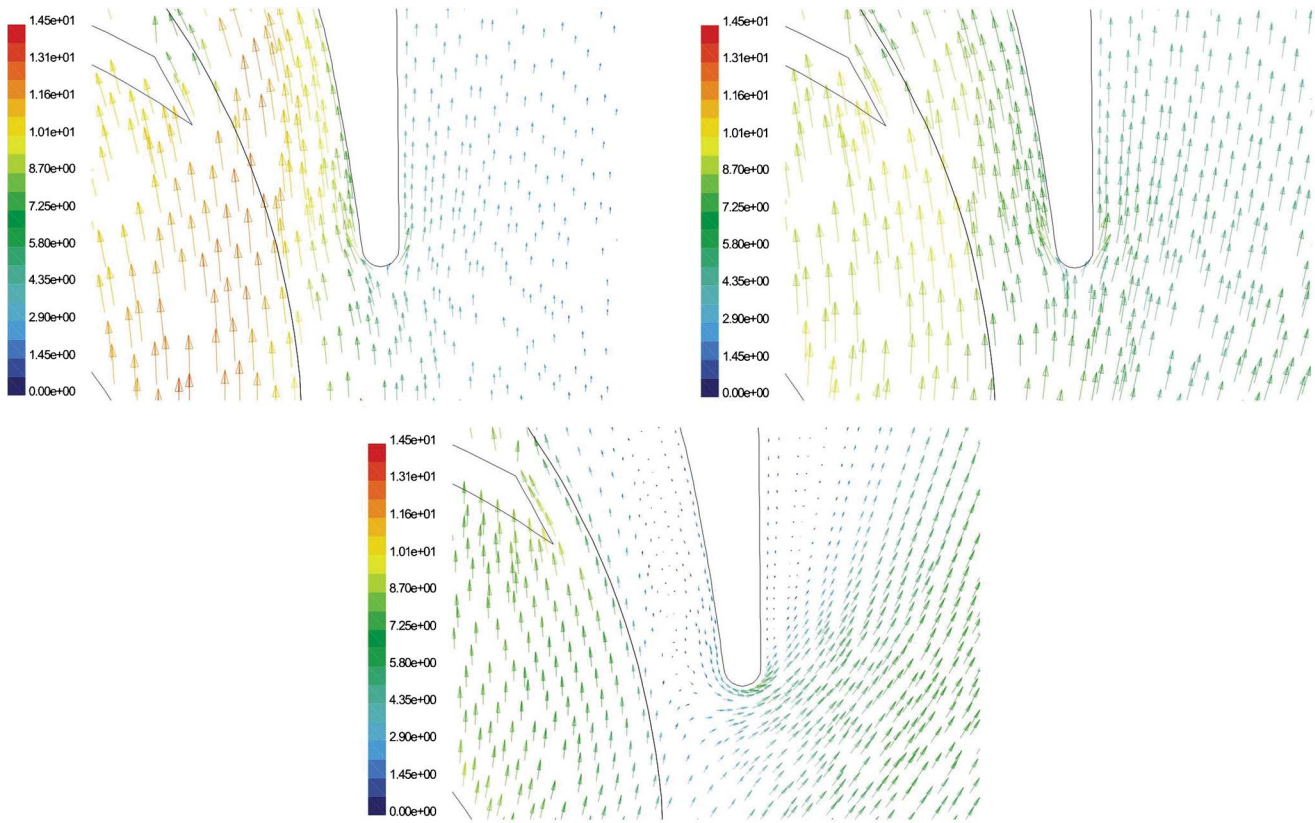


Fig. 9 Nondimensional pressure fluctuation at the  $f_{BP}$  for three axial positions at the volute. The tongue is at  $\varphi=0$  deg and  $Q=1.5 Q_N$ .

Two specific flow features are analysed in the present study: first, the relationship between pressure loading on the blades and torque and, second, a possible correlation between pressure fluctuations and vorticity changes in the volute. In both cases, flow rate dependence is considered for design and off-design conditions. The instantaneous torque and the pressure fluctuations have been already shown and therefore, in what follows, the other two variables will be considered.

**Flow Field as Function of Relative Blade Position.** As a first approach, averaged fields are studied in order to evaluate the overall trends. Although both pressure and velocity are studied, the focus is placed on the velocity fields. Figure 10 shows the absolute velocity vectors in the near tongue region for three different flow rates and for the same blade positions. A midspan pseudostream surface (between hub and shroud) is considered for this figure. As expected from other published data [13], stagnation point moves around the tongue depending on the flow rate, appearing at the volute tongue symmetry position only at the nominal flow rate (Fig. 10, upper right figure). For low flow rates (Fig. 10, upper left figure for  $0.5 Q_N$ ), a low velocity region is obtained on the discharge pipe zone and the stagnation point occurs placed on the pipe side of the volute tongue. For high flow rates (Fig. 10, lower figure, for  $1.5 Q_N$ ), a strong recirculation bubble is found in the impeller side and the stagnation point occurs towards this bubble, whereas another bubble appears in the discharge pipe, decreasing the possible pressure recovery effect of the volute. Considering the volute tongue tip as a semi-cylinder with radius  $R$ , the position of the stagnation point is at the symmetry plane for the nominal flow rate, at  $0.4R$  and in the upstream (exit direction) for the lower flow rate and at  $2.5R$  in the upstream (impeller direction) for the higher one.

Once the averaged fields have been studied and good agreement with the expected trends had been found, instantaneous distributions of the flow variables inside the impeller are considered in order to correlate the different states with the torque needed to cause the impeller movement in each instant. Again, a pseudostream surface placed half-way between hub and shroud is chosen for this flow study. Again, three significant flow rates are considered, namely  $Q=0.5 Q_N$ ,  $Q_N$ , and  $1.5 Q_N$ . Figure 11 shows the pressure in the before-mentioned midspan pseudostream surface for three flow rates and for three different relative impeller-tongue positions (three time instants for a blade passing period, named A, B, and C in Fig. 5). Following a representation in which the three flow rates are presented in three columns and each time instant is presented in the same row, a figure array is built. Therefore, in Fig. 11 each figure row corresponds to one of the three time instants considered and each column corresponds to one of the three



**Fig. 10 Absolute velocities in an intermediate pseudostream surface, plotted in a 0–14.5 m/s scale. Low (upper left figure), nominal (upper right figure) and high flow rate (lower figure).**

flow rates analyzed. The first time instant corresponds to a position in which the blade is in front of the volute tongue and the other two instants (*B* and *C*) correspond to two intermediate positions (the tongue is between two blades). The same scale is kept for all these figures in order to enable comparisons to be made. A really uniform pressure increase through the different channels is maintained for the nominal flow rate, whereas for off-design conditions a departure from this axis-symmetric situation is obtained, as will be explained. To comment on this array of figures, an angle  $\varphi$ , measured in the rotating direction, from the line that connects the rotating center and the volute tongue, will be considered.

In the first column of Fig. 11, a region with higher pressures is found in the range of  $270 \text{ deg} < \varphi < 360 \text{ deg}$  (just preceding the volute tongue, in the rotating direction). The blades seem to be more loaded in the second position (second row or intermediate time instant, instant *B*) because there are more blades with high pressure in this position. A region of low pressure distribution is observable in the range  $0 \text{ deg} < \varphi < 90 \text{ deg}$  (just following the volute tongue). The second (intermediate) column of Fig. 11 depicts a different loading of the blades, with almost equal pressure distribution in all the blade passages, according to the relative vector velocity. Finally, the third column of Fig. 11 shows a contrasting situation in comparison with the first column: that is, a region of high pressure in the range of  $0 \text{ deg} < \varphi < 90 \text{ deg}$  (following the volute tongue) and a region of low pressure distribution in the range  $270 \text{ deg} < \varphi < 360 \text{ deg}$  (preceding the volute tongue). A less axis-symmetric pattern is now found when the blades are not in front of the volute tongue (second row or instant *B*). Therefore, based on the local pressure distribution, the conclusion might be that the off-design conditions show a kind of opposite behavior (maximum loading for blades in front of the volute tongue for low flow rates and minimum for high flow rate), whereas the nominal flow rate produces a more uniform loading for any flow rate.

**Helicity Inside the Volute.** Finally, the helicity in the volute is plotted. Such a study is carried out in order to obtain information on the secondary flow patterns and possible correlation between these helicity values and the axial evolution of the previously analyzed pressure fluctuations. Although both variables are not related to each other, their evolution in the volute could explain some flow behaviors. The pressure fluctuations are obtained as a result of frequency analysis and, due to the numerical and experimental treatment of the signal, are a consequence of the whole flow pattern at the blade passing frequency, whereas the helicity is an instantaneous variable, which only accounts for the secondary flows. On the other hand, there is no dynamic equation that clearly states a relationship between both of them. Therefore, only a qualitative comparison makes sense and would possibly indicate the feasible correlation between these variables, which is searched in this section.

Helicity is defined as the dot product of the vorticity and the velocity vectors, that is:  $(\nabla \times \vec{u}) \cdot \vec{u}$ . It provides information on the vorticity aligned with the fluid stream and has been plotted here to identify secondary flows. Inside the impeller, and due to the momentum exchange, there is an increase of vorticity, but in the volute there should be a kind of vorticity conservation along the stream paths. This feature should be observed in the calculations. For the sake of completeness and summarizing the available results, only the previously mentioned three flow rates are considered:  $Q=0.5 Q_N$ ,  $Q_N$ , and  $1.5 Q_N$ , and the three time instants analyzed so far will also be taken into account (namely positions *A*, *B*, and *C* of the impeller blades).

For the local helicity study, four radial planes, each at  $90 \text{ deg}$  to each other and starting on a position  $10 \text{ deg}$  before the volute tongue (rotating direction) are analyzed. See Fig. 12 for a geometrical description of these four planes. The helicity inside the

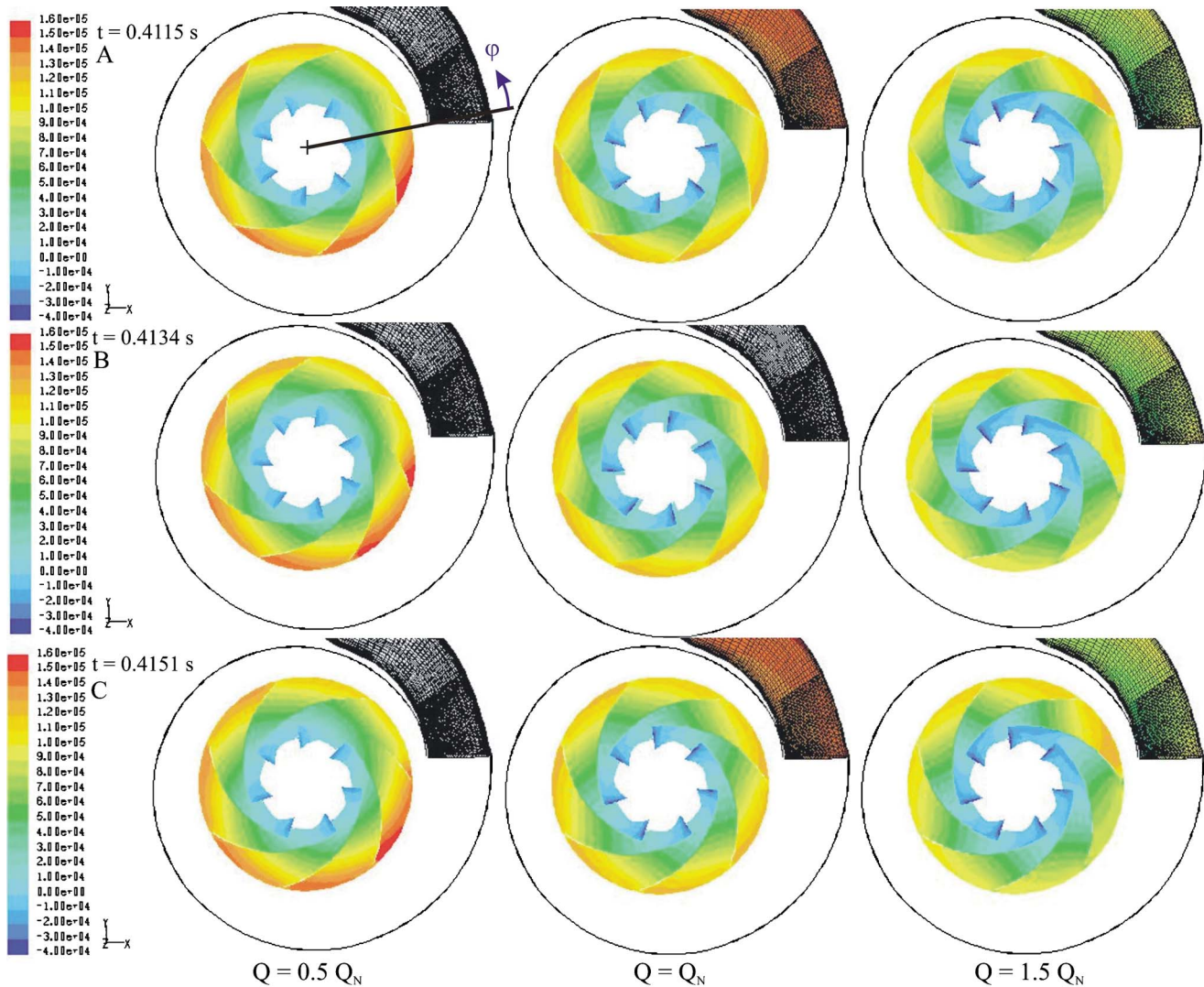


Fig. 11 Static pressure in the middle pseudostream surface inside the impeller for three flow rates and three time instants (A, B, C in respective rows)

volute at the described four angular positions around the volute is mapped for the same time instant previously considered for the torque, and for the nominal flow rate (Fig. 13). Again, as done for the pressure distributions, a figure array is built. Each row corre-

sponds to one of the four radial planes and each column corresponds to three time instants considered (this representation is the same for the three flow rates analyzed, that is for Figs. 13–15). Although the general instantaneous trends are observed to be the

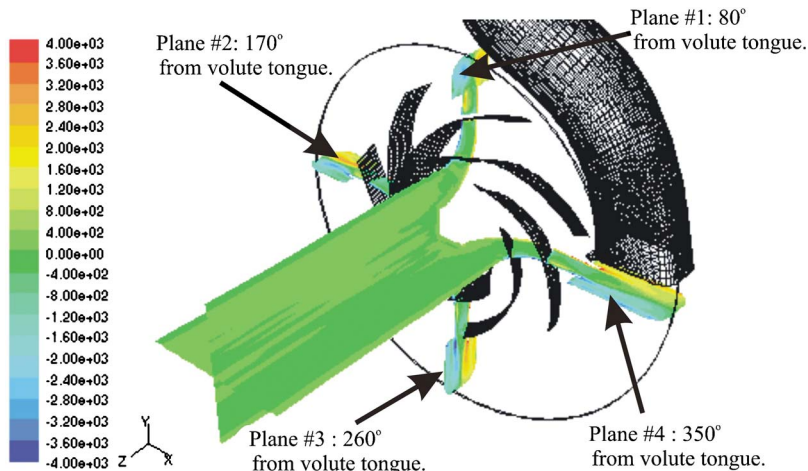


Fig. 12 Location of the reference planes to study the helicity inside the volute

same for any relative blade-tongue position (some previous results have already been reported in Ref. [27]) and, therefore, the consideration of the same time instant does not restrict the overall conclusions, a detailed study is presented considering the same time instants already shown for the torque and pressure maps.

In Fig. 13 and for any of the three time instants considered, two counter-rotating vortices are captured. It can be seen that the vortex centres remain more or less at the same radial distance from the impeller outlet all round the volute (independently of the position  $\varphi$  considered). Only small differences are found at both sides of the center plane (middle surface in the axis direction, “z”). The strength of the vortices (plotted with the same scale for relative comparison) provides a region of higher helicity in the range of  $0 \text{ deg} < \varphi < 180 \text{ deg}$ . From that angle on, the cross section is great enough to provide a diffusion of the vortex strength. In any case, though, the symmetry plane of the volute does describe also the symmetry of the counter rotating vortices.

In the volute, there is no generation of circulation and therefore, an increase of the cross section would produce a decrease in the helicity. This behavior is observed except for section No. 4, just before the position of the volute tongue. The effect of this volute tongue on the secondary flows is therefore made clear.

The same four planes are studied for the other two operating conditions considered, that is off-design conditions, namely  $0.5 Q_N$ , and  $1.5 Q_N$ . The helicity maps numerically obtained for the three relative blade positions considered are plotted in Figs. 14 and 15. As with all the helicity figures (Figs. 13–15) they are plotted to the same scale, to enable direct comparison, although the scale ( $-6e3$  to  $6e3$  has only a qualitative meaning). The higher values of the helicity are found for the lower flow rate (Fig. 14), for a position placed near the volute tongue. In this Fig. 14, the center of the positive vortex is neatly placed on the hub side of the volute, whereas the negative vortex is not so clearly defined. Moreover, it seems that it does not appear in the first two sections analyzed and only can be observed for angles  $\varphi > 180 \text{ deg}$ . Even for these angles, the full structure is more fuzzy and far from the symmetric situation depicted in Fig. 13. The large positive vortex is placed on the hub side of the volute and its strength does not decay so strongly. Again and in parallel with the expected result already commented on for Fig. 13, a decrease in the vortex strength becomes visible as larger sections of the volute are considered.

At higher flow rates (Fig. 15), the symmetry plane again becomes a condition of symmetry for the helicity (similar to the nominal flow rate result). The structure in this figure is very much the same as for Fig. 13. More flow rates are analyzed, but the results does not add more information to the depicted vortex structure.

Although the results of Figs. 7–9 are related to the pressure component only at the blade passing frequency, the existence of a higher pressure at the symmetry section does agree with the appearance of the two counter-rotating vortices. This is clearer for the results obtained for flow rates higher than the nominal.

However, for low flow rates operation (lower than or equal to  $0.5 Q_N$ ), although the pressure pattern at the blade passing frequency would induce a similar conclusion, no symmetric pair of vortices is obtained numerically. This effect may be the result of two different causes: first, for this operating points more intermediate planes would be needed to establish the maximum fluctuations and, second, the partial load phenomena interact with the pressure fluctuations and, therefore, no clear correlation between the local flow and the global pressure obtained is possible. A stronger change in function of time is also found for this flow rate.

Another fact to be taken into account is the existence, for the lower flow rate considered (see the pressure patters obtained in Fig. 7), of a region around the interval  $0 \text{ deg} < \varphi < 60 \text{ deg}$  where the pressure fluctuations at the blade passing frequency for the

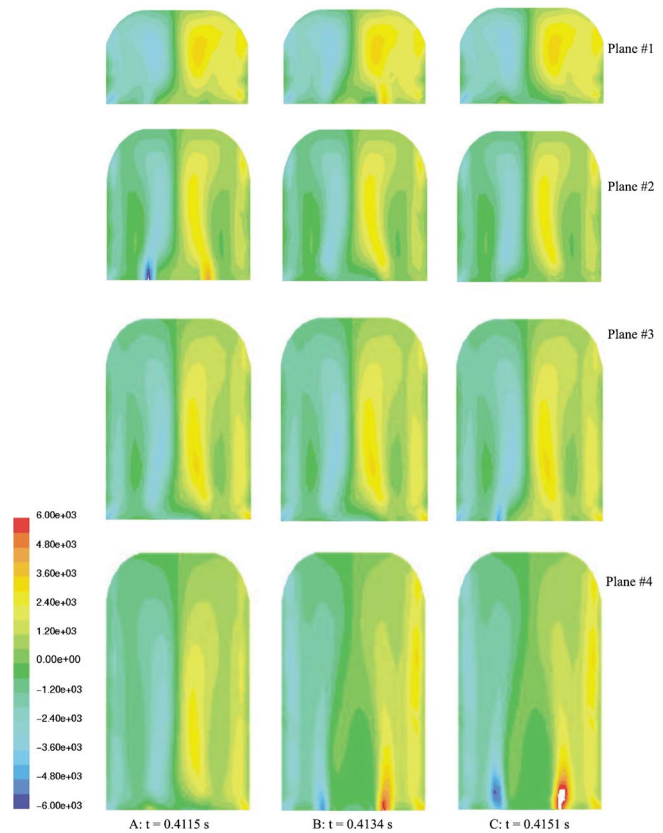


**Fig. 13 Helicity in  $\text{m/s}^2$  for  $Q = Q_N$  at four different volute planes (placed at 80, 170, 260, and 350 deg from the tongue) and three time instants (left to right)**

three different planes collapse. This effect could break the vortex structure found at other flow rates, where the different curves differ more for such locations close to the volute tongue.

In any case, the study of the pressure distributions and the helicity contour maps inside the volute of the pump seem to follow trends very much related one to the other, and a direct correlation is found for a relatively wide range of flow rates. Also, the instantaneous torque evolution seems to be correlated to the observed evolution.

Therefore, and considering the set of Figs. 7–9 and the set of Figs. 13–15, a certain relationship between the maximum of the pressure fluctuations and the helicity fields is revealed. When there is a maximum or a minimum of the pressure fluctuations in the different axial planes, the flow creates a similar behavior, which has been studied here by means of the helicity fields. The strength of the vortices remains more constant for the nominal flow rate, where there is a more constant difference between the pressure fluctuations in the different axial planes, whereas at lower and higher flow rates (off-design conditions) the helicity shows stronger mixing processes.

## Conclusions

The 3D unsteady calculation combined with the sliding mesh technique has proven to be a useful tool to investigate the flow field inside a centrifugal pump including the dynamic effects. This numerical procedure has been used in this work to analyze different flow phenomena, both instantaneously and in a blade passing average basis. Previous works [28,30,32] do validate the model in what refers to static and dynamic performance and extensively compare with existing experimental data.

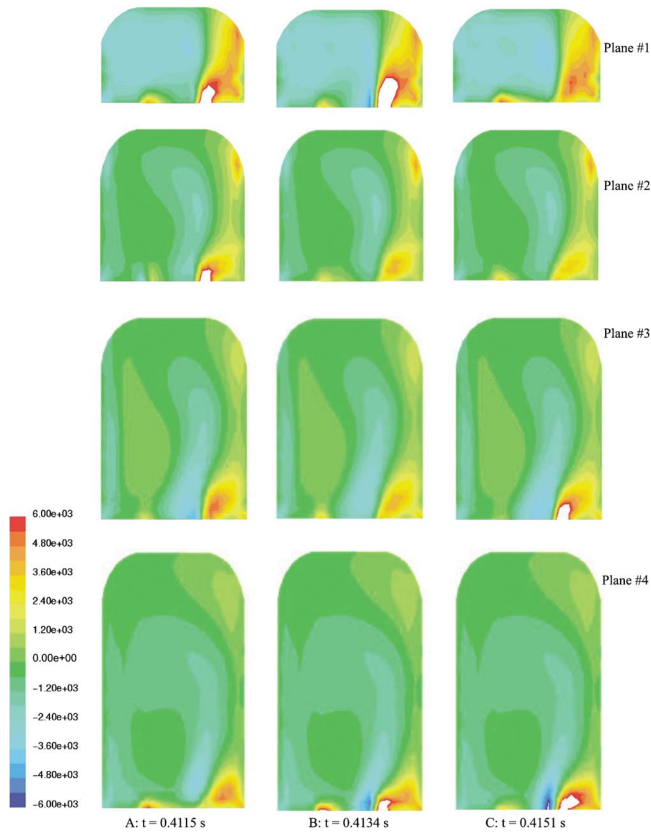


**Fig. 14 Helicity in  $m/s^2$  for  $Q=0.5 Q_N$  at four different volute planes (placed at 80, 170, 260, and 350 deg from the volute tongue) and three time instants (left to right)**

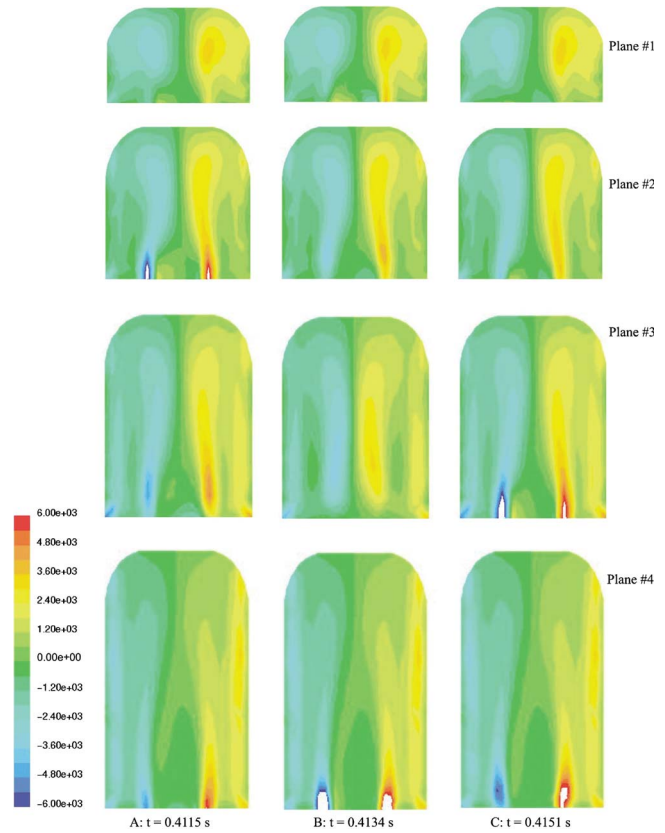


**Fig. 15 Helicity in  $m/s^2$  for  $Q=1.5 Q_N$  at four different volute planes (placed at 80, 170, 260, and 350 deg from the volute tongue) and three time instants (left to right)**

The stagnation point placement on the volute tongue numerically calculated is in agreement with the typical evolution for centrifugal pumps, according to the literature data. The pressure fields in function of the blade position gives rise to the different blade loadings. These different loadings appear to be predominant for the instantaneous torque, over the other possible effects (viscous, etc.). This conclusion has been drawn through the detailed study and comparison of both local and global data. Although both sets of data are results of the numerical model, the torque was validated with experiments in previous studies [32] and only a slight underestimation of the numerical model is found.

The helicity, as a measure of the secondary has been correlated to the pressure fluctuations for the blade passing frequency at different axial planes. Although there is no clear mathematical relationship for those two variables, an intrinsic relationship is found. Actually, except for low flow rates, where other effects are superimposed, a flow structure depending only on such pressure fluctuations seems to be found. These results stresses the predominant role of the pressure fluctuations at the blade passing frequency (impeller-volute interaction) on the flow patterns obtained. Possible interaction with partial load phenomena have been obtained. The boundary condition imposed by the volute and its effects on the circumferential variation of the helicity has been studied for a wide range of operating conditions.

The main goal reached with this study has been the finding of a plausible explanation for the flow structure inside the pump corresponding with the pressure and torque fluctuating values. In other words, a correlation between global and local flow features has been obtained. The pressure fluctuations due to the impeller-volute interaction filtered at the blade passing frequency provide valuable information and explain many flow characteristics in a centrifugal pump.

## Acknowledgment

The research conducted has been sponsored by the Ministerio de Ciencia y Tecnología (Spain) under Projects No. DPI2001-2598, No. DPI2002-04266-C02-02, and No. DPI2003-09712.

## Nomenclature

- $b_2$  = impeller width at outlet, m
- $D_2$  = impeller diameter at outlet, m
- $f_{BP}$  = blade passing frequency, Hz
- $H_N$  = pump head at best efficiency point (nominal), m
- $k$  = turbulent kinetic energy,  $m^2/s^2$
- $p_A$  = pressure, pressure amplitude at the blade passing frequency, Pa
- $Q, Q_N$  = flow rate and flow rate at nominal point,  $m^3/s$
- $R$  = volute tongue tip radius
- $T, \bar{T}$  = torque and averaged torque in a blade passing period, N m
- $\bar{u}$  = flow velocity, m/s
- $U_2$  = peripheral velocity at impeller outlet, m/s
- $z$  = axial coordinate, m
- $\beta_2$  = impeller blade angle (outlet section), deg
- $\varepsilon$  = turbulent dissipation,  $m^2/s^3$
- $\rho$  = density of the fluid (water in this paper),  $kg/m^3$
- $\varphi$  = angular position around impeller, deg
- $\omega$  = rotating speed, rad/s
- $\omega_S$  = specific speed  $\omega_S = \omega Q_N^{1/2} / (g H_N)^{3/4}$ , -

## References

- [1] Laskminarayana, B., 1996, *Fluid Dynamics and Heat Transfer of Turbomachinery*, Wiley Interscience, New York.
- [2] Engeda, A., 1998, "From the Crystal Palace to the Pump Room," International Gas Turbine & Aeroengine Congress, Stockholm, Sweden, 98-GT-22.
- [3] Brennen, C. E., 1994, *Hydrodynamics of Pumps*, Oxford University Press, New York.
- [4] Japikse, D., Marscher, W. D., and Furst, R. B., 1997, *Centrifugal Pump Design and Performance*, Concepts ETI, Inc, Wilder, VT.
- [5] Gopalakrishnan, S., 1997, "Pump Research and Development—Past, Present, and Future. An American Perspective," ASME-FEDSM-97-3387.
- [6] Karassik, I. G., Krutzsch, W. C., Fraser, W. H., and Messina, J. P., 1985, *Pump Handbook*, 2nd ed. McGraw Hill, New York.
- [7] Greitzer, E. M., 1981, "The Stability of Pumping Systems. The 1980 Freeman Scholar Lecture," ASME J. Fluids Eng., **103**, pp. 193–242.
- [8] Morgenroth, M., and Weaver, D. S., 1998, "Sound Generation by a Centrifugal Pump at Blade Passing Frequency," ASME J. Turbomach., **120**, pp. 736–743.
- [9] Chu, S., Dong, R., and Katz, J., 1995, "Relationship Between Unsteady Flow, Pressure Fluctuations, and Noise in a Centrifugal Pump—Part B: Effects of Blade-Tongue Interactions," ASME J. Fluids Eng., **117**, pp. 30–35.
- [10] Binder, R. C., Lafayette, I. N. D., and Knapp, R. T., 1936, "Experimental Determination of the Flow Characteristics in the Volutes of Centrifugal Pumps," Trans. ASME **58-4**, pp. 649–663.
- [11] Bowerman, R. D., and Acosta, A. J., 1957, "Effect of the Volute on Performance of a Centrifugal Pump Impeller," Trans. ASME, **79**, pp. 1057–1069.
- [12] Adkins, D. R., and Brennen, C. E., 1988, "Analysis of Hydrodynamic Radial Forces on Centrifugal Pump Impellers," ASME J. Fluids Eng., **110**, pp. 20–28.
- [13] Miner, S. M., Flack, R. D., and Allaire, P. E., 1992, "Two Dimensional Flow Analysis of a Laboratory Centrifugal Pump," ASME J. Fluids Eng., **114**, pp. 333–339.
- [14] Kaupert, K. A., and Staubli, T., 1999, "The Unsteady Pressure Field in a High Specific Speed Centrifugal Pump Impeller. Part I: Influence of the Volute," ASME J. Fluids Eng., **121**, pp. 621–626.
- [15] Dong, R., Chu, S., and Katz, J., 1997, "Effect of Modification to Tongue and Impeller Geometry on Unsteady Flow, Pressure Fluctuations and Noise in a Centrifugal Pump," ASME J. Turbomach., **119**, pp. 506–515.
- [16] Wuibaut, G., Bois, G., Dupont, P., Caignaert, G., and Stanilas, M., 2002, "PIV Measurements in the Impeller and Vaneless Diffuser of a Radial Flow Pump in Design and Off-Design Operating Conditions," ASME J. Fluids Eng., **124**, pp. 791–797.
- [17] Gunzburger, M. D., and Nicolaides, R. A., 1993, *Incompressible Computational Fluid Dynamics. Trends and Advances*, Cambridge University Press, Cambridge.
- [18] Lakshminarayana, B., 1991, "An Assessment of Computational Fluid Dynamic Techniques in the Analysis and Design of Turbomachinery—The 1990 Freeman Scholar Lecture," ASME J. Fluids Eng., **113**, pp. 315–352.
- [19] Denus, C. K., and Góde, E., 1999, "A Study in Design and CFD Analysis of a Mixed-Flow Pump Impeller," ASME-FEDSM-99-6858.
- [20] Miner, S. M., 2000, "Evaluation of Blade Passage Analysis Using Coarse Grids," ASME J. Fluids Eng., **122**, pp. 345–348.
- [21] Arndt, N., Acosta, A. J., Brennen, C. E., and Caughey, T. K., 1990, "Experimental Investigation of Rotor-Stator Interaction in a Centrifugal Pump with Several Vaned Diffusers," ASME J. Turbomach., **112**, pp. 98–108.
- [22] Baun, D. O., Köstner, L., and Flack, R. D., 2000, "Effect of Relative Impeller-to-Volute Position on Hydraulic Efficiency and Static Radial Force Distribution in a Circular Volute Centrifugal Pump," ASME J. Fluids Eng., **122**, pp. 588–605.
- [23] Aysheshim, W., and Stoffel, B., 2000, "Numerical and Experimental Investigations on a Centrifugal Pump Stage With and Without Vaned Diffuser: Experimental Part," IAHR, *Proceedings of the XXI Symposium on Hydraulic Machinery and Systems*.
- [24] Croba, D., and Kueny, J. L., 1996, "Numerical Calculation of 2D, Unsteady Flow in Centrifugal Pumps: Impeller and Volute Interaction," Int. J. Numer. Methods Fluids, **22**, pp. 467–481.
- [25] Longatte, F., and Kueny, J. L., 1999, "Analysis of Rotor-Stator-Circuit Interactions in a Centrifugal Pump," ASME-FEDSM-99-6866.
- [26] Shi, F., and Tsukamoto, H., 2001, "Numerical Study of Pressure Fluctuations Caused by Impeller-Diffuser Interaction in a Diffuser Pump Stage," ASME J. Fluids Eng., **123**, pp. 466–474.
- [27] Blanco, E., Fernández, J., González, J., and Santolaria, C., 2000, "Numerical Flow Simulation in a Centrifugal Pump with Impeller-Volute Interaction," ASME-FEDSM-00-11297.
- [28] González, J., Fernández, J., Blanco, E., and Santolaria, C., 2002 "Numerical Simulation of the Dynamic Effects Due to Impeller-Volute Interaction in a Centrifugal Pump," ASME J. Fluids Eng., **124**, pp. 348–355.
- [29] British Standard BS-5316 Part-2, 1977, Acceptance Tests for Centrifugal, Mixed Flow and Axial Pumps."
- [30] González, J., 2000, "Modelización Numérica del Flujo no Estacionario en Bombas Centrífugas. Efectos Dinámicos de la Interacción entre Rodete y Voluta, Ph.D. thesis (in Spanish), Universidad de Oviedo, Spain.
- [31] Freitas, C. J., 1993, "Journal of Fluids Engineering Editorial Policy Statement on the Control of Numerical Accuracy," ASME J. Fluids Eng., **115**, pp. 339–340.
- [32] González, J., Santolaria, C., Blanco, E., and Fernández, J., 2002, "Unsteady Flow Structure on a Centrifugal Pump: Experimental and Numerical Approaches," ASME-FEDSM2002-31182.
- [33] Tsukamoto, H., Uno, M., Hamafuku, N., and Okamura, T., 1995, "Pressure Fluctuation Downstream of a Diffuser Pump Impeller," ASME FED, **216**, pp. 133–138.
- [34] Goto, A., and Zangeneh, M., 2002, "Hydrodynamic Design of Pump Diffuser Using Inverse Design Method and CFD," ASME J. Fluids Eng., **124**, pp. 319–328.



# Numerical Study of Unsteady Flows in a Scroll Compressor

**M. M. Cui**  
TRANE Air Conditioning,  
American Standard Companies,  
La Crosse, WI 54601

*Since scroll compressors contain gas pockets whose shapes and sizes change continuously, the flow fields inside the compressors are time dependent and three-dimensional. The spatial and temporal variations inside the gas pockets also induce unsteady flows between the gas pockets. This unsteadiness controls the mechanisms responsible for the behavior of the scroll compressor components and their interactions. The dynamic nature inherent in the scroll compressors affects the performance and reliability of the scroll compressors. To improve and optimize the scroll compressor design for better performance and reliability, information is needed to understand the detailed physics of the unsteady flows inside the scroll compressors. To provide the fundamental information needed, the unsteady flows in a scroll compressor are studied numerically. The system simulated includes upper bearing housing, scrolls, check valve, and discharge plenum. Refrigerant-22 is used as the working fluid. The unsteady flows inside and between the gas pockets are characterized by the instantaneous distributions of field quantities and the area- and mass-averaged parameters. [DOI: 10.1115/1.2243300]*

## 1 Introduction

In a scroll compressor, the working process consists of continuously compressing a series of gas pockets in crescent-shaped volumes. These gas pockets inside a scroll compressor move along a spiral profile. The volume and shape of the gas pockets change with their locations. The variations of pressure and temperature inside the gas pockets also generate leakage flows between the gas pockets. These gas pockets are eventually squeezed out periodically into a check valve through the discharge port. At design working conditions, the gas flow passes the check valve and reaches the discharge plenum, a cylindrical open space. In the plenum, the unsteadiness of the velocity, pressure, and temperature of the gas stream are attenuated. The stabilized gas flow eventually leaves the compressor outlet. The unsteadiness is associated with all aforementioned components. The geometry of the gas flow path through the compressor is complicated. The shape of the volume occupied by gas moves and deforms continuously as the scroll orbits. The complexity of the scroll compressor geometry poses a challenge for numerical simulation of the flow and heat transfer inside the scroll compressors. Typical analyses of scroll compressors are conducted using one-dimensional mathematical models [1,2]. Over the years, a few attempts [3–5] have been made to overcome this obstacle. The two-dimensional pressure, temperature, and velocity distributions for an individual gas pocket were obtained.

In the current study, a scroll compressor has been numerically simulated in an integrated fashion. The components from the inlet to outlet of the scroll compressor along the flow path are included in the simulation (Fig. 1). The asymmetric structure of each component and interaction between them are analyzed. The inlet of the compression chamber is the area at the bottom of Fig. 1(a). Figure 1(b) shows the shape of the scrolls and surrounding structure inside the compressor. The basic parameters of the compressor are listed in Table 1.

## 2 Methodology

To obtain the best predictability, the governing equations are kept in the most general form to solve accurately for given geometry [6]. The first part of the simulation is to prepare the domain,

generate mesh, model fluid properties, and define boundary conditions. A block-structured mesh for the entire scroll compressor is generated. The geometry includes the upper bearing housing, fixed and orbiting scrolls, dummy and discharge ports, and the discharge plenum. Since the scrolls are designed to achieve a preferred porting area schedule at the discharge port, the shapes of the fixed and orbiting scrolls are different. The total mesh has about 700,000 hexahedral elements. The maximum skew of the elements is smaller than 28 deg. The  $y^+$  for the turbulent boundary layer is between 20 and 100. The surface boundary conditions are adiabatic smooth walls for machined surfaces and adiabatic rough walls for casting surfaces with a roughness of 25  $\mu\text{m}$ . The mesh for the domains inside the fixed and orbiting scrolls is regenerated at each time step to accommodate the shape and size change of the gas pockets. The mesh density is automatically adjusted to resolve the leakage flows. The thermodynamic and transport properties of Refrigerant-22 are calculated using the Martin-Hou equation of state and power laws, respectively. The second part of the project is to solve the Navier-Stokes equations with the  $k-\varepsilon$  turbulence model. A commercial coupled-implicit solver based on the finite-volume method is applied to the geometry. The discretization model is a modified linear profile with physical advection correction. For each case calculated, the solution is considered to be converged when the rms residuals of all the governing equations have been reduced by five to six orders of magnitude from their initial values. The calculation continues until the main structure of the flow field shows stable patterns.

The data are recorded after the inlet and outlet gas properties show good agreement with experimental observation. For each time step, the basic field quantities are recorded as functions of time and location. The other field quantities can be calculated from these basic field quantities. The statistic quantities can be obtained following the proper averaging procedures. Some surface, volume, and mass averaging algorithms are listed in Table 2. The overall design and performance parameters are obtained by integrating the field quantities over the domain of interest.

## 3 Overall Features of the Flow Field

The main features of the flow field can be seen in the distribution of the basic flow field quantities: velocity, temperature, and pressure. These field quantities are calculated every 1.5 deg and the data are saved every 3 deg of crank shaft rotation. The equivalent time interval is  $7.143 \times 10^{-6}$  s for 1.5 deg. Figures 2–7 show the velocity, temperature, and pressure distributions on  $z$  and  $x$

Contributed by the Fluids Engineering Division of ASME for publication in the JOURNAL OF FLUIDS ENGINEERING. Manuscript received October 17, 2003; final manuscript received February 21, 2006. Assoc. Editor: Jinkook Lee.

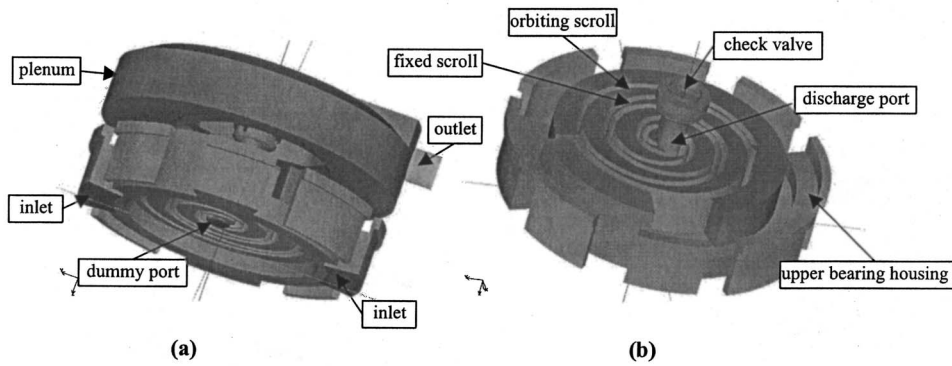


Fig. 1 Flow domain of the scroll compressor: (a) compressor and (b) scroll involute

Table 1 Scroll compressor parameters

Inlet pressure (MPa)	Exit pressure (MPa)	Mass flow rate (kg/s)	Speed (rpm)	Power (kW)
0.6	2.2	0.3473	3500	53

Table 2 Some average algorithms used in the calculation

Volume averaged properties	Area averaged properties
$\bar{V} = \frac{1}{V} \iiint_V dv$	$A = \iint_A dA$
$M = \iiint_V \rho dv$	$\dot{m} = \iint_A \rho \mathbf{V} \cdot \mathbf{n} dA$
$\bar{\Phi} = \frac{1}{V} \iiint_V \Phi dv$	$\bar{\Psi} = \frac{1}{A} \iint_A \Psi dA$
$\bar{\Phi}_m = \frac{1}{M} \iiint_V \rho \Phi dv$	$\bar{\Psi}_m = \frac{1}{\dot{m}} \iint_A \rho \Psi \mathbf{U} \cdot \mathbf{n} dA$

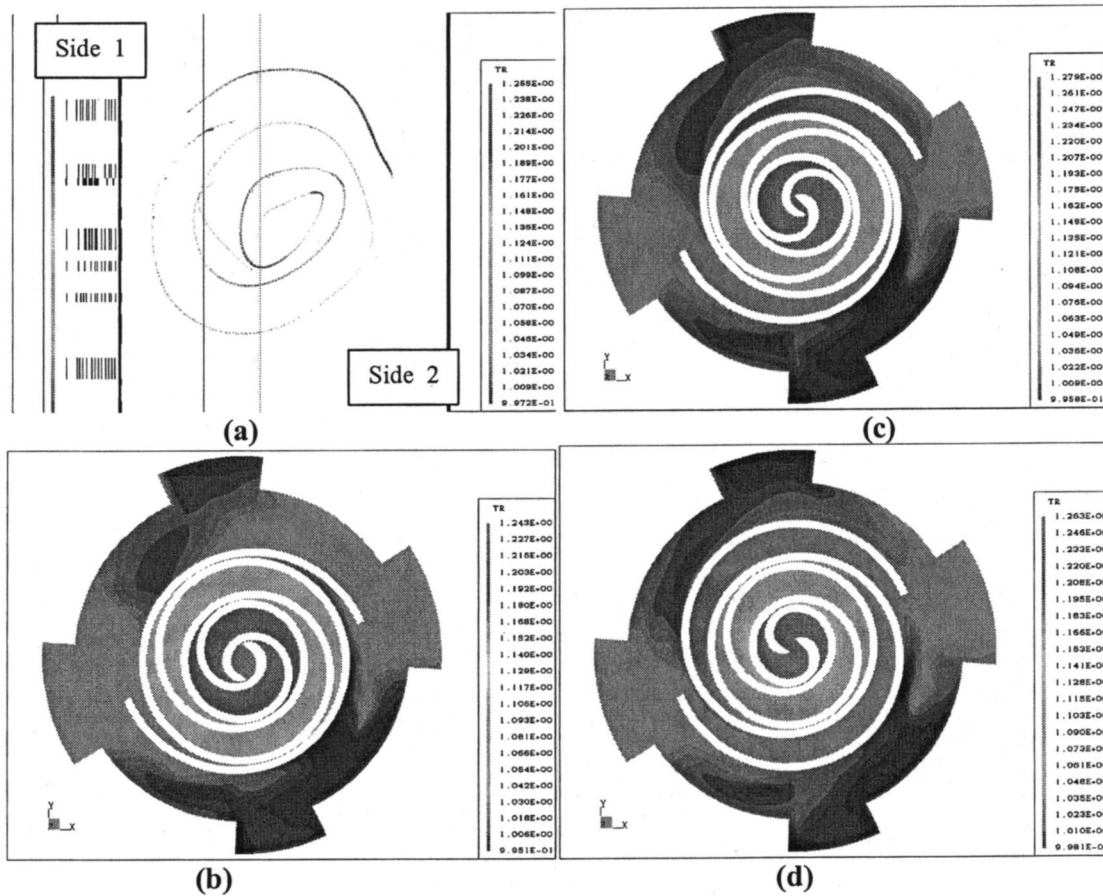


Fig. 2 Temperature distribution inside the scrolls on a cross section area perpendicular to the z axis: crank angle=(a) 0 deg, (b) 180 deg, (c) 360 deg, (d) 540 deg

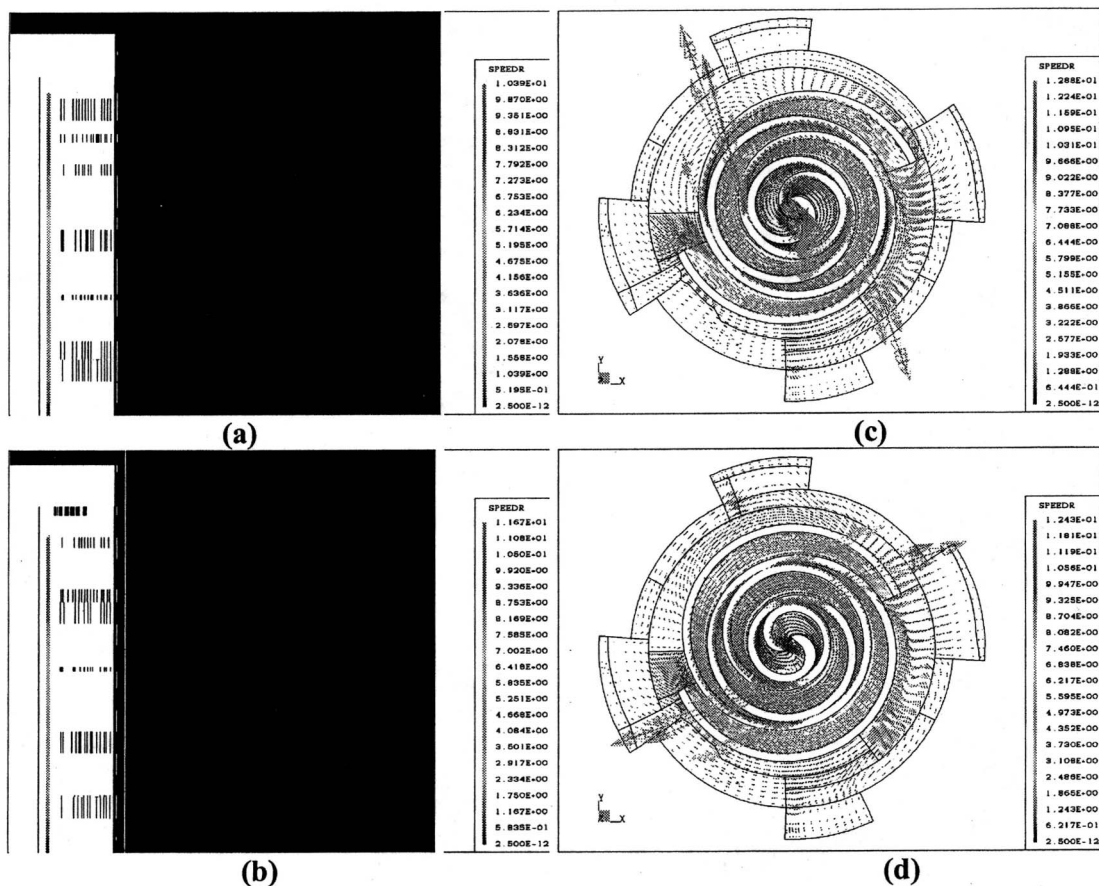


Fig. 3 Vector map on the cross-section area perpendicular to the z axis of a gas pocket: crank angle=(a) 0 deg, (b) 180 deg, (c) 360 deg, (d) 540 deg

planes. Since the scrolls separate the flow field into two similar parts, they are labeled as side 1 and side 2 (Fig. 6(a)).

Temperature distribution inside the scroll compressor is shown in Fig. 2. A total of four temperature maps are shown in Fig. 2, which are for crank angles of 0, 90, 180, and 270 deg, respectively. To generalize the results, the temperature is plotted as a nondimensional quantity using the ratio of the local temperature to the compressor inlet temperature.

At each time instant, the temperature distributions on the z plane show four steps from the compressor shell to center. These steps are represented by the suction side space and first, second, and third gas pockets, respectively (Fig. 2). It becomes the most distinguishable feature of the flow field. Although the gas leakage between the gas pockets exists both upstream and downstream, the mass flow rate of the leakage is not enough to change the temperature distribution significantly in the gas pockets. The temperature variation inside each of the gas pockets is smaller compared to overall temperature range even though the change is visible in Fig. 2. The same linear scale cannot differentiate both large scale between the gas pockets and the small scale inside the gas pockets.

As the gas pockets rotate around the z axis and are pushed into the center, the volume of the gas pockets reduces gradually while the temperature inside the gas pockets increases. The maximum temperature oscillates while the overall pattern is kept the same. As the crankshaft rotates, the compression process repeats itself.

As a gas pocket moves towards the center of the compressor, the volume of the gas pocket decreases. The temperature of the gas pockets increases gradually as the pressure goes up. The maximum of the temperature fluctuates near the center of the involute.

The asymmetric distribution of the temperature can be observed both inside the scrolls in the gas pockets and outside the scrolls in the upper bearing housing.

Figure 3 shows the vector maps inside the scrolls on a cross-section area perpendicular to the z axis. The flow inside the upper bearing housing oscillates around the scroll. Inside the scrolls, the flow is moving counter-clockwise. As the gas pocket reaches the center of the involute, a counter-clockwise vortex is formed. Inside the scrolls, the gas leaks back from higher pressure pockets to lower pressure pockets. The leaking velocity is considerably higher than the orbiting velocity of the scroll. As the scroll orbits around the center, the leaking velocity increases first. When the gas pockets approach the center of the involute, the leaking velocity reaches its maximum value and starts to decrease due to the porting process. The asymmetric flow pattern can be observed at the center of the involute due to the difference in the shapes of the scrolls and ports.

The geometry of the flow domain surrounded by the fixed and orbiting scroll is not symmetric. To obtain the targeted porting schedule, the shapes of the scrolls are designed differently. The casting surrounding the scrolls and ports are also not symmetric. All these asymmetric structures contribute to the distortion of the flow field as the gas pocket reaches the center of the compressor. The activities that deviate from the symmetry can be seen in Fig. 2(c). The three-dimensional distortion induced by the dummy and discharge ports is also shown in Fig. 7.

Figure 4 shows the pressure variation on a cross-section parallel to the x-y plane inside the gas pockets. The four plots represent the crank angles of 0, 180, 360, and 540 deg. To illustrate the pressure variation caused by flow inside the body of the gas

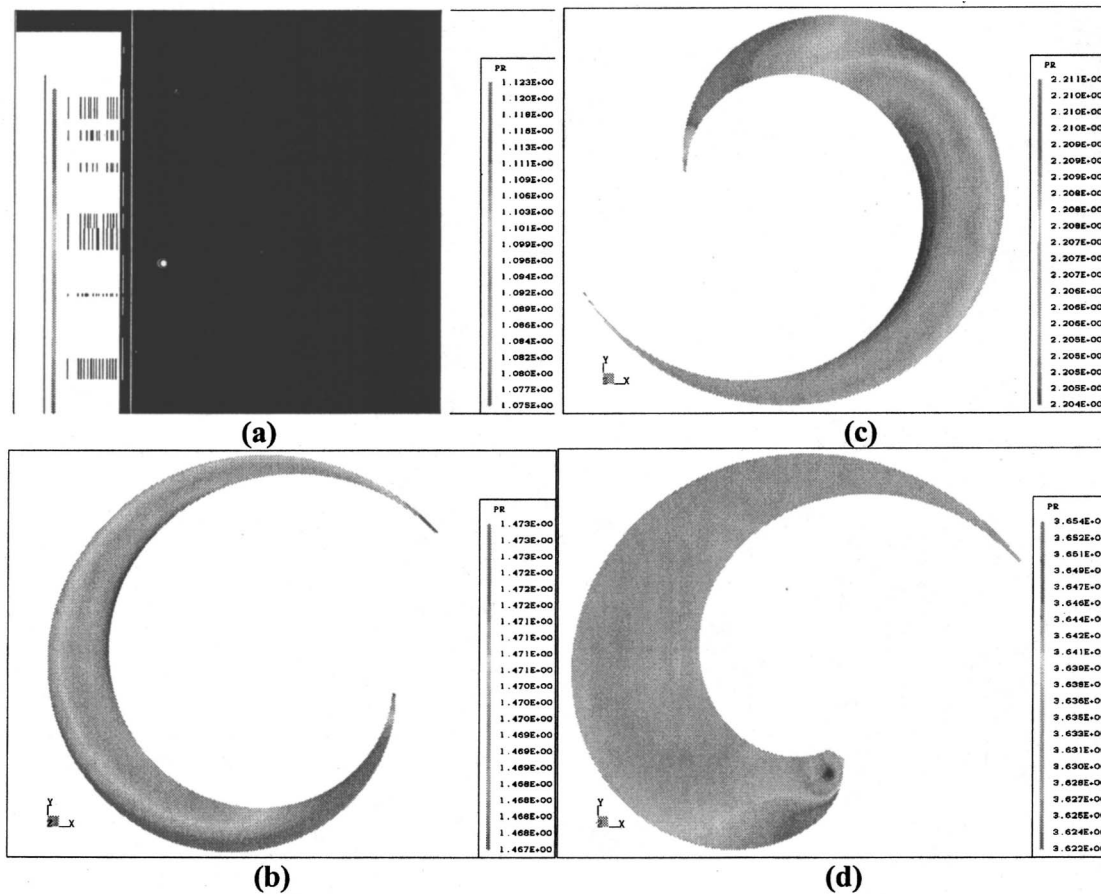


Fig. 4 Pressure distribution inside the scrolls on a cross section area perpendicular to the  $x$  axis: crank angle=(a) 0 deg, (b) 90 deg, (c) 180 deg, (d) 270 deg

pocket, the section near the throat of leakage is not shown in the pictures. The figures are enlarged to show the details of the pressure field. The pressure nonuniformity is caused by two mechanisms: leakage flow and orbiting motion of the scroll. The leakage induced pressure variations are near the tips of the gas pockets. The jets from the upper level gas pockets through the flank gap generate the low-pressure regions near the throat. The leakage also generates vertices downstream. These structures of the vertices can be observed in Figs. 4(c) and 4(d). The high-pressure region is formed as a combined result of velocity and volume change. The pressure waves start from these moving walls and eventually raise the pressure inside the pockets.

Figure 5 shows vector map of the gas pockets. The flows induced by orbiting motion and leakage flows are observable in these plots. The locations of the cross-section planes are the same as the temperature field in Fig. 2. The velocity distributions display the physical mechanisms that are responsible for flow field distortion. The leakage through the flank gap induces the flow field distortion in the form of the vertices at the tips of gas pockets. At the early stage of the compression, the pressure difference between the gas pockets is small. The distortion caused by leakage flows is limited at the tip of the pockets (Figs. 5(a) and 5(b)). As the gas pockets approach to the center of the compressor, the pressure difference becomes larger. The higher pressure difference drives the leakage velocity stronger. The vertices induced by the leakage expand into larger areas (Figs. 5(c) and 5(d)). The orbiting motion of the surrounding walls of the gas pockets drives the gas inside the pockets moving in the same direction. Due to the shape of the involute, the gas velocity shows a more complicated flow

pattern than a circular shape as the involute orbits. The local velocity of the walls around the gas pockets is shown in the velocity maps in Fig. 5.

Since the orbiting scroll moves along a circular path, it drives the gas moving along the same direction. In Figs. 4(a) and 5(a), the upper inner boundary is moving downward. The pressure in the upper part of the gas pocket is lower due to the expanding volume. The lower part of the gas pocket shows a higher value of pressure as the orbiting scroll moves to close the gas pocket. The flow inside the gas pockets is dominated by the orbiting motion of the scroll. The leakage flow is weak at this stage of the compression. The mass leaked into the gas pocket from the upper stream pocket is comparatively small. The leakage induced pressure gain is comparatively small.

Figures 4(b) and 5(b) show the pressure and velocity distributions of the gas pocket as it moves 180 deg counter-clockwise. The velocity pattern induced by the orbiting motion of the scroll is similar to that of 0 deg location in the majority part of gas pocket. In the region close to the upper stream gas pocket, the leakage flow changes this part of vector map. The pressure is higher at this part of the flow field. Two mechanisms generate this phenomenon. The first is the static pressure gain due to the velocity reduction when the leakage flow blocks the flow following the orbiting scroll. The second is the pressure increase caused by the leakage mass flow that carries higher pressure from the upper gas pocket. Consequently, a high-pressure region forms along the flow path of the incoming leakage.

As the gas pockets move along the spiral path toward the center

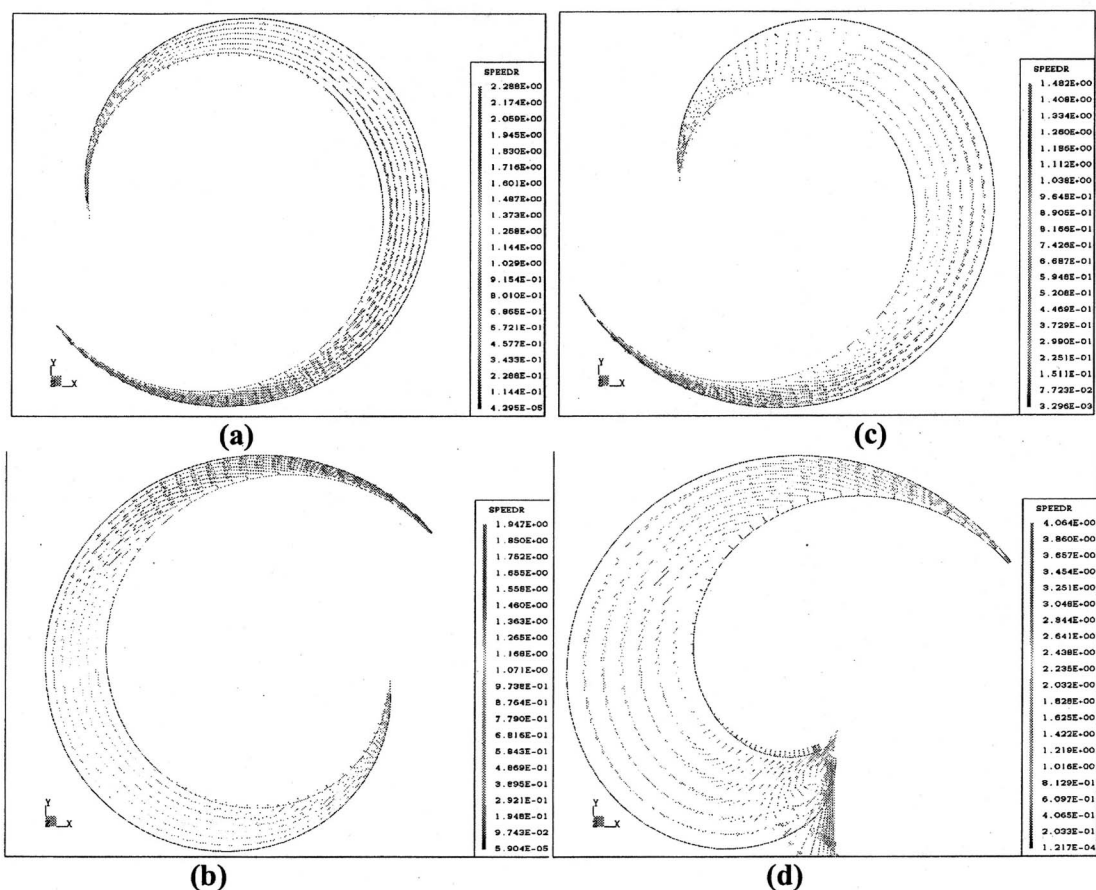


Fig. 5 Vector map inside the scrolls on a cross section area perpendicular to the  $x$  axis: crank angle=(a) 0 deg, (b) 90 deg, (c) 180 deg, (d) 270 deg

of the compressor, the vertices at the area close to the upper stream gas pocket expand. The two mechanisms responsible for the pressure distortion at the previous location become stronger. The high pressure region grows larger compared to the previous location and the shape stays similar.

The gas pocket eventually moves close to the discharge port and starts to merge into the center gas pocket. The pressure difference between the gas pockets becomes smaller. The size of the vortex at the tip of the gas pocket decreases. The penetration distance of the leakage flow is reduced (Figs. 4(d) and 5(d)).

Figure 6 shows the pressure distribution on a cross-section area perpendicular to the  $x$  axis. The shape of the flow domain can be observed in these figures. The four fringe plots of the pressure distribution are for the crank angles of 0, 90, 180, and 270 deg, respectively.

It can be seen that the pressure change along the horizontal ( $y$ ) direction is much larger than the variation in the vertical direction, the  $z$  direction. The compression of gas inside the gas pockets is completed in the horizontal direction. The activity along the vertical direction is the pressure drop caused by the check valve and the pressure recovery from the kinetic energy using discharge plenum. Figures 6(a)–6(d) also indicate that the maximum of the pressure inside the plenum fluctuates.

Figure 5 shows the velocity maps of the flow on the cross section area perpendicular to the  $x$  axis. The velocity distribution can be divided into three regions: suction region, compression region, and recovering region. The suction region is formed by the flow inside the upper bearing housing and is drawn into the gas pockets when they are opening. Due to the complicated geometry, comparatively stable size of volume, and oscillation of the orbit-

ing scroll, the velocity is slow and the flow pattern appears to have many small structures in the suction region. The compression region consists of six gas pockets. The velocity distribution is controlled by two mechanisms: the gas rotation induced by the orbiting scroll and the leakage flow due to the pressure difference of the gas pockets. The pressure recovery region includes the discharge tube, check valve, and pressure plenum. The increasing pressure inside the gas pockets first generates the high-speed gas flow downstream when the compressor starts to port. Then the gas flow goes through the check valve and spreads into the pressure plenum. A portion of the kinetic energy is converted to pressure. The rest of the kinetic energy is dissipated into heat.

The secondary flows are observable in Figs. 7(a)–7(d). The impact of these secondary flows can be seen in temperature distributions (Fig. 2). The energy carried by these secondary flows will be dissipated and not be converted to pressure. The scroll compressor design should be optimized to minimize the secondary flows inside the compressor.

#### 4 Characteristics of Gas Pockets

Inside the scrolls, the gas pockets change their shapes and volumes continuously. These changes and the associated pressure and temperature rises are the fundamental working mechanisms of the scroll compressors. The forms of the shape and volume changes control the forms of the pressure and temperature changes. Figure 8(a) shows the volume change of the gas pockets as a function of the crank angle. In the early stage of the compression, the pocket volume shows a linear behavior as the crank angle increases. As the gas pocket approaches the center of the scrolls, the volume

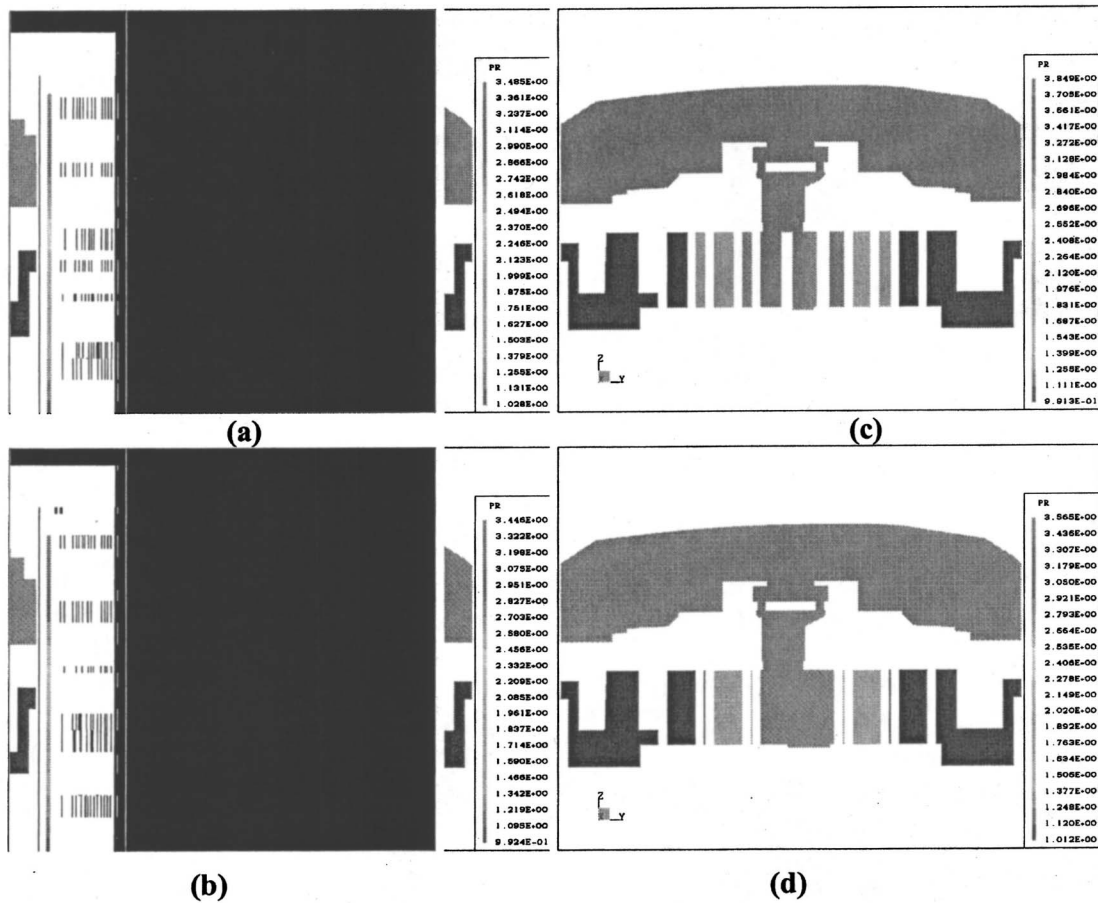


Fig. 6 Pressure distribution inside the scrolls on a cross section are perpendicular to the  $z$  axis: crank angle=(a) 0 deg, (b) 90 deg, (c) 180 deg, (d) 270 deg

change rate begins to deviate from the linear curve and decreases gradually. The change rate of the gas pockets eventually reaches zero. The total mass inside a gas pocket is plotted as a function of its volume (Fig. 8(b)). Compared to the volume, the mass inside a gas pocket is controlled by multiple factors. The shape of the scrolls and upper bearing housing impacts the suction process. The leakage between the gas pockets with different pressures induces the mass flow both to the downstream pockets and from the upstream pockets. As the pockets reach the center of the involute, the dummy and discharge ports provide more channels for gas to flow in and out of the pocket. The balance of these competing mechanisms determines the total mass inside the gas pocket. As a result, the total mass increases gradually during the early compression process and reaches its maximum value as the volume ratio equals 0.35. The total mass then starts to decrease due to the porting process. The change rate of the total mass inside the pocket behaves linearly as the porting progresses. The asymmetric distribution of the total mass also can be observed in Fig. 8(b) even though the volume of the gas pockets is close to symmetric (Fig. 8(a)).

The patterns of the volume-averaged pressure and temperature changes inside the gas pockets are similar (Fig. 9). The isentropic compression curves for the averaged pressure and temperature inside the gas pockets are also plotted for comparison. Since the flow structure is asymmetric, the gas pockets on the two sides of the scroll compressor have different features. Side 1 and side 2 are labeled in Fig. 2(a). The six gas pockets on side 1 and side 2 are named as pocket 1\_1 through 1\_3 and pocket 2\_1 through 2\_3, respectively. The name convention is kept consistent throughout this paper. Before the pressure and temperature reach their maxi-

imum values, the trend of the pressure and temperature curves shows similarity to the isentropic compression curve. As the pressure and temperature curves pass their maximum, the porting process plays an important role. The pressure and temperature curves no longer follow the isentropic curves. During the porting process, the pressure and temperature fluctuate as the orbiting scroll vane scans through the discharge port. The discharge pressure and temperature at the outlet of the pressure plenum are plotted in Fig. 9 for comparison. The overcompression of the gas inside the pockets can be seen in both pressure and temperature plots.

The leakage flows between the gas pockets exist throughout the scroll compressor working process. The flows between the gas pockets can be classified into two categories: leakage and merger flows. Figure 10 shows both the flank gap and the mass flow through the flank gap as functions of the crank angle. The flank gap changes little until the gas pockets move near the center of the involute. The gap then widens rapidly and the flow rate increases. The interesting phenomenon in this process is the leakage flow goes in different directions. The gas flows into the center pocket on one side and flows out of the center pocket on the other side. The same phenomenon shows in Fig. 3(c) as well.

Figure 11(a) shows the pressure difference between two neighboring gas pockets as a function of the crank angle. Both sides of the compression chamber are plotted together. The leakage speeds of two sides are shown in Fig. 11(b). The pressure difference shows a trend of increase before the crank angle reaches 540 deg. The pressure difference then starts to decrease and reaches its lowest point at the crank angle of 900 deg. At this point, the flank gas starts to open and the gas pockets start to merge into the center

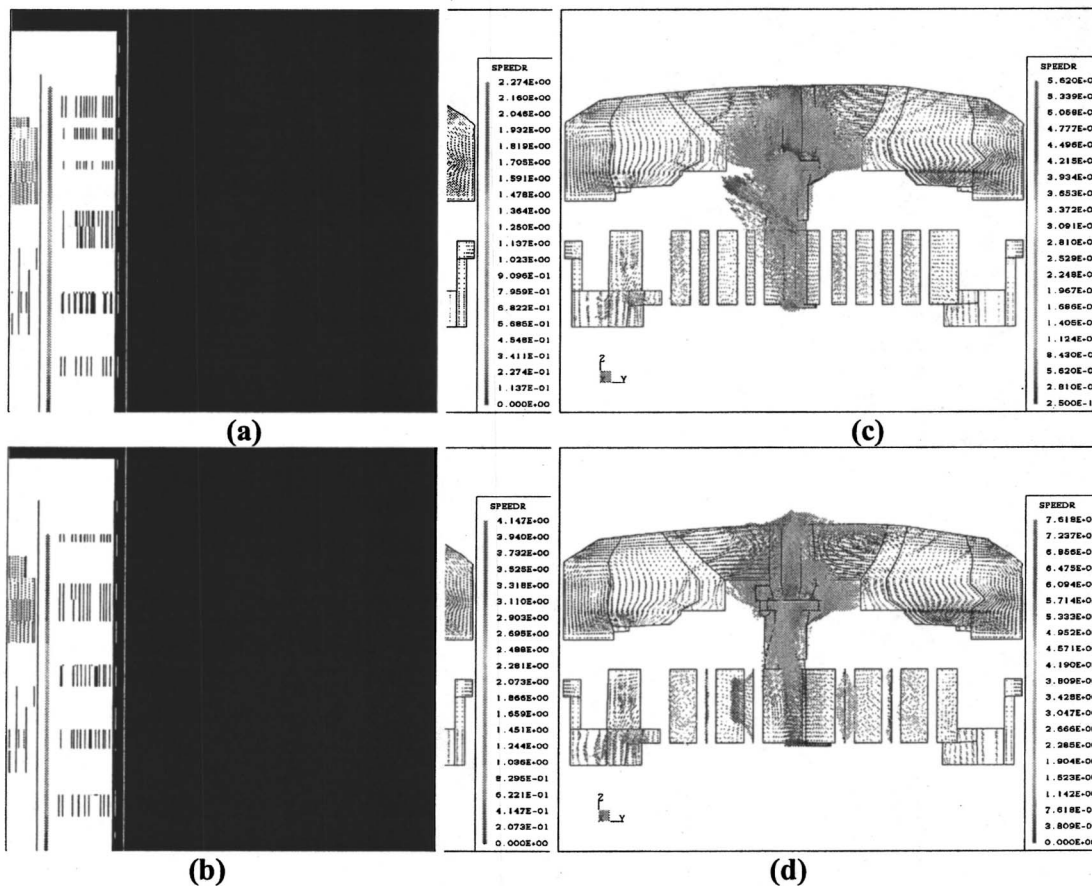


Fig. 7 Vector map inside the scrolls on a cross section area perpendicular to the  $z$  axis: crank angle=(a) 0 deg, (b) 90 deg, (c) 180 deg, (d) 270 deg

gas pocket. An asymmetric flow field is most noticeable at the peak pressure difference and merge point (Figs. 11(a) and 11(b)). The leakage flow appears to be symmetric in the middle section of the compression process. The asymmetric behavior shows when the pockets are just formed near the inlet and reach the center of the compressor. The asymmetric geometry of the upper bearing housing casting and the downstream components, dummy and discharge ports, check valve, etc., contributes to this phenomenon.

The pressure histories of two fixed points in the scroll compressor are plotted in Fig. 12(a). These pressure taps are located on the

wall of pockets 2\_1 and 2\_2 as pocket 2\_1 forms. When the scroll moves, these two fixed taps record the time history of pressure at these locations. The pressure patterns at these locations are similar to the time averaged pressure values. The measured pressure values agree well with the simulated values. The overall profile of the measured pressure history agrees with the existing pressure data of the scroll compressors [7,8]. The compressor performance data are plotted against the prediction in Fig. 12(b). The performance is calculated as the adiabatic efficiency,  $\eta$ :

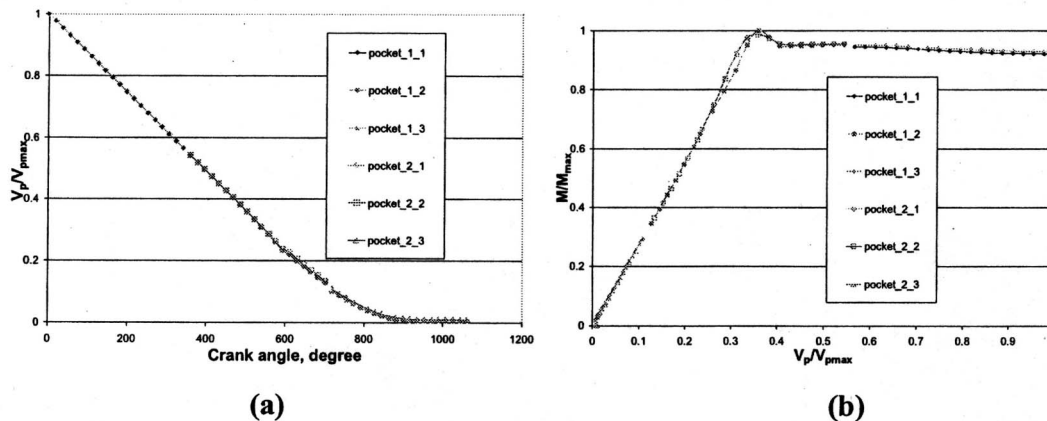


Fig. 8 Volume and mass changes in the gas pockets: (a) volume versus wrap angle and (b) mass versus volume

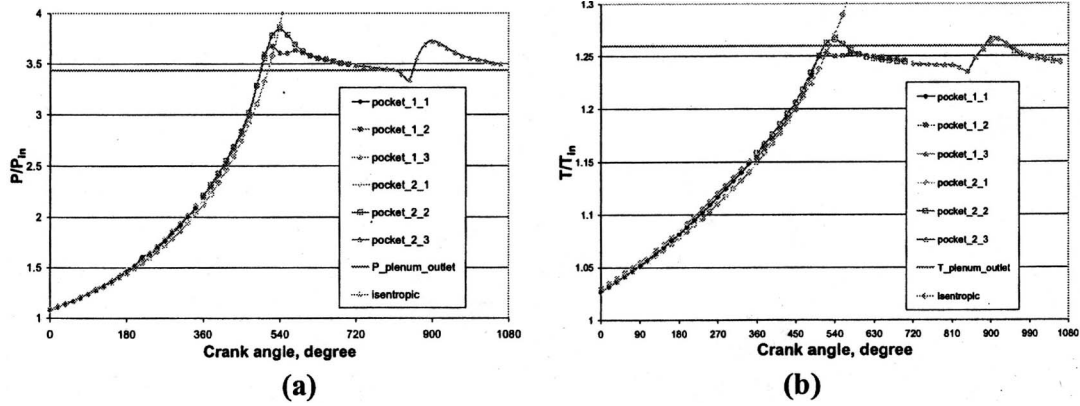


Fig. 9 Volume-averaged pressure (a) and temperature (b) in the gas pockets

$$\eta = \frac{\Delta h_{\text{isentropic}}}{\Delta h_{\text{actual}}} \quad (1)$$

where  $\Delta h_{\text{isentropic}}$  is enthalpy rise in an isentropic compression process and  $\Delta h_{\text{actual}}$  is the enthalpy rise in the actual compression process.

A total of 80 compressor was tested. The largest peak-to-peak value is 8% of the predicted value. The standard deviation is 1.1% of the predicted value.

### 5 Concluding Remarks

The numerical simulation of the operating process of the entire scroll compressor has been accomplished. The results provide a foundation for the further understanding of the detailed physics inside the scroll compressors. The design and performance parameters can be calculated from the data obtained from the current analysis. The information can be applied to the design and optimization of the scroll compressors.

The leakage flow between the gas pockets with different pres-

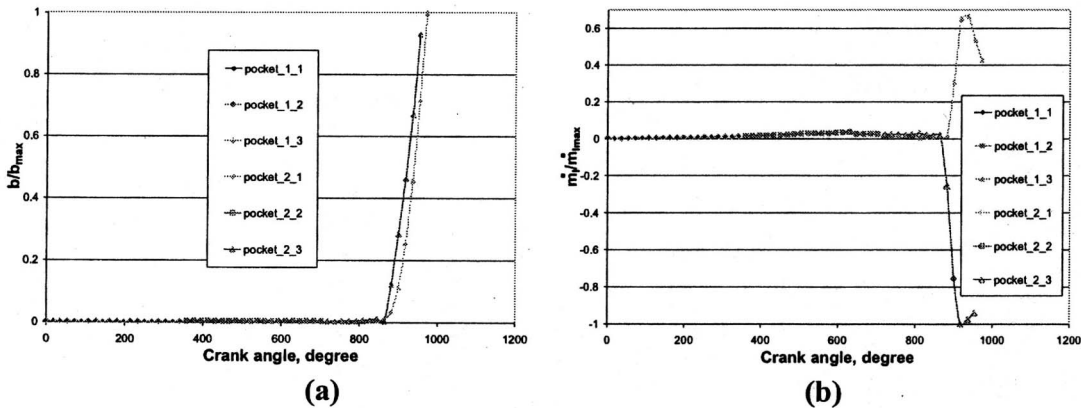


Fig. 10 Flank gap width (a) and mass flow rate between pockets (b)

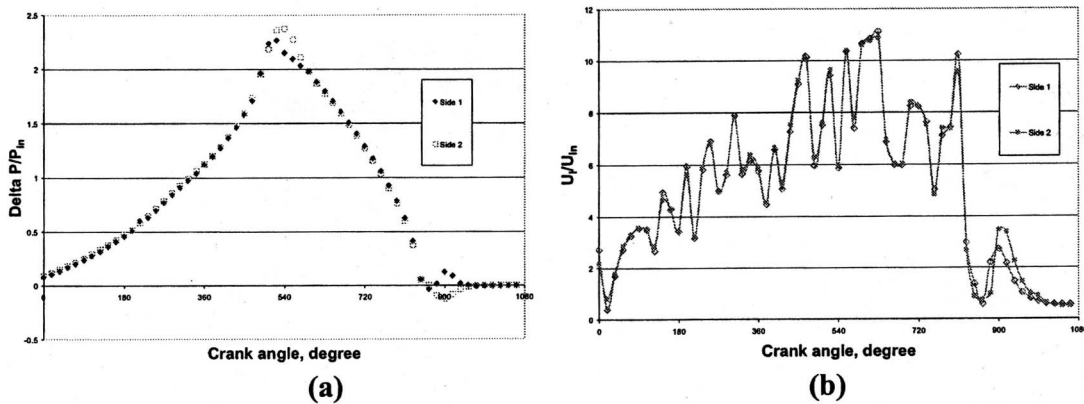


Fig. 11 Pressure difference between two neighboring gas pockets (a) and area-averaged leakage speed through flank gap (b)



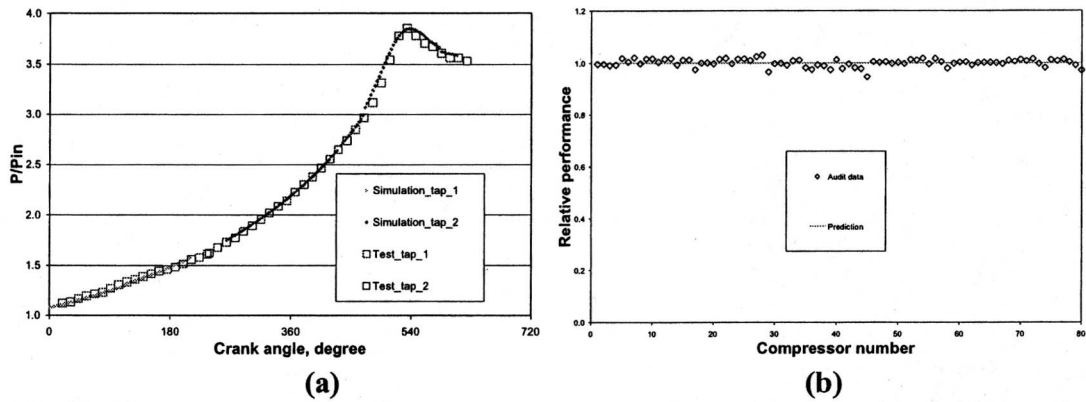


Fig. 12 The pressure at the pressure taps (a) and comparison of predicted performance with measured values (b)

tures is a dynamic process. The flank gap, velocity, pressure difference between the gas pockets, and leakage flow rate change periodically as the orbiting scroll rotates. The total leakage loss is the averaged result of the temporal and spatial variations of these quantities.

Asymmetric distributions of the mass, velocity, pressure, and temperature exist inside the compressor. These asymmetric distributions impact the performance and reliability of the scroll compressors. The information about these asymmetric distributions can be used to optimize the scroll compressor design.

Overcompression of the gas inside the compressor is obtained quantitatively. The overcompression appears to be a time-dependent phenomenon and asymmetric. The work needed to compress the gas over the compressor discharge pressure reduces the efficiency of the compressor. The fundamental understanding of this overcompression can be used to improve the scroll compressor design.

### Acknowledgment

The author would like to thank TRANE Air Conditioning, American Standard Companies, for the permission to publish this paper. Jack Sauls of TRANE Air Conditioning, American Standard Companies, reviewed the manuscript.

### Nomenclature

$A$	= area
$b$	= flank gap width
$h$	= enthalpy
$m$	= local mass flow rate
$M$	= total mass flow rate
$P$	= pressure
$T$	= temperature
$U$	= velocity
$u, v, w$	= component of the velocity
$V$	= gas pocket volume
$\eta$	= adiabatic efficiency

$\rho$  = density  
 $\Phi, \Psi$  = arbitrary physical quantity

### Subscripts

$l$  = leakage  
 $m$  = mass averaged quantity  
 $in$  = value at inlet  
 $out$  = value at outlet  
 $max$  = maximum value  
 $p$  = pocket

### Superscripts

- = average

### References

- [1] Chen, Y., Halm, N. P., Groll, E. A., and Braun, J. E., 2002, "Mathematical Modeling of Scroll Compressors. Part I: Compression Process Modeling," *Int. J. Refrig.*, **25**, pp. 731–750.
- [2] Chen, Y., Halm, N. P., Groll, E. A., and Braun, J. E., 2002, "Mathematical Modeling of Scroll Compressors. Part II: Overall Compressor Modeling," *Int. J. Refrig.*, **25**, pp. 751–764.
- [3] Stosic, N., and Smith, I. K., 1996, "CFD Studies of Flow in Screw and Scroll Compressors," *Proceedings of the International Compressor Engineering Conference at Purdue*, pp. 181–186.
- [4] Ooi, K. T., and Zhu, J., 2004, "Convective Heat Transfer in a Scroll Compressor Chamber: a 2-D Simulation," *Int. J. Therm. Sci.* **43**, pp. 677–688.
- [5] Pietrowicz, S., Yanagisawa, T., Fukuta, M., and Gnutek, Z., 2002, "Mathematical Modeling of Physical Processes in the Scroll Compressor Chamber," *Proceedings of the International Compressor Engineering Conference at Purdue*, p. C20-6.
- [6] Cui, M. M., 2003, "Numerical Study of Unsteady Flows in a Scroll Compressor," *Proceedings of the International Conference on Compressors and Their Systems, London*, pp. 2–10.
- [7] Hase, S., Sano, K., Yamamoto, S., Hirano, H., Kohayakawa, T., and Ishii, N., 1994, "Development of the High-Efficiency Horizontal-Type Scroll Compressor," *Proceedings of the International Compressor Engineering Conference at Purdue*, pp. 447–452.
- [8] Toyama, T., Nishikawa, Y., Yoshida, Y., Hiodoshi, S., and Shibamoto, Y., 2002, "Reduction of Noise and Over-compression Loss by Scroll Compressor With Modified Discharge Check Valve," *Proceedings of the International Compressor Engineering Conference at Purdue*, p. C20-4.

# Numerical Study of Active Flow Control for a Transitional Highly Loaded Low-Pressure Turbine

**Donald P. Rizzetta**

e-mail: donald.rizzetta@afri.af.mil

**Miguel R. Visbal**

e-mail: miguel.visbal@afri.af.mil

Air Force Research Laboratory,  
Computational Sciences Branch,  
Aeronautical Sciences Division,  
AFRL/VAAC, Building 146 - Room 225,  
2210 Eighth Street,  
Wright-Patterson AFB, OH 45433-7512

*Active control was simulated numerically for the subsonic flow through a highly loaded low-pressure turbine. The configuration approximated cascade experiments that were conducted to investigate a reduction in turbine stage blade count, which can decrease both weight and mechanical complexity. At a nominal Reynolds number of 25,000 based upon axial chord and inlet conditions, massive separation occurred on the suction surface of each blade due to uncovered turning. Vortex generating jets were then used to help mitigate separation, thereby reducing wake losses. Computations were performed using both steady blowing and pulsed mass injection to study the effects of active flow control on the transitional flow occurring in the aft-blade and near-wake regions. The numerical method utilized a centered compact finite-difference scheme to represent spatial derivatives, that was used in conjunction with a low-pass Pade-type nondispersive filter operator to maintain stability. An implicit approximately factored time-marching algorithm was employed, and Newton-like subiterations were applied to achieve second-order temporal accuracy. Calculations were carried out on a massively parallel computing platform, using domain decomposition to distribute subzones on individual processors. A high-order overset grid approach preserved spatial accuracy in locally refined embedded regions. Features of the flowfields are described, and simulations are compared with each other, with available experimental data, and with a previously obtained baseline case for the noncontrolled flow. It was found that active flow control was able to maintain attached flow over an additional distance of 19–21% of the blade chord, relative to the baseline case, which resulted in a reduction of the wake total pressure loss coefficient of 53–56%. [DOI: 10.1115/1.2238877]*

*Keywords: active flow control, low-pressure turbine, high-order numerical method*

## Introduction

Uninhabited air vehicles (UAVs) employed for reconnaissance and combat missions commonly utilize low-pressure turbines in their propulsion systems. Due to a reduction in atmospheric density during high-altitude cruise, such low-pressure turbines may encounter Reynolds numbers, based upon blade axial chord and inlet conditions, below 25,000. In this situation, boundary layers along a large extent of blade surfaces can remain laminar, even in the presence of elevated freestream turbulence levels. The laminar boundary layers are then particularly susceptible to flow separation over the aft portion of blade suction surfaces, causing blockage in flow passages and a significant reduction in turbine efficiency. These circumstances may thus result in imposed ceiling limitations for prolonged UAV deployment.

A number of experimental studies [1–8] have identified several factors contributing to performance degradation in low-pressure turbines, which in addition to the Reynolds number include freestream turbulence, pressure gradient, and curvature. Because of the impact upon UAV operations, a number of experiments have focused on flow control as a means of reducing efficiency degradation at altitude. It was found by Lake et al. [9] that boundary-layer separation could be mitigated by modifying the turbine blade geometry. Dimples were recessed into blade suction surfaces in order to maintain the region of attached flow. Although this passive technique increases efficiency at low-Reynolds num-

bers, it may also increase viscous losses at higher Reynolds numbers such as those that occur during takeoff, where unmodified blades perform satisfactorily.

As an alternative, Bons et al. [10–12] and Sondergaard et al. [13] have explored active flow control in the form of both steady and pulsed vortex generator jets, which may be actuated upon demand. Extensive measurements verified that the jets dramatically reduced separation, resulting in decreased losses. In addition to passive control [14], Volino [15] also explored the use of synthetic vortex generator jets for low-pressure turbines. Plasma control has also been demonstrated by Huang et al. [16] to restrict separation. More recent experiments by Sondergaard et al. [17] have investigated the feasibility of increasing the blade spacing at constant chord for a linear low-pressure turbine cascade, thereby raising the per blade loading. For practical applications, a higher loading can reduce the turbine part count and stage weight. Increased blade spacing however, is accompanied by more extensive boundary-layer separation on the suction surface of each blade due to uncovered turning, resulting in a further reduction of efficiency and additional wake losses. Vortex generator jets were then employed to diminish these losses by maintaining attached boundary-layer flow over a greater distance along the blade surface.

Numerical computations of low-pressure turbines have traditionally been predicated on solution of the Reynolds-averaged Navier-Stokes (RANS) equations [18–23]. Although these efforts have been moderately successful in predicting some of the overall features of the turbine flowfields, limitations and deficiencies of RANS turbulence models have precluded an accurate description

Contributed by the Fluids Engineering Division of ASME for publication in the JOURNAL OF FLUIDS ENGINEERING. Manuscript received November 29, 2005; final manuscript received March 9, 2006. Assoc. Editor: Paul Durbin. Paper presented at the 35th AIAA Fluid Dynamics Conference, June 6–9, 2005, Toronto, Ontario, Canada.

of low-Reynolds number separation and the transition to turbulence. Moreover, it is unlikely that the RANS approach will be adequate for simulating active flow control applications in the transitional regime.

Due to advances in the speed and storage capacity of high-performance computing systems, direct numerical simulation (DNS), and large-eddy simulation (LES) have emerged as viable means for the investigation of flows through low-pressure turbines [24–32]. DNS and LES supported by high-order numerical methods improve predictive capability where RANS models fail, and allow for the simulation of flow control strategies. Several previous computations [26,27,30–32] have been related to the experiments of Bons et al. [10–12], Sondergaard et al. [13,17], and Rivir et al. [33]. In particular, the calculations of Rizzetta and Visbal [31] considered the highly loaded low-pressure turbine configuration investigated by Sondergaard et al. [17]. Simulations were carried out for both an uncontrolled baseline case, and a case with active flow control in the form of pulsed vortex generating jets. Although the aft-blade separation was mitigated and wake total pressure losses were decreased by the use of pulsed injection, the jet momentum coefficient employed in the computation was appreciably lower than that of the experiment. Consequently, the amount of control attained by the simulation was less substantial than observed by Sondergaard et al. [17].

Control of the highly loaded low-pressure turbine considered by Sondergaard et al. [17] consisted only of steady vortex generator jets. And while prior investigations verified that separation could be similarly managed by pulsed injection [11,12], it is unclear how the detailed behavior of the individual flow control arrangements differs. The purpose of the present work was to conduct numerical computations of the turbine configuration which approximate the experiment of Sondergaard et al. [17]. Steady vortex generator jet flow control matching the experimental jet momentum coefficient was simulated at a chord inlet Reynolds number of approximately 25,000. In addition, a calculation was also performed for pulsed jet injection, with a duty cycle that was one half that of the steady case. This allows for a direct comparison between the respective flow control situations, as well as with the baseline case, so that characteristics of the flowfields may be elucidated.

## Governing Equations

The governing equations are taken as the unsteady three-dimensional compressible unfiltered Navier-Stokes equations. After introducing a curvilinear coordinate transformation to a body-fitted system, the equations are cast in the following nondimensional conservative form:

$$\frac{\partial}{\partial t} \left( \frac{Q}{J} \right) + \frac{\partial}{\partial \xi} \left( F - \frac{1}{\text{Re}_\infty} F_v \right) + \frac{\partial}{\partial \eta} \left( G - \frac{1}{\text{Re}_\infty} G_v \right) + \frac{\partial}{\partial \zeta} \left( H - \frac{1}{\text{Re}_\infty} H_v \right) = 0 \quad (1)$$

Here  $t$  is the time,  $\xi$ ,  $\eta$ ,  $\zeta$  the computational coordinates,  $Q$  the vector of dependent variables,  $F$ ,  $G$ ,  $H$  the inviscid flux vectors, and  $F_v$ ,  $G_v$ ,  $H_v$  the viscous flux vectors. The vector of dependent variables is given as

$$Q = [\rho \quad \rho u \quad \rho v \quad \rho w \quad \rho E]^T \quad (2)$$

and the vector fluxes by

$$F = \frac{1}{J} \begin{bmatrix} \rho U \\ \rho u U + \xi_x p \\ \rho v U + \xi_y p \\ \rho w U + \xi_z p \\ \rho E U + \xi_{x_i} u_i p \end{bmatrix}, \quad G = \frac{1}{J} \begin{bmatrix} \rho V \\ \rho u V + \eta_x p \\ \rho v V + \eta_y p \\ \rho w V + \eta_z p \\ \rho E V + \eta_{x_i} u_i p \end{bmatrix}, \quad (3)$$

$$H = \frac{1}{J} \begin{bmatrix} \rho W \\ \rho u W + \zeta_x p \\ \rho v W + \zeta_y p \\ \rho w W + \zeta_z p \\ \rho E W + \zeta_{x_i} u_i p \end{bmatrix} \quad (3)$$

$$F_v = \frac{1}{J} \begin{bmatrix} 0 \\ \xi_{x_i} \tau_{i1} \\ \xi_{x_i} \tau_{i2} \\ \xi_{x_i} \tau_{i3} \\ \xi_{x_i} (u_j \tau_{ij} - Q_i) \end{bmatrix}, \quad G_v = \frac{1}{J} \begin{bmatrix} 0 \\ \eta_{x_i} \tau_{i1} \\ \eta_{x_i} \tau_{i2} \\ \eta_{x_i} \tau_{i3} \\ \eta_{x_i} (u_j \tau_{ij} - Q_i) \end{bmatrix}, \quad (4)$$

$$H_v = \frac{1}{J} \begin{bmatrix} 0 \\ \zeta_{x_i} \tau_{i1} \\ \zeta_{x_i} \tau_{i2} \\ \zeta_{x_i} \tau_{i3} \\ \zeta_{x_i} (u_j \tau_{ij} - Q_i) \end{bmatrix} \quad (4)$$

where

$$U = \xi_t + \xi_{x_i} u_i, \quad V = \eta_t + \eta_{x_i} u_i, \quad W = \zeta_t + \zeta_{x_i} u_i \quad (5)$$

$$E = \frac{T}{\gamma(\gamma-1)M_\infty^2} + \frac{1}{2}(u^2 + v^2 + w^2) \quad (6)$$

In the preceding expressions,  $u$ ,  $v$ ,  $w$  are the Cartesian velocity components,  $\rho$  the density,  $p$  the pressure, and  $T$  the temperature. All length scales have been nondimensionalized by the turbine blade axial chord  $c$ , and dependent variables have been normalized by their reference values except for  $p$  which has been nondimensionalized by  $\rho_\infty u_\infty^2$ . Components of the stress tensor and heat flux vector are expressed as

$$Q_i = - \left[ \frac{1}{(\gamma-1)M_\infty^2} \right] \left( \frac{\mu}{\text{Pr}} \right) \frac{\partial \xi_j}{\partial x_i} \frac{\partial T}{\partial \xi_j} \quad (7)$$

$$\tau_{ij} = \mu \left( \frac{\partial \xi_k}{\partial x_j} \frac{\partial u_i}{\partial \xi_k} + \frac{\partial \xi_k}{\partial x_i} \frac{\partial u_j}{\partial \xi_k} - \frac{2}{3} \delta_{ij} \frac{\partial \xi_l}{\partial x_k} \frac{\partial u_k}{\partial \xi_l} \right) \quad (8)$$

The Sutherland law for the molecular viscosity coefficient  $\mu$  and the perfect gas relationship

$$p = \frac{\rho T}{\gamma M_\infty^2} \quad (9)$$

were also employed, and Stokes' hypothesis for the bulk viscosity coefficient has been invoked.

## Numerical Method

Time-accurate solutions to Eq. (1) are obtained numerically by the implicit approximately factored finite-difference algorithm of Beam and Warming [34] employing Newton-like subiterations

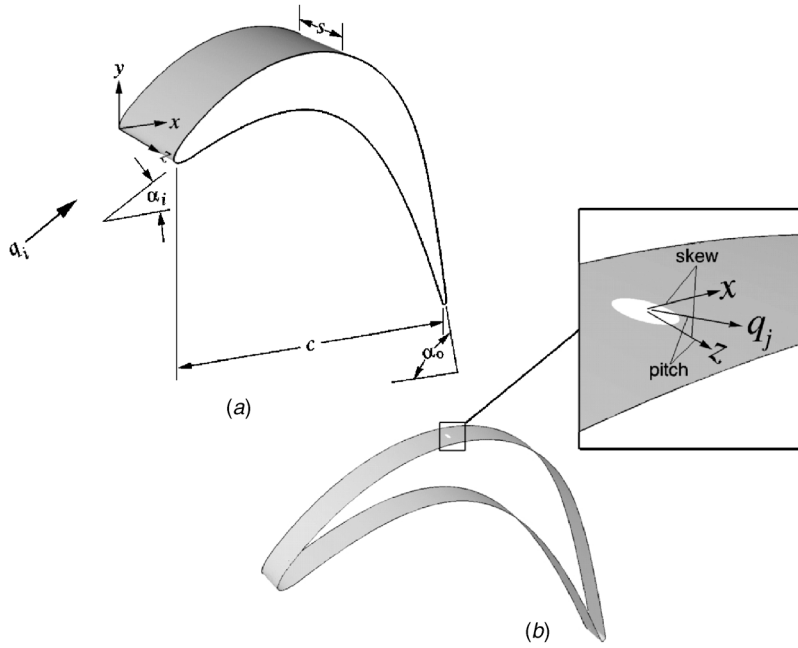


**Fig. 1 Schematic representation of the turbine blade configuration and vortex generator jet geometry**

[35], which has evolved as an efficient tool for generating solutions to a wide variety of complex fluid flow problems, and may be written as follows:

$$\begin{aligned} & \left[ \frac{1}{\mathcal{J}} + \left( \frac{2\Delta t}{3} \right) \delta_{\xi 2} \left( \frac{\partial F^p}{\partial Q} - \frac{1}{\text{Re}_\infty} \frac{\partial F_v^p}{\partial Q} \right) \right] \mathcal{J} \times \left[ \frac{1}{\mathcal{J}} + \left( \frac{2\Delta t}{3} \right) \delta_{\eta 2} \left( \frac{\partial G^p}{\partial Q} \right. \right. \\ & \quad \left. \left. - \frac{1}{\text{Re}_\infty} \frac{\partial G_v^p}{\partial Q} \right) \right] \mathcal{J} \times \left[ \frac{1}{\mathcal{J}} + \left( \frac{2\Delta t}{3} \right) \delta_{\xi 2} \left( \frac{\partial H^p}{\partial Q} - \frac{1}{\text{Re}_\infty} \frac{\partial H_v^p}{\partial Q} \right) \right] \Delta Q \\ & = - \left( \frac{2\Delta t}{3} \right) \left[ \left( \frac{1}{2\Delta t} \right) \left( \frac{3Q^p - 4Q^n + Q^{n-1}}{\mathcal{J}} \right) + \delta_{\xi 4} \left( F^p \right. \right. \\ & \quad \left. \left. - \frac{1}{\text{Re}_\infty} F_v^p \right) + \delta_{\eta 4} \left( G^p - \frac{1}{\text{Re}_\infty} G_v^p \right) + \delta_{\xi 4} \left( H^p - \frac{1}{\text{Re}_\infty} H_v^p \right) \right] \quad (10) \end{aligned}$$

In this expression, which is employed to advance the solution in time,  $Q^{p+1}$  is the  $p+1$  approximation to  $Q$  at the  $n+1$  time level  $Q^{n+1}$ , and  $\Delta Q = Q^{p+1} - Q^p$ . For  $p=1$ ,  $Q^p = Q^n$ . Second-order-accurate backward-implicit time differencing was used to obtain temporal derivatives.

The implicit segment of the algorithm incorporates second-order-accurate centered differencing for all spatial derivatives, and utilizes nonlinear artificial dissipation [36] to augment stability. Efficiency is enhanced by solving this implicit portion of the factorized equations in diagonalized form [37]. Temporal accuracy, which can be degraded by use of the diagonal form, is maintained by utilizing subiterations within a time step. This technique has been commonly invoked in order to reduce errors due to factorization, linearization, diagonalization, and explicit application of boundary conditions. It is useful for achieving temporal accuracy on overset zonal mesh systems, and for a domain decomposition implementation on parallel computing platforms. Any deterioration of the solution caused by use of artificial dissipation and by lower-order spatial resolution of implicit operators is also reduced by the procedure. Three subiterations per time step have been applied to preserve second-order temporal accuracy.

The compact difference scheme employed on the right-hand side of Eq. (10) is based upon the pentadiagonal system of Lele [38], and is capable of attaining spectral-like resolution. This is achieved through the use of a centered implicit difference operator

with a compact stencil, thereby reducing the associated discretization error. For the present computations, a fourth-order tridiagonal subset of Lele's system is utilized, which is illustrated here in one spatial dimension as

$$\alpha \left( \frac{\partial F}{\partial \xi} \right)_{i-1} + \left( \frac{\partial F}{\partial \xi} \right)_i + \alpha \left( \frac{\partial F}{\partial \xi} \right)_{i+1} = a \left( \frac{F_{i+1} - F_{i-1}}{2} \right) \quad (11)$$

with  $\alpha=1/4$  and  $a=3/2$ . The scheme has been adapted by Visbal and Gaitonde [39] as an implicit iterative time-marching technique, applicable for unsteady vortical flows. It is used in conjunction with a sixth-order low-pass Pade-type nondispersive spatial filter developed by Gaitonde et al. [40], which has been shown to be superior to the use of explicitly added artificial dissipation for maintaining both stability and accuracy on stretched curvilinear meshes [39]. The filter is applied to the solution vector sequentially in each of the three computational directions following each subiteration, and is implemented in one dimension as

$$\alpha_f \hat{Q}_{i-1} + \hat{Q}_i + \alpha_f \hat{Q}_{i+1} = \sum_{n=0}^3 \frac{a_n}{2} (Q_{i+n} + Q_{i-n}) \quad (12)$$

where  $\hat{Q}$  designates the filtered value of  $Q$ . Equation (12) represents a one-parameter family of sixth-order filters, where numerical values for  $\alpha_f$  and the  $a_n$ 's may be found in Ref. [41].

The aforementioned features of the numerical algorithm are embodied in a parallel version of the time-accurate three-dimensional computer code FDL3DI [41], which has proven to be reliable for steady and unsteady fluid flow problems, including the simulation of flows over delta wings with leading-edge vortices [42–44], vortex breakdown [43,44], direct numerical simulation of transitional wall jets [45] and synthetic jet actuators [46], and DNS and LES of subsonic [27,47] and supersonic flowfields [48–50].

### Details of the Computations

The experiment Sondergaard et al. [13] consisted of a linear cascade of turbine blades having a span of 0.88 m and an axial chord of 0.089 m. The axial chord to spacing ratio (solidity) was 0.75, the inlet flow angle  $\alpha_i=35.0$  deg, and the design exit flow

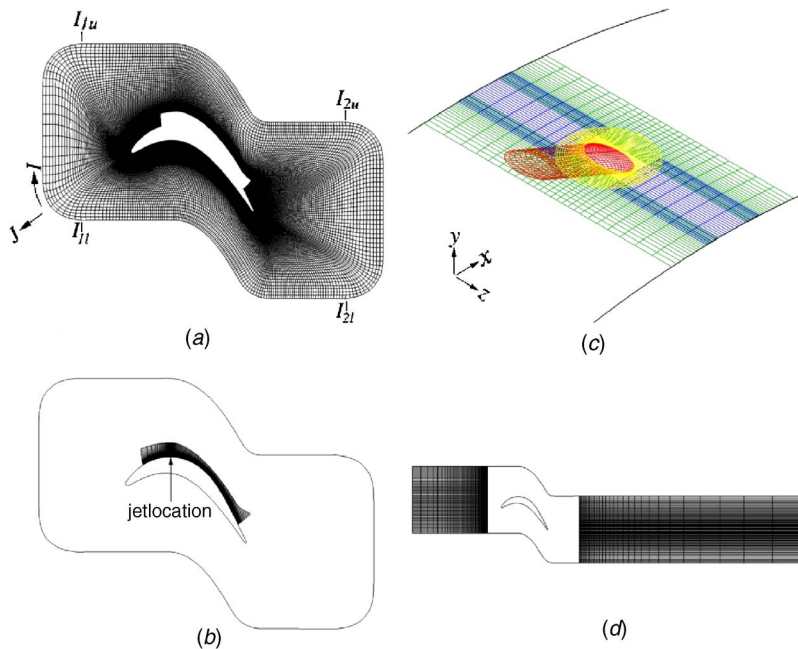


Fig. 2 Turbine blade computational mesh system

angle  $\alpha_j=60.0$  deg. Shown in Fig. 1(a) is a schematic representation of the turbine blade shape, given by the Pratt and Whitney “PakB” research design, which is a Mach number scaled version of geometries typically used in highly loaded low-pressure turbines [10–13,15]. These experiments investigated the use of vortex generator jets to control the flow by mitigating the effects of separation on the blade suction surface. The jets were created by blowing air through holes which had been drilled in the blade surface at a pitch angle of 30 deg and a skew angle of 90 deg. Here, the pitch is defined as the angle the jet makes with the local surface, and the skew is the angle of the projection of the jet on the surface, relative to the “local freestream” direction [12]. The size of the drill used to develop the holes is commonly referred to as the jet diameter  $d$ , which was 0.001 m. Because of the orientation, however, the jet exit geometric shape is elliptic as seen in Fig. 1(b), and the jet exit velocity vector has components only in the blade-normal ( $n$ ) and spanwise ( $z$ ) directions.

**Computational Meshes.** To conserve computational resources, only a single turbine blade passage is considered, and periodic conditions are enforced in the vertical direction ( $y$ ) to represent a single turbine stage flowfield. This situation is somewhat different than the experimental arrangement, which consisted of a small finite number of blades in a linear cascade. The computational domain surrounding the blade was described by a body-fitted mesh system, whose origin was located at the inboard leading edge of the blade (see Fig. 1(a)). The mesh employs an O-grid topology, and was elliptically generated using automated software [51]. Figure 2(a) indicates the baseline grid about the turbine blade, which was comprised of 348 points in the circumferential direction ( $I$ ), 189 points in the blade-normal direction ( $J$ ), and 101 points in the spanwise direction ( $K$ ). Minimum spacing in the  $J$ -direction occurs at the blade surface. Mesh points for  $1 \leq I \leq 5$  and  $I_{\max-4} \leq I \leq I_{\max}$  are coincident in an overlap region at the blade leading edge so that periodic conditions in the circumferential direction may be enforced in order to complete the O-grid construct. To accommodate periodic conditions in the vertical direction, the streamwise ( $x$ ) point locations and vertical spacing along  $I_{1u}-I_{2u}$  is identical to that along  $I_{1l}-I_{2l}$  for  $J_{\max-4} \leq J \leq J_{\max}$ .

To properly capture the correct fluid physics for the flow con-

trol cases, the baseline grid was modified in order to enhance resolution in the jet and jet wake regions. This was done by removing points in the near wall grid, indicated by the blanked area of Fig. 2(a), and replacing them with an embedded refined mesh as seen in Fig. 2(b). This technique is identical to that which was successfully employed by Rizzetta and Visbal [31] in a similar computation. The size of the refined mesh region was  $(313 \times 185 \times 101)$  grid points in  $(I, J, K)$ , respectively. Only every fourth grid line in each coordinate direction appears in the figure. A series of overset grids were used to describe the elliptic jet geometry, and zones upstream, downstream, inboard, and outboard of the jet. These grids connect to each other and with the refined-mesh region as shown in Fig. 2(c). Also seen in the figure is the jet nozzle interior to the blade, which was accounted for in the simulations, and extended a distance of four jet diameters below the surface.

In order to facilitate application of inflow and outflow conditions to the turbine blade domain, overset grids were utilized upstream and downstream of the blade region. These are found in Fig. 2(d), and consisted of  $(46 \times 61 \times 101)$  and  $(31 \times 75 \times 101)$  mesh points in the streamwise, vertical, and spanwise directions for the upstream and downstream domains, respectively. Half the grid points in the vertical direction are seen in the figure. Although the experiment of Sondergaard et al. [17] consisted of a row of jets uniformly distributed along the span of a blade, only a single jet was considered in the simulations. The  $z$ -extent of the domain was taken as the inter-jet spacing  $s=0.112$ , which is equal to 10 jet diameters (as in the experiment) and periodic conditions were invoked at the spanwise boundaries. A nonuniform spanwise mesh distribution was utilized, with grid point clustering near the jet exit. At all overset domain boundaries, a minimum 5-point overlap was constructed. The total number of grid points in all domains was approximately  $13.5 \times 10^6$ . Computational mesh spacings given in wall units for both simulations are presented in Table 1. Results of the grid refinement study performed for the baseline uncontrolled case of Ref. [31], indicate that adequate resolution should be achieved for the present computations.

**Temporal Considerations.** Calculations for the steady jet case were obtained using a time step of  $\Delta t=1.50 \times 10^{-4}$ , where  $t$  is nondimensionalized by reference quantities. Based upon inflow

**Table 1 Computational mesh spacings in wall units**

Case	$\Delta r^+$	$\Delta l_{\min}^+$	$\Delta l_{\max}^+$	$\Delta r_{\min}^+$	$\Delta z_{\min}^+$	$\Delta z_{\max}^+$
steady	0.02	1.63	50.07	0.44	3.09	10.98
pulsed	0.02	1.74	53.39	0.46	3.23	11.47

conditions, this corresponds to a time increment of approximately  $1.18 \times 10^{-4}$  (see Table 1 for the time step in wall units). For the pulsed case, these parameters were  $\Delta t = 1.47 \times 10^{-4}$  and  $\Delta t_i = 1.20 \times 10^{-4}$ , respectively. A slightly smaller time step was employed with unsteady injection so that the pulsing cycle could be described by an integer number of increments (1300 time steps/cycle). Flowfields for each case were initialized from the previously obtained baseline (uncontrolled) solution, and processed for 20,000 time steps in order to remove transients. Final results were then evolved for a subsequent 124,000 steps, during which statistical information was collected. Statistics were monitored to assure that a converged sample was achieved. This duration represents over 14.5 characteristic time units, based upon the inflow velocity, for both simulations.

Experimental investigations [10–13,15] have used several parameters to describe characteristics of vortex generating jets. The jet blowing ratio  $B$  is defined as

$$B = \frac{q_j}{\bar{q}_l} \quad (13)$$

where  $q_j$  is the jet exit velocity magnitude, and  $\bar{q}_l$  is the “local freestream velocity” (see Ref. [11] for the definition of  $\bar{q}_l$ ). In the present computations, the maximum value of the jet blowing ratio  $B_{\max}$  was specified as 4.5. This is identical to the experiment of Sondergaard et al. [17] for the steady case. As a point of reference, typical film cooling holes for turbine applications are designed to operate at an approximate value of  $B_{\max} = 2.0$  [12]. For the present configuration considered here, experimental data is available only for steady blowing flow control. In previous investigations with a smaller inter-blade spacing, however, measurements were also taken using pulsed mass injection. The unsteady jet exit velocity sequence in those experiments consisted of a period of essentially constant blowing, followed by an interval of no blowing. The duty cycle represents that portion of the total duration over which the jet is active, and was 50% for the present case. A nondimensional frequency  $\mathcal{F}$  as formulated in Refs. [10–13] was used to quantify the forcing period where

$$\mathcal{F} = 0.41 c_f / u_{\infty} \bar{q}_l \quad (14)$$

The value of  $\mathcal{F} = 3.1$  was used in the present computations, which was the same as that of some experiments [10–12]. The jet blowing coefficient, defined as

$$c_{\mu} = \mathcal{D}[(\pi/4)d^2 B_{\max}^2] \quad (15)$$

is used to quantify the momentum flux transferred to the turbine blade passage by active control. For the steady blowing case  $c_{\mu} = 2.0 \times 10^{-3}$ , and is one-half this value for pulsed injection owing to the 50% duty cycle.

A representative experimental [12] time history of one blowing cycle obtained by hot wire measurement is shown in Fig. 3. For the pulsed-injection computation, a series of cubic and linear functions were used to approximate the experimental result, as seen in the figure where the 50% duty cycle is apparent. As noted earlier, a single cycle was described by 1300 time steps, and the total computation consisted of 96 cycles.

**Boundary Conditions.** Inflow and outflow conditions for the complete turbine blade domain were obtained in a manner consistent with subsonic internal flows, which have commonly been employed in RANS applications [52]. Along the upstream boundary, the total pressure, total temperature, and inlet flow angle were

specified, and the velocity magnitude was obtained from the interior solution. Downstream, the exit static pressure ( $p_{\infty}$ ) was fixed, and other flow variables were extrapolated from within the domain. Because the inflow velocity develops as part of the solution, the Reynolds number based upon the inflow conditions was not known a priori. A reference Mach number ( $M_{\infty}$ ) of 0.1 was selected for all computations. For the baseline solution, the reference Reynolds number ( $Re_{\infty}$ ) was adjusted to match the desired inflow condition,  $Re$ . This same Reynolds number was then employed in the current simulations. When flow control was applied however, the inflow velocity magnitude increased due to a reduction of blockage in the blade passage. Although this situation was anticipated, the reference Reynolds number was not altered. This is the same approach as utilized in corresponding experiments [10–13,15]. Thus, the inflow Reynolds numbers are somewhat higher than the nominal value of 25,000. For the time-mean flowfields,  $Re = 29,100$  for steady blowing and  $Re = 29,960$  with pulsed mass injection. Therefore, even without flow control, the increase in the Reynolds number might delay separation, although this effect is expected to be small. The treatment for the inflow and outflow boundaries was previously employed by Rizzetta and Visbal [27,31] in similar computations.

Periodic conditions were applied along the upper and lower portions of the turbine blade as indicated previously in Fig. 2(a). Periodic conditions were also applied along upper and lower horizontal boundaries of the upstream and downstream domains seen in Fig. 2(d). The downstream domain was intentionally severely stretched in the streamwise direction to prevent spurious reflections from the outflow boundary. This technique transfers information to high spatial wave numbers, and then dissipates it by the low-pass filter [53]. Flow variables in all regions of noncoincident overlapped meshes were obtained from explicit sixth-order-accurate Lagrangian interpolation formulae. This includes the upstream and downstream domains, the turbine blade grid, the refined-mesh region, all zones surrounding the jet, and the interior jet nozzle. The interpolation approach for high-order numerical

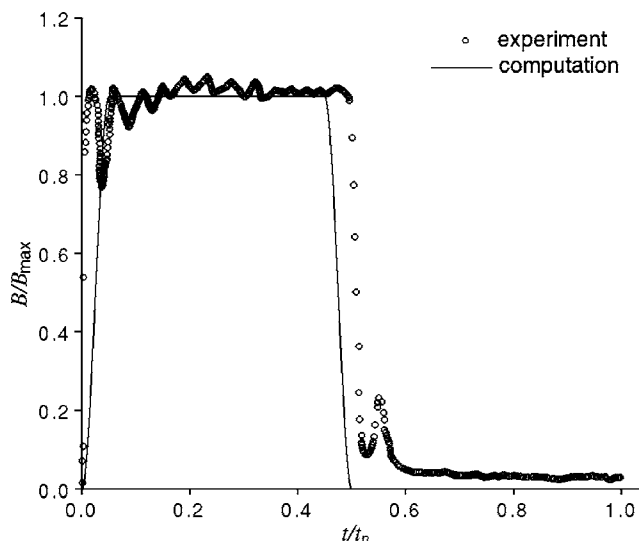


**Fig. 3 Jet blowing ratio time history**

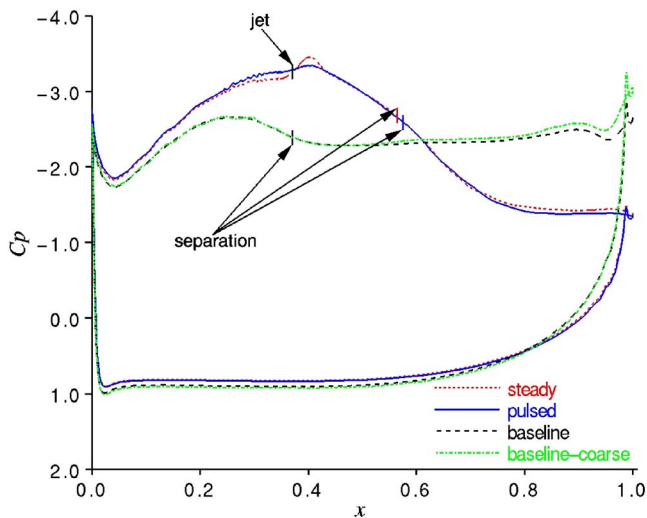


**Fig. 4 Time-mean surface pressure coefficient distributions**

solutions has been successfully applied by Sherer [54] for the simulation of fluid dynamic and acoustic problems. As stated previously, periodic conditions were invoked in the spanwise direction.

On solid surfaces, including the blade boundary and walls of the jet nozzle, the no slip condition was enforced along with an isothermal wall, and a fourth-order-accurate representation of zero normal pressure gradient. At the inflow to the jet nozzle, a velocity profile was specified, the jet was assumed to be isothermal, and the pressure was obtained from the inviscid normal momentum equation. For both the steady and pulsed cases, the velocity profile was taken to be parabolic. In the steady case, the maximum jet blowing ratio was fixed at  $B_{\max}=4.5$ , corresponding to the experiment, while for pulsed injection this ratio varied in time according to the form shown in Fig. 3. It is noted for both cases that the maximum jet velocity is over seven times greater than the magnitude of the blade inflow velocity. The Reynolds number of the jet based upon the maximum blowing ratio and the diameter  $d$  was 2370.

**Domain Decomposition.** For parallel processing, the previously described computational domains were decomposed into a series of subzones, which were then distributed on individual processors of a massively parallel computing platform (IBM SP4, SGI 3900). Decompositions were constructed to provide an approximately equal number of grid points in every subzone, thereby balancing the computational work load among the processors. Faces at the boundaries of each subzone block were overset into adjacent domains, such that an overlap of five planes was established. Although this incurred an overhead due to redundant computation, it maintained the formal high-order accuracy of both the numerical differencing and filtering schemes. Because a vast majority of the overlapping mesh points of the respective decompositions were coincident, no further interpolation was required. Automated software [55] was used to identify donor and recipient grid points in the overlapping domains. Inter-node communication among the processors was established through standard message-passing interface (MPI) library routines [56], which were used to transfer information between the various subzones of the flowfield at domain boundaries. A total of 202 processors were employed for all of the computations reported here.

## Results

**The Time-Mean Flowfields.** Time-mean surface pressure coefficient distributions for the flow control and baseline [31] computations are found in Fig. 4. For the flow control cases, these

distributions were obtained at the spanwise location of the periodic boundary between two jets. As indicated in the figure, the jet was positioned at  $x=0.37$ , which coincides with the separation point of the baseline solution. The large plateau region in the baseline distribution is characteristic of a massively separated flow. Because of reduced blockage and increased inflow velocity, the effect of flow control is to decrease the pressure on the upstream portion of the suction surface, while increasing it downstream, relative to the baseline case. Separation occurs at  $x=0.56$  for the steady blowing result, and at  $x=0.58$  for pulsed injection. Only minor differences, most noticeable near the jet, are observed between the two flow control solutions. Also shown in the figure, is a coarse-mesh distribution for the baseline case, which indicates little sensitivity to grid resolution, except near the trailing-edge region. More extensive results of the grid resolution study for the baseline case are found in Ref. [31].

Profiles of the time-mean velocity magnitude are presented in Figs. 5 and 6. These profiles were extracted along lines ( $n$ ) normal to the blade surface at each  $x$ -station, on the periodic spanwise boundary between jets. The data of Sondergaard et al. [17] for steady blowing also appears in the figures. However, only a qualitative comparison between the experimental and numerical results may be expected due to appreciable differences in the respective flow situations. Among these are the fact that the experiments were conducted in a linear cascade, which had a limited number of blades. Tail boards were attached at the trailing edge of the first and last blades in the cascade, and extended downstream a considerable distance into the wake, thus creating covered turning for a substantial portion of the flowfield. It was found in previous simulations of a similar configuration by Postl et al. [26,30], Gross and Fasel [32], and Rizzetta and Visbal [27,31], that computational results differed from the experiments of Bons et al. [10–12]. Although the numerical solutions of Postl et al. [26,30] and Gross and Fasel [32] compared favorably with those of Rizzetta and Visbal [27,31], none of the simulations reproduced the measured data. At similar Reynolds numbers and flow conditions, the experimental configuration resulted in a much greater region of separated flow along the blade surface than was observed in the computations. This disparity is believed to be caused by the cascade arrangement with tail boards, which cannot be simulated numerically due to limitations of computational resources. In addition, vortex generating jets were fabricated only on the central blade of the experimental cascade. This situation is quite unlike the simulations, where periodic conditions about the blade are enforced. Although experimental data was collected for  $Re=50,000$ , the computations were carried out at a nominal Reynolds number of 25,000. This was done in order to maintain adequate spatial resolution for a direct numerical simulation of the transitional flowfield. Moreover, the lower Reynolds number provides a difficult challenge to the numerical study of active flow control, which is the primary purpose of the investigation. The Reynolds number of 25,000 is more representative of the practical situation for UAVs, and may also be directly compared to the previously obtained baseline case. Differences between the experimental and computational configurations are summarized in Table 2.

Profiles in Figs. 5 and 6 have been normalized by the inflow velocity magnitude. The major effect of flow control is to increase fullness of the profiles through momentum transfer from the jet and mixing with the boundary layer. Only minor variations are observed between the steady and pulsed injection cases. As expected, profiles from the simulations are thicker than those of the experiment due to aforementioned differences in the Reynolds numbers and configurations. Increased fullness of the control profiles from the baseline solution is evident in the figures, even at locations where separation is present ( $x>0.58$ ).

Spanwise turbulent kinetic energy wave-number spectra are provided in Fig. 7. These spectra were generated along lines in the  $z$ -direction at a distance of  $n=0.03$  from the blade surface. This

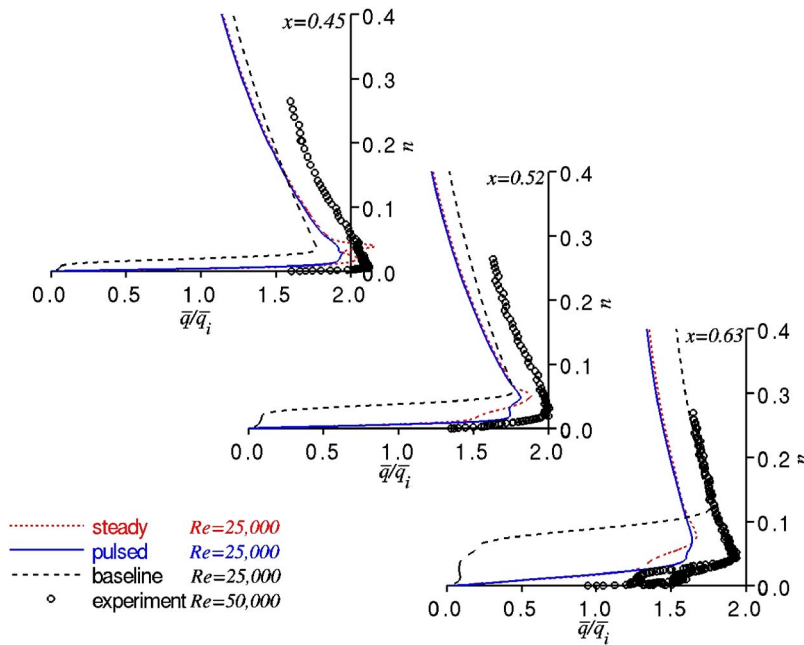


Fig. 5 Time-mean velocity magnitude profiles at upstream stations

location ( $n=0.03$ ) is approximately equal to one-half of the boundary-layer thickness of the time-mean velocity profile upstream of separation. At the two most upstream stations ( $x=0.50, 0.70$ ),  $E_{k_z}$  is higher for the flow control cases than that of the baseline due to energy being added to the flow. In the downstream region ( $x=0.90$ ), flow control has mitigated separation and the associated breakdown into a more chaotic situation, so that the turbulent kinetic energy of the baseline case is higher. Because of the low Reynolds number, it is unclear if any portion of the spectrum lies in the inertial range, indicated by the  $-5/3$  slope.

Time-mean contours of the spanwise component of vorticity are seen in Fig. 8. The contours for the flow control results were taken at the plane of the periodic boundary between jets, while those of

the baseline case have been spanwise averaged. An increased region of attached flow due to flow control is apparent, resulting in a decrease of the wake thickness. The effect of the decrease is quantified by the integrated wake total pressure loss coefficient  $C_w$ , defined as [17]

$$C_w = S \int \left( \frac{P_{ti} - \bar{P}_{to}}{P_{ti} - \bar{p}_i} \right) dy \quad (16)$$

where the integration takes place across the wake profile between the periodic boundaries in the vertical direction. It was determined that  $C_w=1.10$  [31] for the baseline solution,  $C_w=0.52$  for steady blowing, and  $C_w=0.48$  for pulsed injection. Thus even with a 50%

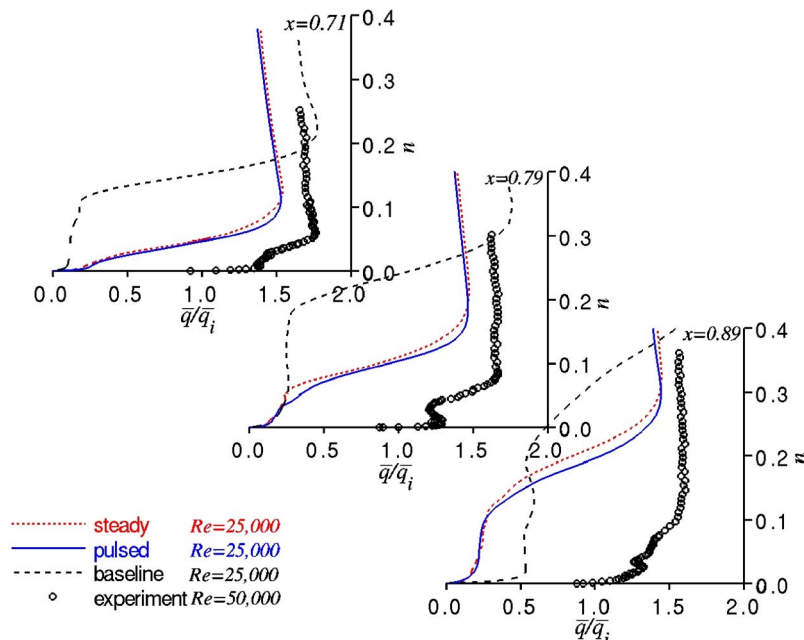


Fig. 6 Time-mean velocity magnitude profiles at downstream stations



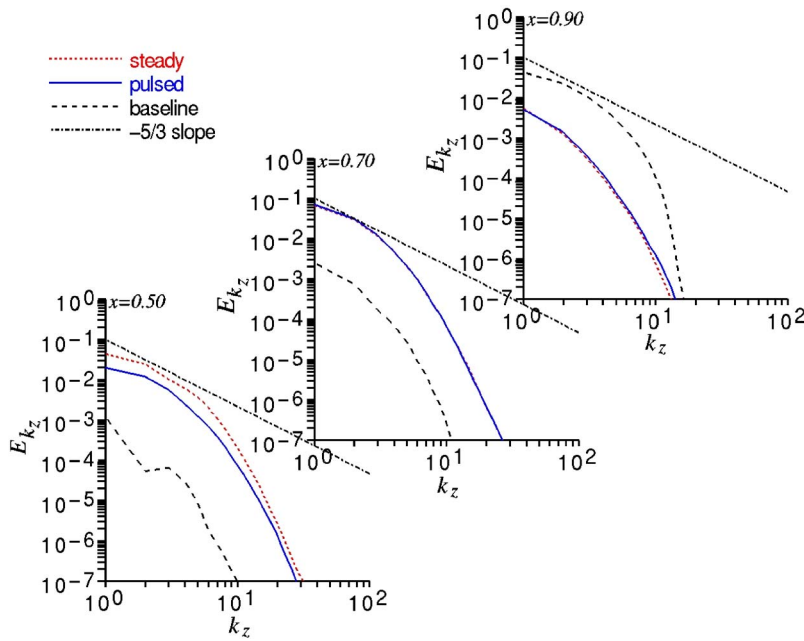


Fig. 7 Time-mean turbulent kinetic energy spanwise wave-number spectra

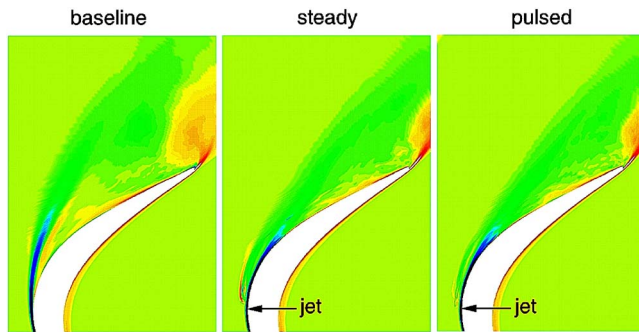


Fig. 8 Time-mean contours of the spanwise component of vorticity

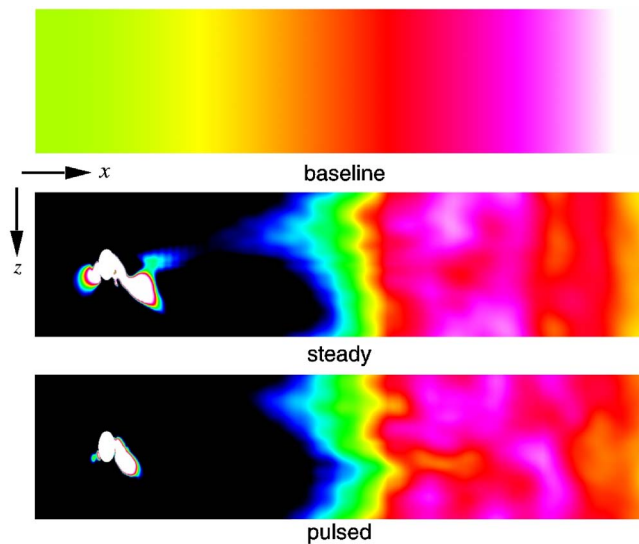


Fig. 9 Time-mean contours of the spanwise component of vorticity on the blade surface

duty cycle, pulsed injection was found to be as effective as steady blowing for the reduction of wake losses. This result is consistent with previous experimental studies [11,12].

Figure 9 represents these same vorticity contours evaluated on the blade surface and viewed from above. Apart from the area immediately surrounding the jet, the flow control cases are remarkably similar. As expected, no symmetry about the spanwise centerline exists due to the pitch angle of the jet. The extremely dark portion of the contours surrounding the jet exit region of the control cases represents attached flow.

**Unsteady Features of the Flowfields.** Profiles of the root-mean-square fluctuating velocity magnitude at several streamwise locations are found in Fig. 10. At the upstream stations ( $x = 0.50, 0.70$ ), the flow control cases differ somewhat from each other, but both produce peak values less than that of the baseline result. Fluctuations in the control cases are related to unsteadiness of the jet, while those of the baseline flow evolve from the shear layer. As a result, the location of the maximum fluctuation occurs further from the blade surface in the baseline solution. At the downstream location ( $x=0.90$ ), a more massive separated region in the baseline flow gives rise to a uniformly high fluctuating velocity in the normal direction, which is more localized in the flow control cases.

Turbulent kinetic energy frequency spectra are shown in Fig. 11. The data used to generate these spectra was collected at  $n = 0.03$ , similar to that of Fig. 7. Like the spanwise wave number spectra of Fig. 7, the frequency spectra for the flow control cases is substantially higher than that of the baseline result at the upstream stations ( $x=0.50, 0.70$ ) because of energy addition. At  $x = 0.50$ , the discrete peaks in  $E_\omega$  for the pulsed injection case cor-

Table 2 Comparison of experimental and computational configurations

Feature	Experiment	Computation
blade arrangement	linear cascade	periodic distribution
tail boards	first and last blades	none
jet arrangement	central blade of cascade only	periodic distribution
Re	50,000	25,000

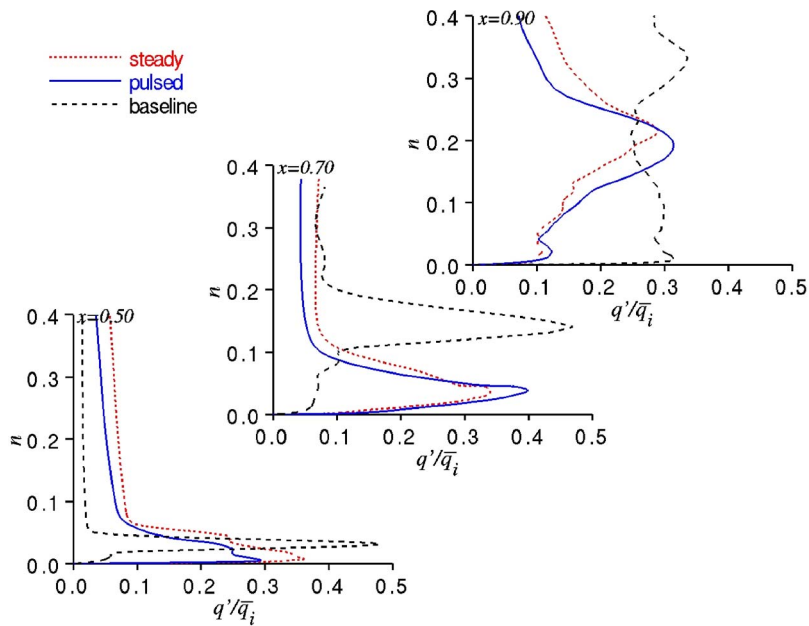


Fig. 10 Time-mean fluctuating velocity magnitude profiles

respond to harmonics of the forcing frequency. The occurrence of this behavior was described in detail in Ref. [31]. As noted previously, turbulent energy of the baseline case exceeds that of the flow control results near the blade trailing edge ( $x=0.90$ ).

Instantaneous contours of the spanwise component of vorticity are presented in Fig. 12. Once again, the baseline result was extracted at the midspan location, while those of the flow control cases were situated between control jets. Similar to the time-mean contours of Fig. 8, it is noted that flow control maintains attached flow and decreases the vertical extent of the wake relative to the baseline case. Unsteady structures are visible in separated flow regions. It is seen in the flow control cases that vorticity is being generated in the boundary layer in close proximity to the blade surface. When the boundary layers separate in these situations, it is much less dramatic than in the uncontrolled case. For the base-

line solution, the extensive unsteady separated flow region has a richer content of small scale structures due to breakdown and a transition to a more complex situation. A three-dimensional representation of the flow is depicted by iso-surfaces of vorticity magnitude in the trailing-edge region seen in Fig. 13. The value of iso-surfaces correspond approximately to that at the edge of the shear layer upstream of separation. Both the vertical and spanwise extent of the turbulent structures are visible for each case.

Instantaneous spanwise vorticity contours on the blade surface viewed from above are displayed in Fig. 14. Although differences in the control cases exist in the near-jet region, the downstream flowfields are quite similar. Iso-surfaces of vorticity magnitude in the near-jet region, as viewed downstream of the jet, are provided in Fig. 15. Unsteadiness can be observed in the jet surface, just

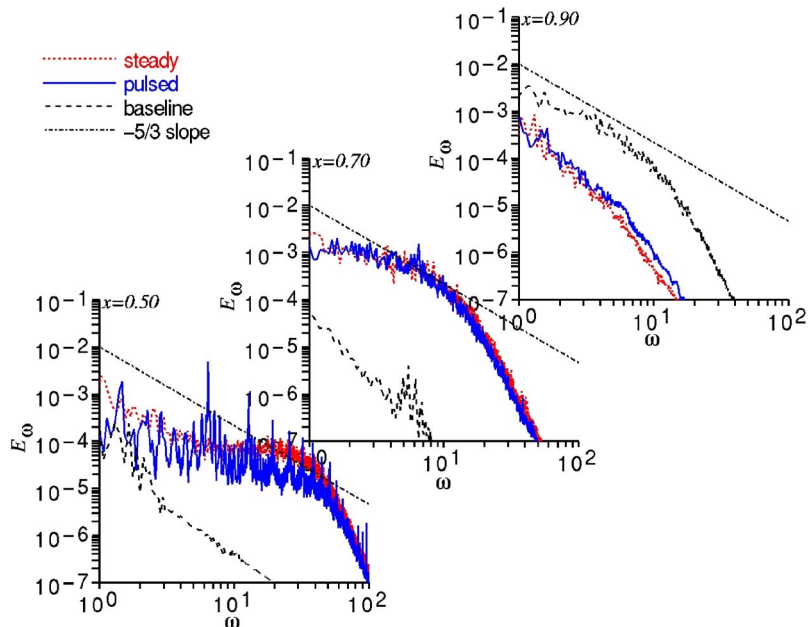


Fig. 11 Turbulent kinetic energy frequency spectra

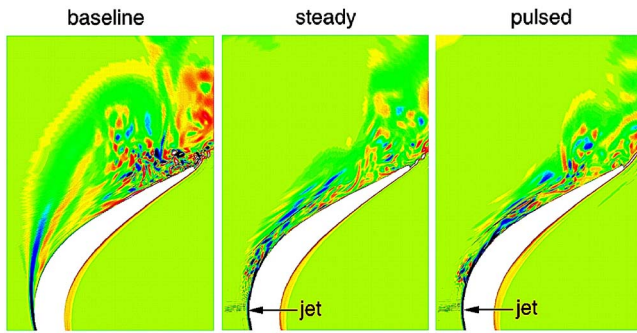


Fig. 12 Instantaneous planar contours of the spanwise component of vorticity

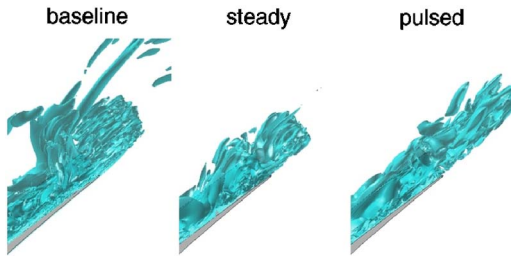


Fig. 13 Instantaneous iso-surfaces of vorticity magnitude in the trailing-edge region

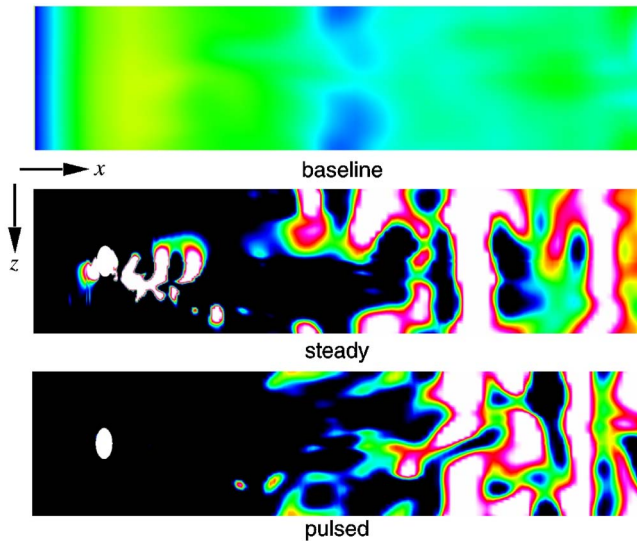


Fig. 14 Instantaneous planar contours of the spanwise component of vorticity on the blade surface

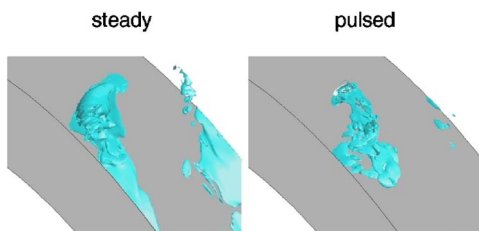


Fig. 15 Instantaneous iso-surfaces of vorticity magnitude in the near-jet region

downstream of the nozzle exit, for the steady blowing case. It is noted that the wake of the jet extends across the spanwise domain. The jet surface for the pulsed case is less coherent.

Instantaneous planar contours of the streamwise component of vorticity are found in Fig. 16. Locations of these contours lie at distances of 1, 5, and 10 jet diameters downstream from the center of the jet. The height of the attached boundary layer ( $\delta$ ) upstream of the jet is indicated in the figure. For the steady injection case of Fig. 16(a), the jet penetrates to a height greater than the boundary-layer thickness, and mixing persists downstream beyond  $x-x_j = 10d$ . In Fig. 16(b), contours are shown for the pulsed case, at a time corresponding to the midpoint of the pulsing cycle ( $t/t_p = 0.5$ ). At this instance, the jet exit velocity is at its maximum and has been active for one-half the cycle (see Fig. 3). Here, the contours look similar to those of the steady injection case, except at the most downstream station. Contours for the pulsed case at the end of the injection cycle appear in Fig. 16(c). For this situation ( $t/t_p = 1.0$ ), no injection has occurred for one-half of the cycle, and effects of the jet are only visible at the most downstream station.

It is perhaps surprising that there are so few differences between the steady blowing and pulsed injection cases. The reason for this is that even in the steady case, the flow immediately downstream of the jet is inherently unsteady. Because of the orientation of the jet transverse to the streamwise flow (blade-normal and spanwise), it is fundamentally unstable and rapidly evolves to a noncoherent form. This process serves to generate mixing, much like the pulsed injection case. The pulsed case, however, provides a much more efficient means of distributing momentum to the flow, since it produces identical benefits with one-half the mass flow rate.

## Summary and Conclusions

Direct numerical simulation was used to describe the transitional subsonic flow through a highly loaded low-pressure turbine at a nominal Reynolds number of 25,000, with both steady blowing and pulsed mass injection flow control. Computations were carried out using a high-order numerical method, and an overset grid methodology for describing the computational flowfield. A high-order interpolation procedure maintained accuracy at boundaries of discrete mesh systems that were used to define the jet region, including its interior nozzle.

For both the steady and pulsed cases, the fundamental effect of flow control was to energize the blade boundary layer due to the transfer of fluid momentum and mixing. This helped maintain attached flow along the blade surface for a distance of 19–21% greater than that of the baseline case. As a result, wake total pressure losses were decreased by 53–56%.

Comparisons were made for both the time-mean and fluctuating components of the respective flowfields. Velocity magnitude profiles qualitatively agreed with experimental measurements that were taken for a somewhat different configuration at a higher Reynolds number. Few differences were observed in characteristics of the flow control solutions. Although the steady blowing case employed no explicit unsteady forcing, due to fluid instability of the jet, the flowfield was inherently unsteady and resulted in features which were quite similar to the pulsed case. Both situations achieved the desired result of decreased wake losses, but the pulsed case required less mass flow to attain the same level of improvement in efficiency.

## Acknowledgment

The work presented here was sponsored by the U.S. Air Force Office of Scientific Research under Task 2307N61A and was monitored by T. Beutner. Computational resources were supported in part by a grant of supercomputer time from the U.S. Department of Defense Major Shared Resource Centers at Stennis Space Center, MS and Wright-Patterson AFB, OH. The authors are grateful to R. Sondergaard for supplying experimental results.

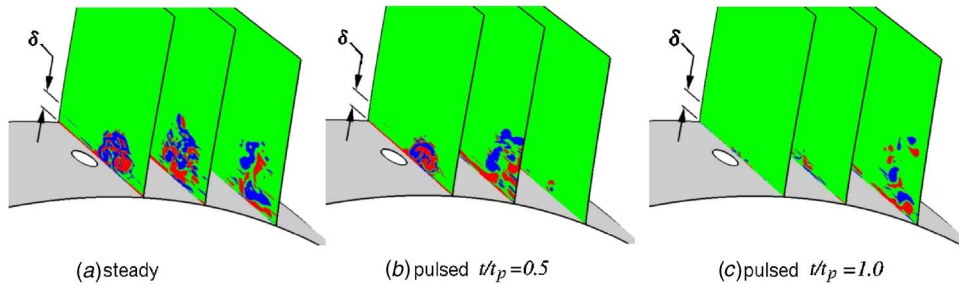


Fig. 16 Instantaneous planar contours of the streamwise component of vorticity for the steady injection case, and the pulsed injection case at  $t/t_p=0.5$  and  $t/t_p=1.0$

## Nomenclature

$C_p$	turbine blade time-mean surface pressure coefficient, $2(\bar{p}-\bar{p}_i)/\rho_i \bar{q}_i^2$
$D$	duty cycle expressed as a decimal fraction
$E_{k_z}, E_\omega$	nondimensional turbulent kinetic energy wave number and frequency spectra
$f$	dimensional jet forcing frequency
$\mathcal{J}$	Jacobian of the coordinate transformation
$k_z$	nondimensional spanwise wave number
$l, n$	nondimensional blade tangential and normal directions
$M$	Mach number
$p$	nondimensional static pressure
$Pr$	Prandtl number, 0.73 for air
$q$	nondimensional planar velocity magnitude, $\sqrt{u^2+v^2}$ or $\sqrt{v^2+w^2}$ for the jet
$Re_\infty$	reference Reynolds number, $\rho_\infty q_\infty c / \mu_\infty$
$Re$	chord inlet Reynolds number, $\rho_i \bar{q}_i Re_\infty / \mu_i$
$t$	nondimensional time based upon the reference velocity, $u_\infty$
$t_p$	nondimensional jet forcing period
$T$	nondimensional static temperature
$u, v, w$	nondimensional Cartesian velocity components in the $x, y, z$ directions
$u_1, u_2, u_3$	$u, v, w$
$U, V, W$	contravariant velocity components
$x, y, z$	nondimensional Cartesian coordinates in the streamwise, vertical, and spanwise directions
$x_1, x_2, x_3$	$x, y, z$
$\alpha$	turbine blade flow angle
$\gamma$	specific heat ratio, 1.4 for air
$\delta$	nondimensional boundary-layer thickness
$\delta_{ij}$	Kronecker delta function
$\delta_{\xi 2}^2, \delta_{\eta 2}^2, \delta_{\zeta 2}^2,$ $\delta_{\xi 4}^4, \delta_{\eta 4}^4, \delta_{\zeta 4}^4$	second-order and fourth-order finite-difference operators in $\xi, \eta, \zeta$
$\Delta l, \Delta n, \Delta z$	nondimensional mesh step sizes in blade tangential, normal, and spanwise directions
$\mu$	nondimensional molecular viscosity coefficient
$\xi_x, \xi_y, \xi_z,$ $\eta_x, \eta_y, \eta_z,$ $\zeta_x, \zeta_y, \zeta_z$	metric coefficients of the coordinate transformation
$\omega$	nondimensional frequency

## Subscripts

$i, o$	inflow and outflow conditions
$j$	corresponding to vortex generator jet
max, min	maximum and minimum values
$l$	"local freestream value"
$\infty$	dimensional reference value

## Superscripts

+	= value given in law-of-the-wall units
$\bar{\cdot}$	= time-mean quantity
$\sqrt{\cdot}$	= root-mean-square fluctuating component

## References

- [1] Halstead, D. E., Wisler, D. C., Okiishi, T. H., Walker, G. J., Hodson, H. P., and Shin, H. W., 1995, "Boundary Layer Development in Axial Compressors and Turbines Part 1 of 4: Composite Picture," ASME Paper No. 95-GT-461.
- [2] Halstead, D. E., Wisler, D. C., Okiishi, T. H., Walker, G. J., Hodson, H. P., and Shin, H. W., 1995, "Boundary Layer Development in Axial Compressors and Turbines Part 3 of 4: LP Turbines," ASME Paper No. 95-GT-463.
- [3] Simon, T. W., and Volino, R. J., 1996, "Separating and Separated Boundary Layers," WL-TR-96-2092, Wright Laboratory, Wright-Patterson AFB, OH.
- [4] Baughn, J. W., Butler, R. J., Byerley, A. R., and Rivir, R. B., 1966, "An Experimental Investigation of Heat Transfer, Transition and Separation on Turbine Blades at Low Reynolds Number and High Turbulence Intensity," WL-TR-96-2093, Wright Laboratory, Wright-Patterson AFB, OH.
- [5] Murawski, C. G., Simon, T. W., Volino, R. J., and Vafai, K., 1997, "Experimental Study of the Unsteady Aerodynamics in a Linear Cascade With Low Reynolds Number Low Pressure Turbine Blades," ASME Paper No. 97-GT-95.
- [6] Qui, S., and Simon, T. W., 1997, "An Experimental Investigation of Transition as Applied to Low Pressure Turbine Suction Surface Flows," ASME Paper No. 97-GT-455.
- [7] Welsh, S. T., Barlow, D. N., Butler, R. J., Van Treuren, K. W., Byerley, A. R., Baughn, J. W., and Rivir, R. B., 1997, "Effects of Passive and Active Air-Jet Turbulence on Turbine Blade Heat Transfer," ASME Paper No. 97-GT-131.
- [8] Murawski, C. G., and Vafai, K., 1999, "Effect of Variable Axial Chord on a Low-Pressure Turbine Blade," J. Propul. Power, **15**(5), pp. 667-674.
- [9] Lake, J. P., King, P. I., and Rivir, R. B., 1999, "Reduction of Separation Losses on a Turbine Blade With Low Reynolds Number," AIAA Paper No. 99-0242.
- [10] Bons, J. P., Sondergaard, R., and Rivir, R. B., 1999, "Control of Low-Pressure Turbine Separation Using Vortex Generator Jets," AIAA Paper No. 99-0367.
- [11] Bons, J. P., Sondergaard, R., and Rivir, R. B., 2001, "Turbine Separation Control Using Pulsed Vortex Generator Jets," ASME J. Turbomach., **123**(2), pp. 198-206.
- [12] Bons, J. P., Sondergaard, R., and Rivir, R. B., 2002, "The Fluid Dynamics of LPT Blade Separation Control Using Pulsed Jets," ASME J. Turbomach., **124**(1), pp. 77-85.
- [13] Sondergaard, R., Rivir, R. B., and Bons, J. P., 2002, "Control of Low-Pressure Turbine Separation Using Vortex Generator Jets," J. Propul. Power, **18**(4), pp. 889-895.
- [14] Volino, R. J., 2003, "Passive Flow Control on Low-Pressure Turbine Airfoils," ASME J. Turbomach., **125**(4), pp. 754-764.
- [15] Volino, R. J., 2003, "Separation Control on Low-Pressure Turbine Airfoils Using Synthetic Vortex Generator Jets," ASME J. Turbomach., **125**(4), pp. 765-777.
- [16] Huang, J., Corke, T. C., and Thomas, F. O., 2003, "Plasma Actuators for Separation Control of Low Pressure Turbine Blades," AIAA Paper No. 2003-1027.
- [17] Sondergaard, R., Bons, J. P., Sucher, M., and Rivir, R. B., 2002, "Reducing Low-Pressure Turbine Stage Blade Count Using Vortex Generator Jet Separation Control," ASME Paper No. GT-2002-30602.
- [18] Eulitz, F., and Engel, K., 1998, "Numerical Investigation of Wake Interaction in a Low Pressure Turbine," AIAA Paper No. 98-GT-563.
- [19] Choi, C. H., and Yoo, J. Y., 1998, "Cascade Flow Calculations Using the  $k-\omega$  Turbulence Model With Explicit-Implicit Solver," AIAA J., **35**(9), pp. 1551-1552.
- [20] Chernobrovkin, A., and Lakshminarayana, B., 1999, "Turbulence Modeling and Computation of Viscous Transitional Flows for Low Pressure Turbines," J. Fluids Eng., **121**(4), pp. 824-833.
- [21] Dorney, D. J., Ashpis, D. E., Halstead, D. E., and Wisler, D. C., 2000, "Study of Boundary-Layer Development in a Two-Stage Low-Pressure Turbine," J. Propul. Power, **16**(1), pp. 160-163.
- [22] Suzen, Y. B., Huang, P. G., Volino, R. J., Corke, T. C., Thomas, F. O., Huang,

- J., Lake, J. P., and King, P. I., 2003 "A Comprehensive CFD Study of Transitional Flows in Low-Pressure Turbines Under a Wide Range of Operating Conditions," AIAA Paper No. 2003-3591.
- [23] Suzen, Y. B., Huang, P. G., Hultgren, L. S., and Ashpis, D. E., 2001, "Predictions of Separated and Transitional Boundary Layers Under Low-Pressure Turbine Airfoil Conditions Using an Intermittency Transport Equation," *ASME J. Turbomach.*, **125**(3), pp. 455–464.
- [24] Raverdy, B., Mary, I., Sagaut, P., and Liamis, N., 2001, "Large-Eddy Simulation of the Flow Around a Low Pressure Turbine Blade," *Direct and Large-Eddy Simulation IV*, ERCOFTAC Series Vol. 8, B. J. Guerts, R. Friedrich, and O. Metais, eds., Kluwer Academic Publishers, Dordrecht, The Netherlands, pp. 381–388.
- [25] Mittal, R., Venkatasubramanian, S., and Najjar, F. M., 2001, "Large-Eddy Simulation of Flow Through a Low-Pressure Turbine Cascade," AIAA Paper No. 2001-2560.
- [26] Postl, D., Gross, A., and Fasel, H. F., 2003, "Numerical Investigation of Low-Pressure Turbine Blade Separation Control," AIAA Paper No. 2003-0614.
- [27] Rizzetta, D. P., and Visbal, M. R., 2003, "Numerical Investigation of Transitional Flow Through a Low-Pressure Turbine Cascade AIAA Paper No. 2003-3587.
- [28] Wissink, J. G., 2003, "DNS of Separating, Low-Reynolds Number Flow in a Turbine Cascade With Incoming Wakes," *Int. J. Heat Fluid Flow*, **24**(4), pp. 626–635.
- [29] Kalitzin, G., Wu, X., and Durbin, P. A., 2003, "DNS of Fully Turbulent Flow in a LPT Passage," *Int. J. Heat Fluid Flow*, **24**(4), pp. 636–644.
- [30] Postl, D., Gross, A., and Fasel, H. F., 2004, "Numerical Investigation of Active Flow Control for Low-Pressure Turbine Blade Separation," AIAA Paper No. 2004-750.
- [31] Rizzetta, D. P., and Visbal, M. R., 2004, "Numerical Simulation of Separation Control for a Highly Loaded Low-Pressure Turbine," *AIAA J.*, **43**(9), pp. 1958–1967.
- [32] Gross, A., and Fasel, H. F., 2004, "Active Control of Separation for Low-Pressure Turbine Blades," AIAA Paper No. 2004-2203.
- [33] Rivir, R. B., Sondergaard, R., Bons, J. P., and Yurchenko, N., 2004, "Control of Separation in Turbine Boundary Layers," AIAA Paper No. 2004-2201.
- [34] Beam, R., and Warming, R., 1978, "An Implicit Factored Scheme for the Compressible Navier-Stokes Equations," *AIAA J.*, **16**(4), pp. 393–402.
- [35] Gordnier, R. E., and Visbal, M. R., 1993, "Numerical Simulation of Delta-Wing Roll," AIAA Paper No. 93-0554.
- [36] Jameson, A., Schmidt, W., and Turkel, E., 1981, "Numerical Solutions of the Euler Equations by Finite Volume Methods Using Runge-Kutta Time Stepping Schemes," AIAA Paper No. 81-1259.
- [37] Pulliam, T. H., and Chaussee, D. S., 1981, "A Diagonal Form of an Implicit Approximate-Factorization Algorithm," *J. Comput. Phys.*, **39**(2), pp. 347–363.
- [38] Lele, S. A., 1992, "Compact Finite Difference Schemes With Spectral-like Resolution," *J. Comput. Phys.*, **103**(2), pp. 16–42.
- [39] Visbal, M. R., and Gaitonde, D. V., 1999, "High-Order-Accurate Methods for Complex Unsteady Subsonic Flows," *AIAA J.*, **37**(10), pp. 1231–1239.
- [40] Gaitonde, D., Shang, J. S., and Young, J. L., 1997, "Practical Aspects of High-Order Accurate Finite-Volume Schemes for Electromagnetics," AIAA Paper No. 97-0363.
- [41] Gaitonde, D., and Visbal, M. R., 1998, "High-Order Schemes for Navier-Stokes Equations: Algorithm and Implementation into FDL3DI," AFRL-VA-WP-TR-1998-3060, Air Force Research Laboratory, Wright-Patterson AFB, OH.
- [42] Gordnier, R. E., and Visbal, M. R., 1998, "Numerical Simulation of Delta-Wing Roll," *Aerosol Sci. Technol.*, **2**(6), pp. 347–357.
- [43] Gordnier, R. E., 1995, "Computation of Delta-Wing Roll Maneuvers," *J. Aircr.*, **32**(3), pp. 486–492.
- [44] Visbal, M. R., 1993, "Computational Study of Vortex Breakdown on a Pitching Delta Wing," AIAA Paper No. 93-2974.
- [45] Visbal, M., Gaitonde, D., and Gogineni, S., 1998, "Direct Numerical Simulation of a Forced Transitional Plane Wall Jet," AIAA Paper No. 98-2643.
- [46] Rizzetta, D. P., Visbal, M. R., and Stanek, M. J., 1999, "Numerical Investigation of Synthetic-Jet Flowfields," *AIAA J.*, **37**(8), pp. 919–927.
- [47] Rizzetta, D. P., Visbal, M. R., and Blaisdell, G. A., 2003, "A Time-Implicit High-Order Compact Differencing and Filtering Scheme for Large-Eddy Simulation," *Int. J. Numer. Methods Fluids*, **42**(6), pp. 665–693.
- [48] Rizzetta, D. P., Visbal, M. R., and Gaitonde, D. V., 2001, "Large-Eddy Simulation of Supersonic Compression-Ramp Flow by a High-Order Method," *AIAA J.*, **39**(12), pp. 2283–2292.
- [49] Rizzetta, D. P., and Visbal, M. R., 2002, "Application of Large-Eddy Simulation to Supersonic Compression Ramps," *AIAA J.*, **40**(8), pp. 1574–1581.
- [50] Rizzetta, D. P., and Visbal, M. R., 2003, "Large-Eddy Simulation of Supersonic Cavity Flowfields Including Flow Control," *AIAA J.*, **41**(8), pp. 452–462.
- [51] Steinbrenner, J. P., Chawner, J. P., and Fouts, C. L., 1991, "The GRIDGEN 3D Multiple Block Grid Generation System, Volume II: User's Manual," WRDC-TR-90-3022, Wright Research and Development Center, Wright-Patterson AFB, OH.
- [52] Gruber, B., and Carstens, V., 2001, "The Impact of Viscous Effects on the Aerodynamic Damping of Vibrating Transonic Compressor Blades-A Numerical Study," *ASME J. Turbomach.*, **123**(2), pp. 409–417.
- [53] Visbal, M. R., and Gaitonde, D. V., 2001, "Very High-Order Spatially Implicit Schemes for Computational Acoustics on Curvilinear Meshes," *J. Comput. Acoust.*, **9**(4), pp. 1259–1286.
- [54] Sherer, S. E., 2003, "Further Analysis of High-Order Overset Grid Method With Applications," AIAA Paper No. 2003-3839.
- [55] Suhs, N. E., Rogers, S. E., and Dietz, W. E., 2003, "PEGASUS 5: An Automated Preprocessor for Overset-Grid Computational Fluid Dynamics," *AIAA J.*, **41**(6), pp. 1037–1045.
- [56] Message Passing Interface Forum, 1994, "MPI: A Message-Passing Interface Standard," Computer Science Department Technical Report CS-94-230, University of Tennessee, Knoxville, TN.

J. Uddin

e-mail: uddinj@maths.bham.ac.uk

S. P. Decent

e-mail: decentsp@for.mat.bham.ac.uk

School of Mathematics,  
University of Birmingham,  
Edgbaston, Birmingham B15 2TT,  
United Kingdom

M. J. Simmons

School of Chemical Engineering,  
University of Birmingham,  
Edgbaston, Birmingham B15 2TT,  
United Kingdom  
e-mail: m.j.simmons@bham.ac.uk

# The Instability of Shear Thinning and Shear Thickening Spiralling Liquid Jets: Linear Theory

*The linear instability of a power law liquid emerging as a jet from an orifice on the surface of a rotating container is investigated, with applications to industrial prilling. Asymptotic methods are used to examine the growth rate and wavenumber of the most unstable traveling wave mode for different flow index numbers. Comparison with Newtonian liquids show that for small rotation rates shear thinning liquids are most stable to disturbances. In contrast for higher rotation rates we find shear thickening liquids are more stable than shear thinning liquids. The influence of viscosity, surface tension, and rotation rate on the growth rates and most unstable wavenumbers associated with both types of liquids are also examined. [DOI: 10.1115/1.2238876]*

## 1 Introduction

The industrial prilling process is a quick and relatively cheap technique used for the production of small spherical pellets. In this process a specially perforated large cylindrical drum rotates about its axis. Molten liquid is pumped into the drum, and long curved jets are produced from the holes in the surface of the drum which break up due to centrifugal and capillary instabilities. Break up leads to the production of droplets, which subsequently solidify, and form pellets. This process is widely used in industry for the manufacture of fertilizers, magnesium, and aluminium pellets (see Andersen and Yttri [1] and Ornek et al. [2]).

A mathematical formulation of this problem for an inviscid fluid was introduced and investigated by Wallwork et al. [3]. The inclusion of the effects of gravity and Newtonian viscosity were investigated by Decent et al. [4–6] who used a temporal and spatial stability analysis to determine breakup lengths and droplet sizes. Nonlinear effects have also been considered by Päråu et al. [7,8] and Wong et al. [9]. Experimental studies by Wong et al. [10] show a good agreement with theory and reveal four different modes of break up depending on jet exit conditions. In that paper, it is found that of all the parameters studied, liquid viscosity has the strongest influence on the jet break up length and the dynamics of jet break up. Since many industrial fluids used in prilling are not Newtonian and, therefore, likely to have varying viscosities, a better understanding of non-Newtonian effects on break up and droplet formation is needed.

Drop formation and the break up of straight liquid jets was first observed and investigated by Savart [11] in the early nineteenth century. Together with the contributions of Lord Rayleigh [12] and Plateau [13] these works are now considered classical. There is no paucity of literature on the stability of liquid jets (e.g., see Goedde and Yuen [14], Keller, Rubinow and Tu [15] and Hilbing and Heister [16]), and the reader is referred to numerous reviews of these works, and in particular Eggers [17] and Lin [18].

For Newtonian fluids we have the familiar constitutive equation given by  $\tau = \mu \gamma$  where  $\tau$  is the stress tensor,  $\gamma$  is the rate of strain (deformation) tensor and  $\mu$  is the dynamic viscosity. Many real fluids such as liquid fertilizer, paint solution, and molten polymers, as well as many household fluids like shampoo and ketchup, do not obey a linear relationship between strain and stress. Such fluids are often better described by a *Power Law* model where the

stress is expressed as a function of the shear rate raised to some power. We note that the power law model, though common in industry, is the simplest non-Newtonian model and does not capture any viscoelastic or visco-plastic effects. In its most general form we have  $\tau = \eta \dot{\gamma}$ , where the apparent viscosity is given by the second invariant of the rate of strain tensor  $\log \eta = \log m + ((\alpha - 1)/2) \log((\dot{\gamma} : \dot{\gamma})/2)$ . The *flow index number*  $\alpha$  is dimensionless and the *fluid consistency number*  $m$  has dimensions of  $\text{Pa} \cdot \text{s}^\alpha$ , both of which are found experimentally. Here Pa is Pascals, and s is seconds. Fluids which follow such a model are termed *shear thinning* or *shear thickening* depending on whether  $\alpha$  is less than or greater than unity. In the special case where  $\alpha = 1$ , we have  $m = \mu$  and the Newtonian fluid is recovered. Hence  $m$  is a measure of the relative viscosity of the fluid, with  $\alpha$  measuring how “non-Newtonian” the fluid is.

The stability of non-Newtonian fluids with power law rheology have already been investigated for a diverse range of flows. These include flow down an inclined plane (Hwang et al. [19] and Balmforth et al. [20]), between concentric cylinders (Coronado-Matutti et al. [21]) as well as gravity driven shear flows (Berezin et al. [22]). In this paper we apply linear stability analysis to slender power law jets.

## 2 Problem Formulation

To model the prilling process we consider a large cylindrical container having radius  $s_0$  and rotating with angular velocity  $\Omega$  along its axis of symmetry. A small orifice is placed at the side of the container having radius  $a$  which is considered small in relation to the radius of the container.

We examine the problem by considering a coordinate system  $(x, y, z)$  which rotates with the container, having an origin at the axis of the container and with the position of the center of the orifice at  $(s_0, 0, 0)$ . In this case the axis of the container lies along the  $y$ -axis and the effects of gravity on the jet can be neglected if the centripetal acceleration of the jet  $s_0 \Omega^2$  is much greater than the acceleration due to gravity  $g$ , as is the case with industrial prilling. Then the jet moves solely in the  $x$ - $z$ -plane and thus we can describe the centerline of the jet by coordinates  $(X(s, t), 0, Z(s, t))$ , where  $s$  is the arclength along the centerline of the jet, measured from the orifice, and  $t$  is time.

The rotation of the container causes the jet to curve on leaving the orifice and any analysis of the jet in the rotating  $(x, y, z)$  coordinate system becomes cumbersome. We, therefore, introduce a coordinate system previously used by Wallwork [23] which is

Contributed by the Fluids Engineering Division of ASME for publication in the JOURNAL OF FLUIDS ENGINEERING. Manuscript received November 27, 2005; final manuscript received March 9, 2006. Assoc. Editor: Dimitris Drikakis.

similar to the approach adopted by Ribe [24] and Entov and Yarin [25], where we have one coordinate lying along the centerline of the jet corresponding to the arc length  $s$  of the jet, with the remaining coordinates as the plane polar coordinates  $n$ ,  $\phi$  (radial and azimuthal) in any cross section of the jet. The associated unit vectors are represented by  $\mathbf{e}_s$ ,  $\mathbf{e}_n$ , and  $\mathbf{e}_\phi$ , respectively, and their derivation is explained further in [4].

To describe the flow we use the velocity vector  $\mathbf{u} = u\mathbf{e}_s + v\mathbf{e}_n + w\mathbf{e}_\phi$  to arrive at the familiar equations of motion (including the continuity equation) given by

$$\rho \left( \frac{\partial \mathbf{u}}{\partial t} + \mathbf{u} \cdot \nabla \mathbf{u} \right) = -\nabla p + \nabla \cdot \boldsymbol{\tau} - 2\boldsymbol{\omega} \times \mathbf{u} - \boldsymbol{\omega} \times (\boldsymbol{\omega} \times \mathbf{r})$$

$$\nabla \cdot \mathbf{u} = 0$$

where  $\rho$  is the constant density of the fluid,  $p$  is the pressure within the jet and  $\boldsymbol{\omega} = (0, \omega, 0)$  is the angular velocity vector of the container.

The surface of the jet can be described by the equation  $n - R(s, t, \phi) = 0$ , where  $R(s, t, \phi)$  is a function giving the free surface position, and a normal vector to this surface is given by  $\nabla(n - R(s, t, \phi))$ . When evaluated this gives the unit normal vector as

$$\mathbf{n} = \frac{1}{E} \left( -\frac{\partial R}{\partial s} \mathbf{e}_s + \mathbf{e}_n - \frac{\partial R}{\partial \phi} \mathbf{e}_\phi \right) \quad \text{where}$$

$$E = \left( 1 + \frac{1}{h_s^2} \left( \frac{\partial R}{\partial s} \right)^2 + \frac{1}{R^2} \left( \frac{\partial R}{\partial \phi} \right)^2 \right)^{1/2}$$

If we let  $\mathbf{r} = \int \mathbf{e}_s ds + n\mathbf{e}_\phi$  denote the position vector of any particle on the free surface then the normal stress condition is given by  $\mathbf{n} \cdot \boldsymbol{\Pi} \cdot \mathbf{n} = \sigma \kappa$ , where  $\boldsymbol{\Pi}$  is the total stress tensor given by  $p\mathbf{I} + \boldsymbol{\tau}$ ,  $\sigma$  is the isotropic surface tension and  $\kappa$  is the curvature of the free surface

$$\kappa = \frac{1}{nh_s} \left( \frac{\partial}{\partial s} \left( -\frac{n}{h_s} \frac{\partial R}{\partial s} \right) + \frac{\partial}{\partial n} \left( \frac{nh_s}{E} \right) + \frac{\partial}{\partial \phi} \left( -\frac{h_s}{n} \frac{\partial R}{\partial \phi} \right) \right)$$

Using the two tangent vectors to our free surface,  $\mathbf{t}_1 = \partial \mathbf{r} / \partial s$  and  $\mathbf{t}_2 = \partial \mathbf{r} / \partial \phi$ , we form our tangential stress conditions  $\mathbf{t}_i \cdot \boldsymbol{\Pi} \cdot \mathbf{n} = 0$  for  $i=1, 2$ . The kinematic condition is given by  $(D/Dt)(R(s, t, \phi) - n) = 0$ , for  $n=R(s, \phi, t)$ .

We nondimensionalize our equations using the transformations

$$\{\bar{u}, \bar{v}, \bar{w}\} = \frac{1}{U} \{u, v, w\}, \quad \bar{p} = \frac{p}{\rho U^2}$$

$$\{\bar{s}, \bar{X}, \bar{Z}, \bar{t}, \bar{\epsilon}\} = \frac{1}{s_0} \{s, X, Z, tU, a\}, \quad \{\bar{n}, \bar{R}\} = \frac{1}{a} \{n, R\}$$

where  $U$  is the exit speed of the jet in the rotating frame,  $\epsilon$  is the aspect ratio of the jet, and  $u$ ,  $v$ , and  $w$  are the tangential, radial, and azimuthal velocity components relative to the centerline of the jet, respectively. For power law fluids the viscosity is not constant and we have that

$$(\nabla \cdot \boldsymbol{\tau})_j = (\nabla \cdot (\eta \boldsymbol{\gamma}))_j = \eta (\nabla \cdot (\nabla \mathbf{u} + \nabla \mathbf{u}^T))_j + \frac{\gamma_{ij}}{h_i} \partial_i \eta$$

$$= (\eta \nabla^2 \mathbf{u})_j + \frac{\gamma_{ij}}{h_i} \partial_i \eta$$

where the free indices go through  $s$ ,  $n$ , and  $\phi$ , and  $h_i$  are the structure functions. Thus our equations of motion will differ from those found in [5,7] through the dynamic viscosity being replaced by  $\eta$  and the inclusion of derivatives of  $\eta$ .

We exploit the fact that the radius of the orifice is small when compared to the radius of the cylinder by expanding  $u, v, w, p$  in

Taylor series in  $\epsilon n$  (see Eggers [17], Hohman et al. [26]), and  $R, X, Z$  in asymptotic series in  $\epsilon$ . We assume that the leading order axial component of the velocity is independent of  $\phi$  and that the centerline of the jet is unaffected by small perturbations. Dropping overbars, this gives

$$u(s, n, \phi, t) = u_0(s, t) + (\epsilon n)u_1 + (\epsilon n)^2 u_2 + \dots$$

$$\{v, w\}(s, n, \phi, t) = (\epsilon n)\{v_1, w_1\} + (\epsilon n)^2 \{v_2, w_2\} + \dots$$

$$p(s, n, \phi, t) = p_0(s, n, \phi, t) + (\epsilon n)p_1 + \dots$$

$$R(s, n, \phi, t) = R_0(s, t) + \epsilon R_1 + \dots$$

$$\{X, Z\}(s, n, \phi, t) = \{X_0, Z_0\}(s) + \epsilon \{X_1, Z_1\}(s, t) + \dots$$

where  $u_1, u_2, v_1, w_1, v_2, w_2, p_1$ , and  $R_1$  are in general functions of  $s$ ,  $\phi$ , and  $t$ . The resulting nondimensional equations are tedious and since they are very similar to those found in [7,5,23] we will only reproduce here terms related to the non-Newtonian effects. It is found that the momentum equations are

$$N.S. + \frac{1}{\epsilon \text{Re}_\alpha} \frac{2\epsilon^2}{h_s} \frac{\partial \eta}{\partial s} \left( \frac{\partial u}{\partial s} + v \cos \phi S - w \sin \phi S \right)$$

$$+ \frac{1}{n} \frac{\partial \eta}{\partial \phi} \left( \epsilon u \sin \phi S + \frac{h_s}{n} \frac{\partial u}{\partial \phi} + \epsilon \frac{\partial w}{\partial s} \right)$$

$$+ \frac{\partial \eta}{\partial n} \left( \epsilon \frac{\partial v}{\partial s} - \epsilon u \cos \phi S + h_s \frac{\partial u}{\partial n} \right) \quad (1)$$

$$N.S. + \frac{1}{\epsilon \text{Re}_\alpha} \left( \frac{\epsilon}{h_s} \frac{\partial \eta}{\partial s} \left( \epsilon \frac{\partial v}{\partial s} - \epsilon u \cos \phi S + h_s \frac{\partial u}{\partial n} \right) \right.$$

$$\left. + \frac{\partial \eta}{\partial n} \left( 2h_s \frac{\partial v}{\partial n} \right) + \frac{h_s}{n} \frac{\partial \eta}{\partial \phi} \left( \frac{\partial w}{\partial n} - \frac{w}{n} + \frac{1}{n} \frac{\partial v}{\partial \phi} \right) \right) \quad (2)$$

and

$$N.S. + \frac{h_s}{\epsilon \text{Re}_\alpha} \left( \frac{\epsilon}{h_s^2} \frac{\partial \eta}{\partial s} \left( \epsilon \frac{\partial w}{\partial s} + \epsilon u \sin \phi S + \frac{h_s}{n} \frac{\partial u}{\partial \phi} \right) \right.$$

$$\left. + \frac{1}{n} \frac{\partial \eta}{\partial n} \left( \frac{\partial v}{\partial \phi} - w + n \frac{\partial w}{\partial n} \right) + \frac{2}{n^2} \frac{\partial \eta}{\partial \phi} \left( \frac{\partial w}{\partial \phi} + v \right) \right) \quad (3)$$

where  $N.S.$  represents the expression for the Navier-Stokes equations found in [7,5,23]. The normal stress condition, the first and second tangential stress conditions and the arclength condition as well as the kinematic condition remain unchanged to those found in [7,5,23]. A number of dimensionless parameters appear in these equations, including the Rossby number  $\text{Rb} = U/(s_0 \Omega)$ , the Weber number  $\text{We} = \rho U^2 a / \sigma$ , the aspect ratio  $\epsilon = a/s_0$ , and the generalized Reynolds number based on the radius of the cylinder  $\text{Re}_\alpha = (\rho/m)s_0^\alpha U^{2-\alpha}$ . To remain consistent with earlier works [6,7] we have chosen to base the Reynolds number on  $s_0$  rather than the characteristic dimension of the jet flow  $a$ . We do, however, go on to use a Reynolds number based on the jet radius. Here  $S = (X_s Z_{ss} - Z_s X_{ss})$ .

From the continuity equation we obtain

$$O(\epsilon n): u_{0s} + 2v_1 + w_{1\phi} = 0, \quad (4)$$

$$O(\epsilon n)^2: u_{1s} + 3v_2 + w_{2\phi} + (3v_1 + w_{1\phi}) \cos \phi S - w_1 \sin \phi S = 0 \quad (5)$$

From the second tangential stress condition we get

$$O(\epsilon n): R_0^3 v_{1\phi} = 0 \quad (6)$$

$$O(\epsilon n)^2: 3R_0^2 R_1 v_{1\phi} + R_0^4 (w_2 + v_{2\phi}) - 2R_0^2 R_1 \phi w_{1\phi} = 0 \quad (7)$$

Thus we see that  $v_{1\phi} = 0$ , and by differentiating (4) we see that  $w_{1\phi\phi} = 0$ . Since  $w_1$  is periodic in  $\phi$  we must have  $w_1 = w_1(s, t)$ .

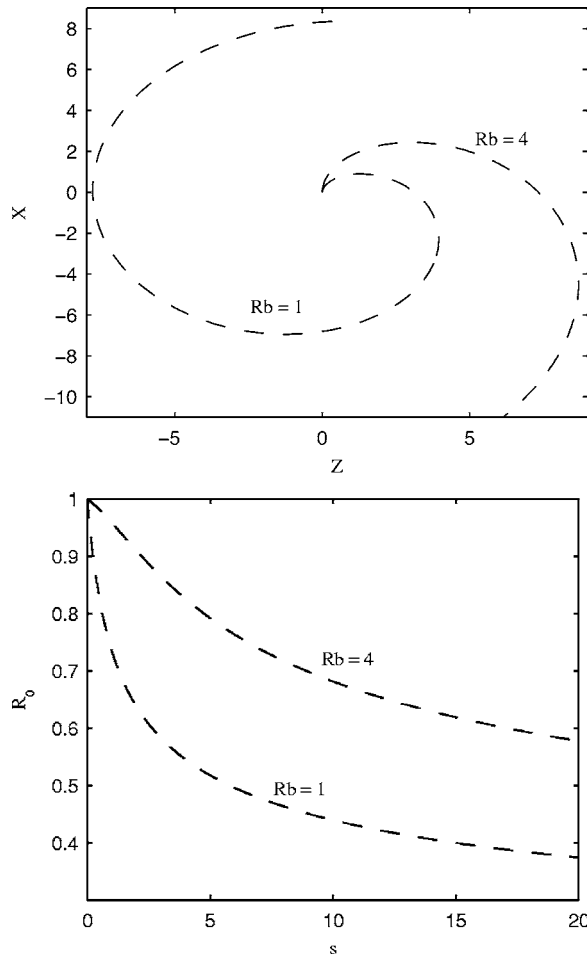


Fig. 1 The trajectory and radius of an inviscid jet when  $We = 20$

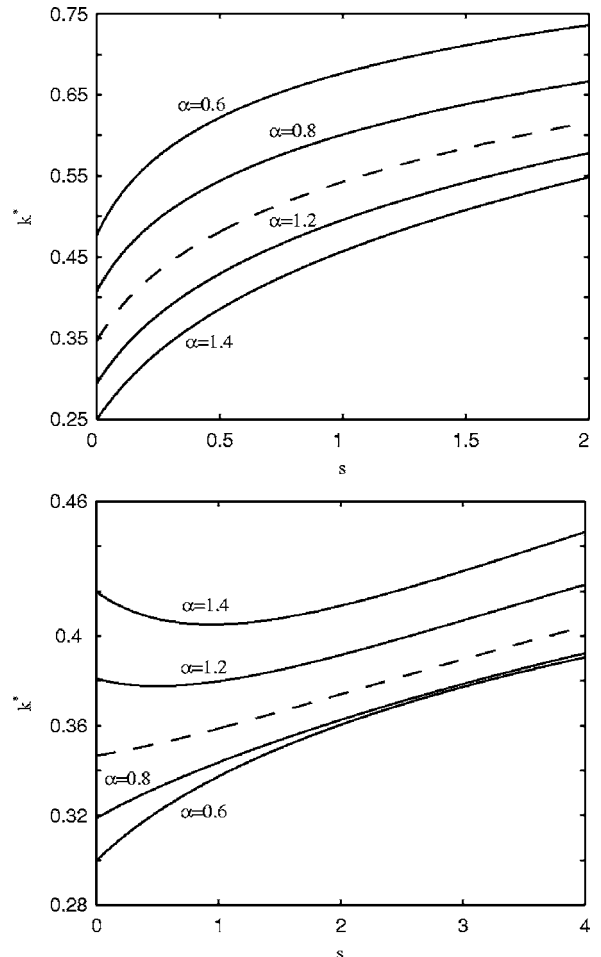


Fig. 2 The most unstable wavenumber against arc length when  $Re_\alpha = 3$  and  $We = 20$  for a high ( $Rb = 0.75$ , top) and a low ( $Rb = 4$ , bottom) rotation rate. The dashed curve represents  $\alpha = 1$ .

Then (4) implies that  $v_1 = -u_{0s}/2$  and from (7) we have  $w_2 + v_2\phi = 0$ , which when differentiated with respect to  $\phi$  leads to  $w_2\phi = -v_2\phi\phi$ . From the first tangential stress condition we have

$$O(\epsilon): u_1 = u_0 S \cos \phi \quad (8)$$

$$O(\epsilon^2): u_2 = \frac{3}{2} u_{0s} \frac{R_{0s}}{R_0} + \frac{u_{0ss}}{4} \quad (9)$$

Periodic solutions for  $v_2$  and  $w_2$  are found to be

$$v_2 = \frac{1}{4} \left( \frac{u_{0s}}{2} S - u_0 S_s \right) \cos \phi + \frac{w_1}{4} S \sin \phi$$

$$w_2 = \frac{1}{4} \left( \frac{u_{0s}}{2} S - u_0 S_s \right) \sin \phi - \frac{w_1}{4} S \cos \phi$$

The apparent viscosity can be expressed as

$$\eta = m |\sqrt{3} u_{0s}|^{\alpha-1} \left( 1 + (\epsilon n) \frac{(\alpha-1)}{u_{0s}} \left( \left( u_0 S_s - \frac{u_{0s}}{2} S \right) \cos \phi - w_1 \sin \phi S \right) + O((\epsilon n)^2) \right) \quad (10)$$

From the second Navier-Stokes equation, we have at leading order  $p_{0n} = 0$ . Thus  $p_0 = p_0(s, \phi, t)$ , i.e.,  $p_0$  is independent of  $n$ . At order  $\epsilon$  we get

$$p_1 = \left( u_0^2 S - \frac{2}{Rb} u_0 + \frac{(X+1)Z_s - ZX_s}{Rb^2} \right) \cos \phi - \frac{|\sqrt{3} u_{0s}|^{\alpha-1}}{Re_\alpha} \left( \frac{6-\alpha}{2} u_{0s} S + \alpha u_0 S_s \right) \cos \phi + (\alpha - 2) \frac{|\sqrt{3} u_{0s}|^{\alpha-1}}{Re_\alpha} w_1 S \sin \phi \quad (11)$$

For simplicity of notation we will relabel  $X_0$  and  $Z_0$  with  $X$  and  $Z$ , respectively.

The Navier-Stokes equation in the azimuthal direction gives at leading order  $p_{0\phi} = 0$  which is automatically satisfied. At order  $\epsilon$  we get the above equation for  $p_1$ . From the normal stress condition we obtain at leading order and order  $\epsilon$

$$p_0 = - \frac{|\sqrt{3} u_{0s}|^{\alpha-1} u_{0s}}{Re_\alpha} + \frac{1}{R_0 We}$$

$$p_1 = \frac{1}{R_0 We} \left( S \cos \phi - \frac{R_{1\phi\phi} + R_1}{R_0^2} \right) + \frac{4 |\sqrt{3} u_{0s}|^{\alpha-1}}{Re_\alpha} v_2$$

If we now substitute the expression for  $p_1$  from (11) into the above equation, and note that  $R$  is periodic in  $\phi$ , we get



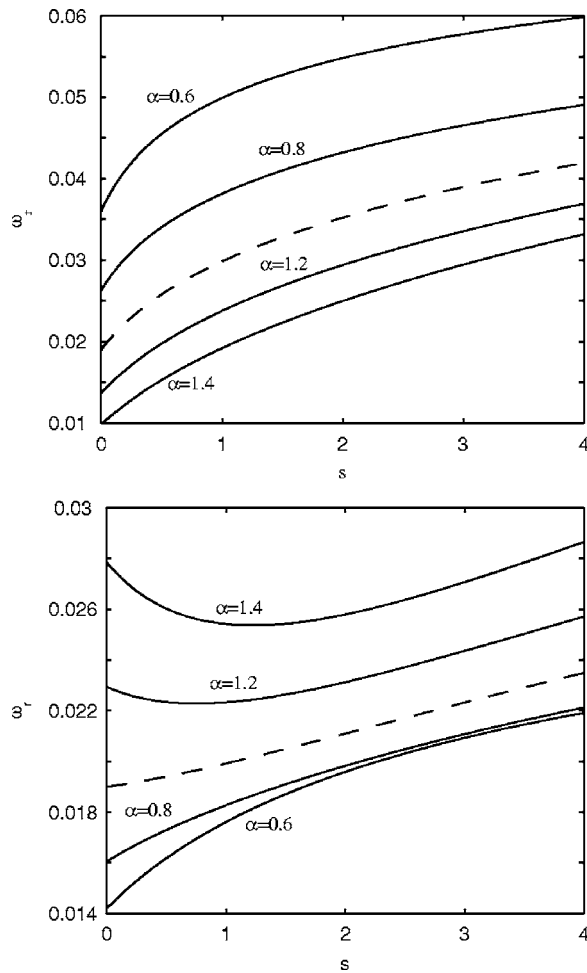


**Fig. 3** The growth rate  $\omega_r$  against arc length when  $\widetilde{Re}_\alpha=3$  and  $We=20$  for a high ( $Rb=0.75$ , top) and a low ( $Rb=4$ , bottom) rotation rate. The dashed curve represents  $\alpha=1$ .

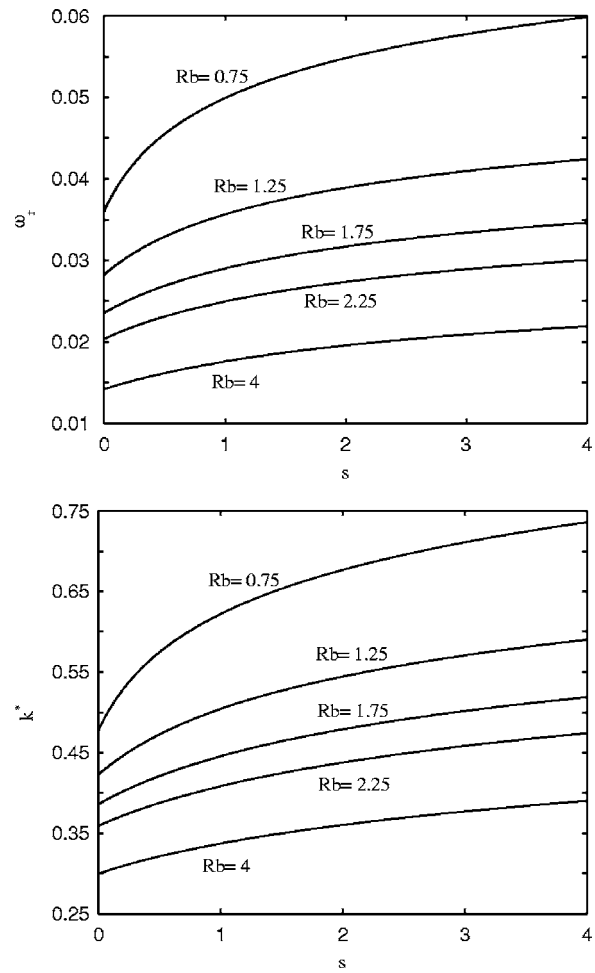


**Fig. 4** The growth rate (top) and most unstable wavenumber (bottom) against  $s$  for different  $Rb$  numbers.  $\alpha=0.6$ ,  $\widetilde{Re}_\alpha=3$ , and  $We=20$ .

$$\begin{aligned}
 S \left( \frac{(7-\alpha)|\sqrt{3}u_{0s}|^{\alpha-1}u_{0s}}{2Re_\alpha} + \frac{1}{R_0We} - u_0^2 \right) \cos \phi \\
 + \left( \frac{2}{Rb}u_0 - \frac{(X+1)Z_s - ZX_s}{Rb^2} \right) \cos \phi \\
 - \frac{(\alpha-1)|\sqrt{3}u_{0s}|^{\alpha-1}}{Re_\alpha} (u_0S_s \cos \phi + w_1 \sin \phi) = 0 \quad (12)
 \end{aligned}$$

The above equation is valid only if the leading order terms in the expansion of  $X$  and  $Z$  are independent of  $t$ . If we had retained leading order translational velocity terms  $v_0$  and  $w_0$  in our expansions for  $v$  and  $w$ , and had  $X_{0t} \neq 0$  and  $Z_{0t} \neq 0$ , then the right hand side of (12) would contain some additional unsteady terms (see [7,8]) in  $E=Z_sX_t - Z_tX_s$ . However,  $E \approx 0$  has already been found in [7,8] to be a very accurate approximation between the orifice and the break up point of the jet. This is backed up by the experimental observations of Wong et al. [10], which show that the center-line of the jet is steady (in the rotating frame), giving  $X_t \approx 0$ ,  $Z_t \approx 0$ , and  $E \approx 0$  for experimental observations. There seems to be no reason to suppose this will be different for non-Newtonian jets. (However, experiments are planned using the same apparatus as in [10] to check this.)

The Navier-Stokes equation in the axial direction, at order  $\epsilon$ , after using the expressions for  $u_2$ ,  $p_0$ , and  $\eta$  becomes

$$\begin{aligned}
 u_{0t} + uu_{0s} = - \frac{1}{We} \left( \frac{1}{R_0} \right)_s + \frac{(X+1)X_s + ZZ_s}{Rb^2} \\
 + \frac{3|\sqrt{3}u_{0s}|^{\alpha-1}}{Re_\alpha} \cdot \left( \alpha u_{0ss} + 2u_{0s} \frac{R_{0s}}{R} \right) \quad (13)
 \end{aligned}$$

From the kinematic condition, we obtain at order  $\epsilon$

$$R_{0t} + \frac{u_{0s}}{2}R_0 + u_0R_{0s} = 0 \quad (14)$$

And finally the last equation to be solved is the arclength equation at leading order

$$X_s^2 + Z_s^2 = 1 \quad (15)$$

We see that we have now four equations (12)–(15) for the four unknowns  $u_0$ ,  $R_0$ ,  $X$ , and  $Z$ .

We now search for steady state solutions to this set of equations. We have the four variables  $u_0$ ,  $R_0$ ,  $X$ , and  $Z$ , all of which we can consider as being functions of  $s$  only in the steady state. For convenience of notation we replace the leading order velocity and radius terms by  $u$  and  $R$ . The resulting steady state equations are

$$\begin{aligned}
 uu_s = - \frac{1}{We} \left( \frac{1}{R} \right)_s + \frac{(X+1)X_s + ZZ_s}{Rb^2} + \frac{3|\sqrt{3}u_s|^{\alpha-1}}{Re_\alpha} \cdot \left( \alpha u_{ss} + 2u_s \frac{R_s}{R} \right) \quad (16)
 \end{aligned}$$

$$\frac{u_s}{2}R + uR_s = 0 \quad (17)$$

as well as (12) and (15).

Using the initial conditions  $R(0)=1$  and  $u(0)=1$  in (17) we have that  $R^2u=1$ , and using this we get a reduced set of equations

$$uu_s = -\frac{u_s}{2We\sqrt{u}} + \frac{(X+1)X_s + ZZ_s}{Rb^2} + \frac{3|\sqrt{3}u_s|^{\alpha-1}}{Re_\alpha} \cdot \left( \alpha u_{ss} - \frac{u_s^2}{u} \right) \quad (18)$$

$$S \left( \frac{(7-\alpha)|\sqrt{3}u_s|^{\alpha-1}u_s}{2Re_\alpha} + \frac{\sqrt{u}}{We} - u^2 \right) \cos \phi + \left( \frac{2}{Rb}u - \frac{(X+1)Z_s - ZX_s}{Rb^2} \right) \cos \phi - \frac{(\alpha-1)|\sqrt{3}u_s|^{\alpha-1}}{Re_\alpha} \times (uS_s \cos \phi - w_1 \sin \phi) = 0 \quad (19)$$

as well as (15).

This system of equations can be solved for  $X$  and  $Z$  (thus giving us a steady trajectory), and for  $u$ , using a finite difference scheme (see [7,8]). However, in the next section, in order to obtain a distinguished limit, it will be shown that we require  $Re_\alpha = O(\epsilon^{-1})$ , so that  $Re_\alpha \rightarrow \infty$  is the correct limit here (This was also found in [5] in the Newtonian case.) This inviscid steady state ( $Re_\alpha \rightarrow \infty$ ) is only a valid approximation for the viscous case when the Ohnesorge number  $Oh = \sqrt{We/Re_\alpha}$  is not very large, so we shall, therefore, confine ourselves to the study of jets where the Ohnesorge number is small or  $O(1)$ . However, Wong et al. [10] has shown that jets do not form unless  $Oh$  is small, which gives confidence to this approximation.

The inviscid centerline problem for  $Re_\alpha = \infty$  is solved using a Runge-Kutta method with the boundary conditions at the nozzle as  $X(0)=Z(0)=Z_s(0)=0$  and  $u(0)=X_s(0)=1$ . Both the trajectory and the jet radius are plotted in Fig. 1.

### 3 Temporal Instability

The length scale over which the jet curves is  $s=O(1)$  but disturbances along the jet are much smaller, typically of the order of the jet radius  $a$ . By considering traveling wave modes of the form  $\exp(ik\bar{s} + \omega\bar{t})$ , where  $\bar{s}=s/\epsilon$  and  $\bar{t}=t/\epsilon$  are small length and time scales, and  $k=k(s)=O(1)$  and  $\omega=\omega(s)=O(1)$  are the wavenumber and frequency of the disturbances, we have a multiple scales formulation with perturbations along the jet having wavelength of  $O(\epsilon)$ , as required. Adding small perturbations to the steady state solution found at the end of the previous section, we have

$$\{u, R, p\}(s, t) = \{u_0, R_0, p_0\}(s) + \delta \{ \hat{u}, \hat{R}, \hat{p} \} \exp(ik\bar{s} + \omega\bar{t}) + O(\delta\epsilon) + c.c.$$

$$\{X, Z\}(s, t) = \{X, Z\}(s) + \delta\epsilon \{ \hat{X}, \hat{Z} \}(\bar{s}, \bar{t}, t) + c.c. \quad (20)$$

where c.c. denotes complex conjugates. The perturbations above are assumed to leave the centerline of the jet unaffected. This assumption, which has been shown to be a very good approximation in most experiments, is explained further in [7].

In the above expansion, the leading order steady state is considered. However, if perturbations are applied to all orders in  $\epsilon$  of the steady solution then we require  $0 < \delta \ll \epsilon^2$  for (20) to remain valid. We should also note that perturbations are applied implicitly to both the radial and azimuthal velocity components since both depend upon the axial velocity  $u$  (see previous section). We note that the  $\epsilon$  term in the perturbation for  $X$  and  $Z$  is needed to avoid the trivial solution  $\hat{X}=\hat{Z}=0$ . (We note that this finding backs up the assumption in the previous section that  $X$  and  $Z$  are time independent at leading order in  $\epsilon$ .) Here  $k$  is the wavenumber of the traveling wave disturbance,  $\omega$  is the frequency and  $\delta$  is a small constant which gives the amplitude of the wave.

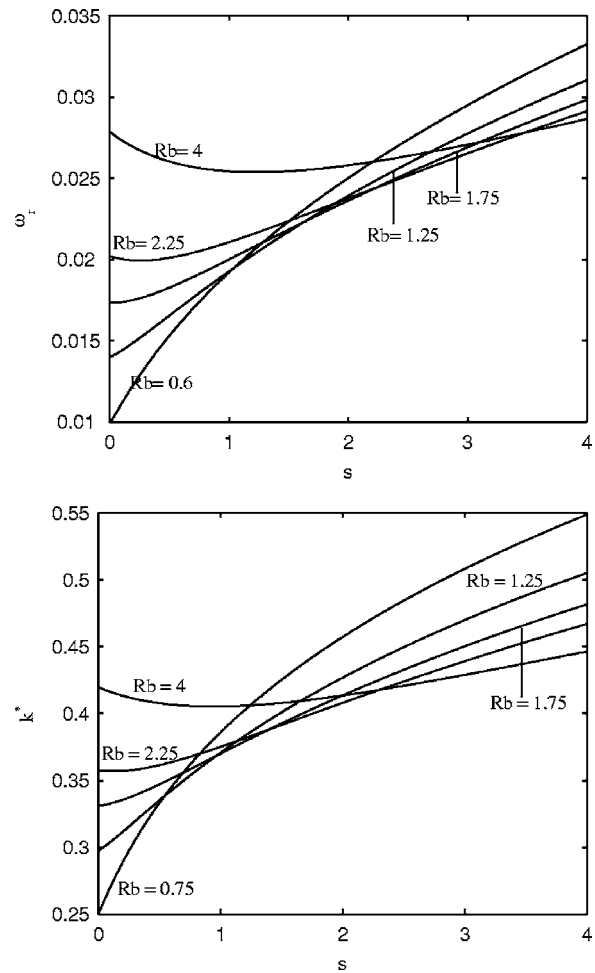


**Fig. 5** The growth rate (top) and most unstable wavenumber (bottom) against  $s$  for different  $Rb$  numbers.  $\alpha=1.4$ ,  $Re_\alpha=3$ , and  $We=20$ .

A new scaling for the Reynolds number based on the initial jet radius, namely  $\widetilde{Re}_\alpha = \epsilon Re_\alpha$  is needed to obtain a distinguished limit in the resulting unstable equations. To prevent instability to modes with zero wavelength we must use the full expression for the curvature, which is,  $1/We((1/R(1+\epsilon^2R_s^2)^{1/2}) - (\epsilon^2R_{ss}/(1+\epsilon^2R_s^2)^{3/2}))$ . Although to leading order the curvature term is  $1/(RWe)$ , the complete expression for the mean curvature term is needed to reproduce equilibrium states in jet breakup (see [17]) and has been used previously by a number of authors including Lee [27] and Garcia and Castellanos [28]. Thus the axial equation of motion becomes

$$u_t + uu_s = -\frac{1}{We} \left( \frac{1}{R(1+\epsilon^2R_s^2)^{1/2}} - \frac{\epsilon^2R_{ss}}{(1+\epsilon^2R_s^2)^{3/2}} \right)_s + \frac{(X+1)X_s + ZZ_s}{Rb^2} + \frac{3|\sqrt{3}u_s|^{\alpha-1}}{Re_\alpha} \left( \alpha u_{ss} + 2u_s \frac{R_s}{R} \right) \quad (21)$$

instead of (13). The scaling in  $\bar{s}=s/\epsilon$  brings the  $O(\epsilon)$  terms in (21) into leading order as required.

Using  $f(s, \alpha) = 3\alpha|\sqrt{3}u_s|^{\alpha-1}$ , substituting our perturbed solution into (12), (14), (15), and (21), we get at leading order the eigenvalue relation

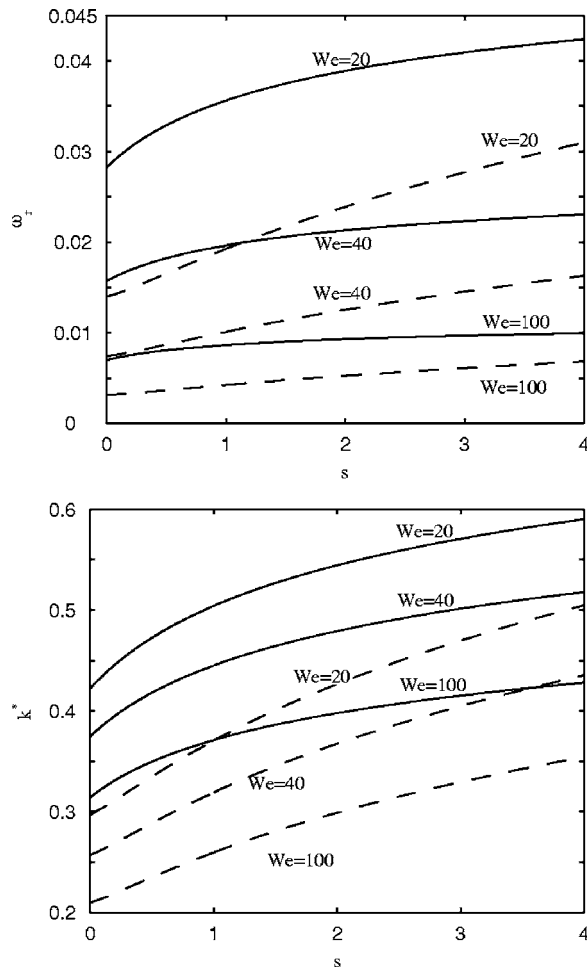


**Fig. 6** The effects of changing the Weber number on  $\omega_r$  (top) and  $k^*$  (bottom) for shear thickening liquids ( $\alpha=1.4$ , -dashed line) and shear thinning liquids ( $\alpha=0.6$ , solid line) where  $Rb=1.25$  and  $\widetilde{Re}_\alpha=3$

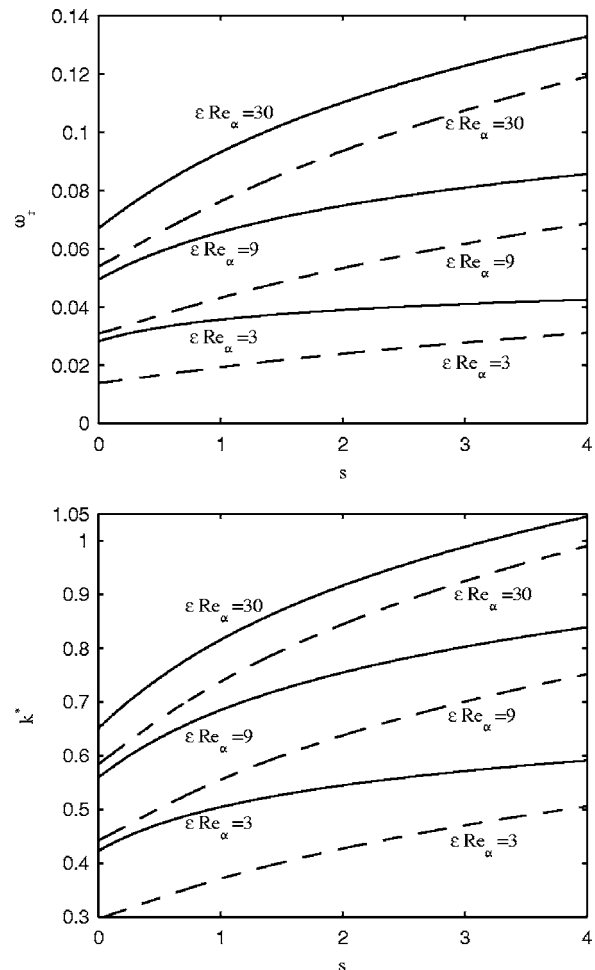


**Fig. 7** The effects of changing the Reynolds number on  $\omega_r$  (top) and  $k^*$  (bottom) for shear thickening liquids ( $\alpha=1.4$ , -dashed line) and shear thinning liquids ( $\alpha=0.6$ , solid line) where  $Rb=1.25$  and  $We=20$

$$(\omega + iku) - \frac{kR}{2We(\omega + iku)} \left( \frac{k}{R^2} - k^3 \right) + \frac{k^2 f}{\widetilde{Re}_\alpha} = 0 \quad (22)$$

after some algebra. Writing  $\omega = \omega_r + i\omega_i$  gives  $\omega_i = -ku$  and

$$\omega_r = - (1/2) \frac{k^2 f}{\widetilde{Re}_\alpha} \pm (k/2) \left( (kf/\widetilde{Re}_\alpha)^2 + 2(RWe)^{-1} (1 - (kR)^2) \right)^{1/2} \quad (23)$$

For unstable disturbances we require that the growth rate  $\omega_r$  be positive (otherwise disturbances decay along the jet) which is satisfied when  $0 < kR < 1$ . This instability range is the same for a straight jet, a result previously found in [12]. We can find the most unstable wavenumber  $k = k^*$  for which  $\omega_r$  is a maximum, and this is

$$k^* = \frac{1}{(2R^3)^{1/4}} \cdot \frac{1}{\sqrt{Ohf + \sqrt{2R}}} \quad (24)$$

Here  $R$  and  $f$  are found as the solution to the steady equations (15), (18), and (19).

We can consider the eigenvalue relationship (22) in two ways, either by a temporal instability analysis or by a spatial instability analysis. In temporal instability analysis we assume that  $k$  is real and that perturbations grow or decay in time, over the entire length of the jet. This is the method adopted above. In a spatial instability analysis disturbances are allowed to grow in space

along the jet: In this case  $\omega$  is assumed to be imaginary and we solve the eigenvalue relationship for  $k$ , finding  $k$  complex. For viscous Newtonian jets, it was shown by [5] that identical results for the most unstable wavenumber and most unstable frequency were obtained in the long wavelength limit for spatial and temporal instability. A similar agreement between temporal instability and spatial instability for non-Newtonian liquids also occurs here, in the long wavelength limit and we have, therefore, omitted a spatial instability analysis in this paper.

The rotation of the container affects both the growth rate and wavenumber of disturbances along the jet. To demonstrate this effect we consider both a high rotation rate ( $Rb=0.75$ ) and a low rotation rate ( $Rb=4$ ) and then compare the wavenumber of the most unstable mode (Fig. 2) and the the growth rate of disturbances (Fig. 3) for different values of  $\alpha$ , with the results plotted against the arclength  $s$ . Note that shear thinning liquids ( $\alpha < 1$ ) have larger values of  $k^*$  and  $\omega_r$  than shear thickening liquids ( $\alpha > 1$ ) for  $Rb=0.75$ , but this comparison is vice versa for  $Rb=4$ . By taking two very different values of  $\alpha$  (Figs. 4 and 5) we see that for shear thinning liquids both  $k^*$  and  $\omega_r$  increase for increasing rotation rates whereas for shear thickening liquids  $k^*$  and  $\omega_r$  initially increase with  $Rb$  but then this trend switches so that jets with high  $Rb$  numbers have smaller values of  $k^*$  and  $\omega_r$  than jets with lower  $Rb$  numbers. In Fig. 6 we see that as the surface tension of the liquid is increased  $k^*$  and  $\omega_r$  increase for both shear thinning and thickening liquids. In the case of viscosity (Fig. 7)

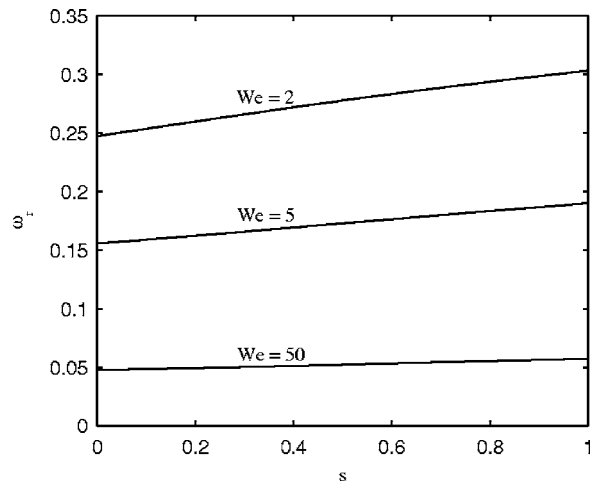


Fig. 8 The growth rate of the most unstable mode for various Weber numbers ( $Rb=2$  and  $\bar{Re}_a=300$ )

we find that decreasing the viscosity of the liquid results in larger values of  $k^*$  and  $\omega_r$ . For very low viscosities we can compare our results to those of an inviscid spiraling jet considered by Wallwork et al. [3]. In this case [3] has shown that the growth rate of disturbances along the jet can be expressed as

$$\omega_r = \sqrt{\frac{1}{We} \left( \frac{1}{R^2} - k^2 \right) k \frac{I_1(kR)}{I_0(kR)}} \quad (25)$$

where  $I_m$  is the modified Bessel function of order  $m$  and the most unstable mode occurs when  $k=k^*=0.697/R$ . Equation (25) is obtained without the need to make the long wavelength limit. Taking the inviscid limit of Eq. (23) we get

$$\omega_r = \sqrt{\frac{k^2(1 - (kR)^2)}{2RWe}} \quad (26)$$

which coincides with (25) if an expansion to the lowest order in  $kR$  is made, i.e., the long wavelength limit of (25) also gives (26). By taking a large value of the Reynolds number so that the jet is effectively inviscid, we can plot the growth rate  $\omega_r$  (as given by (23)) against the arc length  $s$  for various Weber numbers (Fig. 8); reassuringly, this is in agreement with [3].

In all the Figs. 2–7, it can be seen that  $k^*$  and  $\omega_r$  mainly, but not always increase with arclength (for exceptions see Figs. 2, 3, and 5). Therefore, the wavelength ( $=2\pi/k^*$ ) of the most unstable mode mainly (but not always) decreases as it travels upstream along the jet.

#### 4 Conclusions

Linear traveling wave disturbances along curved power law non-Newtonian liquid jets were examined. In particular the growth rates and most unstable wavenumbers associated with shear thinning fluids and a shear thickening fluids were investigated and compared to Newtonian fluids.

It is found that the rotation rate of the container can alter the growth rates and wavenumbers of disturbances for shear thinning and shear thickening liquids. Since disturbances are convected along the jet and  $\omega_r$  is a measure of the growth of these disturbances we expect greater (lesser) instability for larger (smaller) values of  $\omega_r$ , thus leading to shorter (longer) jets. The wavelength of disturbances along the jet is inversely related to the wavenumber  $k^*$  so that for larger (smaller) values of  $k^*$  we expect smaller (larger) droplets. When the cylindrical container rotates with a high rotation rate we can expect longer jets with larger droplets for shear thickening liquids in comparison with shear thinning liquids. In the case of low rotation rates this trend is reversed.

Decent et al. [5] has shown that Newtonian jets are generally longer and produce smaller drops as the rotation rate is increased which corresponds well with the behavior of shear thinning liquids.

For both shear thinning and shear thickening liquids viscosity is found to impede the growth of disturbances so that more viscous jets are longer and produce larger droplets. This agrees with the Newtonian case considered by [5]. Surface tension is found to enhance the growth of disturbances so that jets with high surface tension produce shorter jets and smaller drops. In the case where the Reynolds number is large, we can expect the effects of non-Newtonian viscosity to diminish and our results for the most unstable wavenumbers and growth rates will correspond to those of [3].

We note that while linear theory can be used to give an idea of the instability of power law liquid jets the actual break up of liquid jets and subsequent satellite droplet formation is dominated by nonlinear effects. These effects will be considered in a future paper.

#### Acknowledgment

J. Uddin would like to thank EPSRC for their financial support.

#### References

- [1] Andersen, K. G., and Yttri, G., 1997, Porso vert, Universitets for laget Oslo.
- [2] Ornek, D., Gurkan, T., and Oztin, C., 2000, "Prilling of Aluminium Sulphate," *J. Chem. Technol. Biotechnol.*, **75**(8), pp. 689–694.
- [3] Wallwork, I. M., Decent, S. P., King, A. C., and Schulkes, R. M. S., 2002, "The Trajectory and Stability of a Spiralling Liquid Jet. Part 1, Inviscid Theory," *J. Fluid Mech.*, **459**, pp. 43–65.
- [4] Decent, S. P., King, A. C., and Walwork, I. M., 2002, "Free Jets Spun From a Prilling Tower," *J. Eng. Math.*, **42**, pp. 265–282.
- [5] Decent, S. P., King, A. C., Simmons, M. H., Päråu, E. I., Wong, D. C. Y., and Wallwork, I. M., 2004, "The Trajectory and Stability of a Spiralling Liquid Jet: Part II. Viscous Theory," University of Birmingham preprint series.
- [6] Decent, S. P., Simmons, M. J. H., Parau, E., Wong, D. C., King, A. C., and Partridge, L., 2004, "Liquid Jets From a Rotating Orifice," *Proceedings of 5th International Conference on Multiphase Flow*, Yokohama, Japan, May 30–June 4, 2004, Paper 138, CDROM.
- [7] Päråu, E. I., Decent, S. P., Simmons, M. J. H., Wong, D. C. Y., and King, A. C., 2004, "Nonlinear Viscous Liquid Jets From a Rotating Orifice," *J. Eng. Math.* (to be published).
- [8] Päråu, E. I., Decent, S. P., King, A. C., Simmons, M. J. H., Wong, D. C. Y., 2004, "Nonlinear Travelling Waves on a Spiralling Liquid Jet," *Wave Motion* (to be published).
- [9] Wong, D. C., Simmons, M. J. H., Partridge, L., Parau, E., Decent, S. P., and King, A. C., 2004, "Nonlinear Dynamics and Break-up of Curved Liquid Jets Spun From a Rotating Orifice," *Proceedings of 5th International Conference on Multiphase Flow*, Yokohama, Japan, May 30–June 4, 2004, Paper 303, CDROM.
- [10] Wong, D. C. Y., Simmons, M. J. H., Decent, S. P., Päråu, E. I., and King, A. C., 2004, "Break-up Dynamics and Drop Sizes Distributions Created From Spiralling Liquid Jets," *Int. J. Multiphase Flow*, **30**(5), pp. 499–520.
- [11] Savart, F., 1833, "Memoire sur la Constitution des Veines Liquides Lancees par des Orifices Circulaires en Mince Paroi," *Ann. Chim. Phys.*, **53**, pp. 337–374.
- [12] Rayleigh, W. S., 1878, "On the Instability of Jets," *Proc. London Math. Soc.*, **10**, pp. 4–13.
- [13] Plateau, J., 1873, "Statique Experimentale et Theoretique des Liquides Soumis aux Seules Forces Moleculaires," Gauthier Villars, Paris, **II**, p. 319.
- [14] Goedde, E. F., and Yuen, M. C., 1970, "Experiments on Liquid Jet Instability," *J. Fluid Mech.*, **40**, pp. 495–511.
- [15] Keller, J. B., Rubinow, S. I., and Tu, Y. O., 1973, "Spatial Instability of a Jet," *Phys. Fluids*, **16**, pp. 2052–55.
- [16] Hilbing, J. H., and Heister, S. D., 1996, "Droplet Size Control in Liquid Jet Breakup," *Phys. Fluids*, **8**(6), pp. 1574–81.
- [17] Eggers, J., 1997, "Nonlinear Dynamics and Breakup of Free Surface Flows," *Rev. Mod. Phys.*, **69**(3), pp. 865–929.
- [18] Lin, S. P., 2003, *Breakup of Liquid Sheets and Jets*, Cambridge University Press, United Kingdom.
- [19] Hwang, C., Chen, J., Wang, J., and Lin, J., 1994, "Linear Stability of Power Law Liquid Film Flows Down an Inclined Plane," *J. Phys. D.*, **27**, pp. 2297–2301.
- [20] Balmforth, N. J., Craster, R. V., and Toniolo, C., 2003, "Interfacial Instability

- in Non-Newtonian Fluid Layers,” *Phys. Fluids*, **15**(11), pp. 3370–3384.
- [21] Coronado-Matutti, O., Souza-Mendes, P. R., and Carvalho, M. S., 2004, “Instability of Pseudoplastic Liquid in Couette Flow Between Concentric Cylinders,” *J. Fluids Eng.*, **3**(126), pp. 386–390.
- [22] Berezin, M. P., Hutter, K., and Spodavara, 1998, “Stability Analysis of Gravity Driven Shear Flows With Free Surface for Power Law Fluids,” *Archives of Applied Mathematics*, **68**, pp. 169–178.
- [23] Wallwork, I. M., 2002, “The Trajectory and Stability of a Spiralling Liquid Jet,” Ph.D. thesis, University of Birmingham, Birmingham.
- [24] Ribe, N. M., 2004, “Coiling of Visous Jets,” *Proc. R. Soc. London, Ser. A*, **460**, pp. 3223–3239.
- [25] Entov, V. M., and Yarin, A. L., 1984, “The Dynamics of Thin Liquid Jets in Air,” *J. Fluid Mech.*, **140**, 91–113.
- [26] Hohman, M. M., Shin, M., Rutledge, G., and Brenner, M. P., 2001, “Electrospinning and Electrically Forced Jets. II. Applications,” *Phys. Fluids*, **13**(8), pp. 2221–2236.
- [27] Lee, H. C., 1974, “Drop Formation in a Liquid Jet,” *IBM J. Res. Dev.*, **18**, pp. 364–369.
- [28] Garcia, F. J., and Castellanos, A., 1994, “One-Dimensional Models for Slender Axisymmetric Viscous Liquid Jets,” *Phys. Fluids*, **6**, pp. 2676–2689.

# Transpiration Induced Shock Boundary-Layer Interactions

**B. Wasistho**

Center for Simulation of Advanced Rockets,  
University of Illinois at Urbana-Champaign,  
Urbana, IL 61801

*Steady and unsteady shock boundary-layer interactions are studied numerically by solving the two-dimensional time-dependent Navier-Stokes equations. To validate the numerical method, the steady interaction is compared with measurements and other numerical results reported in the literature. The numerical study of the steady interaction leads to a suitable method for transpiration boundary conditions. The method applies to unsteady flows as well. Using the validated numerical method, we show that an unsteady shock boundary-layer interaction can occur in a supersonic flow over a flat plate subjected to suction and blowing from the opposite side of the plate, even though the imposed transpiration is steady. Depending on the Mach number, the Reynolds number, the distance of the transpiration boundary to the lower wall, and the transpiration profile, the unsteadiness can be inviscid or viscous dominated. The viscous effect is characterized by the occurrence of self-excited vortex shedding. A criterion for the onset of vortex shedding for internal compressible flows is also proposed. [DOI: 10.1115/1.2236127]*

## 1 Introduction

The study of shock boundary-layer interactions (SBLI) is crucial as this phenomenon significantly affects the aerodynamic and structural performance of high speed vehicles. Generally, the occurrence of shocks is undesirable as it causes a sudden increase of momentumless thickness, which implies an increase of drag and a loss of lift. Another undesirable phenomenon is shock buffeting as this puts extra load on the aircraft structure and decreases the aircraft aeroelastic performance through the occurrence of flutter.

Since the early investigations by Ferri [1], Ackeret et al. [2], and Liepmann et al. [3], which reveal the difference between the interaction of a shock with laminar and turbulent boundary layers, many experimental, theoretical, and numerical studies of SBLI have appeared in the literature. Reviews about this topic can be found in Adamson and Messiter [4] and Delery and Marvin [5]. These studies concern mostly steady SBLI. Some investigations have been carried out on shock buffeting in a transonic flow past airfoils, for example a review by Tijdeman and Seebass [6], but the focus is on inviscid flow. Although recently investigations on unsteady SBLI have been performed, the origin of the unsteadiness is restricted to the boundary layer (upstream turbulence/disturbances or vortex shedding), whereas the main, inviscid shock remains steady. This type of unsteady interaction has formed the research subject of, among others, Degrez [7], Dolling [8], and Loth and Matthys [9]. In practical situations, the unsteadiness of both the inviscid shock and the boundary-layer underneath interact with each other. Pressure loads formed by this kind of unsteady interaction are more critical for the structure than that caused by the viscous unsteadiness alone.

In this paper, we present a new type of SBLI where both inviscid and viscous unsteadiness occur, namely SBLI in a flat plate supersonic flow subjected to suction and blowing. The prescribed suction and blowing is fixed in time. Hence, the unsteadiness occurs spontaneously. We study the phenomenon by means of numerical simulations based on the two-dimensional time-dependent Navier-Stokes equations. A steady SBLI simulation induced by a wedge is first conducted, to validate the numerical method. Based on this test, the most appropriate method of imposing boundary conditions is revealed and used in the unsteady interaction case. The unsteady case leads to a new onset criterion for vortex shed-

ding in compressible flows subject to a transpiration boundary. This work provides useful hints for the occurrence and unsteadiness of shocks.

The aim of this paper is, first, to propose an accurate boundary condition to generate an inclined shock identical to that generated by a wedge, hence allowing a simpler rectangular domain and a more accurate discretization to study the shock phenomenon. This would not be possible if the wedge geometry is taken explicitly into account. Second, the paper presents an efficient way to study shock-buffeting phenomena, by means of controlled transpiration. Third, we extend an existing incompressible vortex shedding criterion to compressible flows.

This paper is organized as follows. In Sec. 2, we outline the governing equations and the numerical method. The validation of the numeric and the boundary conditions is presented in Sec. 3 by examining the wedge induced steady SBLI. In Sec. 4, we present SBLI induced by suction and blowing. Finally, we summarize our findings in Sec. 5.

## 2 Numerical Method

In this section we present the basic equations governing the flow, the boundary conditions, and the discretization method.

**2.1 Governing Equations.** Unsteady compressible flow over a flat plate is described by the Navier-Stokes equations that represent conservation of mass, momentum, and energy:

$$\partial_t \rho + \partial_j (\rho u_j) = 0$$

$$\partial_i (\rho u_i) + \partial_j (\rho u_i u_j) + \partial_i p - \partial_j \tau_{ij} = 0 \quad (1)$$

$$\partial_t e + \partial_j [(e + p) u_j] - \partial_j (\tau_{ij} u_i - q_j) = 0$$

The symbols  $\partial_t$  and  $\partial_j$  denote the partial differential operators  $\partial/\partial t$  and  $\partial/\partial x_j$  with respect to time ( $t$ ) and spatial coordinate ( $x_j$ ), respectively;  $\rho$  is the density,  $p$  is the pressure,  $u_i$  is the  $i$ th component of the velocity vector, and  $e$  is the total energy density which is given by:

$$e = \frac{p}{\gamma - 1} + \frac{1}{2} \rho u_i u_i \quad (2)$$

where  $\gamma$  denotes the adiabatic gas constant. Moreover,  $\tau_{ij}$  is the stress tensor which is a function of the dynamic viscosity  $\mu$  and velocity vector  $\mathbf{u}$ :

Contributed by the Fluids Engineering Division of ASME for publication in the JOURNAL OF FLUIDS ENGINEERING. Manuscript received March 22, 2005; final manuscript received January 28, 2006. Assoc. Editor: Subrata Roy.

$$\tau_{ij} = \frac{\mu(T)}{\text{Re}} \left( \partial_j u_i + \partial_i u_j - \frac{2}{3} \delta_{ij} \partial_k u_k \right) \quad (3)$$

where  $\text{Re} = (\rho_\infty u_\infty \delta^*) / \mu(T_\infty)$  is the reference Reynolds number. The dynamic viscosity  $\mu$  can be constant or related to the temperature  $T$  by Sutherland's law. Finally,  $q_j$  is the viscous heat flux vector, given by

$$q_j = - \frac{\mu}{(\gamma - 1) \text{Re Pr M}_\infty^2} \partial_j T \quad (4)$$

where Pr is the Prandtl number and  $M_\infty$  is the reference Mach number. The temperature  $T$  is related to the density  $\rho$  and the pressure  $p$  by the ideal gas law

$$T = \gamma M_\infty^2 \frac{p}{\rho} \quad (5)$$

Throughout we use  $\gamma = 1.4$  and  $\text{Pr} = 0.72$ . The values of the reference Mach number  $M_\infty$  and the Reynolds number Re are specified for each case separately. The variables have been made dimensionless using reference scales, i.e., a reference length  $\delta^*$ , which is taken equal to the displacement thickness of the boundary layer at the inflow boundary, density  $\rho_\infty$ , velocity  $u_\infty$ , temperature  $T_\infty$ , and viscosity  $\mu(T_\infty)$ . The subscript  $\infty$  refers to the free-stream value.

**2.2 Boundary Conditions.** The flow is simulated in two dimensions in a rectangular computational domain. The boundaries consist of inflow, outflow, and upper and lower boundaries. The lower boundary is a no-slip adiabatic wall. Specifically, the velocity components vanish and the other quantities follow by solving the mass and energy conservation equations.

The number of boundary conditions at the other boundaries are based on the well-posedness requirement of a hyperbolic system in two dimensions. On the subsonic part of the inflow boundary (near the wall) we prescribe the pressure or the density and the velocity components, and extrapolate the temperature. The prescribed variables correspond to the compressible Blasius boundary layer. At the supersonic part of the inflow boundary all dependent variables are prescribed.

At the supersonic part of the outflow boundary all dependent variables are extrapolated from the interior domain. In contrast to the inflow boundary, the boundary condition for the subsonic outflow boundary is nontrivial since the flow downstream of the outflow boundary is unknown. Therefore, we apply a so-called non-reflecting condition on the characteristic waves ([10,11]). To be more specific, in two-dimensional compressible flows, four characteristic waves are advected with different speeds. The corresponding wave-amplitude variations  $\Lambda_1, \dots, \Lambda_4$  are defined as

$$\Lambda_1 = \lambda_1 \left( \frac{\partial p}{\partial x_1} - \rho c \frac{\partial u_1}{\partial x_1} \right) \quad (6)$$

$$\Lambda_2 = \lambda_2 \left( c^2 \frac{\partial \rho}{\partial x_1} - \frac{\partial p}{\partial x_1} \right) \quad (7)$$

$$\Lambda_3 = \lambda_3 \frac{\partial u_1}{\partial x_1} \quad (8)$$

$$\Lambda_4 = \lambda_4 \left( \frac{\partial p}{\partial x_1} + \rho c \frac{\partial u_1}{\partial x_1} \right) \quad (9)$$

where  $\lambda_i$  is the velocity at which the corresponding waves propagate in the  $x_2$  direction. These velocities are given by:

$$\lambda_1 = u_1 - c \quad (10)$$

$$\lambda_2 = \lambda_3 = u_1 \quad (11)$$

$$\lambda_4 = u_1 + c \quad (12)$$

where  $c$  is the speed of sound:

$$c^2 = \gamma p / \rho \quad (13)$$

The nonreflecting condition is imposed by setting the amplitude variation of the incoming wave to zero. In other words,  $\Lambda_1 = 0$ . In this way we close the problem at the subsonic outflow boundary.

If the flow is strongly instationary, additional treatments are needed to minimize reflections at the outflow boundary. For this purpose, a buffer domain technique is applied in the vicinity of the outflow boundary. In the buffer region the disturbances are directly reduced to zero by multiplication with a specific damping function. The buffer domain calms the flow gradually into a laminar flow to prevent reflections of upstream disturbances at the outflow boundary [12].

The boundary conditions at the upper boundary must be treated carefully. The suction and blowing along the upper boundary are realized by prescribing the (subsonic) normal velocity, which is positive for suction and negative for blowing. In the case of unsteady flow, the external flow is in general unknown. This leads to a similar situation as found at the subsonic outflow boundary. In the region of (subsonic) negative normal velocity (blowing), theoretically, three variables should be prescribed corresponding to three incoming characteristic waves. Thus, besides the normal velocity, two other variables should be imposed. However, this cannot be done since we have no other information about the external condition than the normal velocity. To resolve this problem we could apply the nonreflecting principle, as described above (next denoted as B1), to the remaining two incoming waves.

Two other boundary condition methods are considered for comparison, B2 and B3. In B2 only the normal velocity is prescribed and the other variables are extrapolated from the interior solution irrespective of the sign of the normal velocity. This leads to an underprescription of boundary conditions. In B3 a boundary condition based on the complete analytical solution is used. This reference boundary condition makes use of the extrapolation technique. Specifically, in the region of positive normal velocity, only one analytical variable is imposed, for which we choose the temperature, and three variables, namely, the velocity components  $u_1$  and  $u_2$  and the pressure are extrapolated from the interior domain. In the region of negative normal velocity, the temperature and the velocity components are prescribed and the pressure is extrapolated from the interior domain to the boundary. A sketch of the three boundary conditions is given in Fig. 1.

**2.3 Discretization Method.** In shock-free flows, a weighted fourth-order central discretization is used for the spatial discretization [12]. In the case of high Mach-number flow in which shocks occur, we use a "hybrid" discretization scheme [13]. In particular, the fourth-order method is used if no shock is detected in the flow field, whereas a third-order MUSCL discretization [14] is employed in the presence of a shock. To maintain the conservation property of the discretization method, the method selected at a certain time-step is applied in the whole domain, while the alteration of the method is time dependent. The upwind scheme is only applied in the direction in which a sufficiently strong shock is detected. The shock sensor in the  $x_i$  direction is defined as

$$s_i = \max \left| \frac{\partial p}{\partial x_i}(t) \right| \frac{\Delta x_i}{p_o} \quad (14)$$

where  $\Delta x_i$  and  $p_o$  denote the grid-spacing and the initial mean pressure respectively, while the maximum is taken over the whole domain. The discretization method is altered when the shock sensor exceeds a threshold value, for which we use the value 0.2. The resolution of the grid is sufficient to capture weaker shocks with the fourth-order method. In this way we obtain an efficient shock capturing scheme while maintaining the conservation property. The time integration is performed by an explicit, second-order accurate, compact-storage, four-stage Runge-Kutta scheme.

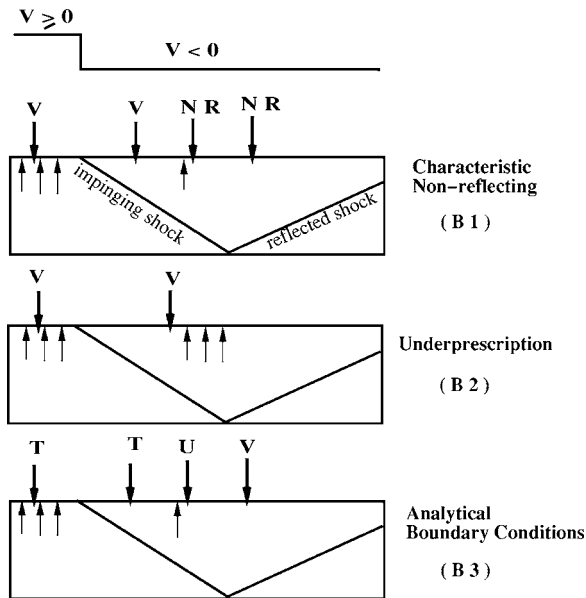


Fig. 1 Three different upper boundary conditions under study: B1: characteristic method, B2: underprescription, B3: prescription of analytical solution. Bold arrows denote prescribed variables while thin arrows denote extrapolations from the interior domain.

### 3 Steady SBLI

For the validation of the numerical method we perform a simulation of steady SBLI, mimicking the experiment by Hakkinen et al. [15]. In addition, comparable numerical results by Katzer [16] are available. The shock is generated by a wedge or corner and impinges onto a flat plate under a certain angle. For a given incoming Mach number and a shock angle  $\sigma$  (see Fig. 2) the relations between the flow properties on both sides of the shock can be derived from gas dynamics [3]:

$$\frac{p_2}{p_1} = 1 + \frac{2\gamma}{\gamma+1}(M_1^2 \sin^2 \sigma - 1) \quad (15)$$

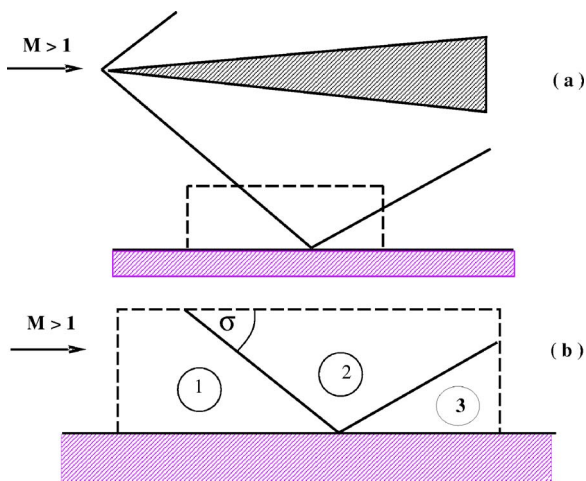


Fig. 2 Impinging steady shock generated by a wedge. The computational domain is bounded by the dashed line (a) and enlarged on (b).  $\sigma$  is the shock angle and 1, 2, and 3 denote the inviscid area upstream of the impinging shock, the area between the impinging shock and the reflected shock, and the area downstream of the reflected shock, respectively.

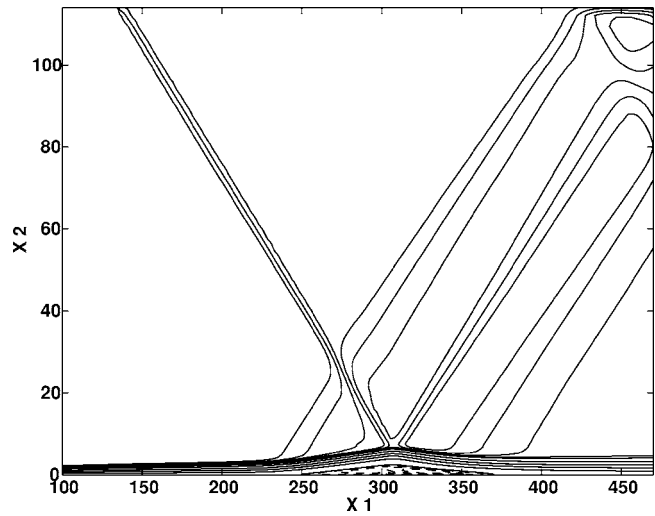


Fig. 3 Mach-field of steady SBLI using upwind scheme in both directions. The shock is induced by wedge/corner.

$$\frac{\rho_2}{\rho_1} = \frac{(\gamma+1)M_1^2 \sin^2 \sigma}{2 + (\gamma-1)M_1^2 \sin^2 \sigma} \quad (16)$$

$$\frac{T_2}{T_1} = \frac{p_2 \rho_1}{p_1 \rho_2} \quad (17)$$

$$\frac{u_{n2}}{u_{n1}} = \frac{\rho_1}{\rho_2} \quad (18)$$

Subscripts 1 and 2 denote the location in front of and behind the shock, respectively, while subscript  $n$  denotes the direction normal to the shock. These properties are useful in providing the external information for the upper boundary condition. The analytical solutions along the upper boundary are step functions, with an increase in  $p$ ,  $\rho$ , and  $T$  and a drop in the velocity component normal to the shock. The tangential velocity component remains unchanged.

The iso-Mach-lines of the flow field are shown in Fig. 3. Since the shock is oblique, their solution is calculated with the MUSCL scheme applied in both directions. The simulation is performed for two different shock strengths. In the first case, the incoming Mach number is 2.0 and the wedge angle is such that the shock angle is 32.58 deg, which yields a ratio of  $p_3/p_1=1.4$ . The subscript 3 and 1 denote the inviscid area defined in Fig. 2. The Reynolds number  $Re_o=2.96 \times 10^5$ , based on the distance between the flat plate leading edge to the shock impingement point, which is equivalent to  $Re=950$ , based on the inflow displacement thickness. In the second case  $Re_o=2.87 \times 10^5$  and the ratio  $p_3/p_1=1.25$ , which results from a shock angle of 31.67°. These cases are selected since they have been used in the comparison study of Hakkinen's and Katzer's results [15,16]. The convergence criterion for the steady state is

$$R(p) = 2 \left[ \frac{1}{N} \sum_{i=1}^N \left( \frac{p^{t+\Delta t}(i) - p^t(i)}{\Delta t} \right)^2 \right]^{1/2} < \epsilon \quad (19)$$

where  $\epsilon=10^{-6}$  and  $N$  is the number of grid points on the wall.

**3.1 Verification of Grid Resolution and Domain Size.** For the case  $p_3/p_1=1.4$  we check the adequacy of the grid resolution and the domain size. The domain dimension is  $400 \times 115$  based on the inflow displacement thickness. The reference grid size is  $151 \times 128$ , comparable to Katzer's grid. Varying the number of grid points in the streamwise direction to 101 and 192 yields almost the same result for the skin friction coefficient,  $c_f$ . A



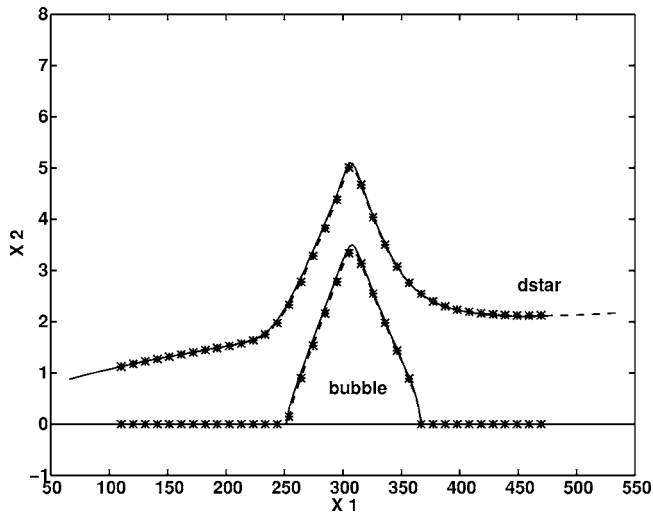


Fig. 4 Displacement thickness and separation bubble of time-averaged flow: reference domain (\*), shifted outflow (dashed), and shifted inflow (solid)

change of the number of grid points in the normal direction to 64 and 192 yields a maximum deviation in  $c_f$  of 8.5% for 64 points and of 1.4% for 128 points compared to the results with 192 points.

The influence of the boundaries and, hence, domain size is examined by shifting their position by about 17%. As can be seen in the plot of the displacement thickness and separation bubble in Figs. 4 and 5, the influence was found to be small. The effects are more appreciable if we lower the upper boundary, as illustrated by the lower peak of the displacement thickness in Fig. 5. This is caused by unavoidable reflections of expansion waves at the upper boundary near the outflow boundary.

**3.2 Effect of Discretization and Boundary Conditions.** A central discretization can be used for flows containing shocks if the shocks are not too strong and the resolution is adequate. The use of the fourth-order central scheme is preferred, since it is more accurate and faster than the third-order upwind scheme. Therefore, we examine combinations of both schemes. Employing the fourth-order central scheme in the streamwise direction results in

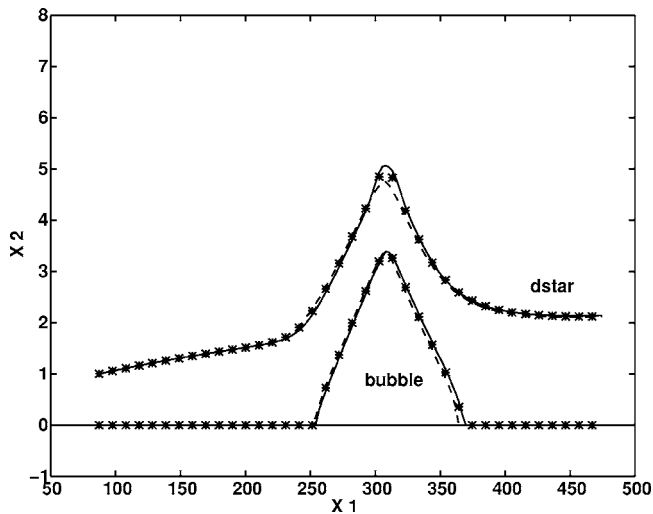


Fig. 5 Displacement thickness and separation bubble of time-averaged flow: reference domain (\*), lower (dashed) and higher upper boundary (solid)

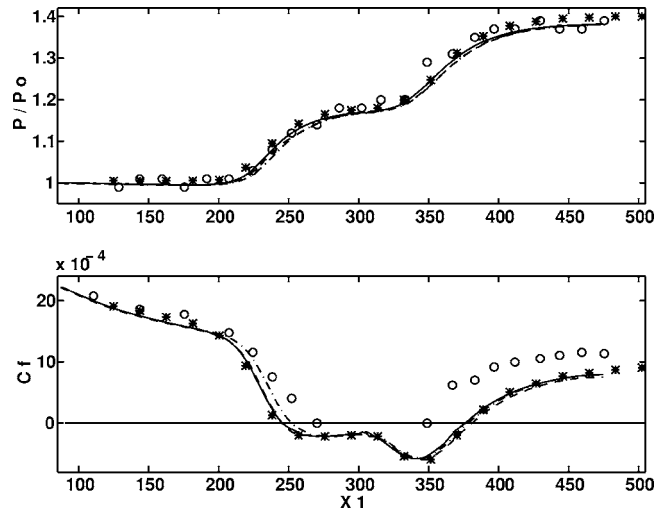


Fig. 6 Wall pressure (above) and skin friction coefficient (below) for  $p_3/p_1=1.4$ : B3 upwind (solid), B1 upwind (dashed-dotted), B1 mixed (dashed), Katzer's numerical result (\*), and Hakkinen et al.'s experiment (o)

odd-even decoupling, indicating that the streamwise gradients are too strong for the central scheme on the reference grid  $151 \times 128$ . Hence, upwind discretization in the  $x_1$  direction is necessary. Comparing the third-order upwind scheme (MUSCL) in both directions with a combination of upwind in the streamwise and central in the normal direction, we observe only small differences in the wall pressure and skin friction coefficient as shown in Fig. 6. However, the latter produces wiggles in the solution as illustrated by the Mach-field in Fig. 7 (compare to Fig. 3). Figure 6 also shows that the results using the upper boundary conditions B1 and B3 show only small deviations.

The underprescribed boundary condition B2 is tested by comparing its temperature to that from B3 and B1, as shown in Fig. 8. In this test, the third-order upwind scheme is applied in both directions. The increasing temperature near the outflow boundary is caused by reflections of compression waves at the upper boundary (Fig. 3). B2 exhibits a large overshoot behind the shock and an increase toward the outflow boundary. B1, in contrast, yields a much better freestream temperature. This difference is also manifest in the other dependent variables. Figure 8 also illustrates that

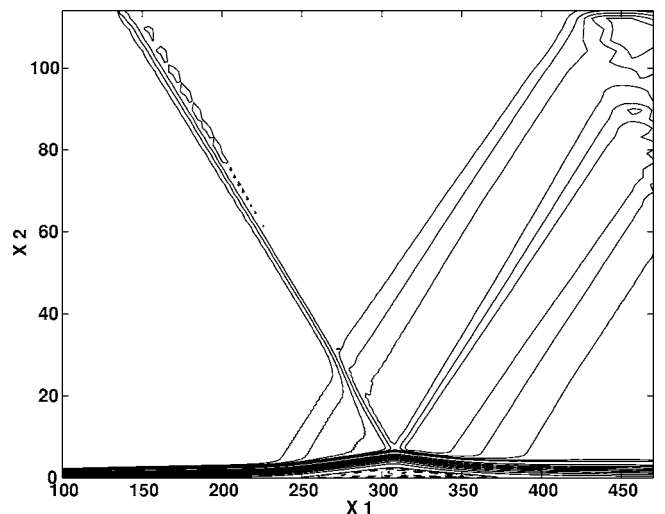


Fig. 7 Mach-field of steady SBLI using central discretization in the  $x_2$  direction and upwind in the  $x_1$  direction

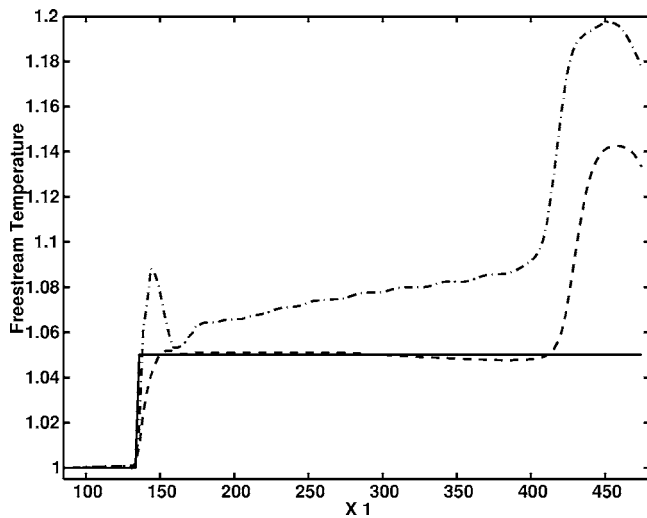


Fig. 8 Temperature along the upper boundary from boundary condition B2 (dashed dotted) and B1 (dashed) compared to theory (solid)

the shock in the case of B1 is smeared over several grid cells, in contrast to B3. The shock sharpens if we employ the central scheme in the normal direction. This also gives a more accurate wall pressure and wall shear stress coefficient, as shown in Fig. 6. Hence, if the shock angle is close to  $90^\circ$  a central scheme is preferred in the normal direction, otherwise an upwind scheme is necessary to avoid wiggles in this direction.

Wall pressure, shear stress coefficient, and streamwise velocity profiles in Figs. 6 and 9–11 show that the present results agree well for both cases of shock strength with the numerical result of Katzer [16] and are comparable to the measurements by Hakkinen et al. In the skin friction plot (Fig. 9), the zero pressure gradient solution is included to show that the presence of the shock has only a local effect. Although Katzer's results are not taken along in all figures, it is confirmed that the overall agreement between his results and the present results is excellent. Katzer solved the 2D Navier-Stokes equations by using the explicit time-split MacCormack scheme where a control of artificial dissipation is employed as a tuning parameter. He addresses the origin of the dif-

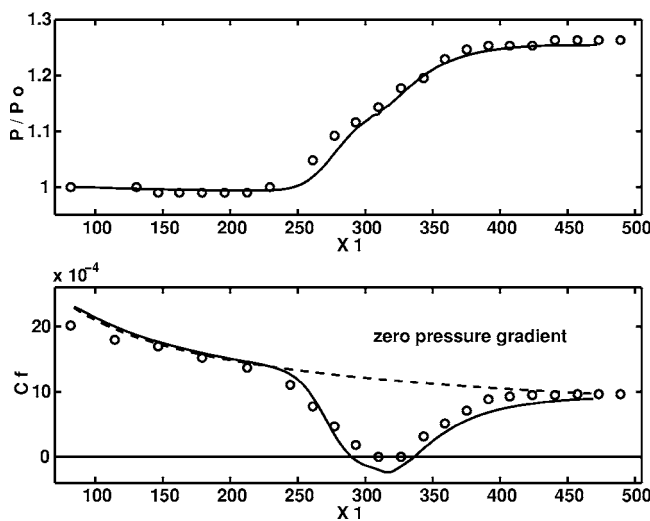


Fig. 9 Wall pressure (above) and skin friction coefficient (below) for  $p_3/p_1=1.25$ : B3 upwind (solid) and Hakkinen's experiment (o). Dashed line corresponds to zero pressure gradient solution.

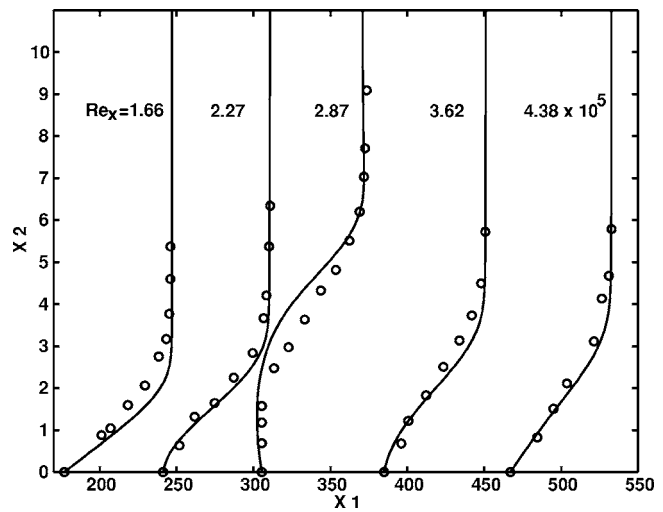


Fig. 10  $u_1$  profiles for  $p_3/p_1=1.40$ : B3 upwind (solid) and Hakkinen's experiment (o)

ference between the calculated and the measured skin friction in the stronger shock case to the fact that in the experimental study the wall shear stress has been measured using a Stanton probe contacting the wall. This may influence the length of the separation bubble. In addition, there is a three-dimensional effect in the experiment due to the presence of side walls. This effect is absent in the numerical simulation.

#### 4 Unsteady SBLI

In this section, we conduct a controlled shock buffeting experiment by means of a transpiration boundary and derive from this a compressible vortex shedding criterion. An arbitrary normal velocity distribution is imposed along the upper boundary in the form of consecutive suction and blowing, as sketched in Fig. 12. Parameters characterizing the suction and blowing are the amplitude  $a$ , the distance between suction and blowing  $d$ , its total width  $w$ , and the angle  $\phi$ . The distribution is fixed in time, and free slip assumption is applied to the streamwise velocity component.

**4.1 Reference Configuration.** As a reference simulation, we use the following configuration. The height and length of the domain are 30 and 500, respectively,  $M=1.3$ , and  $Re=500$  based on

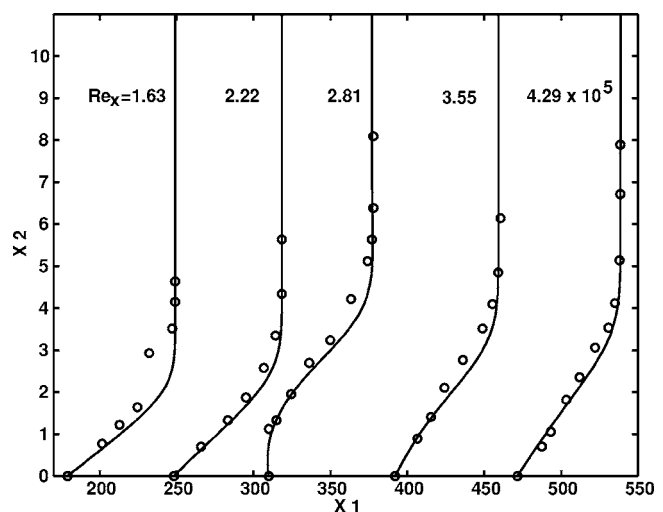


Fig. 11  $u_1$  profiles for  $p_3/p_1=1.25$ : B3 upwind (solid) and Hakkinen's experiment (o)

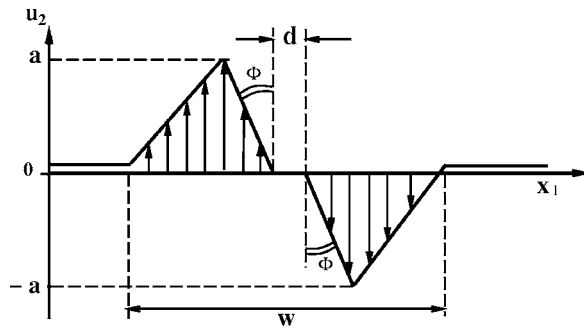


Fig. 12 Characteristics of prescribed  $u_2$  along the upper boundary

the inflow displacement thickness. The suction and blowing parameters are  $a=0.12$ ,  $w=300$ ,  $d=22.5$ , and  $1/\tan(\phi)=du_2/dx_1=-0.0053$ . The grid resolution is  $191 \times 64$  in the  $x_1$  and  $x_2$  directions, respectively, which is found to be sufficient for the present study as illustrated below. In association with channel divergence and convergence, suction and blowing cause the supersonic flow to expand and compress, respectively. Applying only suction forms no shock. The inviscid part of the flow is isentropic and steady in this case. Applying only blowing (compression), on the other hand, generates a steady shock and a separation region upstream of the shock. A consecutive suction and blowing with their distance  $d=0$  results in the occurrence of steady shocks. The shock strength is affected by the angle  $\phi$ . The smaller  $\phi$  is, the stronger the shock. An interesting phenomenon happens when we increase the distance  $d$  up to the reference case value,  $d=22.5$ . The generated shocks then become unsteady, in that they oscillate in the flow direction. This unsteadiness persists with a further increase of  $d$  and, at the same time, the extent of the separation region increases. However, if the distance between suction and blowing is extremely large, their interaction decays and the flow is characterized by a local suction and blowing separately, as described above.

A directional shock sensor, defined in Eq. (14), is used as an indicator for the shock strength and the unsteadiness. As an illustration, the shock sensor corresponding to the reference case is shown in Fig. 13. It functions as a numerical as well as physical indicator. As a numerical indicator, the shock sensor determines whether the upwind or central scheme is used. If  $s_i$  is higher than

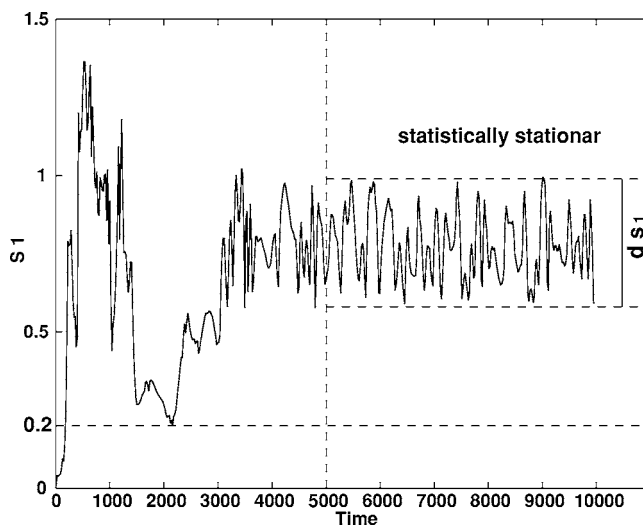


Fig. 13 Shock sensor of reference case with threshold value 0.2 and statistically stationary state beginning at  $t \approx 5000$

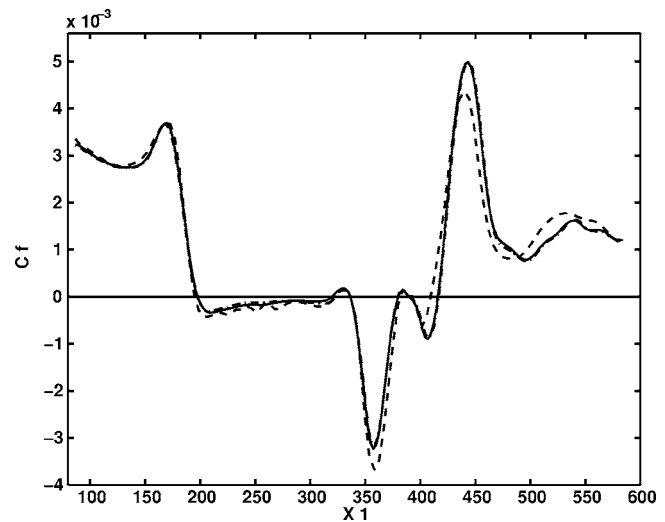


Fig. 14 Skin friction coefficient of time-averaged flow resulting from the resolution  $115 \times 32$  (dashed),  $191 \times 64$  (solid), and  $247 \times 96$  (dashed dotted)

a threshold value, the upwind scheme is activated in the  $x_i$  direction, otherwise the central scheme is used. The threshold value of 0.2 is found to be appropriate. Using this hybrid scheme, we avoid wiggles when a shock occurs, while maintaining in a high accuracy when the flow is shockless. The data sampling is taken after a statistically stationary state is reached. As a physical indicator, the time averaged  $s_i$  measures the shock strength while the shock sensor bandwidth  $ds_i$ , defined as the difference between the maximum and the minimum of  $s_i$  during the data sampling, measures the level of unsteadiness ( $ds_i=0$  means that the shock is steady). The sufficiency of the grid resolution is examined by comparing the skin friction coefficient of the time averaged flow resulting from the resolution  $115 \times 32$ ,  $191 \times 64$ , and  $247 \times 96$ , as shown in Fig. 14. The deviation of the grid  $191 \times 64$  from the finer grid is negligible in comparison with the deviation of the coarse grid, which shows that the resolution is sufficient for the present qualitative study.

**4.2 Effect of Compressibility, Reynolds Number, and Transpiration Strength.** In this section, we consider a consecutive suction and blowing, with a nonzero distance  $d$ , allowing unsteadiness to occur. We study the influence of the domain height ( $h$ ), Mach number ( $M$ ), Reynolds number ( $Re$ ), and the strength of suction and blowing ( $a$ ). The resulting adverse pressure gradient is sufficiently strong that separation always appears, even in the case of  $s_i < 0.2$  (shockless). We investigate the dependence of the shock strength and unsteadiness, the occurrence of vortex shedding, and the properties of the separation region on the above parameters.

**4.2.1 Shock Unsteadiness, Average Shock Strength, and Vortex Shedding.** In the case of sufficiently large channel height ( $h > 60$ ), a shock is first generated at the end of the suction part. The influence of the lower wall boundary-layer thickening to the effective channel cross section is small. We observe a spontaneous vortex shedding from the reattachment region, which is typically located under the blowing region. This shedding of vortices causes a small fluctuation of the shocks. In the case of small channel height ( $h \approx 40$ ), the blowing suppresses the occurrence of vortex shedding. In addition, the thickening of the boundary-layer in the interaction region changes the effective cross section of the domain more significantly. These phenomena are illustrated by the Mach-field and vortex contours in Figs. 15 and 16, respectively. The unsteadiness in the case of small  $h$  can be understood as

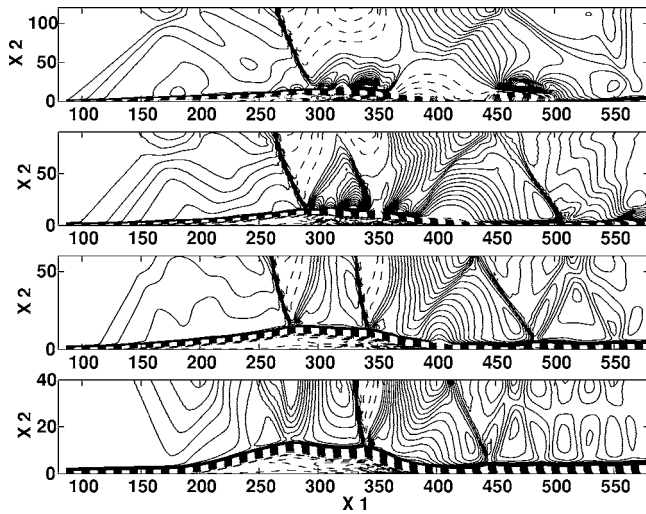


Fig. 15 Mach-field of the flow corresponding to domain height 120, 90, 60, and 40, from above to below. Dashed lines denote subsonic regions.

follows. The presence of a shock results in a change in boundary-layer thickness. This changes the effective cross section of the nozzle, which in turn causes the shocks to migrate to other stream-wise locations, and so on. This process repeats irregularly in time, forming an unsteady shock boundary-layer interaction. Clearly, this type of unsteadiness, which is caused by the continuous change of the channel effective cross section, is different from the shock fluctuation due to vortex shedding in the case of a high upper boundary.

The unsteady interaction described above is localized under the suction and blowing region. Increasing the duration of the simulation considerably we observe that this irregular motion does not decay in time and evolves into a statistically stationary behavior. Varying the length of the computational domain, we confirm that the phenomenon is not caused by a coupling between the outflow and inflow boundaries.

The influence of the parameters on the shock strength and unsteadiness is shown in Figs. 17 and 18, respectively. A further decrease in the distance between the upper boundary and the lower wall removes the unsteadiness and even the shocks (shock strength lower than 0.2). An increase in this distance to above 40,

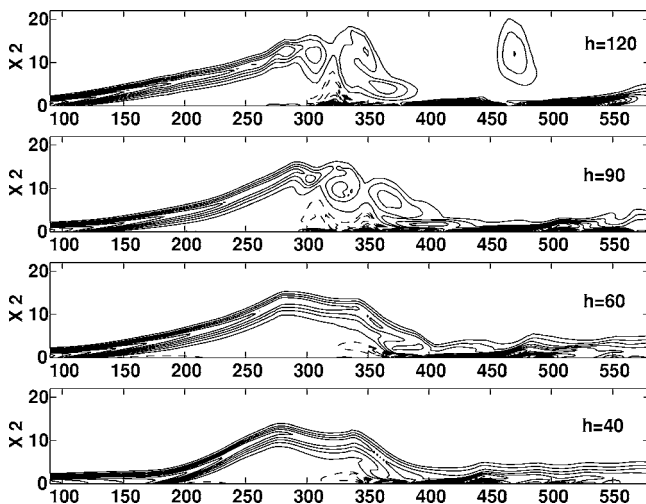


Fig. 16 Vorticity contours corresponding to the domain heights in Fig. 15. Solid line is negative vorticity, dashed line positive.

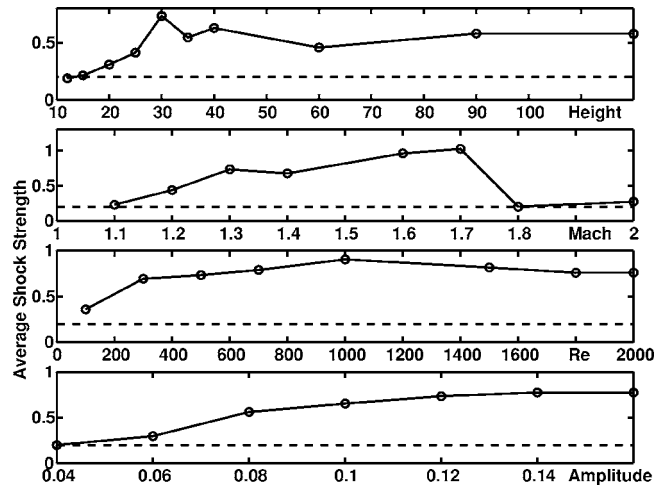


Fig. 17 Average shock strength dependence on domain height, Mach, Re, and suction and blowing amplitude

on the other hand, widens the shock bandwidth, due to the shedding of vortices from the separation region. The region of shock unsteadiness and shock strength is also bounded on both sides by the Mach number. At  $M=1.8$  and higher, the compressions are so weak that shocks disappear from the domain. Decreasing the suction and blowing amplitude and the Reynolds number tends to suppress the unsteadiness and shock strength, which can be expected in view of the shock weakening and increasing viscosity, respectively. The flow with high Reynolds numbers ( $Re \geq 1500$ ) is also characterized by the appearance of vortex shedding. This dependence of the occurrence of spontaneous vortex shedding on the height of the domain and the Reynolds number suggests that both parameters are important for a vortex shedding onset criterion.

**4.2.2 Properties of Separation Region.** The influence of the physical parameters on the size of the separation bubble and the reverse flow intensity is shown in Figs. 19 and 20 in terms of the bubble height and the minimum skin friction coefficient, respectively. The separation bubble in this case is taken from the time averaged flow, and the bubble height is defined as the maximum value of  $x_2$  where  $\int_0^{x_2} \rho u_1 dx_2 = 0$ . The length of the separation bubble varies proportionally to its height, so the height is representative for the size of the separation bubble. In Fig. 19, we see that the separation region grows with increasing height of the

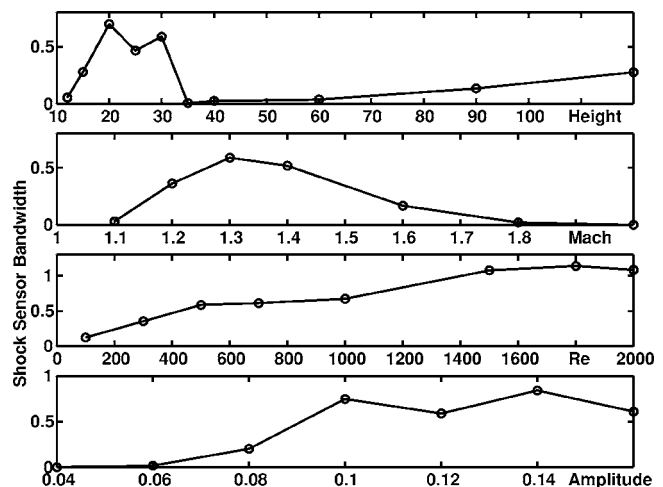


Fig. 18 Shock unsteadiness dependence on domain height, Mach, Re, and suction and blowing amplitude

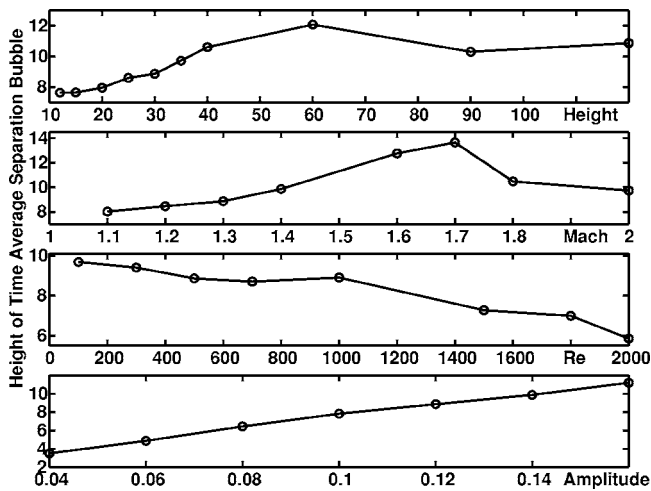


Fig. 19 Separation bubble height as function of domain height, Mach, Re, and suction and blowing amplitude

upper boundary up to  $h=60$ . Above this height, the bubble bursts into shed vortices, resulting in a decrease in bubble size. This vortex shedding results in a decrease of reverse flow intensity (lower negative  $c_f$  in Fig. 20). Increasing the amplitude of suction and blowing results in larger separation bubble and increase in reverse flow intensity due to the stronger shock. The bubble size decreases with increasing Reynolds number. This is a consequence of the fact that the boundary layer grows more slowly at higher Reynolds numbers. The steep decrease in reverse flow intensity above  $Re=1000$  is due to a transition from a closed laminar bubble to a bubble which sheds vortices. The bubble size grows with increasing Mach number up to  $M=1.7$ , above which the ratio decreases sharply due to the disappearance of the shock, as shown previously in Fig. 17. Accordingly, the intensity of the reverse flow also decreases considerably above this Mach number.

**4.3 Vortex Shedding Onset Criterion.** For boundary-layer flows under an adverse pressure gradient, Pauley et al. [17] proposed the following criterion for the onset of vortex shedding (in dimensionless form):

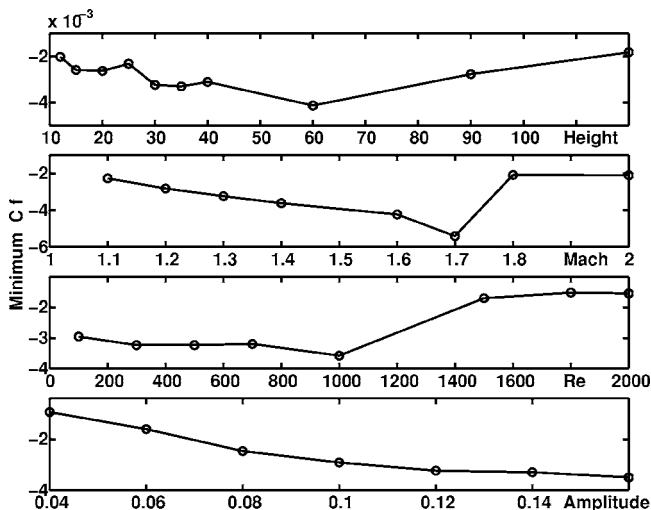


Fig. 20 Minimum  $c_f$  as function of domain height, Mach, Re, and suction and blowing amplitude

$$P_{\max} = \theta_s^2 \text{Re} \left( \frac{du_{in}}{dx_1} \right)_{\max} \approx -0.24 \quad (20)$$

where  $\theta_s$  is the momentum thickness at the separation point and  $(du_{in}/dx_1)_{\max}$  is the maximum (negative) inviscid velocity gradient along the separation region. However, applying this criterion to the present flow results in large discrepancies. It was found that the influence of  $\theta_s$  on the vortex shedding is not consistent. This is manifest in an unclear correlation between  $P_{\max}$  and the occurrence of vortex shedding, as can be seen in the plot of  $P_{\max}$  versus Reynolds number based on the domain height,  $R_h$  in Fig. 21 (left). The data have the same Mach number. The overlapping area of  $P_{\max}$ , in which both vortex shedding cases and nonvortex shedding cases occur, is large. The configuration of each case is presented in Table 1, while the corresponding values of  $P_{\max}$  are given in Table 2. Furthermore, the maximum inviscid velocity gradient in the present flows containing shocks is so much higher than in shockless flows that even in cases where no vortex shedding occurs the value of  $P_{\max}$  is far beyond the threshold value proposed by Pauley. Employing the maximum (negative) velocity gradient  $(du_e/dx_1)_{\max}$  along the boundary layer edge instead of the maximum gradient in the inviscid part

$$P_{\max} = \theta_s^2 \text{Re} \left( \frac{du_e}{dx_1} \right)_{\max} \quad (21)$$

does not improve the result considerably, as shown in Fig. 21 (right). The edge velocity,  $u_e$ , is defined based on the constant pressure assumption across the boundary layer:

$$u_e = \left[ \frac{2}{(\gamma-1)M^2} (1 - \bar{p}_w^{(\gamma-1)/\gamma}) + 1 \right]^{1/2} \quad (22)$$

with  $\bar{p}_w$  the dimensionless wall pressure  $p_w/p_\infty$ . In Fig. 21 (right), we observe that the low values of  $P_{\max}$  are mostly occupied by the data of no vortex shedding and the opposite is true for the high values. The overlapping area is, however, still large. Pauley's criterion is clearly not applicable for flows with strong compressibility effects, such as shocks. The criterion is not designed for compressible flows in the first place. It has been shown, on the other hand, that the domain height and Reynolds number have an important effect on the occurrence of vortex shedding (for example, Fig. 16). This correlation between  $Re$  and  $h$  can also be seen in Fig. 21. The vortex shedding occurs at high values of  $R_h = Re \times h$  for a fixed Mach number. This suggests that replacing the length parameter  $\theta_s$  by the domain height  $h$  forms a logical step toward a better shedding criterion for flows under suction and blowing. We should also notice that in the present study  $\theta_s$  cannot be seen as a local parameter for vortex shedding, which occurs at the reattachment region. The distance between the separation point and the reattachment point is quite large, so that the influence of the upper boundary may be more profound than the influence of the boundary layer at the separation point.

Based on this motivation, we define the following shedding parameter

$$P_{\max} = h^2 \text{Re} \left( \frac{du_e}{dx_1} \right)_{\max} \quad (23)$$

where  $h$  is the height of the upper boundary and  $(du_e/dx_1)_{\max}$  is the maximum (negative) gradient of the edge velocity as given above. Plotting this  $P_{\max}$  against  $Re$ ,  $h$ , and  $R_h$  in Fig. 22, we see a better correlation between  $P_{\max}$  and the occurrence of vortex shedding. The overlapping interval of the shedding parameter is small. However, including the data at various Mach numbers widens the overlapping area as shown in Fig. 23 (left). This suggests to take the Mach number explicitly into account, which is natural for a compressible flow. From the data we learn that a decreasing Mach number tends to trigger vortex shedding. Hence, a decrease in Mach number should increase the shedding parameter value.

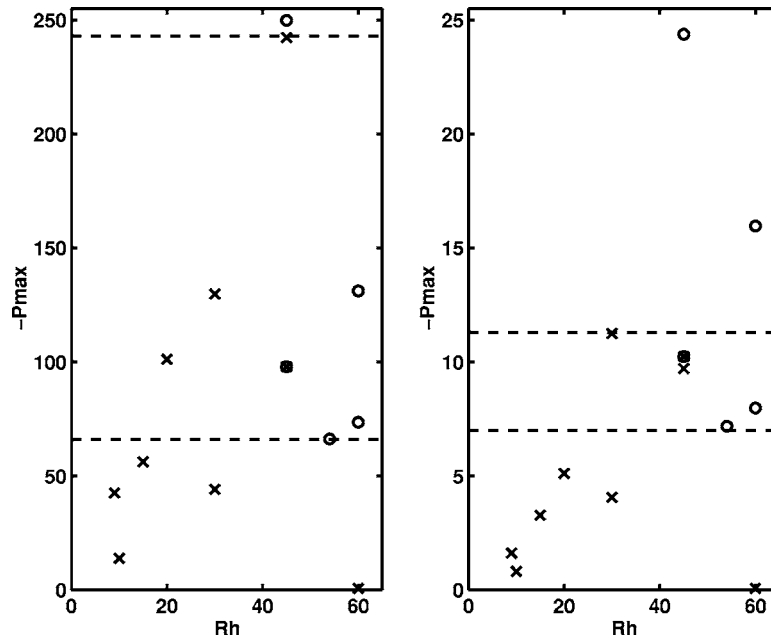


Fig. 21 Vortex shedding parameter as function of  $R_h$ , where  $\circ$  denotes separation with vortex shedding,  $\times$  without vortex shedding, and  $\otimes$  a transition between the two, as defined by Eq. (20) (left figure) and Eq. (21) (right figure) for  $M=1.3$ . Area between dash lines denotes overlapping regime.

A way to determine the quantitative influence of Mach number on the vortex shedding is by curve-fitting the numerical data with a Mach-number-dependent function. To this purpose we multiply Eq. (23) by a function,  $1/(C+M^k)$ . The two constants,  $C$  and  $k$ , can be determined from the limiting behavior in which  $M$  tends to zero and to infinity. Fitting to our numerical results at high and low Mach number cases we found  $k=4$  and  $C=0.11$  to be appropriate,

in the sense that the overlapping area becomes smallest. The data of the low Mach number cases are taken from an earlier study on separated flow at  $M=0.2$  [18]. Other expressions for the Mach number effect yield similar or worse results.

From the above outline, the following criterion is appropriate for the onset of vortex shedding in compressible flows subject to transpiration boundary,

Table 1 Time-averaged result of  $R_{\theta_s}$ ,  $\max(-du_{in}/dx_1)$  and  $\max(-du_e/dx_1)$  from cases with varying  $Re$ ,  $h$ ,  $M$ , and amplitude of suction and blowing.

No.	$Re$	$h$	$M$	$a$	$R_h \times 10^{-3}$	$R_{\theta_s}$	$\max(-du_{in}/dx_1)$	$\max(-du_e/dx_1)$
1	300	30	1.3	0.12	9	457.64	6.085e-2	2.302e-3
2	500	30	1.3	0.12	15	725.86	5.334e-2	3.110e-3
3	1000	30	1.3	0.12	30	1340.62	7.221e-2	6.257e-3
4	1500	30	1.3	0.12	45	1821.38	4.428e-2	4.629e-3
5	1800	30	1.3	0.12	54	1746.91	3.906e-2	4.238e-3
6	2000	30	1.3	0.12	60	1941.01	4.752e-2	5.797e-3
7	500	20	1.3	0.12	10	408.96	4.145e-2	2.429e-3
8	500	40	1.3	0.12	20	889.55	6.397e-2	3.232e-3
9	500	60	1.3	0.12	30	680.50	4.765e-2	4.387e-3
10	500	90	1.3	0.12	45	1528.75	5.346e-2	5.215e-3
11	500	120	1.3	0.12	60	1384.28	3.420e-2	4.165e-3
12	500	90	1.3	0.06	45	1811.54	3.692e-2	1.481e-3
13	500	30	1.1	0.12	15	713.14	5.747e-2	2.128e-3
14	500	30	1.6	0.12	15	414.19	7.123e-2	4.698e-3
15	500	30	1.8	0.12	15	636.30	7.507e-2	1.99e-3
16	500	30	2.0	0.12	15	644.17	1.125e-1	1.89e-3
17	500	120	1.3	0.006	60	350.96	2.527e-3	2.735e-4
18	330	30	0.2	0.037	9.9	204.10	6.693e-2	6.411e-4
19	330	30	0.2	0.055	9.9	221.97	1.181e-2	1.042e-3
20	330	30	0.2	0.055	9.9	221.97	1.270e-2	4.231e-3
21	1000	120	1.3	0.12	120	3277.36	3.370e-2	4.999e-3
22	600	40	1.01	0.07	24	504.63	2.009e-2	3.735e-3
23	700	40	1.005	0.10	28	741.31	2.759e-2	5.713e-3

**Table 2** Shedding parameters Eq. (20), Eq. (21), and Eq. (24) corresponding to the cases in Table 1.  $\circ$  is vortex shedding case,  $\times$  is non vortex shedding case and  $\otimes$  is transition between the two.

No.	$-P_{\max}$ Eq. (24)	$-P_{\max}$ Eq. (20)	$-P_{\max}$ Eq. (21)	Shedding
1	209.70	42.48	1.61	$\times$
2	471.66	56.21	3.28	$\times$
3	1898.45	129.77	11.25	$\times$
4	2106.81	97.93	10.24	$\otimes$
5	2314.82	66.22	7.19	$\circ$
6	3517.75	73.58	7.98	$\circ$
7	163.85	13.86	0.81	$\times$
8	871.51	101.23	5.11	$\times$
9	2662.08	44.13	4.06	$\times$
10	7120.46	249.86	24.38	$\circ$
11	10110.92	131.08	15.96	$\circ$
12	2022.18	242.34	9.72	$\times$
13	555.87	63.96	2.37	$\times$
14	366.92.31	21.13	1.39	$\times$
15	107.94	47.54	1.26	$\times$
16	74.67	65.94	1.11	$\times$
17	663.83	0.62	0.067	$\times$
18	1702.51	0.84	0.081	$\times$
19	2777.78	1.76	0.155	$\circ$
20	11254.48	1.90	0.632	$\circ$
21	24273.96	361.99	53.7	$\circ$
22	3116.62	8.53	1.58	$\circ$
23	5662.08	21.66	4.49	$\circ$

$$2100 \leq -P_{\max} = -h^2 \text{Re} \left( \frac{du_e}{dx_1} \right)_{\max} (0.11 + M^4)^{-1} \leq 2700 \quad (24)$$

Below 2100 vortex shedding does not occur and above 2700 it always occurs. The result using this shedding parameter is shown

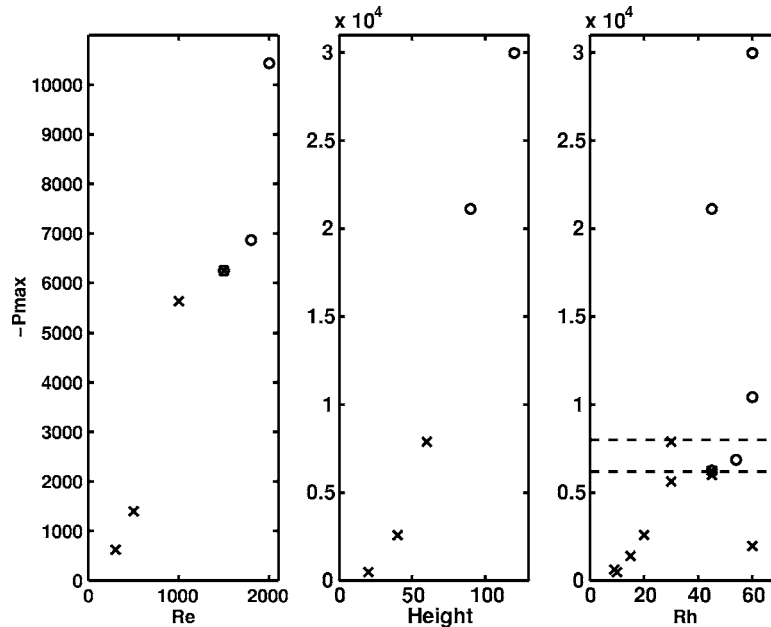


**Fig. 22** Vortex shedding parameter defined by Eq. (23) as function of  $Re$  (fixed  $h$ ),  $h$  (fixed  $Re$ ), and  $R_h$  for  $M=1.3$

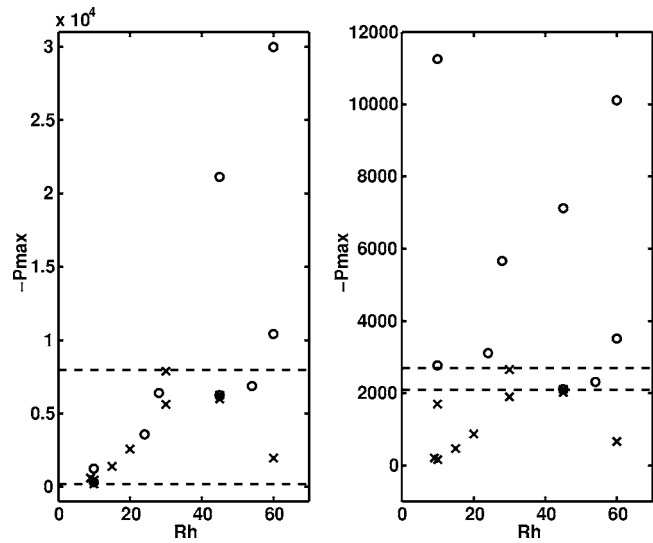


**Fig. 23** Vortex shedding parameter defined by Eq. (23) (left figure) and Eq. (24) (right figure) including data at different Mach numbers

in Fig. 23 (right). Since we also use data of low Mach number cases, this criterion is not only applicable to shock cases, but also to virtually incompressible flows.

## 5 Conclusion

We summarize our contributions as follows. The employed numerical method provides results which agree well with other numerical and experimental results in steady SBLI. In addition, the good performance of the characteristic suction and blowing boundary condition is established for flows containing shocks. We show that in a flat plate supersonic flow with a free pressure at the outlet, applying only suction at the upper boundary creates no shock wave in the flow. Applying only blowing, on the other hand, generates a steady shock and a separation region upstream of it. A wedge induced shock can be reproduced in this way without inclined boundary, avoiding grid skewness.

Unsteady SBLI can occur if we apply a consecutive suction and blowing at the upper boundary. This forms an effective shock buffeting generator. A substantial unsteadiness is not only found in the separated boundary layer, but also in the inviscid shock. The shock unsteadiness occurs in a closed range of domain height and Mach number and weakens with decreasing suction and blowing amplitude and Reynolds number. The viscous unsteadiness, in the form of spontaneous vortex shedding, occurs in the high values of Reynolds number and domain height. The average shock strength decreases with decreasing Reynolds number, domain height, and suction and blowing amplitude. Further, a maximum shock strength is encountered in a bounded range of Mach number.

It was found that the shedding criterion due to Pauley et al. [17] is not applicable to the highly compressible flow containing shocks. A new shedding criterion suitable for compressible flows is proposed, based on the present results.

### Acknowledgment

This work is supported by the Koninkelijke Nederlandse Academie van Wetenschappen (Royal Netherlands Academy of Arts and Sciences, KNAW).

### References

- [1] Ferri, A., 1940, "Experimental Results with Airfoils Tested in the High-Speed Tunnel in Guidonia," NACA TM 946.
- [2] Ackeret, J., Feldmann, F., and Rott, N., 1947, "Investigations of Compression Shocks and Boundary Layers in Gases Moving at High Speed," NACA TM 1113.
- [3] Liepmann, H. W., and Roshko, A., 1966, *Elements of Gasdynamics*, J Wiley, New York.

- [4] Adamson, T. C., and Messiter, A., F., 1980, "Analysis of Two-Dimensional Interaction between Shock Waves and Boundary Layers," *Annu. Rev. Fluid Mech.* **12**, pp. 103–138.
- [5] Delery, J., and Marvin, J. G., 1986, "Shock-Wave Boundary Layer Interactions," AGARDograph-AG-180.
- [6] Tijdeman, H., and Seebass, R., 1980, "Transonic Flow Past Oscillating Airfoils," *Annu. Rev. Fluid Mech.* **12**, pp. 181–222.
- [7] Degrez, G., 1981, "Exploratory Experimental Investigation of the Unsteady Aspects of Blunt Fin-Induced Shock Wave Turbulent Boundary Layer Interactions," M.S.E. thesis, Mechanical and Aerospace Eng. Dept., Princeton Univ., Princeton, NJ.
- [8] Dolling, D. S., 1993, "Fluctuating Loads in Shock Wave/Turbulent Boundary Layer Interaction: Tutorial and Update," AIAA Paper No. 93-0284.
- [9] Loth, E., and Matthys, M. W., 1995, "Unsteady Low Reynolds Number Shock Boundary Layer Interactions," *Phys. Fluids* **7**(5), pp. 1142–1150.
- [10] Thompson, K. W., 1987, "Time Dependent Boundary Conditions for Hyperbolic Systems," *J. Comput. Phys.* **68**, pp. 1–24.
- [11] Poinot, T. J., and Lele, S. K., 1992, "Boundary Conditions for Direct Simulations of Compressible Viscous Flows," *J. Comput. Phys.* **101**, pp. 104–129.
- [12] Wasistho, B., Geurts, B. J., and Kuerten, J. G. M., 1997, "Spatial Simulation Techniques for Time-Dependent Compressible Flow over a Flat Plate," *Comput. Fluids* **26**, pp. 713–739.
- [13] Vreman, A. W., 1995, "Shocks in Direct Numerical Simulation of the Confined Three Dimensional Mixing Layer," *Phys. Fluids* **7**, pp. 2105–2107.
- [14] Van Leer, B., 1974, "Towards the Ultimate Conservative Difference Scheme II. Monotonicity and Conservation Combined in a Second-Order Scheme," *J. Comput. Phys.* **14**, pp. 361–370.
- [15] Hakkinen, R. J., Greber, I., Trilling, L., and Abarbanel, S. S., 1959, "The Interaction of an Oblique Shock Wave With a Laminar Boundary Layer," NASA Memo 2-18-59W.
- [16] Katzer, E., 1989, "On the Lengthscales of Laminar Shock Boundary-Layer Interaction," *J. Fluid Mech.* **206**, pp. 477–496.
- [17] Pauley, L. L., Moin, P., and Reynolds, W. C., 1990, "The Structure of Two-Dimensional Separation," *J. Fluid Mech.* **220**, pp. 397–411.
- [18] Wasistho, B., Geurts, B. J., and Kuerten, J. G. M., 1997, "Numerical Simulation of Separated Boundary-Layer Flow," *J. Eng. Math.* **32**, pp. 179–196.



# Measurement of Permeability and Slip Coefficient of Porous Tubes

N. M. Brown  
School of Engineering,  
University of Technology,  
Kingston, Jamaica

F. C. Lai<sup>1</sup>  
School of Aerospace and Mechanical  
Engineering,  
University of Oklahoma,  
Norman, OK 73019

Experiments have been conducted to measure the permeability and slip coefficient of seven porous tubes. They were made from fiberglass and nylon nettings with various wall thicknesses. Tests show that these tubes have a distinct permeability in the longitudinal and radial directions. In addition, the slip coefficient which is important in many applications was determined. From the results obtained, one can conclude that both permeabilities depend on the material, but the radial permeability also depends on the wall thickness. The slip coefficient depends not only on the material but also on the Reynolds number, permeabilities, and wall thickness. [DOI: 10.1115/1.2234783]

## Introduction

It has been shown by Gari and Loehrke [1] that a porous manifold is effective in the promotion and maintenance of thermal stratification in a liquid storage tank. In particular, a porous manifold is able to reduce the plume entrainment and mixing of fluids induced by the charging flow, the two most important factors that have been identified to have adverse effects on the performance of thermal storage tanks [2]. In search of the optimal design conditions for a thermal storage tank, Yee and Lai [3] have performed a comprehensive numerical study to examine the effectiveness of a porous manifold. In their formulation, the flow in the porous manifold was based on Darcy's law and a slip coefficient was introduced in the interface condition between the fluid layer and the porous wall. Although their study has covered a wide range of the parameters involved, the slip coefficient was limited to those reported by Beavers et al. [4] for some specific foam metals. Based on the available data, they show that a porous manifold may actually have an adverse effect on the formation of thermal stratification if the permeability of the porous manifold is too small. From the contour plots presented in their study, one observes that very little fluid is able to penetrate the porous wall at a low Richardson number because of the low permeability of the wall. Intuitively, if one were to use a more permeable porous manifold, a more favorable condition for the formation of thermal stratification might be attainable. Thus, the present study is focused on the testing of two new materials (i.e., fiberglass and nylon screens) for their use in the proposed porous manifold. To achieve our goal, we have extended the model proposed by Beavers and Joseph [5] from planar systems to radial systems. To our knowledge, no such attempt has been made before. The only related study may be that of Siginer and Bakhtiyarov [6] for flows in a tube with two sections of porous medium with distinct permeability in series. The following discussion provides the basis for our extended study.

## Theoretical Background

For a steady, fully developed flow in a tube bounded by a permeable wall (Fig. 1), the velocity profile is given by

$$v_z = \left( -\frac{dP}{dz} \right) \left[ \frac{r_i^2}{4\mu} + \frac{K_z}{\mu} - \frac{\sqrt{K_z} r_i}{\gamma} - \frac{r^2}{4\mu} \right] \quad (1)$$

which can be readily obtained from solving the Poiseuille flow in a tube with a proper interface condition. The interface condition employed is based on the model proposed by Beavers and Joseph [5] in which it assumes the presence of a slip velocity on the wall. In addition, it assumes that the velocity gradient in fluid near the wall is proportional to the difference between the slip velocity and flow velocity in the porous medium. That is

$$r = r_i, \quad \frac{\partial v_z}{\partial r} = \frac{\gamma}{\sqrt{K_z}} (v_s - u_m) \quad (2)$$

The slip coefficient  $\gamma$  depends on the material of which the porous wall is composed and  $K_z$  is the longitudinal permeability, which is also a property of the wall material. The slip velocity at the interface  $v_s$  is given by

$$v_s = \frac{K_z}{2\mu} \left( -\frac{dP}{dz} \right) \left[ 2 - \frac{1}{\gamma \sqrt{Da}} \right] \quad (3)$$

It should be mentioned that the model by Beavers and Joseph [5] is not the only model dealing with the interface between fluid and porous layer, but is chosen here because of its simplicity. Other more involved models, such as Brinkman-extended Darcy model [7], also involve empirical constants which need to be determined by experiments. The determination of these constants may not be as straightforward or well defined as the slip coefficient [8].

Using the velocity profile obtained in Eq. (1), the volumetric flow rate through the tube with porous wall can be calculated to give

$$Q = \frac{\pi r_i^4}{8\mu} \left( -\frac{dP}{dz} \right) \left[ 1 - \frac{4}{\gamma} \sqrt{Da} + 8Da \right] \quad (4)$$

On the other hand, for a tube bounded by an impermeable wall, the volumetric flow rate is shown to be

$$Q^* = \frac{\pi r_i^4}{8\mu} \left( -\frac{dP}{dz} \right) \quad (5)$$

If the thickness of the porous wall and pressure gradient along the tube are fixed, the ratio of these two volumetric flow rates is given by

$$\frac{Q}{Q^*} = \left[ 1 - \frac{4}{\gamma} \sqrt{Da} + 8Da \right] \quad (6)$$

Given the permeability of the porous wall, one can first calculate the Darcy number,  $Da$ . Then, with the measurement of the volu-

<sup>1</sup>Corresponding author.

Contributed by the Fluids Engineering Division of ASME for publication in the JOURNAL OF FLUIDS ENGINEERING. Manuscript received May 22, 2004; final manuscript received February 11, 2006. Review conducted by Joseph Katz.

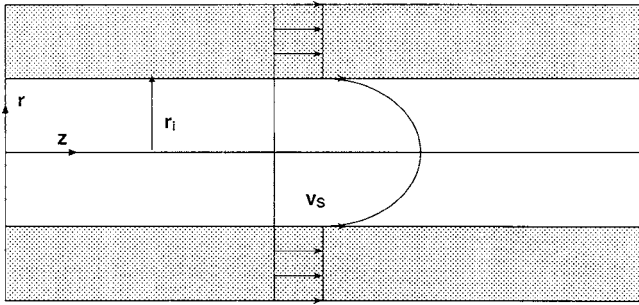


Fig. 1 A fully developed flow in a tube bounded by porous wall

metric flow rate ratio  $Q/Q^*$ , one can solve for the slip coefficient  $\gamma$  from Eq. (6).

To determine the longitudinal permeability, it is assumed that the flow in the porous annulus is in the Darcy's flow regime [9], which requires

$$Re_m = \frac{v_z \sqrt{K_z}}{\nu} \ll 1 \quad (7)$$

Assuming the validity of Darcy's law (Eq. (8))

$$v_z = -\frac{K_z}{\mu} \frac{dP}{dz} = -\frac{K_z}{\mu} \frac{\Delta P}{L} \quad (8)$$

one can express the volumetric flow rate as

$$Q = -\frac{K_z A}{\mu} \frac{\Delta P}{L} \quad (9)$$

Thus, for a given pressure gradient, the longitudinal permeability can be determined from the above equation as soon as the volumetric flow rate is known.

For a radial flow, Darcy's law can be expressed as (Amyx et al. [10] and Dake [11])

$$Q = -\frac{K_r A}{\mu} \frac{dP}{dr} \quad (10)$$

If the flow rate is maintained constant, the pressure gradient across any annular layer can be determined by

$$\int_{p_i}^{p_o} dP = \frac{1}{2\pi K_r L} \int_{r_i}^{r_o} \frac{dr}{r} \quad (11)$$

and which leads to the following expression

$$\Delta P = \frac{1}{2\pi K_r L} \ln \frac{r_o}{r_i} \quad (12)$$

Thus, from the measurement of volumetric flow rate and pressure gradient across an annular layer, the radial permeability can be determined by

$$K_r = \frac{1}{\pi 2L} \frac{Q \mu \ln(r_o/r_i)}{\Delta P} \quad (13)$$

## Experimental Setup and Procedure

**Measurement of Longitudinal Permeability.** The experimental apparatus used to determine the longitudinal permeability of a porous tube is shown in Fig. 2, which consists of upstream plenum, downstream plenum, test section, and a reservoir. The upstream plenum was fabricated from a 12.7-mm-thick Plexiglas sheet. It was equipped with four overflow weirs so that the water level in the plenum could be maintained at any desired height by using a proper overflow weir. Two stiff fiberglass screens were used as dampers to rid the plenum of any ripple or pressure fluctuation. The upstream plenum was fitted with one *J*-type thermocouple to measure the water temperature. The downstream plenum

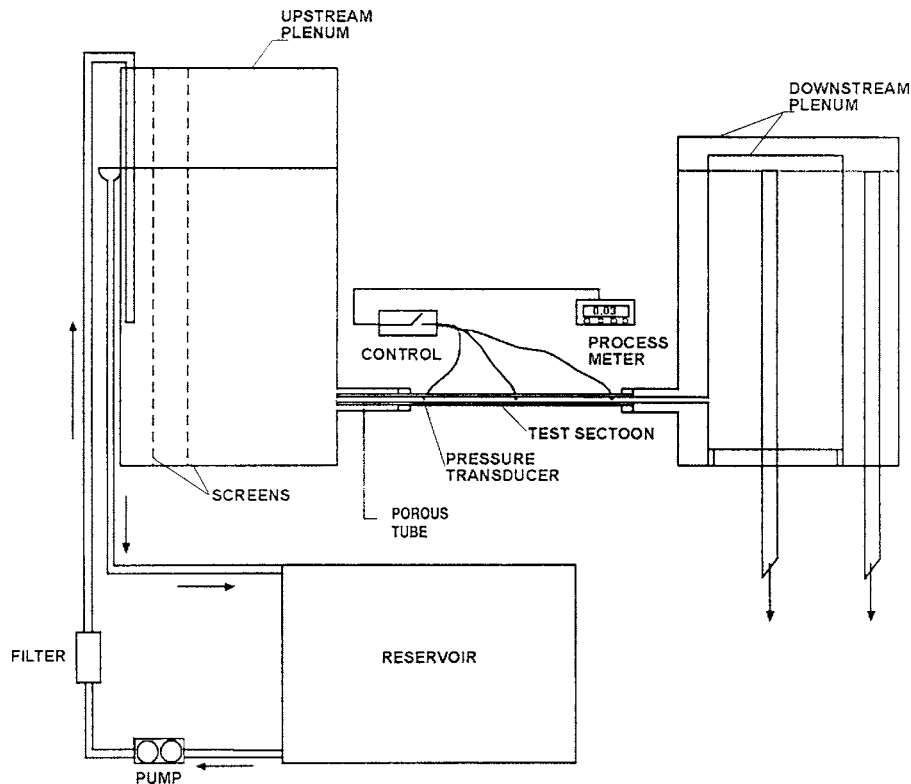


Fig. 2 Schematics of the experimental setup for the measurement of longitudinal permeability

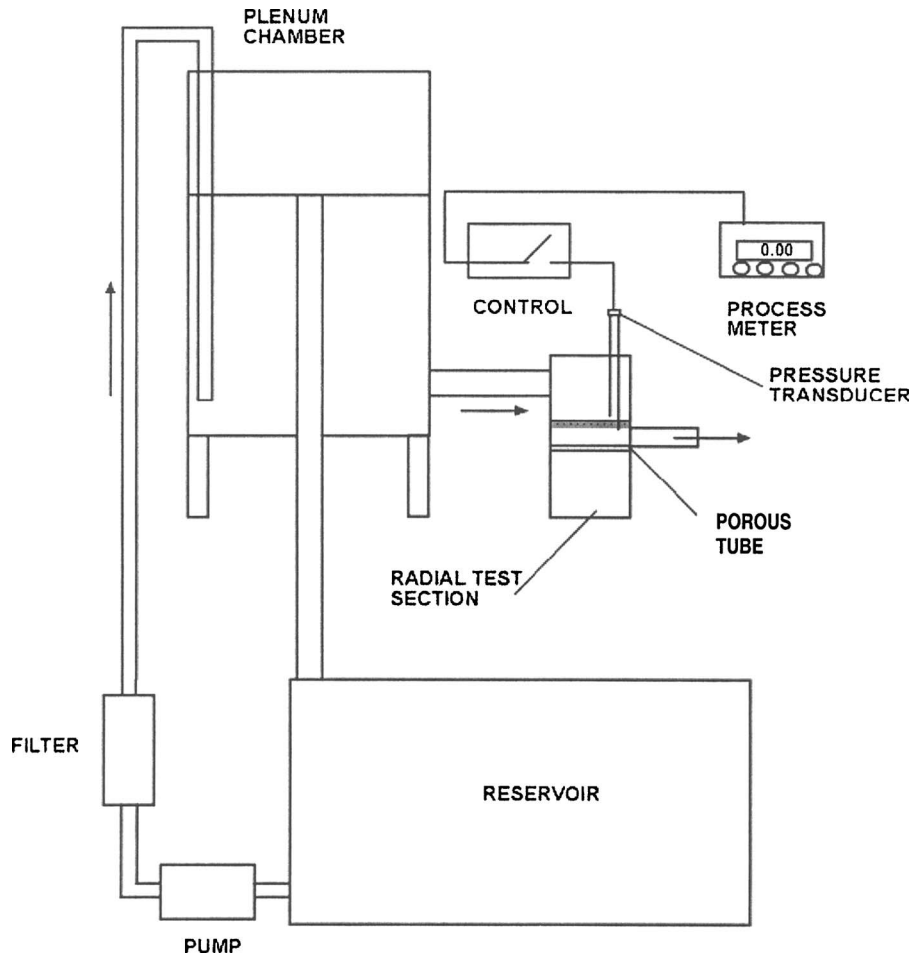


Fig. 3 Schematics of the experimental setup for the measurement of radial permeability

was also fabricated from a 12.7-mm-thick Plexiglas sheet. There were two tanks in the downstream plenum, which were connected to the exit of the test section. To allow for an independent measurement and control of flow through the test section, the smaller tank was placed inside the larger tank. The water level inside each tank of the downstream plenum was controlled by an adjustable weir. These two adjustable weirs provided an easy way not only to balance the transverse pressure difference, but also to maintain the pressure gradient in the test section.

The test section is basically a Plexiglas tube fitted with a porous annulus (i.e., the porous tube to be tested) of various thicknesses. The tube has a length of 685.8 mm and an outer diameter of 25.4 mm. The thickness of the Plexiglas tube is 3 mm. The porous tubes were made from fiberglass mesh commonly used as mosquito net for windows and doors and nylon mesh used in the building industry to hold insulation in sheet racks. The mesh with a porosity ranging from 0.84 to 0.9 was carefully wrapped around rods of various diameters to form the shape of a tube. When the outer diameter of the porous tube reached 19.4 mm (i.e., the inner diameter of the Plexiglas tube), the outer layer of the mesh was sewed in place to form a straight porous annulus that would conform to the Plexiglas outer tube. Seven porous tubes were fabricated with a thickness of 3.2, 4.8, and 6.4 mm, respectively.

Three sets of pressure transducers were installed along the test section to measure the pressure gradient in the flow direction. To avoid the entrance effect, the first set of pressure ports was installed 216 mm downstream of the inlet and the other two were located at an interval of 203.2 mm along the length of the tube. The pressure ports were installed directly opposite to each other to ensure that measurement was taken at exactly the same location

along the porous tube. Three pressure taps were used to measure pressures inside the porous annulus while another three were used to measure pressures in the fluid region. The measurement was taken using Omega PX26 series differential and gage pressure transducers and read out by an Omega DP25B-S meter. The pressure transducers had a reading accuracy of  $6.895 \text{ N/m}^2$  (0.001 psi) and were able to compensate temperature fluctuation from 0 to  $50^\circ\text{C}$ .

From the discussion in the last section, it is clear that the determination of longitudinal permeability and slip coefficient of a porous tube requires the establishment of a unidirectional, fully developed flow field inside the tube and the porous wall. This condition is realized when the differential pressure across both porous annulus and tube is identical, which can be readily achieved by adjusting the overflow weirs in the downstream plenum.

To facilitate the determination of slip coefficients, one first needs to measure the longitudinal permeability of the porous tubes. In all, four tubes were tested; three of them were made from fiberglass mesh (with a thickness of 3.2, 4.8, and 6.4 mm, respectively) and the other was made from more permeable nylon mesh (with a thickness of 6.4 mm). Two of the fiberglass tubes, which had a thickness of 3.2 and 6.4 mm, were tightly wrapped and the other (with a thickness of 4.8 mm) was loosely wrapped. For the tightly wrapped tubes, there were five layers of mesh per millimeter thickness while for the loosely wrapped tube, it had about 3.5 layers over the same thickness. The nylon tube was wrapped about the same tightness as those tightly wrapped fiberglass tubes.

To measure the longitudinal permeability of a porous tube, a

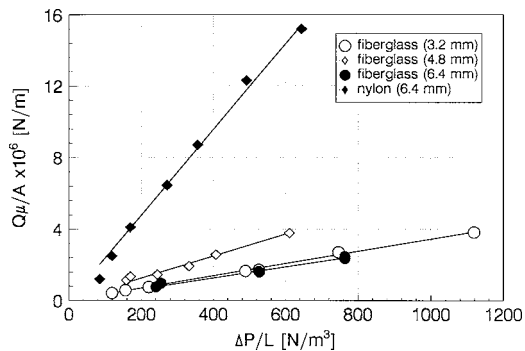


Fig. 4 Longitudinal permeability of porous tubes with various wall thicknesses

rod with the same inner diameter of the porous tube was first inserted to the test section to block the flow in the core region. Then the water level in the upper and downstream plenums was adjusted to produce a steady flow through the porous tube. The water flowing out of the downstream plenum was collected in a beaker and its volume was recorded. The time required to collect a given amount of water was also noted and the volumetric flow rate was determined. On average, measurement was taken over a 5-min period. Additional measurements were made by adjusting the overflow weirs in the downstream plenum to increase the pressure gradient through the test section. This procedure was repeated five more times.

**Determination of the Slip Coefficient.** To determine the slip coefficient, the rod which was inserted in the test section in earlier experiments for longitudinal permeability was removed. The overflow weirs in the downstream plenum were adjusted so that the required pressure gradient was achieved in the test section. A steady flow of water was allowed to flow through both porous annulus and core region in the test section. Toward the exit, water was separated into two streams by a thin separator pipe, which directed water from the core region to the inner tank in downstream plenum, and water from the porous annulus to the outer tank. The flows from both tanks were collected and measured. Since the length of the flow separator pipe is quite short (less than 4 in.), the pressure drop due to its presence is believed to be small to cause any significant difference in the flow rates.

**Measurement of Radial Permeability.** A slightly different setup was used to measure the radial permeability (Fig. 3). Only one plenum was used to provide the required hydrostatic head for the test section. To facilitate the measurements, one pressure probe was inserted through the porous tube wall to measure the pressure at the center of the tube, the other probe was placed a few millimeters from the outer surface of the tube to measure the outside pressure. Water was first pumped to the plenum chamber

Table 1 Measured longitudinal and radial permeabilities of porous tubes

Tube wall thickness (mm)	Longitudinal permeability (m <sup>2</sup> )	Radial permeability (m <sup>2</sup> )
6.4 (FG) <sup>a</sup>	3 × 10 <sup>-9</sup>	6 × 10 <sup>-10</sup>
4.8 (FG)	6 × 10 <sup>-9</sup>	7 × 10 <sup>-10</sup>
3.2 (FG)	3 × 10 <sup>-9</sup>	4 × 10 <sup>-10</sup>
6.4 (N) <sup>a</sup>	3 × 10 <sup>-8</sup>	1 × 10 <sup>-9</sup>
3.2 (N)		1 × 10 <sup>-9</sup>
1.6 (N)		7 × 10 <sup>-10</sup>
6.4 (N) <sup>b</sup>		1.05 × 10 <sup>-8</sup>

<sup>a</sup>FG—fiberglass, N—nylon.

<sup>b</sup>With an outer diameter of 0.10 m.

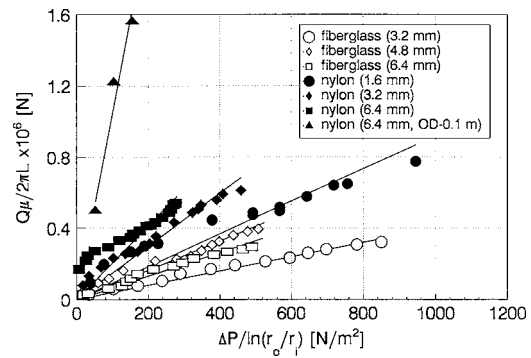


Fig. 5 Radial permeability of porous tubes with various wall thicknesses

from the reservoir. At a given hydrostatic head, water was forced to flow through the porous tube radially because of the pressure gradient across the porous wall. The overflow weir was adjusted to vary the hydrostatic head that controlled the flow rate across the porous wall. Ten different hydrostatic pressures were used for each tube.

Prior to the experiment, the pressure transducers were individually calibrated. To confirm that the pressure transducers were properly calibrated, the volumetric flow rate through a solid wall tube was compared to that obtained using the Hagen-Poiseuille's equation, Eq. (5). For the conditions given, Eq. (5) is reduced to

$$Q = 4.9463 \times 10^{-7} \Delta P \quad (14)$$

An excellent agreement (with discrepancy less than 1.5%) was found when one compared the measured volumetric flow rates with those obtained from Eq. (14). The maximum uncertainty of the measured flow rates was calculated to be ±2.3%. The low experimental errors demonstrate that the experimental setup and data collection were done properly.

## Results and Discussion

To determine the longitudinal permeability, the measured volumetric flow rates are plotted against the pressure gradient along the porous tube in Fig. 4. From Eq. (9), one recognizes that the slope of these data points represents the longitudinal permeability, which is summarized in Table 1. The maximum uncertainty for the longitudinal permeabilities thus obtained is calculated to be 11.1%. A complete set of the data can also be found in Ref. [12].

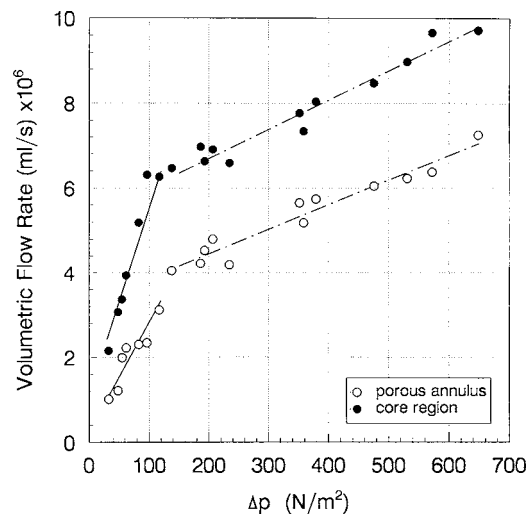


Fig. 6 Variation of volumetric flow rates as a function of the pressure drop (fiberglass tube with a wall thickness of 6.4 mm)

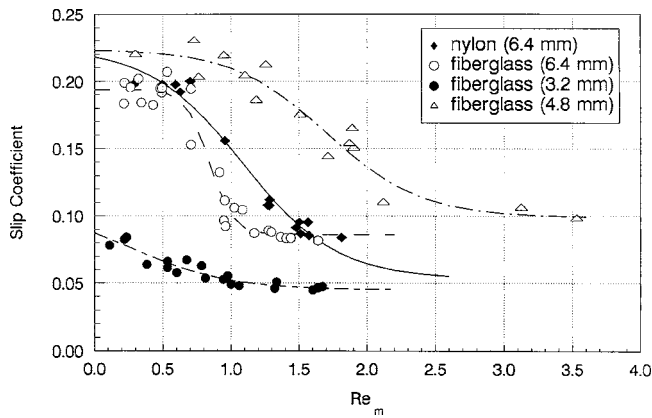


Fig. 7 Slip coefficient as a function of the Reynolds number for fiberglass and nylon tubes with various wall thicknesses

The results show that the nylon tube has the highest longitudinal permeability. This is due to the fact that the nylon tube has a larger mesh than the fiberglass tubes. As water flows through the tube, it encounters less resistance from the nylon mesh than fiberglass mesh. For fiberglass, the tightly wrapped tubes have about the same permeability while the loosely wrapped tube has a permeability that is twice of others. This finding has suggested that the longitudinal permeability of a porous tube is less dependent on the wall thickness, but more on how tightly the tube is wrapped and how large the mesh size is. If the tube is loosely wrapped and the mesh has a larger pore, it would allow more fluid to seep through between mesh layers and thus leads to an increase in the longitudinal permeability.

Figure 5 shows the variation of volumetric flow rate as a function of the radial pressure gradient across a porous tube. Again, the slope of each curve represents the radial permeability of that particular porous tube, which is also summarized in Table 1. The maximum uncertainty of the radial permeabilities thus obtained is calculated to be 33.4%, which is higher than that of longitudinal permeabilities because of more quantities involved in the calculation. It is observed that tubes with the same wall thickness display a similar trend. Also, the loosely wrapped tube (4.8 mm) has the highest permeability among the three fiberglass tubes tested. One may expect at first that a thicker porous tube would have a smaller radial permeability. However, the results show that as the wall thickness doubled, the increase in logarithmic radius ratio outweighs the reduction in flow rate. As a result, a tube with a thicker wall (6.4 mm) has a higher permeability than that with a thinner wall (3.2 mm). The same trend is observed in the nylon tubes. Since nylon tubes have a larger mesh than fiberglass tubes, they have a higher radial permeability than the fiberglass tubes for a given wall thickness. Thus, one can conclude that radial perme-

Table 2 Correlations of slip coefficient with the Reynolds number for various porous tubes

	$a$	$b$	$c$	$d$	Correlation coefficient
Fiberglass (3.2 mm)	0.045	0.062	0.267	0.357	0.885
Fiberglass (4.8 mm)	0.099	0.125	1.702	0.346	0.927
Fiberglass (6.4 mm)	0.086	0.108	0.839	0.086	0.959
Nylon (6.4 mm)	0.053	0.172	1.087	0.343	0.974

ability is also dependent on the diameter of a tube. Given the same wall thickness, a tube with a larger diameter has a higher radial permeability.

As discussed in the last section, one needs to measure the longitudinal permeability along with the separate flow rates through the porous annulus and core region to determine the slip coefficient. The flow rates through the porous annulus and core region are shown in Fig. 6 as a function of the total pressure drop for the fiberglass tube with a wall thickness of 6.4 mm. The other tubes show a similar trend. From Fig. 6, one notices that the volumetric flow rate is basically a linear function of the pressure drop. However, one also observes that there is a change in the slope when the total pressure drop is about 140 N/m<sup>2</sup>, which indicates that there is a transition from the Darcy flow regime to non-Darcy flow regime. This transition in the flow regime has important implication for the slip coefficient that will be elaborated in the following discussion.

The slip coefficients  $\gamma$  are plotted in Fig. 7 as a function of the modified Reynolds number. The maximum uncertainty for the slip coefficients is calculated to be 16.3%. From the figure, one observes that slip coefficient assumes a constant value at low Reynolds numbers ( $Re_m < 1$ ) where Darcy's law is valid. As Reynolds number increases, the value of slip coefficient first decreases sharply, then approaches an asymptotic value when the Reynolds number is further increased. As expected, the fiberglass tube with a thickness of 4.8 mm (which has a higher permeability and a higher flow rate) also has a higher slip coefficient. For fiberglass tubes with a thickness of 3.2 and 6.4 mm, their slip coefficients are very different despite of having about the same longitudinal permeability, which indicates that there may be other factors at work.

The slip coefficients obtained from the present study can be best correlated with the Reynolds number in the following form:

$$\gamma = a + \frac{b}{1 + \exp[(Re_m - c)/d]} \quad (15)$$

where  $a$ ,  $b$ ,  $c$ , and  $d$  are constants, which are summarized in Table 2. In this form, the transition in slip coefficient with the flow condition can be best presented.

## Conclusions

Experiments have been performed to determine the slip coefficient, longitudinal and radial permeabilities of several porous tubes. From the results obtained, longitudinal permeability is found to depend more on the tightness that a mesh is wrapped into the shape of a tube than the actual thickness of the tube wall. Radial permeability is found also dependent on the diameter of a tube in addition to wall thickness. Slip coefficient on the other hand is found to depend on factors other than the material property. For instance, slip coefficient also depends on the Reynolds number, permeability, and thickness of the tube wall. For a given porous tube, slip coefficient reduces from a constant value in the Darcy flow regime and approaches an asymptotic value in the non-Darcy flow regime when the Reynolds number increases ( $Re_m > 1$ ). While the present study has extended the previous work of Beavers et al. [5] in the determination of slip coefficient of radial porous walls, the results obtained are not only a good supplement to the existing literature, but also provide useful information for the design of thermal storage tanks using a porous manifold.

## Nomenclature

- $A$  = cross-sectional area normal to the flow direction, m<sup>2</sup>
- $Da$  = Darcy number,  $Da = K/r_i^2$
- $K$  = permeability of porous medium, m<sup>2</sup>
- $L$  = length of porous tube, m
- $P$  = pressure, Pa

$Q$  = volumetric flow rate,  $m^3/s$   
 $r$  = radial coordinate, m  
 $r_i$  = inner radius of porous tube, m  
 $r_o$  = outer radius of porous tube, m  
 $Re$  = Reynolds number,  $Re=ur_i/\nu$   
 $Re_m$  = modified Reynolds number for porous media,  
 $Re_m=u_m K^{1/2}/\nu$   
 $t$  = time, s  
 $u_i$  = inlet velocity in the  $z$ -direction, m/s  
 $u_m$  = flow velocity in porous medium in the  
 $z$ -direction, m/s  
 $v_r$  = velocity in the  $r$ -direction, m/s  
 $v_s$  = slip velocity  
 $v_z$  = velocity in the  $z$ -direction, m/s  
 $z$  = axial coordinates, m

#### Greek Symbol

$\gamma$  = slip coefficient  
 $\mu$  = dynamic viscosity of fluid, kg/m s  
 $\nu$  = kinematic viscosity of fluid,  $m^2/s$

#### References

- [1] Gari, H. N., and Loehrke, R. I., 1982, "A Controlled Buoyant Jet for Enhanc-

- ing Stratification in a Liquid Storage Tank," ASME J. Fluids Eng., **104**, pp. 475–481.
- [2] Hollands, K. T. G., and Lightstone, M. F., 1989, "A Review of Low-Flow, Stratified-Tank Solar Water Heating System," Sol. Energy, **43**(2), pp. 97–105.
- [3] Yee, C. K., and Lai, F. C., 2001, "Effect of Porous Manifold on Thermal Stratification in Liquid Storage Tank," Sol. Energy, **71**(4), pp. 241–254.
- [4] Beaver, G. S., Sparrow, E. M., and Magnuson, R. A., 1970, "Experiments on Coupled Parallel Flows in a Channel and a Bounding Porous Medium," ASME J. Basic Eng., **92**, pp. 843–848.
- [5] Beaver, G. S., and Joseph, D. D., 1967, "Boundary Condition at a Naturally Permeable Wall," J. Fluid Mech., **30**, pp. 197–207.
- [6] Siginer, D. A., and Bakhtiyarov, S. I., 2001, "Flow in Porous Media of Variable Permeability and Novel Effects," ASME J. Appl. Mech., **68**, pp. 312–319.
- [7] Brinkman, H. C. A., 1947, "A Calculation of the Viscous Force Exerted by a Flowing Fluid on a Dense Swarm of Particles," Appl. Sci. Res., Sect. A, **1**, pp. 27–34.
- [8] Givler, R. C., and Altobelli, S. A., 1994, "A Determination of the Effective Viscosity for the Brinkman-Forchheimer Flow Model," J. Fluid Mech., **258**, pp. 355–370.
- [9] Nield, D. A., and Bejan, A., 1998, *Convection in Porous Media*, 2nd ed., Springer-Verlag, New York.
- [10] Amyx, J. W., Bass, D. M., and Whiting, R. L., 1960, *Petroleum Reservoir Engineering, Physical Properties*, McGraw-Hill, New York.
- [11] Dake, L. P., 1978, *Fundamentals of Reservoir Engineering*, Elsevier, New York.
- [12] Brown, N. M., 2003, "Enhancement of Thermal Stratification in a Storage Tank Using a Porous Manifold," Ph.D. dissertation, University of Oklahoma, Norman, OK.

# Pressure-Driven Flows of Bingham Plastics Over a Square Cavity

Evan Mitsoulis<sup>1</sup>  
e-mail: mitsouli@metal.ntua.gr

S. Marangoudakis

M. Spyrtos

Th. Zisis

School of Mining Engineering and Metallurgy,  
National Technical University of Athens,  
Zografou 157 80,  
Athens, Greece

Nikolaos A. Malamataris

Department of Mechanical Engineering,  
Technological Educational Institution of Western  
Macedonia,  
Kozani 501 00,  
Macedonia, Greece  
e-mail: nikolaos@vergina.eng.auth.gr

*Pressure-driven flows over a square cavity are studied numerically for Bingham plastics exhibiting a yield stress. The problem is encountered whenever pressure measurements are made by a drilled-hole based pressure transducer. The Bingham constitutive equation is used with an appropriate modification proposed by Papanastasiou, which applies everywhere in the flow field in both yielded and practically unyielded regions. Newtonian results are obtained for a wide range of Reynolds numbers ( $0 < Re \leq 1000$ ) for the cavity vortex position and intensity, and the excess pressure drop (entrance correction) in the system. To reduce the length of the computational domain for highly convective flows, an open boundary condition has been implemented at the outflow. For viscoplastic fluids the emphasis is on determining the extent and shape of yielded/unyielded regions along with the cavity vortex shape, size, and intensity for a wide range of Bingham numbers ( $0 \leq Bn < \infty$ ). The entrance correction is found to be an increasing sigmoidal function of the  $Bn$  number, reaching asymptotically the value of zero. It is shown that for viscoplastic fluids not exhibiting normal stresses in shear flow (lack of viscoelasticity), the hole pressure is zero opposite the center of the hole. Thus, any nonzero pressure hole measured by this apparatus would signify the presence of a normal-stress difference in the fluid. [DOI: 10.1115/1.2236130]*

*Keywords: yield stress, Bingham model, cavity flow, recirculation, inertia flow, viscoplasticity, pressure-hole error*

## 1 Introduction

An important class of non-Newtonian materials exhibits a yield stress, which must be exceeded before significant deformation can occur. A list of several materials exhibiting yield was given in a seminal paper by Bird et al. [1]. The models presented for such so-called *viscoplastic* materials included the Bingham, Herschel-Bulkley, and Casson models. Analytical solutions were provided for the Bingham plastic model in simple flow fields. Since then a renewed interest has developed among several researchers for the study of these materials in nontrivial flows (see recent review by Barnes [2]).

Because of the irregularity inherent in models with a yield stress, several methods have been proposed in the literature. The augmented Lagrangian method (ALM) [3], based on variational inequalities, is well suited for such models as evidenced in the works by Fortin et al. [4] and Huilgol and Panizza [5]. On the other hand, a variety of regularization methods have also been proposed and implemented with good results [6,7].

A popular approach to regularize the ideal Bingham model has been the exponential modification proposed by Papanastasiou [8]. With this model, Abdali et al. [9] solved the benchmark entry flow problem of Bingham plastics through planar and axisymmetric 4:1 contractions, and the exit flow problem, and determined the extrudate swell. That work showed the evolution of the phenomenon of viscoplasticity as a dimensionless yield stress or Bingham number ( $Bn$ ) increased from the Newtonian to the fully plastic limit. Further work involved non-isothermal viscoplastic simulations in entry and exit die flows of a propellant dough with the Herschel-Bulkley model [10].

In the case of inertial flows, the expansion benchmark problem

has been the object of a number of studies [11–16]. Different models of viscoplasticity have been used, and the effect of Reynolds ( $Re$ ) and Bingham ( $Bn$ ) numbers has been fully addressed.

An interesting problem of relevance to the rheological community is the pressure-driven (Poiseuille) flow over a cavity, which is used for pressure measurements by drilling a hole in the conduit and positioning a pressure transducer in the hole. In the context of viscoelastic fluids, this gives rise to the “pressure-hole error” [17,18], which can be used to measure normal stress effects. Results for viscoelastic fluids have been obtained [19,20] with good agreement between experiments and simulations. However, no work appears to have been done for viscoplastic fluids.

In the present work, we wish to examine this rheological benchmark problem of a pressure-driven flow over a square cavity for a wide range of Bingham numbers ( $0 \leq Bn \leq 3000$ ) and Reynolds numbers ( $0 \leq Re \leq 1000$ ). The results include both the yielded/unyielded regions as well as kinematic and dynamic quantities, such as vortex size and intensity and excess pressure losses (entrance correction) as functions of  $Bn$  and  $Re$  numbers.

## 2 Mathematical Modeling

The flow is governed by the usual conservation equations of mass and momentum for an incompressible fluid under isothermal, laminar flow conditions. These are:

$$\text{Mass: } \nabla \cdot \bar{u} = 0 \quad (1)$$

$$\text{Momentum: } \rho(\bar{u} \cdot \nabla \bar{u}) = -\nabla p + \nabla \cdot \bar{\tau} \quad (2)$$

where  $\bar{u}$  is the velocity vector,  $p$  is the scalar pressure, and  $\bar{\tau}$  is the extra stress tensor.

The relevant Reynolds number ( $Re$ ) for laminar flow is a measure of the convective forces compared to the viscous forces, and is defined as [11,12]:

<sup>1</sup>Corresponding author.

Contributed by the Fluids Engineering Division of ASME for publication in the JOURNAL OF FLUIDS ENGINEERING. Manuscript received December 12, 2005; final manuscript received March 9, 2006. Assoc. Editor: Dennis Siginer.

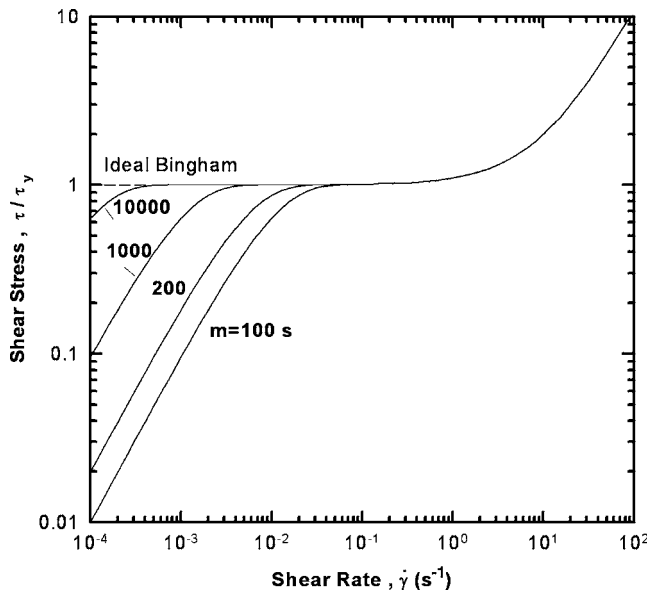


Fig. 1 Shear stress versus shear rate according to the modified Bingham constitutive equation (2) for several values of the exponent  $m$

$$Re = \frac{\rho VH}{\mu} \quad (3)$$

where  $\rho$  is the fluid density,  $\mu$  is the fluid viscosity,  $V$  is the average velocity, and  $H$  is a characteristic length, usually taken as the diameter of a pipe or the gap of a channel. The creeping flow approximation gives  $Re=0$ , while usual ranges for laminar flow are in the order of  $10^{-3} \leq Re \leq 10^{+3}$ .

For viscoplastic fluids and in order to model the stress-deformation behavior of Bingham plastics, the ideal Bingham constitutive equation has been proposed [1]. In simple shear flow it takes the form (see also Fig. 1):

$$\tau = \tau_y + \mu \dot{\gamma}, \quad \text{for } |\tau| > \tau_y \quad (4a)$$

$$\dot{\gamma} = 0, \quad \text{for } |\tau| \leq \tau_y \quad (4b)$$

where  $\tau$  is the shear stress,  $\dot{\gamma}$  is the shear rate,  $\tau_y$  is the yield stress, and  $\mu$  is a constant plastic viscosity. Note that when the shear stress  $\tau$  falls below  $\tau_y$  a solid structure is formed (unyielded). To avoid the discontinuity inherent in any viscoplastic model, Papanastasiou [8] proposed a modification in the equation by introducing a material parameter, which controls the exponential growth of stress. This way the equation is valid for both yielded and unyielded areas. Papanastasiou's modification when applied to the Bingham model becomes:

$$\tau = \tau_y [1 - \exp(-m\dot{\gamma})] + \mu \dot{\gamma} \quad (5)$$

where  $m$  is the stress growth exponent. As shown in Fig. 1, this equation mimics the ideal Bingham fluid for large enough  $m$ . In viscoplastic flows, it is customary and convenient to show the results as a function of a dimensionless yield stress  $\tau_y^*$  or Bingham number  $Bn$ , defined respectively by:

$$\tau_y^* = \frac{\tau_y H/2}{\mu V_N} \quad (6)$$

$$Bn = \frac{\tau_y H}{\mu V} \quad (7)$$

where  $H$  is a characteristic length (the channel gap),  $V_N$  is a characteristic speed taken as the average velocity of a corresponding Newtonian liquid with viscosity  $\mu$  at the same pressure gradient, and  $V$  is the average velocity of the Bingham plastic in a fully developed flow region inside a channel. In all cases, the Newtonian fluid corresponds to  $\tau_y^* = Bn = 0$ . However, at the other extreme of an unyielded solid,  $Bn \rightarrow \infty$ , while  $\tau_y^*$  reaches a dimensionless pressure gradient  $\Delta P^*$  defined by

$$(\text{planar}) \quad \Delta P^* = \left( \frac{\Delta P}{\Delta L} \right) \frac{H^2}{4\mu V_N} = 3 \quad (8)$$

In full tensorial form the constitutive equation (5) is then written as:

$$\bar{\tau} = \bar{\eta} \bar{\dot{\gamma}} \quad (9)$$

where  $\eta$  is the apparent viscosity given by

$$\eta = \mu + \frac{\tau_y}{|\dot{\gamma}|} [1 - \exp(-m|\dot{\gamma}|)] \quad (10)$$

and  $|\dot{\gamma}|$  is the magnitude of the rate-of-strain tensor  $\bar{\dot{\gamma}} = \nabla \bar{v} + \nabla \bar{v}^T$ , which is given by

$$|\dot{\gamma}| = \sqrt{\frac{1}{2} II_{\dot{\gamma}}} = \left[ \frac{1}{2} \{\bar{\dot{\gamma}} : \bar{\dot{\gamma}}\} \right]^{1/2} \quad (11)$$

where  $II_{\dot{\gamma}}$  is the second invariant of  $\bar{\dot{\gamma}}$ . To track down yielded/unyielded regions, we shall employ the criterion that the material flows (yields) only when the magnitude of the extra stress tensor  $|\tau|$  exceeds the yield stress  $\tau_y$ , i.e.,

$$\text{yielded: } |\tau| = \sqrt{\frac{1}{2} II_{\tau}} = \left[ \frac{1}{2} \{\bar{\tau} : \bar{\tau}\} \right]^{1/2} > \tau_y \quad (12a)$$

$$\text{unyielded: } |\tau| \leq \tau_y \quad (12b)$$

### 3 Method of Solution

The constitutive equation (9) for the Bingham plastic must be solved together with the conservation equations (1) and (2) and

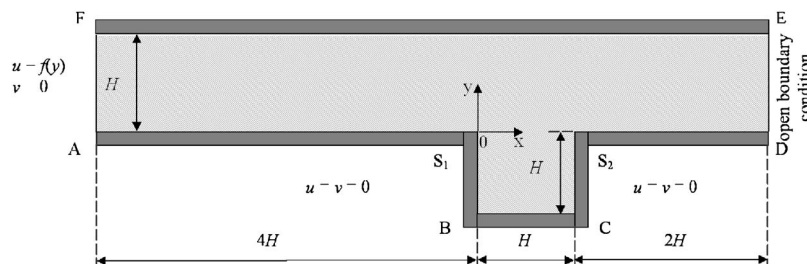
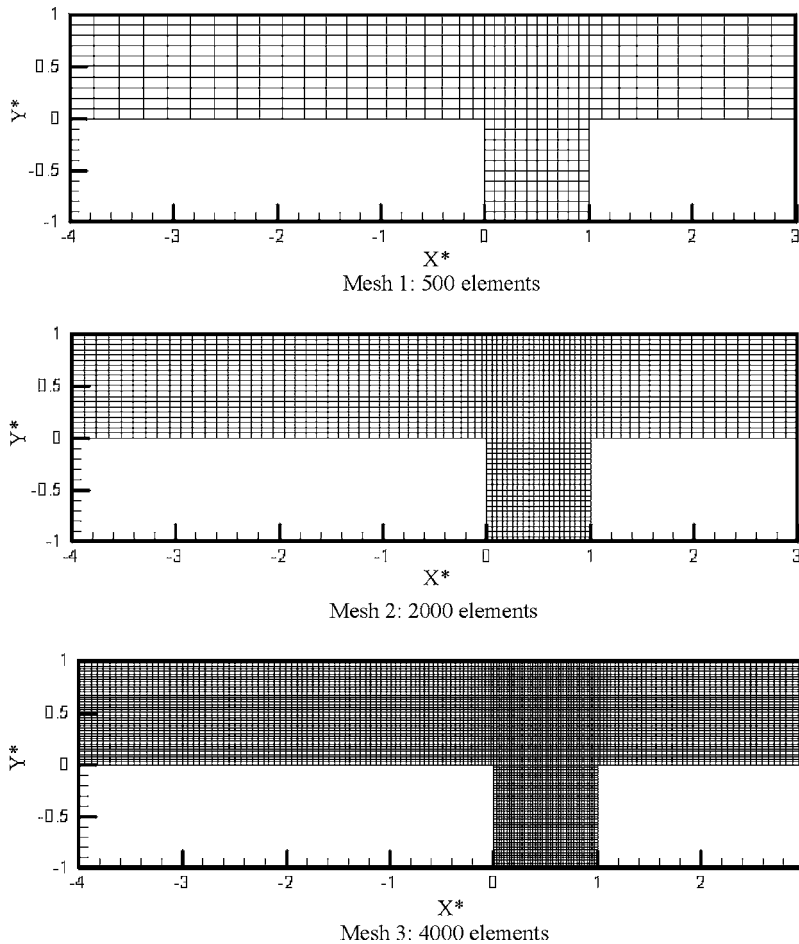


Fig. 2 Schematic diagram of pressure-driven flow over a square cavity, notation, and boundary conditions. The flow is from left to right.





**Fig. 3 Finite elements meshes used in the computations for a pressure-driven flow over a square cavity**

appropriate boundary conditions. Figure 2 shows the solution domain and boundary conditions for the pressure-driven flow over a square cavity representing the hole geometry. Note the presence of two singular points  $S_1$  and  $S_2$  at the corners of the hole-cavity. The origin is set at point  $S_1$ . The boundary conditions are set for a Cartesian coordinate system (planar geometry, see Fig. 2) [20]:

- no slip condition along the walls  $AS_1BCS_2D$  and  $EF(u=v=0)$ ,
- fully developed velocity profile ( $u(y)=f(y), v=0$ ), along the entry boundary  $AF$ ,
- *open* boundary condition [21] along the exit boundary  $DE$ .

The open boundary condition is basically the extension of the Navier-Stokes equations at the artificial outflow boundary (see below).

Because of the last boundary condition, which has been well documented and used in the past both for Newtonian [22] and

non-Newtonian flows [23], it is not necessary to extend the domain length much downstream, even for highly inertial flows. Thus, the domain length extends from  $-4H$  to  $+3H$  from the origin (point  $S_1$ ). The square cavity is of  $H \times H$  dimensions.

All lengths are scaled with the gap  $H$ , all velocities with the average Newtonian velocity  $V_N$ , and all pressures and stresses with  $\mu V_N/H$ .

The numerical solution is obtained with the finite element method (FEM), employing as primary variables the two velocities and pressure (*u-v-p formulation*) [9]. We use Lagrangian quadrilateral elements with biquadratic interpolation for the velocities and bilinear interpolation for the pressures. Whereas in our previous works [9,10,16] we have used the Picard scheme (direct substitution showing linear convergence) for the solution of the non-linear system of equations, in this work we have experimented with the Newton-Raphson iterative scheme, which shows quadratic convergence. In this case, we write the continuity and momentum equations as residuals  $R_i^C$  and  $R_i^M$ , weighted with the bilinear  $\psi^j$  and biquadratic  $\phi^j$  basis functions, respectively, over the domain  $\Omega$ :

$$R_i^C = \int \int_{\Omega^*} (\nabla^* \cdot \bar{u}^*) \psi^j d\Omega^* = \int \int_{\Omega^*} \left( \frac{\partial u^*}{\partial x^*} + \frac{\partial v^*}{\partial y^*} \right) \psi^j d\Omega^* \quad (13)$$

$$\bar{R}_i^M = \int \int_{\Omega^*} \left( \bar{u}^* \cdot \nabla^* \bar{u}^* + \nabla^* p^* - \frac{1}{\text{Re}} \nabla^* \cdot \bar{\tau}^* \right) \phi^j d\Omega^* \quad (14)$$

**Table 1 Finite element mesh characteristics used in the simulations**

F.E. mesh	No. of elements	No. of nodes	No. of unknowns	No. of nodes at inlet/outlet
Mesh 1 (M1)	500	2121	4357	21
Mesh 2 (M2)	2000	8241	17717	41
Mesh 3 (M3)	4000	16301	35707	81

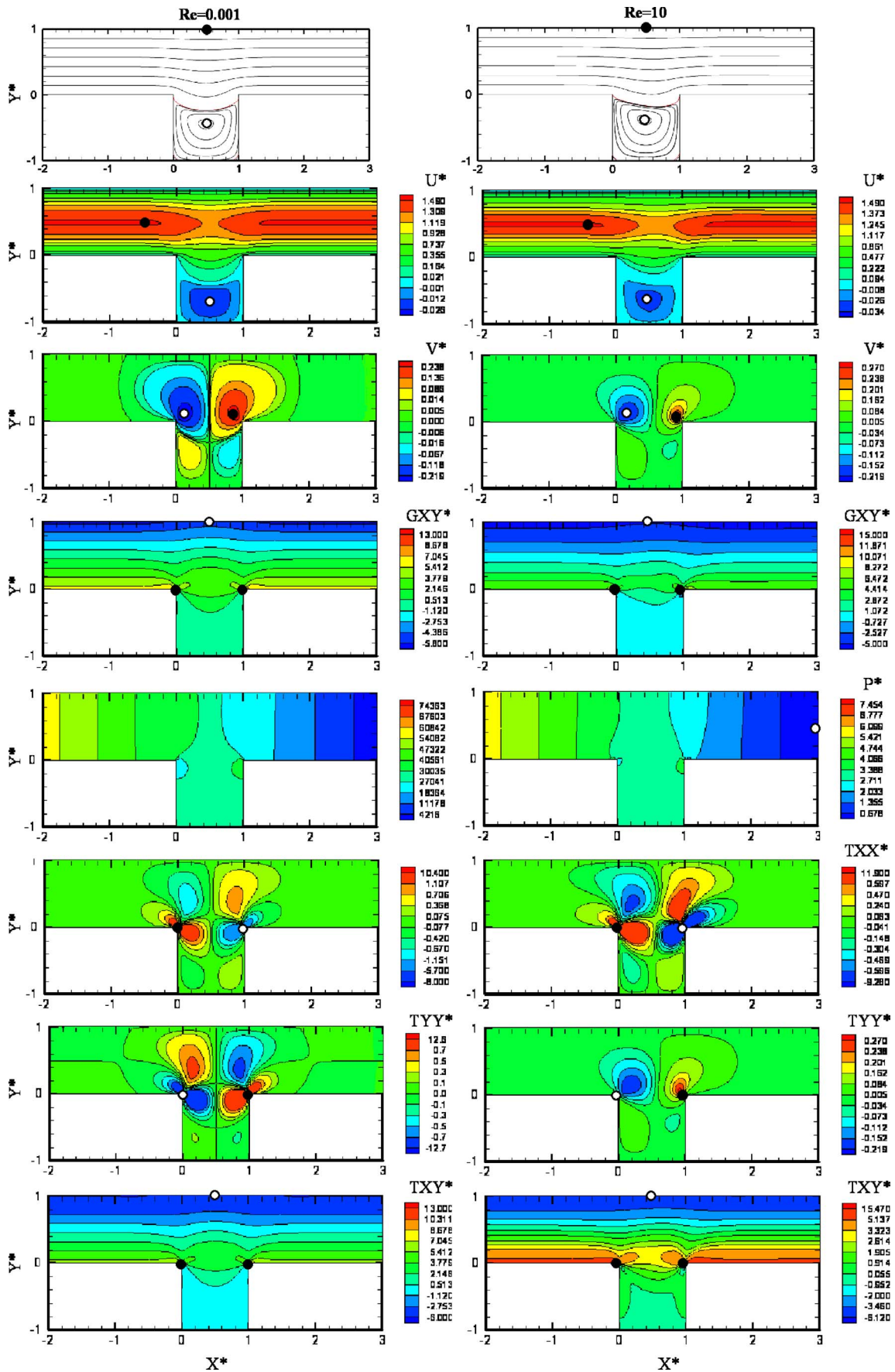


Fig. 4 Streamlines and contours of kinematic and dynamic variables for a Newtonian fluid flowing under pressure over a square cavity. Left, creeping flow,  $Re=10^{-3}$ ; right, weak inertial flow,  $Re=10$ .

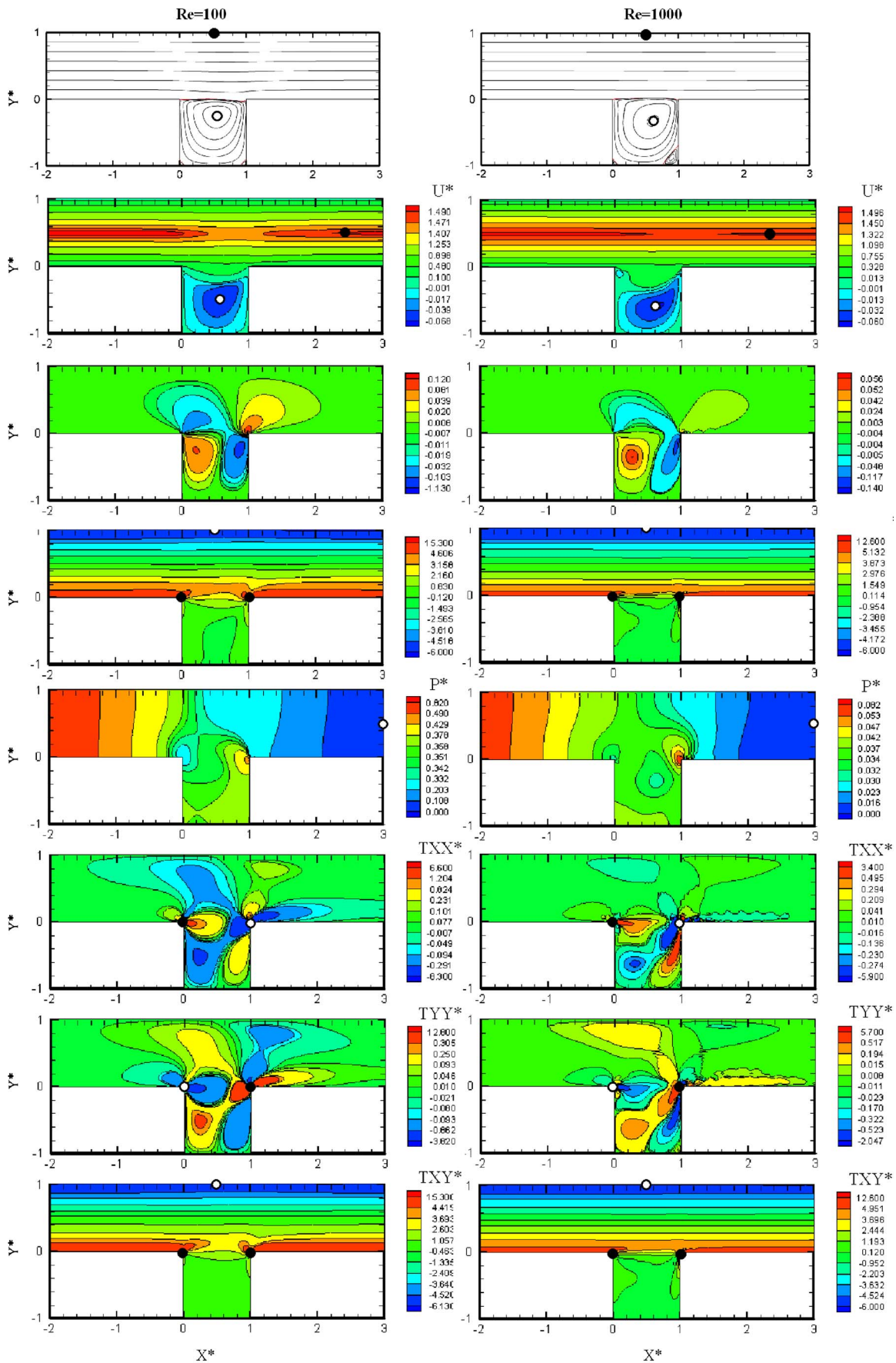


Fig. 5 Streamlines and contours of kinematic and dynamic variables for a Newtonian fluid flowing under pressure over a square cavity. Left, moderate inertial flow,  $Re=100$ ; right, strong inertial flow,  $Re=1000$ .

The momentum residuals (Eq. (14)) require further manipulations to lead to the following standard form:

$$\begin{aligned}
 \bar{R}_i^M &= \int \int_{\Omega^*} (\bar{u}^* \cdot \nabla^* \bar{u}^*) \phi^i d\Omega^* + \int \int_{\Omega^*} \left( -p^* \bar{l}^i \right. \\
 &\quad \left. + \frac{1}{\text{Re}} \bar{\tau}^i \right) \cdot \nabla^* \phi^i d\Omega^* - \int \int_{\Omega^*} \nabla^* \cdot \left[ \left( -p^* \bar{l}^i + \frac{1}{\text{Re}} \bar{\tau}^i \right) \phi^i \right] d\Omega^* \\
 &= \int \int_{\Omega^*} \left[ \left( u^* \frac{\partial u^*}{\partial x^*} + v^* \frac{\partial u^*}{\partial y^*} \right) \phi^i \right. \\
 &\quad \left. + \left( u^* \frac{\partial v^*}{\partial x^*} + v^* \frac{\partial v^*}{\partial y^*} \right) \phi^i \right] dx^* dy^* \\
 &\quad - \int \int_{\Omega^*} \left[ \frac{\partial}{\partial x^*} \left[ \left( -p^* + \frac{1}{\text{Re}} \tau_{xx}^* \right) \phi^i \right] + \frac{\partial}{\partial y^*} \left( \frac{1}{\text{Re}} \tau_{yx}^* \phi^i \right) \right] \\
 &\quad - \int \int_{\Omega^*} \left[ \frac{\partial}{\partial x^*} \left( \frac{1}{\text{Re}} \tau_{xy}^* \phi^i \right) + \frac{\partial}{\partial y^*} \left[ \left( -p^* + \frac{1}{\text{Re}} \tau_{yy}^* \right) \phi^i \right] \right] \\
 &\quad \times dx^* dy^* - \oint_{\partial\Omega_{\text{outflow}}^*} \begin{bmatrix} -p^* + \frac{1}{\text{Re}} \tau_{xx}^* \\ \frac{1}{\text{Re}} \tau_{yx}^* \end{bmatrix} \phi^i dy^* \quad (15)
 \end{aligned}$$

In the above, the stresses are expressed in terms of the velocity gradients by the constitutive equation (9). The last term in Eq. (15) represents the open boundary condition at the outflow. It is implemented by simply evaluating the surface integrals of the momentum equations in terms of the, as of yet, unknown outflow nodal values  $u-v-p$  along with the volume integrals. The stars denote dimensionless variables, while  $\partial\Omega$  is the outflow part of the boundary where integration takes place.

By taking the partial derivatives of the residuals with respect to the unknown nodal variables  $u-v-p$ , the Jacobian matrix is evaluated analytically and the nonlinear system of equations is solved by the Newton-Raphson iterative scheme, which when correctly done exhibits quadratic convergence within four to five iterations. The norm-of-the-error for convergence was set to  $10^{-8}$  for the velocities and  $10^{-6}$  for the pressures.

For smooth quadratic convergence, continuation in a parameter is necessary, and we have used many steps either by increasing the Re or Bn numbers carefully (see below). The numerical simulations have been performed with three meshes, which are shown in Fig. 3 in full view. Their characteristics are given in Table 1. Mesh 1 (M1) was used for preliminary calculations to gain experience, mesh 2 (M2) was used as the workhorse for all simulations, while mesh 3 (M3) was used for test cases to check the independence of results for such mesh refinement. Mesh 2 has 2000 quadrilateral Lagrangian elements, 8241 nodes, and 18,603 unknown degrees of freedom (DOF) with 41 points in the transverse  $y$  direction at entry.

Simulations are carried out for a wide range of Bingham numbers ( $0 \leq \text{Bn} \leq 3000$ ). In order to come as close as possible to the ideal Bingham model, we have used in the modified apparent-viscosity equation (10) a value for the dimensionless stress exponent  $M = mV_N/H = 200$ , as done also in other works [13,14]. It is well known and shown clearly in Fig. 1 that a higher value of  $m$  (hence  $M$ ) comes closer to the ideal Bingham plastic for which  $m \rightarrow \infty$ . However, as explained in detail by Alexandrou et al. [14], a very high value of  $M$  produces unrealistic and undesirable zig-zag numerical oscillations and should be avoided. Also the Newton-Raphson iterative scheme becomes very stiff to converge for  $M=1000$ , while a value of  $M=200$  was found as the best compromise between accuracy and efficiency of the numerical code.

For a given Bingham number, a zeroth-order continuation scheme has been used to increase the  $M$  parameter. The solution

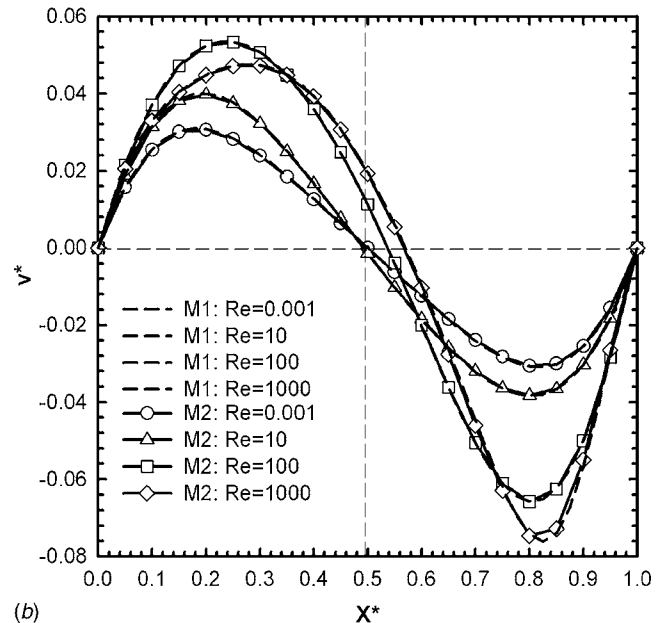
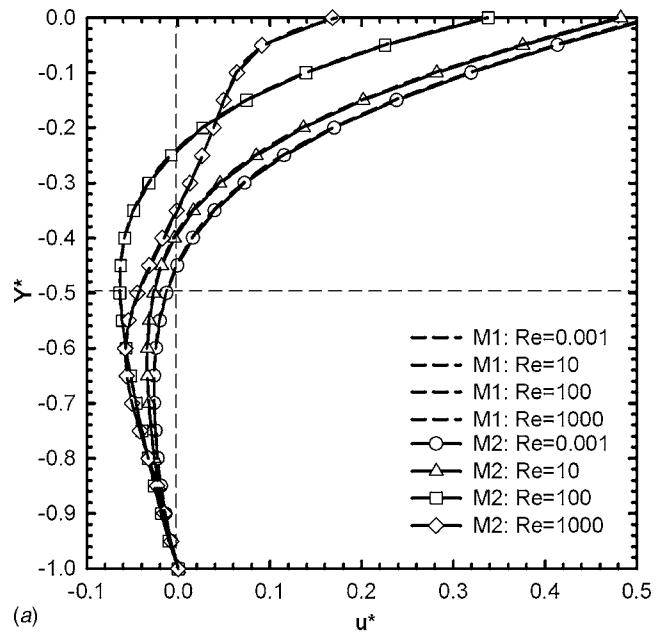


**Fig. 6 Velocity profiles: (a)  $u$  components and (b)  $v$  components in vertical and horizontal section, respectively, passing through the geometric center of the cavity ( $0.5H, -0.5H$ ) for various Re numbers**

process started from the Newtonian solution ( $M=0$ ), which was used to obtain a first approximation. Newton-Raphson iterations were performed until convergence of the solution for the current  $M$  value was achieved. The new solution was then used as an

**Table 2 Newtonian results for the characteristic variables ( $\text{Re}=10^{-3}$ )**

F.E. mesh	Vortex location ( $X_v, Y_v$ )	Vortex intensity $-\psi_{v,max}^*$ (%)	Entrance correction, $n_{en}$
Mesh 1 (M1)	(0.5, -0.45)	1.7356	-0.2427
Mesh 2 (M2)	(0.5, -0.45)	1.7553	-0.2398
Mesh 3 (M3)	(0.5, -0.45)	1.7567	-0.2397

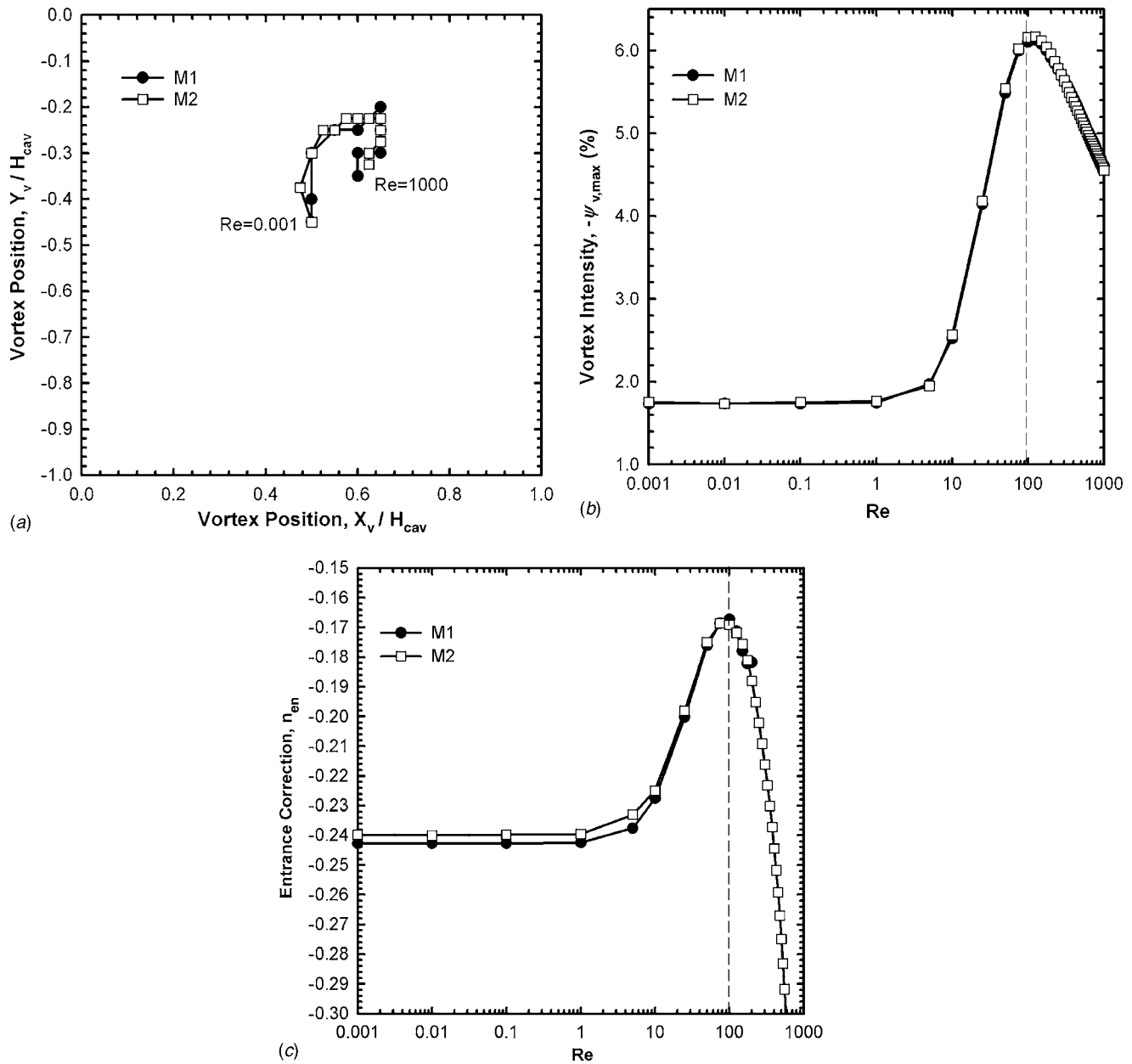


Fig. 7 (a) Location of the eye of the main vortex in the square cavity, (b) its intensity, and (c) entrance correction as a function of Re number

initial estimate for a higher  $M$  value to obtain a solution for a higher level of viscoplasticity, until the final value of  $M=200$  was reached. The converged solution at this  $M$  level was then the solution for the set Bn number. The same procedure was used when increasing the Re number, where now the continuation was simply done on the Re parameter.

## 4 Results and Discussion

**4.1 Newtonian Results.** We first applied our numerical scheme to the calculation of the laminar inertial flow of a Newtonian fluid in the range  $0.001 \leq Re \leq 1000$ . We have increased the Re number in 44 steps for this range. We present contours of the kinematic and dynamic variables for four Re numbers ( $Re = 0.001, 10, 100, 1000$ ) in Figs. 4 and 5. The dimensionless kinematic variables are the stream function  $\psi^*$ , the velocities  $U^*$  and  $V^*$  and the shear rates  $GXY^*$ . The dimensionless dynamic variables are the pressure  $P^*$ , the normal stresses  $TXX^*$ ,  $TYY^*$ , and the

shear stresses  $TXY^*$ . Eleven contours are drawn between the minimum and maximum values (0–100%) at select values to offer a better representation of the flow field. The maximum is shown as a solid circle while the minimum is an open circle. For the streamlines, the stream function has been obtained a posteriori by solving the Poisson equation with boundary conditions set to 1 on the upper wall and zero at the lower and cavity walls. Thus, the zero-line (in a color plot designated as red) separates the main flow from the flow in the cavity, where a main recirculation occurs with secondary ones at elevated Re numbers.

From these figures we can observe the following:

- For creeping flow of a Newtonian fluid ( $Re=0.001$ ), the streamlines are symmetric with regard to  $X^*=0.5$  (Fig. 4, top left). Increasing the Re number, symmetry is no longer valid, and the main recirculation in the cavity is skewed towards the right cavity lip. At the same time, its size is reduced because of the development of two sec-

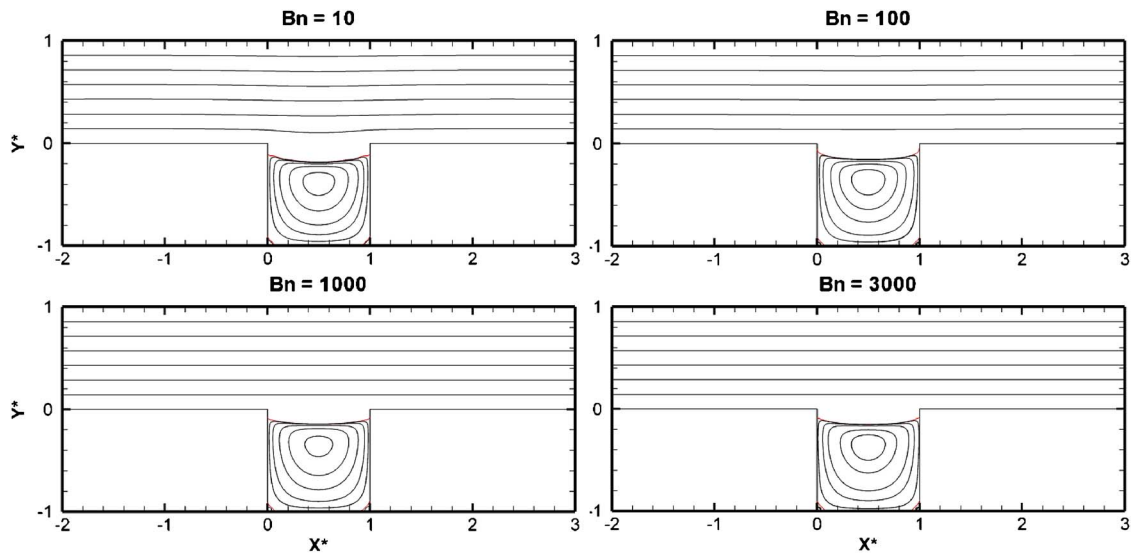


**Fig. 8** Streamlines for  $Bn=10, 100, 1000, 3000$  in creeping pressure-driven flow of a viscoplastic Bingham-Papanastasiou fluid over a square cavity ( $Re=10^{-3}$ )

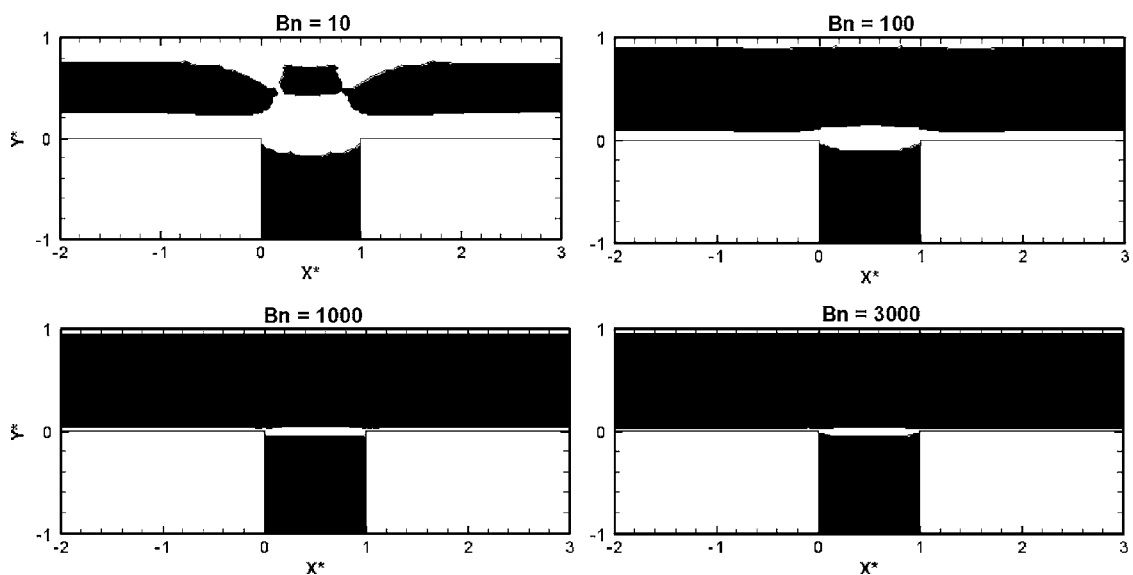
oundary recirculations appearing in the bottom corners. For  $Re=1000$  (Fig. 5, top right), the outermost streamline of the main recirculation in the cavity is parallel to the streamlines of the main flow, and there is no bending of the streamlines due to the high inertia. Also at  $Re=1000$ , from the two secondary corner vortices in the cavity, the one on the right is substantially larger than the left one.

- The isobars (Figs. 4 and 5, middle) are perpendicular to the flow in the region away from the cavity due to the fully developed flow there, especially for low to moderate  $Re$  numbers. As the  $Re$  number increases, inertia bends the isobars from the vertical. However, farther upstream (at  $-4H$ , not shown) the isobars are still perpendicular due to the fully developed flow there.
- There are stress concentrations (Figs. 4 and 5, bottom) at the singular points  $S_1$  and  $S_2$  (see also Fig. 2). At  $S_2$  the stresses are higher in absolute value than at  $S_1$ , because

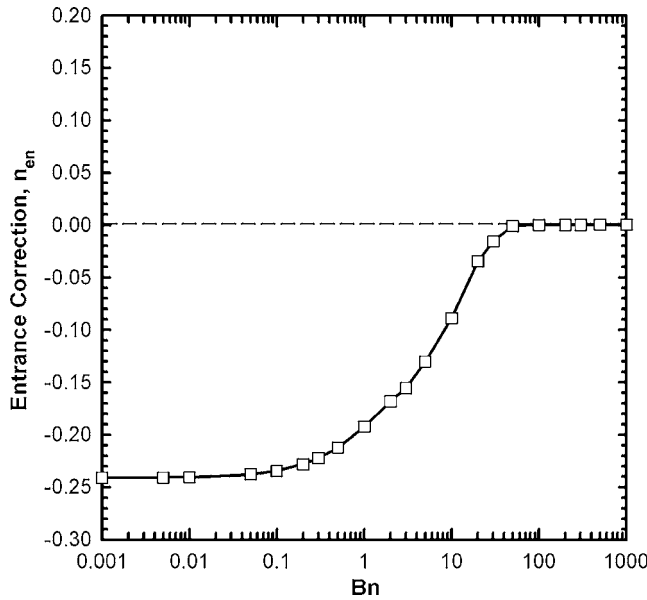
the fluid passes over  $S_1$  and hits  $S_2$  with the force of inertia. The increase in the size of the main recirculation, which is a consequence of the increasing  $Re$  number, reduces the stresses at these points because it impedes the fluid from entering into the cavity.

Figure 6 shows the customary  $u$ - and  $v$ -velocity profiles in the cavity for the four  $Re$  numbers of choice. These profiles are similar but not exactly the same to those of the lid-driven cavity problem, due to the different boundary conditions of the latter [24]. From such profiles we find the recirculation center (eye of the vortex) for various  $Re$  numbers. At this point the  $u$ - and  $v$  velocities are zero (vertical dashed line in Fig. 6(a) and horizontal dashed line in Fig. 6(b), respectively). Also in Fig. 6 results are shown from M1 (500 elements) and M2 (2000 elements) verifying the independence of these from mesh influence.

The numerical flow simulations give rise to the following quan-



**Fig. 9** Yielded/unyielded (shaded black) regions for  $Bn=10, 100, 1000, 3000$  in creeping pressure-driven flow of a viscoplastic Bingham-Papanastasiou fluid over a square cavity ( $Re=10^{-3}$ )



**Fig. 10 Entrance correction as a function of the Bn number in creeping pressure-driven flow of a viscoplastic Bingham-Papanastasiou fluid over a square cavity ( $Re=10^{-3}$ )**

titles of interest, which have been used traditionally as a measure of the flow kinematics and dynamics in contractions/expansions [11,12] and lid-driven cavities [24]:

- i. the dimensionless *vortex position*,  $(X_v^*, Y_v^*)$ , defined in the cavity by

$$X_v^* = \frac{X_v}{H_{cav}}, \quad Y_v^* = \frac{Y_v}{H_{cav}} \quad (16)$$

where  $H_{cav}=H$  is the cavity width (see Fig. 2);

- ii. the dimensionless *vortex intensity*,  $-\psi_{v,max}^*$  defined by

$$-\psi_{v,max}^* = \frac{\psi_{v,max} - \psi_{uw}}{\psi_{lw} - \psi_{uw}} \quad (17)$$

where  $\psi_{v,max}$  is the stream function value in the eye of the vortex,  $\psi_{uw}$  is the stream function value at the upper wall, and  $\psi_{lw}$  is the stream function value at the lower wall of the conduit. Note that  $-\psi_{v,max}^*$  is equivalent to the percentage of flow rate that recirculates in the cavity; and

- iii. the dimensionless *entrance correction*,  $n_{en}$ , defined by

$$n_{en} = \frac{\Delta P - \Delta P_0}{2\tau_w} \quad (18)$$

where  $\Delta P$  is the overall pressure drop in the flow domain,  $\Delta P_0$  is the pressure drop based on fully developed flow at the inlet (at  $-4H$ ), and  $\tau_w$  is the shear stress for fully developed flow at the inlet wall. It should be noted that  $\tau_w = (\Delta P_0/L)(H/2)$ , where  $L=7H$ .

The entrance correction is a very sensitive quantity as a representation of the goodness of the pressure results, as it is a difference between two big numbers ( $\Delta P$  and  $\Delta P_0$ ). For this reason both inlet and outlet profiles must be taken into account and correctly accounted for. Thus,  $\Delta P = P(-4, 1) - P(3, 1)$  is the pressure difference calculated at the upper walls at inlet and outlet. At inlet the profile must be the fully developed one, corresponding to a unit average velocity, which in the case of non-Newtonian viscoplastic fluids is found by using the first column of finite elements to solve the 1-D problem. This solution also gives the pressure

gradient and the shear stress at the wall for a fully developed shear flow. At outlet and due to the open boundary condition imposed there, the pressure values may be small but are not zero and must be taken into account in the calculation of  $\Delta P$ .

For the creeping flow case ( $Re=10^{-3}$ ), the numerical values of the above characteristic variables for the three meshes used are given in Table 2, where it becomes obvious the mesh convergence of the results with mesh refinement. The results from the overall calculations are given in Fig. 7 for the simulation range of Re numbers. We observe the following:

- The eye of the vortex shifts to the top right with increasing Re number. The uppermost point occurs at  $Re = 350$ , after which it tends to move to its initial position in a cyclic manner (Fig. 7(a)).
- The vortex intensity in the cavity increases with Re up to  $Re=100$ , reaching 6.2% of the flow rate, following which it decreases (Fig. 7(b)). The secondary recirculations increase in magnitude with Re but remain at small orders of magnitude, almost negligible in comparison to the main one.
- The same behavior as with the vortex intensity is observed with the entrance correction as a function of the Re number (Fig. 7(c)). The negative values of  $n_{en}$  correspond to the existence of subpressure in the cavity. The result for the creeping flow ( $Re=10^{-3}$ ) is  $-0.24$ , which is the limit found in hole-pressure results for Newtonian fluids [18–20]. We also note that the entrance correction is the most sensitive quantity and thus is more dependent on the mesh. For the M1 mesh, results above  $Re=100$  were not reliable.

**4.2 Viscoplastic Results.** Because of the usually high viscosity and yield stress values of viscoplastic materials, the flow of a viscoplastic fluid obeying the Bingham-Papanastasiou constitutive equation is considered creeping ( $Re=0.001$ ) and is solved in the range  $0.001 \leq Bn \leq 3000$ . Starting from a zero value for the stress exponent  $M$  (Newtonian fluid), we proceeded in 801 consecutive steps to reach the value of  $M=200$  for  $Bn=0.001$ . The same procedure was used for all Bn numbers in 5 Bn increments in every logarithmic decade to reach the highest value of 3000.

The results are presented in Fig. 8 for the streamlines for four Bn numbers (10, 100, 1000, and 3000). The stream function has been again made dimensionless taking the value of 1 on the upper wall and 0 along the lower and cavity walls. The separating streamline, which also has the value of zero, bends inside the cavity and separates the main flow in the channel from the secondary flow in the cavity. Because of the creeping flow conditions ( $Re=0.001$ ) the flow appears symmetric with regard to  $X^*=0.5$  line. The streamlines within the cavity indicate the presence of recirculation. The vortex intensities of the recirculation are in the order of  $10^{-4}\%$  of the flow rate (cf. 1.75–6% for the Newtonian inertial case for which  $Bn=0$ ) and are slightly decreasing with increasing Bn number.

The presence of recirculation is counter to what is expected from the presence of unyielded (black) regions there, which are not supposed to deform. Indeed, in Fig. 9 we see the yielded/unyielded (shaded black) regions for the same Bn numbers. Regarding the flow in the channel, as the Bn number increases, the unyielded regions get larger, leaving only small boundary yielded layers near the walls. The unyielded regions are parallel to the walls of the channel for some distance, expressing a fully developed Bingham flow there. The results in the inlet and outlet regions are fully in agreement with the 1-D solution for pressure-driven flow of a Bingham fluid between parallel walls. Regarding the flow in the cavity, it appears totally unyielded (black) for  $Bn \geq 10$ .

This rather surprising result of cavity recirculation, which has already been observed in the lid-driven cavity problem [24], is a

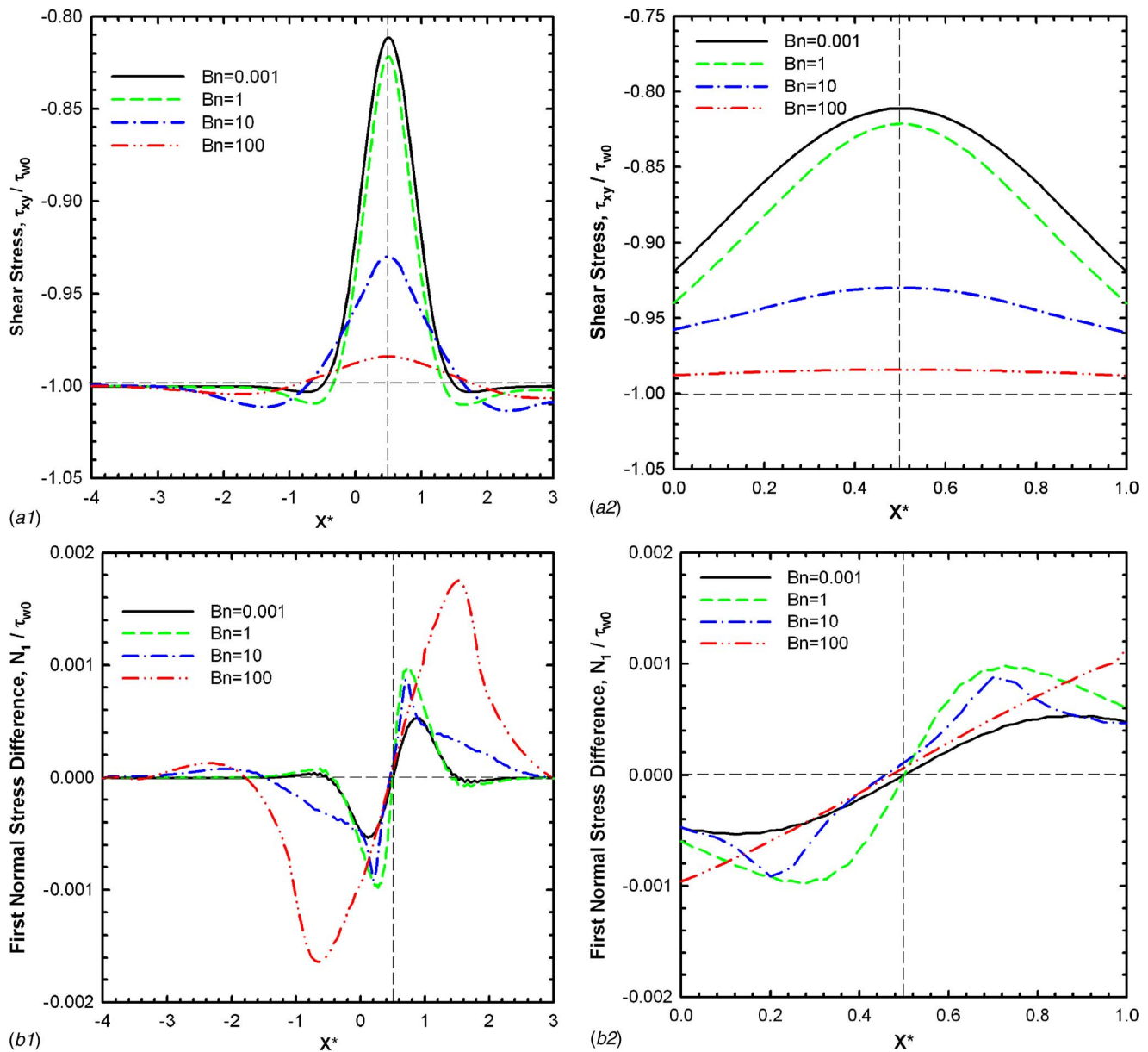


**Fig. 11** Dimensionless shear stress  $\tau_{xy}$  (a1) and first normal stress difference  $N_1$  (b1) profiles along the upper wall for different  $Bn$  numbers in creeping pressure-driven flow of a viscoplastic Bingham-Papanastasiou fluid over a square cavity ( $Re=10^{-3}$ ). Blown-up profiles along the upper wall above the cavity for  $\tau_{xy}$  (a2) and  $N_1$  (b2). Note that at  $(x,y)=(0.5,1.0)$ ,  $N_1 = \tau_{xy} = 0$  ( $\tau_{w0}$  is the fully developed shear stress value at the inlet wall).

direct consequence of using the Bingham-Papanastasiou model, which is valid in both fluid regions (yielded-unyielded). Within the cavity, the velocity and its derivatives are very small (orders of magnitude smaller than in the main flow) but not indentially zero. The area within the cavity is referred to as *apparently unyielded region* (AUR), while the unyielded region in the main flow is referred to as *truly unyielded region* (TUR). In AUR regions the velocity is nearly zero and so are its derivatives ( $\dot{\gamma} \approx 0$ ). On the other hand, in TUR regions the velocity is definitely nonzero but has a pluglike profile, leading again to its derivatives being almost zero ( $\dot{\gamma} \approx 0$ ), and the viscoplastic fluid flows fast but deforms little. So in the main flow in the conduit, the unyielded regions are TUR while in the cavity they are AUR. The cavity vortex remains similar in shape and intensity for all  $Bn$  numbers, indicating the very slow flow within, which leads to an apparently unyielded region.

Figure 10 shows the entrance correction as a function of  $Bn$ . In this case, the negative pressures (subpressures due to the cavity) start from the Newtonian creeping flow value of  $-0.24$  and increase in a sigmoidal manner, reaching asymptotically zero as  $Bn \rightarrow \infty$  (in our case for values of  $Bn > 100$ ). This result is similar in trend to previous results for the entrance correction in entry flows through contractions [9] and expansions [16] and reflects the substantial pressure needed to overcome the high yield stress effects for elevated  $Bn$  numbers. As the  $Bn$  number becomes very high, all the material passes essentially over the cavity corresponding to a fully developed pluglike flow in the channel with no excess pressure losses, thus resulting in a zero entrance correction.

Returning to the pressure-hole method, it is known from viscoelastic computations [18–20] that the limit of the hole pressure  $P_H$  is given by



$$P_H = -cN_1, \quad (19)$$

where  $P_H$  is the pressure at the upper wall opposite the center of the cavity; here at  $(x, y) = (0.5, 1.0)$ ,  $N_1 = \tau_{xx} - \tau_{yy}$  is the first normal stress difference, and  $c$  a constant, which equals either 0.25 from theory [18] or 0.24 from computations [20]. Another formula for  $P_H$  is given by Higashitani and Pritchard's theory [19,20] as the integral:

$$P_H = - \int_0^{\tau_w} \frac{N_1}{2\tau} d\tau, \quad (20)$$

where  $\tau_w$  is the shear stress at the wall unperturbed by the presence of the slot, and  $\tau$  is the shear stress. The two formulas have been shown to give similar results for viscoelastic flows [20].

It is well known that for Newtonian fluids  $P_H = 0$ , and the streamlines are symmetric about the centerline of the hole. The same is expected to hold for viscoplastic fluids without inertia, where again symmetric streamlines are found. To check the validity of this assumption, we plot in Fig. 11 the values of  $N_1$  and  $\tau_w$  along the upper wall for different values of Bn. We observe that there is antisymmetry in the profiles, but right at  $(x, y) = (0.5, 1.0)$ ,  $N_1 = \tau_{xy} = 0$ . Either Eq. (19) or (20) would give a zero value for  $P_H$ . This was borne out by our computations. Thus, any nonzero value found in experiments with such a device serves to indicate the presence of viscoelastic effects in the viscoplastic fluid, which may be the case for some visco-plastic-elastic materials, such as propellant doughs [25].

## 5 Conclusions

Finite element simulations were carried out for pressure-driven flows of Newtonian fluids and Bingham plastics over a square cavity corresponding to the pressure-hole method for measurements with a transducer. The Bingham constitutive equation was modified as proposed by Papanastasiou [8] with an exponential growth term to make it valid in both the yielded and unyielded regions, thus eliminating the need for tracking the location of yield surfaces. An open boundary condition at the outlet [21] allowed solutions for high Re number flows ( $Re = 1000$ ) in a short domain without encountering any problems of convergence with the Newton-Raphson iterative scheme.

The present results offer benchmark solutions for inertial flows of Newtonian fluids regarding kinematic and dynamic variables, including the vortex location in the cavity and its intensity, as well as the associated excess pressure drop in the system (entrance correction) as a function of the Re number. For viscoplastic Bingham fluids and creeping flow conditions, it was noted that this type of flow gives rise to unyielded regions in the main flow and in the cavity, called truly unyielded (TUR) and apparently unyielded (AUR), respectively. These regions increase as the dimensionless yield stress or Bingham number increases. Furthermore, the extent and shape of yielded/unyielded regions have been well captured using the criterion of the magnitude of the extra stress tensor exceeding the yield stress. The entrance correction increases substantially in a sigmoidal form and reaches asymptotically zero as  $Bn \rightarrow \infty$ . Finally, it was verified that the pressure-hole method for purely viscoplastic fluids will not work, since the hole pressure is zero. Thus, any nonzero measurements will indicate the presence of viscoelasticity in the material.

## Acknowledgment

Part of this research is supported by the "HERAKLEITOS" program of the Ministry of Education and Religious Affairs of Greece (No. 68/0655). The project is co-funded by the European Social Fund (75%) and National Resources (25%). Financial support from "HERAKLEITOS" is gratefully acknowledged.

## References

- [1] Bird, R. B., Dai, G. C., and Yarusso, B. J., 1983, "The Rheology and Flow of Viscoplastic Materials," *Rev. Chem. Eng.*, **1**, pp. 1–70.
- [2] Barnes, H. A., 1999, "The Yield Stress—A Review or *πάντα ρεῖ*—Everything Flows?," *J. Non-Newtonian Fluid Mech.*, **81**, pp. 133–178.
- [3] Fortin, M., and Glowinski, R., 1983, *Augmented Lagrangian Methods*, North-Holland, Amsterdam.
- [4] Fortin, A., Côté, D., and Tanguy, P. A., 1991, "On the Imposition of Friction Boundary Conditions for the Numerical Simulation of Bingham Fluid Flows," *Comput. Methods Appl. Mech. Eng.*, **88**, pp. 97–109.
- [5] Huilgol, R. R., and Panizza, M. P., 1995, "On the Determination of the Plug Flow Region in Bingham Fluids Through the Application of Variational Inequalities," *J. Non-Newtonian Fluid Mech.*, **58**, pp. 207–217.
- [6] Bercovier, M., and Engelman, M., 1980, "A Finite-Element Method for Incompressible Non-Newtonian Flows," *J. Comput. Phys.*, **36**, pp. 313–326.
- [7] O'Donovan, E. J., and Tanner, R. I., 1984, "Numerical Study of the Bingham Squeeze Film Problem," *J. Non-Newtonian Fluid Mech.*, **15**, pp. 75–83.
- [8] Papanastasiou, T. C., 1987, "Flow of Materials With Yield," *J. Rheol.*, **31**, pp. 385–404.
- [9] Abdali, S. S., Mitsoulis, E., and Markatos, N. C., 1992, "Entry and Exit Flows of Bingham Fluids," *J. Rheol.*, **36**, pp. 389–407.
- [10] Mitsoulis, E., Abdali, S. S., and Markatos, N. C., 1993, "Flow Simulation of Herschel-Bulkley Fluids Through Extrusion Dies," *Can. J. Chem. Eng.*, **71**, pp. 147–160.
- [11] Scott, P. S., Mirza, F., and Vlachopoulos, J., 1988, "Finite-Element Simulation of Laminar Viscoplastic Flows With Regions of Recirculation," *J. Rheol.*, **32**, pp. 387–400.
- [12] Scott, P. S., Mirza, F. A., and Vlachopoulos, J., 1986, "A Finite Element Analysis of Laminar Flows Through Planar and Axisymmetric Abrupt Expansions," *Comput. Fluids*, **14**, pp. 423–432.
- [13] Burgos, G. R., and Alexandrou, A. N., 1999, "Flow Development of Herschel-Bulkley Fluids in a Sudden Three-Dimensional Square Expansion," *J. Rheol.*, **43**, pp. 485–498.
- [14] Alexandrou, A. N., McGilvray, T. M., and Burgos, G., 2001, "Steady Herschel-Bulkley Fluid Flow in Three-Dimensional Expansions," *J. Non-Newtonian Fluid Mech.*, **100**, pp. 77–96.
- [15] Alleborn, N., Nandakumar, K., Raschler, H., and Durst, F., 1997, "Further Contributions on the Two-Dimensional Flow in a Sudden Expansion," *J. Fluid Mech.*, **330**, pp. 169–188.
- [16] Mitsoulis, E., and Huilgol, R. R., 2004, "Entry Flows of Bingham Plastics in Expansions," *J. Non-Newtonian Fluid Mech.*, **122**, pp. 45–54.
- [17] Bird, R. B., Armstrong, R. C., and Hassager, O., 1987, *Dynamics of Polymeric Liquids, Vol. 1: Fluid Mechanics*, 2nd ed. Wiley, New York.
- [18] Tanner, R. I., 2000, *Engineering Rheology*, 2nd ed., Oxford P., Oxford.
- [19] Tanner, R. I., 1988, "Pressure-Hole Errors—An Alternative Approach," *J. Non-Newtonian Fluid Mech.*, **28**, pp. 309–318.
- [20] Sugeng, F., Phan-Thien, N., and Tanner, R. I., 1988, "A Boundary-Element Investigation of the Pressure-Hole Effect," *J. Rheol.*, **32**, pp. 215–233.
- [21] Papanastasiou, T. C., Malamataris, N., and Ellwood, K., 1992, "A New Out-flow Boundary Condition," *Int. J. Numer. Methods Fluids*, **14**, pp. 587–608.
- [22] Heinrich, J. C., and Vionnet, C. A., 1995, "On Boundary Conditions for Unbounded Flows," *Commun. Numer. Methods Eng.*, **11**, pp. 179–185.
- [23] Park, S. J., and Lee, S. J., 1999, "On the Use of Open Boundary Condition Method in the Numerical Simulation of Non-isothermal Viscoelastic Flow," *J. Non-Newtonian Fluid Mech.*, **87**, pp. 197–214.
- [24] Mitsoulis, E., and Zisis, T., 2001, "Flow of Bingham Plastics in a Lid-Driven Square Cavity," *J. Non-Newtonian Fluid Mech.*, **101**, pp. 173–180.
- [25] Carter, R. E., and Warren, R. C., 1987, "Extrusion Stresses, Die Swell, and Viscous Heating Effects in Double-Base Propellants," *J. Rheol.*, **31**, pp. 151–173.

# Air Flow Through Compressed and Uncompressed Aluminum Foam: Measurements and Correlations

**Nihad Dukhan**

Associate Professor  
Department of Mechanical Engineering,  
University of Detroit Mercy,  
Detroit, MI 48221  
e-mail: nihad.dukhan@udmercy.edu

**Rubén Picón-Feliciano**

Undergraduate Student  
Department of Mechanical Engineering,  
University of Puerto Rico-Mayagüez,  
Mayagüez, PR 00681  
e-mail: ruben-picon@hotmail.com

**Ángel R. Álvarez-Hernández**

Thermal Analyst  
NASA Johnson Space Center,  
Houston, TX 77058  
e-mail: angel-alvarez-hernandez@yahoo.com

*Wind-tunnel steady-state unidirectional pressure-drop measurements for airflow through nine compressed and uncompressed isotropic open-cell aluminum foam samples, having different porosities and pore densities, were undertaken. The compressed foam produced significantly higher pressure drop, which increased with increasing Darcian velocity following the quadratic Forchheimer equation. The permeability and the inertia coefficient data for the compressed foam showed less scatter compared to those for the uncompressed foam. Both were correlated using an Ergun-like equation, with the correlation being better for the permeability. The permeability correlation predicted the results of some previous studies very well. The friction factor correlated well with the Reynolds number. [DOI: 10.1115/1.2236132]*

*Keywords: pressure drop, permeability, metal foam, porous media*

## Introduction

Metal foams are a relatively new class of materials with low densities and novel thermal, mechanical, and acoustic properties. They were initially developed in 1960s by the US Navy for cooling interballistic missile components and were maintained under secrecy until the early 1980s when they became commercially available in the US. Recently (1990s) they have been considered by the academic enterprise. The recent development of a variety of processes for producing them at lower cost, yet with improved properties, has increased their applications [1]. They have been used in aerospace applications [2,3], geothermal operations, and petroleum reservoirs [4]. Nickel foams have been used in high-power batteries for portable electronics [3]. Some metal foams have been considered for use in fuel cells [5], while others are used in many chemical and medical applications [6], and by the electrochemical industry [1]. As the mother metal, aluminum has emerged as the prime material due to its low density, high thermal conductivity, and its relatively low price.

Thermal management applications of metal foams include compact heat exchangers for airborne equipment and compact heat sinks for power electronics [2]. The open porosity, low relative density, and high thermal conductivity of the cell edges, large accessible surface area per unit volume, and the ability to mix the cooling fluid by promoting eddies [7] all make metal foam thermal management devices efficient, compact, and light-weight.

Due to their novelty and random structure, metal foams are still incompletely characterized. The recent upsurge of utilizing them in contemporary technologies makes the need for fully characterizing them more urgent. Central to this need is an accurate evaluation of the flow characteristics to assist in any trade-off analysis between the increased heat transfer and the associated increase in the pressure drop for foam heat exchanger and heat sink designs. An extensive review of the topic of fluid flow in porous media in general can be found in [8–11].

The porous matrix of metal foam consists of tortuous irregularly shaped flow passages with a continuous disruption of any

hydrodynamic and thermal boundary layers. The flow recirculates at the back of the solid fibers, and turbulence and unsteady flows usually occur [12]. The geometric complexity prevents exact solutions of the transport equations inside the pores [7,13,14]. This led researchers to rely heavily on experimentation and empirical models, and to a lesser degree on analytical models, as described below.

Seguin et al. [15] provided experimental characterization of flow regimes in various porous media. The onset of turbulent regime for the Reynolds number based on the pore diameter was 470. This corresponds to 0.093 using the permeability-based Reynolds number,  $Re_K$ . Lage and Antohe [13] revisited the famous report of Darcy and argued that the ratio between the form and the viscous forces should be used to mark the transition from the linear to the quadratic regimes of the pressure drop behavior. They concluded that the transition is media specific and depends on the internal geometry of the porous medium.

Decker et al. [16] provided detailed experimental characterization and numerical modeling of the heat and mass transport in highly porous nickel-chromium alloy foam. They used an additional pressure drop term in the momentum equation, which depended on the properties of the foam. The fluid flow models for packed beds did not apply to metal foam, but they contained and described all the relevant transport effects [16].

Bastawros [7] and Bastawros et al. [12] provided experimental measurements of the thermal and hydraulic aspects of cellular metals subject to transverse airflow in the transition regime, i.e.,  $Re_K \sim 1.01$ . They used 30 pore per inch (ppi) open cell aluminum foam with a porosity of 91.5%. The pressure drop followed a power law when plotted against the flow velocity.

Crosnier et al. [5] studied 20 and 40 ppi aluminum foam and 20 ppi stainless steel foam using air. All the porosities were above 90%. The transition from the laminar to the turbulent regime took place at a Darcian velocity of about 1 m/s. They stated that the larger the pore diameter (i.e., the smaller the ppi) the higher the permeability  $K$  and the smaller the pressure drop; and that the smaller the pore size, the higher the surface area and thus the higher the mechanical energy dissipation.  $K$  scaled well with the square of the pore size, while the non-Darcian permeability (called the passability), which is the ratio of the inertia coefficient  $c$  to the square root of  $K$ , scaled well with the pore size. The

Contributed by the Fluids Engineering Division of ASME for publication in the JOURNAL OF FLUIDS ENGINEERING. Manuscript received June 17, 2005; final manuscript received January 31, 2006. Review conducted by Joseph Katz.

permeability and the passability were functions of the porosity, the pore size, the surface area, and the solid structure of the foam.

Khayargoli et al. [6] studied the relationship between the permeability and the structural parameters for air flow in nickel and nickel-chromium foams. The velocity ranged from 0 to 15 m/s, while the porosity ranged from 83 to 90%. As the pore size decreased, the surface area increased, creating additional flow resistance. Increasing the thickness of the foam in the flow direction did not affect  $K$ .  $K$  increased and  $c$  decreased with increasing the pore diameter, but did not show any clear correlation with the porosity. They argued that for large-pore foam,  $K$  was large and the pressure drop was mainly due to form drag force. For this case the pressure drop correlated with the square of the velocity. The two types of foam tested produced different values of  $K$  and  $c$  which was due to the difference in their structure. They concluded that while the flow in the foam is very complex,  $K$  and  $c$  could be predicted by an Ergun-like model using appropriate constants. The Ergun model will be presented later.

Tadrist et al. [17] investigated the use of aluminum foam for compact heat exchangers. The porosities of the foam were over 90%. They experimentally determined  $K$  and  $c$  and used an Ergun-type relation between the pressure drop and the velocity in the foam.

Kim et al. [18] carried out systematic experiments to study the friction and the heat transfer characteristics of porous fins in a plate-fin heat exchanger using water. The foam fins had porosity in the range 89 to 96% and a thickness of 3 cm (1.18 in.) in the flow direction. Both the friction and the heat transfer were significantly affected by the permeability and the porosity of the foam fin. They determined the permeability using the Forchheimer model and correlated the friction factor with the Reynolds number, the Darcy number, and the geometry.

Paek et al. [19] experimentally determined the permeability and the Ergun's coefficient (same as the inertia coefficient  $c$ ) for water flow through aluminum foam in the porosity range of 89 to 96%. At a fixed porosity, as the cell size decreased, the surface-area-to-volume ratio increased, which increased the resistance to the flow and thus lowered the permeability and increased the pressure drop. The friction factor was correlated with the  $Re_K$ . The inertia coefficient was very sensitive to the roughness of the foam, which depended on the shape of the ligament and the cell structure.

Current models for packed beds are not suitable for high porosity metal foam [4] due to the vast different structure of the foam. Bhattacharya et al. [20] provided analytical and experimental results for the permeability and the friction coefficient for aluminum foam. They represented the foam by a two-dimensional array of hexagonal cells and proposed models for the inertia coefficient and the friction factor. Experiments covered the high range of porosities from 90 to 98% and pore densities of 5, 10, 20, and 40 ppi.  $K$  increased with the pore diameter and the porosity, while the friction factor depended only on the porosity. They used the Forchheimer equation to describe the pressure drop in the foam, which was fully saturated with air and water separately.

Du Plessis et al. [21] provided a geometrical model for the fluid dynamics in metal foam. The model was verified using water and a glycerol solution flow in metallic foams having 45, 60, and 100 ppi, and porosities of 97.8, 97.5, and 97.3%, respectively. Fourie and Du Plessis [22] enhanced the above work by developing expressions for the characteristic dimension as a function of the cell size and the porosity. They applied the new model to the experimental results of Bastawros et al. [12]. The characteristic dimension correlated well with the cell size.

Despois and Mortensen [23] presented a microstructure-based model for the permeability of porous metal, and used pure aluminum foam saturated with water and glycerin separately, to validate the model. The porosity ranged from 69 to 88%. The Darcy-regime data showed a strong dependence of the permeability on the square of the pore size.

Boomsma et al. [24] modeled the flow in aluminum foam using

a periodic unit of eight cells. The pressure drop predicted by the model was 25% lower than values obtained by experiment. This difference was reduced to 12% after the wall effects were included in the simulation, which were probably important due to the small size of the foam sample (12 mm by 38 mm by 80 mm long). The Reynolds number based on the pore diameter was more applicable than the permeability-based Reynolds number for metal foams. The surface area controlled the viscous drag, which was the dominant factor for the pressure drop in the foam.

Few researches [25–28] used three-dimensional x-ray computed tomography to investigate the microstructure of metal foam. Olurin et al. [27] indicated that it was unclear how to precisely characterize the microstructure and the internal architecture of the foam, and that there was no simple standard experimental technique for such characterization. Scheffler et al. [28] studied some 20 ppi aluminum foam's morphology and reported that the pores were nearly sphere-like. The ligament diameter showed a maximum at 0.25 mm (0.009 in.) and the cell size showed a bimodal distribution with maxima at 0.75 and 1.9 mm cell diameter (0.029 and 0.074 in.)

Zhou et al. [1] investigated the microstructure and macrostructure of aluminum foam using a combination of optical and scanning electron microscopy. They noted that the cells in 10, 20, and 40 ppi foam were elongated, and that the actual structure was somewhat different from the tetrakaidecahedron model that had been accepted and used to describe the cells. They recorded significant variations in both the face size and the ligament length. In addition, there were numerous closed-cell faces observed [20,24].

The high range of porosities (>90%) of uncompressed foam is not optimal for heat exchange devices. They are structurally weak and the moderate enhancement in the heat transfer does not justify the increase in the pressure drop. For the foam to be an excellent heat transfer medium with justifiable pressure drop, it needs to be compressed to lower porosities, i.e., 70 to 80%, when using air as the working fluid. Compressing the foam increases the metal density, makes the foam more suitable for brazing, which improves the heat transfer across the solid-foam interface, and improves the structural rigidity. It also substantially increases the surface area density, which enhances the heat transfer in the foam.

Compressed foam received relatively little attention. There are only two sets of data available in the open literature that are summarized here. References [14,29–31] studied 40 ppi compressed foam, while [14] studied compressed 10 ppi foam. Boomsma et al. [29] and Boomsma and Poulikakos [30] measured the hydraulic and thermal performance of open-cell, 40 ppi aluminum foam, compressed and uncompressed, with porosities between 60.8 and 88.2%. They used the Forchheimer equation to fit their experimental pressure drop data. The compressed foam heat exchangers generated thermal resistances that were two to three times lower than the commercially available heat exchangers, while requiring the same pumping power. Decreasing the pore diameter dramatically decreased the permeability and increased the form coefficient. No correlations were given by [29] and [30].

Lage et al. [13] presented experimental pressure drop data for airflow through compressed 40 ppi metal foam with porosities in the range 32 to 62%. For  $Re_K \sim O(10)$ , there was a third regime beyond the Forchheimer region in which the pressure drop correlated with the velocity using a cubic polynomial.

Hwang et al. [14] studied the friction drag for airflow in compressed aluminum foam initially having 10 ppi and porosities of 70, 80, and 95%. The permeability and the inertia coefficient were determined from the Forchheimer relation. The friction factor was correlated with the Reynolds number using a power law. It increased with decreasing the porosity at a fixed Reynolds number. The best thermal performance was for the 80% porous foam for a given pumping power. No correlations were given for the permeability or the inertia coefficient.

Antohe et al. [31] experimentally determined the permeability and the inertia coefficients for air and poly-alpha-olefin oil flow in

compressed 40 ppi aluminum foam in the porosity range of 30 to 70%. The permeability decreased with decreasing the porosity. The inertial coefficient did not have a monotonic variation, but a general tendency to increase with decreasing porosity. They used the permeability-based Reynolds number of one to indicate the transition from the linear to the quadratic regimes of the pressure drop. The discrepancy between the results obtained with air and oil were 18% for the permeability and 51% for the inertia coefficient.

In general metal foam has not been studied to the same extent as that of other types of porous materials. Paek et al. [19] observed that the experimental pressure drop data for metal foam in the literature seemed to be at variance with each other. For packed beds, such data are substantially consistent.

While compressed 40 ppi [30,31] and 10 ppi [14] foam were tested, the 20 ppi compressed foam has never been tested, to the knowledge of the current authors. It has different geometrical parameters, which may offer some performance gains over the other pore densities. In addition, there are no correlations for the inertia coefficient or the permeability in the previous studies. The existing analytical models [20–22], on the other hand, all assume uniform cell structure, which is not applicable to the deformed cells of compressed foam.

This study presents the experimental results of airflow through a considerable spectrum of commercially available aluminum foam—compressed and uncompressed, including the 20 ppi foam. It also provides an empirical model for the pressure drop in metal foam using easily measurable parameters. It proposes that the Ergun-type dependence of the permeability on the porosity is valid, and it determines a few coefficients from experiments. The new information and correlations provided by the present work are crucial for computing the pumping power for foam heat exchanger designs and optimization.

## Empirical Model

For high enough flow velocities ( $>0.1$  m/s [30]), form drag becomes important and a second order polynomial is used to describe the pressure drop in the foam, which is named the Forchheimer equation (also the Forchheimer extended Darcy's equation and the Hazen-Dupuit-Darcy equation):

$$\frac{\Delta p}{L} = \frac{\mu}{K} V + \frac{\rho c}{\sqrt{K}} V^2 \quad (1)$$

where  $L$  is the length of the porous medium in the flow direction,  $c$  is a dimensionless form drag coefficient, and  $K$  is the permeability, both of which are strongly dependent on the structure of the porous medium. The Darcian velocity  $V$  (also called the superficial or the seepage velocity) is calculated by dividing the volumetric flow rate by the cross-sectional area. For creeping flow (very low speed) in porous media, the first order term is the only term present, and Eq. (1) reduces to the famous Darcy's law [9].

The Ergun model is a pioneer empirical relation for describing the pressure drop through porous media based on the porosity and a geometrical length scale [5]:

$$\frac{\Delta p}{L} = A \frac{(1-\varepsilon)^2 H \mu}{\varepsilon^3 d_{par}^2} V + B \frac{(1-\varepsilon) H \rho}{\varepsilon^3 d_{par}} V^2 \quad (2)$$

where  $A$  and  $B$  are empirical constants,  $H$  is the height of the porous bed, and  $d_{par}$  is the particle diameter. This model was originally developed for porous beds made out of solid spherical particles.

The pressure drop in metal foam depends on the microstructure, which is characterized by the porosity (or the relative density), cell size, cell shape, and the morphology of the ligaments forming the network of pores. The main difficulty in modeling the flow through metal foam lies in accurately determining the structural characteristics of the foam. Khayargoli et al. [6] argued that there was a difficulty in assuming that the three-dimensional web-like

cellular structure of metal foam has a corresponding particle diameter. Zhou et al. [1] noted that the cells in aluminum foam were elongated, and that the actual structure was somewhat different from the uniform tetrakaidecahedron shape that has been used to model the cells [20,24]. Reference [1] recorded significant variations in both the face size and the ligament length. In addition, there were numerous closed-cell faces observed. These issues are further complicated by compressing the foam. If the compression is done in one direction, the geometrical arguments of Refs. [20–22] do not apply, as the cells are significantly deformed. Therefore we have to rely on empirical models. The current analysis will use the following Ergun-like model:

$$\frac{\Delta p}{L} = \alpha \left( \frac{(1-\varepsilon)^2}{\varepsilon^3 d} \right)^m \mu V + \beta \left( \frac{(1-\varepsilon)^2}{\varepsilon^3 d} \right)^n \rho V^2 \quad (3)$$

where  $\alpha$  and  $\beta$  are empirical constants (to be determined by experiment) that depend on the actual geometry of the foam and  $d$  is the mean ligament diameter. The other geometrical characteristics of the foam will be combined in the values of the exponents  $m$  and  $n$ , which will be determined by the experiment as well. These exponents are used to capture the difference in the architecture between open-cell metal foam and other porous media. Using the ligament diameter as the length scale simplifies the analysis and avoids making further idealizations regarding the foam structure. Also, the diameter is an easily measurable quantity using common microscopy. Even though it exhibits some variations, a mean value can be usually ascertained.

Comparing the empirical model in Eq. (3) to Eq. (1), we obtain

$$K = \frac{1}{\alpha} \left( \frac{(1-\varepsilon)^2}{\varepsilon^3 d} \right)^{-m} \quad (4)$$

$$c = \frac{\beta}{\sqrt{\alpha}} \left( \frac{(1-\varepsilon)^2}{\varepsilon^3 d} \right)^{n-m/2} \quad (5)$$

The friction factor for porous media is given by [14,20,29]

$$f = \frac{(\Delta p/L) \sqrt{K}}{\rho V^2} \quad (6)$$

It is expected to correlate with the Reynolds number using a power law [14,18]:

$$f = a(\text{Re}_K)^b \quad (7)$$

where  $a$  and  $b$  are constants to be determined from the experimental data, and the Reynolds number based on the permeability as the length scale is given by [24]

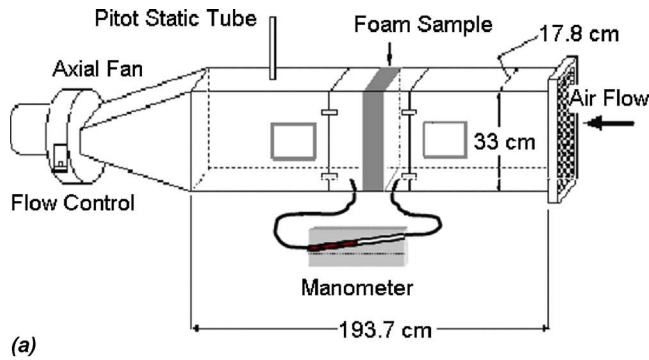
$$\text{Re}_K = \frac{\rho V \sqrt{K}}{\mu} \quad (8)$$

Some researches [14,30] used the pore diameter as the length scale.

## Experiment

Experiments were performed in a small open-loop tunnel shown schematically in Fig. 1(a). Room air was forced to flow into this tunnel by a suction fan located close to its exit. The exit had a sliding plate that changed the size of the exit area, thus controlling the volumetric flow rate through the tunnel. A 5 cm (2 in.) thick section of flow straightener was placed close to the entrance. The size of the tunnel's test section was 14.9 cm by 30.2 cm (5.875 in. by 11.875 in.), and it had an integrated Pitot-static tube connected to a manometer for pressure measurements in mm of water.

A total of nine samples of commercially available aluminum foam (manufactured by ERG Materials and Aerospace) were separately investigated. Each sample measured 5.08 cm (2.00 in.) in



(a)



(b)

Fig. 1 (a) Schematic of wind tunnel. (b) Photograph of foam sample mounted in test section.

the flow direction and had a cross-sectional area of 10.16 cm (4.00 in.) by 24.13 cm (9.50 in.). The foam parameters are given in Table 1.

The samples were all made from aluminum alloy 6101-T6 and were homogeneous. Visual inspection did not reveal any nonuniformity in the foam structure.

The four sides of each foam sample that constituted its outer perimeter were covered with 1 in. thick Styrofoam sheets, and the sample was placed in the tunnel's test section, as shown in Fig. 1(b). The other two sides were perpendicular to the flow direction and remained open to the airflow. The Styrofoam ensured that the flow would travel through the foam only, allowing a negligible flow between the foam and the tunnel's walls. The flow rate was varied between 10 and 100% of the tunnel's exit opening, in increments of 10%. For each flow rate, the steady-state unidirectional static pressure drop was measured using pressure taps located about 2 cm (0.79 in.) before and after the foam sample and the monometer. The average velocity in the tunnel was measured using an Omega HH-30A digital anemometer with a range of 0.2 to 40 m/s (0.6 to 131.2 ft/s). The air was certainly incompressible for the velocity range covered by the experiment, i.e., 0.77 to 2.73 m/s (2.53 to 8.96 ft/s).

The measurements were repeated three times for each sample and the average of the three runs was reported. This experimental technique has produced reliable results that compared well with the published literature [32].

The uncertainty in the pressure measurements had a contribution from the calibration ( $e_{cal}=1.02$  Pa) of the monometer and from its precision ( $e_{pre}=0.98$  Pa). The root-sum-squares method [33] states that total uncertainty in the pressure values  $\delta_p$  is given by

$$\delta_p = \pm \sqrt{e_{cal}^2 + e_{pre}^2} \quad (9)$$

This results in  $\delta_p$  of  $\pm 9.85$  Pa ( $\pm 0.001$  psia).

The length was measured using a scale with an uncertainty of  $\delta_L = \pm 0.008$  m (0.315 in.). The resulting uncertainty in the linear pressure drop is given by [33]

$$\delta_{(\Delta P/L)} = \pm \sqrt{\left(\frac{\partial(\Delta P/L)}{\partial \Delta P}\right)^2 \delta_p^2 + \left(\frac{\partial(\Delta P/L)}{\partial L}\right)^2 \delta_L^2} \quad (10)$$

This gives a maximum  $\delta_{\Delta P/L}$  of  $\pm 81.6$  Pa/m ( $\pm 0.004$  psia/ft).

The average air velocity in the tunnel was measured using a digital anemometer. The reported uncertainties by the manufacturer included a fixed error of  $\pm 0.25\%$  of the full scale and an error of  $\pm 0.75\%$  of the reading. The resolution error was 0.01 m/s (0.033 ft/s). Using the root-sum-squares method, and using a reference velocity of 1 m/s, the maximum relative uncertainty in the air velocity is  $\delta_v = \pm 11.2\%$ .

Table 1 Foam parameters

Sample	Pores per inch (ppi)	Porosity $\varepsilon$ %	Mean ligament diameter $d$ , mm (in.)	Surface area density $\sigma$ , m <sup>2</sup> /m <sup>3</sup> (in. <sup>2</sup> /in. <sup>3</sup> )
1	10	91.9	0.406 (0.016)	792.1 (20.1)
2	10	91.5	0.406 (0.016)	809.1 (20.6)
3	10	79.4	0.406 (0.016)	
4	Compressed 10	68.2	0.406 (0.016)	2053.1 (52.2)
5	Compressed 20	91.9	0.203 (0.008)	3169.3 (80.5)
6	20	92.4	0.203 (0.008)	1265.7 (32.2)
7	20	77.4	0.203 (0.008)	1240.2 (31.5)
8	Compressed 20	67.9	0.203 (0.008)	3593.7 (91.3)
9	Compressed 40	92.3	0.102 (0.004)	5104.3 (129.6) 1800.8 (45.7)

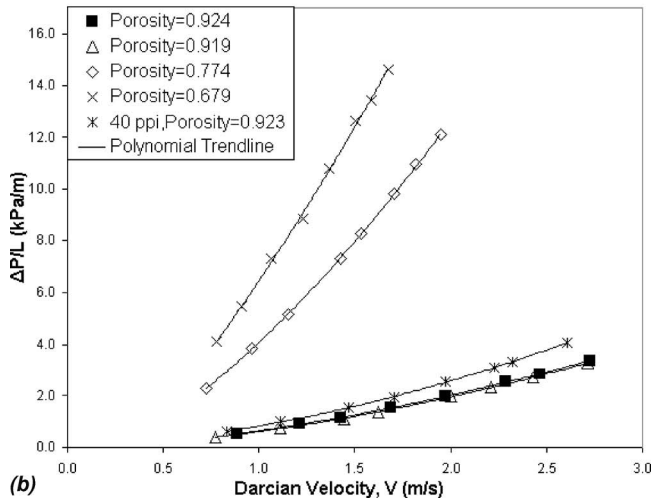
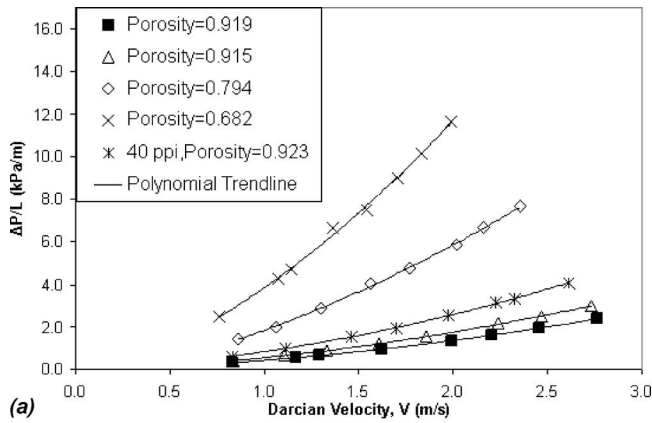


Fig. 2 Pressure drop versus Darcian velocity (a) for 10 ppi and (b) for 20 ppi foam

## Results and Discussion

Parts (a) and (b) of Fig. 2 are plots of the pressure drop divided by the thickness of the 10 and 20 ppi foam samples versus the Darcian velocity. The pressure drop for the 40 ppi sample is also plotted. The pressure drop for both of the foam samples increases with increasing velocity in a quadratic fashion, as shown by the quadratic curve fits in Eq. (1). The general trends of the pressure drop are in qualitative agreement with previous studies [13,20,30]. The pressure drop is significantly higher for the lower-porosity compressed foam. This effect is stronger for the 20 ppi foam at the same velocity and the same approximate porosity. The 40 ppi foam produces higher pressure drop than the 10 and 20 ppi of comparable porosity. This may be explained by the fact that the surface area density is much higher for this foam than the 10 and the 20 ppi foam, as shown in Table 1. This large surface area is responsible for more energy dissipation [19,24]. In the high porosity regime above 90%, the change in porosity has little effect on the pressure drop for the 20 ppi sample. The curves for 92.4 and 91.9% porosity are extremely close. The effect of the porosity for the 10 ppi foam seems to be stronger for the 91.5 and 91.9% porosity foam.

Figure 3 is a plot of the permeability versus the Darcian velocity. Part (a) is for the 10 ppi foam, while part (b) is for the 20 ppi foam sample. The permeability for the 40 ppi foam is also plotted for comparison. The values of  $K$  and  $c$  were determined from curve fitting of the data according to Eq. (1) at each flow velocity and iterating. The behavior of  $K$  shows some scatter, which is not uncommon [20,30]. The average  $K$  values are printed on the plots. It

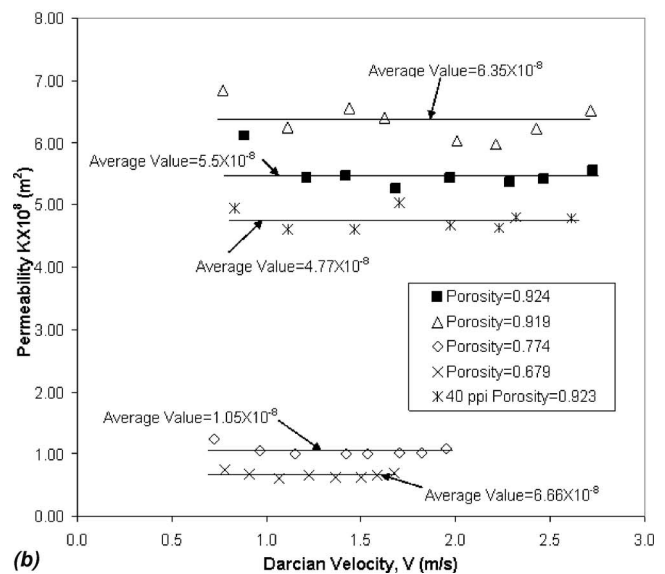
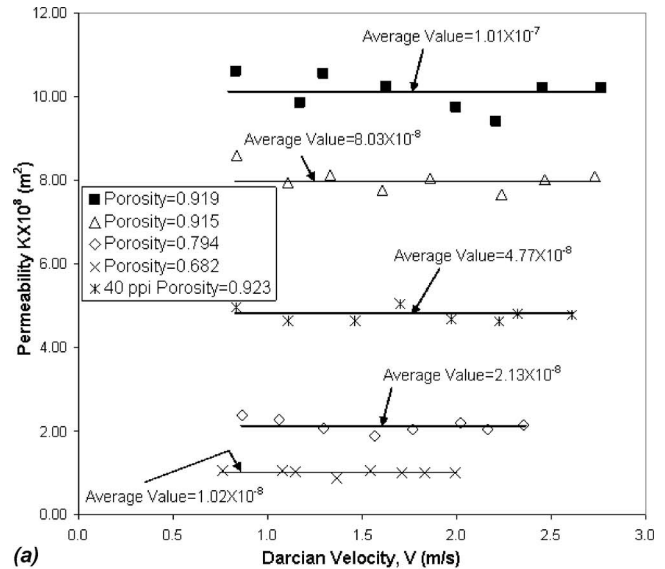


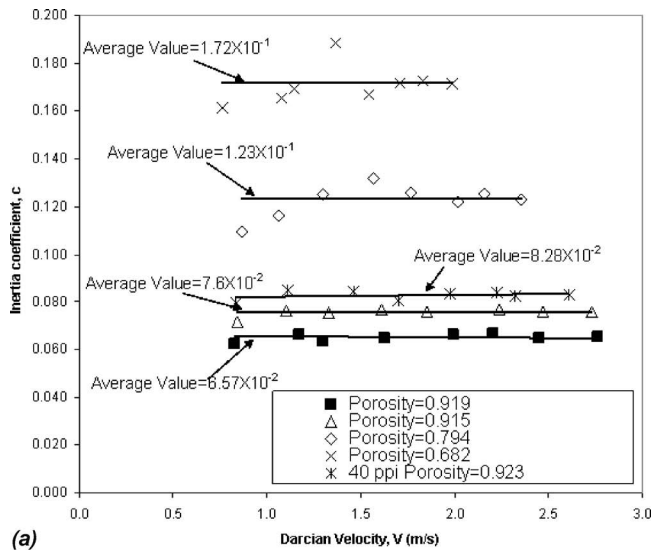
Fig. 3 Permeability versus Darcian velocity (a) for 10 ppi and (b) for 20 ppi foam

is clear that compressing the foam significantly decreases the permeability, i.e., increases the resistance to the flow. This can be explained by the increase in the surface area density, as shown in Table 1. The permeability of the 40 ppi foam is lower than the permeability for the 10 and 20 ppi foam having almost the same porosity. This is explained by the difference in the distribution of the solid aluminum in the foam, e.g., smaller-diameter ligaments for the 40 ppi foam, and thus more obstruction to the flow and more surface area [19,20].

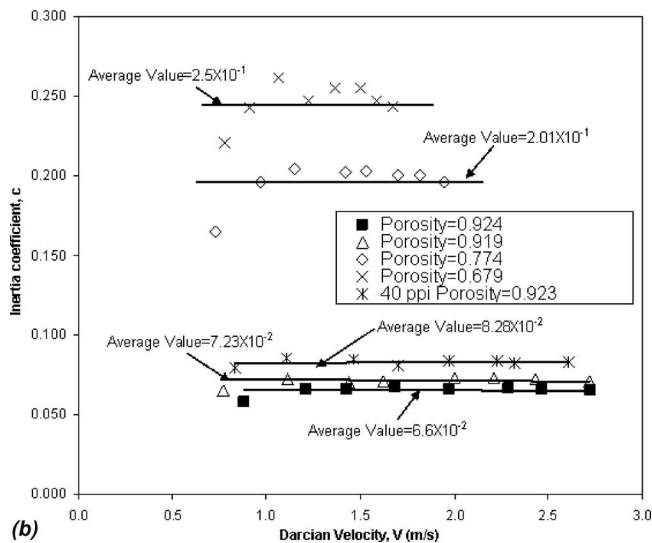
It is worth noting here that, unlike the high-porosity uncompressed foam, the permeability of compressed foam seem to be well behaved, showing significantly less scatter. This is true for both the 10 and 20 ppi compressed foam.

Figure 4 is a plot of the inertia coefficient  $c$  versus the velocity. This coefficient was determined from curve fitting of the linear pressure drop versus the superficial velocity according to Eq. (1) at each flow velocity and iterating. Like the permeability, the inertia coefficient shows some scatter, which was also observed in previous studies [20,30]. The inertia coefficient is significantly higher for the compressed foam cases.

Figure 5 is a plot of the friction factor  $f$  versus the Reynolds



(a)



(b)

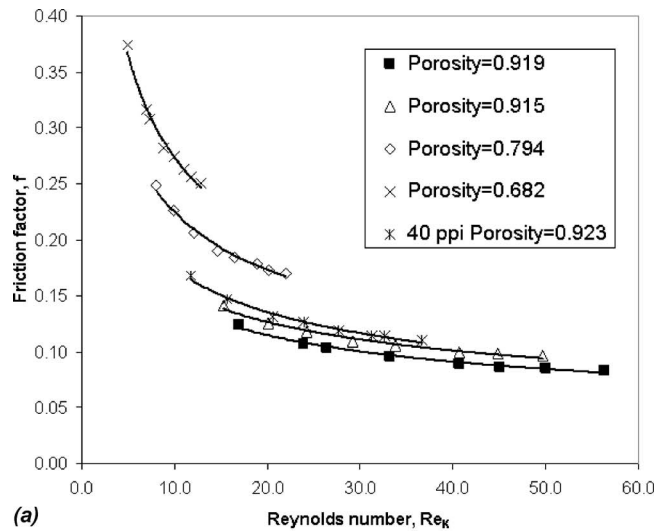
**Fig. 4 Inertia coefficient versus Darcian velocity (a) for 10 ppi and (b) for 20 ppi foam**

number  $Re_K$ . The Reynolds number was calculated using Eq. (8), and the friction factor was calculated according to Eq. (6). The solid lines represent the power law fit of Eq. (7). The flow regime is turbulent according to Refs. [14,15], which stated that for  $Re > 3$ , the flow is fully turbulent. For the compressed foam, the friction factor seems to be reaching a constant value after Reynolds number of about 35.

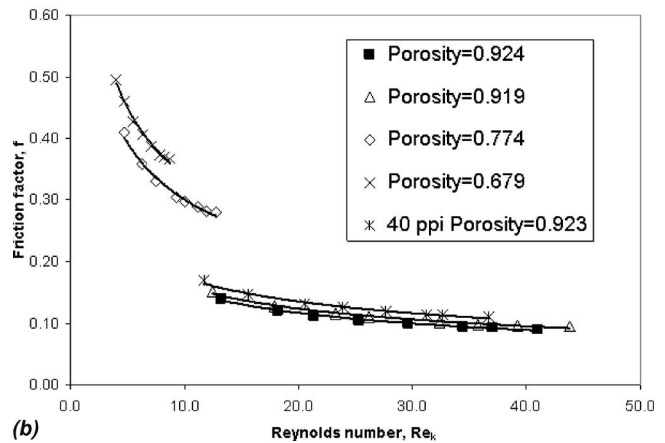
The compression is seen to significantly increase the friction factor, which is consistent with the increase in the pressure drop as shown in Fig. 2. The friction factor is higher for the 20 ppi foam compared to the 10 ppi foam. The 20 ppi foam has a smaller pore size, which means more ligaments obstructing the flow. The surface area density is also a lot higher for the 20 ppi foam, as shown in Table 1.

### Comparison to Other Studies

Some comparisons to previously published data were possible—both for the compressed and the uncompressed foam. For the uncompressed foam, comparisons are made with Crosnier et al. [5], Kim et al. [18], Bhattacharya et al. [20], and Boomsma et al. [29]. For the compressed foam, comparisons are made with Hwang et al. [14], Boomsma and Poulikakos [30], and Antohe et al. [31]. The comparisons are more qualitative than quantitative



(a)



(b)

**Fig. 5 Friction factor versus Reynolds number (a) for 10 ppi and (b) for 20 ppi foam**

due to the differences in the structural parameters of the foam tested by the current authors and those tested by [5,14,18,20,29–31].

For the uncompressed foam cases, Table 2 provides a quick comparison with a few of the previous studies [5,18,20,29]. The average value of the permeability for the 10 ppi 91.9 and 91.5% porous samples are  $10.10 \times 10^{-8}$  and  $8.03 \times 10^{-8}$  m<sup>2</sup>, respectively, which compare well with the results of Bhattacharya et al. [20] for similar foam, but are significantly different from the results reported by Kim et al. [18] and Boomsma et al. [29]. The same is true for the inertia coefficient: the reported values of this study are 0.0657 and 0.0760 for the above samples, and are 0.070 and 0.082 for Bhattacharya et al. [20] for similar foam. For the inertia coefficient, there is an agreement with Boomsma et al. [29] who reported a value of 0.070. Kim et al. [18] did not report any inertia coefficients.

For the 20 ppi foam samples of 92.4 and 91.1% porosities, the permeabilities are  $5.50 \times 10^{-8}$  and  $6.35 \times 10^{-8}$  m<sup>2</sup>, respectively, which are closer to the result of Crosnier et al. [5] ( $7.58 \times 10^{-8}$  m<sup>2</sup>) and significantly different from the values reported by Bhattacharya et al. [20] and Boomsma et al. [29]. The opposite is true for the values of the inertia coefficient: they agree with Bhattacharya et al. [20] and Boomsma et al. [29] and are very different from the values reported by Crosnier et al. [5].

As for the 40 ppi foam, the agreement is generally good for both the permeability and the inertia coefficient. The permeability values of this study and those reported by [5,18,20,29] are com-

**Table 2 Comparison to previous work with uncompressed foam**

ppi	$\varepsilon$ (%)	$K \times 10^8 [\text{m}^2]$					$c \times 10^2$			
		Current study	Kim et al. [18]	Bhattacharya et al. [20]	Boomsma et al. [29]	Crosnier et al. [5]	Current study	Bhattacharya et al. [20]	Boomsma et al. [29]	Crosnier et al. [5]
10	92.1	...	...	...	35.29	...	...	...	7.1	...
10	92	...	23.6	...	...	...	...	...	...	...
10	91.9	10.10	...	...	...	...	6.57	...	...	...
10	91.5	8.03	...	...	...	...	7.6	...	...	...
10	91.38	...	...	11.0	...	...	...	7.0	...	...
10	90.9	...	...	11.1	...	...	...	8.2	...	...
20	93.5	...	...	...	...	8.25	...	...	...	0.10
20	93.2	...	...	...	...	8.76	...	...	...	0.10
20	92.8	...	...	...	...	7.58	...	...	...	0.10
20	92.45	...	...	11.0	...	...	...	10.4	...	...
20	92.4	5.5	...	...	...	...	6.6	...	...	...
20	92	...	10.7	...	10.89	...	...	...	7.9	...
20	91.9	6.35	...	...	...	...	7.23	...	...	...
20	90.6	...	...	8.54	...	...	...	8.5	...	...
40	93.4	...	...	...	...	4.83	...	...	...	0.11
40	93.1	...	...	...	...	4.62	...	...	...	0.12
40	93	...	...	...	...	5.17	...	...	...	...
40	92.9	...	...	...	...	5.06	...	...	...	...
40	92.8	...	...	...	7.12	...	...	...	9.7	...
40	92.72	...	...	6.1	...	...	...	8.9	...	...
40	92.6	...	...	...	...	4.56	...	...	...	0.12
40	92.3	4.77	...	...	...	...	8.28	...	...	...
40	92	...	7.15	...	...	...	...	...	...	...
40	91.32	...	...	5.3	...	...	...	8.4	...	...

parable, while the inertia coefficient of this study is comparable to the values reported by [20,29], and it is an order of magnitude higher than that reported by [5] for similar foam.

It is clear that there is a disagreement between different researches' results, including the current study. This is explained by the fact that the permeability and the inertia coefficient both strongly depend on other geometrical parameters of the foam,

such as the fiber diameter and the pore size, and not just its porosity and pore density (ppi). The disagreement is not unusual [19]. One may also conclude that an agreement on the permeability results may not guarantee an agreement on the inertia coefficient.

Table 3 provides a quick comparison with the few available previous studies for the compressed foam cases [14,30,31]. The

**Table 3 Comparison to previous work with compressed foam**

ppi	$\varepsilon$ (%)	$K \times 10^8 (\text{m}^2)$				$c \times 10^2$			
		Current study	Antohe et al. [31]	Hwang et al. [14]	Boomsma and Poulikakos et al. [30]	Current study	Antohe et al. [31]	Hwang et al. [14]	Boomsma and Poulikakos et al. [30]
10	80	...	...	2	...	...	...	6.8	...
10	79.4	2.13	...	...	...	12.3	...	...	...
10	70	...	...	0.88	...	...	...	11	...
10	68.2	1.02	...	...	...	17.2	...	...	...
20	77.4	1.05	...	...	...	20.1	...	...	...
20	67.9	0.67	...	...	...	25	...	...	...
40	88.2	...	...	...	0.444	...	...	...	7.8
40	87.4	...	...	...	0.367	...	...	...	6.9
40	82.5	...	...	...	0.230	...	...	...	8.6
40	80.5	...	...	...	0.197	...	...	...	12.0
40	76.1	...	...	...	0.139	...	...	...	12.5
40	72.2	...	...	...	0.0807	...	...	...	11.6
40	72	...	0.1136	...	...	37.1	...	...	...
40	68.9	...	...	...	0.0525	...	...	...	10.8
40	66.9	...	...	...	0.0388	...	...	...	10.9
40	64	...	0.0585	...	...	39.7	...	...	...
40	60.8	...	...	...	0.0246	...	...	...	13.6
40	60	...	0.0924	...	...	38.3	...	...	...
40	58	...	0.0606	...	...	47.1	...	...	...
40	56	...	0.037	...	...	45.1	...	...	...
40	50	...	0.0272	...	...	83.8	...	...	...
40	46	...	0.0317	...	...	53.4	...	...	...
40	44	...	0.0536	...	...	41.8	...	...	...
40	44	...	0.0175	...	...	41.3	...	...	...



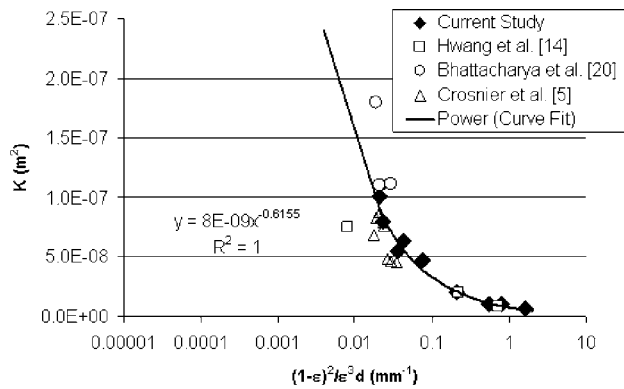


Fig. 6 Permeability versus Ergun parameter

permeability of the 79.4% porous 10 ppi foam of this study is  $2.13 \times 10^{-8} \text{ m}^2$ , which is very close to  $2 \times 10^{-8} \text{ m}^2$  reported by Hwang et al. [14] for his 80% porous foam. The comparison is also very good for the 68.2% porous foam, as seen in Table 3. As for the inertia coefficient, the agreement is not as good.

There are no available data for compressed 20 ppi foam to compare to. The reported data of Antohe et al. [31] and Boomsma and Poulidakos [30] for compressed 40 ppi foam show some significant difference for both the permeability and the inertia coefficient. However, there is a clear tendency for the permeability to decrease, and for the inertia coefficient to increase, with decreasing porosity.

### Correlations and Predictions

Figure 6 is a plot of the permeability versus the parameter  $(1-\epsilon)^2/\epsilon^3d$ . The best curve fit of the experimental data is given in the figure and is shown by the solid line. The curve-fit's constant and exponent shown on the figure produced the best  $R$  value and are given in Table 4. Also plotted are the experimental data of three previous studies [5,14,20]. Other experimental data were available in the literature but could not be plotted here since it did not include any values for the average ligament diameter [18,30,31].

Only a few points from Ref. [20] were included here. These were selected based on their porosity. The very high porosities (in the order of 97%) of some of the samples of [20] produced high permeabilities that could not fit in the above plot without compromising its clarity. The agreement with Hwang et al. [14] is exceptionally good. It should be noted here that two of the Cosnier [5] samples were stainless steel foam. The curve fit seems to predict those very well also. All of this adds to the confidence of the current proposed correlation as given by Eq. (3).

Figure 7 is a plot of the inertia coefficient versus the parameter  $(1-\epsilon)^2/\epsilon^3d$ . The experimental results correlate well with this parameter. The curve fit is shown by the solid line and the values of

Table 4 Empirical coefficients

Sample	$\alpha$	$\beta$	$m$	$n$	$a$	$b$
1	$1.25 \times 10^8$	1336.7	0.6155	0.6184	0.3119	-0.3332
2					0.3355	-0.3251
3					0.5362	-0.3775
4					0.7152	-0.4169
5					0.3791	-0.3734
6					0.3771	-0.3904
7					0.7376	-0.3892
8					0.8578	-0.3999
9					0.3119	-0.3332

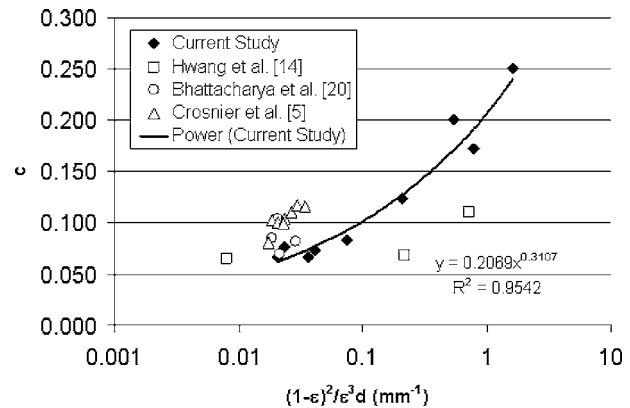


Fig. 7 Inertia coefficient versus Ergun parameter

the empirical constants of Eq. (3) are given in Table 4. The correlation is not as good as that of the permeability shown in Fig. 6. This was observed for the model of Bhattacharya et al. [20], which worked well for the permeability but not as well for the inertia coefficient. In Fig. 7 the maximum difference between the model and the experimental data of the current work is about 16%. The prediction of the previous studies using this correlation is rather poor, especially for Hwang et al. [14].

The friction factor correlated well with the Reynolds number using a power law. Hwang et al. [14] also used a power law for the friction factor as a function of the Reynolds number. A comparison with their results could not be made due to the difference in the definition of the Reynolds number and the friction factor used in their study. The curve fit constants produced by this study are listed in Table 4, and the power law curve fits are all shown by the solid lines in Fig. 5.

### Summary

Experimental data sets were presented for the pressure drop of air flow through samples of compressed and uncompressed open-cell aluminum foam having different porosities and pore densities. The pressure drop behaved in a quadratic fashion when plotted against the superficial velocity following the Forchheimer equation and was significantly higher for the compressed foam. The permeability and the inertia coefficient were both determined from the curve fit of the pressure drop versus the superficial velocity. The results of this study were contrasted with a few previous results for uncompressed foam, and with the few previous results of compressed foam. The agreement was generally better for the permeability. The agreement for the permeability did not guarantee an agreement for the inertia coefficient. Both the permeability and the inertia coefficient were correlated using an Ergun-like model with the ligament diameter as the length scale. This approach worked very well for the current study and predicted the result of some of the previous workers, especially for the permeability. The inertia coefficient correlation was not as good and did not predict the reported data in the open literature. The authors feel that this issue should be investigated further. The friction factor decayed asymptotically with the Reynolds number, and this decay was weak for Reynolds numbers greater than about 35.

### Acknowledgment

This work was supported in part by the ERC Program of the National Science Foundation under Award No. EEC-9731677 with the help of Dr. Miguel Vélez and Dr. Elaine Scott, and also by Pratt & Whitney with the help of David Cloud, for which the authors are very thankful. Pablo D. Quiñones-Ramos, currently at the University of Michigan, has been instrumental in providing

many of the references needed for completing this paper, for which the authors are deeply grateful.

## Nomenclature

- $a$  = empirical constant in Eq. (7)  
 $b$  = empirical constant in Eq. (7)  
 $c$  = inertia coefficient  
 $d$  = mean ligament diameter  
 $f$  = friction factor  
 $K$  = permeability  
 $L$  = thickness of foam sample in the flow direction  
 $m$  = empirical coefficient in Eq. (3)  
 $n$  = empirical coefficient in Eq. (3)  
 $p$  = static pressure  
 $\text{ppi}$  = number of pores per inch  
 $\text{Re}_K$  = Reynolds number based on permeability, Eq. (8)  
 $V$  = Darcian velocity

## Greek Symbols

- $\alpha$  = empirical coefficient in Eq. (3)  
 $\beta$  = empirical coefficient in Eq. (3)  
 $\Delta$  = change  
 $\delta$  = uncertainty  
 $\varepsilon$  = porosity  
 $\mu$  = kinematic viscosity of air  
 $\rho$  = density of air  
 $\sigma$  = surface area per unit volume of foam

## References

- Zhou, J., Mercer, C., and Soboyejo, W. O., 2002, "An Investigation of the Microstructure and Strength of Open-Cell 6010 Aluminum Foam," *Metall. Mater. Trans. A*, **33A**(5), pp. 1413–1427.
- Ashby, M. F., Evans, A. G., Fleck, N. A., Gibson, L. J., Hutchinson, J. W., and Wadley, H. N. G., 2000, *Metal Foams, a Design Guide*, Butterworth-Heinemann, Woburn, MA, Chap. 1, pp. 181–188.
- Sullines, D., and Daryabeige, K., 2001, "Effective Thermal Conductivity of High Porosity Open Cell Nickel Foam," *Proc. 35th AIAA Thermophysics Conference*, Anaheim, CA, June 11–14, IAAA Paper No. 2001–2819.
- Vafai, K., and Tien, C. L., 1982, "Boundary and Inertia Effects on Convective Mass Transfer in Porous Media," *Int. J. Heat Mass Transfer*, **25**(8), pp. 1183–1190.
- Crosnier, S., Rivam, R., Bador, B., and Blet, V., 2003, "Modeling of Gas Flow through Metallic Foams," *Presented at the 1st European Hydrogen Energy Conference*, Sept. 2–5, Alpexpo-Alpes Congrès, Grenoble, France.
- Khayargoli, P., Loya, V., Lefebvre, L. P., and Medraj, M., 2004, "The Impact of Microstructure on the Permeability of Metal Foams," *Proc. the CSME 2004*, June 1–4, London, Canada, pp. 220–228.
- Bastawros, A. F., 1998, "Effectiveness of Open-Cell Metallic Foams for High Power Electronic Cooling," *Presented at Symposium on the Thermal Management of Electronics*, IMECE, Anaheim, CA.
- Kaviany, M., 1995, *Principles of Heat Transfer in Porous Media*, Springer-Verlag, New York, Chap. 2.
- Lage, J. L., 1998, "The Fundamental Theory of Flow through Permeable Media from Darcy to Turbulence," in *Transport Phenomena in Porous Media*, D. B. Ingham and I. Pop, eds., Pergamon, New York, pp. 1–30.
- Nield, D. A., 2002, "Modeling Fluid Flow in Saturated Porous Media and at Interfaces," in *Transport Phenomena in Porous Media II*, D. B. Ingham and I. Pop, eds., Pergamon, New York, pp. 1–19.
- Nield, D. A., and Bejan, A., 1999, *Convection in Porous Media*, 2nd ed., Springer, New York, Chap. 1.
- Bastawros, A. F., Evans, A. G., and Stone, H. A., 1998, "Evaluation of Cellular Metal Heat Transfer Media," MECH 325, Harvard University Report, Cambridge, MA.
- Lage, J. L., Antohe, B. V., and Nield, D. A., 1997, "Two Types of Nonlinear Pressure-Drop Versus Flow-Rate Relation Observed for Saturated Porous Media," *ASME J. Fluids Eng.*, **119**, pp. 700–706.
- Hwang, J. J., Hwang, G. J., Yeh, R. H., and Chao, C. H., 2002, "Measurement of Interstitial Convective Heat Transfer and Frictional Drag for Flow Across Metal Foams," *ASME J. Heat Transfer*, **124**, pp. 120–129.
- Seguin, D., Montillet, A., and Comiti, J., 1998, "Experimental Characterization of Flow Regimes in Various Porous Media-I: Limit of Laminar Flow Regime," *Chem. Eng. Sci.*, **53**(21), pp. 3751–3761.
- Decker, S., Mößbauer, S., Nemoda, D. T., and Zapf, T., 2000, "Detailed Experimental Characterization and Numerical Modeling of Heat and Mass Transport Properties of Highly Porous Media for Solar Receivers and Porous Burners," *Lehrstuhl für Strömungsmechanik Universität Erlangen-Nürnberg Cauerstr. 4, D-91058 Erlangen, Germany*.
- Tadrist, L., Miscevic, M., Rahlh, O., and Topin, F., 2004, "About the Use of Fibrous Materials in Compact Heat Exchangers," *Exp. Therm. Fluid Sci.*, **28**, pp. 193–199.
- Kim, S. Y., Paek, J. W., and Kang, B. H., 2000, "Flow and Heat Transfer Correlations for Porous Fin in a Plate-Fin Heat Exchanger," *ASME J. Heat Transfer*, **122**, pp. 572–578.
- Paek, J. W., Kang, B. H., Kim, S. Y., and Hyun, J. M., 2000, "Effective Thermal Conductivity and Permeability of Aluminum Foam Materials," *Int. J. Thermophys.*, **21**(2), pp. 453–464.
- Bhattacharya, A., Calmidi, V. V., and Mahajan, R. L., 2002, "Thermophysical Properties of High Porosity Metal Foams," *Int. J. Heat Mass Transfer*, **45**, pp. 1017–1031.
- Du Plessis, J. P., Montillet, A., Comiti, J., and Legrand, J., 1994, "Pressure Drop Prediction for Flow through High Porosity Metallic Foams," *Chem. Eng. Sci.*, **49**, pp. 3545–3553.
- Fourie, J. G., and Du Plessis, J. P., 2002, "Pressure Drop Modeling in Cellular Metallic Foams," *Chem. Eng. Sci.*, **57**, pp. 2781–2789.
- Despois, J. F., and Mortensen, A., 2005, "Permeability of Open-Cell Microcellular Materials," *Acta Mater.*, **53**, pp. 1381–1388.
- Boomsma, K., Poulikakos, D., and Ventikos, Y., 2003, "Simulation of Flow through Open Cell Metal Foams Using an Idealized Periodic Cell Structure," *Int. J. Heat Fluid Flow*, **24**, pp. 825–834.
- Schmierer, E. N., Razani, A., Keating, S., and Melton, T., 2004, "Characterization of High Porosity Open-Celled Metal Foam Using Computed Tomography," *Proc. the ASME International Mechanical Engineering Congress*, Nov. 13–20, Anaheim, CA.
- Benouali, A., Froyen, L., Delerue, J. F., and Wevers, M., 2002, "Mechanical Analysis and Microstructure Characterization of Metal Foams," *Mater. Sci. Technol.*, **18**, pp. 489–494.
- Olurin, O. B., Arnold, M., Körner, C., and Singer, R. F., 2002, "The Investigation of Morphometric Parameters of Aluminum Foams Using Micro-Computed Tomography," *Mater. Sci. Eng., A*, **328**, pp. 334–343.
- Scheffler, F., Herrmann, R., Schwiager, W., and Scheffler, M., 2004, "Preparation and Properties of an Electrically Heatable Aluminum Foam/Zelite Composite," *Microporous Mesoporous Mater.*, **67**, pp. 53–59.
- Boomsma, K., Poulikakos, D., and Zwick, F., 2003, "Metal Foams As Compact High Performance Heat Exchangers," *Mech. Mater.*, **35**, pp. 1161–1176.
- Boomsma, K., and Poulikakos, D., 2002, "The Effect of Compression and Pore Size Variations on the Liquid Flow Characteristics in Metal Foams," *ASME J. Fluids Eng.*, **124**, pp. 263–272.
- Antohe, B., Lage, J. L., Price, D. C., and Weber, R. M., 1997, "Experimental Determination of the Permeability and Inertial Coefficients of Mechanically Compressed Aluminum Porous Matrices," *ASME J. Fluids Eng.*, **119**, pp. 404–412.
- Dukhan, N., and Alvarez, A., 2004, "Pressure Drop Measurements for Air Flow through Open-Cell Aluminum Foam," *Proc. ASME International Engineering Congress*, Nov. 13–19, Anaheim, CA.
- Figliola, R., and Beasley, D., 2000, *Theory and Design for Mechanical Measurements*, Wiley, New York, pp. 152–160.

**R. N. Mondal**  
Graduate School of Natural Science and  
Technology,  
Okayama University,  
Okayama 700-8530, Japan

**Y. Kaga**  
Research Center for Energy Conversion,  
Doshisha University,  
Tataratsu-dani 1-3,  
Kyo-tanabe city,  
Kyoto 610-0394, Japan

**T. Hyakutake**

**S. Yanase**  
e-mail: yanase@mech.okayama-u.ac.jp

Department of Mechanical Engineering,  
Faculty of Engineering,  
Okayama University,  
Okayama 700-8530, Japan

# Effects of Curvature and Convective Heat Transfer in Curved Square Duct Flows

*Non-isothermal flows with convective heat transfer through a curved duct of square cross section are numerically studied by using a spectral method, and covering a wide range of curvature,  $\delta$ ,  $0 < \delta \leq 0.5$  and the Dean number,  $Dn$ ,  $0 \leq Dn \leq 6000$ . A temperature difference is applied across the vertical sidewalls for the Grashof number  $Gr=100$ , where the outer wall is heated and the inner one cooled. Steady solutions are obtained by the Newton-Raphson iteration method and their linear stability is investigated. It is found that the stability characteristics drastically change due to an increase of curvature from  $\delta = 0.23$  to  $0.24$ . When there is no stable steady solution, time evolution calculations as well as their spectral analyses show that the steady flow turns into chaos through periodic or multi-periodic flows if  $Dn$  is increased no matter what  $\delta$  is. The transition to a periodic or chaotic state is retarded with an increase of  $\delta$ . Nusselt numbers are calculated as an index of horizontal heat transfer and it is found that the convection due to the secondary flow, enhanced by the centrifugal force, increases heat transfer significantly from the heated wall to the fluid. If the flow becomes periodic and then chaotic, as  $Dn$  increases, the rate of heat transfer increases remarkably. [DOI: 10.1115/1.2236131]*

*Keywords: curved duct, secondary flow, Dean number, curvature, heat transfer*

## 1 Introduction

Flows and heat transfer in curved ducts have attracted considerable attention because of the diversity of their practical applications in fluids engineering, such as in fluid transportation, heat exchangers, cooling systems, chemical reactors, gas turbines, centrifugal pumps, passages in biological systems, and ducting in internal combustion engines. The flow through a curved duct shows physically interesting features under the action of the centrifugal force caused by the curvature of the duct, that is, the existence of a variety of secondary vortices. A lot of theoretical and experimental work has been done concerning developing and fully developed flows. The review articles by Berger et al. [1], Nandakumar and Masliyah [2], Itoh [3], and Berger [4] may be referenced.

Developing flows in curved ducts with square and rectangular cross sections were studied, both experimentally and numerically, by Ghia and Sokhgey [5], Humphrey et al. [6], Yee et al. [7], Taylor et al. [8], Hille et al. [9], Sankar et al. [10], and Sugiyama et al. [11]. The numerical study of Soh [12] showed that, depending on the inlet condition for a given flow rate, the flow might develop into the two-cell and four-cell states predicted by the bifurcation study of Winters [13]. So et al. [14] performed a numerical investigation of developing flows through 180 deg curved bends of circular cross section for the inlet conditions of uniform flow, potential vortex, and parabolic flow, where separation was embedded within the Dean cells. Probably the most complete study of developing flow in a curved square duct for smaller  $Dn$ 's is that by Bara et al. [15]. They investigated both experimentally and numerically the flow characteristics through a curved square duct for  $\delta=0.066$  at  $\theta=270$  deg from the inlet. Velocity measurements of the developing flow at small  $Dn$ 's were in good agreement with simulations using the developing flow code by Sankar et al. [10] and fully developed flow code by Shantini and Nandakumar [16]. The entry length for a developing flow to become

fully developed depends on curvature, as shown in Yao and Berger [17]. As predicted by numerical calculations and experiments by Soh [12], Bara et al. [15], and Mees et al. [18,19], developing flow in a curved duct quickly attains a fully developed two-dimensional (2-D) state, at most 240 to 270 deg from the inlet. This motivated the present study to do 2-D analysis of curved duct flows assuming the uniformity in the main flow direction.

On the assumption of two-dimensionality, lots of bifurcation studies have been performed for fully developed (2-D) flows through curved ducts with square and rectangular cross sections, for example, Cheng et al. [20], Joseph et al. [21], Shantini and Nandakumar [16], and Wang and Yang [22] for a square duct, and Winters [13], Daskopoulos and Lenhoff [23], Finlay and Nandakumar [24], Thangam and Hur [25], and Yanase et al. [26] for a rectangular duct. An early complete bifurcation study of 2-D flows was conducted by Winters [13] for square and rectangular duct flows. Recently, a comprehensive numerical study of bifurcation structure and stability of 2-D flows in a curved duct of square cross section was made by Wang and Yang [22], where three new solution branches were found. In the succeeding paper, Wang and Yang [27] compared their 2-D calculations with experimental observations at  $\theta=270$  deg and showed that 2-D calculation can accurately predict oscillating unsteady flows. Very recently, Mondal et al. [28] performed a numerical investigation of fully developed flows through a curved duct of square cross section and found a close relationship between unsteady solutions and the bifurcation diagram of steady solutions. They also investigated the effects of curvature on the flow characteristics.

One of the most important effects of curved duct flow may be the enhancement of thermal exchange between two differentially heated vertical sidewalls, because secondary flows promote fluid mixing and heat transfer in the fluid (McCormack et al. [29] and Sturgis and Mudawar [30]). Cheng and Akiyama [31] and Mori et al. [32] numerically predicted steady, fully developed laminar forced convection in channels with uniform heat flux boundary conditions. In both investigations, clear evidence of secondary flows was shown in both velocity and temperature profiles. Ru and Chang [33] considered combined free and forced convections

Contributed by the Fluids Engineering Division of ASME for publication in the JOURNAL OF FLUIDS ENGINEERING. Manuscript received June 16, 2005; final manuscript received March 3, 2006. Assoc. Editor: Subrata Roy.

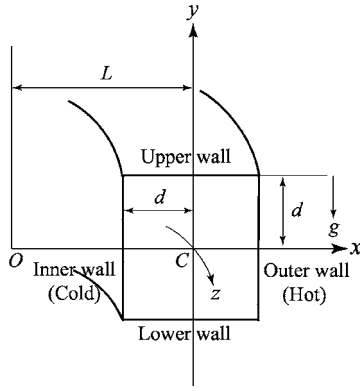


Fig. 1 Coordinate system of the curved square duct

for fully developed flows in uniformly heated curved tubes. Ligrani et al. [34] studied channels of aspect ratio 40 and showed that the formation of secondary vortices is affected more by external heating on the outer wall than on the inner wall of the passage. Chandratilleke and Nursubyakto [35] presented numerical calculations to describe the secondary flow characteristics and convective heat transfer for fully developed laminar flows through curved rectangular ducts of aspect ratios 1 to 8 heated on the outer wall, where they obtained a good agreement between the numerical results and their experimental data. Recently, Yanase et al. [36,37] performed numerical investigations for isothermal and non-isothermal flows through a curved rectangular duct of aspect ratio 2 and studied the effect of secondary flows on convective heat transfer for differentially heated vertical sidewalls.

Studies on fully developed flows through a curved duct for small curvature have been made, experimentally or numerically, by many authors. However, some tubes could have large curvature, in practice, which makes the action of the centrifugal force large and the flow characteristics more complicated. Yanase et al. [38] numerically studied the effect of curvature on dual solutions for the fully developed laminar flow through a curved duct of circular cross section. They found that a four-vortex solution remains unstable even if  $\delta$  is increased up to 0.8. To the best of the authors' knowledge, however, there has not yet been any substantial work done studying the effect of curvature over a wide range for a curved duct flow with square or rectangular cross section. It is, therefore, quite interesting to investigate the non-isothermal flows through a curved duct with the presence of buoyancy effects by varying curvature over a wide range because this type of flow is often encountered in engineering applications.

In the present paper, numerical results are presented for the fully developed (2-D) flow through a curved duct of square cross section whose outer wall is heated and inner one cooled. Flow characteristics are studied over a wide range of  $\delta$  and  $Dn$  based on the bifurcation study, that is, by finding steady solutions, investigating their linear stability, and calculating nonlinear time evolutions with the spectral analysis of the unsteady solutions. Studying the effects of curvature on the flow characteristics as well as the enhancement of convective heat transfer by secondary flows are important objectives of the present paper.

## 2 Governing Equations

Consider a hydrodynamically and thermally fully developed 2-D flow of viscous incompressible fluid through a curved duct with square cross section whose width (or height) is  $2d$ . The coordinate system with the relevant notation is shown in Fig. 1, where  $C$  is the center of the duct cross section,  $O$  is the center of curvature, and  $L$  is the radius of curvature. The  $x$ ,  $y$ , and  $z$  axes are taken to be in the horizontal, vertical, and axial directions, respectively. It is assumed that the outer wall of the duct is heated while the inner one is cooled. The temperature of the outer wall is  $T_0$

+ $\Delta T$  and that of the inner wall is  $T_0 - \Delta T$  where  $\Delta T > 0$ . It is also assumed that the flow is uniform in the axial direction and driven by a constant pressure gradient  $G$  along the center line of the duct, i.e., the main flow in the  $z$  direction as shown in Fig. 1. All the variables are nondimensionalized by using the representative length  $d$ , the representative velocity  $U_0 = \nu/d$ , the representative time  $d/U_0 = d^2/\nu$ , where  $\nu$  is the kinematic viscosity, and the representative temperature  $\Delta T$ . Velocity components in the  $x$  and  $y$  directions are nondimensionalized by  $U_0$  and in the  $z$  direction by  $U_0/\sqrt{2\delta}$ , where  $\delta = d/L$  is the curvature of the duct, and temperature is nondimensionalized by  $\Delta T$ . Henceforth, all the variables are nondimensionalized if not specified.

Velocity components in the  $x$ ,  $y$ , and  $z$  directions are  $u$ ,  $v$ , and  $w$ , respectively. Since the flow field is uniform in the  $z$  direction, the sectional stream function  $\psi$  is introduced as

$$u = \frac{1}{1 + \delta x} \frac{\partial \psi}{\partial y}, \quad v = -\frac{1}{1 + \delta x} \frac{\partial \psi}{\partial x} \quad (1)$$

The basic equations for  $w$ ,  $\psi$ , and  $T$  are derived from the Navier-Stokes equations and the energy equation under the Boussinesq approximation as,

$$(1 + \delta x) \frac{\partial w}{\partial t} + \frac{\partial(w, \psi)}{\partial(x, y)} - Dn + \frac{\delta^2 w}{1 + \delta x} = (1 + \delta x) \Delta_2 w - \frac{\delta}{(1 + \delta x)} \frac{\partial \psi}{\partial y} w + \delta \frac{\partial w}{\partial x} \quad (2)$$

$$\begin{aligned} \left( \Delta_2 - \frac{\delta}{1 + \delta x} \frac{\partial}{\partial x} \right) \frac{\partial \psi}{\partial t} = & -\frac{1}{(1 + \delta x)} \frac{\partial(\Delta_2 \psi, \psi)}{\partial(x, y)} + \frac{\delta}{(1 + \delta x)^2} \\ & \times \left[ \frac{\partial \psi}{\partial y} \left( 2\Delta_2 \psi - \frac{3\delta}{1 + \delta x} \frac{\partial \psi}{\partial x} + \frac{\partial^2 \psi}{\partial x^2} \right) \right. \\ & \left. - \frac{\partial \psi}{\partial x} \frac{\partial^2 \psi}{\partial x \partial y} \right] + \frac{\delta}{(1 + \delta x)^2} \\ & \times \left( 3\delta \frac{\partial^2 \psi}{\partial x^2} - \frac{3\delta^2}{1 + \delta x} \frac{\partial \psi}{\partial x} \right) - \frac{2\delta}{1 + \delta x} \frac{\partial}{\partial x} \Delta_2 \psi \\ & + w \frac{\partial w}{\partial y} + \Delta_2^2 \psi - Gr(1 + \delta x) \frac{\partial T}{\partial x} \quad (3) \end{aligned}$$

$$\frac{\partial T}{\partial t} + \frac{1}{(1 + \delta x)} \frac{\partial(T, \psi)}{\partial(x, y)} = \frac{1}{Pr} \left( \Delta_2 T + \frac{\delta}{1 + \delta x} \frac{\partial T}{\partial x} \right) \quad (4)$$

where

$$\Delta_2 \equiv \frac{\partial^2}{\partial x^2} + \frac{\partial^2}{\partial y^2}, \quad \frac{\partial(f, g)}{\partial(x, y)} \equiv \frac{\partial f}{\partial x} \frac{\partial g}{\partial y} - \frac{\partial f}{\partial y} \frac{\partial g}{\partial x} \quad (5)$$

The Dean number  $Dn$ , the Grashof number  $Gr$ , and the Prandtl number  $Pr$ , which appear in Eqs. (2) to (4), are defined as

$$Dn = \frac{Gd^3}{\mu\nu} \sqrt{\frac{2d}{L}}, \quad Gr = \frac{\gamma g \Delta T d^3}{\nu^2}, \quad Pr = \frac{\nu}{\kappa} \quad (6)$$

Here  $\mu$ ,  $\gamma$ ,  $\kappa$ , and  $g$  are the viscosity, the coefficient of thermal expansion, the coefficient of thermal diffusivity, and the gravitational acceleration, respectively. In the present study,  $Dn$  and  $\delta$  are varied while  $Pr$  and  $Gr$  are fixed as  $Pr=7.0$  (water) and  $Gr=100$ .

The rigid boundary conditions for  $w$  and  $\psi$  are

$$\begin{aligned} w(\pm 1, y) = w(x, \pm 1) = \psi(\pm 1, y) \\ = \psi(x, \pm 1) \\ = \frac{\partial \psi}{\partial x}(\pm 1, y) = \frac{\partial \psi}{\partial y}(x, \pm 1) \\ = 0 \quad (7) \end{aligned}$$

and the temperature  $T$  is assumed to be constant on the walls as

$$T(1,y) = 1, \quad T(-1,y) = -1, \quad T(x, \pm 1) = x \quad (8)$$

It should be noted that Eqs. (2) to (4) are invariant under the transformation of the variables

$$\begin{aligned} y &\Rightarrow -y \\ w(x,y,t) &\Rightarrow w(x,-y,t) \\ \psi(x,y,t) &\Rightarrow -\psi(x,-y,t) \\ T(x,y,t) &\Rightarrow -T(x,-y,t) \end{aligned} \quad (9)$$

Therefore, the case of heating the inner sidewall and cooling the outer sidewall can be deduced directly from the results obtained in this paper.

### 3 Numerical Calculations

**3.1 Method of Numerical Calculation.** In the present numerical calculations, the spectral method is used in which variables are expanded in a series of functions consisting of the Chebyshev polynomials. That is,  $\Phi_n(x)$  and  $\Psi_n(x)$  are expressed as

$$\Phi_n(x) = (1-x^2)C_n(x), \quad \Psi_n(x) = (1-x^2)^2C_n(x) \quad (10)$$

where

$$C_n(x) = \cos[n \cos^{-1}(x)] \quad (11)$$

is the  $n$ th order Chebyshev polynomial.  $w(x,y,t)$ ,  $\psi(x,y,t)$ , and  $T(x,y,t)$  are expanded in terms of the expansion functions  $\Phi_n(x)$  and  $\Psi_n(x)$  as

$$\begin{aligned} w(x,y,t) &= \sum_{m=0}^M \sum_{n=0}^N w_{mn}(t) \Phi_m(x) \Phi_n(y) \\ \Psi(x,y,t) &= \sum_{m=0}^M \sum_{n=0}^N \psi_{mn}(t) \Psi_m(x) \Psi_n(y) \\ T(x,y,t) &= \sum_{m=0}^M \sum_{n=0}^N T_{mn}(t) \Phi_m(x) \Phi_n(y) + x \end{aligned} \quad (12)$$

where  $M$  and  $N$  are the truncation numbers of the polynomial series in the  $x$  and  $y$  directions, respectively. The expansion coefficients  $w_{mn}$ ,  $\psi_{mn}$ , and  $T_{mn}$  are then substituted into the basic Eqs. (2)–(4) and the collocation method is applied. As a result, nonlinear equations for  $w_{mn}$ ,  $\psi_{mn}$ , and  $T_{mn}$  are obtained. The collocation points are taken to be

$$x_i = \cos \left[ \pi \left( 1 - \frac{i}{M+2} \right) \right], \quad y_j = \cos \left[ \pi \left( 1 - \frac{j}{N+2} \right) \right] \quad (13)$$

where  $i = 1, \dots, M+1$  and  $j = 1, \dots, N+1$ . The steady solutions are obtained by the Newton-Raphson iteration method assuming all the coefficients to be time independent, and the convergence is assured by taking  $\epsilon_p < 10^{-10}$ , where subscript  $p$  denotes the iteration number and  $\epsilon_p$  is defined as

$$\epsilon_p = \sum_{m=0}^M \sum_{n=0}^N [(w_{mn}^{(p+1)} - w_{mn}^{(p)})^2 + (\psi_{mn}^{(p+1)} - \psi_{mn}^{(p)})^2 + (T_{mn}^{(p+1)} - T_{mn}^{(p)})^2]$$

Linear stability of the steady solutions is investigated against 2-D ( $z$ -independent) perturbations. To do this, the eigenvalue problem is solved which is constructed by the application of the function expansion method together with the collocation method to the perturbation equations obtained from Eqs. (2)–(4). In order to calculate unsteady solutions of the flow, the Crank-Nicolson and Adams-Bashforth methods together with the function expansion (12) and collocation methods are applied.

**Table 1 The values of  $\lambda$  and  $w(0,0)$  for various  $M$  and  $N(=M)$  at  $Dn=1000$ ,  $Gr=100$ , and  $\delta=0.1$**

$M$	$N$	$\lambda$	$w(0,0)$
14	14	0.241 883 50	360.1056
16	16	0.241 817 54	360.5243
18	18	0.241 855 67	360.7442
20	20	0.241 855 38	360.9000
22	22	0.241 854 46	360.9539

**3.2 Numerical Accuracy.** In the present numerical calculations, for sufficient accuracy of the solutions,  $M=20$  and  $N=20$  have been used. The values of  $\lambda$  and  $w(0,0)$ , obtained for  $Dn=1000$  and  $Gr=100$  at  $\delta=0.1$ , are shown in Table 1 for various values of  $M$ , where  $\lambda$  is the resistance coefficient defined in Eq. (14) and  $w(0,0)$  is the axial velocity of the steady solution at  $(x,y)=(0,0)$ . It is found that  $\lambda$  changes 0.0272% from  $M=14$  to  $M=16$ , 0.0157% from  $M=16$  to  $M=18$ , 0.0001% from  $M=18$  to  $M=20$ , and 0.0003% from  $M=20$  to  $M=22$ .  $w(0,0)$  changes 0.116% from  $M=14$  to  $M=16$ , 0.060% from  $M=16$  to  $M=18$ , 0.043% from  $M=18$  to  $M=20$ , and 0.015% from  $M=20$  to  $M=22$ . Therefore, it is concluded that the values  $M=20$  and  $N=20$  give sufficient accuracy for the present numerical calculations.

### 4 Resistance Coefficient and the Nusselt Number

In the present study, the resistance coefficient  $\lambda$  is used as the representative quantity of the flow state. It is also called the *hydraulic resistance coefficient* and is generally used in fluids engineering, defined as

$$\frac{P_1^* - P_2^*}{\Delta z^*} = \frac{\lambda}{4d} \rho \langle w^* \rangle^2 \quad (14)$$

where quantities with an asterisk denote dimensional ones,  $\langle \rangle$  stands for the mean over the cross section of the duct, and  $\rho$  is the density. The mean axial velocity  $\langle w^* \rangle$  is calculated by

$$\langle w^* \rangle = \frac{\nu}{4\sqrt{2}\delta d} \int_{-1}^1 dx \int_{-1}^1 w(x,y,t) dy \quad (15)$$

Since  $(P_1^* - P_2^*)/\Delta z^* = G$ ,  $\lambda$  is related to the mean nondimensional axial velocity  $\langle w \rangle$  by

$$\lambda = \frac{4\sqrt{2}\delta Dn}{\langle w \rangle^2} \quad (16)$$

where  $\langle w \rangle = \sqrt{2}\delta d \langle w^* \rangle / \nu$ . It should be remarked that  $\lambda \propto Dn^{-1}$  in the limit of  $Dn \rightarrow 0$  with  $\delta$  keeping constant, since  $\langle w \rangle \propto Dn$  in this limit. In this paper,  $\lambda$  is used to denote the steady solution branches and to pursue the time evolution of the unsteady solutions.

The Nusselt number,  $Nu$ , which is used as an index of the heat transfer from the walls to the fluid, is defined as

$$Nu_c = \frac{1}{2} \int_{-1}^1 \left( \frac{\partial T}{\partial x} \right)_{x=-1} dy, \quad Nu_h = \frac{1}{2} \int_{-1}^1 \left( \frac{\partial T}{\partial x} \right)_{x=1} dy \quad (17)$$

for steady solutions. For unsteady solutions, on the other hand, it is defined as

$$Nu_{rc} = \frac{1}{2} \int_{-1}^1 \left\langle \left\langle \frac{\partial T}{\partial x} \right|_{x=-1} \right\rangle \right\rangle dy, \quad (18)$$

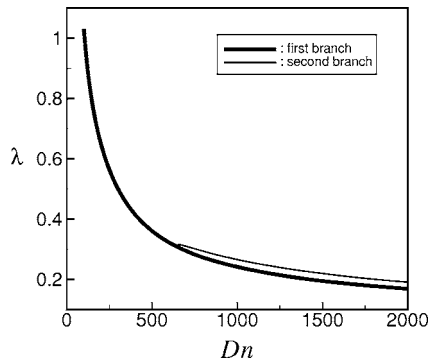


Fig. 2 Steady solution branches for  $\delta=0.1$  and  $100 \leq Dn \leq 2000$  for  $Gr=100$

$$Nu_{\tau_h} = \frac{1}{2} \int_{-1}^1 \left\langle \left\langle \frac{\partial T}{\partial x} \Big|_{x=1} \right\rangle \right\rangle dy,$$

where  $\langle \langle \rangle \rangle$  denotes an average over a time interval  $\tau$ . When the field is periodic,  $\tau$  is taken as one period, and if it is chaotic,  $\tau$  is chosen to be an appropriate time interval.

## 5 Results

### 5.1 Steady Solutions and Their Linear Stability Analysis.

After a comprehensive survey over the parametric ranges, two branches of steady solutions are found for the curvature in the range  $0 < \delta \leq 0.5$  over a wide range of the Dean number,  $0 \leq Dn \leq 6000$ , for a fixed Grashof number  $Gr=100$ . A bifurcation diagram, for example, is shown in Fig. 2 for  $\delta=0.1$  and  $100 \leq Dn \leq 2000$  using  $\lambda$ , the representative quantity of the solutions. The two steady solution branches are named the *first steady solution branch* (first branch, thick solid line) and the *second steady solution branch* (second branch, thin solid line), respectively. The steady solution branches are distinguished by the nature and number of secondary flow vortices appearing in the cross section of the duct (for details, see Yanase et al. [36]). It is found that the two branches are independent and there exists no bifurcating relationship between them in the parameter range investigated in this paper. The first branch varies monotonically, as  $Dn$  varies, while the second branch consists of the upper and lower branches that are connected at the turning point  $Dn \approx 654.7$ . For other values of  $\delta$ , the bifurcation diagram is topologically unchanged from Fig. 2. In this respect, it is interesting to note that for the isothermal flow in a curved square duct, Mondal et al. [28] observed a topological change in the bifurcation diagram as the curvature was increased from  $\delta=0.27$  to  $\delta=0.28$ . They found that for smaller  $\delta$  ( $\delta \leq 0.27$ ), the bifurcation diagram remains topologically unchanged having three branches of steady solutions; for larger  $\delta$  ( $\delta \geq 0.28$ ), on the other hand, they noticed another type of bifurcation diagram with two branches of solutions. In the present study, however, it is found that the bifurcation diagram for the non-isothermal flow at any  $\delta$ , whether small or large, is completely similar to that for  $\delta \geq 0.28$  of isothermal flow predicted by Mondal et al. [28].

Linear stability of the steady solutions is then investigated. It is found that only the first branch is linearly stable while the other branch is linearly unstable. The first branch is linearly stable in two distinct intervals of  $Dn$  for  $0 < \delta \leq 0.23$ , but in a single interval of  $Dn$  for  $0.24 \leq \delta \leq 0.5$ . It is found that the stability characteristics are changed due to an increase of curvature from  $\delta=0.23$  to  $\delta=0.24$ , which are illustrated in Fig. 3 for  $0 < \delta \leq 0.5$  and  $0 \leq Dn \leq 4500$ . In this figure, the regions of stable and unstable solutions are separated by broken lines where the circles denote stable solutions on the boundary calculated in this study. As seen in Fig. 3, there exist two unstable regions. One unstable

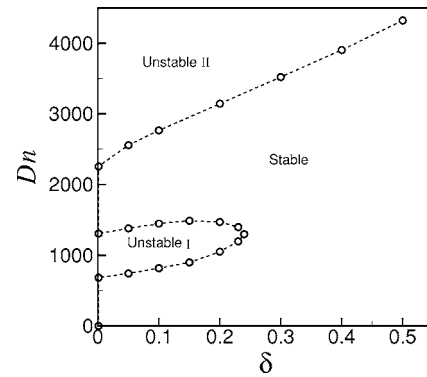


Fig. 3 Stability criterion on the  $Dn-\delta$  plane (circle with broken line: boundary between the regions of stable and unstable solutions)

region, say region I, exists for smaller  $Dn$  and vanishes suddenly as  $Dn$  increases. This region becomes narrower as  $\delta$  increases and terminates at  $\delta \approx 0.24$ . The other unstable region, say region II, on the other hand, exists for larger  $Dn$  and is not stabilized any more as  $Dn$  or  $\delta$  increases. It is observed that the stability region increases as  $\delta$  increases (see Fig. 3). In this regard, it should be noted that in the present study no qualitative change of the bifurcation diagram is found due to the change of curvature, except the linear stability characteristics of the first branch as  $\delta$  increases from 0.23 to 0.24. In the paper by Mondal et al. [28], however, it was found that the change of the curvature from  $\delta=0.27$  to  $\delta=0.28$  crucially affects the branching pattern of the bifurcation diagram as well as their linear stability characteristics.

To see the effects of curvature on the flow patterns and temperature distributions, contours of typical secondary flow and temperature profile are drawn for the two steady solution branches at several values of  $\delta$  and  $Dn$ . Contours of secondary flow and temperature profile for the first steady solution branch at  $Dn=1000$  are shown in Fig. 4(a) and those for  $Dn=4000$  in Fig. 4(b), where the contours of  $\psi$  and  $T$  are drawn with increments  $\Delta\psi=0.6$  and  $\Delta T=0.2$ , respectively. The same increments of  $\psi$  and  $T$  are used for all the figures in this paper, if not specified. The right-hand side of each box is in the outside direction of the duct curvature. In the figures of secondary flow, solid lines ( $\psi \geq 0$ ) show that the secondary flow is in the counter-clockwise direction while dotted lines ( $\psi < 0$ ) are in the clockwise direction. In the figures of temperature field, on the other hand, solid lines are those for  $T \geq 0$  and dotted ones for  $T < 0$ . As seen in Fig. 4, the first steady solution branch consists of a two-vortex solution irrespective of  $Dn$  and  $\delta$ .

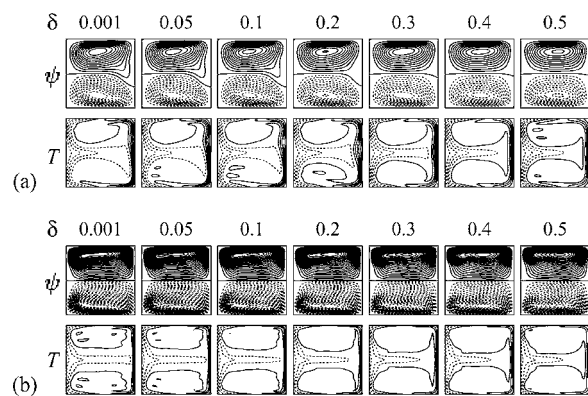
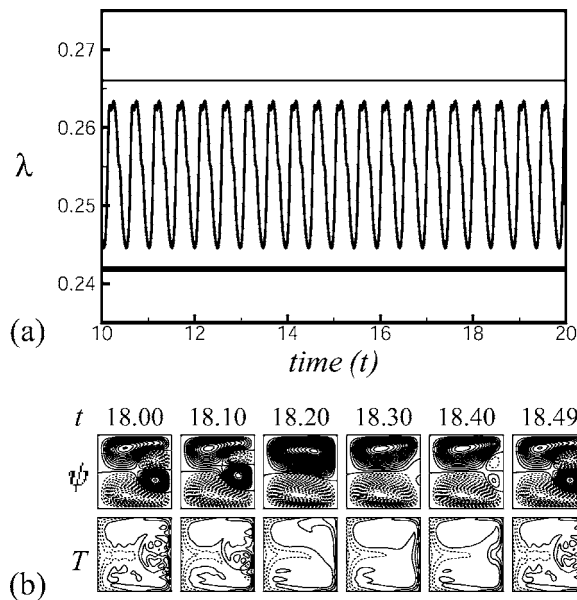


Fig. 4 Contours of secondary flow (top) and temperature profile (bottom) on the first steady solution branch for various  $\delta$ . (a)  $Dn=1000$ , (b)  $Dn=4000$ .



**Fig. 5** The results for  $\delta=0.1$  and  $Dn=1000$ . (a) Time evolution of  $\lambda$  and the values of  $\lambda$  for the steady solutions for  $10 \leq t \leq 20$ . (b) Contours of secondary flow (top) and temperature profile (bottom) for  $18.00 \leq t \leq 18.49$ .

If  $\delta$  increases, the flow becomes more symmetric with respect to the plane  $y=0$  for  $Dn=1000$  (Fig. 4(a)). For large  $Dn$  ( $Dn=4000$ , Fig. 4(b)), on the other hand, the symmetry with respect to  $y=0$  exists even for small  $\delta$ . The reason is that the centrifugal force, which maintains symmetry of the flow with respect to  $y=0$ , is strong even for small  $\delta$  if  $Dn$  is large. Contours of secondary flow and temperature profile on the second steady solution branch are also obtained but they are not shown here for brevity. It is found that the asymmetric two-vortex solution (on the lower branch) gradually changes to a nearly symmetric four-vortex solution (on the upper branch) whether  $\delta$  is small or large.

**5.2 Time Evolution and Spectral Analysis.** In order to study the nonlinear behavior of the unsteady solutions, time evolution calculations as well as their spectral analyses are performed for the curvature in the range  $0 < \delta \leq 0.5$ . In Sec. 5.2.1, the results of the time evolution calculations and their spectral analyses are discussed, in detail, for  $\delta=0.1$  at different values of  $Dn$ , and those for other values of  $\delta$  in Sec. 5.2.2, which covers the whole range of the curvature investigated in this paper.

**5.2.1 Time Evolution and Spectral Analysis for  $\delta=0.1$ .** Time evolutions of  $\lambda$  for  $Dn \leq 818$  at  $\delta=0.1$  show that the value of  $\lambda$  quickly approaches that of the stable solution on the first branch. In order to see what happens when the steady solution is linearly unstable in the first unstable region (region I,  $819 \leq Dn \leq 1450$ ), time evolution calculation is then performed for  $Dn=1000$  as shown in Fig. 5(a). The initial condition is the steady solution on the first branch. As seen in Fig. 5(a), the unsteady flow at  $Dn=1000$  is a periodic solution. Then, to observe the relationship between the periodic solution and the steady states, the values of  $\lambda$  on the steady solution branches at  $Dn=1000$  are also shown in the same figure by straight lines using the same kind of lines as were used in the bifurcation diagram in Fig. 2. As seen in Fig. 5(a), the periodic solution at  $Dn=1000$  oscillates in the region between the first and the second steady solution branches. To observe the change of the flow characteristics, as time proceeds, contours of secondary flow and temperature profile, for one period of oscillation, are shown in Fig. 5(b) for  $18.00 \leq t \leq 18.49$ , where it is observed that the periodic solution at  $Dn=1000$  oscillates

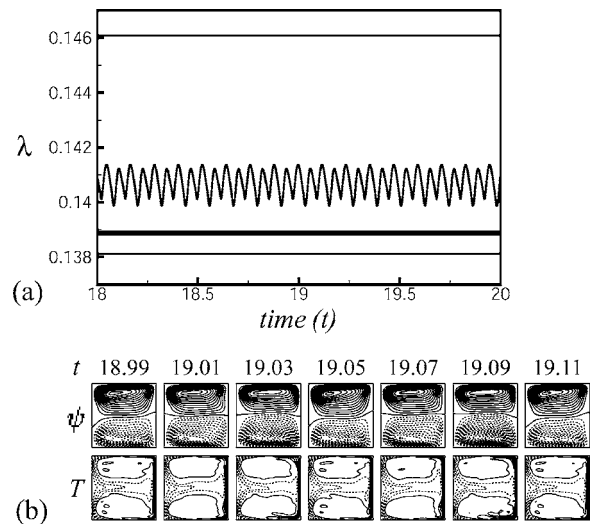


**Fig. 6** The results for  $\delta=0.1$  and  $Dn=3000$ . (a) Time evolution of  $\lambda$  and the values of  $\lambda$  for the steady solutions for  $18 \leq t \leq 20$ . (b) Contours of secondary flow (top) and temperature profile (bottom) for  $18.99 \leq t \leq 19.11$ .

between the asymmetric two- and four-vortex solutions.

Time evolutions of  $\lambda$  for  $1451 \leq Dn \leq 2767$  show that the value of  $\lambda$  quickly approaches that of the stable solution on the first branch. In order to see what happens when this branch becomes unstable for  $Dn \geq 2768$  (second unstable region), time evolution calculation of  $\lambda$  is then performed for  $Dn=3000$  as shown in Fig. 6(a). In this figure, the values of  $\lambda$  for the steady solution branches are also plotted with straight lines. It is found that the flow oscillates multi-periodically in the region between the first and second steady solution branches where the oscillation takes place comparatively close to the first branch, which is a two-vortex solution. Secondary flow patterns, drawn for one period of the main oscillation, are depicted in Fig. 6(b), which shows that the unsteady flow at  $Dn=3000$  is an asymmetric two-vortex solution. If  $Dn$  is increased further, the periodic oscillation turns into a chaotic oscillation via multi-periodic oscillation. Time evolutions of  $\lambda$  together with the values of  $\lambda$  for the steady solution branches, indicated by straight lines, are shown in Figs. 7(a) and 8(a) for  $Dn=3500$  and  $3600$ , respectively, where the initial conditions are the steady solutions on the first branch. Figure 7(a) shows that the flow exhibits a multi-periodic oscillation at  $Dn=3500$ , while Fig. 8(a) shows that the flow oscillates irregularly with the large windows of quasi-periodic oscillations at  $Dn=3600$ , which suggests that the flow is chaotic then. Both the oscillations take place close to the first branch. Contours of secondary flow and temperature profiles for  $Dn=3500$ , for one period of oscillation at  $25.95 \leq t \leq 27.0$  (one longer period), are shown in Fig. 7(b) and that for  $Dn=3600$  at  $8.0 \leq t \leq 10.0$  in Fig. 8(b), where the increment  $\Delta\psi = 1.2$  is used to draw the contours of secondary flow. As seen in the secondary flow patterns, the time-dependent solutions at  $Dn=3500$  and  $Dn=3600$  are composed of asymmetric two-vortex solutions. The periodic solutions, obtained by the 2-D calculations in the present study, signify the existence of three-dimensional traveling wave solutions.

Next, time evolutions of  $\lambda$  together with the values of  $\lambda$  for the steady solution branches, indicated by straight lines, are shown in Figs. 9(a) and 10(a) for  $Dn=4000$  and  $Dn=5500$ , respectively, where it is seen that the flow is chaotic in both cases. Initial condition independence has also been examined for the chaotic solution at  $Dn=4000$  using the initial condition on the second steady solution branch, and it is found that the chaotic solution fluctuates around the same place ( $\lambda \approx 0.13$ ) even if two different initial conditions are used. In this regard, it should be noted that

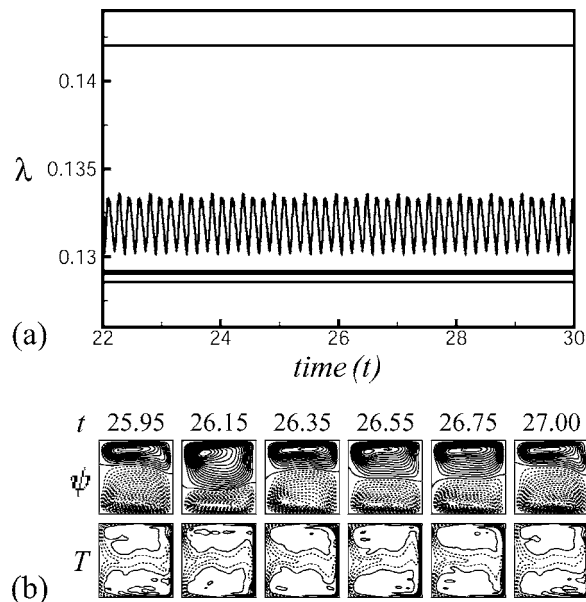


Fig. 7 The results for  $\delta=0.1$  and  $Dn=3500$ . (a) Time evolution of  $\lambda$  and the values of  $\lambda$  for the steady solutions for  $22 \leq t \leq 30$ . (b) Contours of secondary flow (top) and temperature profile (bottom) for  $25.95 \leq t \leq 27.0$ .

the unsteady solution at  $Dn=4000$  drifts between the first and the second steady solution branches while that for  $Dn=5500$  fluctuates above all the steady solution branches, and the upper part of the second branch, which has the maximum  $\lambda$  ( $\lambda=0.1120881$ ) at  $Dn=5500$ , looks like an envelope of this chaotic solution. The chaotic solution for  $Dn=4000$  is considered to be *weak chaos* and that for  $Dn=5500$  *strong chaos*, since the chaotic solution at  $Dn=5000$  is still trapped among the steady solution branches but that for  $Dn=5500$  tends to get away from them. In order to observe the change of the flow patterns and temperature distributions, contours of secondary flow and temperature profile for  $6.0 \leq t \leq 8.0$

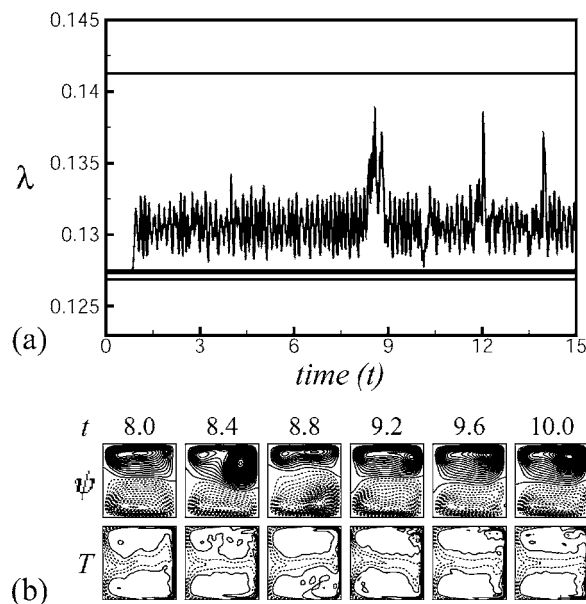


Fig. 8 The results for  $\delta=0.1$  and  $Dn=3600$ . (a) Time evolution of  $\lambda$  and the values of  $\lambda$  for the steady solutions for  $0 \leq t \leq 15$ . (b) Contours of secondary flow (top) and temperature profile (bottom) for  $8.0 \leq t \leq 10.0$ .

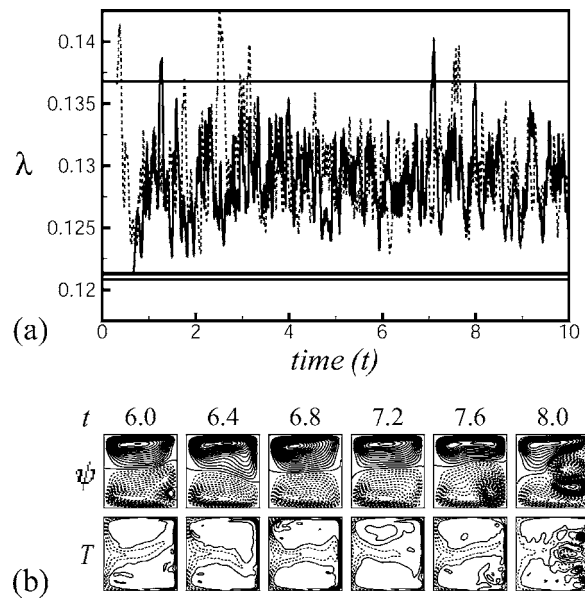


Fig. 9 The results for  $\delta=0.1$  and  $Dn=4000$ . (a) Time evolution of  $\lambda$  and the values of  $\lambda$  for the steady solutions for  $0 \leq t \leq 10$ . (b) Contours of secondary flow (top) and temperature profile (bottom) for  $6.0 \leq t \leq 8.0$ .

are shown in Figs. 9(b) and 10(b) for  $Dn=4000$  and  $Dn=5500$ , respectively, where the increments  $\Delta\psi=1.2$  and  $\Delta T=0.4$  are used to draw the contours of secondary flow and temperature profile, respectively. As seen in the secondary flow patterns, the chaotic solution at  $Dn=4000$  is a two- and four-vortex solution while that for  $Dn=5500$  is composed of two- and multi-vortex solutions. The chaotic solutions, obtained in the present study, indicate the existence of three-dimensional turbulence in real flows.

Now, in order to investigate the transition from a periodic solution to the chaotic one in more detail, the power spectra of the time change of  $\lambda$  are obtained for  $3000 \leq Dn \leq 5500$ . The power

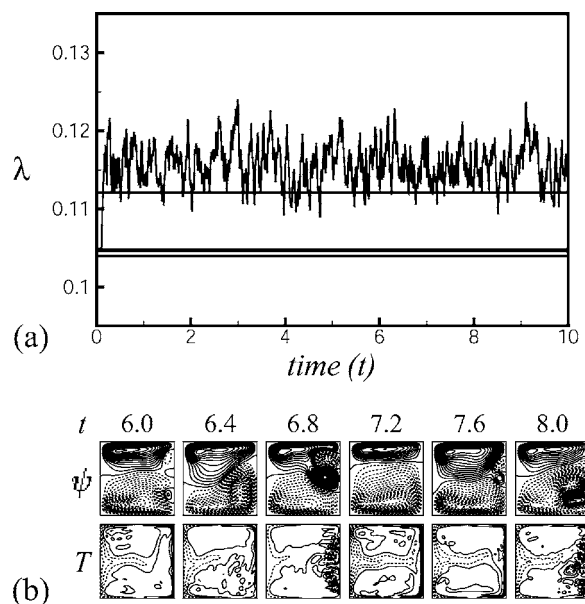
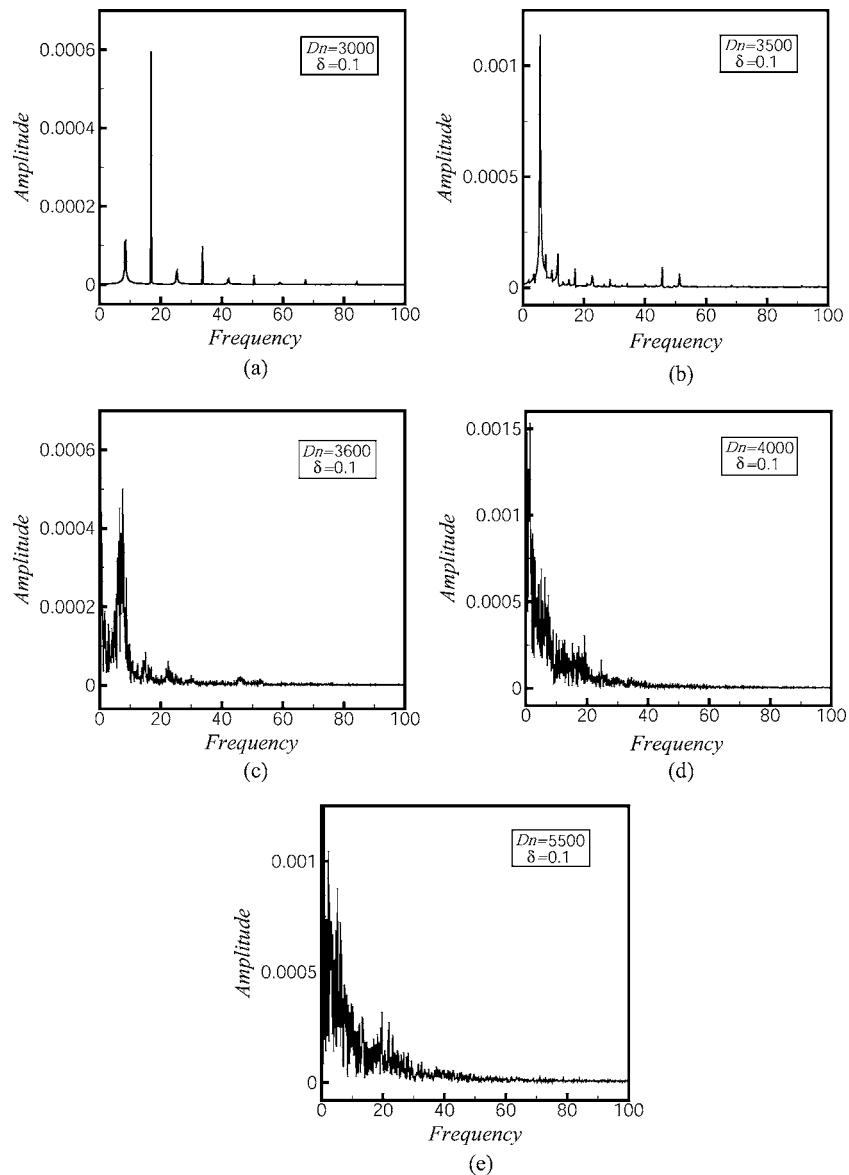


Fig. 10 The results for  $\delta=0.1$  and  $Dn=5500$ . (a) Time evolution of  $\lambda$  and the values of  $\lambda$  for the steady solutions for  $0 \leq t \leq 10$ . (b) Contours of secondary flow (top) and temperature profile (bottom) for  $6.0 \leq t \leq 8.0$ .





**Fig. 11** Power spectra of the time evolution of  $\lambda$  at various  $Dn$  for  $\delta=0.1$ . (a)  $Dn=3000$ , (b)  $Dn=3500$ , (c)  $Dn=3600$ , (d)  $Dn=4000$ , and (e)  $Dn=5500$ .

spectrum for  $Dn=3000$  is shown in Fig. 11(a). It is found that the line spectrum of the fundamental frequency ( $f=16.84$  Hz) and its harmonics as well as the subharmonics appear. The power spectrum for  $Dn=3500$  is shown in Fig. 11(b), in which not only the line spectrum of the fundamental frequency ( $f=5.61$  Hz) and its harmonics but also the other line spectrum ( $f=45.65$  Hz) and its harmonics can be seen. This result clearly shows that the oscillation presented in Fig. 7(a) is multi-periodic. It is interesting that the frequency of the fundamental mode for  $Dn=3500$  ( $f=5.61$  Hz) is smaller than that for  $Dn=3000$  as seen in Fig. 11(b). It is therefore concluded that the oscillation displayed in Fig. 7(a) ( $Dn=3500$ ) is qualitatively different from that in Fig. 6(a) ( $Dn=3000$ ). If  $Dn$  is increased further, an alternating occurrence of the oscillating and chaotic states is observed as shown in Fig. 8(a) for  $Dn=3600$ . The corresponding power spectrum (Fig. 11(c)) shows that it consists of the line spectrum with nearly the same frequency as for  $Dn=3500$  and a continuous spectrum. It is clear that the former corresponds to the periodic state and the latter to the chaotic one. If  $Dn$  is increased still further, the line spectra disappear as shown in Fig. 11(d) for  $Dn=4000$ , which is considered to

be weak chaos because the orbit of  $\lambda$  is trapped among the steady solution branches (see Fig. 9(a)). Finally, the power spectrum for  $Dn=5500$  is shown in Fig. 11(e), which is considered to be strong chaos because the orbit of  $\lambda$  tends to get away from the steady solution branches (see Fig. 10(a)). Though it is difficult to find an appreciable difference in the time evolution curves for  $Dn=4000$  and  $Dn=5500$  (Figs. 9(a) and 10(a)), the difference in the power spectrum is very clear for these two cases. For  $Dn=5500$ , the spectrum occurs remarkably in larger frequencies than that for  $Dn=4000$ , which may support us to distinguish the strong chaos from the weak chaos. The appearance of the two modes with different frequencies for  $Dn=3000$  and  $Dn=3500$  may suggest that the Ruelle-Takens [39] mechanism plausibly works for the occurrence of chaos in the present system.

By the time evolution calculations, it is found that stable steady solutions occur in the regions for  $0 < Dn \leq 818$  and  $1451 \leq Dn \leq 2767$ , periodic solutions for  $819 \leq Dn \leq 1450$  and  $2768 \leq Dn \leq 3500$ , and chaotic solutions for  $3600 \leq Dn \leq 6000$  at  $\delta=0.1$ . Linear stability analysis indicates that the stable steady solution exists for  $0 < Dn \leq 818.52$  and  $1450.81 \leq Dn \leq 2767.15$ . There-

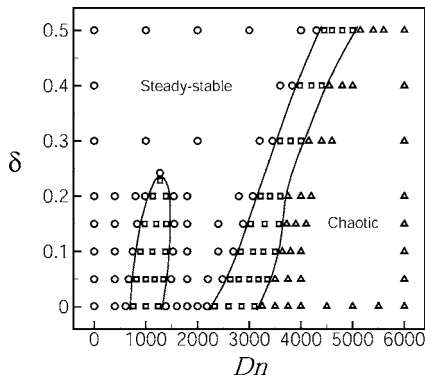


**Fig. 12** Distribution of the time-dependent solutions in the  $(Dn-\delta)$  plane for  $0 \leq Dn \leq 6000$  and  $0 < \delta \leq 0.5$  (○: steady-stable solution, □: periodic solution, △: chaotic solution, and the solid line shows a rough boundary of the periodic solutions)

fore, the results of the linear stability analysis and those of the time evolution calculations are consistent. In this study, the time evolution calculations for other values of  $\delta$  show that the time-dependent behavior is similar to that for  $\delta=0.1$ .

**5.2.2 Phase Diagram in the  $Dn-\delta$  Plane.** In this subsection, the distribution of the steady, periodic, and chaotic solutions, obtained by the time evolution calculations, is presented in Fig. 12 in the  $(Dn-\delta)$  domain for  $0 \leq Dn \leq 6000$  and  $0 < \delta \leq 0.5$ . In this picture, the circles indicate stable steady solutions, the squares periodic solutions, and the triangles chaotic solutions. As seen in Fig. 12, the steady flows turn into chaotic flows through periodic or multi-periodic flows if  $Dn$  is increased keeping  $\delta$  fixed. However, for smaller  $\delta$  ( $\delta \leq 0.23$ ) there exist two exclusive regions of  $Dn$  where the solution is time periodic, and in this case the flow undergoes “*steady*→*periodic*→*steady*→*periodic*→*chaotic*” if  $Dn$  is increased. And as  $\delta$  increases further ( $\delta \geq 0.24$ ), the region of the stable steady solution increases at a stretch and consequently the occurrence of the periodic state and hence the chaotic state is delayed as  $Dn$  increases.

**5.3 Nusselt Number.** The Nusselt number,  $Nu$ , defined in Eq. (17), can be used as an index of horizontal heat transfer from the walls to the fluid. If the flow field is not steady, the time average of the Nusselt number,  $Nu_{\tau}$ , is used as defined in Eq. (18). To study the convective heat transfer for differentially heated vertical sidewalls, variation of  $Nu$  with  $Dn$  for the first steady solution branch at  $\delta=0.1$  is shown in Fig. 13, where a thick solid line denotes  $Nu_c$  on the inner sidewall and a thin solid line  $Nu_h$  on the outer sidewall. Since only the first branch is linearly stable, calculation of the steady values of  $Nu$  is meaningful only for this branch. The time average of  $Nu$ , calculated by the time evolution computations on the inner and outer sidewalls at several values of  $Dn$ , is also shown in the same figure. In order to study the phenomena for the convective heat transfer from the walls to the fluid, temperature gradients on the inner (cooled) and outer (heated) sidewalls are calculated which are shown in Figs. 14(a) and 14(b), respectively.

As seen in Fig. 13, the steady values of  $Nu$  are a little different on both sidewalls at  $Dn=0$ . On the inner sidewall  $Nu$  is larger than that on the outer sidewall. This is due to the bend of the duct. The relative magnitude of  $Nu$ , however, reverses as  $Dn$  increases as seen in Fig. 13. In Fig. 14(a), it is shown that  $\partial T/\partial x$  on the inner (cooled) sidewall decreases in the central region around  $y=0$  as  $Dn$  increases. This is caused by the advection of the secondary flow in the outward direction around  $y=0$  due to the centrifugal force. In the same figure, it is also shown that  $\partial T/\partial x$  tends to increase in the regions other than the central region for  $Dn \geq 100$ . This is caused by the advection of the secondary flow in

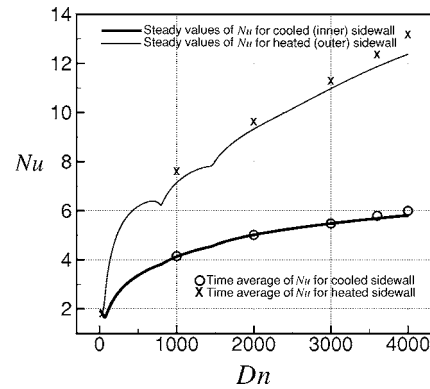


**Fig. 13** Variation of the Nusselt number ( $Nu$ ) with the Dean number ( $Dn$ ) for the first steady solution branch at  $\delta=0.1$

the inward direction there, which is a reverse flow of the outward secondary flow in the central region. As seen in Fig. 14(b),  $\partial T/\partial x$  increases monotonically over the whole region, as  $Dn$  goes up from zero. This is because the secondary flow enhances  $\partial T/\partial x$  not only in the central region but in other regions as well if  $Dn$  is increased.

Time average of  $Nu$ , obtained by the time evolution computation of  $Nu$  for the inner and outer sidewalls, is calculated at several values of  $Dn$  for both the periodic and chaotic solutions and is plotted with the steady values of  $Nu$  in Fig. 13. As seen in Fig. 13, the time-averaged values of  $Nu$  are larger than the steady values of  $Nu$  on the first steady solution branch for both the inner and outer sidewalls, which suggests that the occurrence of the periodic or chaotic flow enhances heat transfer in the flow. It should be remarked that the tendency of increasing  $Nu$  is larger on the outer sidewall than that on the inner sidewall for larger  $Dn$ , which can be explained by the fact that many subsidiary secondary vortices are generated near the outer sidewall [35]. To compare the convective heat transfer of a curved duct with that of a straight channel, an additional calculation of  $Nu$  for a straight channel is conducted. It is found that at the specific Dean number,  $Dn=3600$ , which is equivalent to the Reynolds number  $Re=Dn/\sqrt{2\delta}=8050$ ,  $Nu$  for the curved duct is approximately 400% larger than that of the corresponding straight channel. This result indicates that heat transfer is more strongly enhanced by the curved duct than that in a straight channel, and that heat is transferred a great deal as  $Dn$  becomes large.

## 6 Discussion

In this section, a brief discussion on the plausibility of applying 2-D calculations to study curved duct flows will be given. As explained in the Introduction, it has been shown by many experimental and numerical studies that curved duct flows easily attain asymptotic fully developed 2-D states (uniform in the main flow direction) at most 270 deg from the inlet. In this concern, a question may arise that 2-D analysis is valid if the asymptotic state is steady, but its applicability is doubtful if it is not steady, such as periodic. However, a recent work by Wang and Yang [27] gives a clear answer to the question that even periodic flows can be analyzed by 2-D calculations. They showed that for an oscillating flow, there exists a close similarity between the flow observation at 270 deg and 2-D calculation. In fact the periodic oscillation, observed in the cross section of their duct, was a traveling wave advancing in the downstream direction. Therefore, it is found that 2-D calculations can predict the existence of three-dimensional traveling wave solutions as an appearance of 2-D periodic oscillation.

Traveling waves were also observed by Mees et al. [18,19]. It is noteworthy that even a curved duct flow that does not attain an asymptotic state can be analyzed by 2-D calculations. In the paper

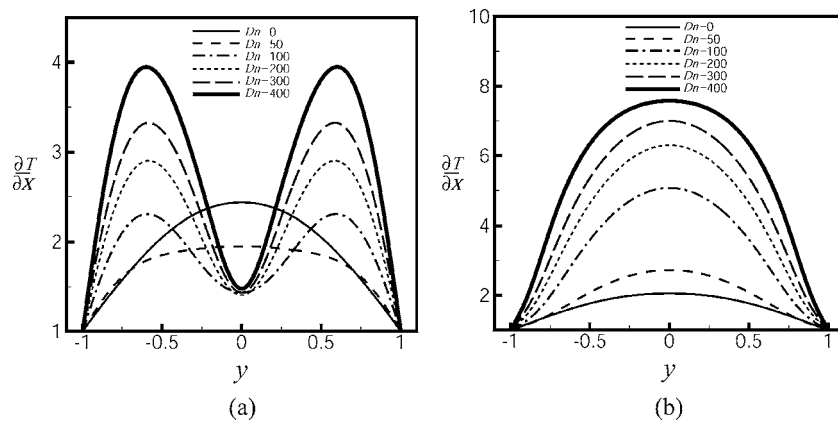


Fig. 14 Temperature gradients for  $\delta=0.1$  (a) at the cooled sidewall and (b) at the heated sidewall

by Mees et al. [40], they observed the change of secondary flow pattern far downstream using a spiral duct, where  $Dn$  increases in the downstream due to an increase of  $\delta$  as the radius of the duct becomes smaller. It was found that the flow exhibits an oscillation between two- and four-vortex flows first, but turns to a steady two-vortex flow downstream. This can be explained by the present bifurcation study as follows. In Fig. 12 of the present paper, we presented the bifurcation diagram where it is shown that there exists a region of stable steady solutions (two-vortex solutions) in the lowest  $Dn$  region, and oscillating solutions appear if  $Dn$  is increased (an oscillation of two- and four-vortex solutions). If  $Dn$  is increased further, a region of stable steady solutions again appears when two-vortex solutions are observed. Though the present paper treats non-isothermal flows, nearly the same change of the solution occurs in the bifurcation diagram for the isothermal case ( $Gr=0$ ) [28]. Therefore, it is found that the flow change in the downstream of the spiral duct can be explained by 2-D bifurcation analysis.

There is some evidence showing that the occurrence of chaotic or turbulent flow may be predicted by 2-D analysis. Yamamoto et al. [41] investigated linear stability of helical pipe flows with respect to 2-D perturbations and compared the results with the experimental data obtained by Yamamoto et al. [42]. There was a good agreement between the numerical results and the experimental data, which shows that even the transition to turbulence can be predicted by 2-D analysis to some extent, though it is true that the full transition process cannot be elucidated by 2-D analysis. The transition to chaos of the periodic oscillation, obtained by the 2-D calculation in the present paper, may correspond to destabilization of traveling waves in the curved duct flows like that of Tollmien-Schlichting waves in a boundary layer. Our 2-D analysis, therefore, may contribute to the study of curved duct flows. First, it gives an outline of the behaviors for not only fully developed but developing curved duct flows. Second, the asymptotic behavior is obtained by only 2-D analysis and, without the knowledge of an asymptotic behavior of the flows, it is difficult to have a good physical insight into the curved duct flows. Finally, the complete bifurcation study, which is hardly possible in three-dimensional analysis, gives a firm framework for the three-dimensional study of steady, periodic, and chaotic curved duct flows.

## 7 Conclusions

A detailed numerical study of fully developed two-dimensional flow and heat transfer through a curved duct of square cross section has been performed by using the spectral method. In the present study, a temperature difference is applied across the vertical sidewalls where the outer wall is heated and the inner one

cooled. Numerical calculations are carried out covering a wide range of curvature,  $0 < \delta \leq 0.5$ , and the Dean number,  $0 \leq Dn \leq 6000$ , for the Grashof number  $Gr=100$ .

After a comprehensive survey over the range of the parameters, two branches of asymmetric steady solutions are obtained for any  $\delta$  lying in the range. Linear stability of the steady solutions reveals that only the first branch is linearly stable while the other branch is linearly unstable. The first branch is linearly stable in two distinct intervals of  $Dn$  for smaller  $\delta$  ( $\delta \leq 0.23$ ); for larger  $\delta$  ( $\delta \geq 0.24$ ), on the other hand, the same branch is found to be linearly stable in a single but wide interval of  $Dn$ . It is found that the Hopf bifurcation occurs at  $Dn$  on the boundary between the stable and unstable solutions. Time evolution calculations as well as their spectral analyses show that in the first unstable region ( $\delta \leq 0.23$ ) the flow undergoes “steady-periodic-steady-periodic-chaotic;” in the second unstable region ( $\delta \geq 0.24$ ), however, the steady flow turns into chaos through periodic or multi-periodic oscillations in the straightforward scenario “steady-periodic-chaotic,” if  $Dn$  is increased. It is found that the transition to periodic or chaotic state is retarded consistently with an increase of  $\delta$ . In order to investigate the transition from the multi-periodic oscillations to the chaotic states in more detail, the spectral analysis is found to be very useful. In this regard, it is interesting to notice that the chaotic solution is weak for smaller  $Dn$ , where the solution drifts among the steady solution branches; for larger  $Dn$ , on the other hand, the chaotic solution becomes strong, where the solution gets away from the steady solution branches. It is worth mentioning that irregular oscillation of the isothermal flow through a curved duct has been observed experimentally by Ligrani and Niver [34] for the large aspect ratio and by Wang and Yang [22,27] in a square duct.

Steady values of  $Nu$ , calculated for the first steady solution branch, show that the larger  $Dn$  is, the larger  $Nu$  becomes on the outer sidewall. Time-averaged values of  $Nu$  have also been calculated for cases when the field is periodic or chaotic, and consequently it is suggested that the periodic or chaotic flow enhances heat transfer in the flow. The rate of convective heat transfer at the outer sidewall is found to be enhanced significantly more than that in a straight channel and is seen to increase as secondary flow activities become stronger.

## Acknowledgment

The authors gratefully acknowledge the reviewers for their critical but constructive comments and suggestions on the original manuscript. R. N. Mondal, one of the authors, would like to acknowledge gratefully the financial support from the Japanese Min-

## Nomenclature

- $d$  = half width (or height) of the duct cross section  
 $D_n$  = Dean number  
 $g$  = gravitational acceleration  
 $G$  = mean pressure gradient in the main flow direction  
 $Gr$  = Grashof number  
 $L$  = radius of the duct curvature  
 $Nu$  = Nusselt number  
 $Pr$  = Prandtl number  
 $t$  = time  
 $T$  = temperature  
 $u$  = velocity component in the  $x$  direction  
 $v$  = velocity component in the  $y$  direction  
 $w$  = velocity component in the  $z$  direction  
 $x$  = horizontal axis  
 $y$  = vertical axis  
 $z$  = axis in the direction of the main flow

## Greek Letters

- $\gamma$  = coefficient of thermal expansion  
 $\delta$  = curvature of the duct  
 $\kappa$  = thermal diffusivity  
 $\lambda$  = resistance coefficient  
 $\mu$  = viscosity  
 $\nu$  = kinematic viscosity  
 $\rho$  = density  
 $\psi$  = sectional stream function

## References

- Berger, S. A., Talbot, L., and Yao, L. S., 1983, "Flow in Curved Pipes," *Annu. Rev. Fluid Mech.*, **35**, pp. 461–512.
- Nandakumar, K., and Masliyah, J. H., 1986, "Swirling Flow and Heat Transfer in Coiled and Twisted Pipes," *Adv. Transp. Processes*, **4**, pp. 49–112.
- Ito, H., 1987, "Flow in Curved Pipes," *JSME Int. J.*, **30**, pp. 543–552.
- Berger, S. A., 1991, "Flow and Heat Transfer in Curved Pipes and Tubes," AIAA Paper No. 91-0030, pp. 1–19.
- Ghia, K. N., and Sokhey, J. S., 1977, "Laminar Incompressible Viscous Flow in Curved Ducts of Rectangular Cross-section," *ASME J. Fluids Eng.*, **99**, pp. 640–648.
- Humphrey, J. A. C., Taylor, A. M. K., and Whitelaw, J. H., 1977, "Laminar Flow in a Curved Duct of Strong Curvature," *J. Fluid Mech.*, **83**, pp. 509–527.
- Yee, G., Chilukuri, R., and Humphrey, J. A. C., 1980, "Developing Flow and Heat Transfer in Strongly Curved Ducts of Rectangular Cross Section," *ASME J. Heat Transfer*, **102**, pp. 285–291.
- Taylor, A. M. K. P., Whitelaw, J. H., and Yianneskis, M., 1982, "Curved Ducts with Strong Secondary Motion: Velocity Measurements of Developing Laminar and Turbulent Flow," *ASME J. Fluids Eng.*, **104**, pp. 350–359.
- Hille, P., Vehrenkamp, R., and Schulz-Dubois, E. O., 1985, "The Development and Structure of Primary and Secondary Flow in a Curved Square Duct," *J. Fluid Mech.*, **151**, pp. 219–241.
- Sankar, S. R., Nandakumar, K., and Masliyah, J. H., 1988, "Oscillatory Flows in Coiled Square Ducts," *Phys. Fluids*, **31**, pp. 1348–1358.
- Sugiyama, S., Aoi, T., Yamamoto, M., and Narisawa, N., 1989, "Measurements of Developing Laminar Flow in a Curved Rectangular Duct by Means of LDV," *Experimental Heat Transfer, Fluid Mechanics and Thermodynamics*, R. K. Shah et al., eds., pp. 1185–1191.
- Soh, W. Y., 1988, "Developing Flow in a Curved Duct of Square Cross-Section and its Fully Developed Dual Solutions," *J. Fluid Mech.*, **188**, pp. 337–361.
- Winters, K. H., 1987, "A Bifurcation Study of Laminar Flow in a Curved Tube of Rectangular Cross-Section," *J. Fluid Mech.*, **180**, pp. 343–369.
- So, R. M. C., Zhang, H. S., and Lai, Y. G., 1991, "Secondary Cells and Separation in Developing Laminar Curved-Pipe Flows," *Theor. Comput. Fluid Dyn.*, **3**, pp. 141–162.
- Bara, B., Nandakumar, K., and Masliyah, J. H., 1992, "An Experimental and Numerical Study of the Dean Problem: Flow Development Towards Two-Dimensional Multiple Solutions," *J. Fluid Mech.*, **244**, pp. 339–376.
- Shantini, W., and Nandakumar, K., 1986, "Bifurcation Phenomena of Generalized Newtonian Fluids in Curved Rectangular Ducts," *J. Non-Newtonian Fluid Mech.*, **22**, pp. 35–60.
- Yao, L. S., and Berger, S. A., 1975, "Entry Flow in a Curved Pipe," *J. Fluid Mech.*, **67**, pp. 177–196.
- Mees, P. A. J., Nandakumar, K., and Masliyah, J. H., 1996, "Instability and Transitions of Flow in a Curved Square Duct: The Development of the Two Pairs of Dean Vortices," *J. Fluid Mech.*, **314**, pp. 227–246.
- Mees, P. A. J., Nandakumar, K., and Masliyah, J. H., 1996, "Secondary Instability of Flow in a Curved Duct of Square Cross Section," *J. Fluid Mech.*, **323**, pp. 387–409.
- Cheng, K. C., Lin, R. C., and Ou, J. W., 1975, "Graetz Problem in Curved Square Channels," *ASME J. Heat Transfer*, **97**, pp. 244–248.
- Joseph, B., Smith, E. P., and Adler, R. J., 1975, "Numerical Treatment of Laminar Flow in Helically Coiled Tubes of Square Cross Section," *AIChE J.*, **21**, pp. 965–974.
- Wang, L., and Yang, T., 2004, "Bifurcation and Stability of Forced Convection in Curved Ducts of Square Cross-Section," *Int. J. Heat Mass Transfer*, **47**, pp. 2971–2987.
- Daskopoulos, P., and Lenhoff, A. M., 1989, "Flow in Curved Ducts: Bifurcation Structure for Stationary Ducts," *J. Fluid Mech.*, **203**, pp. 125–148.
- Finlay, W. H., and Nandakumar, K., 1990, "Onset of Two-Dimensional Cellular Flow in Finite Curved Channels of Large Aspect Ratio," *Phys. Fluids A*, **2**, pp. 1163–1174.
- Thangam, S., and Hur, N., 1990, "Laminar Secondary Flows in Curved Rectangular Ducts," *J. Fluid Mech.*, **217**, pp. 421–440.
- Yanase, S., Kaga, Y., and Daikai, R., 2002, "Laminar Flows Through a Curved Rectangular Duct Over a Wide Range of the Aspect Ratio," *Fluid Dyn. Res.*, **31**, pp. 151–183.
- Wang, L., and Yang, T., 2005, "Periodic Oscillation in Curved Duct Flows," *Physica D*, **200**, pp. 296–302.
- Mondal, R. N., Kaga, Y., Hyakutake, T., and Yanase, S., 2005, "Unsteady Solutions and the Bifurcation Diagram for the Flow Through a Curved Square Duct," *Fluid Dyn. Res.* (revised again and submitted).
- McCormack, P. D., Welker, H., and Kelleher, M., 1970, "Taylor Goertler Vortices and Their Effect on Heat Transfer," *ASME J. Heat Transfer*, **92**, pp. 101–112.
- Sturgis, J. C., and Mudawar, I., 1999, "Single-Phase Heat Transfer Enhancement in a Curved Rectangular Channel Subjected to Concave Heating," *Int. J. Heat Mass Transfer*, **42**(7), pp. 1255–1272.
- Cheng, K. C., and Akiyama, M., 1970, "Laminar Forced Convection Heat Transfer in Curved Rectangular Channels," *Int. J. Heat Mass Transfer*, **13**, pp. 471–490.
- Mori, Y., Uchida, Y., and Ukon, T., 1971, "Forced Convective Heat Transfer in Curved Channel with a Square Cross Section," *Int. J. Heat Mass Transfer*, **14**, pp. 1787–1805.
- Ru, Y., and Chang, S. F., 1994, "Combined Free and Forced Convection for Developed Flow in Curved Pipes with Finite Curvature Ratio," *Int. J. Heat Fluid Flow*, **15**(6), pp. 470–476.
- Ligrani, P. M., and Niver, R. D., 1988, "Flow Visualization of Dean Vortices in a Curved Channel with 40 to 1 Aspect Ratio," *Phys. Fluids*, **31**, pp. 3605–3617.
- Chandratilleke, T. T., and Nursubyakto, 2003, "Numerical Prediction of Secondary Flow and Convective Heat Transfer in Externally Heated Curved Rectangular Ducts," *Int. J. Therm. Sci.*, **42**, pp. 187–198.
- Yanase, S., Mondal, R. N., Kaga, Y., and Yamamoto, K., 2005, "Transition from Steady to Chaotic States of Isothermal and Non-Isothermal Flows Through a Curved Rectangular Duct," *J. Phys. Soc. Jpn.*, **74**(1), pp. 345–358.
- Yanase, S., Mondal, R. N., and Kaga, Y., 2005, "Numerical Study of Non-Isothermal Flow with Convective Heat Transfer in a Curved Rectangular Duct," *Int. J. Therm. Sci.*, **44**(11), pp. 1047–1060.
- Yanase, S., Yamamoto, K., and Yoshida, T., 1994, "Effects of Curvature on Dual Solutions of Flow Through a Curved Circular Tube," *Fluid Dyn. Res.*, **13**, pp. 217–228.
- Ruelle, D., and Takens, F., 1971, "On the Nature of Turbulence," *Commun. Math. Phys.*, **20**, pp. 167–192.
- Mees, P. A. J., Nandakumar, K., and Masliyah, J. H., 1996, "Steady Spatial Oscillations in a Curved Duct of Square Cross-Section," *Phys. Fluids*, **8**(12), pp. 3264–3270.
- Yamamoto, K., Yanase, S., and Jiang, R., 1998, "Stability of the Flow in a Helical Tube," *Fluid Dyn. Res.*, **22**, pp. 153–170.
- Yamamoto, K., Akita, T., Ikeuchi, H., and Kita, Y., 1995, "Experimental Study of the Flow in a Helical Circular Tube," *Fluid Dyn. Res.*, **16**, pp. 237–249.

# Numerical Simulation of Two-Dimensional Laminar Incompressible Wall Jet Flow Under Backward-Facing Step

P. Rajesh Kanna  
Research Scholar

Manab Kumar Das<sup>1</sup>  
Associate Professor  
e-mail: manab@iitg.ernet.in

Department of Mechanical Engineering,  
Indian Institute of Technology Guwahati,  
North Guwahati, Guwahati-781039, Assam,  
India

*Two-dimensional laminar incompressible wall jet flow over a backward-facing step is solved numerically to gain insight into the expansion and recirculation of flow processes. Transient streamfunction vorticity formulation of the Navier-Stokes equation is solved with clustered grids on the physical domain. The behavior of the jet has been studied for different step geometry (step length,  $l$ , step height,  $s$ ) and Reynolds number ( $Re$ ). It is found that the presence of a step in the wall jet flow creates recirculation and the reattachment length follows an almost linear trend within the range considered for both parameters  $Re$  and step geometry. Simulations are made to show the effect of entrainment on recirculation eddy. Detailed study of  $u$  velocity decay is reported. The velocity profile in the wall jet region shows good agreement with experimental as well as similarity results. The distance where the similarity profile forms is reduced by increasing the step geometry whereas an increment in  $Re$  increases this distance. The effects of  $Re$ , step length, and step height on wall vorticity are presented. The parametric study is helpful to predict the reattachment location for wall jet flows over step. [DOI: 10.1115/1.2243298]*

*Keywords:* wall jet, recirculation, wall vorticity, similarity, backward-facing step

## 1 Introduction

Depending upon the distance of the confining boundaries from the discharge, a jet can be analyzed as a free jet or a bounded one. If the boundaries (parallel to inlet axis) are sufficiently away from the origin of the jet, the flow is termed as a free jet. However, a bounded jet will occur when it interacts with a parallel wall. Bounded jet flows occur in many engineering applications such as environmental discharges, heat exchangers, fluid injection systems, cooling of combustion chamber wall in a gas turbine, automobile demister, and others. Bounded jets can be classified into three types: (a) impinging jet aimed towards the boundary, (b) wall jet where fluid is discharged at the boundary, and (c) offset jet from a vertical wall of a stagnant pool issuing parallel to a horizontal solid wall.

The flow emanating from a two-dimensional (2D) plane wall jet is shown in Fig. 1(a) where the main features and regions of interest are depicted. Fluid is discharged from a slot along the vertical wall into the ambient near a horizontal solid boundary parallel to the inlet jet direction. The jet flow features are different in various regions. In the near-field up to the step from the point of discharge, the jet behaves like a plane wall jet. Further the jet expands across the step. Due to entrainment between the solid wall and the jet there is a reduction of pressure in this region, forcing the jet to deflect towards the boundary and eventually attach with it. This is called the Coanda effect. In the region around the attachment point, that is, the impingement region and part of the recirculation region, the jet can be partly characterized as an impingement jet. The jet becomes a wall jet in the far field. Other factors like free-stream velocity, ambient stratification, buoyancy (density difference), discharge orientation, etc., further complicate the jet-boundary interaction and the behavior of a wall jet.

<sup>1</sup>Author to whom all correspondence should be addressed.

Contributed by the Fluids Engineering Division of ASME for publication in the JOURNAL OF FLUIDS ENGINEERING. Manuscript received January 27, 2005; final manuscript received January 25, 2006. Review conducted by Joseph Katz.

Wall jet flow over the step has many practical applications. Wall jet flow is commonly used in the windshield defroster system in automobiles. A jet of hot air is blown along the windshield to protect the surface from its surroundings. Introducing a recirculation by means of a step to enhance the heat transfer is an interesting study on this situation. The recirculation is used to shift the peak Nusselt number location in the downstream direction. Another example can be found from the cooling of electronic components. Steplike geometries are very often found in multi-processor electronic components. For better performance, they are designed to maintain at constant low temperature. Wall jets are used to cool such hot surfaces. The knowledge of recirculation eddy size is technically important from the design point of view in connection with  $Re$  and the step length and height. It is a common belief that the peak Nusselt number will occur near the reattachment location. So, it is very important to find the reattachment location in connection with  $Re$  and geometry. Wall jet flow over a step has several similar applications like a refrigerated air curtain, the paper industry, etc. The understanding of the flow behavior of the wall jet over a step is important in engineering practices. If attachment is not desired for more mixing, a knowledge of calculation and design is required to prevent it. For a case where attachment is desirable, study of the involved variables is required so that a precise location of the attachment point and the containment of the flow can be established. Moreover, this simulation will be helpful to set approximate guidelines for carrying out experiments.

Analytical solutions of the wall jet are available, based on the self-similarity of the velocity field [1,2]. However, these solutions are valid only far away from the jet inlet and, in most applications, the near-field development holds the key to important features of the jet flow and recirculation. Therefore, the near-field development of a wall jet has been the subject of a lot of research in recent years.

Amitay and Cohen [3] have reported the effects of wall blowing and suction on the stability characteristics of a laminar incompressible two-dimensional plane wall jet. Cohen et al. [4] did

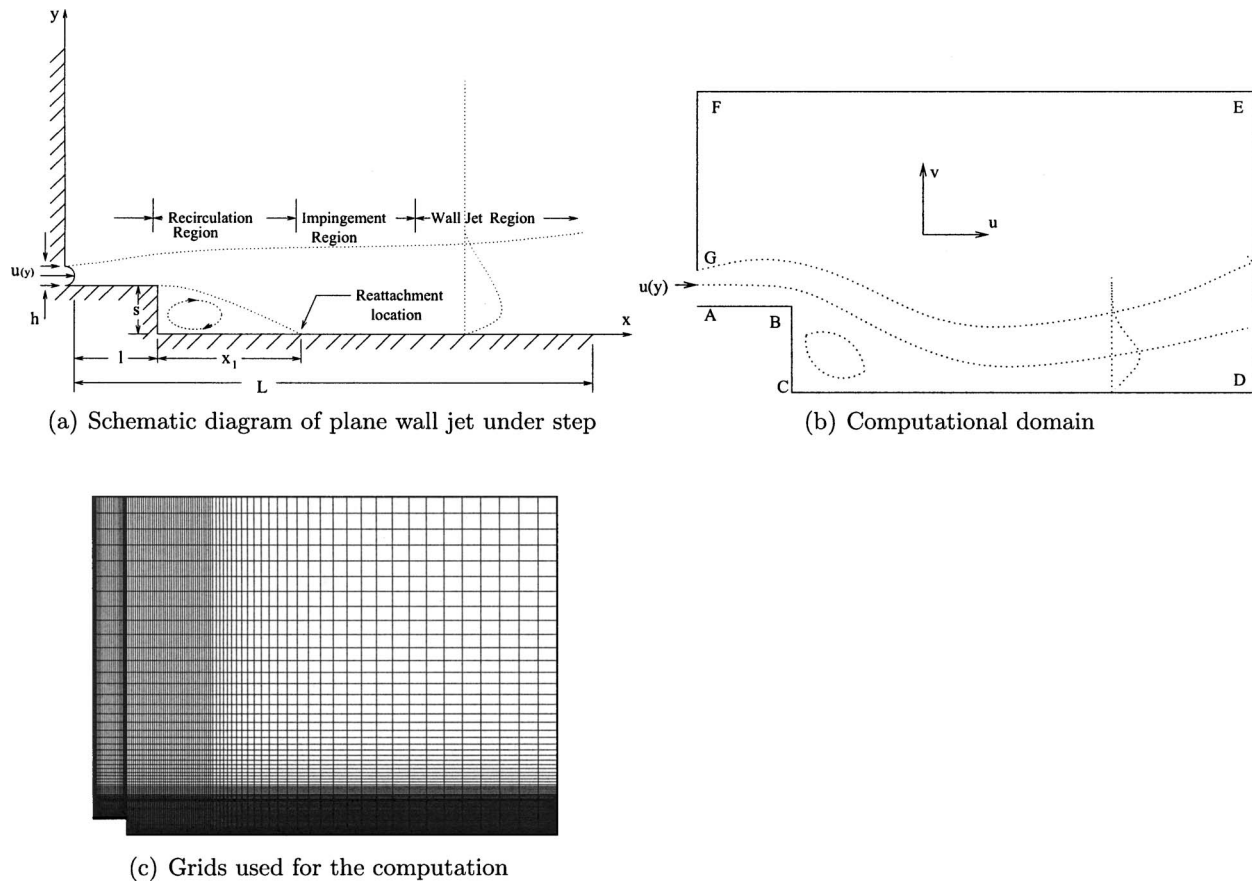


Fig. 1 Schematic diagram and boundary conditions in a wall jet under backward-facing step problem

work on transition of wall jets subjected to blowing and suction. Quintana et al. [5] experimentally investigated the mean and fluctuating characteristics of a plane unsteady laminar wall jet for constant wall temperature. Seidel [6] has done numerical work to find the effect of high amplitude forcing on laminar and turbulent wall jets over a heated flat plate. Seidel has used DNS for laminar case and RANS for turbulent wall jet. Recently, Bhattacharjee and Loth [7] simulated laminar and transitional cold wall jets. They have investigated the significance of three different inlet profiles, viz., parabolic, uniform, and ramp, and presented the detailed results of time-averaged wall jet thickness and temperature distribution. They used the RANS approach for higher Reynolds number and DNS approach for three-dimensional wall jet.

The stability of 2D free jets was studied experimentally by Sato [8] and Sato and Sakao [9]. Theoretical analyses for axisymmetric free jets were carried out by Batchelor and Gill [10] and Cohen and Wygnanski [11]. Sarma et al. [12] have studied 2D incompressible jet development inside a duct in the laminar flow regime for cases with and without entrainment of ambient fluid. The effect of channel length in the backward-facing step is studied by Barton [13]. For similar geometry for the pulsatile inlet condition heat transfer, results were reported by Valencia and Hinojosa [14]. Jacob et al. [15] investigated the sound radiation by a backward-facing step under a plane wall jet.

Though many studies have been conducted on wall jets, the available literature on theoretical simulation of plane laminar wall jets over step jet flow is not carried by anybody. The case of an entraining jet located near the jet discharge, which occurs in several practical applications, has not been studied. In the present study, a time marching incompressible flow solver has been applied for simulating the flow features of wall jet for a range of step geometry (step length,  $l$ , step height,  $s$ ) and Reynolds number.

## 2 Mathematical Formulation

An incompressible two-dimensional laminar wall jet under backward-facing step jet flow is considered. For the sake of simplicity, the jet is assumed to be isothermal and have the same density as the ambient fluid. Also, the velocity profile at the jet inlet is taken as parabolic.

The governing equations for incompressible laminar flow are solved by stream-function-vorticity formulation. The transient nondimensional governing equations in the conservative form are

$$\nabla^2 \psi = -\omega \quad (1)$$

Vorticity equation

$$\frac{\partial \omega}{\partial t} + \frac{\partial(u\omega)}{\partial x} + \frac{\partial(v\omega)}{\partial y} = \frac{1}{\text{Re}} \nabla^2 \omega \quad (2)$$

where  $\psi$  is the stream function,  $u = \partial\psi/\partial y$ ,  $v = -\partial\psi/\partial x$ , and  $\omega = \partial v/\partial x - \partial u/\partial y$ .

The variables are scaled as

$$u = \frac{\bar{u}}{\bar{U}}; \quad v = \frac{\bar{v}}{\bar{U}}; \quad x = \frac{\bar{x}}{h}; \quad y = \frac{\bar{y}}{h}; \quad \omega = \frac{\bar{\omega}}{\bar{U}/h}; \quad t = \frac{\bar{t}}{h/\bar{U}}$$

with the overbar indicating a dimensional variable and  $\bar{U}$ ,  $h$  denoting the average jet velocity at the nozzle exit and the jet width, respectively.

The boundary conditions needed for the numerical simulation have been prescribed. For an offset jet with entrainment, the following dimensionless conditions have been enforced as shown in Fig. 1(b). The inlet slot height is assumed as  $h=0.05$  m.

At the jet inlet, along AG (Fig. 1(b)),

$$u(y) = 120y - 2400y^2; \quad \omega(y) = 4800y - 120;$$

$$\psi(y) = 60y^2 - 800y^3 \quad (3a)$$

Along  $FG$ ,  $AB$ ,  $BC$ , and  $CD$  due to no-slip condition,

$$u = v = 0 \quad (3b)$$

Along  $EF$ ,

$$\frac{\partial u}{\partial x} = 0 \quad (3c)$$

At the downstream boundary, the condition of zero first-derivative has been applied for velocity components. This condition implies that the flow has reached a developed condition. Thus, at  $(DE)$ ,

$$\frac{\partial u}{\partial x} = \frac{\partial v}{\partial x} = 0 \quad (3d)$$

### 3 Numerical Procedure

The unsteady vorticity transport equation (2) in time is solved by alternate direction implicit scheme (ADI). The central differencing scheme is followed for both the convective as well as the diffusive terms [16]. It consists of two half time-steps.

The first half time-step:

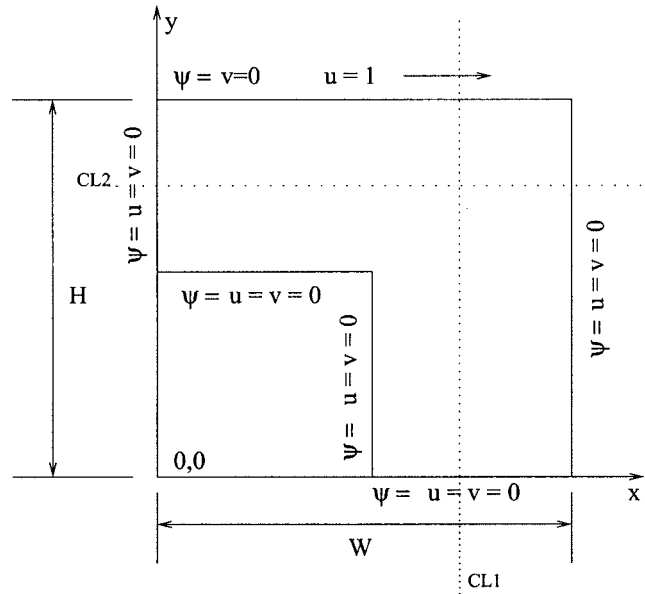
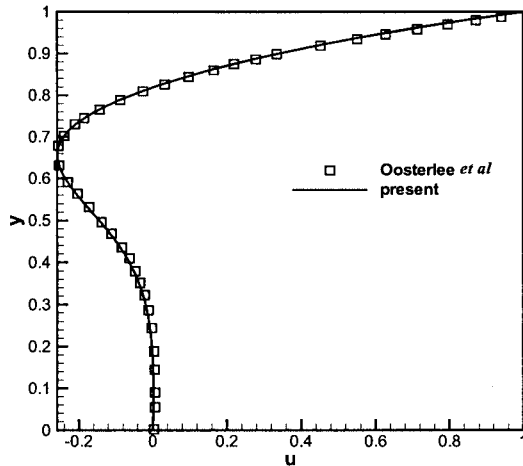
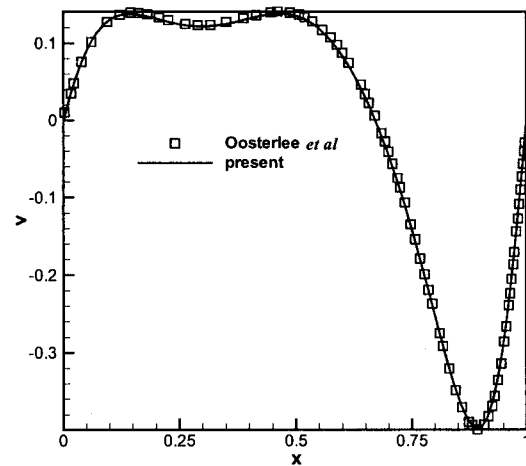


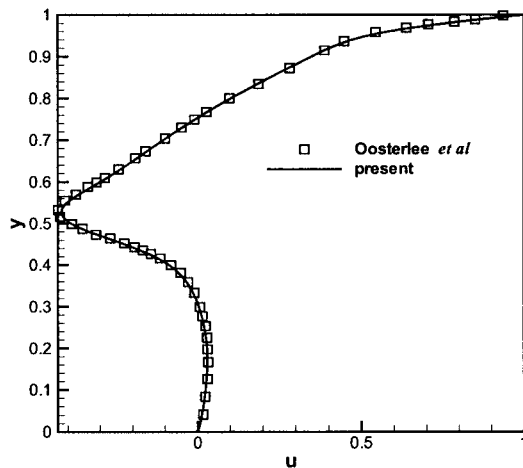
Fig. 2 Schematic diagram and boundary conditions of L-shaped lid driven cavity flow problem [30]



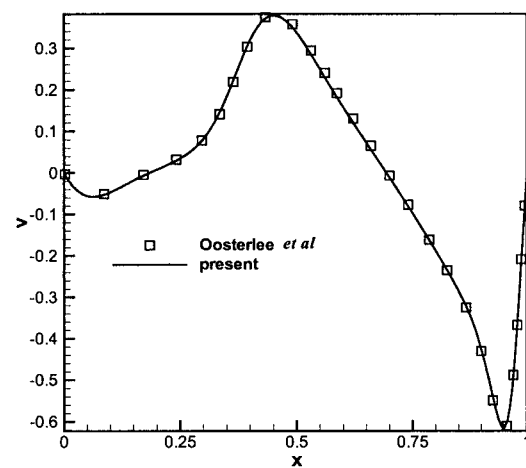
(a)  $u$ -velocity (CL1),  $Re = 100$



(b)  $v$ -velocity (CL2),  $Re = 100$

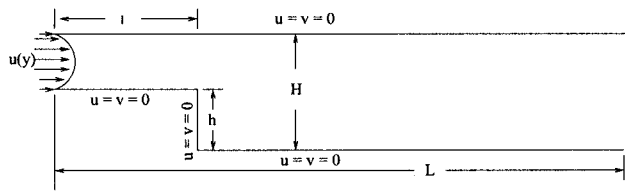


(c)  $u$ -velocity (CL1),  $Re = 1000$

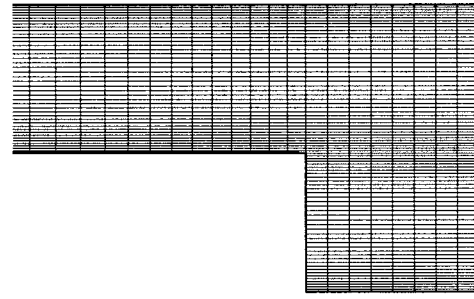


(d)  $v$ -velocity (CL2),  $Re = 1000$

Fig. 3 Velocity profiles along CL1 and CL2



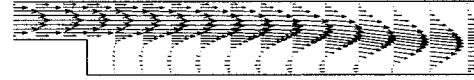
(a) Schematic diagram



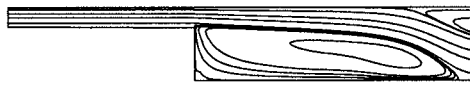
(b) Clustered grids used near the step: ER=0.5



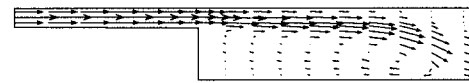
(c)  $Re = 500$ ,  $ER=0.5$ . Streamline contour



(d)  $Re = 500$ ,  $ER=0.5$ . Velocity vector



(e)  $Re = 200$ ,  $ER=0.75$ . Streamline contour



(f)  $Re = 500$ ,  $ER=0.75$ . Velocity vector

**Fig. 4 Backward-facing step flow with upstream channel problem. (Domain shown near the step.)**

$$\frac{\omega_{i,j}^{n+1/2} - \omega_{i,j}^n}{\Delta t/2} + Lx(u\omega)_{i,j}^{n+1/2} + Ly(v\omega)_{i,j}^n - \frac{1}{Re} [Lxx(\omega)_{i,j}^{n+1/2} + Lyy(\omega)_{i,j}^n] = 0 \quad (4a)$$

The second half time-step:

$$\frac{\omega_{i,j}^{n+1} - \omega_{i,j}^{n+1/2}}{\Delta t/2} + Lx(u\omega)_{i,j}^{n+1/2} + Ly(v\omega)_{i,j}^{n+1} - \frac{1}{Re} [Lxx(\omega)_{i,j}^{n+1/2} + Lyy(\omega)_{i,j}^{n+1}] = 0 \quad (4b)$$

where,

$$Lx(u\omega)_{i,j} = \frac{(u\omega)_{i+1,j} - (u\omega)_{i-1,j}}{\Delta x_i + \Delta x_{i-1}}, \quad Ly(v\omega)_{i,j} = \frac{(v\omega)_{i,j+1} - (v\omega)_{i,j-1}}{\Delta y_j + \Delta y_{j-1}} \quad (5a)$$

$$Lxx(\omega)_{i,j} = \frac{\omega_{i-1,j} - 2\omega_{i,j} + \omega_{i+1,j}}{\Delta x_i * \Delta x_{i-1}}, \quad (5b)$$

$$Lyy(\omega)_{i,j} = \frac{\omega_{i,j-1} - 2\omega_{i,j} + \omega_{i,j+1}}{\Delta y_j * \Delta y_{j-1}}$$

Equations (4a) and (4b) are rearranged to give the following equations (6a) and (6b).

$$\begin{aligned} &= (C_x u_{i-1,j}^n + S_x) \omega_{i-1,j}^{n+1/2} + (1 + 2S_x) \omega_{i,j}^{n+1/2} - (-C_x u_{i+1,j}^n + S_x) \omega_{i+1,j}^{n+1/2} \\ &= (C_y v_{i,j-1}^n + S_y) \omega_{i,j-1}^{n+1/2} + (1 - 2S_y) \omega_{i,j}^{n+1/2} + (-C_y v_{i,j+1}^n + S_y) \omega_{i,j+1}^{n+1/2} \end{aligned} \quad (6a)$$

$$\begin{aligned} &- (C_y v_{i-1,j}^n + S_y) \omega_{i-1,j}^{n+1} + (1 + 2S_y) \omega_{i,j}^{n+1} - (-C_y v_{i,j+1}^n + S_y) \omega_{i,j+1}^{n+1} \\ &= (C_x u_{i-1,j}^n + S_x) \omega_{i-1,j}^{n+1/2} + (1 - 2S_x) \omega_{i,j}^{n+1/2} \\ &+ (-C_x u_{i+1,j}^n + S_x) \omega_{i+1,j}^{n+1/2} \end{aligned} \quad (6b)$$

where

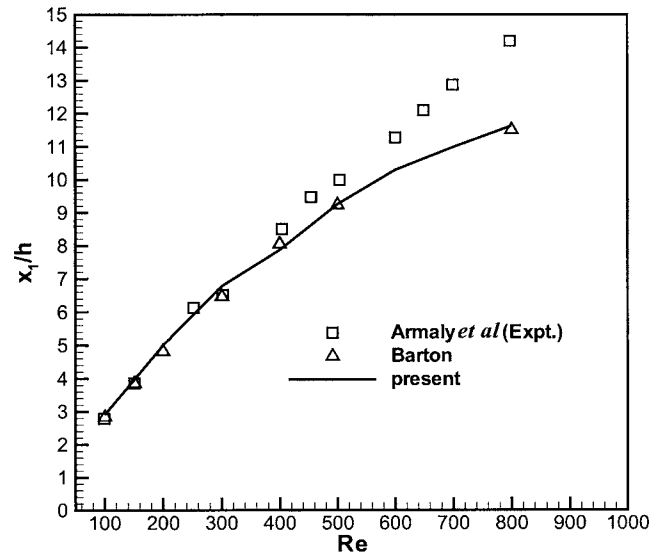


**Fig. 5 Reattachment length for different Reynolds number: parabolic inlet profile**



**Table 1 Primary vortex reattachment length (ER=0.25, Re =500)**

[32]	[14]	Present
0.84628	1.1158	1.0707

**Table 2 Primary vortex reattachment length (ER=0.75, Re =200)**

[32]	[14]	Present
6.4868	7.0261	7.1469

$$C_x = \frac{\Delta t}{2(\Delta x_i + \Delta x_{i-1})}, \quad C_y = \frac{\Delta t}{2(\Delta y_j + \Delta y_{j-1})},$$

$$S_x = \frac{\Delta t}{\text{Re} \Delta x_i} \frac{1}{(\Delta x_i + \Delta x_{i-1})}, \quad S_y = \frac{\Delta t}{\text{Re} \Delta y_j} \frac{1}{(\Delta y_j + \Delta y_{j-1})}$$

The discretization of Eq. (1) is given by:

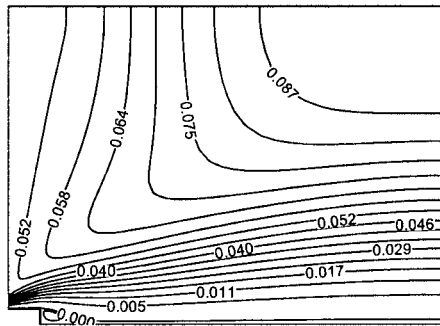
$$Lxx(\psi) + Lyy(\psi) = -\omega_{i,j} \quad (7)$$

The velocity components are updated by the following equations:

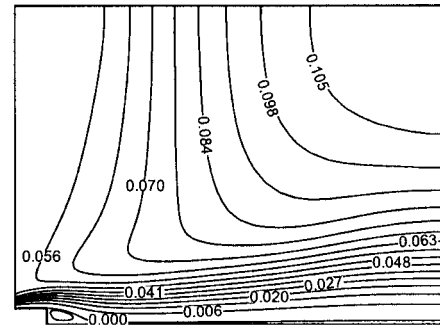
$$u = \frac{\partial \psi}{\partial y} = \frac{\psi_{i,j+1} - \psi_{i,j-1}}{\Delta y_j + \Delta y_{j-1}} \quad (8a)$$

$$v = -\frac{\partial \psi}{\partial x} = \frac{\psi_{i+1,j} - \psi_{i-1,j}}{\Delta x_i + \Delta x_{i-1}} \quad (8b)$$

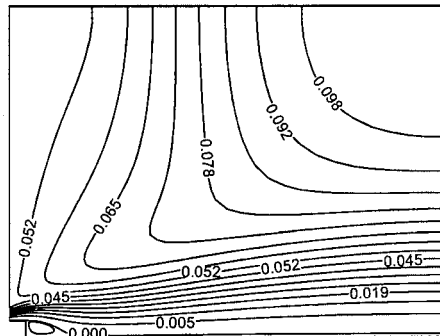
The velocities (Eqs. (6a) and (6b)) are calculated at the  $n$ th level while advancing to the  $(n+1)$ th time level. Because of this approximation in the nonlinear terms, the second-order accuracy



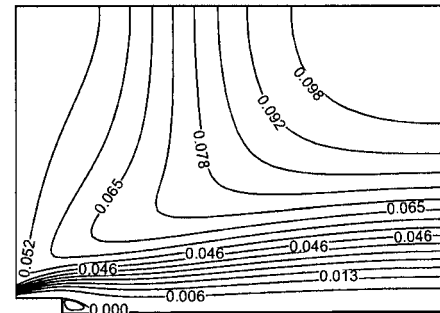
(a)  $l = 2h, s = 1h, Re = 300$



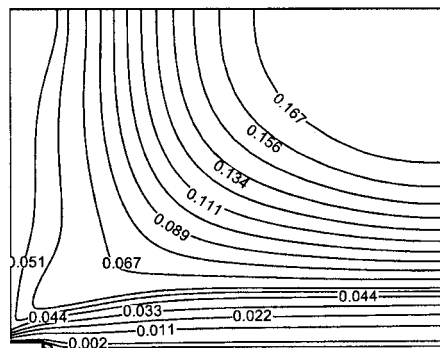
(b)  $l = 2h, s = 1h, Re = 600$



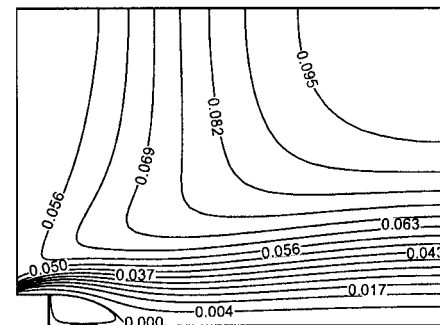
(c)  $l = 1h, s = 1h, Re = 400$



(d)  $l = 3h, s = 1h, Re = 400$



(e)  $l = 2h, s = 0.5h, Re = 400$



(f)  $l = 2h, s = 2h, Re = 400$

**Fig. 6 Streamline contour**

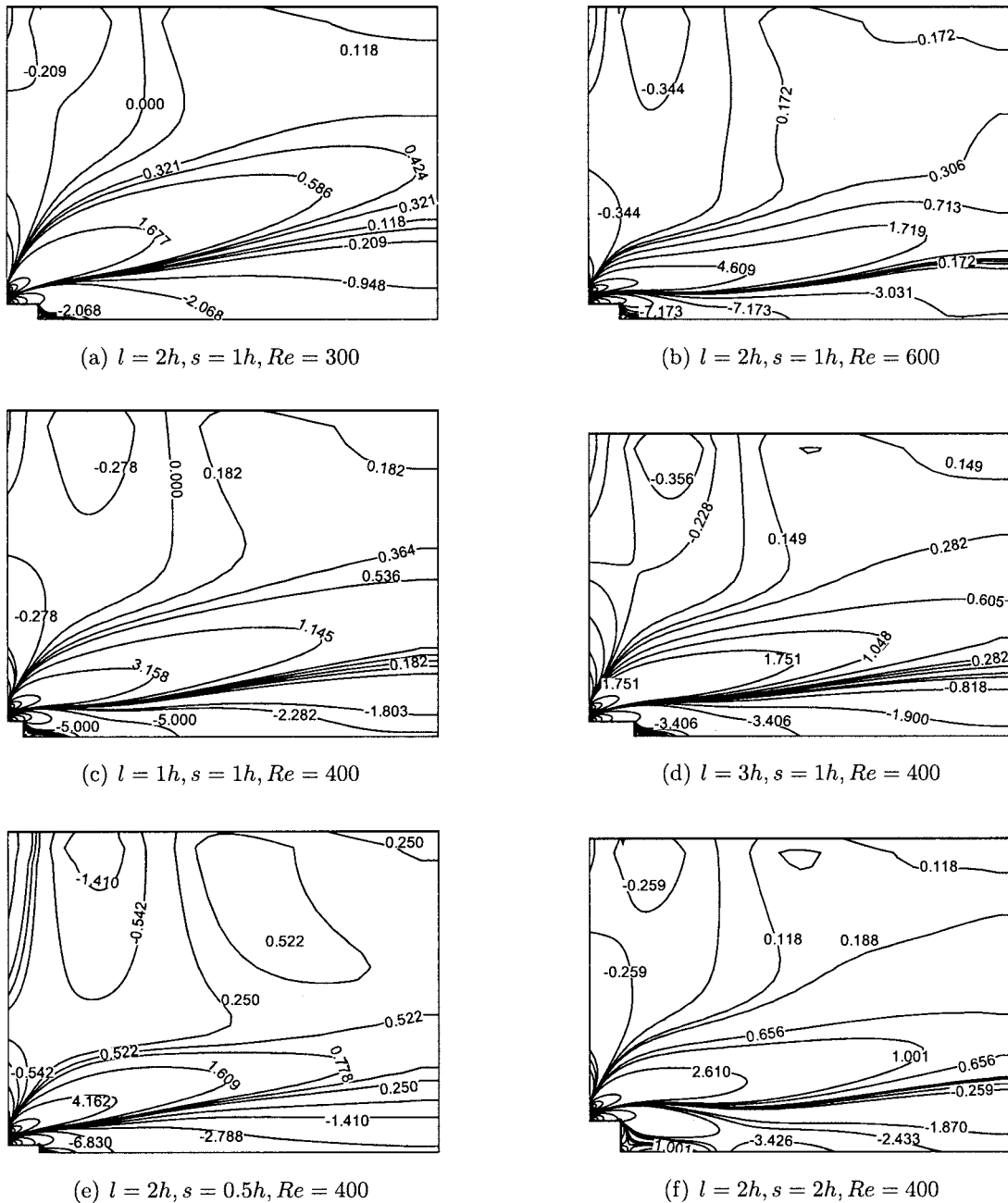


Fig. 7 Vorticity contour

of the method is somewhat lost. However, something of the second-order accuracy of the linearized system is retained if the velocity field is slowly varying [16].

It is first-order accurate in time and second-order accurate in space  $O(\Delta t, \Delta x^2, \Delta y^2)$  and is unconditionally stable. The Poisson equation (7) is solved explicitly by five-point Gauss-Seidel methods. Thom's vorticity condition has been used to obtain the wall vorticity as given below.

$$\omega_w = -\frac{2(\psi_{w+1} - \psi_w)}{\Delta n^2} \quad (9)$$

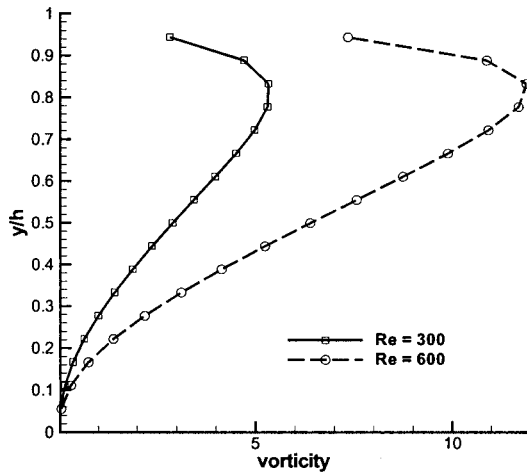
where  $\Delta n$  is the grid space normal to the wall. It has been shown by Napolitano et al. [17] and Huang and Wetton [18] that convergence in the boundary vorticity is actually second order for steady problems and for time-dependent problems when  $t > 0$ . Roache [16] has reported that for a Blasius boundary-layer profile, nu-

merical tests verify that this first-order form is more accurate than second-order form.

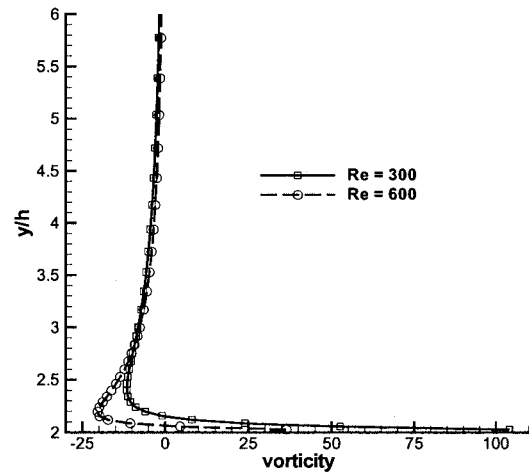
The wall jet consists of an inner region and an outer region. It is a combination of boundary layer flow over a flat plate at the inner region and plane free jet at the outer region [19]. The velocity profile has a point of inflexion. The surrounding medium of the wall jet may be quiescent or co-flow or counter-flow depending upon the applications. In the present case, the surrounding is considered to be quiescent.

At the bottom wall and the left side wall, constant stream lines are assumed based on inlet flow. At the outlet in the downstream direction, stream-wise gradients are assumed to be zero. At the entrainment boundary, the normal velocity gradient is zero [20].

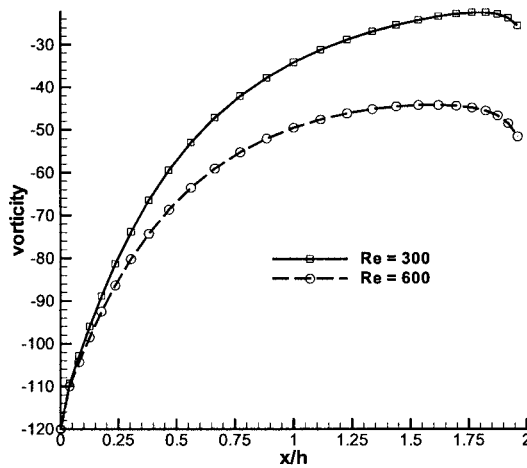
The detailed boundary conditions are, along  $FE$  (Fig. 1(b)),



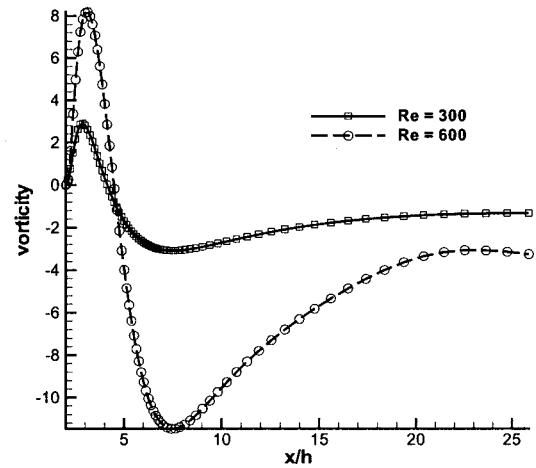
(a) Vorticity along step height, BC



(b) Vorticity along left wall, FG



(c) Vorticity along step length, AB



(d) Vorticity along  $(L-l)/h$ , CD

Fig. 8 Effect of Re on wall vorticity:  $l=2h$ ,  $s=1h$

$$\omega(y) = \frac{2(\psi_w - \psi_{w+1})}{\Delta x_i * \Delta x_{i-1}}; \quad \psi = 0.05 \quad (10a)$$

along BA,

$$\omega(y) = \frac{2(0 - \psi_{w+1})}{\Delta x_i * \Delta x_{i-1}}; \quad \psi = 0 \quad (10b)$$

along BC,

$$\omega(x) = \frac{2(0 - \psi_{w+1})}{\Delta y_j * \Delta y_{j-1}}; \quad \psi = 0 \quad (10c)$$

The rationality of the entrainment and exit boundary conditions are given in detail in [21].

The solution approaches steady state asymptotically while the time reaches infinity. The computational domain considered here is clustered Cartesian grids. For unit length, the grid space at  $i$ th node is [22],

$$x_i = \left[ \frac{i}{i_{max}} - \frac{\kappa}{\vartheta} \sin\left(\frac{i\vartheta}{i_{max}}\right) \right] \quad (11)$$

where  $\vartheta$  is the angle and  $\kappa$  is the clustering parameter.  $\vartheta=2\pi$  stretches both ends of the domain whereas  $\vartheta=\pi$  clusters more grid points near one end of the domain.  $\kappa$  varies between 0 and 1. When it approaches 1, more points fall near the end.

For the computation, time step 0.0001 is used. It has been observed that for coarse grids, a larger time step can be used, whereas, for fine grids, the solution diverges with large time step. While selecting  $\kappa$ , a time step also needs to be considered. The maximum vorticity error behavior is complicated as explained by Roache [16]. While marching in time for the solution, it has been observed that the maximum vorticity error gradually decreases. It then increases drastically and finally decreases asymptotically, leading to a steady-state solution. The convergence criterion is to be set in such a way that it should not terminate at false stage. At steady state, the error reaches the asymptotic behavior. Here it is set as the sum of the vorticity error reduced to either the convergence criteria  $\varepsilon$  or large total time.

$$\sum_{i,j=1}^{i_{max},j_{max}} (\omega_{i,j}^{t+\Delta t} - \omega_{i,j}^t) < \varepsilon \quad (12)$$

Comini et al. [23] used low Re steady-state solution as an initial guess value for high Re flow for stream function and vorticity. The same practice is followed here also.

#### 4 Validation of the Code

To validate the developed code, the two-dimensional lid-driven square-cavity flow problem [24] and the backward-facing flow

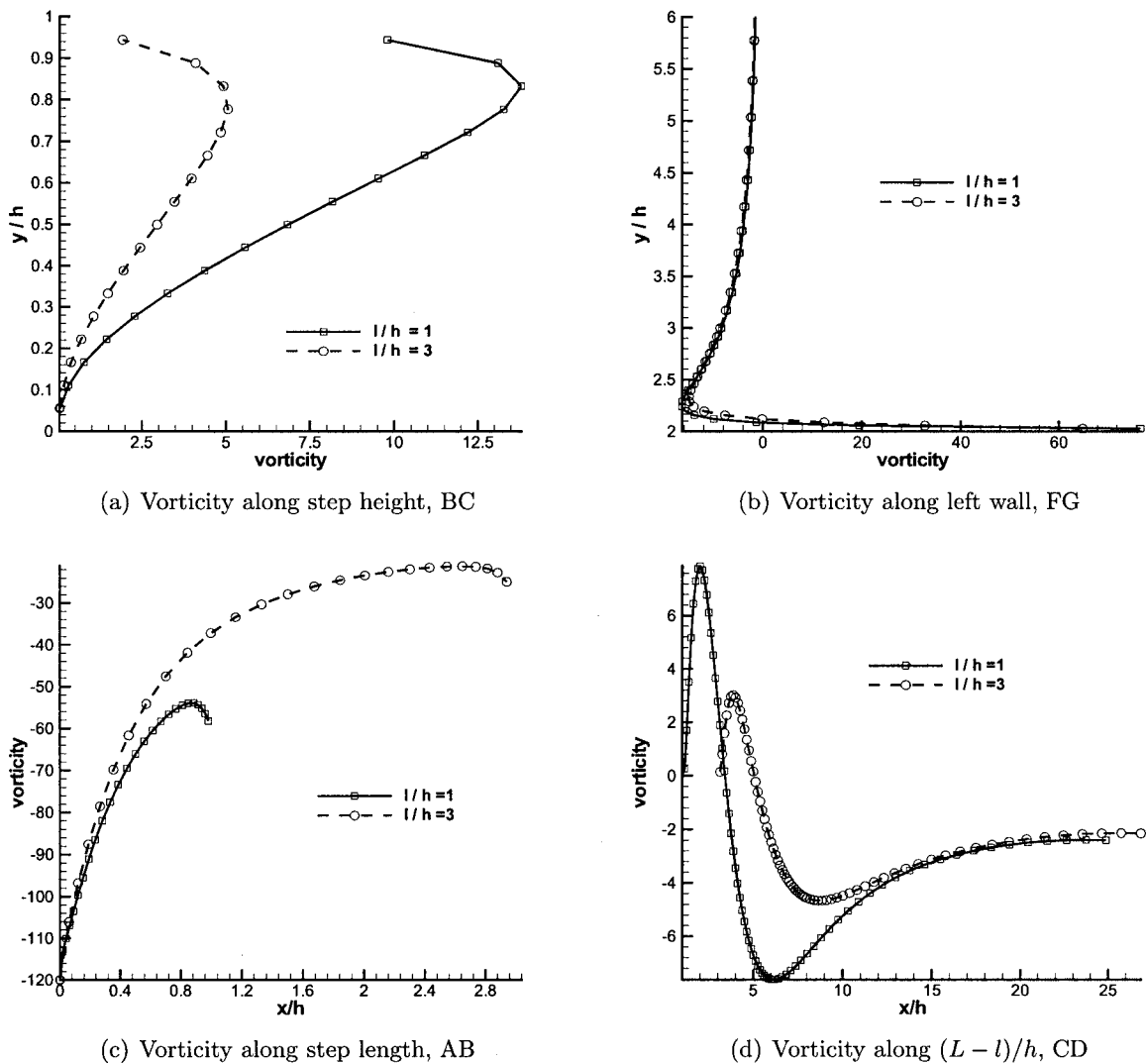


Fig. 9 Effect of step length on wall vorticity:  $Re=400$ ,  $s=1h$

problem [25,26] have been solved. Excellent agreement has been obtained with the benchmark solutions and reported elsewhere [27]. The laminar plane wall jet problem then has been solved and the computed velocity profiles are compared with the similarity solutions of Glauert [1] and the experimental results of Quintana et al. [5] in a similar way as represented by Seidel [6]. Details are given by Kanna and Das [27].

To validate the present numerical procedure, the sudden expansion flow problem and split domain problems are solved. The computational domain reported by Durst et al. [28] is considered for sudden expansion flow. The details of the comparison are given by Kanna and Das [29].

Due to scarcity of experimental results of the present geometry, the following two split domain problems are solved and compared with the published results.

1. L-shaped lid driven cavity problem.
2. Backward-facing step flow with upstream channel.

**4.1 L-shaped Lid Driven Cavity Problem.** The schematic diagram and boundary conditions of the problem are shown in Fig. 2. The geometry considered is similar to that of Oosterlee et al. [30]. The top lid is moving in the positive  $x$  direction. Along the solid walls a no-slip condition is applied. Results are compared at two locations named CL1 and CL2 (Fig. 2).  $u$ - and

$v$ -velocity components at these locations are compared with [30] for  $Re=100$  and  $Re=1000$  (Fig. 3) and excellent agreement is obtained.

#### 4.2 Backward-Facing Step Flow With Upstream Channel.

Backward-facing step with upstream channel flow is the problem of interest for the study of sudden expansion flows. Armaly et al. [25] have reported the experimental results in which the geometry has a long inlet channel and fully developed flow is expected at the expansion. To simulate the experimental situation, the inlet channel is considered in the numerical computation also. Kondoh et al. [31] reported heat transfer study on backward-facing step flow with upstream channel geometry. They considered various expansion ratios. However, their reattachment length ( $ER=2.0$ ,  $Re=100$ ,  $x_1/h=4.8$ ) is larger than the other published work ( $x_1/h=2.8$  [25,14]). Barton studied in detail the effect of the inlet channel [13]. He has reported the reattachment length by setting the inlet at different upstream locations in the channel for various Reynolds numbers. Thangam and Knight [32] studied the effect of step height in the sudden expansion flow.

The geometry considered here is similar to the one considered by Barton [13], which is having  $10 \times h$  as the upstream channel length. The schematic diagram of the problem and boundary conditions are shown in Fig. 4(a). Clustered grids are used near the

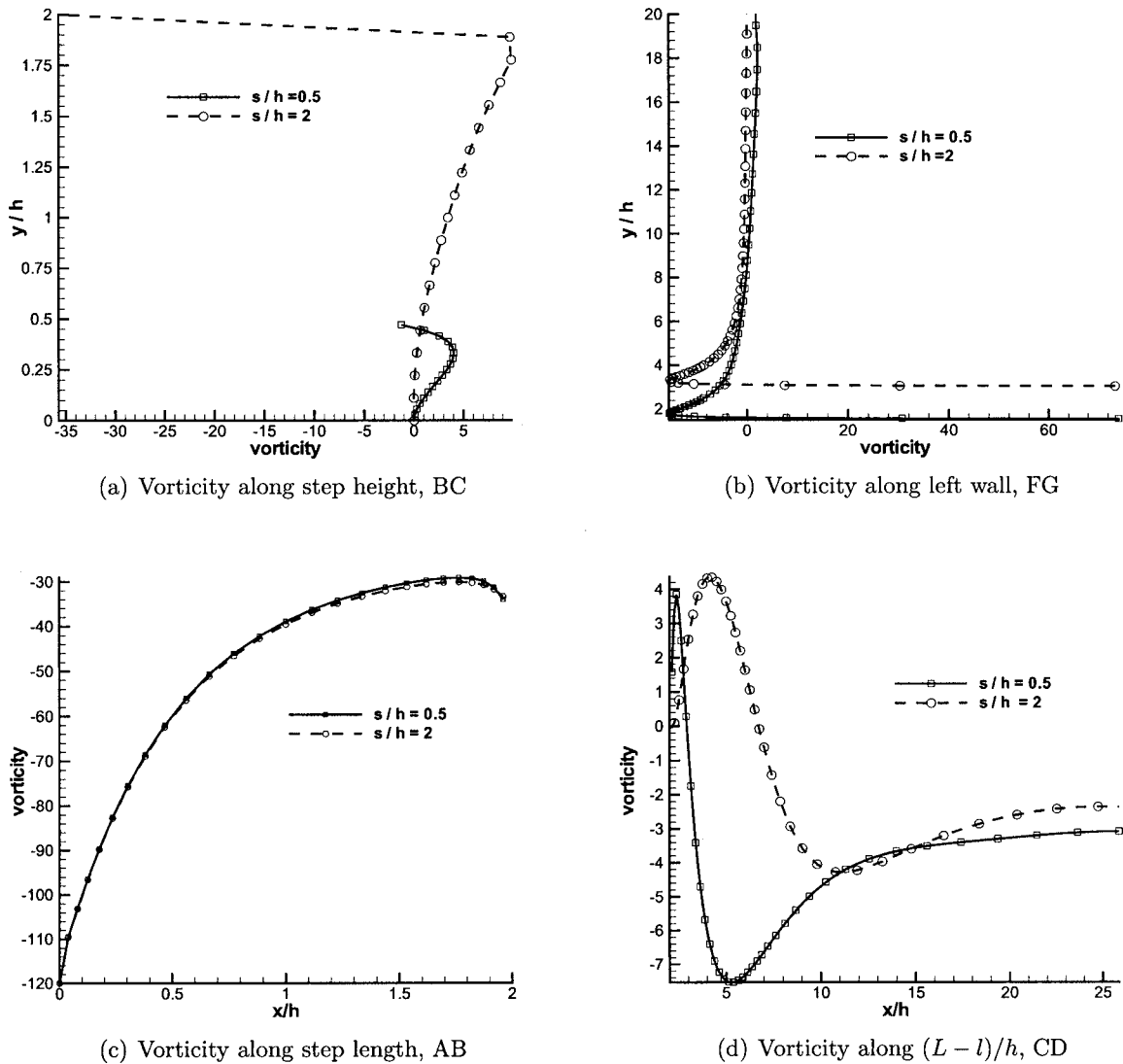


Fig. 10 Effect of step height on wall vorticity:  $Re=400$ ,  $l=2h$

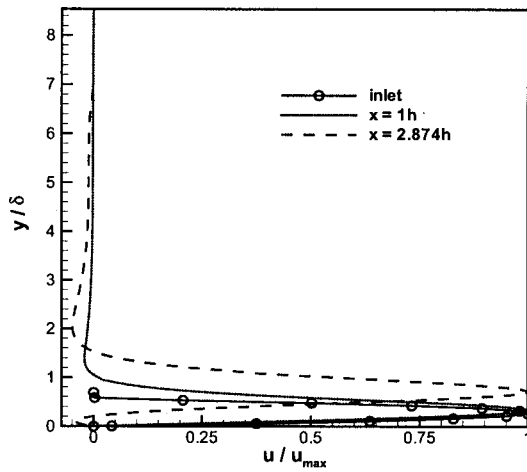
step, which is shown in Fig. 4(b). At the inlet, the parabolic velocity profile is assumed and at exit the fully developed condition is assumed. The expansion ratio (ER) is defined as  $h/H$ . The streamline contour and velocity vector are shown in Figs. 4(c) and 4(d), respectively for  $Re=500$  and  $ER=0.5$ . The  $ER=0.75$  case is considered to visualize the effect of ER. Results are shown for  $Re=200$ ,  $ER=0.75$  in Figs. 4(e) and 4(f). For large values of  $Re$  the primary vortex reattachment length is compared with [25,13] (Fig. 5). The present computations show excellent agreement with computational results and up to  $Re=400$  with experimental results. Backward-facing steps with different expansion ratios are tested and the reattachment length is compared with the published results and good agreement is obtained (Tables 1 and 2).

## 5 Results and Discussion

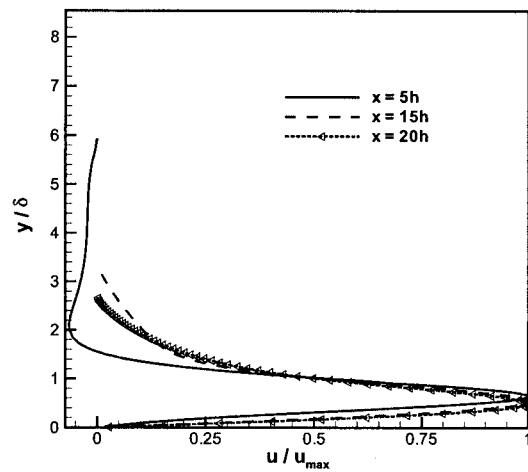
The parabolic profile, issuing from the inlet slot, spreads over a plane wall and further expands across a backward-facing step. It reattaches on the bottom wall due to the Coanda effect and spreads along the wall (Fig. 1(a)). The length between the step and the reattachment point is called the reattachment length ( $x_1$ , Fig. 1(b)). The flow in the domain has the nature of the wall jet, recirculation, developing, and the wall jet at far downstream. Before flow expands from the step, it behaves like a plane wall jet. However, due to entrainment, self-similarity nature is not obtained

at this length. To understand the flow physics of the present situation, three parameters considered here are  $Re(=\bar{U}h/\nu)$ , step length ( $l$ ), and step height ( $s$ ). Results are presented here for  $l=1h, 2h, 3h$  and  $s=0.5h, 1h, 2h$ . Since at low  $Re$  the jet has difficulty overcoming the downstream friction [33],  $Re$  has been chosen between 300 and 600. The experimental study of the laminar plane wall jet is presented in [19]. Based on the jet exit Reynolds number, they reported that the laminar wall jet results up to  $Re=770$ . Bhattacharjee and Loth [7] reported that early transition begins at about  $Re=700$  for the plane wall jet. Kanna and Das [29] have shown that the laminar wall attaching the offset jet can be possible up to  $Re=600$ . Based on these results, the maximum  $Re$  for the wall jet flow over a step is set as  $Re=600$ .

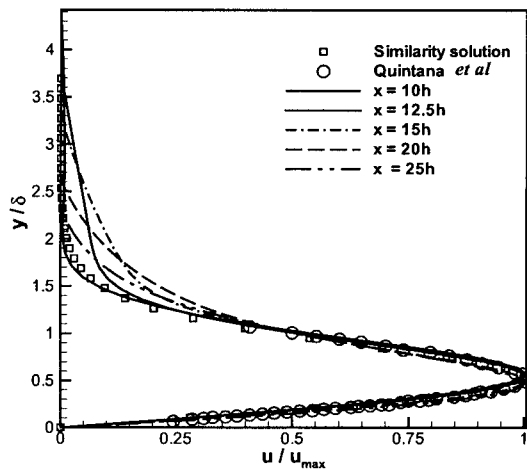
The clustered grids are used for the computations. The domain has been chosen as  $25 \times h$  in the streamwise direction from the step and  $20 \times h$  in normal direction. For the grid independence study the reference case considered is  $Re=400$ ,  $l=2h$ , and  $s=1h$ . Three grid systems  $71 \times 61$ ,  $97 \times 85$ , and  $127 \times 125$  are considered. The variation in the reattachment length is less than 2.5% and the  $97 \times 85$  grid system is used for the entire computation. The grids are clustered near the step and solid walls. Uniform grids are considered for the inlet to ensure that the parabolic velocity profile falls exactly at the inlet slot. Typical grids are shown in Fig. 1(c).



(a) Downstream location  $u$  velocity. contd.



(b) Downstream location  $u$  velocity. contn.



(c) Comparison of  $u$  velocity profile: Wall jet region

Fig. 11 Similarity profile  $Re=400, l=2h, s=1h$

Figure 6 shows the streamline contours for a range of the parameters  $Re$ ,  $l$ , and  $s$ . The streamline contours illustrate the main jet flow, recirculation, and entrainment flow. When  $Re$  increases from 300 to 600, the main flow is confined towards the bottom wall. Particularly after the step, the jet deflects towards the bottom wall (Figs. 6(a) and 6(b)). The size of the recirculation eddy is increased considerably. At low  $Re$  the jet spreads more in the normal direction, which causes the reduction in ambient fluid flow. It is noticed that the increase in the length of the step reduces the reattachment length (Figs. 6(c) and 6(d)). When the height of the step is increased, the main flow deflects towards the bottom wall. Recirculation eddy size is increased (Figs. 6(e) and 6(f)). At exit, the streamlines become parallel and thus the assumption for fully developed flow is satisfied. Near the bottom wall, streamlines are less dense in order to satisfy the no-slip conditions along

Table 3 Effect of  $Re$  on wall jet similarity region distance.  $l=2h, s=1h$ .

$Re$	$x/h$
300	7.72
400	7.74
500	7.99
600	8.33

the walls. The effect of these parameters on vorticity is shown in Fig. 7. Near the bottom wall the  $u$  velocity gradient is greater in the normal direction than the  $v$  velocity gradient in the streamwise direction. It is noticed that when  $Re$  increases this is magnified (Figs. 7(a) and 7(b)). For longer step, vorticity values are reduced (Figs. 7(c) and 7(d)). However, when height of the step is increased, the  $u$ -velocity normal direction gradient is increased (Figs. 7(e) and 7(f)).

Walls are the sources of vorticity. Here solid walls are assumed as impermeable which exist along  $AB$ ,  $BC$ ,  $CD$ , and  $FG$  (Fig. 1(b)). It may have either positive or negative values depending upon the velocity gradients. Since walls are a source of vorticity, the magnitude of vorticity along the wall will be higher than other parts of the domain. Thus the distribution of vorticity along the

Table 4 Effect of step length on wall jet similarity region distance.  $Re=300, s=1h$ .

Length of the step	$x/h$
$l=1h$	8.84
$l=2h$	7.72
$l=3h$	6.42
$l=0h$ [29]	14.24

**Table 5 Effect of step height on wall jet similarity region distance.  $Re=300, l=2h$ .**

Height of the step	$x/h$
$s=0.5h$	9.65
$s=1h$	7.74
$s=2h$	7.56

solid walls is important for understanding the physics of the flow. The effect of  $Re$  and step geometry on wall vorticity is presented in detail in Figs. 8–10. Vorticity distributions are shown for vertical walls followed by horizontal walls. The effect of  $Re$  on vorticity along  $BC$  is shown in Fig. 8(a). Along step height the vorticity is in the positive direction and its value is increased when  $Re$  is increased. However, the maximum vorticity occurred at the same height ( $y=0.833h$ ). It is important to note that along  $BC$  there exist two singular corner points. Roache [16] reported in detail about how to treat these corner singular points. However, at high  $Re$ , he concluded that those forms are less efficient. Above the inlet, the left wall causes vorticity mainly due to the entrainment of the ambient fluid. Vorticity is generated by the left wall up to a maximum of  $y=2h$  above the inlet and further it approaches zero (Fig. 8(b)). At higher  $Re$  it increases in the negative direction. This is attributed to the high entrainment towards the inlet. The vorticity is generated due to negative  $v$  velocity gradient. The vorticity variation along step length is shown in Fig. 8(c). When  $Re$  increases it tends towards negative direction because the normal direction  $u$  gradient is increased. Along  $CD$  the wall vorticity varies from positive to negative in the downstream direction (Fig. 8(d)). From the step it increases in the positive direction and then decreases. After reattachment its direction is changed to the negative direction. At far from the reattachment it becomes invariant at high  $Re$ .

The effect of step length on vorticity is shown in Fig. 9. It is noticed that when the length of the step is increased, wall vorticity on  $BC$  is decreased (Fig. 9(a)). However, the maximum values occur at the same height. When length is increased, the left wall vorticity is decreased (Fig. 9(b)) due to the reduction of entrainment. Figure 9(c) shows the effect of change in step length on vorticity. It is observed that when length increases, the wall vorticity is decreased for the same distance. Along the length of the step, the vorticity value tends towards positive direction. It is noticed that the vorticity along  $CD$  is affected by the upstream step length (Fig. 9(d)). The peak value of the vorticity in any direction

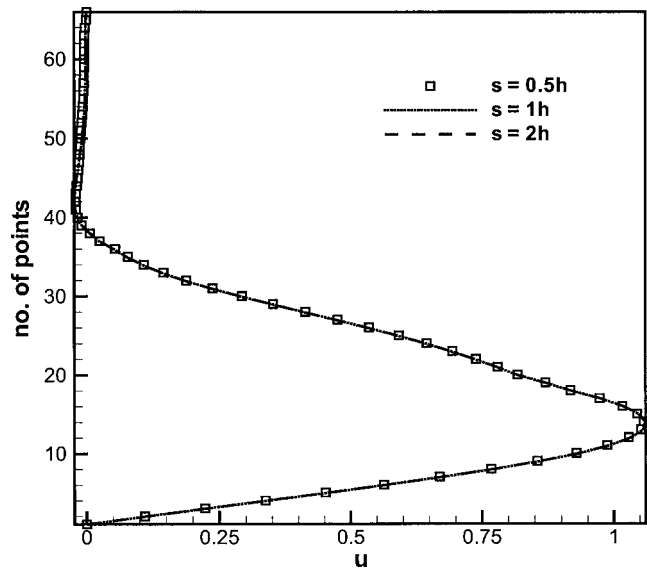
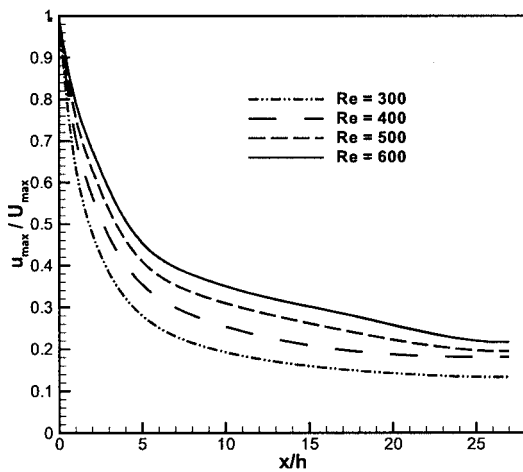


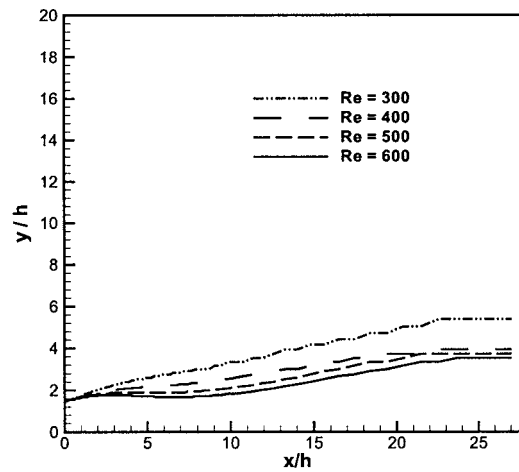
**Fig. 12 Effect of step height on upstream velocity at  $x=1h$ :  $Re=400, l=2h$**

is reduced for longer step length. However, far downstream, the effect of step length is less significant. The effect of step height is shown in Fig. 10. Along  $BC$  the vorticity is increased in the positive direction to a maximum value. As the top corner is approached, it tends towards the negative direction. The magnitude is increased when step height is increased (Fig. 10(a)) due to large recirculation, which causes more positive  $v$  velocity gradient. Along  $FG$ , the magnitude of the vorticity is less affected by the variation in height. However, due to more entrainment at high step height, negative vorticity is generated far away from the inlet (Fig. 10(b)). The variation in step height does not have significant effect on the vorticity along the step length (Fig. 10(c)). Thus the separation in the flow is less significant for the upstream flow wall vorticity. It is noticed that the positive direction peak value is higher for  $s=2h$  and the negative direction peak value is higher for  $s=0.5h$  (Fig. 10(d)).

The wall jet boundary layer thickness ( $\delta$ ) is the normal distance where  $u=0.5u_{max}$ . The similarity  $u$  velocity profile at different downstream locations is compared with experimental [5] and similarity [1] results (Fig. 11) for  $Re=400, l=2h$ , and  $s=1h$ . The



(a) Decay of local  $u_{max}$



(b) Location of local  $u_{max}$

**Fig. 13 Local maximum  $u$  velocity:  $l=2h, s=1h$**

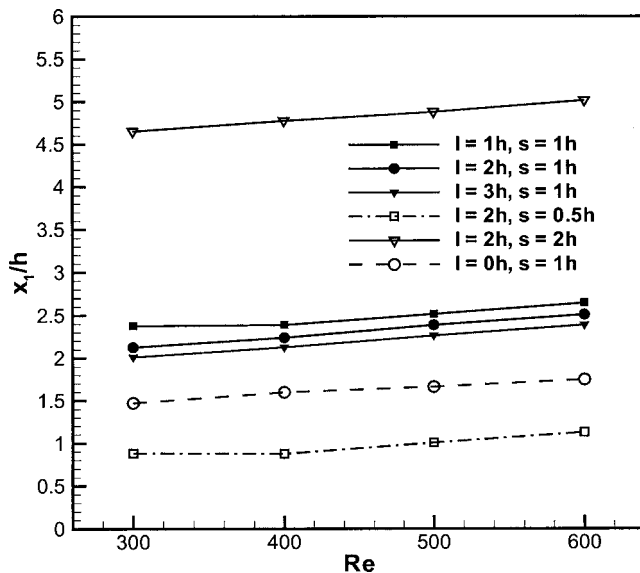


Fig. 14 Reattachment length for different geometry and Reynolds number:  $l=0h$ ,  $s=1h$  [29]

$u$  velocity profiles at locations in the middle of step length ( $x=1h$ ), reattachment point ( $x=2.874h$ ), and inlet are shown in Fig. 11(a). Due to entrainment, a negative direction velocity value is present. The same is shown at a few downstream locations (Fig. 11(b)). After reattachment, flow is under development to a certain distance. Location  $x=5h$  corresponds to the developing region velocity profile. Similarity profiles in the wall jet region are shown in Fig. 11(c). Present computations show excellent agreement with experimental and similarity results for the inner region as well as the outer region of the wall jet. However, at further downstream locations, the jet expands in the normal direction and thus it does not have agreement with the similarity solution at the entrainment location, i.e., free shear layer. The experimental result shown here is chosen from one particular location where it satisfies the similarity solution. The length from the step to the wall jet region, i.e., where the similarity profiles begin and closed-form solutions of the wall jet can be applicable, is measured for different Re and step geometry. It is observed that when Re is increased, due to more entrainment, distance where the similarity principle can be applied is also increased (Table 3). When length increases, this distance is reduced due to reduction of entrainment. However, this distance is larger for the zero step length case (Table 4). This is caused by the entrainment. It is observed that when step height increases this distance is reduced (Table 5).

The effect of the step height on the upstream velocity is shown in Fig. 12. The local  $u$  velocity at the  $x=1h$  location is compared with different step height. It is noticed that the downstream step height variation does not affect the local  $u$  velocity upstream. The maximum  $u$  velocity in the normal direction from the entire downstream direction is presented for different Re and shown in Fig. 13. The local normalized (i.e.,  $u_{max}/U_{max}$ )  $u_{max}$  decays monotonically in the downstream direction, finally reaching an asymptotic condition. The corresponding normalized  $y$  location

Table 6 Effect of step length on primary vortex reattachment length. Percentage of reduction from  $l=1h$ :  $s=1h$ .

Re	$x_1/h$ for $l=1h$	% of reduction if $l=2h$	% of reduction if $l=3h$
300	2.378	10.51	15.39
400	2.389	6.28	11.01
500	2.514	5.09	10.02
600	2.643	5.15	9.72

Table 7 Effect of step height on primary vortex reattachment length. Percentage of variation from  $s=1h$ :  $s=1h$ .

Re	$x_1/h$ for $s=1h$	% of increment if $s=2h$	% of reduction if $s=0.5h$
300	2.128	118.65	58.51
400	2.239	113.31	60.87
500	2.386	104.48	57.88
600	2.507	100.03	55.08

(i.e.,  $y/h$ ) is shown in Fig. 13(b). It is noticed that when Re increases, the jet  $u_{max}$  location ( $y/h$ ) shifts down. The reattachment lengths of all the cases considered here are presented in Fig. 14. It is observed that the increase in step length reduces the reattachment length. However, it is noticed that the reattachment length is reduced when the step length is absent [29]. This is mainly due to the large entrainment near the expansion of the jet. When step height increases, increase in recirculation length is observed. However, the variation in  $x_1$  is more sensitive to step height than step length (Tables 6 and 7).

## 6 Conclusions

The two-dimensional incompressible nonbuoyant laminar wall jet over backward-facing step is solved by stream function and vorticity formulation considering the problem as an asymptotic solution to the transient equation. The flow characteristics like strength of recirculation eddy, impingement length, decay of local velocity, and wall jet region are studied in detail for a range of flow property and physical property. The entrainment is increased for high Re and it is less affected with change in step length. The reattachment length follows almost a linear trend with Re and step geometry for the range considered. However, it is more sensitive to step height than length. The upstream flow properties are not affected by expansion in the geometry. Vorticity from the solid wall is affected by Re. The maximum vorticity location is independent of Re and step geometry. Vorticity from the step height is increased for higher Re and decreased if step length is increased. From the left wall, vorticity is generated to a few inlet slot heights and further it is independent of Re and step geometry. At the bottom wall, vorticity becomes a negative value from a positive value after reattachment point. The  $u_{max}$  location shifts down when Re is increased. Similarity is not observed along step length due to entrainment. Similarity exists for the wall jet far away from the reattachment. Similarity profile formation distance is reduced by increasing the step geometry whereas an increment in Re increases this distance. The bottom wall vorticity is considerably affected near the impingement region.

## Nomenclature

- $h$  = inlet slot height, m
- $i$  =  $x$ -direction grid point
- $j$  =  $y$ -direction grid point
- $l$  = step length, m
- $n$  = normal direction
- Re = Reynolds number for the fluid
- $s$  = step height, m
- $\bar{t}$  = dimensional time, s
- $t$  = nondimensional time
- $\bar{u}, \bar{v}$  = dimensional velocity components along  $(x, y)$  axes, m/s
- $u, v$  = dimensionless velocity components along  $(x, y)$  axes
- $\bar{U}$  = inlet mean velocity, m/s
- $\bar{x}, \bar{y}$  = dimensional Cartesian coordinates along and normal to the plate, m



$x, y$  = dimensionless Cartesian coordinates along and normal to the plate

### Greek Symbols

$\delta$  = wall jet boundary layer thickness  
 $\varepsilon$  = convergence criterion  
 $\eta$  = similarity variable  
 $\kappa$  = clustering parameter  
 $\psi$  = dimensionless stream function  
 $\omega$  = dimensionless vorticity

### Subscripts

$max$  = maximum  
 $w$  = wall

### References

- [1] Glauert, M. B., 1956, "The Wall Jet," *J. Fluid Mech.*, **1**(1), pp. 1–10.
- [2] Schlichting, H., and Gersten, K., 2000, *Boundary Layer Theory*, 8th ed. Springer, New York.
- [3] Amitay, M., and Cohen, J., 1997, "Instability of a Two-Dimensional Plane Wall Jet," *J. Fluid Mech.*, **344**, pp. 67–94.
- [4] Cohen, J., Amitay, M., and Bayly, B. J., 1992, "Laminar-Turbulent Transition of Wall-Jet Flows Subjected to Blowing and Suction," *Phys. Fluids A*, **4**, pp. 283–289.
- [5] Quintana, D. L., Amitay, M., Ortega, A., and Wygnanski, I. J., 1997, "Heat Transfer in the Forced Laminar Wall Jet," *ASME J. Heat Transfer*, **119**, pp. 451–459.
- [6] Seidel, J., 2001, "Numerical Investigations of Forced Laminar and Turbulent Wall Jets Over a Heated Surface," Ph.D. thesis, Faculty of the Department of Aerospace and Mechanical Engineering, The Graduate College, The University of Arizona, Tucson, AZ.
- [7] Bhattacharjee, P., and Loth, E., 2004, "Simulations of Laminar and Transitional Cold Wall Jets," *Int. J. Heat Fluid Flow*, **25**, pp. 32–43.
- [8] Sato, H., 1960, "The Stability and Transition of a Two-Dimensional Jet," *J. Fluid Mech.*, **7**, pp. 53–80.
- [9] Sato, H., and Sakao, F., 1964, "An Experimental Investigation of the Instability of a Two-Dimensional Jet at Low Reynolds Numbers," *J. Fluid Mech.*, **20**, pp. 337–352.
- [10] Batchelor, G. K., and Gill, A. E., 1962, "Analysis of the Stability of Axisymmetric Jets," *J. Fluid Mech.*, **14**, pp. 529–551.
- [11] Cohen, J., and Wygnanski, I., 1987, "The Evolution Instabilities in the Axisymmetric Jet. Part I. The Linear Growth of Disturbances Near the Nozzle," *J. Fluid Mech.*, **176**, pp. 191–219.
- [12] Sarma, A. S. R., Sundararajan, T., and Ramjee, V., 2000, "Numerical Simulation of Confined Laminar Jet Flows," *Int. J. Numer. Methods Fluids*, **33**, pp. 609–626.
- [13] Barton, I. E., 1997, "The Entrance Effect of Laminar Flow Over a Backward-Facing Step Geometry," *Int. J. Numer. Methods Fluids*, **25**, pp. 633–644.
- [14] Valencia, A., and Hinojosa, L., 1997, "Numerical Solution of Pulsating Flow and Heat Transfer Characteristics in a Channel With Backward-Facing Step," *Heat Mass Transfer*, **32**, pp. 143–148.
- [15] Jacob, M. C., Louisot, A., Juve, D., and Guerrand, S., 2001, "Experimental Study of Sound Generated by Backward-Facing Steps Under Wall Jet," *AIAA J.*, **39**(7), pp. 1254–1260.
- [16] Roache, P. J., 1998, *Fundamentals of Computational Fluid Dynamics*, Hermosa, Albuquerque, NM, Chap. 3.
- [17] Napolitano, M., Pascasio, G., and Quartapelle, L., 1999, "A Review of Vorticity Conditions in the Numerical Solution of the  $\zeta$ - $\psi$  Equations," *Comput. Fluids*, **28**, pp. 139–185.
- [18] Huang, H., and Wetton, B. R., 1996, "Discrete Compatibility in Finite Difference Methods for Viscous Incompressible Fluid Flow," *J. Comput. Phys.*, **126**, pp. 468–478.
- [19] Bajura, R. A., and Szewczyk, A. A., 1970, "Experimental Investigation of a Laminar Two-Dimensional Plane Wall Jet," *Phys. Fluids*, **13**, pp. 1653–1664.
- [20] Kang, S. H., and Greif, R., 1992, "Flow and Heat Transfer to a Circular Cylinder With a Hot Impinging Air Jet," *Int. J. Heat Mass Transfer*, **35**(9), pp. 2173–2183.
- [21] Kanna, P. R., and Das, M. K., 2006, "A Short Note on the Entrainment and Exit Boundary Conditions," *Int. J. Numer. Methods Fluids*, **50**(8), pp. 973–985.
- [22] Kuyper, R. A., Van Der Meer, T. H., Hoogendoorn, C. J., and Henkes, R. A. W. M., 1993, "Numerical Study of Laminar and Turbulent Natural Convection in an Inclined Square Cavity," *Int. J. Heat Mass Transfer*, **36**(11), pp. 2899–2911.
- [23] Comini, G., Manzan, M., and Nonino, C., 1994, "Finite Element Solution of the Streamfunction-Vorticity Equations for Incompressible Two-Dimensional Flows," *Int. J. Numer. Methods Fluids*, **19**, pp. 513–525.
- [24] Ghia, U., Ghia, K. N., and Shin, C. T., 1982, "High Re Solutions for Incompressible Flow Using the Navier-Stokes Equations and Multigrid Method," *J. Comput. Phys.*, **48**, pp. 387–411.
- [25] Armaly, B. F., Durst, F., Pereira, J. C. F., and Schonung, B., 1983, "Experimental and Theoretical Investigation of Backward-Facing Step Flow," *J. Fluid Mech.*, **127**, pp. 473–496.
- [26] Gartling, D. K., 1990, "A Test Problem for Outflow Boundary Conditions-Flow Over a Backward-Facing Step," *Int. J. Numer. Methods Fluids*, **11**, pp. 953–967.
- [27] Kanna, P. R., and Das, M. K., 2005, "Conjugate Forced Convection Heat Transfer From a Flat Plate by Laminar Plane Wall Jet Flow," *Int. J. Heat Mass Transfer*, **48**, pp. 2896–2910.
- [28] Durst, F., Pereira, J. C. F., and Tropea, C., 1993, "The Plane Symmetric Sudden-Expansion Flow at Low Reynolds Numbers," *J. Fluid Mech.*, **248**, pp. 567–581.
- [29] Kanna, P. R., and Das, M. K., 2005, "Numerical Simulation of Two-Dimensional Laminar Incompressible Offset Jet Flows," *Int. J. Numer. Methods Fluids*, **49**(4), pp. 439–464.
- [30] Oosterlee, C. W., Wesseling, P., Segal, A., and Brakkee, E., 1993, "Benchmark Solutions for the Incompressible Navier-Stokes Equations in General Coordinates on Staggered Grids," *Int. J. Numer. Methods Fluids*, **17**, pp. 301–321.
- [31] Kondoh, T., Nagano, Y., and Tsuji, T., 1993, "Computational Study of Laminar Heat Transfer Downstream of a Backward-Facing Step," *Int. J. Heat Mass Transfer*, **36**(3), pp. 577–591.
- [32] Thangam, S., and Knight, D. D., 1989, "Effect of Step Height on the Separated Flow Past to Backward Facing Step," *Phys. Fluids A*, **1**, pp. 604–606.
- [33] Chiriac, V. A., and Ortega, A., 2002, "A Numerical Study of the Unsteady Flow and Heat Transfer in a Transitional Confined Slot Jet Impinging on an Isothermal Surface," *Int. J. Heat Mass Transfer*, **45**, pp. 1237–1248.

**M. Bahrami**

Assistant Professor  
Department of Mechanical Engineering,  
University of Victoria,  
BC, V8W 3P6, Canada  
e-mail: mbahrami@uvic.ca

**M. M. Yovanovich**

Distinguished Professor Emeritus  
Fellow ASME

**J. R. Culham**

Associate Professor, Director  
Mem. ASME

Microelectronics Heat Transfer Laboratory,  
Department of Mechanical Engineering,  
University of Waterloo,  
200 University Avenue West,  
ON, N2L 3G1, Canada

# Pressure Drop of Fully-Developed, Laminar Flow in Microchannels of Arbitrary Cross-Section

*The pressure drop of fully developed, laminar, incompressible flow in smooth mini- and microchannels of arbitrary cross-section is investigated. A compact approximate model is proposed that predicts the pressure drop for a wide variety of shapes. The model is only a function of geometrical parameters of the cross-section, i.e., area, perimeter, and polar moment of inertia. The proposed model is compared with analytical and numerical solutions for several shapes. Also, the comparison of the model with experimental data, collected by several researchers, shows good agreement. [DOI: 10.1115/1.2234786]*

## 1 Introduction

Advances in microfabrication make it possible to build microchannels with small characteristic lengths, in the order of micrometers. Micro- and minichannels show promising potential for being incorporated in a wide variety of unique, compact, and efficient cooling applications such as in microelectronic devices. These micro heat exchangers or heat sinks feature extremely high heat transfer surface area per unit volume ratios, high heat transfer coefficients, and low thermal resistances [1]. Microchannels can be produced directly by techniques such as chemical etching on silicon wafers. As a result, the cross-section of the channels depends on a variety of factors, such as the crystallographic nature of the silicon used. According to Morini [2], when a KOH-anisotropic etching technique is employed, it is possible to obtain microchannels which have a fixed cross-section. The shape of the cross-section depends on the orientation of the silicon crystal planes. For instance, the microchannels etched in 100 or 110 silicon will have a trapezoidal cross-section with an apex angle of 54.7 deg imposed by the crystallographic morphology of the silicon or a rectangular cross-section, respectively [2].

Tuckerman and Pease [3] were the first to demonstrate that planar integrated circuit chips can be effectively cooled by laminar water flowing through microchannels with hydraulic diameters of 86 to 95  $\mu\text{m}$ . However, due to small channel dimensions, the pressure drop and the required pumping power dramatically increase. Therefore, simultaneous hydrodynamic and thermal analyses must be performed to investigate the effects of both flow and heat transfer in micro- or minichannels.

In recent years, a large number of papers have reported pressure drop data for laminar flow of liquids in microchannels with various cross-sections. However, published results are often inconsistent. According to [4], some of these authors conducted experiments in noncircular microchannels, but compared their pressure drop data with the classical values of  $f Re = 16$  or 64 of circular pipes. Some of the discrepancies in the published data can be

explained within the limits of continuum fluid mechanics; Bahrami et al. [5] developed a model that captures the observed trends in rough microchannels. Recently, Liu and Garimella [6] and Wu and Cheng [7] conducted experiments in smooth rectangular and trapezoidal microchannels, respectively; they reported that the Navier-Stokes equations are valid for laminar flow in smooth microchannels.

In the literature there are no comprehensive and encompassing models or correlations that predict pressure drop in arbitrary cross-sections. Thus the objective of this work is to develop a compact approximate model that provides the pressure drop in micro- and minichannels of arbitrary cross-section. The model estimates the pressure drop (within 8% accuracy) and provides tools for basic design, parametric studies, and optimization analyses required for microchannel heat exchangers and heat sinks.

## 2 Problem Statement

Consider fully-developed, steady-state laminar flow in a channel with the boundary  $\Gamma$ , constant cross-sectional area  $A$ , and constant perimeter  $P$ , as shown in Fig. 1. The flow is assumed to be incompressible and have constant properties. Moreover, body forces such as gravity, centrifugal, Coriolis, and electromagnetic do not exist. Also, the rarefaction and surface effects are assumed to be negligible and the fluid is considered to be a continuum. For such a flow, the Navier-Stokes equations reduce to the momentum equation which is also known as *Poisson's equation*. In this case, the source term in Poisson's equation is the constant pressure gradient along the length of the duct,  $\Delta p/L$ . The governing equation for fully developed laminar flow in a constant cross-sectional area channel is [8]:

$$\nabla^2 w = \frac{1}{\mu} \frac{dp}{dz} \quad \text{with } w = 0 \text{ on } \Gamma \quad (1)$$

where  $w$  and  $z$  are the fluid velocity and the flow direction, respectively. The boundary condition for the velocity is the no-slip condition at the wall.

The velocity profile is constant in the longitudinal direction; thus the pressure gradient applied at the ends of the channel must be balanced by the shear stress on the wall of the channel

$$\bar{\tau} PL = \Delta p A \quad (2a)$$

where

Contributed by the Fluids Engineering Division of ASME for publication in the JOURNAL OF FLUIDS ENGINEERING. Manuscript received March 13, 2005; final manuscript received January 30, 2006. Assoc. Editor: Kenneth Breuer. Paper presented at the 3rd International Conference on Microchannels and Minichannels (ICMM2005), June 13–15, 2005, Toronto, Ontario, Canada.

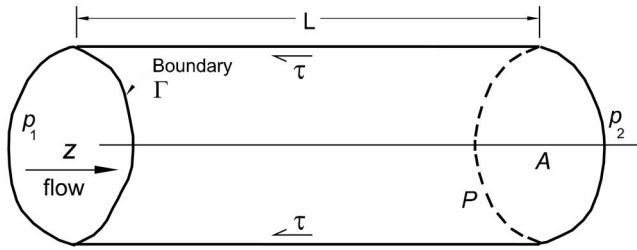


**Fig. 1 Microchannel of arbitrary constant cross-section,  $L \gg \sqrt{A}$**

$$\bar{\tau} = \frac{1}{A_L} \int_{\Gamma} \tau dA_L \quad (2b)$$

where  $A_L = P \cdot L$  is the lateral surface area of the channel.

### 3 Exact Solutions

In this section, relationships are derived for pressure drop and the product of Reynolds number and Fanning friction factor,  $fRe$ , of fully developed laminar flow for various cross-sections using existing analytical solutions. The analytical solutions for the relevant flow fields can be found in fluid mechanics textbooks such as White [9] and Yovanovich [10]. The following method, described for the elliptical microchannels, can be applied for other shapes listed in Table 1. Therefore, it is left to the reader to apply the steps for other cross-sections.

The governing equation is the Poisson's equation, Eq. (1). An analytical solution exists for the laminar fluid flow in elliptical microchannels with the following mean velocity

$$\bar{w} = \frac{b^2 c^2}{4(b^2 + c^2)} \frac{\Delta p}{\mu L} \quad (3)$$

where  $b$  and  $c$  are the major and minor semi-axes of the cross-section,  $b \geq c$ . An aspect ratio is defined for the elliptical microchannel

$$0 \leq \varepsilon \equiv \frac{c}{b} \leq 1 \quad (4)$$

For an elliptical microchannel, the cross-sectional area and the perimeter are

$$A = \pi bc$$

$$P = 4bE(\sqrt{1 - \varepsilon^2}) \quad (5)$$

where  $E(x) = \int_0^{\pi/2} \sqrt{1 - x^2 \sin^2 t} dt$  is the complete elliptic integral of the second kind. The mean velocity can be presented in terms of the aspect ratio,  $\varepsilon$ ,

$$\bar{w} = \frac{c^2}{4(1 + \varepsilon^2)} \frac{\Delta p}{\mu L} \quad (6)$$

which can be rearranged as

$$\frac{\Delta p}{L} = \frac{4(1 + \varepsilon^2)}{c^2} \mu \bar{w} \quad (7)$$

Combining Eqs. (2a), (2b), and (7), the mean wall shear stress is

$$\bar{\tau} = \frac{4\mu(1 + \varepsilon^2)\bar{w}}{c^2} \frac{A}{P} \quad (8)$$

The ratio of the cross-sectional area over the perimeter for elliptical microchannels is

$$\frac{A}{P} = \frac{\pi c}{4E(\sqrt{1 - \varepsilon^2})} \quad (9)$$

The mean wall shear stress becomes

$$\bar{\tau} = \frac{\pi\mu(1 + \varepsilon^2)\bar{w}}{cE(\sqrt{1 - \varepsilon^2})} \quad (10)$$

A relationship can be found between the minor axis  $c$  and the area, Eq. (5),

$$c = \sqrt{\frac{A\varepsilon}{\pi}} \quad (11)$$

Substituting Eq. (11) into Eq. (10), one finds

$$\bar{\tau} = \frac{\pi\sqrt{\pi}(1 + \varepsilon^2)\bar{w}}{\sqrt{\varepsilon}E(\sqrt{1 - \varepsilon^2})\sqrt{A}} \quad (12)$$

It is conventional to use the ratio of area over perimeter  $D_h = 4A/P$ , known as the hydraulic diameter, as the characteristic length scale for noncircular channels. However, as can be seen in Eq. (12), a more appropriate length scale is the square root of area,  $\sqrt{A}$ . Muzychka and Yovanovich [11] showed that the apparent friction factor is a weak function of the shape of the geometry of the channel by defining aspect ratios for various cross-sections. Later, it will be shown that the selection of the square root of area as the characteristic length leads to similar trends in  $fRe_{\sqrt{A}}$  for elliptical and rectangular channels with identical cross-sectional area.

With the square root of area,  $\sqrt{A}$ , as the characteristic length scale, a nondimensional wall shear stress can be defined as:

$$\bar{\tau}^* = \frac{\bar{\tau}\sqrt{A}}{\mu\bar{w}} = \frac{\pi\sqrt{\pi}(1 + \varepsilon^2)}{\sqrt{\varepsilon}E(\sqrt{1 - \varepsilon^2})} \quad (13)$$

It should be noted that the right-hand side of Eq. (13) is only a function of the channel aspect ratio (geometry).

The Fanning friction factor is defined as

$$f = \frac{\bar{\tau}}{\frac{1}{2}\rho\bar{w}^2} \quad (14)$$

Using Eq. (12), the Fanning friction factor for elliptical microchannels becomes

**Table 1 Analytical solutions of  $fRe$  for various cross-sections**

Cross-section	Analytical mean velocity	$fRe_{\sqrt{A}}$
	$\frac{c^2}{4(1 + \varepsilon^2)} \frac{\Delta p}{\mu L}$	$\frac{2\pi\sqrt{\pi}(1 + \varepsilon^2)}{\sqrt{\varepsilon}E(\sqrt{1 - \varepsilon^2})}$
	$\frac{\Delta p c^2}{\mu L} \left[ \frac{1}{3} - \frac{64\varepsilon}{\pi^5} \tanh \frac{\pi}{2\varepsilon} \right]$	$\frac{12}{\left(1 - \frac{192}{\pi^5} \varepsilon \tanh \frac{\pi}{2\varepsilon}\right) (1 + \varepsilon)\sqrt{\varepsilon}}$
	$\frac{1}{60} \frac{\Delta p a^2}{\mu L}$	$\frac{20}{3^{1/4}} = 15.197$
	$\frac{\Delta p a^2}{\mu L} g(\phi)^{  }$	$\frac{\phi\sqrt{\phi}}{(1 + \phi)g(\phi)^{  }}$
	$\frac{\Delta p b^2}{8\mu L} \left[ \varepsilon^2 - 1 + \frac{2\ln(1/\varepsilon) + \varepsilon^2 - 1}{\ln(1/\varepsilon)} \right]$	$\frac{8\sqrt{\pi}(1 - \varepsilon)\sqrt{1 - \varepsilon^2}}{\left(\varepsilon^2 - 1 + \frac{2\ln(1/\varepsilon) + \varepsilon^2 - 1}{\ln(1/\varepsilon)}\right)}$
$   g(\phi) = \frac{\tan(2\phi) - 2\phi}{16\phi} - \frac{128\phi^3}{\pi^5} \sum_{n=1}^{\infty} \frac{1}{(2n-1)^2(2n-1+4\phi/\pi)^2(2n-1-4\phi/\pi)}$		$\varepsilon = \frac{c}{b}$

$$f = \frac{2\pi\sqrt{\pi}(1+\varepsilon^2)}{\sqrt{\varepsilon E(\sqrt{1-\varepsilon^2})}} \frac{\mu}{\rho\bar{w}\sqrt{A}} \quad (15)$$

The Reynolds number can be defined based on the square root of area  $\sqrt{A}$

$$\text{Re}_{\sqrt{A}} = \frac{\rho\bar{w}\sqrt{A}}{\mu} \quad (16)$$

Combining Eqs. (15) and (16) becomes

$$f \text{Re}_{\sqrt{A}} = \frac{2\pi\sqrt{\pi}(1+\varepsilon^2)}{\sqrt{\varepsilon E(\sqrt{1-\varepsilon^2})}} \quad (17)$$

Similar to  $\bar{\tau}^*$ ,  $f \text{Re}_{\sqrt{A}}$  is only a function of the channel geometry. Thus, a relationship can be found between the nondimensional wall shear stress  $\bar{\tau}^*$  and  $f \text{Re}_{\sqrt{A}}$

$$f \text{Re}_{\sqrt{A}} = 2\bar{\tau}^* \quad (18)$$

Following the same steps described above, relationships for  $f \text{Re}_{\sqrt{A}}$  are determined for other microchannel cross-sections and they are summarized in Table 1. With respect to Table 1, the following should be noted:

1. The original analytical solution for the mean velocity in rectangular channels is in the form of a series. However, when  $\varepsilon=1$  (square), the first term of the series gives the value  $f \text{Re}_{\sqrt{A}}=14.132$  compared with the exact value (full series solution) of 14.23. The maximum difference of approximately 0.7% occurs at  $\varepsilon=1$ . For smaller values of  $\varepsilon$ , the agreement with the full series solution is even better. Therefore, only the first term is employed in this study.
2. For rectangular microchannels, two asymptotes can be recognized, i.e., the very narrow rectangular and square channels [12]

$$\begin{aligned} f \text{Re}_{\sqrt{A}} &= \frac{12}{\sqrt{\varepsilon}} & \varepsilon \rightarrow 0 \\ f \text{Re}_{\sqrt{A}} &= 14.13 & \varepsilon = 1 \end{aligned} \quad (19)$$

3. For elliptical microchannels, the asymptotes are the very narrow elliptical and circular microchannels [12]

$$\begin{aligned} f \text{Re}_{\sqrt{A}} &= \frac{11.15}{\sqrt{\varepsilon}} & \varepsilon \rightarrow 0 \\ f \text{Re}_{\sqrt{A}} &= 14.179 & \varepsilon = 1 \end{aligned} \quad (20)$$

Note that the  $f \text{Re}_{\sqrt{A}}$  values and trends for elliptical and rectangular channels are very close at both asymptotes. Figure 2 shows the comparison between  $f \text{Re}_{\sqrt{A}}$  relationships for the rectangular and elliptical microchannels reported in Table 1. In spite of the different forms of the  $f \text{Re}_{\sqrt{A}}$  for rectangular and elliptical microchannels, trends of both formulas are very similar as the aspect ratio varies between  $0 < \varepsilon \leq 1$ . The maximum relative difference is less than 8%.

Elliptical and rectangular cross-sections cover a wide range of singly-connected microchannels. With the similarity in the trends of solutions for these cross-sections, one can conclude that a general, purely geometrical, relationship may exist that predicts  $f \text{Re}_{\sqrt{A}}$  for arbitrary singly-connected cross-sections. Based on this observation, an approximate model is developed in the next section.

#### 4 Approximate Solution

Exact relationships for  $f \text{Re}_{\sqrt{A}}$  are reported for the elliptical, rectangular, and some other shapes in the previous section. However,

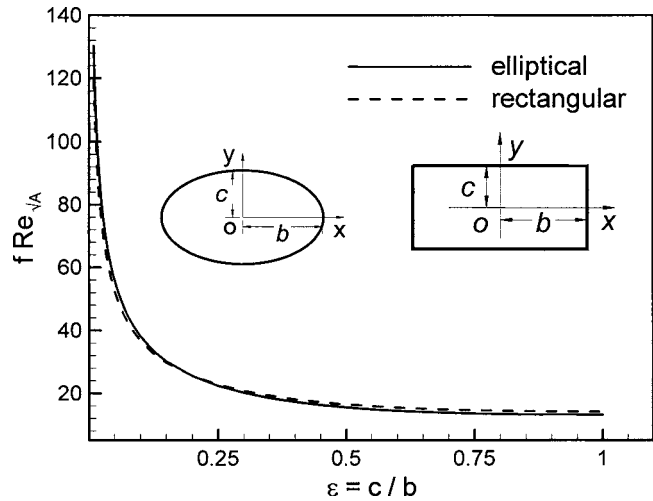


Fig. 2 Comparison of  $f \text{Re}_{\sqrt{A}}$  for elliptical and rectangular microchannels

finding exact solutions for many practical, singly-connected cross-sections, such as trapezoidal microchannels, is complex and/or impossible. In many practical instances such as basic design, parametric study, and optimization analyses, it is often required to obtain the trends and a reasonable estimate of the pressure drop. Moreover, as a result of recent advances in fabrication technologies in MEMS and microfluidic devices, trapezoidal cross-sections have become more important. Therefore, an approximate compact model that estimates pressure drop of arbitrary cross-sections will be of great value.

Torsion in beams and fully developed laminar flow in ducts are similar because the governing equation for both problems is Poisson's equation, Eq. (1). Comparing various singly-connected cross-sections, the torsional rigidity of a shaft could be accurately approximated by using an equivalent elliptical cross-section, where both cross-sectional area and polar moment of inertia are maintained the same as the original shaft [13]. With a similar approach as Saint-Venant, a model will be developed for predicting pressure drop in channels of arbitrary cross-section based on the solution for an elliptical duct.

The elliptical channel is considered, not because it is likely to occur in practice, but rather to utilize the unique geometrical property of its velocity solution. The mean velocity of elliptical channels is known, Eq. (3). The polar moment of inertia  $I_p = \int_A (x^2 + y^2) dA$ , where  $x$  and  $y$  are distances from  $x$  and  $y$  axes for an ellipse is

$$I_p = \frac{\pi bc(b^2 + c^2)}{4} \quad (21)$$

Equation (7) can be rearranged in terms of the polar moment of inertia, about its center, as follows:

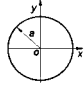
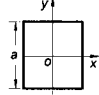
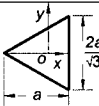
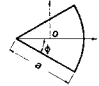
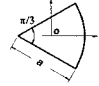
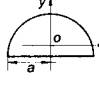
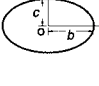
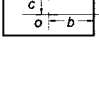
$$\frac{\Delta p}{L} = \frac{16\pi^2 \mu \bar{w}}{A^3} I_p = \frac{16\pi^2 \mu \bar{w}}{A} I_p^* \quad (22)$$

where  $I_p^* = I_p/A^2$  is a nondimensional geometrical parameter which we call the *specific polar moment of inertia*. Combining Eqs. (2a), (2b), and (22), one can write

$$\bar{\tau} = \frac{16\pi^2 \mu \bar{w}}{\sqrt{A}} \frac{\sqrt{A}}{P} I_p^* \quad (23)$$

Note that  $\sqrt{A}/P$  is also a nondimensional parameter. Using Eq. (23), the Fanning friction factor, Eq. (14), can be determined

**Table 2 Approximate model for various cross-sections**

Cross-section	$I_p^*$	$\sqrt{A}/P$	$f Re_{\sqrt{A}}$	
			$32\pi^2 I_p^* \sqrt{A}/P$	exact
	$\frac{1}{2\pi}$	$\frac{1}{2\sqrt{\pi}}$	14.18	14.18
	$\frac{1}{6}$	$\frac{1}{4}$	13.16	14.13
	$\frac{\sqrt{3}}{9}$	$\frac{\sqrt{3}}{6(3)^{1/4}}$	13.33	15.19
	$\frac{9\phi^2 - 8\sin^2 \phi}{18\phi^3}$	$\frac{\sqrt{\phi}}{2(1+\phi)}$	$\frac{(9\phi^2 - 8\sin^2 \phi)\sqrt{\phi}}{36\phi^3(1+\phi)}$	$\frac{\phi\sqrt{\phi}}{(1+\phi)g(\phi)^{[1]}}$
	Circular sector	$\phi = \frac{\pi}{6}$	13.57	14.92
	Semi-circle	$\phi = \frac{\pi}{2}$	15.67	16.17
	$\frac{1+\epsilon^2}{4\pi\epsilon}$	$\frac{\sqrt{\pi\epsilon}}{4E(\sqrt{1-\epsilon^2})}$	$\frac{2\pi\sqrt{\pi}(1+\epsilon^2)}{\sqrt{\epsilon E}(\sqrt{1-\epsilon^2})}$	$\frac{2\pi\sqrt{\pi}(1+\epsilon^2)}{\sqrt{\epsilon E}(\sqrt{1-\epsilon^2})}$
	$\frac{1+\epsilon^2}{12\epsilon}$	$\frac{\sqrt{\epsilon}}{2(1+\epsilon)}$	$\frac{4\pi^2(1+\epsilon^2)}{3\sqrt{\epsilon}(1+\epsilon)}$	$\frac{12}{\left(1 - \frac{192}{\pi^5} \epsilon \tanh \frac{\pi}{2\epsilon}\right)(1+\epsilon)\sqrt{\epsilon}}$
		$[1] g(\phi) = \frac{\tan(2\phi) - 2\phi}{16\phi} - \frac{128\phi^3}{\pi^5} \sum_{n=1}^{\infty} \frac{1}{(2n-1)^2(2n-1+4\phi/\pi)^2(2n-1-4\phi/\pi)}$		$\epsilon = \frac{c}{b}$

$$f = 32\pi^2 \frac{\mu}{\rho w \sqrt{A}} \frac{\sqrt{A}}{P} I_p^* \quad (24)$$

or,

$$f Re_{\sqrt{A}} = 32\pi^2 I_p^* \frac{\sqrt{A}}{P} \quad (25)$$

Using Eq. (18), one can find the nondimensional shear stress

$$\bar{\tau} = \frac{1}{2} f Re_{\sqrt{A}} = 16\pi^2 I_p^* \frac{\sqrt{A}}{P} \quad (26)$$

The right-hand side of Eqs. (25) and (26) are general geometrical functions since  $I_p$ ,  $A$ , and  $P$  are general geometrical parameters. Therefore the approximate model assumes that for constant fluid properties and flow rate in a constant cross-section channel,  $\bar{\tau}$  and  $f Re_{\sqrt{A}}$  are only functions of the nondimensional geometric parameter,  $I_p^* \sqrt{A}/P$ , of the cross-section.

Employing Eq. (25), one only needs to compute the nondimensional parameter  $I_p^* \sqrt{A}/P$  of the channel to determine the  $f Re_{\sqrt{A}}$  value. On the other hand, using the conventional method, Poisson's equation must be solved to find the velocity field and the mean velocity; then the procedure described in the previous section should be followed to find  $f Re_{\sqrt{A}}$ . This clearly shows the convenience of the approximate model.

To validate the approximate model, the exact values of  $f Re_{\sqrt{A}}$  for some cross-sections are compared with the approximate model, i.e., Eq. (25), in Table 2. Also the geometric parameter  $I_p^* \sqrt{A}/P$  is reported for a variety of cross-sections in Table 2. The approximate model shows relatively good agreement, within 8% relative difference, with the exact solutions for the cross-sections considered, except for the equilateral triangular channel. Moreover, the nondimensional geometric parameter is derived for regular polygons and trapezoidal channels; the approximate model is compared with the numerical values for these shapes published by Shah and London [8].

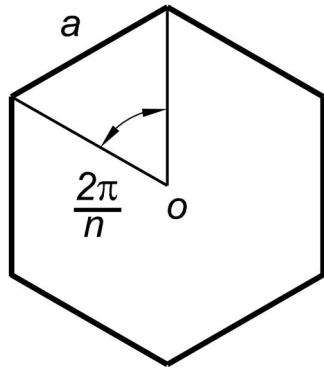


Fig. 3 Cross-section of a regular polygon channel

**4.1 Regular Polygons.** Figure 3 illustrates a regular polygon microchannel of the side length  $a$ . For regular polygons, cross-sectional area, perimeter, and the polar moment of inertia are

$$A = \frac{na^2}{4 \tan(\pi/n)}$$

$$P = na$$

$$I_p = \frac{na^4}{96 \tan(\pi/n)} \left( 1 + \frac{3}{\tan^2(\pi/n)} \right) \quad (27)$$

Thus, one can obtain  $fRe_{\sqrt{A}}$

$$fRe_{\sqrt{A}} = \frac{8\pi^2 \tan(\pi/n)}{3n\sqrt{n} \tan(\pi/n)} \left( 1 + \frac{3}{\tan^2(\pi/n)} \right) \quad (28)$$

Table 3 lists the geometric parameter  $I_p^*$ ,  $\sqrt{A}/P$ , and  $fRe_{\sqrt{A}}$  for regular polygons. Table 3 also shows the comparison between the approximate model with the numerical results reported for regular polygons by Shah and London [8]. The following relationship is used to convert the Reynolds number Fanning friction factor product based on  $D_h$  to  $\sqrt{A}$

$$fRe_{\sqrt{A}} = \frac{P}{4\sqrt{A}} fRe_{D_h} \quad (29)$$

The approximate model shows good agreement, within 8% relative difference, with the numerical results of [8] except for the equilateral triangular ( $n=3$ ); the agreement improves as the num-

Table 3 Geometric parameter for regular polygons

$n$	$I_p^*$	$\sqrt{A}/P$	$fRe_{\sqrt{A}}$	
			model	Numerical [8]
3	0.192	0.219	13.332	15.196
4	0.167	0.250	13.159	14.227
5	0.162	0.262	13.410	14.044
6	0.160	0.269	13.607	14.009
7	0.160	0.272	13.743	14.055
8	0.160	0.275	13.838	14.028
9	0.159	0.276	13.906	14.045
10	0.159	0.277	13.956	14.060
$\infty$	0.159	0.282	14.180	14.180

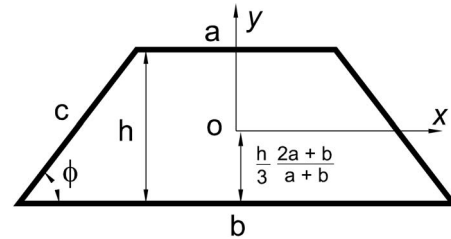


Fig. 4 Cross-section of an isosceles trapezoidal channel

ber of sides increases toward the circular channel ( $n \rightarrow \infty$ ). Using a mapping approach, a compact model is developed in the Appendix which predicts the  $fRe_{\sqrt{A}}$  for isosceles triangular channels with a maximum difference of less than 3.5%.

**4.2 Trapezoidal Microchannel.** The cross-section of a trapezoidal microchannel is shown in Fig. 4. This is an important shape since some microchannels are manufactured with trapezoidal cross-sections as a result of the etching process in silicon wafers. Furthermore, in the limit when the top side length,  $a$ , goes to zero, it yields an isosceles triangle. At the other limit when  $a = b$ , it yields a rectangular channel, and a square microchannel when  $a = b = h$ . An aspect ratio is defined

$$\varepsilon \equiv \frac{a+b}{2h} \quad (30)$$

The aspect ratio should work for all above-mentioned limiting cases. As shown in Table 4, the defined aspect ratio covers the triangular, rectangular, and square limiting cases. The cross-sectional area, perimeter, and polar moment of inertia (about its center) are

$$A = \varepsilon h^2$$

$$P = 2h(\varepsilon + \sqrt{\varepsilon^2 - \beta\varepsilon^2 + 1})$$

$$I_p = \frac{A^2[2(3\varepsilon^2 + 1) + \beta(1 - 3\varepsilon^2)]}{36\varepsilon} \quad (31)$$

where  $\beta$ , another nondimensional parameter, is defined as

$$\beta \equiv \frac{h^2 ab}{A^2} = \frac{4ab}{(a+b)^2} \quad (32)$$

Note that the parameter  $\beta$  is zero for triangular and 1 for rectangular and square channels. The angle  $\phi$  (see Fig. 4) can be found from  $\varepsilon$  and  $\beta$

Table 4 Limiting cases of isosceles trapezoid

Cross-section	$\varepsilon$	$\beta$	$I_p^*$	$\sqrt{A}/P$
Triangular <sup>1</sup>	$\frac{b}{2h}$	0	$\frac{3\varepsilon^2 + 1}{18\varepsilon}$	$\frac{\sqrt{\varepsilon}}{2(\varepsilon + \sqrt{\varepsilon^2 + 1})}$
Triangular <sup>2</sup>	$\frac{1}{\sqrt{3}}$	0	$\frac{\sqrt{3}}{9}$	$\frac{\sqrt{3}}{6(3)^{1/4}}$
Rectangular	$\frac{b}{h}$	1	$\frac{\varepsilon^2 + 1}{12\varepsilon}$	$\frac{\sqrt{3}}{2(1 + \varepsilon)}$
Square	1	1	$\frac{1}{6}$	$\frac{1}{4}$
isosceles				equilateral

$$\sin \phi = \frac{1}{\sqrt{\varepsilon^2 - \beta \varepsilon^2 + 1}} \quad (33)$$

One can obtain  $fRe_{\sqrt{A}}$

$$fRe_{\sqrt{A}} = \frac{8\pi^2(3\varepsilon^2 + 1) + \beta(1 - 3\varepsilon^2)}{9\sqrt{\varepsilon(\varepsilon + \sqrt{\varepsilon^2 - \beta\varepsilon^2 + 1})}} \quad (34)$$

Shah and London [8] reported numerical values for  $fRe_{Dh}$  for laminar fully-developed flow in trapezoidal channels. They presented  $fRe_{Dh}$  values as a function of  $\alpha^* = h/a$  for different values of angles  $\phi$ . The nondimensional geometrical parameters  $\varepsilon$  and  $\beta$ , defined in this work, are related to  $\alpha^*$  and  $\phi$  in [8] as follows:

$$\varepsilon = \frac{1}{\alpha^*} + \frac{1}{\tan \phi}$$

**Table 5 Model versus data [8], trapezoidal channels**

$\alpha^*$	$fRe_{Dh}$	$\varepsilon$	$\beta$	$fRe_{\sqrt{A}}$		
				model	[8]	%diff.
$\phi = 85^\circ$						
8	17.474	0.212	0.830	23.384	23.054	1.41
4	16.740	0.337	0.933	18.563	19.325	-4.11
2	15.015	0.587	0.978	14.516	15.587	-7.38
4/3	14.312	0.837	0.989	13.318	14.398	-8.11
1	14.235	1.087	0.994	13.203	14.274	-8.11
3/4	14.576	1.421	0.996	13.774	14.825	-7.63
1/2	15.676	2.087	0.998	15.806	16.770	-6.10
1/4	18.297	4.087	1.000	22.648	23.038	-1.72
1/8	20.599	8.087	1.000	33.804	32.926	2.60
$\phi = 75^\circ$						
8	14.907	0.393	0.535	15.745	16.982	-7.85
4	14.959	0.518	0.732	14.725	16.142	-9.62
2	14.340	0.768	0.878	13.499	14.754	-9.30
4/3	14.118	1.018	0.931	13.244	14.365	-8.46
1	14.252	1.268	0.955	13.520	14.576	-7.81
3/4	14.697	1.601	0.972	14.304	15.311	-7.04
1/2	15.804	2.268	0.986	16.430	17.332	-5.49
1/4	18.313	4.268	0.996	23.165	23.505	-1.47
1/8	20.556	8.268	0.999	34.155	33.254	2.64
$\phi = 60^\circ$						
8	13.867	0.702	0.324	13.540	15.364	-13.47
4	13.916	0.827	0.513	13.544	15.162	-11.95
2	13.804	1.077	0.713	13.623	14.842	-8.95
4/3	13.888	1.327	0.811	13.953	14.960	-7.21
1	14.151	1.577	0.866	14.484	15.392	-6.26
3/4	14.637	1.911	0.909	15.384	16.230	-5.49
1/2	15.693	2.577	0.950	17.482	18.241	-4.34
1/4	18.053	4.577	0.984	23.908	24.184	-1.15
1/8	20.304	8.577	0.995	34.582	33.735	2.45
$\phi = 45^\circ$						
8	13.301	1.125	0.210	14.669	15.921	-8.53
4	13.323	1.250	0.360	14.796	15.874	-7.28
2	13.364	1.500	0.556	15.123	15.899	-5.13
4/3	13.541	1.750	0.673	15.573	16.194	-3.99
1	13.827	2.000	0.750	16.125	16.691	-3.51
3/4	14.260	2.333	0.816	16.973	17.492	-3.06
1/2	15.206	3.000	0.889	18.869	19.377	-2.69
1/4	17.397	5.000	0.960	24.760	24.952	-0.77
1/8	19.743	9.000	0.988	34.958	34.268	1.97
$\phi = 30^\circ$						
8	12.760	1.857	0.130	17.923	18.058	-0.75
4	12.782	1.982	0.236	18.013	18.077	-0.35
2	12.875	2.232	0.398	18.277	18.235	0.23
4/3	13.012	2.482	0.513	18.633	18.509	0.66
1	13.246	2.732	0.598	19.062	18.961	0.53
3/4	13.599	3.065	0.681	19.720	19.672	0.25
1/2	14.323	3.732	0.785	21.220	21.249	-0.14
1/4	16.284	5.732	0.909	26.178	26.295	-0.44
1/8	18.479	9.732	0.968	35.489	34.747	2.09

$$\beta = 1 - \frac{1}{\varepsilon^2 \tan^2 \phi} \quad (35)$$

Table 5 shows the comparison between the approximate model and the numerical data reported by [8]. As can be seen, except for a few points, the agreement between the approximate model and the numerical values is reasonable (less than 10%).

## 5 Comparison With Experimental Data

The present model is compared with experimental data collected by several researchers [6,7,14] for microchannels. The accuracy of the experimental data is in the order of 10%.

Wu and Cheng [7] conducted experiments and measured the friction factor of laminar flow of deionized water in smooth silicon microchannels of trapezoidal cross-sections. Table 6 summarizes geometric parameters of their microchannels.

Figures 5 and 6 are examples of the comparison between the approximate model and the data of [7] for channels N1-100 and N2-200, respectively. As shown the approximate model shows good agreement with these data.

The frictional resistance  $fRe_{\sqrt{A}}$  is not a function of Re number, i.e., it remains constant for the laminar regime as the Reynolds number varies. Therefore, the experimental data for each set are averaged over the laminar region. As a result, for each experimental data set, one  $\varepsilon$ , one  $\beta$ , and one  $fRe_{\sqrt{A}}$  value can be obtained.

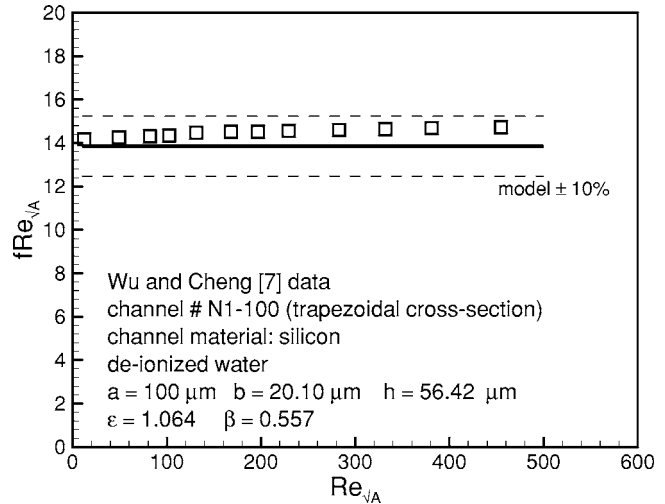


**Fig. 5 Comparison of experimental data [7] with model**

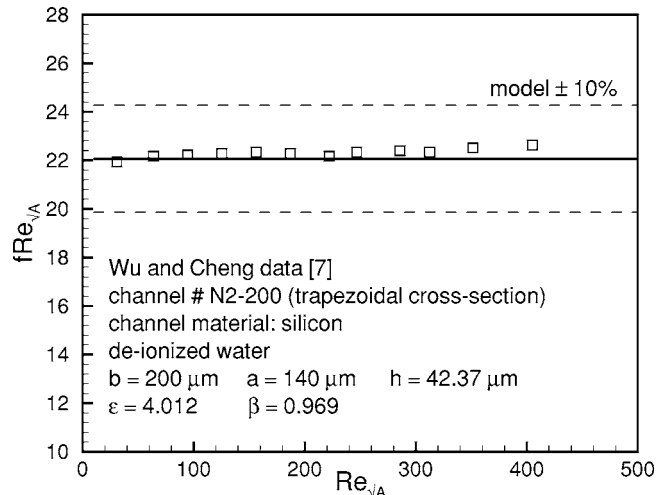


**Fig. 6 Comparison of experimental data [7] with model**

**Table 6 Trapezoidal microchannels data [7]**

Channel	<i>b</i>	<i>a</i>	<i>h</i>	$\epsilon$	$\beta$	<i>fRe<sub>vA</sub></i>		% diff.
	( $\mu\text{m}$ )	( $\mu\text{m}$ )	( $\mu\text{m}$ )	( $\mu\text{m}$ )	( $\mu\text{m}$ )	model	data	
N1-100	100	20.1	56.4	1.06	0.56	13.85	14.48	-4.5
N1-150	150	70.1	56.4	1.95	0.87	15.61	15.95	-2.2
N1-200	200	120.2	56.4	2.84	0.94	18.34	18.74	-2.2
N1-500	500	420	56.5	8.14	0.99	33.38	31.55	5.5
N1-1000	1000	920	56.5	16.99	1.00	50.86	45.76	10.0
N1-4000	4000	3920	56.5	70.10	1.00	108.32	93.13	14.0
N2-50	50	0	35.3	0.71	0.00	13.50	13.95	-3.3
N2-100	100	39.9	42.4	1.65	0.82	14.83	14.91	-0.6
N2-150	150	89.9	42.4	2.83	0.94	18.29	18.22	0.4
N2-200	200	140	42.4	4.01	0.97	22.06	22.30	-1.1
N2-500	500	440	42.4	11.09	1.00	39.95	38.08	4.7
N2-1000	1000	940	42.4	22.89	1.00	59.94	54.60	8.9
N2-4000	4000	3940	42.4	93.70	1.00	125.76	110.70	12.0
N3-50	50	0	35.3	0.71	0.00	13.50	13.62	-0.9
N3-100	100	0	70.6	0.71	0.00	13.50	14.29	-5.8
N3-150	150	0	105.9	0.71	0.00	13.50	14.03	-3.9
N3-200	200	0	141.2	0.71	0.00	13.50	14.66	-8.6
N3-500	500	284	152.5	2.57	0.92	17.48	17.47	0.0
N3-1000	1000	784	152.5	5.85	0.99	27.46	26.45	3.7
N3-2000	2000	1784	152.5	12.40	1.00	42.59	39.57	7.1
N3-4000	4000	3784	152.5	25.52	1.00	63.57	57.07	10.2
N4-100	100	0	70.6	0.71	0.00	13.50	13.98	-3.5
N4-200	200	27.2	122.0	0.93	0.42	13.76	15.10	-9.7
N4-500	500	327	122.2	3.38	0.96	20.08	20.99	-4.5
N4-1000	1000	827	122.2	7.48	0.99	31.75	31.54	0.6
N4-4000	4000	3828	121.5	32.22	1.00	72.07	69.88	3.0
N5-150	150	47.4	72.5	1.36	0.73	14.24	14.87	-4.5
N6-500	500	279	156.1	2.50	0.92	17.24	17.07	1.0

Table 6 presents the predicted  $fRe_{vA}$  values by the approximate model and the averaged values of the reported experimental values of  $fRe_{vA}$  [7]. As shown, the agreement between the predicted values and the experimental values are good and within the experiment uncertainty. The channels considered by [7] cover a wide range of geometrical parameters, i.e.,  $0.71 \leq \epsilon \leq 97.70$  and  $0 \leq \beta \leq 1$ ; as a result the data include triangular and rectangular microchannels. It should be noted that, in spite of the different dimensions, channels N2-50, N3-50, N3-100, N3-150, N3-200, and N4-100 have the same values of  $\beta$  and  $\epsilon$ ; thus they are geometrically equivalent. It is interesting to observe that the predicted and measured  $fRe_{vA}$  values are identical for these channels, as expected. Figure 7 illustrates the comparison between all trapezoidal data [7] and the proposed model. The  $\pm 10\%$  bounds are also shown in the plot, to better demonstrate the agreement between the data and the model.

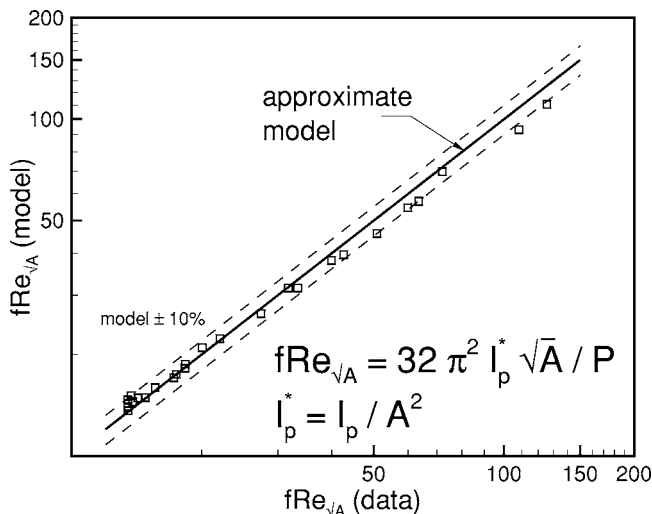


**Fig. 7 Comparison between model and all trapezoidal data [7]**

Liu and Garimella [6] carried out experiments and measured the friction factor in rectangular microchannels. They did not observe any scale-related phenomena in their experiments and concluded that the conventional theory can be used to predict the flow behavior in microchannels in the range of dimensions considered. They [6] measured and reported the relative surface roughness of the channels to be negligible, thus their channels can be considered smooth (see Fig. 8 for channels dimensions). Figure 8 also shows the comparison between the model and the channel L3 of data [6].

Gao et al. [14] experimentally investigated laminar fully developed flow in rectangular microchannels. They designed their experiments to be able to change the height of the channels tested while the width remained constant at 25  $\mu\text{m}$ . They conducted several experiments with several channel heights; see Fig. 9 for the channels dimensions used in this study. Gao et al. [14] measured the roughness of the channel and reported negligible relative

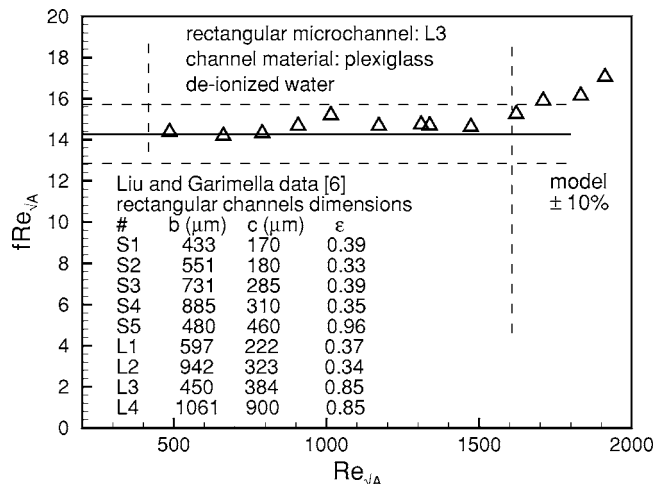


**Fig. 8 Comparison of experimental data [6] with model**



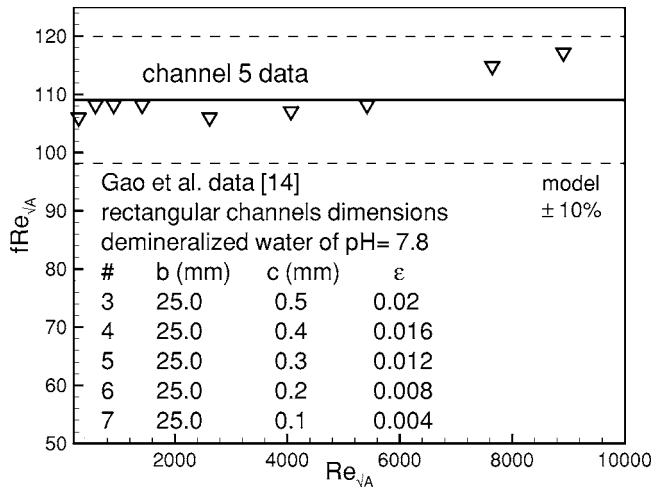


Fig. 9 Comparison of experimental data [15] with model

roughness, thus their channels can be considered smooth. Figure 9 shows the comparison of the model and data [14].

Following the same method described for trapezoidal data, the reported values of  $fRe_{\sqrt{A}}$  for rectangular microchannels are averaged and plotted against both approximate and exact models in Fig. 10. As previously discussed, the maximum difference between the exact and approximate solutions for the rectangular channel is less than 8%. As shown in Fig. 10, the collected data cover a wide range of the aspect ratio  $\epsilon=c/b$ , almost three decades; also the relative difference between the data and model is within the accuracy of the experiments.

## 6 Summary and Conclusions

The pressure drop of fully-developed laminar flow in smooth arbitrary cross-sections channels is studied. Using existing analytical solutions for fluid flow, relationships are derived for  $fRe_{\sqrt{A}}$  for selected cross-sections. It is observed through analysis that the square root of area  $\sqrt{A}$ , as the characteristic length scale, is superior to the conventional hydraulic diameter,  $D_h$ . Thus it is recommended to use  $\sqrt{A}$  instead of  $D_h$ .

A compact approximate model is proposed that predicts the pressure drop of fully developed, laminar flow in channels of arbitrary cross-section. The model is only a function of geometrical parameters of the cross-section, i.e., area, perimeter, and polar

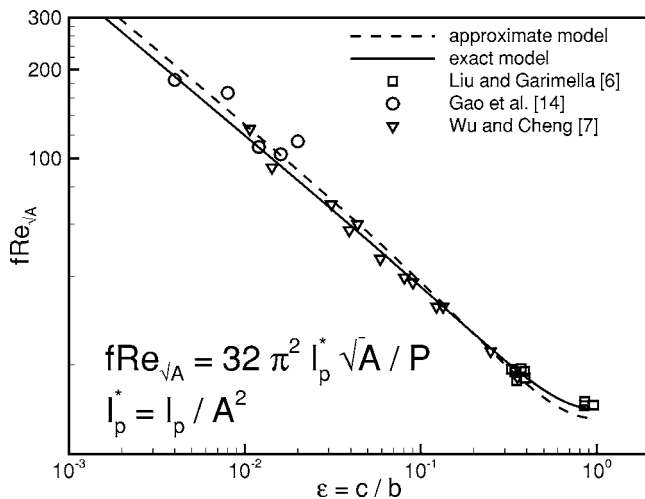


Fig. 10 Comparison between model and all rectangular data [6,7,15]

moment of inertia. The proposed model is compared with analytical and numerical solutions for several shapes. Except for the equilateral triangular channel (with 14% difference), the present model successfully predicts the pressure drop for a wide variety of shapes with a maximum difference on the order of 8%. Moreover, a compact model is developed using a mapping approach, which predicts the  $fRe_{\sqrt{A}}$  for isosceles triangular channels with a maximum difference of less than 3.5%.

The proposed model is also validated with either experimental data or exact analytical solutions for rectangular, trapezoidal, triangular (isosceles), square, and circular cross-sections collected by several researchers and shows good agreement.

## Acknowledgment

The authors gratefully acknowledge the financial support of the Centre for Microelectronics Assembly and Packaging, CMAP, and the Natural Sciences and Engineering Research Council of Canada, NSERC.

## Nomenclature

- $A$  = cross-sectional area,  $m^2$
- $b, c$  = channel semi-axes,  $m$
- $D_h$  = hydraulic diameter  $4A/P$ ,  $m$
- $E(\cdot)$  = complete elliptic integral of the second kind
- $f$  = Fanning friction factor,  $2\tau/\rho\bar{w}^2$
- $h$  = height of trapezoidal channel,  $m$
- $I_p$  = polar moment of inertia,  $m^4$
- $I_p^*$  = specific polar moment of inertia,  $I_p/A^2$
- $L$  = microtube length,  $m$
- $n$  = number of sides, regular polygons
- $P$  = perimeter,  $m$
- $Re_{\sqrt{A}}$  = Reynolds number,  $\rho\bar{w}\sqrt{A}/\mu$
- $w$  = fluid velocity,  $m/s$
- $\bar{w}$  = mean fluid velocity,  $m/s$
- $z$  = flow direction

## Greek Symbols

- $\alpha^*$  = aspect ratio trapezoidal duct,  $h/a$
- $\beta$  = dimensionless parameter trapezoidal duct
- $\epsilon$  = aspect ratio,  $c/b$
- $\rho$  = fluid density,  $kg/m^3$
- $\mu$  = fluid viscosity,  $kg/m.s$
- $\tau$  = wall shear stress,  $N/m^2$
- $\tau^*$  = nondimensional wall shear stress
- $\phi$  = trapezoidal channel angle,  $rad$
- $\Delta p$  = pressure drop,  $Pa$
- $\Gamma$  = boundary of duct

## Subscripts

- $\sqrt{A}$  = square root of cross-sectional area,  $m$

## Appendix: Isosceles Triangular Channels

To calculate the pressure drop in isosceles triangular channels, a *mapping approach* is used. Shah and London [8] reported numeri-

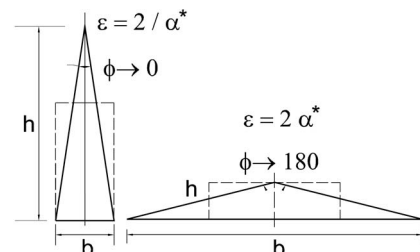


Fig. 11 Two limits of isosceles triangular channel

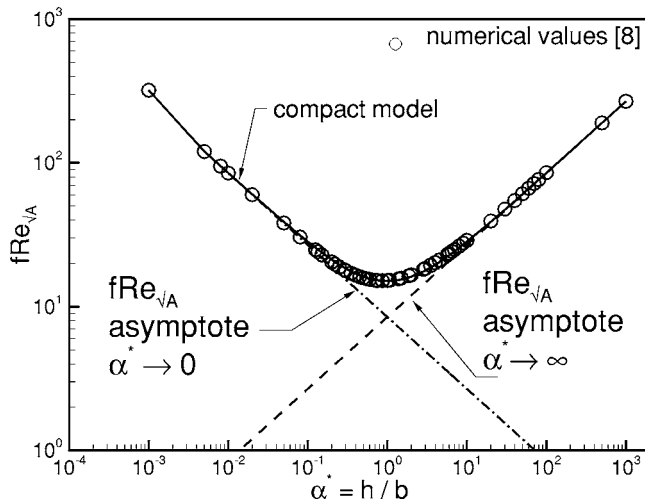


Fig. 12  $fRe_{\sqrt{A}}$  for isosceles triangular channels

cal values of  $fRe_{Dh}$  for isosceles triangular channels as a function of the aspect ratio defined as  $\alpha^*$

$$\alpha^* = \frac{h}{b} \quad (\text{A1})$$

The reported numerical values [8] were converted to  $fRe_{\sqrt{A}}$ . Plotting  $fRe_{\sqrt{A}}$  versus  $\alpha^*$  reveals that the solution has two asymptotes corresponding to the angle  $\phi$  as it approaches 0 and 180 deg as shown in Fig. 11. It is interesting to observe that these two asymptotes are both similar to very narrow rectangular channels. Thus Eq. (19) can be used to predict  $fRe_{\sqrt{A}}$  in both limits. Equation (19) can be written in terms of  $\alpha^*$ , defined by [8], as follows:

$$fRe_{\sqrt{A}} = \begin{cases} \frac{12}{\sqrt{2\alpha^*}} & \alpha^* \rightarrow 0 \\ \frac{12\sqrt{\alpha^*}}{\sqrt{2}} & \alpha^* \rightarrow \infty \end{cases} \quad (\text{A2})$$

To find relationships between  $\alpha^*$  of the triangular channel and  $\varepsilon$  of the equivalent rectangular channel, the cross-sectional area of the equivalent rectangular is set equal to the triangular channel (see Fig. 11). Using the blending technique of Churchill and Usagi [15], a compact correlation can be developed by combining the above asymptotes as follows:

$$fRe_{\sqrt{A}} = 6 \left[ \left( \frac{2}{\alpha^*} \right)^{n/2} + (2\alpha^*)^{n/2} \right]^{1/n} \quad (\text{A3})$$

The value of the fitting parameter  $n$  can be obtained by comparing the compact correlation with the numerical values for  $\alpha^*$  in the range [0.5, 2]. If we choose  $\alpha^* = 1$ , then  $fRe_{\sqrt{A}} = 15.24$ , and the value of  $n = 1.184$  gives excellent agreement at this point. If we select  $n = 1.20$ , the maximum difference of about 3.5% occurs at  $\alpha^* = 0.3$ . For the equilateral triangle where  $\alpha^* = \sqrt{3}/2$ , the compact model with  $n = 1.20$ , gives  $fRe_{\sqrt{A}} = 15.24$ , which is about 0.3% greater than the numerical value of 15.19. Figure 12 presents the numerical values of  $fRe_{\sqrt{A}}$  reported by [8], the two asymptotes, and the compact model, Eq. (A3), with  $n = 1.20$ .

## References

- [1] Yang, C., Wu, J., Chien, H., and Lu, S., 2003, "Friction Characteristics of Water, R-134a, and Air in Small Tubes," *Microscale Thermophys. Eng.*, **7**, pp. 335–348.
- [2] Morini, G. L., 2004, "Laminar-To-Turbulent Flow Transition in Microchannels," *Microscale Thermophys. Eng.*, **8**, pp. 15–30.
- [3] Tuckerman, D. B., and Pease, R. F., 1981, "High-Performance Heat Sinking For VLSI," *IEEE Electron Device Lett.*, **5**, pp. 126–129.
- [4] Pfund, D., Rector, D., Shekarriz, A., Popescu, A., and Welty, J., 2000, "Pressure Drop Measurements in a Microchannel," *AICHE J.*, **46**(8), pp. 1496–1507.
- [5] Bahrami, M., Yovanovich, M. M., and Culham, J. R., 2006, "Pressure Drop of Fully-Developed, Laminar Flow in Rough Microtubes," *ASME J. Fluids Eng.*, **128**, pp. 632–637. Also *ASME 3rd International Conference on Microchannels*, 2005, Paper No. ICMM 2005-75108, July 13–15, Univ. of Toronto, Toronto, Canada.
- [6] Liu, D., and Garimella, S., 2004, "Investigation of Liquid Flow in Microchannels," *J. Thermophys. Heat Transfer*, **18**(1), pp. 65–72.
- [7] Wu, H. Y., and Cheng, P., 2003, "Friction Factors in Smooth Trapezoidal Silicon Microchannels With Different Aspect Ratios," *Int. J. Heat Mass Transfer*, **46**, pp. 2519–2525.
- [8] Shah, R. K., and London, A. L., 1978, *Laminar Flow Forced Convection In Ducts*, Academic, New York.
- [9] White, F. M., 1974, *Viscous Fluid Flow*, McGraw-Hill, New York.
- [10] Yovanovich, M. M., *Advanced Heat Conduction*, Chap. 12 (in preparation).
- [11] Muzychka, Y. S., and Yovanovich, M. M., 1998, "Modeling Friction Factors in Non-Circular Ducts For Developing Laminar Flow," *2nd AIAA Theoretical Fluid Mechanics Meeting*, June 15–18, Albuquerque, NM.
- [12] Muzychka, Y. S., and Yovanovich, M. M., 2002, "Laminar Flow Friction and Heat Transfer in Non-Circular Ducts and Channels Part 1: Hydrodynamic Problem," *Proceedings of Compact Heat Exchangers, A Festschrift on the 60th Birthday of Ramesh K. Shah*, Grenoble, France, pp. 123–130.
- [13] Timoshenko, S. P., and Goodier, J. N., 1970, *Theory of Elasticity*, McGraw-Hill, New York, Chap. 10.
- [14] Gao, P., Person, S. L., and Favre-Marinet, M., 2002, "Scale Effects on Hydrodynamics and Heat Transfer in Two Dimensional Mini and Microchannels," *Int. J. Therm. Sci.*, **41**, pp. 1017–1027.
- [15] Churchill, S. W., and Usagi, R., 1972, "A General Expression For the Correlation of Rates of Transfer and Other Phenomena," *AICHE J.*, **18**, pp. 1121–1128.

# Design of a Low-Turbulence, Low-Pressure Wind-Tunnel for Micro-Aerodynamics

Michael J. Martin  
e-mail: martinm2@asme.org

Kevin J. Scavazze

Iain D. Boyd

Luis P. Bernal

Department of Aerospace Engineering,  
University of Michigan,  
Ann Arbor, MI 48109-2140

*A novel wind-tunnel facility has been designed for measurement of lift and drag on micromachined airfoils. The tunnel is designed to operate with pressures ranging from 0.15 to 1.0 atmosphere, over a velocity range of 30 to 100 m/s, allowing for independent control of Reynolds and Knudsen number. The tunnel is designed for testing of airfoils with chords of 10 to 100 microns, giving a range of Reynolds numbers from 10 to 600, with Knudsen numbers reaching 0.01. Due to the structural constraints of the airfoils being tested, the wind tunnel has a 1 cm cross-section. This small size allows the use of a 100-1 contraction area, and extremely fine turbulence screens, creating a low turbulence facility. Computational fluid dynamics is used to show that an ultra-short 100-1 contraction provides uniform flow without separation, or corner vortices. Velocity data obtained with impact and hot-wire probes indicate uniform flow and turbulence intensities below 0.5%. [DOI: 10.1115/1.2236128]*

## Introduction

As micro-electro-mechanical systems (MEMS) technology improves, the number of flow configurations to be considered is rapidly increasing [1]. Several applications, including micro air vehicles, micromachined hotwires, and micropropulsion systems require analysis of external flow geometries. As the scale of these applications shrinks to take advantage of MEMS technologies, the flow around these objects will enter a rarefied regime. While there has been considerable work on MEMS scale airflows in internal flow geometries, such as microchannels [2], there are few experimental results of external-flow configurations. Potential complications of external flow configurations include flow separation and a large variation in local Knudsen numbers. While some of these effects have been studied in internal flows [3,4], they will become more significant in rarefied external flows [5].

The planned experiments at these scales require a low-turbulence facility, with the ability to vary velocity from 10 to 100 m/s and pressure from 0.1 to 1.0 atmosphere. Due to the force sensors used, the width of the test section is limited to approximately 1.0 cm. Additionally, the facility should be designed to give approximately uniform flow over this range of velocities and pressures.

This paper deals with issues in designing a low-turbulence, uniform flow facility for these test conditions. After outlining facility requirements, a facility configuration is proposed. The design of a 100-1 contraction section, intended for both turbulence suppression and to achieve uniform velocity in the test section, is outlined. Computational fluid dynamics studies are used to predict the contraction effectiveness. Because of the novel configuration and flow requirements, extensive computational fluid dynamics (CFD) studies are made of flow over a wide range of flow conditions. After fabrication of the contraction, impact probe and hot-wire measurements are used to show that the goal of a uniform-flow, low-turbulence facility is met.

## Facility Requirements

Because flow visualization for gases at the MEMS scale is still under development [6], this experiment is designed to measure lift

and drag forces on micromachined airfoils. A modified Blasius boundary layer solution, using a slip boundary condition, shows that on airfoils with a chord of less than 100  $\mu\text{m}$ , the slip flow effects will cause a reduction in drag of 1–10%, depending on conditions [7]. Computational results for flow over a 20  $\mu\text{m}$  flat plate, performed using a hybrid particle-continuum method, show larger forces than the Blasius solution, but the same relative decrease in drag due to slip effects [8].

Previous work has shown that an integrated microdevice, as shown in Fig. 1, incorporating a flat-plate airfoil with piezoresistive sensors, can measure lift and drag on airfoils with chords ranging from 40 to 100  $\mu\text{m}$  [9]. Based on the expected forces on the airfoils, structural considerations limit the maximum span of the devices to approximately 1 cm. Because the piezoresistive sensors are integrated to the side of the airfoil, the maximum width of the test section for these airfoils is also 1 cm.

The wind-tunnel facility to be used in this experiment is a unique design, intended to allow testing of a 1 cm span airfoil under a wide range of flow conditions. In order to carry out the desired measurements, the facility must meet the following requirements:

1. The facility is designed to allow pressure to be varied from 0.1 to 1.0 atm, with a velocity range of 30 to 100 m/s. This approach allows independent control of Knudsen number and Reynolds number for a given test airfoil.
2. Turbulence intensity should be as close to zero as possible, to allow easier comparison of results, and to avoid velocity fluctuations within the system that may be of the same order of magnitude as slip velocities at the surface of the airfoil. As a design goal, the turbulence intensity should be kept less than 0.5%.
3. The velocity profile in the test section should be kept as uniform as possible, with a minimal boundary layer thickness along the wall.

## Facility Configuration

A schematic of the facility is shown in Fig. 2.

The small size of the test section allows for conventional methods of turbulence control to be carried to their limits. Both theoretical and experimental studies [10,11] have shown that stream-wise turbulence is reduced by contractions in the flow. Typical

Contributed by the Fluids Engineering Division of ASME for publication in the JOURNAL OF FLUIDS ENGINEERING. Manuscript received March 23, 2005; final manuscript received February 13, 2006. Assoc. Editor: Kenneth Breuer.

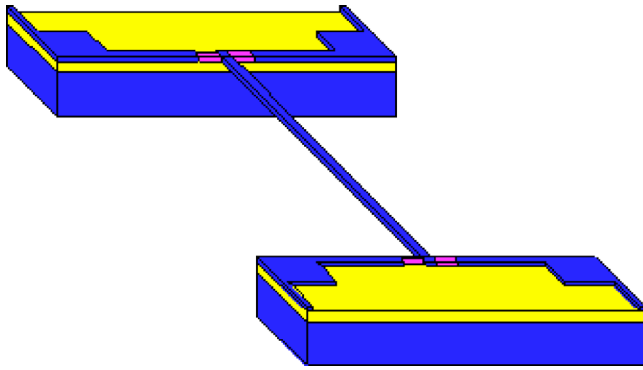


Fig. 1 Integrated flat plate airfoil and sensor design

wind-tunnel facilities use a 25:1 or 16:1 ratio contraction for turbulence suppression. Because of the small size of the microscale facility, a 100:1 ratio inlet can be used.

### Turbulence Suppression Strategies

Theoretical results show that the reduction in the streamwise turbulent velocity fluctuation  $u'$  is given by:

$$\frac{\overline{u_2'^2}}{\overline{u_1'^2}} = \frac{3}{4c^2} [\ln(4c^3 - 1)] \quad (1)$$

where  $u_1'$  is the precontraction turbulent streamwise fluctuation,  $u_2'$  is the postcontraction turbulent fluctuation, and  $c$  is the area ratio [10]. For a 100:1 reduction, we expect the rms fluctuations to decrease by a factor of 0.022.

This model indicates that the normal turbulent velocity fluctuations  $v'$  and  $w'$  will increase, based on the following equation:

$$\frac{\overline{v_2'^2}}{\overline{v_1'^2}} = \frac{\overline{w_2'^2}}{\overline{w_1'^2}} = \frac{3c}{4} \quad (2)$$

where  $v_1'$  and  $w_1'$  are the precontraction turbulent normal fluctuations, and  $v_2'$  and  $w_2'$  are the postcontraction turbulent normal fluctuations. For a 100:1 reduction, we would expect the rms fluctuations to increase by a factor of 8.7.

Although the high contraction ratio leads to increased normal velocity fluctuations, these can be controlled by use of a honeycomb structure, which will filter out large-scale turbulent motions while generating small-scale turbulence. The small-scale turbulent fluctuations will dissipate downstream of the honeycomb, based on the following expression:

$$\left(\frac{q'}{U_\infty}\right)^2 = \frac{0.03}{x/D} \quad (3)$$

where  $q'$  is the turbulent fluctuation,  $U_\infty$  is the free-stream velocity,  $x$  is the downstream distance, and  $D$  is the honeycomb diameter [12].

The high contraction ratio leads to extremely low velocities at the inlet of the system. This means that an extremely fine honeycomb can be used without causing high pressure drops. For this

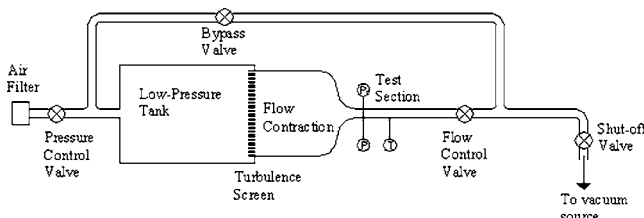


Fig. 2 Schematic of test facility

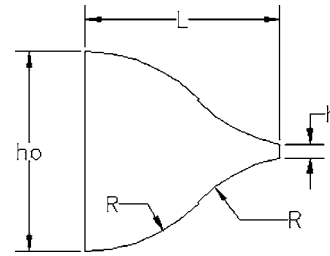


Fig. 3 Contraction geometry

facility, a honeycomb of 2.5 cm long, 0.2 cm diameter tubes is selected. Modeling the turbulence in the facility requires an estimate of the streamwise turbulent velocity fluctuations prior to the honeycomb. In the settling chamber, the velocity will be 1 m/s or less. If we assume a turbulence intensity of 10% in the settling chamber, then the magnitude of the fluctuations is 0.1 m/s. Because 10% is a high level of turbulence, typical of reacting flows [13], this is a conservative estimate.

Assuming initial turbulence fluctuations of 0.1 m/s, modeling the change in  $u'_{rms}$  using Eq. (1), and modeling the changes in  $v'_{rms}$  and  $w'_{rms}$  using Eqs. (2) and (3), we can estimate the magnitude of the turbulent fluctuations after the contraction. For a 10 cm pre-contraction length, using a 0.2 cm diameter honeycomb, these models indicate that all turbulent fluctuations will be below 0.2% regardless of initial velocity.

Use of the 100-1 contraction will, however, result in anisotropic turbulence, since streamwise fluctuations are damped much more effectively than normal fluctuations. Depending upon the intended application for testing, this may have a major effect on the results. For the application described here, minimizing streamwise fluctuations was held to be of much greater importance than minimizing normal fluctuations. This is because one of the objectives of the tunnel is to allow measurement as the airfoils approach the slip flow regime, where a small wall velocity may appear.

### Inlet Design: CFD Results

The major difficulty in design of this facility involves the shape of the contraction section. While there has been much work on the design of both axisymmetric and square wind-tunnel contractions [14], the high contraction ratio and small size of this contraction are unique. A commercial CFD solver [15] is used to study several 100:1 square inlet configurations, with a final width of 1 cm.

All potential configurations are studied with final velocities of 30 and 100 m/s, at a pressure of 1 atm. Following the same approach as previous researchers [14], the contraction is built from two curves, meeting at an inflection point. All inlets use  $h$  equal to 0.01 m and  $h_0$  equal to 0.1 m, and the length was varied from 0.45 to 0.2 m. To simplify the analysis, the curves chosen are circles, and the inflection point is taken as the midpoint of the converging section, as shown in Fig. 3.

Based on the previous analysis, a laminar flow solver is used to compute the flow. Initial calculations were made using a 20 by 20 by 60 mesh that included only the contraction section. Detailed calculations were made using a 20 by 20 by 100 mesh that included the upstream volume. A sample three-dimensional mesh is shown as Fig. 4. Symmetries exist in the  $x$ - $y$  and  $x$ - $z$  planes, allowing the tunnel to be simulated using one-quarter of the total cross section. All cases use a uniform velocity inlet and a uniform pressure outlet boundary condition. All cases were repeated using a 40 by 40 by 200 mesh, to ensure grid independence, and accurate resolution of the boundary layer.

The velocity profiles 1 cm into the test section are compared based on boundary layer thickness and free-stream velocity uniformity. The position is nondimensionalized based on the test section width:

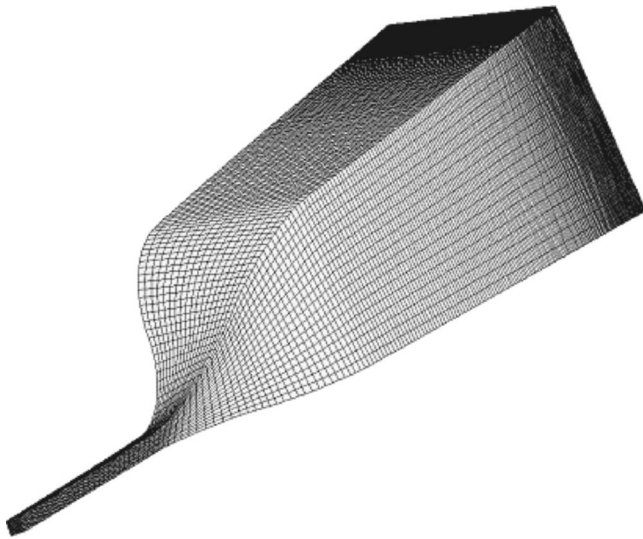


Fig. 4 Sample mesh

$$y^* = \frac{y}{h} \quad (4)$$

where  $y^*$  is the nondimensional position. All velocities are nondimensionalized using the following expression:

$$u^* = \frac{u}{\bar{u}} \quad (5)$$

where  $u^*$  is the nondimensional velocity, and  $\bar{u}$  is the average velocity across the entire test section. The results are shown in Fig. 5.

These results show that the 0.45 m contraction has the thinnest boundary layer, with the least velocity overshoot in the core of the flow. This geometry is then retested for four cases: velocities of 30 and 100 m/s, and pressures of 0.1 and 1.0 atm.

The results show that the shortest inlet possible is the most effective design for this application. Boundary layer growth for these conditions is a much larger concern than flow separation.

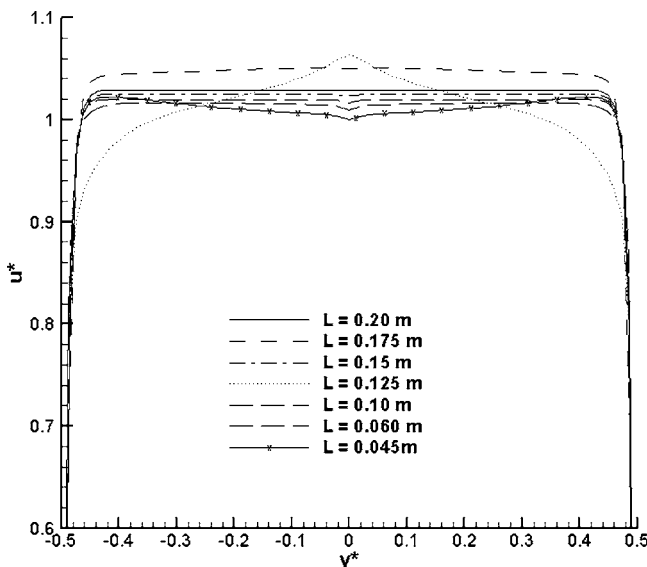


Fig. 5 Velocity profiles for sample contractions

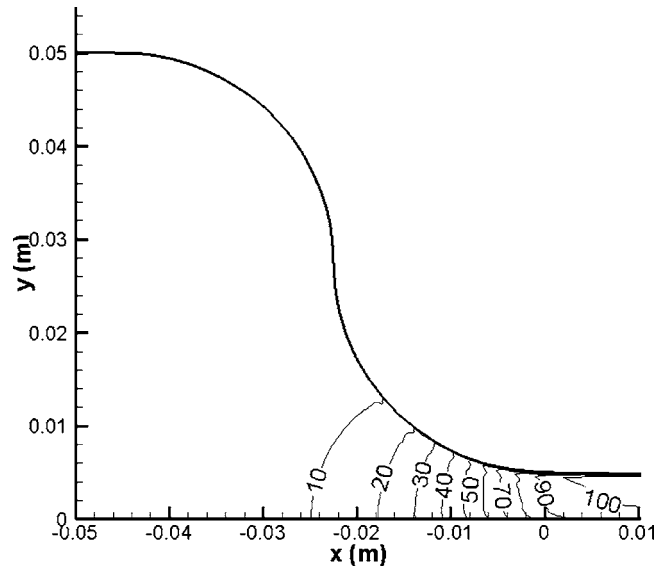


Fig. 6 Contours of  $U$ , 0.045 m contraction,  $U=100$  m/s,  $P=1.0$  atm

Figure 6 shows the contours of  $U$  in a 0.045 m contraction, indicating that the fluid acceleration occurs in the second half of the contraction.

Figure 7 shows the streamlines for the 0.045 m contraction. These streamlines indicate that, in spite of the large change in area in a relatively short distance, there is no flow separation. The streamlines also indicate that, although a boundary layer does develop, there does remain a core of relatively uniform flow in the system.

Figures 8 and 9 show the velocity profiles at the end of the contraction, and 1 cm downstream in the test section, for design 7, for both high-pressure and low-pressure cases.

These results show that the shortest possible inlet should be used for the inlet of a microscale wind-tunnel facility. While there is a velocity overshoot of 7% from the mean velocity at the end of the contraction, this smooths out within the first 1 cm of the test section.

An additional concern was the possible appearance of corner vortices in the contraction section. The normal velocity vectors at the end of the contraction section are shown in Fig. 10. These results show a net flow from the wall area to the center of the test section, and that there is no development of corner vortices in the tunnel contraction section.

The inlet is built using a length of 0.045 m. Additional CFD analysis on the selected design is performed to cover the entire range of pressures and velocities. The cases studied cover a range of pressures from 0.15 to 1.0 atm, with a range of velocity from 10 to 100 m/s. The cases can be characterized using a channel Reynolds number, as given by Eq. (6).

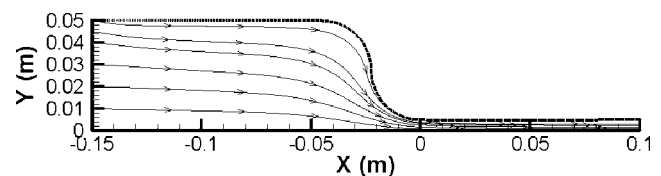


Fig. 7 Streamlines for 0.045 m contraction,  $U=100$  m/s,  $P=1.0$  atm

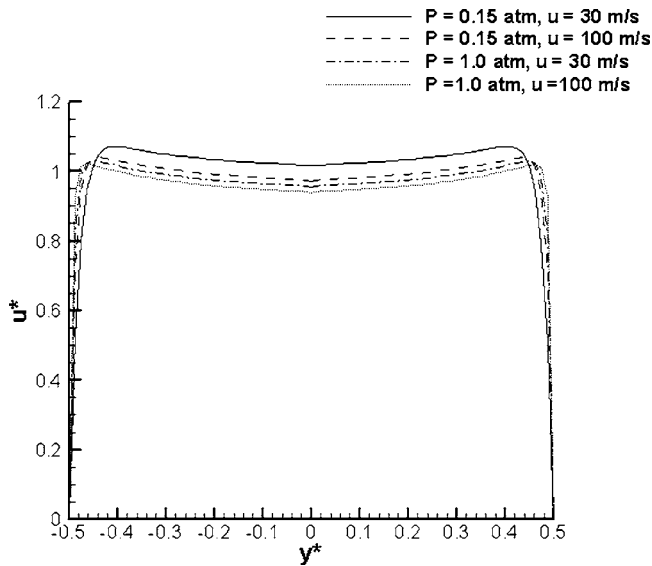


Fig. 8 Normalized velocity profiles at end of 0.045 m contraction

$$Re_h = \frac{\rho \bar{u} h}{\mu} \quad (6)$$

where  $h$  is the test section width,  $\rho$  is the air density, and  $\mu$  is the viscosity.

Because the tunnel is designed to allow independent control of velocity and pressure, the channel Reynolds number will vary considerably. The minimum Reynolds number, at a pressure of 0.15 atmosphere, a temperature of 298 K, and a velocity of 10 m/s, is 1010. The peak Reynolds number, at a pressure of 1.0 atm and a velocity of 100 m/s, is 67,000.

For fully developed channel flows, transition to turbulence typically begins at a Reynolds number of around 2300, and a flow is considered to be fully turbulent at a Reynolds number of 10,000. These criteria apply for both round and square channels [16]. The majority of cases studied here are turbulent by these criteria. However, all CFD studies are performed using laminar flow mod-

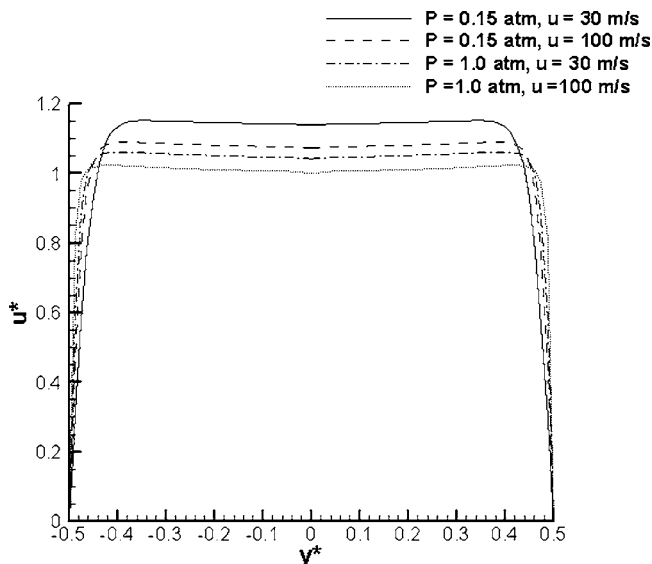


Fig. 9 Normalized velocity profiles 1 cm into test section

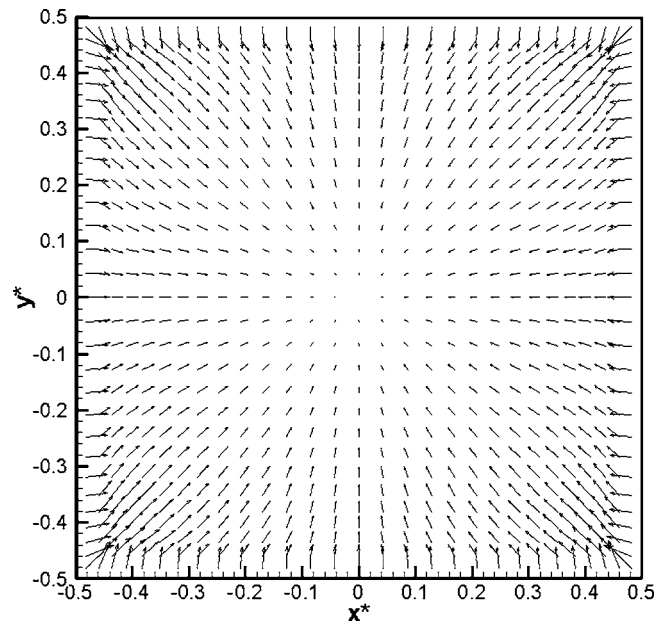


Fig. 10 Normal velocity vectors at end of contraction section

els. The turbulence suppression system detailed earlier in this chapter is assumed to be effective enough that turbulence intensities are extremely low.

CFD analysis was performed for pressures ranging from 0.15 to 1.0 atm and for velocities ranging from 10 to 100 m/s. All of results show a core of uniform flow, and a boundary layer thinner than 0.0005 m for velocities greater than 30 m/s. As expected, the boundary layer thins with increasing velocity and increasing density. When nondimensionalized using average velocity and channel Reynolds number, the velocity profiles 1 cm into the test section collapsed onto each other, as shown in Fig. 11.

The velocity profiles are analyzed to determine the momentum deficit, velocity deficit, and boundary layer thickness. All of these results are plotted versus the channel Reynolds number and provide some indication of how close the channel is to achieving the design goal of uniform flow. They also provide some indication of possible transition to turbulence within the boundary layer.

The boundary layer thickness prior to the contraction can be found by using the Blasius boundary layer for a flat plate:

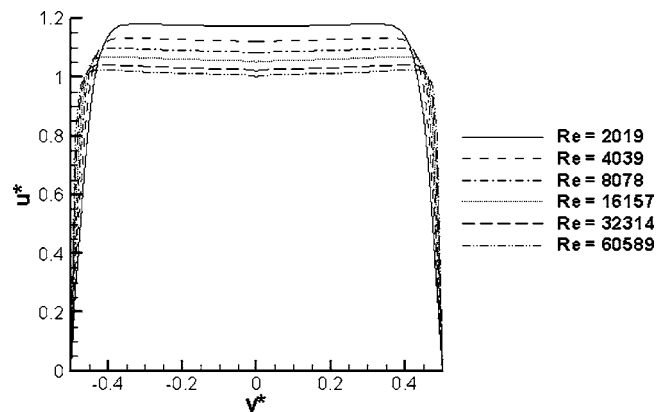


Fig. 11 Nondimensional velocity profiles

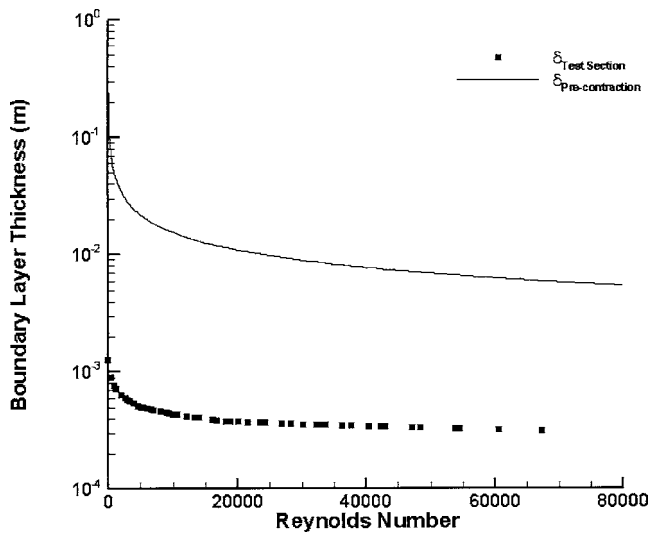


Fig. 12 Boundary layer thickness versus Reynolds number

$$\delta_1 = \frac{5.0}{\sqrt{\rho u_1 / \mu l}} \quad (7)$$

where  $\delta_1$  is the precontraction boundary layer thickness,  $l$  is the length of the settling chamber, and  $u_1$  is the precontraction velocity. The settling chamber length will be assumed to be 0.30 m.

Assuming a constant density,  $u_1$  can be found using continuity, leading to the expression:

$$\delta_1 = \sqrt{\frac{hc}{l}} \frac{5.0l}{\sqrt{Re_h}} \quad (8)$$

The precontraction and postcontraction boundary layer thickness are shown as Fig. 12. The contraction reduces the boundary layer thickness by two orders of magnitude. Equation (9) is used to calculate the nondimensional momentum thickness [17].

$$\theta = \int_0^{h/2} \frac{u}{u_{\max}} \left(1 - \frac{u}{u_{\max}}\right) dy \quad (9)$$

where  $\theta$  is the momentum deficit,  $h$  is the height of the test section, and  $u$  is the downstream velocity at a given point ( $y$ ).

The velocity thickness is calculated using Eq. (10) [16]:

$$\delta^* = \int_0^{h/2} \left(1 - \frac{u}{u_{\max}}\right) dy \quad (10)$$

The momentum and velocity thickness are nondimensionalized using the channel height and are shown in Fig. 13.

These results show that the length scales of the momentum and velocity deficits are both small relative to the tunnel width and vary predictably with Reynolds number.

The results of this analysis can also be used to predict possible transition to turbulence within the boundary layer of the tunnel. A Reynolds number based on velocity thickness is calculated, as shown in Eq. (11):

$$Re_{\delta^*} = \frac{\rho \bar{u} \delta^*}{\mu} \quad (11)$$

where  $\delta^*$  is the velocity thickness found using Eq. (8).  $Re_{\delta^*}$  as a function of tunnel Reynolds number is plotted as Fig. 14.

Previous researchers have found that laminar boundary layers become unstable when  $Re_{\delta^*}$  approaches 520 [17,18]. Based on these criteria, at a tunnel Reynolds number of above 20,000, the boundary layer may transition to turbulence.

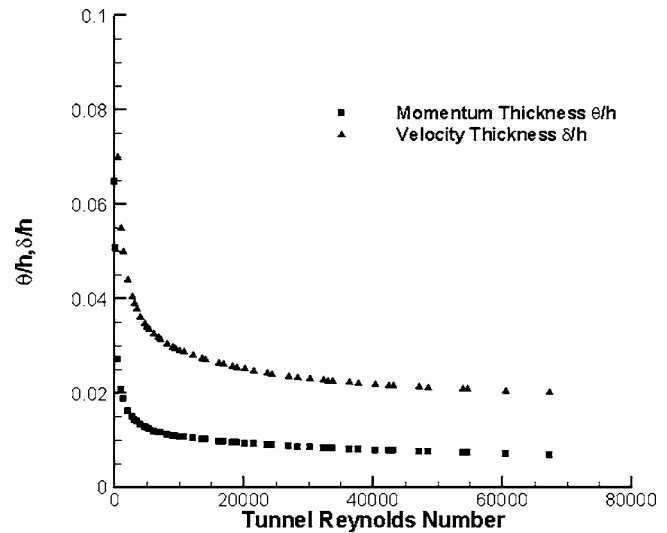


Fig. 13 Momentum and velocity deficits versus Reynolds number

These computational results show that the nondimensional velocity profile, as well as flow characteristics such as the momentum thickness, velocity deficit, and boundary layer thickness, collapse onto the same curve based on Reynolds number. They also show that the tunnel flow is much more uniform than what would normally be expected for a channel flow.

These results show that as the airfoil Knudsen number is changed by varying tunnel conditions, the velocity profile will be identical for any given tunnel Reynolds number. This will allow results for any given Reynolds number test structure to be compared for various Knudsen numbers.

**Tunnel Fabrication.** The completed facility is shown as Fig. 15.

The flow direction of the tunnel in this photograph is from left to right. The air is drawn in through a small-engine air filter and passes through a gated flow-control valve. The air is then drawn through a 30 cm long settling chamber, with a 20 cm by 20 cm cross-section. Even at peak flow, the velocities in the settling chamber will remain below 1 m/s. At the end of the settling chamber, the air is drawn through a honeycomb of 0.2 cm diameter straws. The air then travels down a 10 cm straight section and

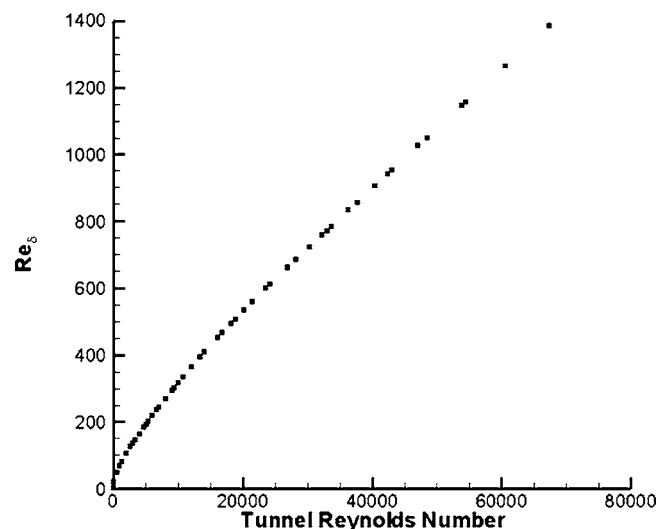


Fig. 14  $Re_{\delta^*}$  versus tunnel Reynolds number

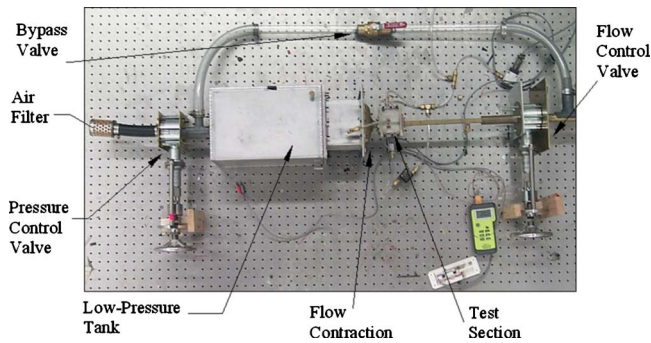


Fig. 15 Operational facility

into the 100-1 contraction. Immediately after the contraction is the test section. After the test section, air then flows through a second valve, used to control the flow velocity. A second 2.5 cm diameter flow line is installed in parallel, to serve as a bypass. This allows low pressure to be maintained in the settling chamber even when there is very little airflow through the test section. These two lines then meet and run to the vacuum system.

**Test Section Instrumentation.** The instrumented test section is shown in Fig. 16.

An impact probe to measure dynamic pressure, a static pressure port, and a thermocouple are installed in the test section. The 0.0008 m diameter impact probe is moved across the test section by using the attached vertical stage. A schematic of this apparatus is shown as Fig. 17.

**Test Section Velocity Measurements.** The velocity profiles in the test section are measured for pressures ranging from 0.3 to 1.0 atm and are shown as Figs. 18–21. Due to geometric con-

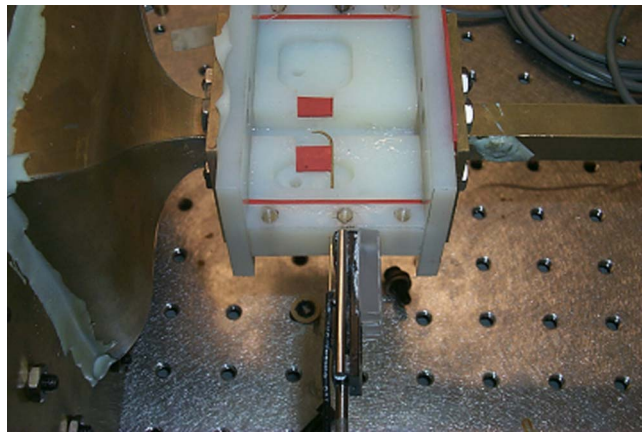


Fig. 16 Test section instrumentation

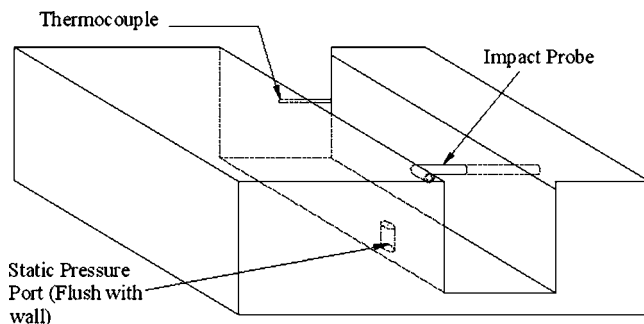


Fig. 17 Test section instrumentation installation

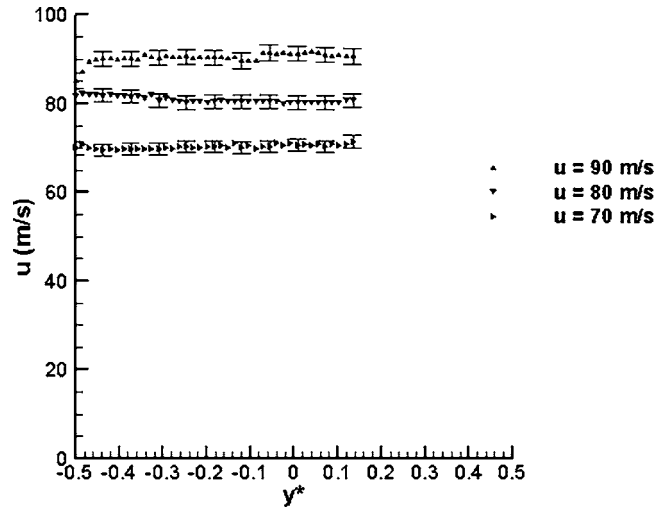


Fig. 18 Velocity profiles for  $P=0.3$  atm

straints on the impact probe, the velocity is measured from one wall to past the mid-point of the test section, instead of across the entire test section.

These results show a core of uniform flow, as predicted by the CFD modeling. They also show possible transition to turbulence in the boundary layer at high Reynolds numbers, as predicted by the modeling of the boundary layer. Therefore, independent measurements were taken of turbulence in the core of the flow, to ensure that the channel flow remains laminar.

### Test Section Turbulence Measurements

The turbulence at the centerline of the test section is characterized using a TSI hot-film probe, as shown in Fig. 22. The hot-film probe is mounted in the same  $y$ - $z$  plane as the impact probe, avoiding flow interference.

The probe is then calibrated by comparison with the impact probe. This method of calibration is selected since external calibration would not be reliable at lower pressures. Testing shows that the commercial hot-wire system is not reliable for low pressures, so measurements of turbulence intensity are taken at 0.6 atm and 100 m/s, and 0.9 atm and 90 m/s. Because of potential interference problems with the probes, the turbulence numbers

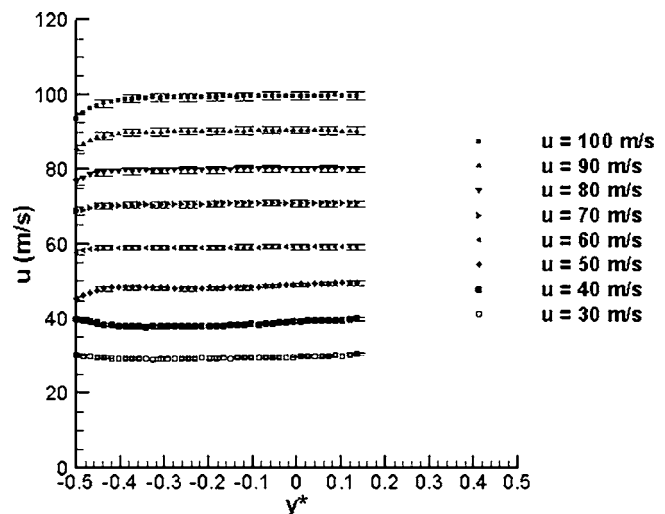


Fig. 19 Velocity profiles for  $P=0.5$  atm



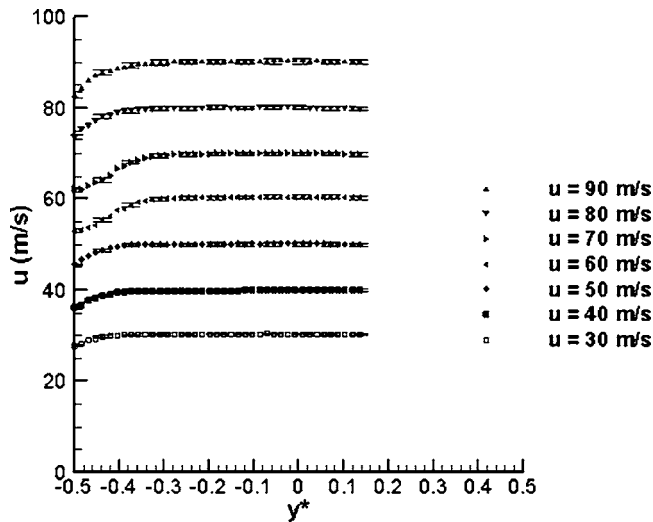


Fig. 20 Velocity profiles for  $P=0.9$  atm

given by the hot-wire should be taken as an upper bound on the turbulence in the tunnel. Typical hot-wire traces are shown in Fig. 23.

These results show that the flow is steady over the duration of planned tests. The voltage fluctuations due to turbulence in the hot-wire system are low enough to be on the same order of mag-

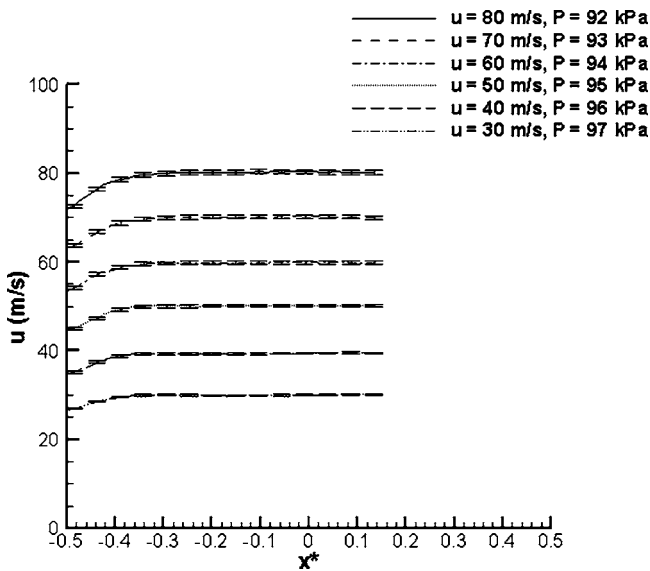


Fig. 21 Velocity profiles for  $P=1.0$  atm

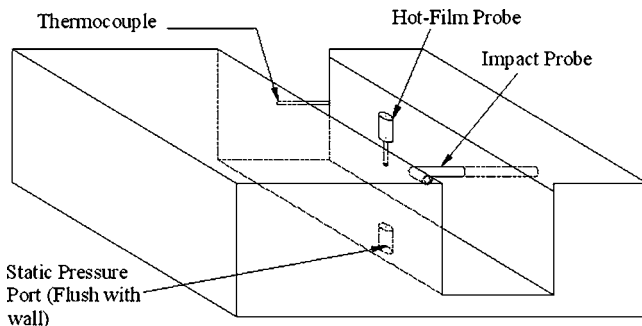


Fig. 22 Test section instrumentation with hot film probe

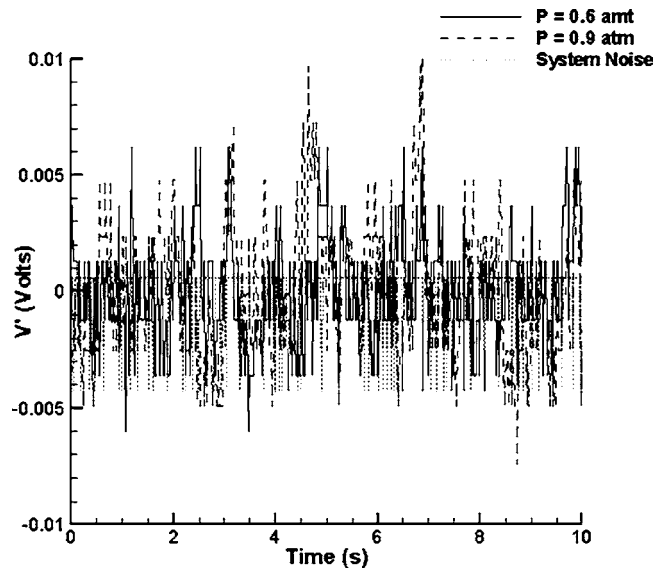


Fig. 23 Centerline hot-wire voltage fluctuations

nitude as the electrical noise in the system. The electrical noise is removed from the rms calculations using the following equation:

$$V(\text{turb})'_{\text{rms}} = \sqrt{V'^2 - V(\text{noise}')^2_{\text{rms}}} \quad (12)$$

where  $V(\text{turb})'_{\text{rms}}$  is the voltage fluctuation due to turbulence,  $V'$  is the voltage fluctuation in the signal, and  $V(\text{noise}')_{\text{rms}}$  is the measured signal noise. After removal of signal noise, the measured turbulence intensity is 0.2% for 0.6 atm and 100 m/s, and 0.4% for 0.9 atm and 90 m/s. Due to the intrusive nature of the probe in a confined channel, these should be taken as upper limits on the turbulence values.

## Conclusions

Computational fluid dynamics analysis showed that high contraction ratios are possible for wind-tunnel usage without incurring flow separation or corner vortices. These results were confirmed by experimental measurements that show that uniform flow profiles were achieved with minimal turbulence. Boundary layer growth is minimal, and a core of uniform flow was maintained. Additional study may be undertaken to determine the limits of 100-1 contractions as a flow control tool.

Experimental study showed that the design goals of the test facility were partially met. The full range of desired pressures and velocities could not be achieved. However, the results suggest that any future low-pressure wind-tunnel built on a draw-through design should be designed with a high bypass ratio to the test section. This will improve the flexibility of the design for testing at low-speed, low-pressure conditions.

## Acknowledgment

The authors gratefully acknowledge support for this work from the Air Force Office of Scientific Research through MURI Grant No. F49620-98-1-043. The authors also wish to thank Terry Larrow, David McLean, Eric Kirk, Chris Chartier, and Tom Griffin for their assistance in fabrication and installation of this facility.

## References

- [1] Ho, C. M., and Tai, Y. C., 1998, "Micro-Electro-Mechanical-Systems (MEMS) and Fluid Flows," *Annu. Rev. Fluid Mech.*, **30**, pp. 579-612.
- [2] Arkilic, E. B., Schmidt, M. A., and Breuer, K. S. 1997, "Gaseous Slip Flow in Long Microchannels," *J. Microelectromech. Syst.*, **6**(2), pp. 167-178.
- [3] Lee, Y. L., Wong, M., and Zohar, Y., 2002, "Pressure Loss in Constriction Microchannels," *J. Microelectromech. Syst.*, **11**(3), pp. 236-244.

- [4] Karniadakis, G. E., and Beskok, A., 2002, *Micro Flows: Fundamentals and Simulation*, Springer-Verlag, New York, Chap. 3.
- [5] Gampert, B., 1978, "Low Reynolds Number TAC-Slip Flow Past a Circular Cylinder," *Proceedings 11th Rarefied Gas Dynamics Symposium*.
- [6] Lempert, W. R., Jiang, N., Sethuram, S., and Samimy, M., 2002, "Molecular Tagging Velocimetry Measurements in Supersonic Micro Jets," *AIAA J.*, **40**(6), pp. 1065–1070.
- [7] Martin, M. J., and Boyd, I. D., 2000, "Blasius Boundary Layer Solution With Slip Flow Conditions," *Proceedings 22nd Rarefied Gas Dynamics Symposium*, AIP Conf. Proc., Melville, NY, Vol. 585, pp. 518–253.
- [8] Sun, Q., Boyd, I. D., and Candler, G. V., 2002, "Numerical Simulation of Gas Flow over Micro-Scale Airfoils," *J. Thermophys. Heat Transfer*, **16**(2), pp. 171–179.
- [9] Martin, M. J., Kurabayashi, K., and Boyd, I. D., 2001, "Measurement of Lift and Drag on MEMS Scale Airfoils in Slip Flow," *Proceedings of 2001 ASME FEDSM*, American Society of Mechanical Engineers, New York.
- [10] Batchelor, G. K., 1953, *Theory of Homogeneous Turbulence*, Cambridge U. P., Cambridge, UK, Chap. 4.
- [11] Uberoi, M. S., 1956, "Effect of Wind-Tunnel Contraction on Free Stream Turbulence," *J. Aeronaut. Sci.*, **23**(8), pp. 754–764.
- [12] Lumley, J. L., and McMahon, J. F., 1967, "Reducing Water Tunnel Turbulence by Means of a Honeycomb," *ASME J. Basic Eng., Series D*, **89D**(4), pp. 764–770.
- [13] Lefebvre, A. H., 1998, *Gas Turbine Combustion*, Taylor & Francis Group, Philadelphia, PA.
- [14] Mikhail, M. N., and Rainbird, W. J., 1978, "Optimum Design of Wind Tunnel Contractions," *AIAA Paper No. 1978-819*.
- [15] FLUENT/UNS User's Guide: Release 3.2. 1995, Fluent Inc., Lebanon, NH.
- [16] Schlichting, H., 1999, *Boundary-Layer Theory*, Springer-Verlag, New York.
- [17] White, F. M., 1991, *Viscous Fluid Flow*, McGraw-Hill, New York.
- [18] Holman, J. P., 2000, *Experimental Methods for Engineers*, McGraw-Hill, Inc., New York.

# Design Optimization of Micro Synthetic Jet Actuator for Flow Separation Control

**Oktay Baysal**

Professor, Eminent Scholar and Dean  
e-mail: obaysal@odu.edu

**Mehti Köklü**

Graduate Research Assistant  
e-mail: mkoklu@odu.edu

**Nurhak Erbaş**

Graduate Research Assistant  
e-mail: nerbas@odu.edu

Frank Batten College of Engineering and  
Technology,  
Old Dominion University,  
Norfolk, VA 23529-0236

*A computational analysis and design methodology is presented for effective microflow control using synthetic jets. The membrane is modeled as a moving boundary to accurately compute the flow inside the jet cavity. Compressible Navier-Stokes equations are solved with boundary conditions for the wall slip and the temperature jump conditions encountered for a specific range of Knudsen numbers. For validation, microchannel flow and microfilter flow are successfully computed. Then, flow past a backward-facing step in a microchannel is considered. Analysis is coupled with a design methodology to improve the actuator effectiveness. The objective function is selected to be the square of the vorticity (enstrophy) integrated over a separated region. First, from a design of experiments study, orifice and actuator cavity widths are identified as the most effective design variables. Then, a response surface method is constructed to find the improved control of the flow. This optimization results in more than 83% reduction of the enstrophy of the recirculation region. [DOI: 10.1115/1.2236134]*

## 1 Introduction

Fluid flow in small devices differs from those in macroscopic devices, and understanding the unfamiliar physics of fluids involved in microflows is a key issue for microfluidics. A key non-dimensional parameter for gas micro flows is the Knudsen (Kn) number. Depending on the Kn range, a full continuum or a full free-molecular analysis may be applicable. In the present study, flows in the Kn range of less than 0.1 are considered and they are modeled using a conventional Navier-Stokes solution method. As demonstrated by Baysal and Aslan [1], however, new wall boundary conditions need to be developed to account for the slip velocity and temperature jump conditions encountered in these micro sized geometries.

Synthetic jets are popular actuators for external flow control and have been proposed as potential actuators for microelectromechanical (MEMS) applications (Aslan et al. [2]). This, however, requires a careful system design in order to achieve effective control. In a synthetic jet, the actuating flow is generated at the orifice of a cavity by oscillating a membrane opposite to the orifice as illustrated in Fig. 1. A wide variety of geometries have been proposed and built for the design of synthetic jets. A triangular cavity has been shown to be more efficient when compared to a rectangular cavity (Edis et al. [3]) and hence it is selected as the test geometry for the present design optimization study. Synthetic jets have also been studied as actuators to control flow separation by Jain et al. [4] and Rediniotis et al. [5]. Major differences in the present study are twofold. First, the present focus is on microflows where the flow physics is different. To the best of the authors' knowledge, there have been only a few studies on micro-sized synthetic jets; also they have only been modeled assuming continuum flow regime with no-slip at the walls. Second, the present study includes a high-fidelity modeling of the geometry to include both the cavity and the motion of the piezoelectric membrane.

Typical practice of MEMS design process is performed in a trial-and-error fashion. Such a practice requires prohibitive iterations before the performance requirements of a given device are finally satisfied. However, if an effective computational approach were to be developed, it could be used within an automated design

optimization methodology (Baysal [6]). Accurate information on mass flow rates, shear stress distributions, and heat transfer in an optimally controlled flow could lead to devices that can be designed effectively, hence rendering lower initial and operational costs.

To demonstrate the presently proposed design methodology, flow past a micro backward-facing step is considered. Here the separation occurs downstream of the step resulting in a significant variation of the mean free path of the gas molecules and the wall shear stress (Fig. 2). The separation characteristics can be altered using a synthetic jet pumped into the channel flow.

The present paper is organized in the following way. First, we include a brief description of the mathematical model for micro gas flows. This is followed by the introduction of both the design of experiments and the response surface methods in the Optimization Methodology section. Finally, we present the results of our study and discussion of our results, followed by the summary and some concluding remarks.

## 2 Mathematical Model

For the present investigation, an existing Navier-Stokes solver, CFL3D, has been modified to account for the slip velocity and temperature jump conditions encountered in MEMS geometries for the Kn numbers up to 0.1. CFL3D solves the three-dimensional, time-dependent, compressible Navier-Stokes equations subject to various boundary conditions. An implicit approximately factored, finite volume, upwind and multigrid algorithm is used for the solution of the equations. The details of the code CFL3D can be found in the references by Rumsey et al. [7] and Baysal et al. [8].

Moving and deforming mesh simulations require time accurate computations with subiterations. The integral form of time-dependent compressible Navier-Stokes equations on dynamic meshes is presented below

$$\frac{\partial}{\partial t} \int_{\forall} \int \int \mathbf{Q} d\forall + \int \int_{\Omega} \mathbf{F}(\mathbf{Q}) \cdot \hat{n} d\Omega = 0 \quad (1a)$$

$$\mathbf{Q} = \{\rho \quad \rho u \quad \rho v \quad \rho w \quad \rho e_0\}^T \quad (1b)$$

Contributed by the Fluids Engineering Division for publication in the JOURNAL OF FLUIDS ENGINEERING. Manuscript received August 10, 2005; final manuscript received March 8, 2006. Assoc. Editor: Ali Beskok.

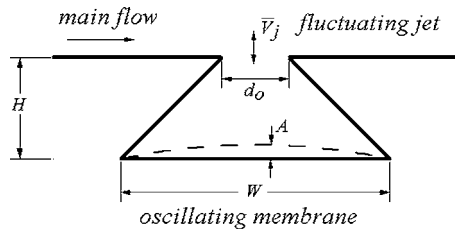


Fig. 1 Schematic of the synthetic jet and its operation

Here, vector  $\mathbf{Q}$  consists of density and the conserved variables of momentum, and total energy per unit volume. The flux vector  $\mathbf{F}$  is given by

$$\mathbf{F}(\mathbf{Q}) \cdot \hat{\eta} = (\mathbf{V} \cdot \hat{\eta}) \begin{Bmatrix} \rho \\ \rho u \\ \rho v \\ \rho w \\ \rho e_0 + p \end{Bmatrix} + p \begin{Bmatrix} 0 \\ \eta_x \\ \eta_y \\ \eta_z \\ a_t \end{Bmatrix} + \begin{Bmatrix} 0 \\ \tau_{kx} \cdot \eta_{,k} \\ \tau_{ky} \cdot \eta_{,k} \\ \tau_{kz} \cdot \eta_{,k} \\ (u_r \tau_{kr} - q_k) \cdot \eta_{,k} \end{Bmatrix}_{\text{sum over } k,r} \quad (1c)$$

where  $p$ ,  $q_k$ , and  $\tau$  are the pressure, heat flux and shear stress terms, respectively. The adjusted velocity is computed relative to the mesh motion as each cell face can move and deform

$$\mathbf{V} = \{(u - x_t), (v - y_t), (w - z_t)\} \quad (1d)$$

with a contravariant face speed computed as

$$a_t = x_t \eta_x + y_t \eta_y + z_t \eta_z \quad (1e)$$

The boundary conditions for the velocity and temperature at a wall are augmented to account for the slip flow and temperature jumps encountered in MEMS devices. The first-order Maxwell-Smoluchowski slip-boundary conditions (Gad-el-Hak [9], Beskok [10], and Agarwal et al. [11]) in Cartesian coordinates are

$$U_s - U_w = \frac{2 - \sigma_v}{\sigma_v} \frac{2}{\rho} \sqrt{\frac{\pi}{8RT_w}} \tau_s + \frac{3 \text{Pr}(\gamma - 1)}{4 \gamma R \rho T_w} (-q_s) \quad (2)$$

$$T_s - T_w = \frac{2 - \sigma_T(\gamma - 1)}{\sigma_T} \frac{4}{\gamma + 1} \frac{1}{\rho R} \sqrt{\frac{\pi}{8RT_w}} (-q_n) \quad (3)$$

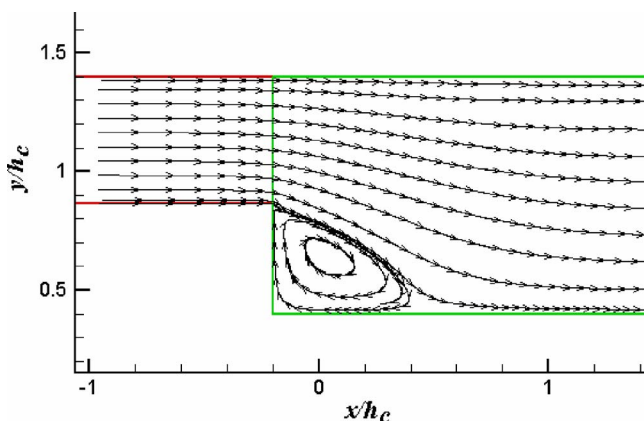


Fig. 2 Separated flow (without control) in a channel with backward-facing step ( $Re=20$ ).  $h_c$ : Outlet channel height.

In these equations, subscript  $s$  denotes the slip flow variables on the solid surface of the body;  $\gamma$  is the ratio of specific heats,  $\rho$  is the density, and  $R$  is the specific gas constant;  $q_n$  and  $q_s$  are the normal and tangential heat-flux components and  $\tau_s$  is the shear stress component pertaining to the skin friction;  $U_w$  and  $T_w$  are the reference wall velocity and temperature, respectively;  $\text{Pr}$  is the Prandtl number.  $\sigma_v$  and  $\sigma_T$  are the tangential momentum and energy “accommodation” coefficients that determine the effectiveness of tangential momentum and energy exchange of the molecules with the walls. The values of the accommodation coefficients are characteristics of the gas/surface pair and may depend on the surface roughness and temperature. In the present study, full diffuse reflection is assumed both for the tangential momentum and energy exchange ( $\sigma_v = \sigma_T = 1$ ). The slip and jump boundary conditions given above are first-order in Knudsen number. The application of boundary condition formulations requires the variation of tangential velocity in the normal direction to the wall. Also coded and used herein is a second-order extension of the Maxwell’s slip velocity boundary condition (Beskok et al. [12])

$$U_s - U_w = \frac{2 - \sigma_v}{\sigma_v} \left[ \frac{\text{Kn}}{1 - b \text{Kn}} \left( \frac{\partial U}{\partial n} \right)_s \right] \quad (4)$$

where  $b$  is the general slip coefficient determined analytically in the slip and early transition flow regimes. For the present examples, the value of  $b=-1$  is employed and the thermal creep term has been omitted.

Since an actuator is being designed herein to control flow separation, a quantitative indicator is needed for its mathematical formulation and the choice of this indicator is not trivial. Several metrics used by the authors in the past included energy loss, reattachment point and area of the separation region. Searching the literature, it was found, for example, that Ravindran [13] and Desai et al. [14] have successfully used enstrophy as an objective function. Enstrophy is the square of vorticity integrated over a region. Selection of enstrophy as the objective function is motivated by the fact that potential flows (zero vorticity) are frictionless and incurs low energy dissipation. Enstrophy constitutes a quantifiable measure of separation that involves recirculation. As such, effectiveness of actuation in reducing separation can be quantified by analytically monitoring the enstrophy of the separated region. Therefore, enstrophy within the separated region is used as the objective function when optimizing the actuator

$$\bar{J}_{\text{ens}} = \frac{1}{2T} \int_0^T \int_{\Omega_s} |\nabla \times \mathbf{U}|^2 d\Omega_s dt \quad (5)$$

where  $T$  is the time period for a one membrane oscillation cycle. The objective function is calculated in  $\Omega_s \subset \Omega$ , where  $\Omega$  is the area of the computational domain and  $\Omega_s$  is the region where the flow is separated, hence, recirculating.  $\Omega_s$  is always computed at a given instant. Then, an indicator of flow separation control effectiveness may be selected as the percent reduction of enstrophy

$$\% \text{ reduction} = \frac{(\bar{J}_{\text{ens}})_{\text{reference}} - (\bar{J}_{\text{ens}})}{(\bar{J}_{\text{ens}})_{\text{reference}}} \times 100 \quad (6)$$

It should be noted that the reference case (Table 4) does not have the actuator, hence, the value of  $(\bar{J}_{\text{ens}})_{\text{reference}}$  or  $\Omega_s$  do not vary in time for the reference case. As for the controlled cases,  $\Omega_s$  values are calculated at four instants during one membrane oscillation cycle after the flowfield reaches a periodic behavior.

### 3 Optimization Methodology

**3.1 Design of Experiments.** The design of experiments method (DOE) is used in many engineering problems in order to understand how the responses are influenced by the design variables. To gain the most information with the least effort is the

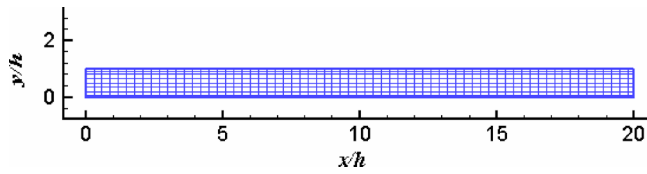


Fig. 3 Computational domain for straight channel: One of every third grid point is shown

main reason for the choice of this approach. A DOE study requires building an empirical model relating the response to the factors. This is called response surface (RS) model and can be approximated by various mathematical approximations. For more information on DOE and RS model, see Ref. [15]. The empirical model for the present study is an approximation to the following relation:  $\bar{J}_{\text{ens}} = \text{function}(W, d_o, A, f)$ , where  $W, d_o, A$ , and  $f$  are the cavity width, orifice width, maximum membrane oscillation amplitude, and membrane oscillation frequency, respectively.

RS model is built with some combinations of design variables and response values. A particular arrangement of these design variables is known as the design of experiments. Considering each combination of the design variables as a point, a proper selection of points could improve the quality of the RS model. A design matrix  $D$  is constructed using the selected points. Design of experiments, which was initially developed for physical experiments, is also essential for the computations to help increase the efficiency. Because the responses obtained from computer experiments are deterministic, there are no random or measurement errors which can be encountered in physical experiments. Thus, the design points should be chosen so as to fill the design space in order to treat all regions of the design space equally. In the current study, Latin hypercube design (LHD), which was first introduced by McKay et al. [16], is used. The Latin hypercube design is formed according to the specified number of points,  $N$ , in the design and it is well suited particularly for the computer experiments. To create a LHD, the range of each variable is divided into  $N$  nonoverlapping intervals on the basis of equal probability. One value from each interval is selected at random with respect to the probability density in the interval.

**3.2 Response Surface Method.** The response surface method (RSM) can be an efficient optimization technique if the cost of analyzing a single design is high. RSM relies on creating an explicit approximation to the objective function and its specified constraints, and then it uses this approximation to perform the optimization. Once the approximation function is constructed, it is used to find the optimum solution instead of carrying out some additional computationally expensive analyses. Another advantage of RSM is its capability of escaping local minima. Although not an issue in a computational simulation, RSM's robustness towards possible noisy behaviors of the responses is another advantage, when data is obtained from experimental study. Since RSM is based on responses only, there is no need to compute the design sensitivities, that are often difficult to derive analytically, or if finite-difference approximations are used, then they require very high computational cost. RSM also allows using the previously analyzed results. One of the most important disadvantages of RSM is that the optimum is identified with less accuracy.

## 4 Results

**4.1 Straight Micro Channel.** To verify the computational model and its boundary conditions flow through a two-dimensional, isothermal, subsonic microchannel with a channel length-to-height ratio of 20 ( $L/h$ ) is considered (Fig. 3). The Kn number at channel outlet is  $Kn_{\text{out}}=0.2$  while at inlet it is  $Kn_{\text{in}}=0.088$ . Inlet-to-outlet pressure ratio is 2.28. The reference Mach ( $M$ ) and Reynolds ( $Re$ ) numbers are 0.0725 and 1.22, respec-

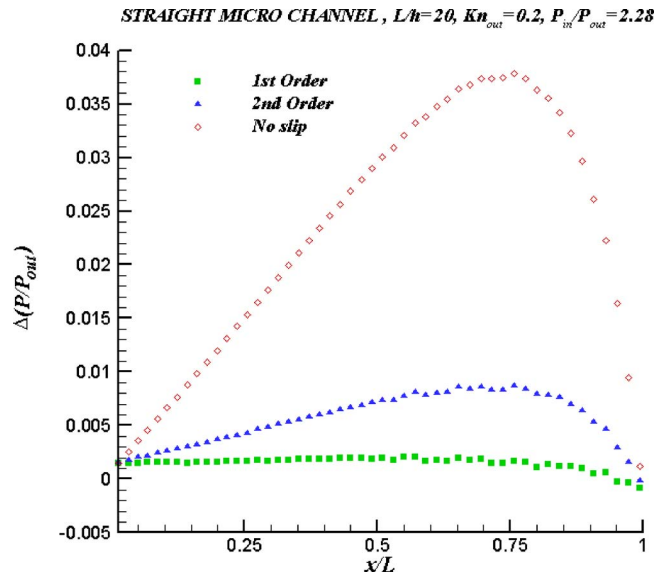


Fig. 4 Deviation of centerline pressure (Eq. (8)) distribution through the micro duct for different computational models,  $Kn_{\text{in}}=0.088$

tively, while 273 K is taken as the reference temperature. This flow is laminar and can be considered to be in the slip flow regime, i.e.,  $Kn \approx 0.1$ . The working fluid is nitrogen. This geometry has also been studied by Beskok [10] using both a DSMC solver and a spectral-element-based continuum CFD solver, and by Agarwal et al. [11] using a higher order fluid dynamics model of the Burnett equations.

In the present computations, both the first order (Eq. (2)) and the second order (Eq. (4)) velocity slip boundary formulations have been employed. Excellent agreement has been obtained with the analytical solutions available for the centerline pressure distribution through the channel (Beskok et al. [12]). The effect of compressibility, even at such low speeds, has also been observed. The pressure distribution is nonlinear and slightly lower in magnitude compared to the no-slip solution. As seen in Fig. 4, the centerline pressure distribution is not deemed sensitive to the order of accuracy of the slip wall formulation and there is at least an order of magnitude difference between the no slip and slip cases. In Fig. 4, the deviation of the computed centerline pressure from the analytically obtained pressure,  $\Delta(p/p_{\text{out}})$ , is plotted

$$\Delta(p/p_{\text{out}}) = (p/p_{\text{out}})_{\text{analytical}} - (p/p_{\text{out}})_{\text{computational model}} \quad (7)$$

where  $p_{\text{out}}$  is the exit channel pressure used to normalize the centerline pressure values.

The computed wall slip velocity distributions, in comparison with the results of Beskok [10] and Agarwal et al. [11] and the analytical solution, are presented in Fig. 5. The results with the first order slip boundary condition match exactly the analytical results, which are based on first order approximations as well. The second order results match the Navier-Stokes and Burnett equation solutions of Agarwal et al. [11] perfectly. The DSMC results of Beskok [10] are slightly different for the first half of the channel but match the other results towards the exit of the duct. The increase in the mass flow due to the wall slip is about 13% as also predicted by Agarwal et al. [11]. In conclusion, the present implementation of both the first and the second order slip boundary condition formulations has been deemed appropriate for microflows.

**4.2 Micro Filter.** Another validation case considered for the present study is a flow through a micro-filter. Analysis of gas flows through micro-filters requires the consideration of three fundamental issues: *Rarefaction, compressibility, and geometric com-*

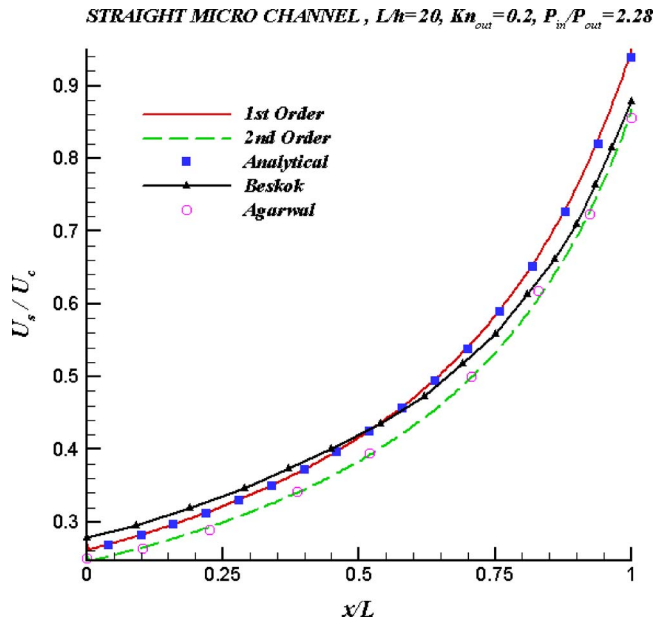


**Fig. 5** Variation of slip velocity along the microduct wall,  $Kn_{in}=0.088$

plexity (Ahmed et al. [17]). The rarefaction is due to the small characteristic length scales of micro-filters ( $L$ ), which are comparable to the local mean free path ( $\lambda$ ). Compressibility effects are important when there are large density variations in the micro fluidic system, particularly, when there are pressure and/or temperature fluctuations. In their simplest form, a micro-filter is a very short channel or sudden constriction. A schematic view and characteristic dimensions of a section of a rectangular micro-filter array are presented in Fig. 6. In Fig. 7, the numerical grid used for the computations is shown.

Experimental and numerical studies have shown that the flow in the micro-filters strongly depends on the opening factor  $\beta$ , the ratio of the hole-height ( $h$ ) to the total filter length ( $L$ ). Considering that the filter holes repeat in a periodic fashion and the symmetry between the two periodic sides, gas flow through only one-half hole is computed by imposing the symmetry boundary conditions in the streamwise direction. In the present study, the ratio of the height to the length at the hole opening is  $h/l=1.5$ , with an opening factor  $\beta=h/L=0.6$ , where  $h=1.2$ ,  $l=0.8$ , and  $L=2$  microns. The gray shaded areas correspond to physical surfaces of the micro-filter, where fully accommodating, diffuse re-

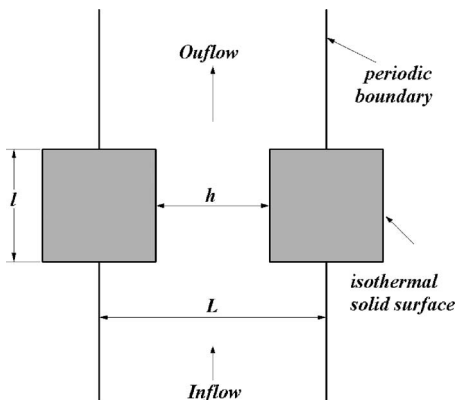


**Fig. 6** Cross-sectional view and the characteristics dimensions of the micro filter

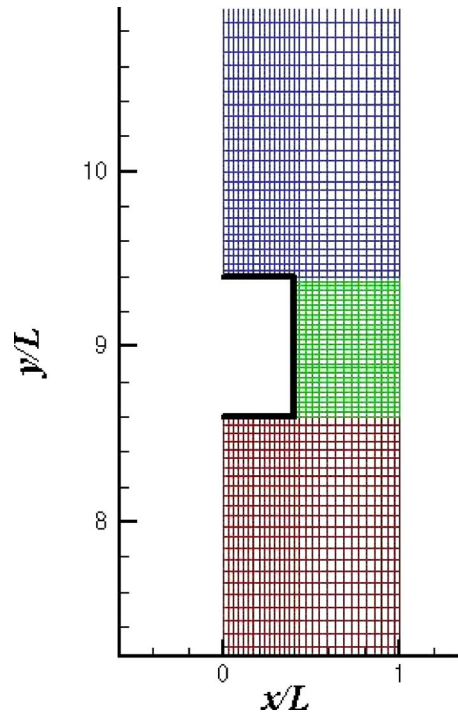


**Fig. 7** Micro filter and its computational domain

flexion boundary conditions are applied. The surface temperature is kept at 300 K. The reference length scale used in the definition of  $Kn$  and  $Re$  is the hole-height  $h$  (Fig. 6).

The predictions from Case I (Table 1) are compared with the computational results of Ahmed et al. [17], where the geometry differs from the present one only with its rounded corners. The streamwise velocity and temperature values, normalized with corresponding inflow values along the centerline of the filter, are in good agreement with those of Ahmed et al. [17] (Fig. 8). The flow which is uniform up to  $y/L=3.3$ , starts to develop before it reaches the filter inlet located  $y/L=4.3$ .

The rarefaction effects are investigated by comparing the results of two different outlet  $Kn$  simulations. Rarefaction is known to cause skin friction reduction. In Fig. 9, the shear stress distribution normalized with inlet dynamic pressure is presented on the filter surface as a function of the surface length for both Cases I and II. In this figure, the nondimensional values of distance at 0, 0.33, 1, and 1.33, correspond to bottom first point, first corner, second corner, and top last point along the filter surface, respectively. The shear stress values are lower for the higher  $Kn$  flow of Case I (top figure). Comparisons of the slip with no-slip cases reveal that shear stresses decrease as a result of the velocity slip on the walls. In Fig. 9, sign reversal in the shear stress indicates local flow separation. The recirculation region is larger in the case of larger  $Re$  flow of Case II (bottom figure).

**4.3 Backward Facing Step.** Flow past a backward facing step is computed to study the effect of slip boundary conditions on a separated flow. The outlet channel height  $h_c$  is  $1.25 \mu\text{m}$  with a ratio of channel length-to-exit height of 5.6. The entry to the channel is also simulated. The channel inlet is located at  $x/h_c=0.86$

**Table 1** Case definitions for the micro filter

Case	$M_{in}$	$M_{out}$	$Re$	$Kn_{in}$	$Kn_{out}$
I	0.17	0.23	7.51	0.054	0.071
II	0.21	0.28	8.82	0.036	0.047

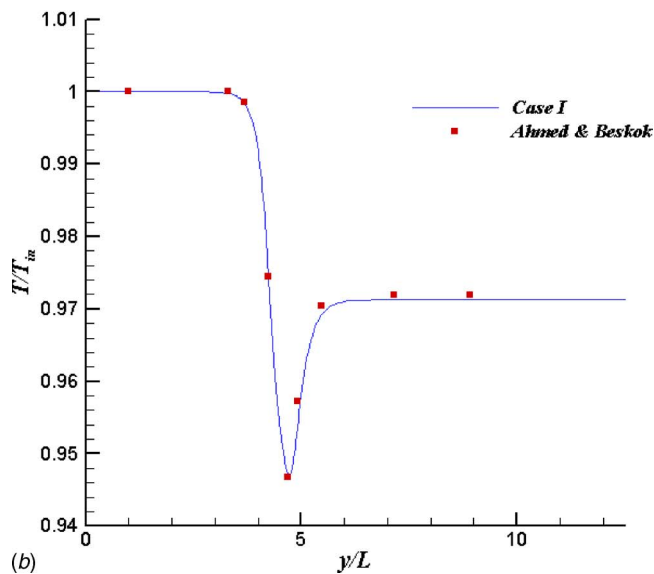
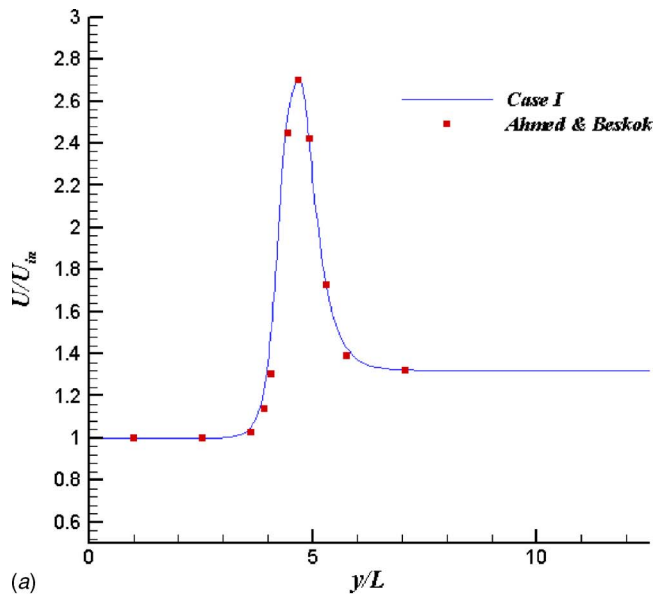


Fig. 8 (a) Normalized streamwise velocity variations along the centerline of micro filter. (b) Normalized streamwise temperature variations along the centerline of micro filter.

and the step height  $s$  is taken as  $s/h_c=0.467$  (Fig. 10). The first and second order slip boundary conditions are employed. Simulation is performed for inlet Mach number  $M=0.47$  and inlet Re number  $Re=80$ . The outlet Kn number is 0.018. Sample results are presented for an inlet-to-outlet pressure ratio of  $P_{in}/P_{out}=2.32$  and inlet temperature is 330 K. The walls are kept at a constant temperature of 300 K. The working fluid is nitrogen.

The computational grid employed consists of two domains. The grid before the step (Sec. 1) is  $49 \times 17$ , and the domain after (Sec. 2) step has a grid of  $161 \times 33$  cells (Fig. 10). To test the grid independency, a finer grid of  $97 \times 33$  cells (Sec. 1) and  $241 \times 65$  cells (Sec. 2) have also been used. Results from both grids were identical up to the fifth digit. The mass flow is monitored for convergence until a constant mass flow is achieved throughout the channel.

For this case, the streamwise pressure variation, normalized with the inlet dynamic head, ( $q_{in}=0.5\rho_{in}U_{in}^2$ ), and the streamwise velocity, normalized with the local speed of sound  $a$ , at about the

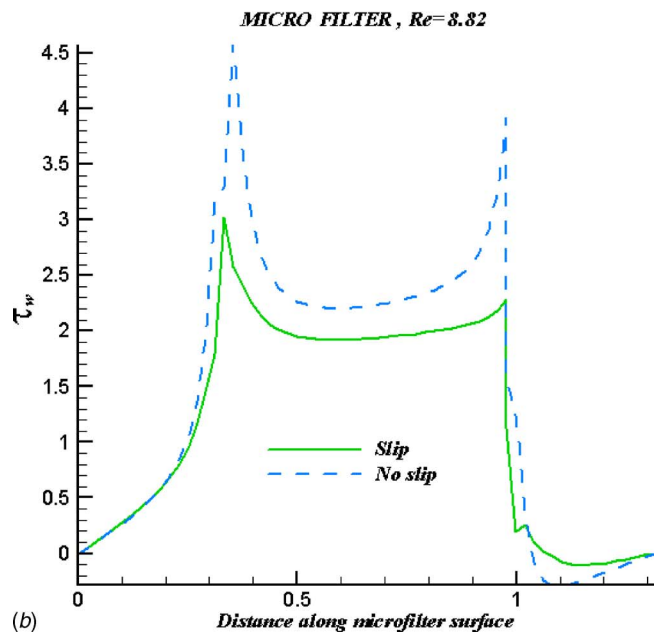
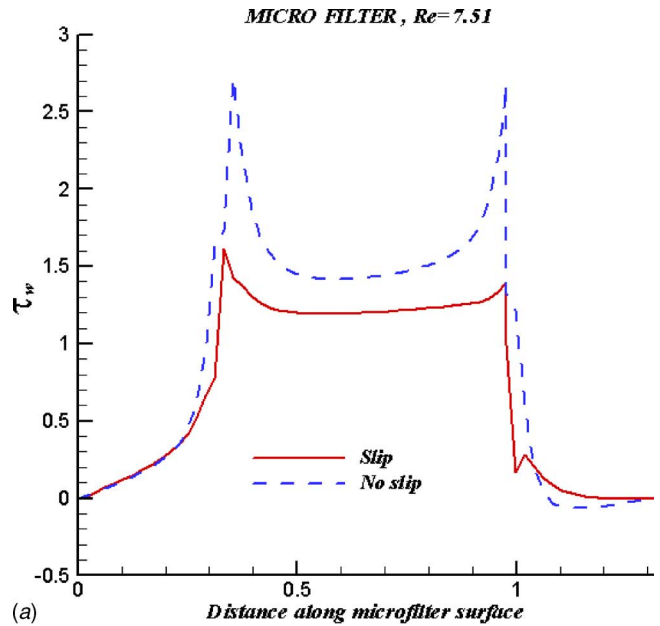


Fig. 9 Variation of shear stress along micro filter wall. Case I (top) and Case II (bottom).

center of entrance  $y/h_c=0.755$  are shown in Figs. 11 and 12, respectively. The results compare well with the DSMC computations of Beskok [10], where the results are for a slightly different flow condition of  $Kn=0.04$ .

**4.4 Synthetic Jet Flow.** In a synthetic jet, the actuating flow is generated at the orifice of a cavity by oscillating a membrane opposite to the orifice. In Fig. 1,  $A$  denotes the maximum membrane oscillation amplitude,  $d_o$  is the orifice width,  $H$  is the cavity height, and  $W$  is the cavity width. Fluctuating jet flow with a jet velocity  $\bar{V}_j$ , produced by the oscillatory motion of the membrane, interacts with the main flow and transfers linear momentum to the main flow. It has previously been shown that the geometric and actuation parameters have profound effects on the mean flow to be controlled (Edis et al. [3]). In order to demonstrate control of flow separation in a micro-fluidic device using a micro synthetic jet,

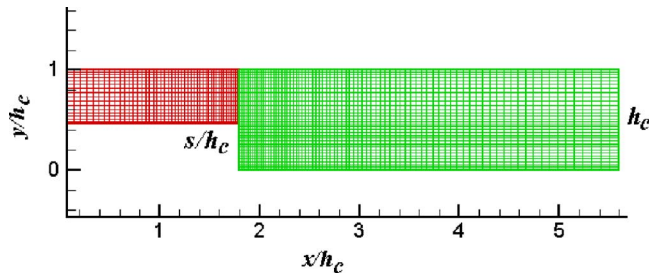


Fig. 10 Micro backward facing step

present authors (Baysal et al. [18]) have originally used a rectangular-cavity synthetic jet actuator placed downstream of the step. This study successfully demonstrated the effect of actuator dimensions as well as membrane motion parameters on altering the separation region, but then suggested that a more thorough optimization study with multiple design parameters was needed.

**4.5 Design Optimization of Synthetic Jet Flow.** For the present design optimization cases, the outlet channel height  $h_c$  is taken to be  $12.5 \mu\text{m}$ . The step height  $s$  is taken as  $s/h_c=0.467$ . The cavity height  $H$  of this actuator is  $0.4h_c$  and it is kept constant during the design process. A representative grid used for the triangular cavity configuration is shown in Fig. 13 (for clarity, only every fourth grid line is shown). In the computational domain, the channel length is considered to be  $5.6h_c$ . The domain consists of three blocks: Cavity (horizontal\*vertical:  $417*81$  cells), upstream of the step ( $129*65$  cells), and downstream of the step regions ( $689*129$  cells). The cavity is placed on the corner downstream of the step for all controlled cases. Results are obtained for an inlet-to-outlet pressure ratio of 2.32. The inlet temperature is 330 K and the walls are assumed to be adiabatic. The inflow velocity is specified for  $M=0.054$  and  $Re=13.3$ . Note that due to the membrane oscillations, the flowfield is unsteady. This requires time-accurate computations of the flowfield governing equations. Running on a single 64-bit AMD-Opteron processor, unit CPU time is 12 microseconds/cell/iteration. When running the code in the time-inaccurate mode, the total CPU time needed to reduce the residual by three orders of magnitude on the same processor is about one hour. When running the code in a time-accurate mode to resolve and track the unsteady flows, a meaningful measure is

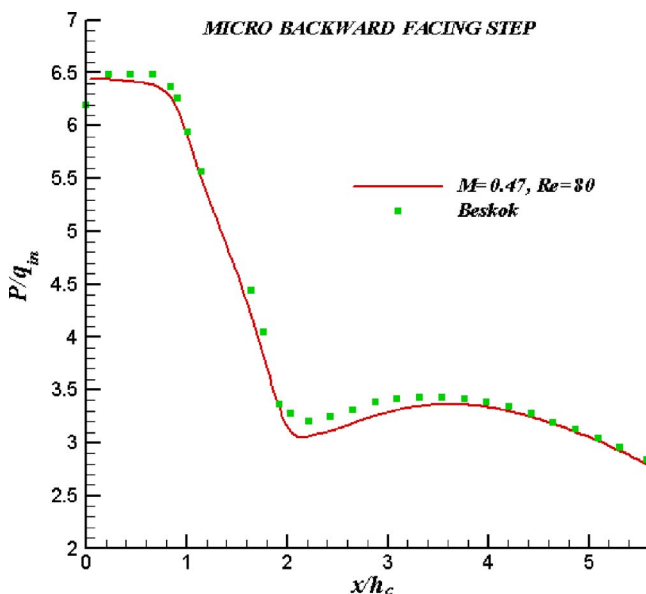


Fig. 11 Streamwise variation of pressure

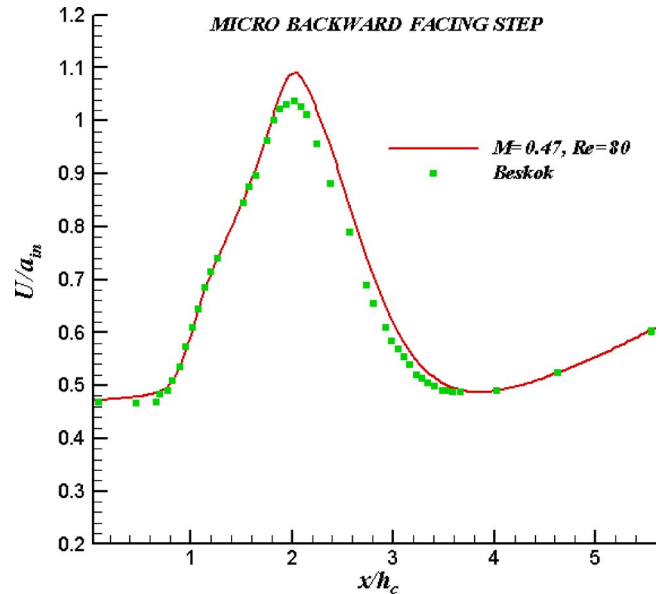


Fig. 12 Variation of normalized streamwise component of velocity

deemed to be the CPU time for one complete membrane oscillation cycle, and it is just under one hour. When the code is run using multiple processors, CPU time scales down almost proportionately to the number of processors.

Initially, a very slow ( $M=0.0001$ ) flow in the channel is considered to ensure that the synthetic jet formation and vortex shedding are both realized. The synthetic jet actuator is placed  $0.4h_c$  from corner of the step and the orifice width is taken as  $1.25 \mu\text{m}$  for this case. Slip boundary conditions are implemented since the jet Knudsen number, based on the jet velocity and the orifice width, is  $Kn_{jet} \approx 0.06$ . Plot of vorticity contours at maximum expulsion stage of the cycle are shown in Fig. 14(a). For the four membrane stages, the velocity profiles at the orifice exit are plotted in Fig. 14(b). The maximum expulsion corresponds to the instant when the membrane is at level position and moving with maximum vertical velocity towards the orifice. The minimum volume corresponds to the instant when the membrane is in its highest position. The maximum ingestion is the level position that occurs following the minimum volume case. The membrane is at its lowest level for the maximum volume stage. Here the velocities are in nondimensional form.

For the optimization study, the cavity width,  $W$ , orifice width,  $d_o$ , membrane oscillation frequency,  $f$ , and membrane oscillation amplitude,  $A$ , are selected as the design variables. Presented in Table 2 are the definitions of the 15 cases that form the design matrix  $D$  constructed for latin hypercube design (LHD) of DOE. Listed in Table 3 are the one-way analysis of variance (ANOVA)

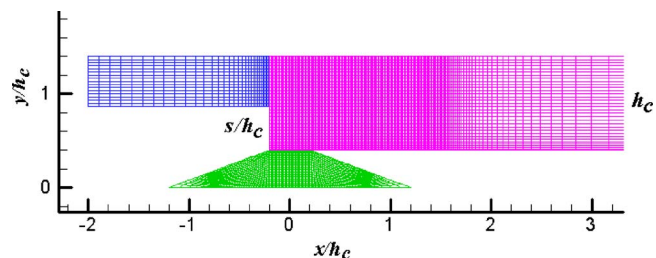
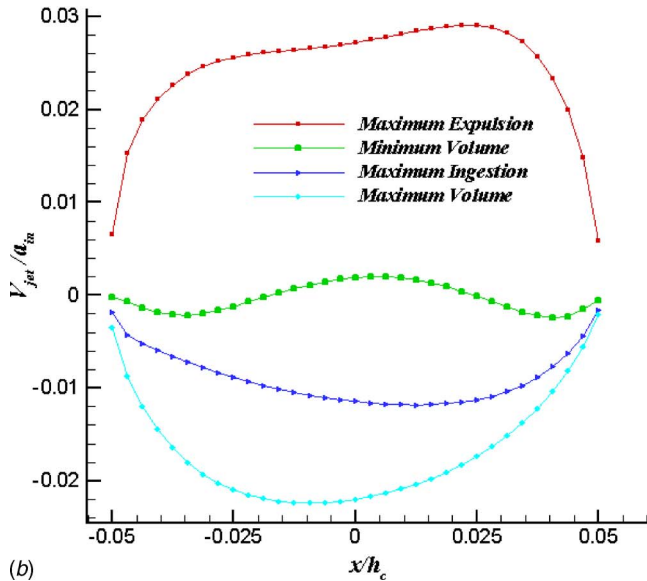
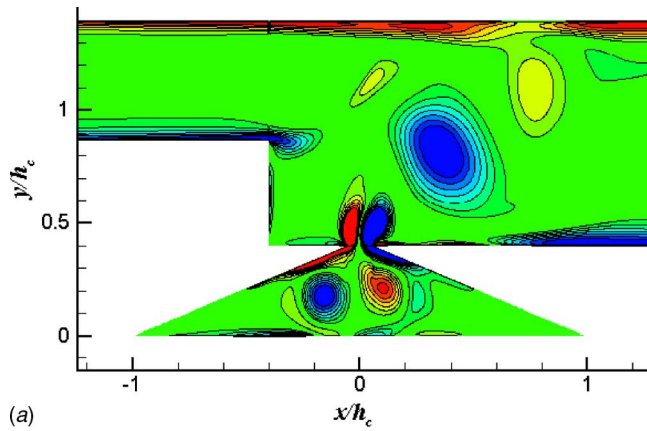


Fig. 13 Geometry of channel with backward facing step and synthetic jet actuator (oscillating membrane, triangular cavity, and orifice). For clarity, only every fourth grid line shown.





**Fig. 14** (a) Plot of vorticity contours at maximum expulsion stage of the synthetic jet cycle.  $h_c$ : Outlet channel height. (b) Velocity profile at the orifice exit for four different stages of the synthetic jet cycle.

results obtained from LHD. At this range of design variables, it is clearly discernible from Table 3 that  $d_o$  has a major effect on the response. Also,  $W$ ,  $A$ , and the interactions between  $A$ - $W$ ,  $A$ - $d_o$ , and  $W$ - $f$ , have a significant effect on the response. On the other hand  $f$  and the interactions of  $f$ - $A$ ,  $f$ - $d_o$ , and  $W$ - $d_o$  have minor effects

**Table 2** Design matrix,  $D$ ,  $Re=13.3$ ,  $h_c=12.5 \mu m$ ;  $H=0.4h_c$

Case no	$f$ (kHz)	$A/h_c$	$W/h_c$	$d_o/h_c$
1	357.1	0.091	1.600	0.174
2	471.4	0.051	1.657	0.046
3	300.0	0.040	1.714	0.149
4	642.9	0.109	1.771	0.136
5	528.6	0.069	1.829	0.033
6	557.1	0.103	1.886	0.200
7	328.6	0.086	1.943	0.020
8	442.9	0.080	2.000	0.187
9	414.3	0.074	2.057	0.084
10	614.3	0.057	2.114	0.110
11	585.7	0.120	2.171	0.059
12	500.0	0.114	2.229	0.123
13	385.7	0.097	2.286	0.097
14	671.4	0.063	2.343	0.161
15	700.0	0.046	2.400	0.071

**Table 3** Analysis of variance obtained by latin hypercube design

Source	Sum of Squares	% Contribution
$f$	16.81	1.06
$A$	143.06	9.02
$d_o$	384.16	24.22
$W$	276.93	17.46
$f$ - $A$	37.03	2.33
$f$ - $d_o$	27.86	1.76
$f$ - $W$	137.24	8.65
$A$ - $d_o$	179.21	11.30
$A$ - $W$	124.43	7.84
$W$ - $d_o$	41.85	2.64
Residual	217.55	13.72

when compared to the other factors and their interactions.

The results for all 15 cases are presented in Table 4. As a reference case, the flow without any actuator control is also computed and its enstrophy calculated in the separation region to be  $\bar{J}_{ens}=33.68$ . This case is used to calculate the percent reduction of enstrophy. For the controlled cases,  $\Omega_s$  is the area of the separation region calculated for the four important instants during one cycle of the membrane oscillation. As observed from Table 4, with synthetic jet control, the separation region and its enstrophy are mostly reduced as compared to the reference case. For some cases, the separation region is totally eliminated during the minimum volume and maximum volume stages (this point will be revisited with Fig. 16). Note that the enstrophy values are calculated to be zero as  $\Omega_s$  vanishes at the corresponding stages. Further, the separation region appears to be more sensitive to the changes in the design variables at minimum volume stage rather than the other stages. During maximum volume stages of Cases 7-9, separation region actually grows. Also, the enstrophy of Case 15 increases (shown as negative percentage in Table 4) despite a reduction in the area of separation.

Next, the design problem is defined for the response surface method (RSM). The results from authors' previous studies (Baysal et al. [18,19]) have been relied upon when selecting the design variables and defining the ranges for these variables. The objective function, enstrophy of the separation region ( $\bar{J}_{ens}$ ) is to be minimized with the design variables within their respective prescribed side constraints:

$$\begin{aligned}
 &\text{Minimize} && \bar{J}_{ens} \text{ in } \Omega_s \\
 &\text{Subject to} && 1.6 \leq W/h_c \leq 2.4 \\
 &&& 0.02 \leq d_o/h_c \leq 0.2 \\
 &&& 0.04 \leq A/h_c \leq 0.12 \\
 &&& 300 \leq f \text{ (kHz)} \leq 700
 \end{aligned}$$

The best control achieved for the flow past the micro backward-facing step is presented in Table 5. Also presented in this table are the comparisons between the RSM-predicted target values for  $\bar{J}_{ens}$  with the target value obtained by the full CFD simulation. This point will be further discussed later. Using this "best-design" synthetic jet, about 83% reduction in the enstrophy of the separation region is obtained.

The response surface for the best values of  $d_o/h_c=0.09$  and  $W=1.76$  is plotted in Fig. 15(a). It is observed that as the membrane amplitude and frequency increase, the response,  $\bar{J}_{ens}$ , tends to decrease. The effect of the amplitude, for the smaller values of frequency, is to decrease the response. However, for the larger values of frequency, increasing amplitude slightly increases the response. On the other hand, for the smaller values of amplitude, the objective function decreases as the frequency increases. Fi-

**Table 4 Results for computational cases of design matrix,  $D, Re=13.3, H=0.4h_c$ .**

Case	$\Omega_s$ min volume	$\Omega_s$ max ingestion	$\Omega_s$ max volume	$\Omega_s$ max expulsion	$\bar{J}_{ens}$	% reduction
reference	0.136	0.136	0.136	0.136	33.684	n/a
1	0.091	0.116	0.092	0.122	24.926	26.0
2	0.052	0.071	0.058	0.097	16.313	51.6
3	0.057	0.084	0.049	0.091	17.540	47.9
4	0.000	0.078	0.003	0.075	14.724	56.3
5	0.066	0.038	0.005	0.028	9.927	70.5
6	0.000	0.055	0.004	0.044	7.384	78.1
7	0.000	0.093	0.188	0.033	15.422	54.2
8	0.000	0.039	0.506	0.045	11.080	67.1
9	0.000	0.023	0.230	0.037	24.601	26.9
10	0.000	0.021	0.000	0.037	23.467	30.3
11	0.000	0.061	0.000	0.062	10.180	69.7
12	0.000	0.012	0.000	0.021	7.764	76.9
13	0.000	0.043	0.000	0.046	18.153	46.1
14	0.000	0.028	0.000	0.042	24.743	26.5
15	0.000	0.059	0.000	0.060	79.009	-134.5

nally, as we approach to the maximum value of the amplitude, the frequency only gradually changes the response. Overall, the results from Fig. 15(a) indicate that the selected ranges of  $A$  and  $f$  provide effective separation control as compared to the no-control case.

The response surface for the best values of  $A/h_c=0.08$  and  $f=550.9$  kHz is plotted in Fig. 15(b). It is shown that increasing the cavity width always has a positive effect on the response. This effect is more apparent for the higher values of the orifice width. The effect of changing the orifice width, however, is mixed and depends on the cavity width value. Although, increasing the orifice width results in a favorable change of the response for higher values of the cavity width, for smaller values of cavity width, increasing the orifice width yields an increase in the response. Moreover, smaller values of cavity width and higher values of orifice width yield worse results than the reference case.

Finally, the flowfield for the “best design” case, predicted by RSM and its design variables as previously given in Table 5, is simulated using full CFD computations (Fig. 16). The best values of the enstrophy obtained from RSM [20] (5.73) and CFD simulation (5.48) differ by only 4.5%. The instantaneous stream traces of this flow at four stages of one membrane-oscillation cycle (Figs. 16(b)–16(e)) are compared to the flow without control (Fig. 16(a)) to observe the differences, particularly, in the separation region. As seen in this figure, the separation region is decreased during maximum expulsion and maximum ingestion stages, and it is totally eliminated during minimum volume and maximum volume stages. This further confirms the results presented in Table 4.

### 5 Concluding Remarks

A computational analysis and design methodology is presented for effective microflow control using synthetic jets. For analysis, a Navier-Stokes flow solver has been modified to account for the slip velocity and temperature jump conditions encountered in MEMS geometries for the Kn number range of 0.001–0.1. For validation purposes, simulations have been successfully performed for a micro channel and a micro filter. The computed

**Table 5 Best values from response surface method [20] and comparison of RSM-predicted target value with simulation code target value at this point.  $h_c=12.5 \mu\text{m}$ .**

	$f^*$ (kHz)	$(A/h_c)^*$	$(W/h_c)^*$	$(d_o/h_c)^*$	$\bar{J}_{ens}^*$	% reduction
RSM	550.9	0.08	1.76	0.09	5.73	82.9
CFD	550.9	0.08	1.76	0.09	5.48	83.7

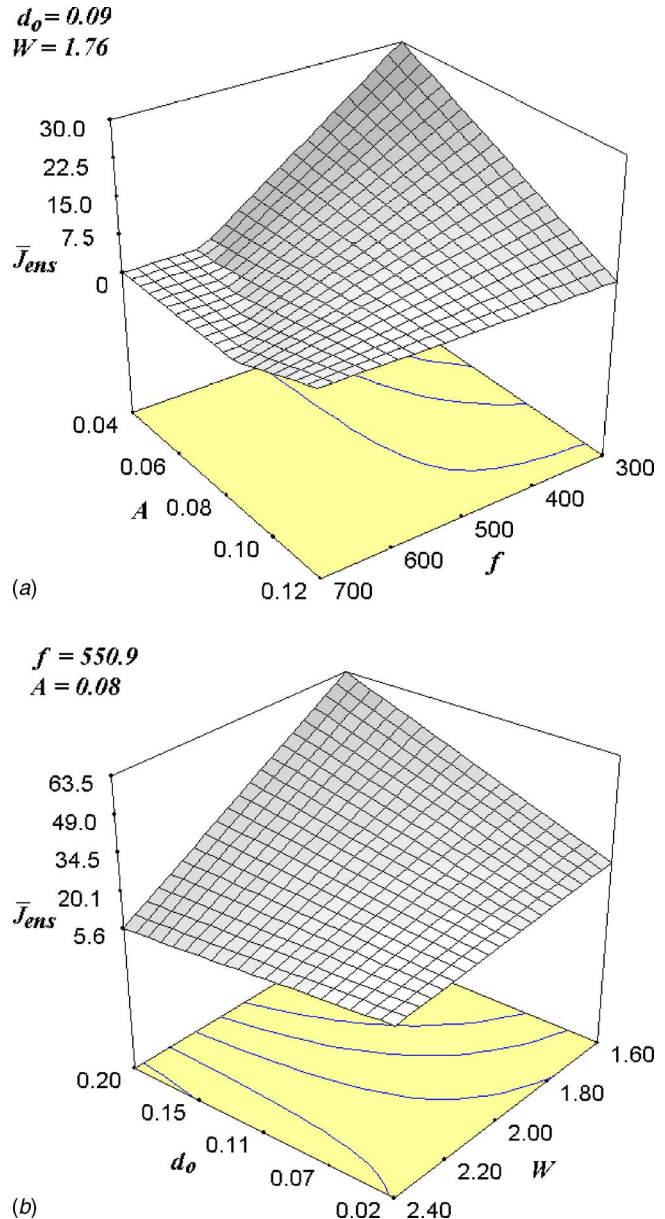


**Fig. 15 (a) Approximate surface enstrophy,  $\bar{J}_{ens}$  = function( $A, f$ );  $d_o$  and  $W$  at their best values. (b) Approximate surface enstrophy,  $\bar{J}_{ens}$  = function( $d_o, W$ );  $A$  and  $f$  at their best values.**

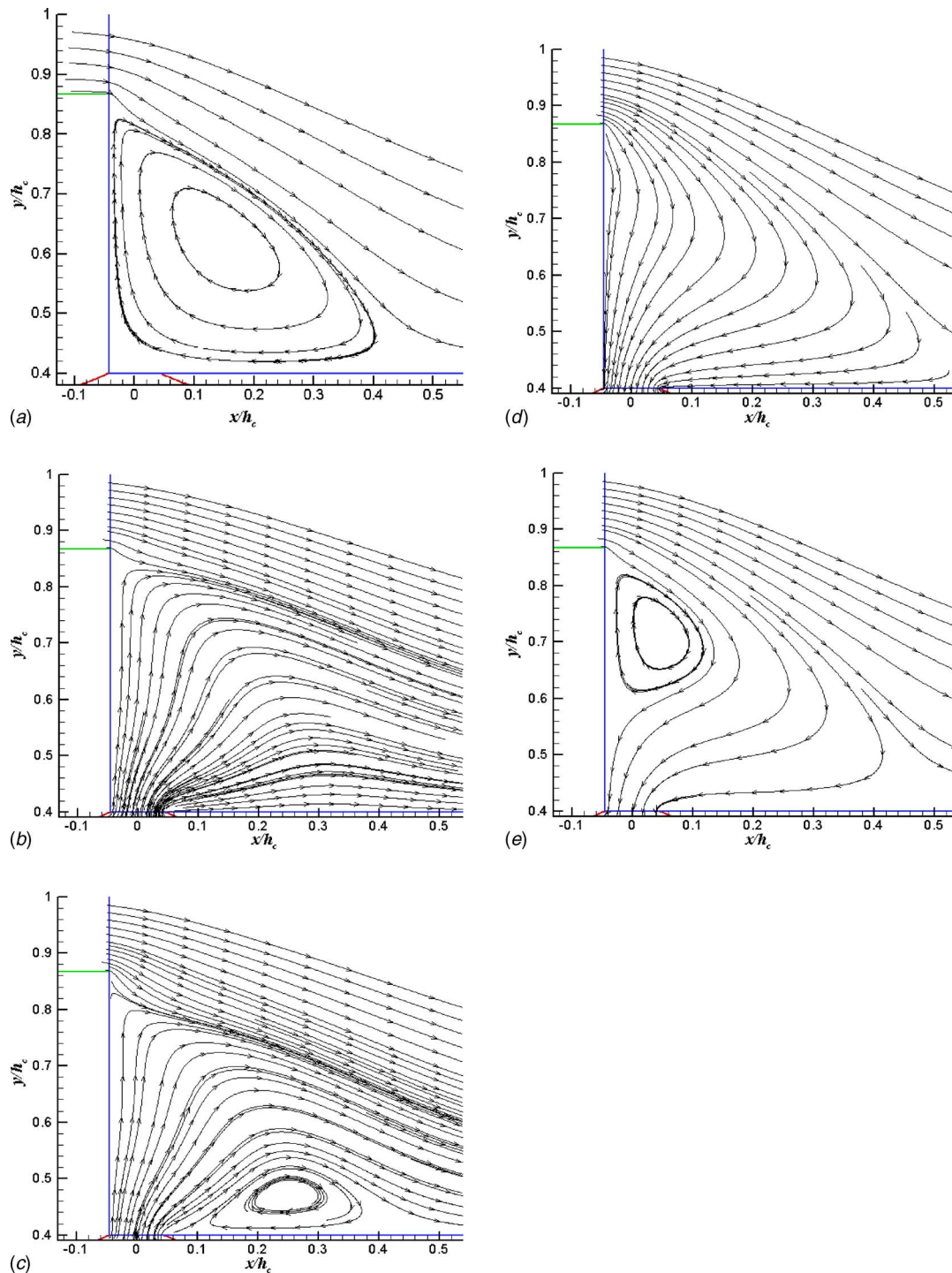


**Fig. 16** Obtained best case: Instantaneous stream traces of separation region, (a) no-control case (b) minimum volume stage, (c) maximum ingestion stage, (d) maximum volume stage, (e) maximum expulsion stage

velocity, temperature, and pressure fields agree very well with the analytical formula and other independent computations available in the literature.

Then, the present computational flow analysis has been coupled with a design methodology to improve the effectiveness of a proposed synthetic jet actuator. For demonstration, a flow past a micro backward-facing step has been considered. Four parameters of the synthetic jet actuator have been selected as the design variables. The objective function to be minimized is selected to be the

entropy of the flow separation region. First, a design of experiments study has been conducted, which identified the orifice width and the cavity width as the most effective design variables. Then, a response surface method has been constructed to optimize and find the improved control of the flow. For the problem defined herein, this optimization has resulted in over 83% reduction of the entropy. The present study is a demonstration of a design methodology using high-fidelity flow simulation that is beyond the current common practices, such as, a cut-and-try approach.

## References

- [1] Baysal, O., and Aslan, R. A., 2002, "Computing Effect of Flow Separation in MEMS Applications," Paper FEDSM2002-31157, *Proceedings of ASME FEDSM'02*, ASME Fluids Engineering Division Summer Meeting, Montreal, Quebec, Canada.
- [2] Aslan, R. A., Baysal, O., and Edis, F. O., 2002, "Computing Micro Synthetic Jet in Slip Regime With Moving Membrane," Paper IMECE2002-33770, *Proceedings of 2002 ASME International Mechanical Engineering Congress and Exposition*, New Orleans, LA.
- [3] Edis, F. O., Erbas, N., Baysal, O., and Aslan, R. A., 2003, "Micro Synthetic Jets and Their Interaction With a Cross Flow in Slip Regime," *Proceedings of International Conference on Recent Advances in Space Technologies - RAST 2003*, Istanbul, Turkey.
- [4] Jain, H., Agarwal, R. K., and Cary, A. W., 2003, "Numerical Simulation of the Influence of a Synthetic Jet on Recirculating Flow Over a Backward Facing Step," AIAA Paper 2003-1125, 41st Aerospace Sciences Meeting, Reno, NV.
- [5] Rediniotis, O. K., Ko, J., Yue, X., and Kurdilla, A. J., 1999, "Synthetic Jets, Their Reduced Order Modelling and Applications to Flow Control," AIAA Paper 99-1000, 37th Aerospace Sciences Meeting, Reno, NV.
- [6] Baysal, O., 1999, "Aerodynamic Shape Optimization: Methods and Applications," *SAE Trans.*, **108**, pp. 794–802.
- [7] Rumsey, C., Biedron, R., and Thomas, J., 1997, *CFL3D: Its History and Some Recent Applications*, NASA TM-112861.
- [8] Baysal, O., Fouladi, K., and Lessard, V. R., 1990, "A Multigrid and Upwind Viscous Flow Solver on Three-Dimensional Overlapped and Embedded Grids," *AIAA J.*, **29**, pp. 903–910.
- [9] Gad-el-Hak, M., 2002, "Flow Physics," *MEMS Handbook*, M. Gad-el-Hak, ed., CRC Press, New York, Chap. 4.
- [10] Beskok, A., 2001, "Validation of a New Slip Model for Separated Gas Micro-Flows," *Numer. Heat Transfer, Part B*, **40**(6), pp. 451–471.
- [11] Agarwal, R., and Yun, K., 2002, "Burnett Simulations of Flows in Micro-devices," *MEMS Handbook*, M. Gad-el-Hak, ed., CRC Press, New York, pp. 7.1–7.36.
- [12] Beskok, A., Karniadakis, G. E., and Trimmer, W., 1996, "Rarefaction and Compressibility Effects in Gas Microflows," *J. Fluids Eng.*, **118**, pp. 448–456.
- [13] Ravindran, S. S., 2004, "Numerical Approximation of Optimal Control of Unsteady Flows Using SQP and Time Decomposition," *Int. J. Numer. Methods Fluids*, **45**, pp. 21–42.
- [14] Desai, M., and Ito, K., 1994, "Optimal Controls of Navier-Stokes Equations," *SIAM J. Control Optim.*, **32**(5), pp. 1428–1446.
- [15] Montgomery, D. C., 2001, *Design and Analysis of Experiments*, 5th ed., Wiley, New York.
- [16] McKay, M. D., Conover, W. J., and Beckman, R. J., 1979, "A Comparison of Three Methods for Selecting Values of Input Variables in the Analysis of Output from a Computer Code," *Technometrics*, **21**(2), pp. 239–245.
- [17] Ahmed, I., and Beskok, A., 2002, "Rarefaction Compressibility and Viscous Heating in Gas Micro Filters," *J. Thermophys. Heat Transfer*, **16**, pp. 161–170.
- [18] Baysal, O., Erbas, N., and Koklu, M., 2004, "Control of Separated Flow Past Backward-Facing Step in Microchannel," Paper ICMM2004-2351, *Proceedings of 2004 ASME Microchannels and Minichannels*, Rochester, NY; Also in *Microfluidics and Nanofluidics*, 1(1), pp. 86–92.
- [19] Baysal, O., Koklu, M., and Erbas, N., 2004, "Design of Micro Synthetic Jet Actuator for Flow Control," *Transport Phenomena of Micro and Nano Devices*, October 17–21, Kona, HI.
- [20] DESIGN-EXPERT, Version 6: [www.statease.com/soft\\_abs.html](http://www.statease.com/soft_abs.html)

## Tadashi Shiraishi

e-mail: tadashi\_shiraishi@mhi.co.jp

## Hisato Watakabe

Senior Research Engineer

Thermal System Laboratory,  
Takasago R&D Center,  
Mitsubishi Heavy Industries Ltd.,  
2-1-1 Shinhama, Arai-cho,  
Takasago-shi, Hyogo, 676-8686, Japan

## Hiromi Sago

Engineering Manager

Advanced Nuclear Plant Designing Section,  
Nuclear Plant Designing Department,  
Kobe Shipyard & Machinery Works,  
Mitsubishi Heavy Industries Ltd.,  
1-1, Wadasaki-cho 1-chome,  
Hyogo-ku, Kobe-shi, Hyogo, 652-8585, Japan  
e-mail: hiromi\_sago@mhi.co.jp

## Mamoru Konomura

Prime Scientist

Advanced Nuclear System Research and  
Development Directorate,  
Japan Atomic Energy Agency,  
4002 Narita-cho,  
Oarai, Ibaraki, 311-1393, Japan  
e-mail: konomura.mamoru@jaea.go.jp

## Akira Yamaguchi

Professor

Quantum and Energy Engineering,  
Division of Sustainable Energy and Environment  
Engineering,  
Graduate School of Engineering,  
Osaka University,  
2-1 Yamadaoka, Suita, Osaka, 565-0871, Japan  
e-mail: yamaguchi@nucl.eng.osaka-u.ac.jp

## Tadashi Fujii

FBR System Design Group,

FBR System Engineering Unit,

Advanced Nuclear System Research and

Development Directorate,

Japan Atomic Energy Agency,

4002 Narita-cho, Oarai, Ibaraki, 311-1393, Japan

e-mail: fujii.tadashi@jaea.go.jp

# Resistance and Fluctuating Pressures of a Large Elbow in High Reynolds Numbers

*For the Japan Atomic Energy Agency sodium-cooled fast reactor, an experimental study on the fluctuating pressure of the hot legs was carried out with tests in a 1/3-scale model. The total resistance coefficient is consistent with published data, and, additionally, our research has given data up to the Reynolds number of  $8.0 \times 10^6$ . The flow visualization and velocity measurement confirmed the independence of the flow on the Reynolds number. Pressures on the pipe wall were statistically examined to predict the characteristics of fluctuating pressures of the hot legs. It reveals that generation of fluctuating pressure is dominant on the boundary of flow separation and reattachment.*

[DOI: 10.1115/1.2236126]

*Keywords:* fast reactor, sodium-cooled, cooling system, elbow, flow separation, resistance coefficient, fluctuating pressure, variance, skewness, kurtosis

## Introduction

A conceptual design study of the JAEA (Japan Atomic Energy Agency) sodium-cooled fast reactor (JSFR) is in progress in "Feasibility Study on Commercialized Fast Reactor Cycle Systems" [1]. The cooling system of the reactor is composed of two loops in order to economize the plant construction cost. Due to the small

loop number, large-diameter piping is adopted in the primary cooling system, and mean sodium velocity in the pipes increases to over 9 m/s. Figure 1 shows the configuration of the primary cooling system of the JSFR. One of the issues for the piping design is to understand the behavior of flow-induced vibration that is caused by the hydraulic characteristics at high Reynolds number ( $10^7$  order level) conditions. Figure 2 shows a flow-induced vibration test facility that simulates the hot leg piping with a 1/3-scale model so that we can investigate flow patterns in it and fluctuating pressures on the pipe wall. The storage pool contains 1000 metric tons of water. The total maximum flow rate of the two

Contributed by the Fluids Engineering Division of ASME for publication in the JOURNAL OF FLUIDS ENGINEERING. Manuscript received March 8, 2005; final manuscript received February 15, 2006. Assoc. Editor: James A. Liburdy.

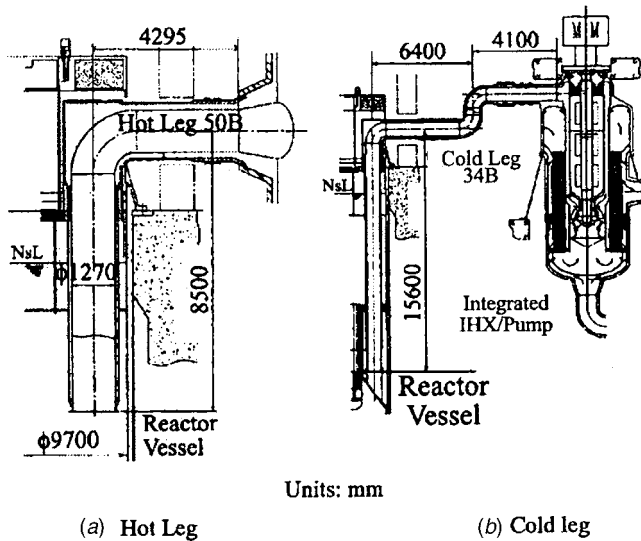


Fig. 1 The configuration of the primary cooling system of the JSFR. NsL is the nominal sodium level in the reactor vessel.

pumps is  $2 \text{ m}^3/\text{s}$  ( $1 \text{ m}^3/\text{s}$  per pump). Water is pumped up through the ultrasonic flow meters to the 7 m high intermediate tank which has a diameter of 2 m. The flow meters are set in the straight pipes (pipe inner diameter=492.2 mm each) with a length of more than 30 times the diameter to secure the accuracy of flow rate. The intermediate tank has an air chamber at its top to suppress fluctuating pressures produced by the pumps. Water is supplied from the intermediate tank to the 6 m high rectifying tank which has a diameter of 3.43 m. The high rectifying tank has a rectifier consisting of grids and pipes built-in so that a uniform velocity distribution can be obtained at the inlet of the model pipe. Figure 3 shows the picture of the model pipe. The pressure in the test loop can be controlled from atmospheric pressure to 0.3 MPa in order to prevent cavitation. Flexible pipes are installed in the auxiliary pipelines to isolate the model pipe from mechanical vibrations. The support of the model pipe has no natural frequency under 30 Hz to ensure the reliability of measured fluctuating pressures. The working fluid is water both at room temperature (285 to 288 K) and at 333 K. The maximum mean velocity in the pipe is 9.2 m/s, the same velocity as the nominal operating velocity of the hot legs of the JSFR. The maximum Reynolds number is  $3.7 \times 10^6$  for water at room temperature and  $8.0 \times 10^6$  at 333 K. In order to extrapolate the flow patterns and fluctuating pressures at

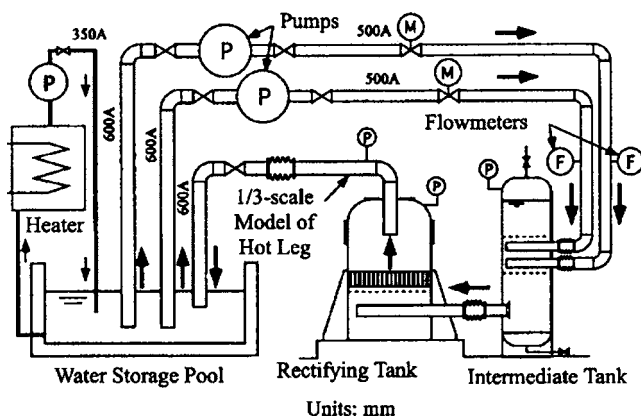


Fig. 2 Schematic of the test facility. 350A, 500A, and 600A are 14B, 20B, and 24B of pipes, respectively.



Fig. 3 1/3-scale model pipe installed on the top of the rectifying tank (inner diameter=412.7 mm)

the high Reynolds number of  $4.2 \times 10^7$  from the experimental data, we investigated their dependence on Reynolds number.

### Total Resistance Coefficient

Figure 4 shows the model of the hot leg pipe with inner diameter of  $D=412.7 \text{ mm}$ . There is a  $5.60D$  long (2309 mm) straight tube between the bellmouth at the inlet and the elbow. There is another  $8.77D$  long (3621 mm) straight tube downstream of the elbow partly shown in Fig. 4. The bending radius of the elbow is  $1.026D$  (423.3 mm). Totally 124 pressure transducers (12 at each section, except 6 at A, 11 at B' and C', 2 at G, I, J and L, and 1 at A', A'', K' and K'') are flush-mounted on the inner wall of the

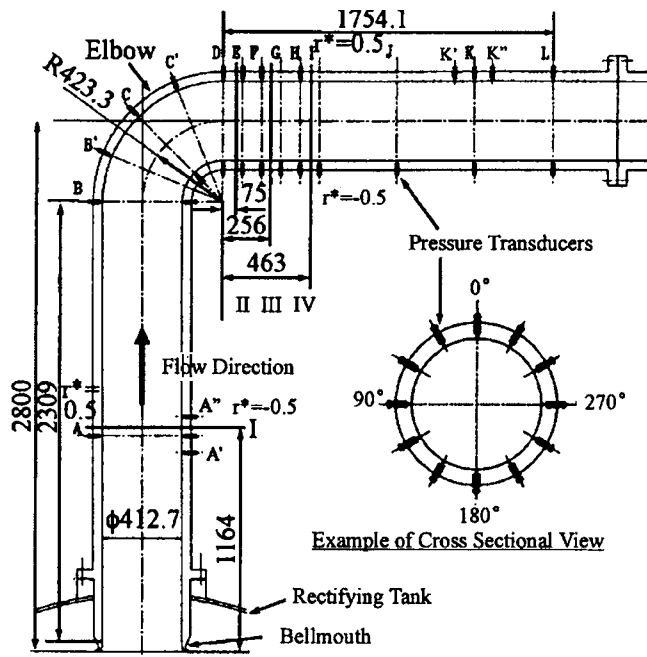
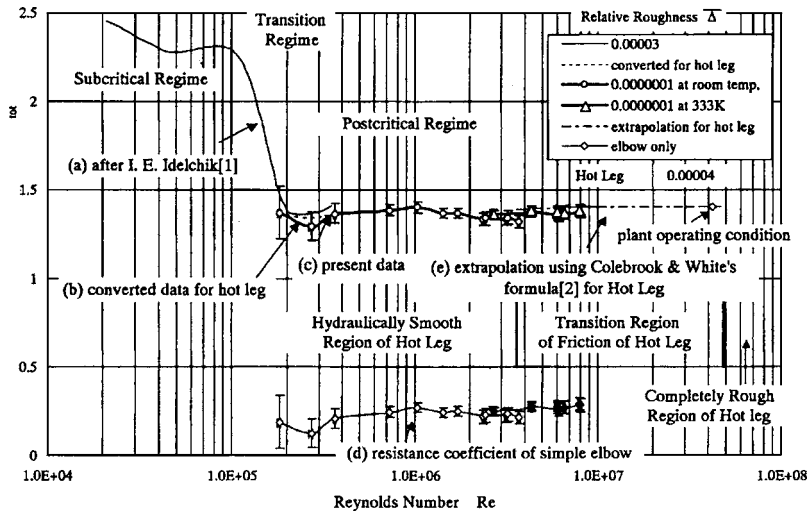


Fig. 4 1/3-scale model of the hot leg with pressure transducers. Velocity distributions were measured in Sections I-IV by laser Doppler velocimeter. Dimensionless radius is  $r^*=r/D$ , where  $r$  is a radius and  $D$  the diameter of the pipe. Totally 124 pressure transducers are flush-mounted on the inner wall of the pipe; 12 at locations B, C, D, E, F, H, and K, 6 at A, 11 at B' and C', 2 at G, I, J, and L, and 1 at A', A'', K', and K''.



**Fig. 5 Total resistance coefficient: (a) published data of a bend after Idelchik [2], (b) converted data from (a) for the hot-leg dimension, (c) present data of 1/3-scale hot leg model, (d) resistance coefficient of elbow only from (c), and (e) extrapolation using Colebrook and White's formula [3]**

pipe in all sections from A to L. We indicate every measuring point with an index such as A 180 deg for the measuring point at the circumferential angle of 180 deg in Section A. The pressure drop of the hot leg pipe from the rectifying tank to Section L was measured and compensated for the sensor-elevation differences. Section L is  $4.25D$  (1754.1 mm) away from the exit of the elbow.

Since energy of turbulence is supplied from main flow, energy flux to turbulence can be evaluated with pressure resistance coefficient,  $\zeta$ . Selected data of resistance coefficients of elbows with short pipes are published for Reynolds numbers up to  $3.6 \times 10^5$  [2]. Resistance coefficients of an elbow are comparable to those of a bend. Idelchik measured the resistance coefficient,  $\zeta$ , of a bend with width of  $b_0$  and bending radius of  $0.8b_0$ . There was a  $1.45b_0$  long straight tube between the bellmouth and the bend, and another  $0.78b_0$  long straight tube downstream of the bend. He defined the pressure resistance coefficient,  $\zeta_{tot}$ , as the total pressure drop including the velocity pressure losses at the exit from the bend into the atmosphere divided by the kinetic pressure. In our case, the total pressure drop is  $P_{in} - P_{out}$ , where  $P_{in}$  is the total pressure in the rectifying tank in which the kinetic pressure is negligible, and  $P_{out}$  is the mean static pressure in Section L. The kinetic pressure is  $\rho U^2/2$ , where  $\rho$  is the density of fluid and  $U$  is the mean velocity in the pipe. We, hence, follow his definition in this paper as:

$$\zeta_{tot} = \frac{P_{in} - P_{out}}{\rho U^2/2} \quad (1)$$

The surface roughness of the hot leg,  $\Delta$ , is estimated to be about  $50 \mu\text{m}$  for commercial pipes, so the relative roughness of the hot leg is  $\bar{\Delta} = \Delta/D = 4 \times 10^{-5}$ . The measured mean surface roughness of the acrylic-resin pipe was  $0.05 \mu\text{m}$ , so the relative roughness of the model elbow was  $\bar{\Delta} = 1.2 \times 10^{-7}$ . Figure 5 shows (a) previously published data of a bend for  $\bar{\Delta} = 3 \times 10^{-5}$  after Idelchik [2], (b) the converted data of the data (a) for the hot leg configuration using the method mentioned in the following paragraph, and (c) the present data of the model elbow at room temperature ( $\circ$ : circle) and at 333 K ( $\Delta$ : triangle). Idelchik explained that the phenomenon in a bend installed close to a smooth entrance is similar to that observed for a flow around a cylinder or a sphere, and the boundary layer is laminar at relatively small Reynolds numbers. The critical Reynolds number is characterized by transition from laminar to turbulent flow. As a result, the pressure resistance co-

efficient is divided into three regimes: the subcritical regime, the transition regime, and the postcritical regime. Almost all the present data (c) are in the postcritical regime. The vertical and horizontal bars of the present data show the ranges of instrumental errors, which came from the ultrasonic flow meters and the pressure transducers.

We converted the previously published data into the hot leg configurations to evaluate the consistency of the present data with them. The resistance coefficient of the elbow's bellmouth was about 0.02, and that of the bend also seemed to be 0.02, judging by the configuration in Ref. [2]. A pipe with relative roughness of  $\bar{\Delta} = 3 \times 10^{-5}$  is hydraulically smooth for Reynolds numbers less than  $5.0 \times 10^6$ . Therefore, we used the Prandtl's universal law of friction for smooth pipes [3] to evaluate the friction effect. The ratio of the curvature effect of the bend to that of the elbow was evaluated for  $Re \geq 2 \times 10^5$  by the formula suggested by Abramovich cited in Idelchik [2]. As a result, the converted data (b) was given for the hot leg. Comparison of the present data (c) with the converted data (b) shows that they agree well with each other. Although there is a slight difference at  $Re = 2.7 \times 10^5$ , the converted data (b) is within the error bar of the present data (c). Consequently, the consistency of the present data with the previously published data is excellent and satisfactory.

The present data give the resistance coefficient of the acrylic-resin elbow for Reynolds numbers up to  $3.7 \times 10^6$  at room temperature ( $\circ$ ) and  $8.0 \times 10^6$  at 333 K ( $\Delta$ ). The acrylic-resin pipe with  $\bar{\Delta} = 1.21 \times 10^{-7}$  is hydraulically smooth for a Reynolds number less than  $1.8 \times 10^9$  that covers all the present data. The values of the data at 333 K ( $\Delta$ ) are slightly higher than those at room temperature ( $\circ$ ), but the difference is demonstrated in the error bars. Since the present data are in the hydraulically smooth region of a pipe, it is reasonable that the friction affects the resistance coefficient by gradually decreasing as the Reynolds number increases in the postcritical regime. However, the resistance coefficient has a tendency to decrease to a constant value of about  $\zeta_{tot} = 1.38$ , according to the higher Reynolds data ( $\Delta$ ). It means the friction is not dominant for the higher Reynolds numbers but the local resistance of a bend is. The slight increase of the resistance coefficient for the Reynolds numbers from  $4 \times 10^5$  to  $10^6$  comes from the effect of separation in the elbow. The resistance coefficient of the simple elbow is the curve (d) calculated from the

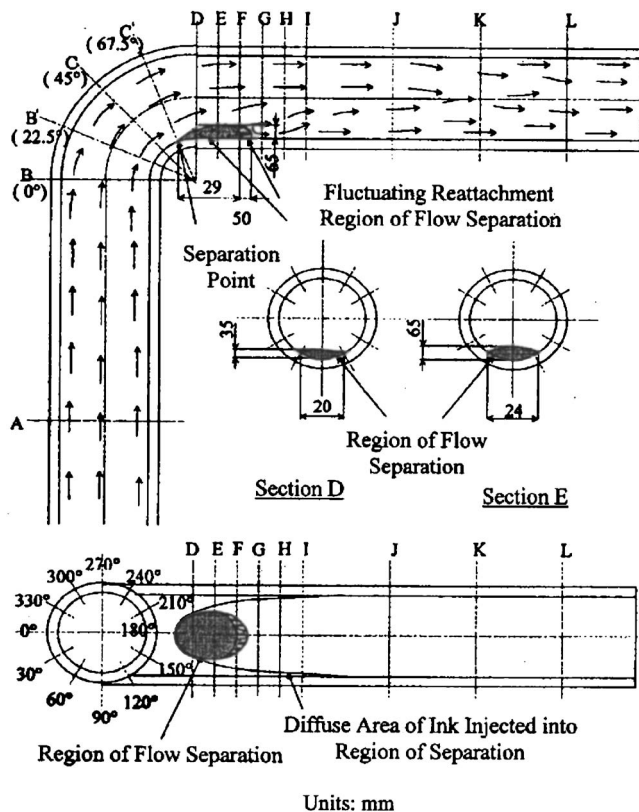


Fig. 6 Flow pattern in the model pipe for mean velocity of 9.2 m/s at room temperature

present data using Prandtl's universal law of friction for smooth pipes and becomes almost constant for a Reynolds number larger than  $10^6$ . Therefore, the decrease of the resistance coefficient for a Reynolds number larger than  $10^6$  comes only from the friction in the smooth pipe. The hot leg with  $\bar{\Delta}=4 \times 10^{-5}$  is hydraulically smooth for a Reynolds number less than  $3.6 \times 10^6$  and in the transition region of friction for a Reynolds number from  $3.6 \times 10^6$  to  $4.9 \times 10^7$ . The plant operating condition of the JSFR,  $Re=4.2 \times 10^7$ , is in the latter region. Using Colebrook and White's formula [3] to evaluate the friction in the transition region, the plant operating condition was extrapolated from present data as the curve (e). Consequently, the extrapolated value of the total resistance coefficient is  $\zeta_{tot}=1.40$  for the plant operating condition.

## Flow Pattern and Velocity Distributions

We observed the flow patterns in the model pipe by the ink-injection method for mean velocities of 0.8, 3.0, 7.0, and 9.2 m/s. Figure 6 schematically shows local flow directions by arrows and the size and the location of flow separation for a mean velocity of 9.2 m/s at room temperature. Flow separation occurred at the point on the internal wall of the elbow near Section C' (or 67.5 deg from the inlet of the elbow), and the separation region spreads from 290 to 340 mm downstream and 65 mm in height. The reattachment point of the flow fluctuated about 50 mm in flow direction on the pipe wall, being synchronized with vortex shedding from the separation bubble. The flow was fairly uniform from the bellmouth to the elbow in the vertical pipe. The flow patterns for the mean velocity from 0.8 to 7.0 m/s were very similar to that for 9.2 m/s. The sizes and the locations of the regions of flow separation were identical to those for 9.2 m/s. Therefore, we can conclude the flow pattern in the hot leg is independent of the Reynolds number in the postcritical regime. These results of the observation were quantitatively confirmed by velocity distributions along the horizontal centerline in Section I and the vertical centerlines in Sections II-IV indicated in Fig. 4.

Figure 7 shows the dimensionless velocity distributions along these centerlines with respect to the dimensionless radius at room temperature. The open symbols indicate axial velocity components, and the solid symbols circumferential ones. The dimensionless velocity,  $u^*$ , is local velocity normalized by the mean velocity in the pipe, and the dimensionless radius,  $r^*$ , is the radius normalized by the pipe diameter,  $D=412.7$  mm. The dimensionless velocity distributions at different mean velocities aligned with each other and the data were confirmed to be reproducible. Figure 7(a) shows a very flat velocity distribution except near the wall in Section I that quantitatively verifies the fairly uniform condition at the inlet of the pipe. Figure 7(b) shows the velocity distributions in Section II at 75 mm downstream of the exit of the elbow that agreed with each other for mean velocities of 0.8, 3.0, 7.0, and 9.2 m/s. There was reverse flow indicating the height of the separation to be  $0.13D$  or 54 mm. The slight difference between the measured height and the observed height, 65 mm, may come from the diffusion of ink in the shear layer next to the separation bubble. The maximum velocity appeared at the top of the shear layer, or  $r^*=-0.2$ , the flow of which came from the location of the maximum velocity in the inner region of the elbow shown in Fig. 8. The axial velocity component is nearly flat in the upper half of Section II, the flow of which comes from the outer region of the elbow. Figure 7(c) shows the velocity distributions in Section III at 256 mm downstream of the elbow's exit and in the reattachment region of flow. There is a jet on the lower wall of the pipe. We first suspected instrumental error for the jet. But the reproducibility of data was good, and the dimensionless velocity distribu-

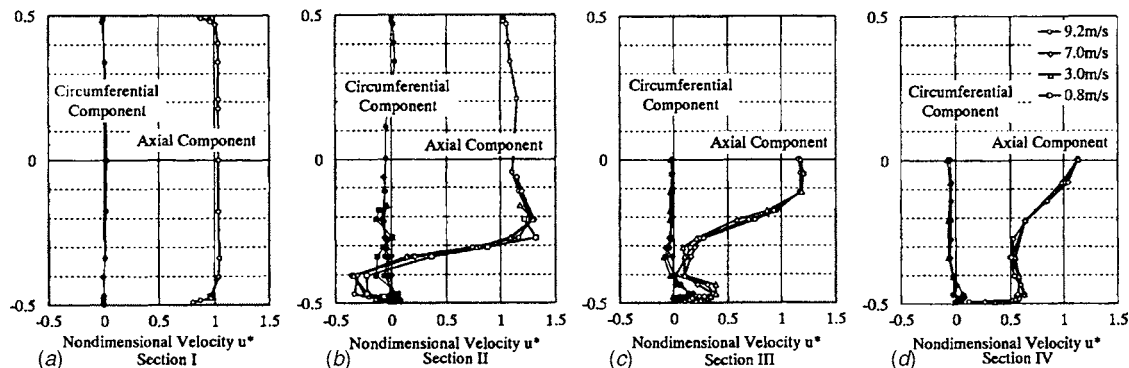


Fig. 7 Dimensionless velocity distributions in Sections I-IV at room temperature. The open symbols indicate axial velocity components, and the solid symbols circumferential ones.



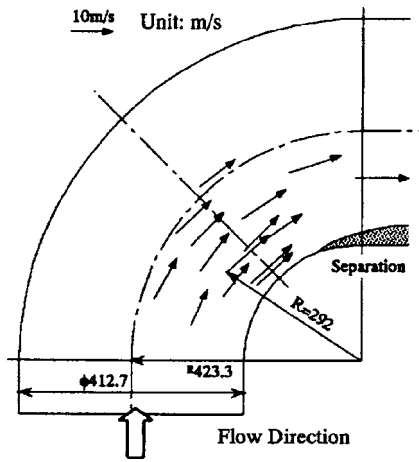


Fig. 8 Local velocities in the elbow for mean velocity of 9.18 m/s at room temperature, which is slightly slower than 9.28 m/s for quantitative measurement. Velocities are measured using pictures of injected bubbles taken by a high-speed camera with a small time interval. The deviation due to the refraction of the acrylic-resin wall is compensated. The frame rate is 4500 frames/second and migration lengths of bubbles are about 10 to 60 mm.

tions collapsed into one line and hence one can clearly deduce the jet's existence. The shear layer between the separation bubble and the main flow in Section II rises to form a low velocity region beneath itself in Section III. The cause of the jet on the pipe's lower wall is the flow on the sides of the separation bubble along the pipe wall that converge in the reattachment region. Figure 7(d)

shows the velocity distributions in Section IV at 463 mm downstream of the elbow's exit, the point at which the low velocity region vanished. Consequently, the dimensionless velocity distribution is also independent of the Reynolds number in the post-critical regime.

Knowing the value and the location of the maximum velocity in the elbow is necessary to prevent erosion. Instantaneous local velocities in the elbow were measured using picture images of small bubbles taken by a high-speed camera with a small time interval for mean velocity of 9.2 m/s at room temperature. The bubbles were injected in the rectifying tank and carried by the flow into the test pipe. The deviation due to the refraction of the pipe's acrylic-resin wall was compensated by calculating more precise locations of the bubbles. Since the turbulence of flow in this region is very small, the instantaneous local velocity is close to its time-averaged local velocity. Figure 8 shows the maximum velocity of 14.1 m/s, or  $u^* = 1.53$  at the location of 33 deg in the angle from the elbow's inlet and 292 mm in the radius, or  $R/D = 0.71$ . There are dimensionless velocities of  $u^* = 1.2$  to 1.5 close to the inner wall near the location of the maximum velocity. The local velocities in the elbow's outer region must be smaller than the mean velocity. The flow separation occurs downstream of the location of the maximum velocity. This is reasonable because flow separation occurs in a pressure recovery area.

### Fluctuating Turbulent Pressure on the Inner Wall of the Pipe

Total energy flux to turbulence can be evaluated with pressure resistance coefficient  $\zeta_{tot}$  as mentioned before. Then, the extrapolation of characteristics of fluctuating turbulent pressure at the plant operating condition with  $Re = 4.2 \times 10^7$  is necessary for evaluating turbulence generated by flow separation of the elbow.

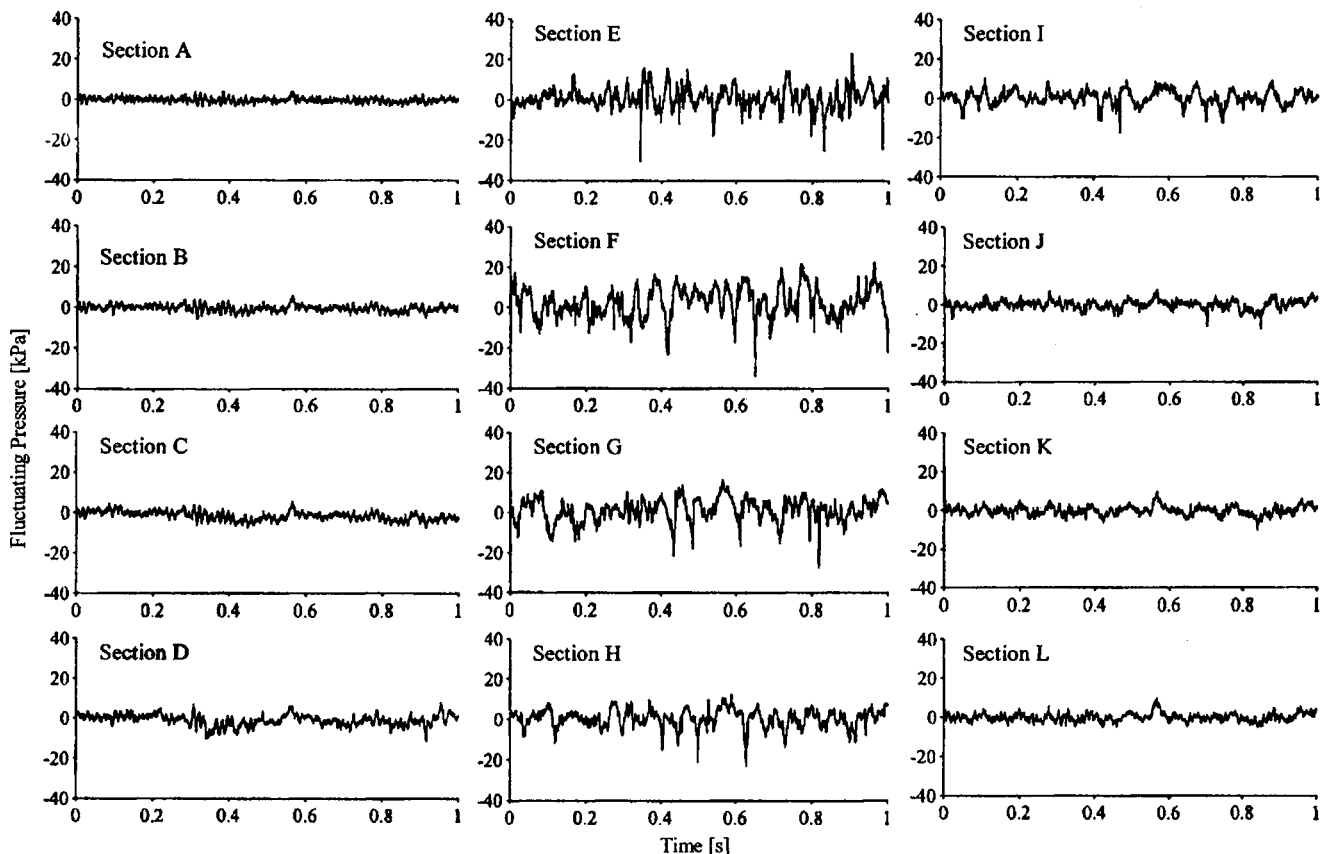


Fig. 9 Fluctuating pressures at the circumferential angle of 180 deg for mean velocity of 9.28 m/s at room temperature

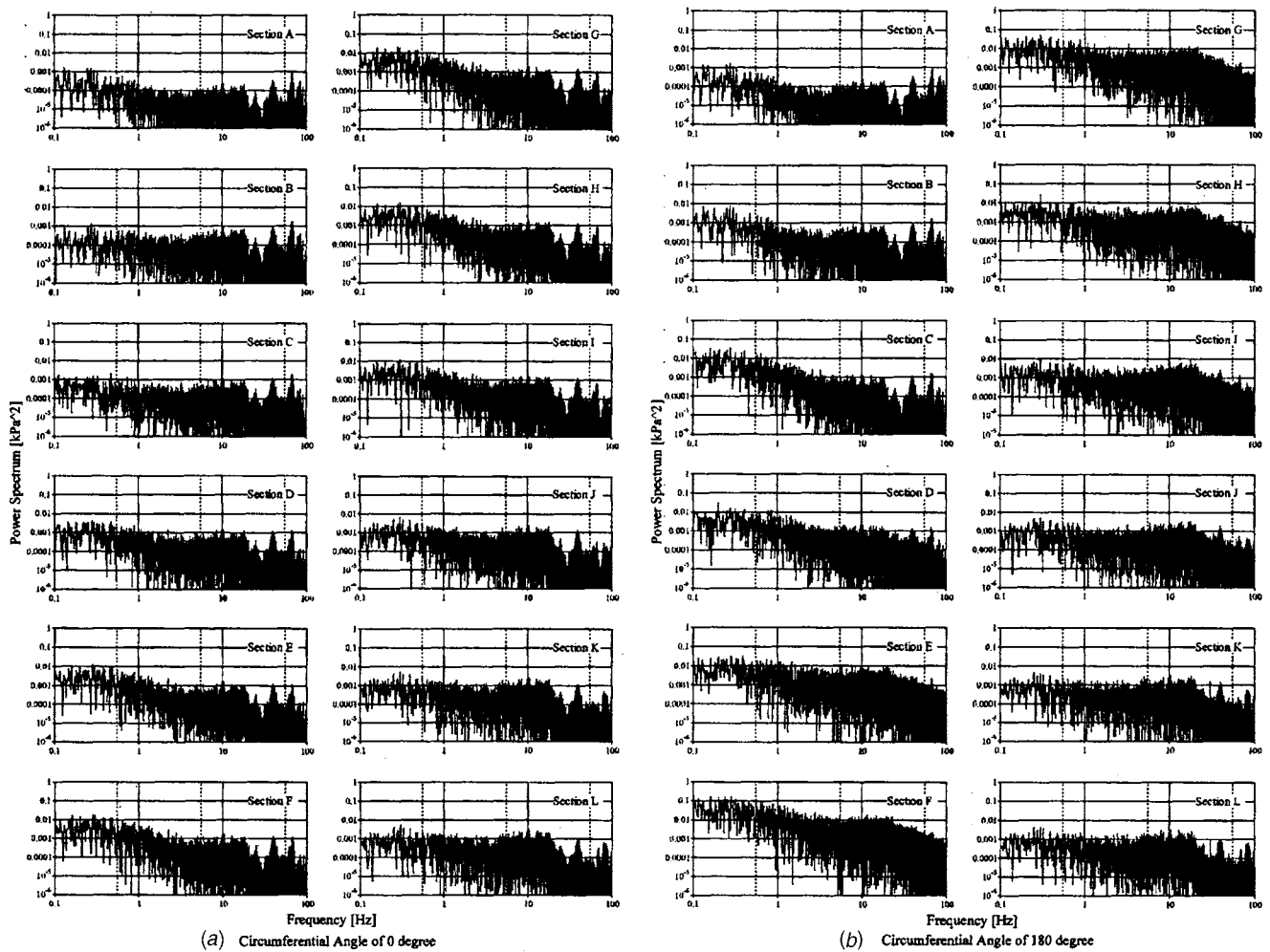


Fig. 10 Power spectra of fluctuating pressures at the circumferential angles of 0 and 180 deg for mean velocity of 9.28 m/s at room temperature

Complex Fourier transformation of pressure fluctuation,  $p(t)$ , at every measuring point,  $x$ , at mean velocity,  $U$ , is consist of frequency,  $\omega$ , and amplitude,  $C(\omega)$ , as its characteristic quantities [4,5].

$$p(t) = \frac{1}{\sqrt{2\pi}} \int_{-\infty}^{\infty} C(\omega) e^{i\omega t} d\omega \quad (2)$$

$$C(\omega) = \frac{1}{\sqrt{2\pi}} \int_{-\infty}^{\infty} p(\xi) e^{-i\omega\xi} d\xi \quad (3)$$

Specifically, power spectra, autocorrelations, cross-correlations, and probability densities of fluctuating pressure are examined. In order to quantitatively evaluate probability densities, standard deviation (or variance), skewness, and kurtosis are measured. The

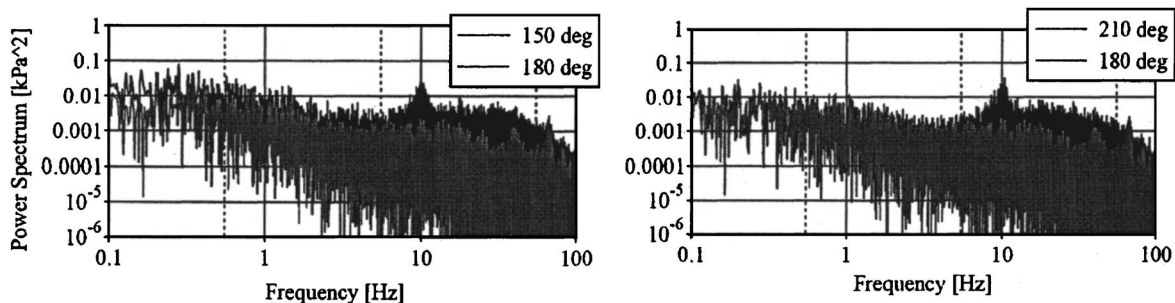


Fig. 11 Power spectra at the circumferential angles of 150 and 210 deg compared with that at 180 deg near the boundary of separation in Section D for mean velocity of 9.28 m/s at room temperature

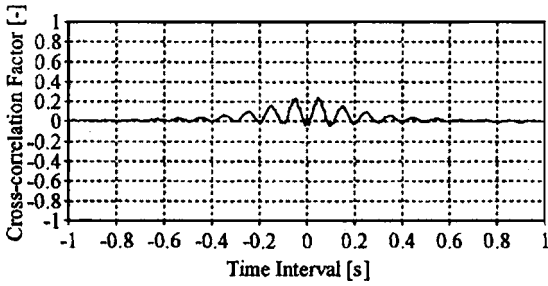


Fig. 12 Cross-correlation factor of fluctuating pressure at the circumferential angles of 150 and 210 deg in section D for mean velocity of 9.28 m/s at room temperature

dimensional analysis will be helpful in finding the analogy of the characteristics of fluctuating pressure, so that standard deviation is divided by kinetic pressure to yield dimensionless standard deviation.

The turbulence causing fluctuating pressure can be classified into the following four categories:

1. turbulence coming from the rectifying tank, or the inlet condition of the model pipe;
2. turbulence generated in the boundary layer of the pipe wall;
3. turbulence generated by the flow separation and its accompanying phenomena, e.g., reattachment and vortex shedding; and
4. turbulence generated in the outer region of the elbow.

Statistical work showed that there were comparatively large skewness and kurtosis in the outer region of the elbow, indicating generated turbulence for  $Re=0.32 \times 10^6$ , but these results vanished when the Reynolds number was larger. Therefore, turbulence generated in the outer region of the elbow is trivial.

Figure 9 shows the fluctuating pressures at a circumferential angle of 180 deg in Sections A to L for the mean velocity of 9.28 m/s at room temperature for the first 1 s. The measuring speed of fluctuating pressures was 5000 Hz, and the measuring time was 10 min. The line connecting the sections at a circumferential angle of 180 deg goes through the center of the flow separation. The amplitude of the fluctuating pressure at A 180 deg near the entrance of the model pipe was small. It showed that the turbulence from the rectifying tank was small because of its good rectification. The amplitudes of the fluctuating pressures at B 180 deg and C 180 deg in the elbow were slightly larger than that at A 180 deg. Therefore, the turbulence generated in the boundary layer of the straight pipe wall was not dominant. The amplitude of the fluctuating pressure at D 180 deg at the elbow's exit was larger than those in the foregoing sections. Die injection showed the flow separation started at a point between C180 deg and D 180 deg in the elbow. Larger amplitude and negative spikes of the fluctuating pressure were measured at E 180 deg in the region of flow separation. The maximum amplitude and negative spikes of the fluctuating pressure were measured at F180 deg in the region of flow reattachment. The amplitude thereafter became smaller and smaller as the measuring point went from G180 deg to L 180 deg. Consequently, the fluctuating pressure in the region of flow separation and its reattachment is dominant and nontrivial for random vibrations of the hot leg.

Figure 10 shows the power spectra of fluctuating pressure at circumferential angles of 180 and 0 deg for mean velocity of 9.28 m/s at room temperature. The power spectra are about  $10^{-3}$  to  $10^{-4}$   $kPa^2$  for both points at A180 deg and A0 deg near the entrance of the model pipe. At the beginning of the elbow for frequencies less than 3 Hz the power spectrum at B180 deg becomes slightly larger than that at B0 deg. The flow near the point at B180 deg is forced to change its direction by the elbow's curvature to yield a slight increase of the power spectrum at low frequencies. The power spectrum at C180 deg just before the separation point becomes much larger than that at C0 deg in the

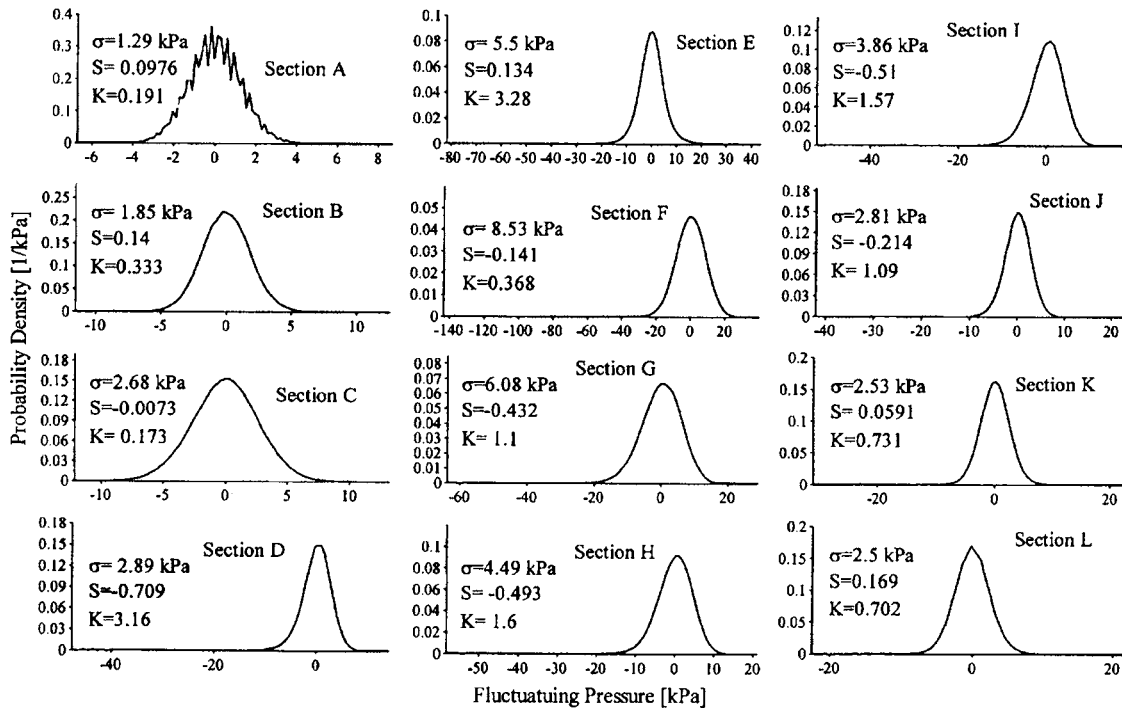


Fig. 13 Probability densities of fluctuating pressure at the circumferential angle of 180 deg for mean velocity of 9.28 m/s at room temperature. The coordinates are self-adjustable scales in order to indicate negative pressure spikes and to compare the shapes of the probability densities each area of which is one.

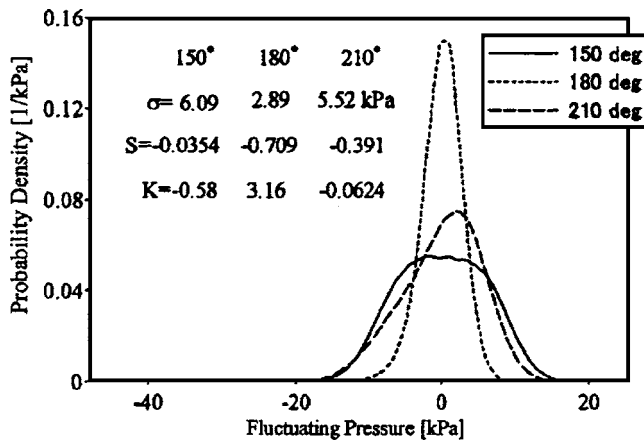
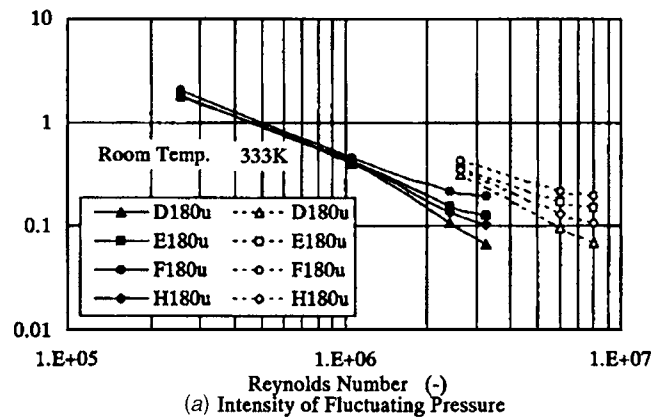


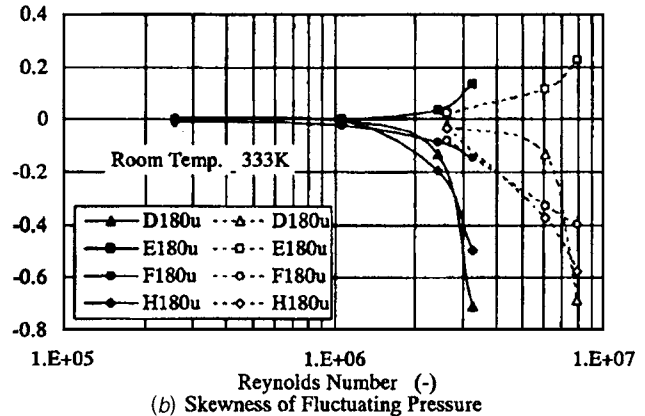
Fig. 14 Probability densities near the boundary of separation in Section D for mean velocity of 9.28 m/s at room temperature

elbow for frequencies less than 6 Hz. These data are the evidence that turbulent energy is supplied from flow into fluctuating pressure at low frequencies. The power spectra at D0 deg to L0 deg downstream of the elbow are almost unchanged. The power spectrum at D180 deg at the exit of the elbow becomes larger even for frequencies up to 100 Hz. The power spectrum at D0 deg also becomes larger than before. The power spectrum at E180 deg becomes much larger and the valleys of the spectrum are filled in the region of the flow separation, while that at E0 deg almost remains as it is at D0 deg. The power spectrum at E180 deg is almost constant up to 20 Hz and descends as the frequency goes up thereafter. The power spectrum at F180 deg in the region of the flow reattachment becomes the largest on the whole, while that at F0 deg almost remains as it is at D0 deg. The power spectrum at F180 deg becomes the largest for frequencies less than 3 Hz. This result suggests turbulence is supplied to the low frequencies again by the reattachment of flow. Comparing the features of the power spectra at D180 deg, E180 deg and F180 deg mentioned above, it can be explained that turbulence is generated in the reattachment of flow and carried upstream by backflow in the region of flow separation. The power spectra at G180 deg to J180 deg downstream of the reattachment of flow decrease more gradually for frequencies below 3 Hz than those at J180 deg to L180 deg.

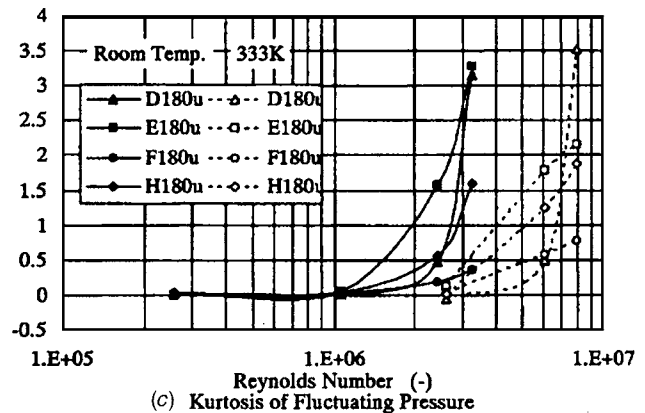
Figure 11 shows the power spectra of fluctuating pressure at D150 deg and D210 deg near the boundary of flow separation for mean velocity of 9.28 m/s at room temperature. For comparison the power spectrum at D180 deg is also plotted in the figure. There are peaks at the frequency of 10 Hz at D150 deg and D210 deg for the mean velocity of 9.28 m/s at room temperature. Comparing the power spectra for other mean velocities that are not shown here, the frequency of the fluctuating pressure is proportional to the mean velocity in the pipe and its Strouhal number is  $St=fD/U=0.45$ , where  $f$  is the frequency,  $D$  is the pipe diameter, and  $U$  is the mean velocity. There is no peak at D180 deg in the separation. The peaks are the largest at D150 deg and D210 deg among all at the measuring points in Section D. This indicates there is a systematic movement of the boundary of flow separation. Figure 12 shows the cross-correlation factor of fluctuating pressure at D150 deg and D210 deg at room temperature. There is a cyclic correlation with period of 0.1 s that is consistent with the peak at the frequency of 10 Hz. The phase difference is about 180 deg, so the fluctuation of 10 Hz alternately occurs at D150 deg and D210 deg. Dye injection reveals the backflow swaying from side to side in the separation bubble that sheds vortices into the downstream. The backflow seems to fluctuate the flow at the boundary of the separation bubble from side to side so that the phase difference is 180 deg.



(a) Intensity of Fluctuating Pressure



(b) Skewness of Fluctuating Pressure



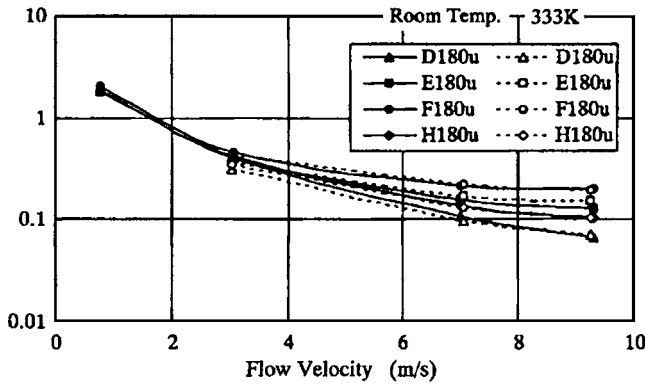
(c) Kurtosis of Fluctuating Pressure

Fig. 15 Dependency of fluctuating pressures on the Reynolds number

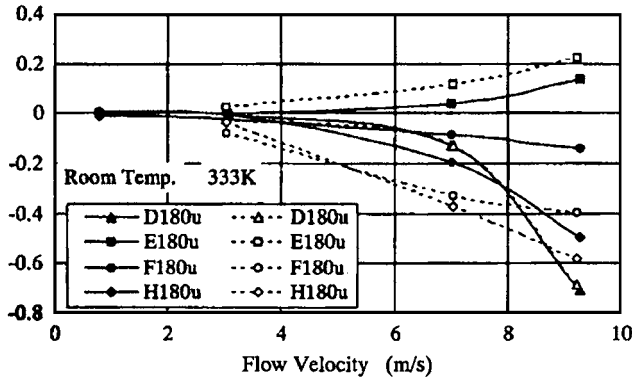
### Statistical Evaluation of Fluctuating Pressures

Figure 13 shows probability densities of fluctuating pressures at the circumferential angle of 180 deg for mean velocity of 9.28 m/s at room temperature. The fluctuating pressure is divided into 100 intervals from the minimum to the maximum values. The probability density at A180 deg has irregularity because the fluctuating pressure is so small that it approaches the minimum resolution of the pressure transducers which is 0.258 to 0.288 kPa. Standard deviation,  $\sigma$ , skewness,  $S$ , and kurtosis,  $K$ , are defined [6–9] as:

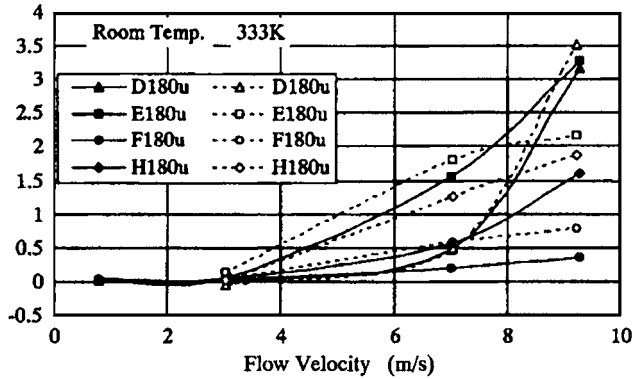
$$\sigma = \sqrt{\frac{1}{n-1} \sum_{i=1}^n \Delta p_i^2} \quad (4)$$



(a) Intensity of Fluctuating Pressure



(b) Skewness of Fluctuating Pressure



(c) Kurtosis of Fluctuating Pressure

Fig. 16 Dependency of fluctuating pressures on flow velocity

$$S = \frac{(1/n) \sum_{i=1}^n \Delta p_i^3}{\sqrt{\left( (1/n) \sum_{i=1}^n \Delta p_i^2 \right)^3}} \quad (5)$$

and

$$K = \frac{(1/n) \sum_{i=1}^n \Delta p_i^4}{\left( (1/n) \sum_{i=1}^n \Delta p_i^2 \right)^2} - 3 \quad (6)$$

where  $\Delta p_i$  is fluctuating pressure, and  $n=3,000,001$  for  $10 \text{ min} \times 5 \text{ kHz}$ . Standard deviation,  $\sigma$ , skewness,  $S$ , and kurtosis,  $K$ , quantitatively represent the magnitude, asymmetry, and flatness of

density distribution of fluctuating pressure respectively. Both  $S$  and  $K$  equal 0 for a normal distribution, which is the case that fluctuating pressure is random. If  $S$  and/or  $K$  are not 0, fluctuating pressure is not random, and there may be some characteristics of turbulent flow. In this case we need to know the dependency of the characteristics of turbulent flow on a Reynolds number.

The maximum value of the standard deviation is  $\sigma=8.53 \text{ kPa}$  at F180 deg. In other words the intensity of fluctuating pressure is maximum at flow reattachment. D180 deg and E180 deg show that the standard deviation in the separation bubble is smaller than that at the reattachment. The standard deviation in the flow downstream of the reattachment becomes smaller again. The abscissa is a self-adjustable scale, and a few negative pressure spikes give wide negative ranges at D180 deg to J180 deg. The skewness is  $S=-0.709$  and the kurtosis is  $K=3.16$  at D180 deg, and  $S=0.134$  and  $K=3.28$  at E180 deg. These results demonstrate that the probability density slightly deviates from its symmetrical shape, and the fraction of fluctuating pressure with small amplitudes is more in the separation bubble than that of the normal distribution. The kurtosis at F180 deg is smaller than those at E180 deg and G180 deg. The kurtosis at H180 deg is larger than that at G180 deg. This means that the fraction of fluctuating pressure with small amplitudes in the region of reattachment is similar to that of the normal distribution. Moreover, the accelerated flow at G180 deg and H180 deg has a greater amount of fluctuating pressure with small amplitudes than that in the region of reattachment. The flow in the region of reattachment is near the moving stagnation point, and turbulence is generated in it. The pressure fluctuation of the generated turbulence is almost random. The feature of the turbulence in the accelerated flow is that turbulence energy is transferred from large to small eddies so that the fraction of fluctuating pressure with small amplitudes increases. The kurtosis of the fluctuating pressure in the flow downstream of H180 deg becomes smaller. This means that the dissipation of turbulence energy is larger than the supply of turbulence energy in the flow far downstream of the reattachment. The symmetric property of the probability density is well preserved through the model pipe at the circumferential angle of 180 deg, except a few negative spikes in the flow near the separation and the reattachment. Figure 14 shows the probability densities at D150 deg, D180 deg and D210 deg for mean velocity of  $9.28 \text{ m/s}$  at room temperature. The boundary of the separation gives negative kurtosis of  $K=-0.58$  and  $-0.0624$  at D150 deg and D210 deg, while the separation bubble gives  $K=3.16$  at D180 deg. This means that the fraction of fluctuating pressure with large amplitudes is larger on the boundary of the separation than that of the normal distribution. Therefore, the boundary flutters to make fluctuating pressure with large amplitudes.

### Dependency of Fluctuating Pressures on Mean Velocity/ Reynolds Number

The dimensionless Navier-Stokes equation indicates that the fluid density,  $\rho$ , can be included in pressure,  $p$ , so that dimensionless pressure,  $p/\rho U^2$ , is common for water and sodium, and the fluid property will affect flow in the pipe only through a Reynolds number. Figure 15 shows the dependency of intensity, skewness, and kurtosis of fluctuating pressure on the Reynolds number at D180 deg to H180 deg. The standard deviations are normalized by kinetic pressure to yield the intensity of fluctuating pressure,  $I=\sigma/(\rho U^2/2)$ . The data at the temperature of 333 K are similar in form but remain separated from those at room temperature. Thus, the statistical values do not depend on the Reynolds number.

We now try to investigate the influence of viscosity on turbulence. The size of the flow separation is  $290 \times 65 \times 240 \text{ mm}$ . A Lagrangian integral scale of time,  $T$ , is defined as [6,7]:

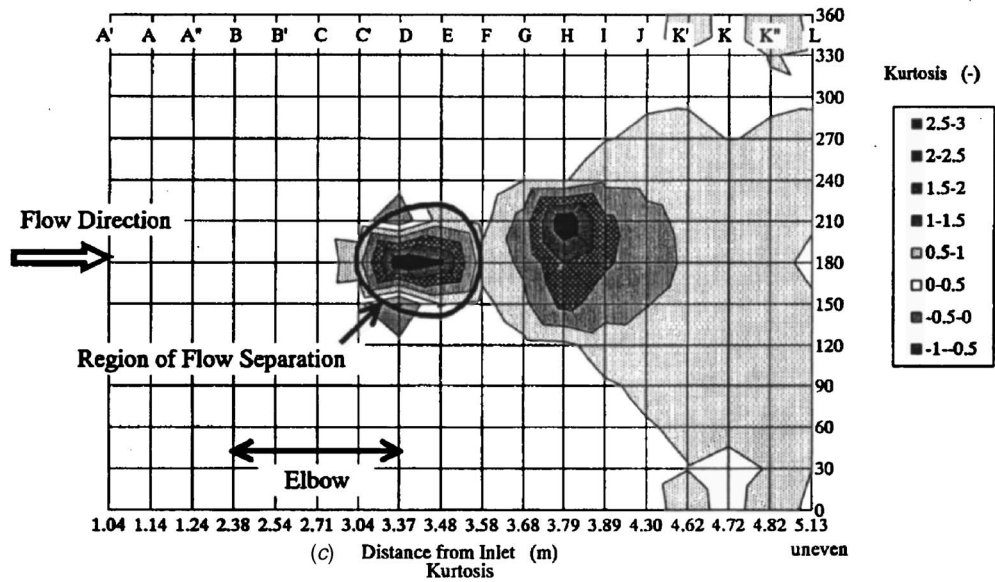
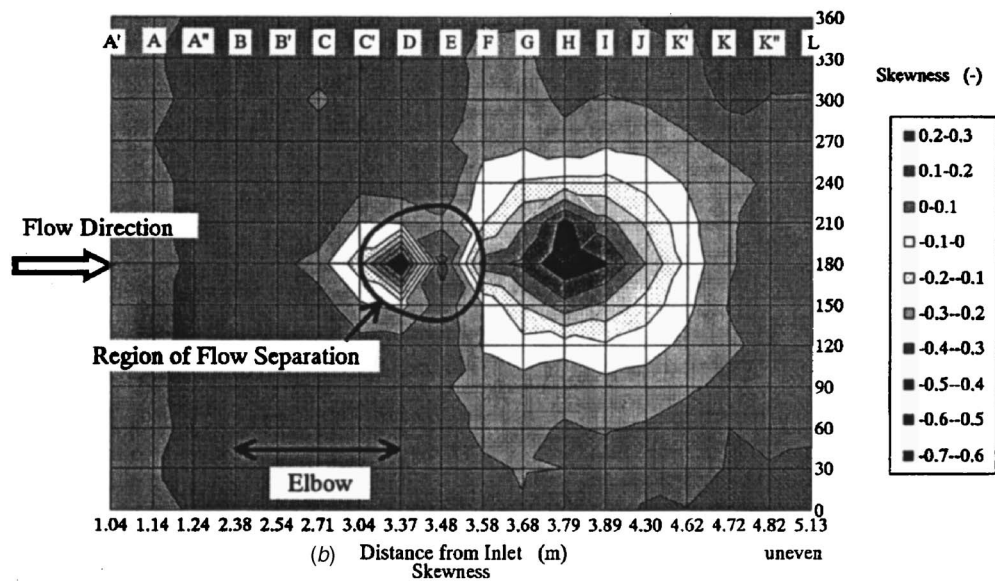
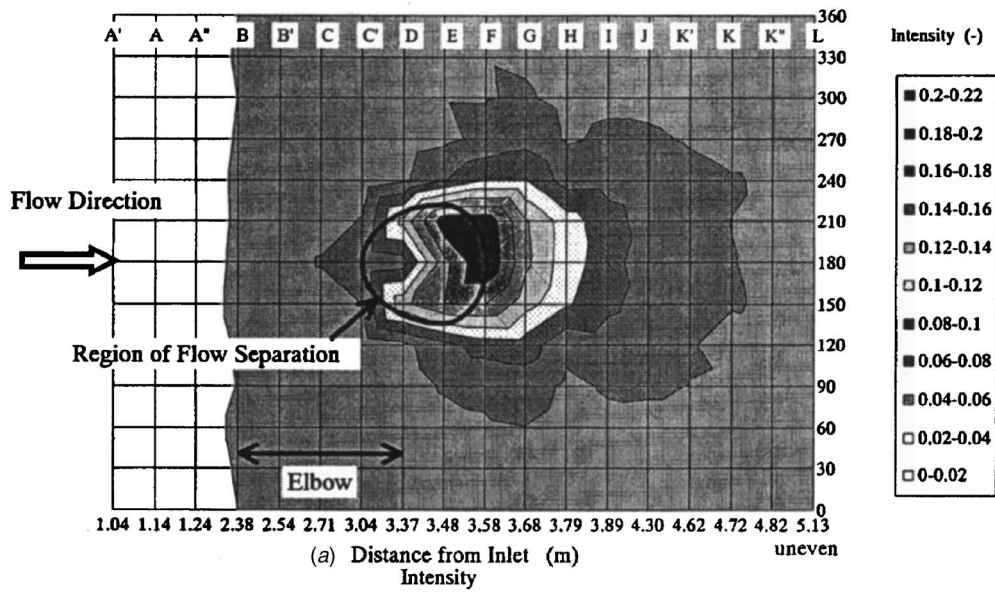


Fig. 17 Distribution of intensity, skewness, and kurtosis of fluctuating pressures

$$T = \int_0^t c(\tau) d\tau \quad (7)$$

where  $c(\tau) = \overline{\Delta p(t)\Delta p(t-\tau)} / \Delta p^2$  is an autocorrelation factor. We take  $t=1$  s to lessen the accumulation of errors. The Lagrangian integral scale of time at F180 deg is  $T=0.1298$  s, and the local velocity is about  $u=0.4$  m/s as shown in Fig. 7(c). At this point, the Lagrangian integral scale of length is  $\ell_L = T \times u = 52$  mm. Therefore, the size of fluctuation must be the order of 50 mm. Kolmogorov's microscale of the local flow [6,7] is the order of  $\eta = 57 \mu\text{m}$  ( $\eta = (\nu^3 / u^3)^{1/4}$ , kinematic viscosity:  $\nu = 1.18 \text{ mm}^2/\text{s}$ , the inner diameter of the pipe:  $\ell = 412.7$  mm, and the local velocity:  $u = 0.4$  m/s), which is 1/1000 times  $\ell_L$ . Thus, the viscosity of the fluid will not affect the generation of fluctuation. This suggests that the statistical values depend on the absolute velocity of the pipe. Figure 16 shows those statistical values with respect to mean velocity of the pipe flow. The data at the temperature of 333 K agree fairly well with those at room temperature. The reason is that the power spectra consist of both frequencies depending on and independent of the mean velocity,  $U$ . Some peaks of frequencies give constant Strouhal numbers for the different mean velocities, and the others do not. The peaks of the frequencies of the constant Strouhal numbers are made by flow. One of the causes of frequencies independent of mean velocity may be the pipe wall. But the rest of the power spectra may be made by middle scale eddies that are far from both the large eddies characterized by the Lagrangean integral scale and the small eddies characterized by the Kolmogorov's microscale. Therefore, the parameter to simulate the distribution and the statistical values of the power spectral shall be not a dimensionless group but the prototypical velocity,  $U$ . Consequently, we can use the statistical values only at the velocity of  $U=9.2$  m/s to extrapolate the standard deviations, skewness, and kurtosis of fluctuating pressure of the hot leg at the Reynolds number of  $4.2 \times 10^7$ .

### Distributions of Fluctuating Pressures in Flow Direction

Figure 17 shows the distributions of the intensity, skewness, and kurtosis of the fluctuating pressure at mean velocity of 9.2 m/s given from the measured data and some interpolation. These are the predicted results of the hot legs. The abscissa is the distance from the inlet of the model pipe with uneven pitch. The ordinate is the circumferential angle of the pipe. The region of flow separation is also indicated in these figures. Figure 17(a) shows that the region of maximum intensity of fluctuating pressure lies on the downstream boundary of flow separation, F180 deg, where the separated flow reattaches to the wall. This means flow reattachment on the wall generates the maximum fluctuating pressures. The front of the boundary of flow separation, C' 180 deg, has relatively small intensity, while the both sides of the boundary, D150–E150 deg and D210–E210 deg, have large intensity. We observed that the flow in front of the separation is more stable and that both sides of the boundary fluctuate from side to side. The intensity gradually decreases downstream of the reattachment. Hence, high intensity of fluctuating pressure is localized in the regions of flow separation, the reattachment, and the area downstream of the reattachment. Figure 17(b) shows that

both minimum and maximum skewnesses lie in the region of flow separation, D180 deg and E180 deg, respectively. This means that flow separated away from the wall yields negative skewness on the wall downstream flow separation, and back flow of the reattaching flow, F180 deg, yields positive skewness in the region of flow separation. There is another minimal skewness downstream from the point of flow reattachment, H180 deg, caused by the rebound of reattaching flow off the wall. Figure 17(c) shows the maximum kurtosis in the region of flow separation, D180 deg, and a maximal kurtosis downstream from the flow reattachment, H210 deg. These regions almost coincide with those of the minimal skewnesses. Hence, there are negative pulses in the regions with negative skewness and positive kurtosis. There are negative kurtoses on both sides of the boundary of flow separation, D150 deg and D210 deg, while those at the other points are all positive. Fluctuating pressure at these points consists of relatively regular amplitudes that indicate some organized movements of the boundary generating turbulence. The power spectra of fluctuating pressure have peaks at the frequency of 10 Hz at D150 deg and D210 deg for the mean velocity of 9.28 m/s, while there is no peak at D180 deg as shown in Fig. 11.

Consequently, generation of fluctuating pressure is dominant on the boundary of flow separation and reattachment.

### Conclusions

The total resistance coefficient of a model pipe is well consistent with published data, and additionally we have provided the data up to Reynolds numbers of  $8.0 \times 10^6$ . The flow visualization and velocity measurement confirmed the independency of the flow on the Reynolds number. Pressures on the inner pipe wall were statistically examined to predict the characteristics of fluctuating pressures on the hot leg. Not a Reynolds number but mean velocity of the pipe flow can be a parameter of the variances, skewnesses, and kurtosis, because the fluctuating pressure consists of both frequencies depending on and independent of the mean velocity of the pipe. The power spectra on the boundary of both sides of separation unveiled fluctuating pressure with exclusive frequency depending on flow velocity. It also revealed that generation of fluctuating pressure is dominant on the boundary of flow separation and reattachment.

### References

- [1] Shimakawa, Y., Kasai, S., Konomura, M., and Toda, M., 2002, "An Innovative Concept of the Sodium-Cooled Reactor to Pursue High Economic Competitiveness," *Nucl. Technol.*, **140**, pp. 1–17.
- [2] Idelchik, I. E., 1986, *Handbook of Hydraulic Resistance*, 2nd ed., Hemisphere, New York.
- [3] Schlichting, H., 1968, *Boundary-Layer Theory*, translated by J. Kestin, 6th ed., McGraw-Hill, New York.
- [4] Beckenbach, E. F., 1961, *Second Series Modern Mathematics for the Engineer*, McGraw-Hill, New York.
- [5] Harris, C. M., and Crede, C. E., 1961, *Shock and Vibration Handbook*, McGraw-Hill, New York.
- [6] Tennekes, H., and Lumley, J. L., 1972, *A First Course in Turbulence*, MIT, Boston, MA.
- [7] Kambe, T., and Drazin, P. G., 1998, *Fluid Dynamics Stability and Turbulence*, University of Tokyo, Tokyo.
- [8] Hinze, J. O., 1965, *Turbulence*, McGraw-Hill, New York.
- [9] Everitt, B. S., 1988, *The Cambridge Dictionary of Statistics*, Cambridge U.P., Cambridge.

# A Computational Study of Torque and Forces Due to Compressible Flow on a Butterfly Valve Disk in Mid-stroke Position

Zachary Leutwyler<sup>1</sup>

e-mail: zleutwyler@houston.rr.com

Charles Dalton

e-mail: dalton@uh.edu

Department of Mechanical Engineering,  
University of Houston,  
Houston, TX 77204-4006

*The ability to accurately predict the aerodynamic torque and lift and drag forces on a 2-D model of a 0.18 aspect ratio biconvex circular-arc disk operating in a compressible flow using computational fluid dynamics (CFD) was investigated. Fluent 6.0 was the CFD package utilized to perform these calculations. Grid-convergence and time-convergence/stability were analyzed first, followed by a qualitative study of the Spalart-Allmaras,  $k-\epsilon$ , and  $k-\omega$  turbulence models with their enhancement features and model variants. Fluent was used to predict the pressure profile on the disk surface for disk positions 30, 45, and 60 deg (where 0 deg is the fully closed position) and over a range of pressure ratios. The pressure ratios were selected to determine the capability of CFD to accurately predict the flow field and resulting torque in flows ranging from nearly incompressible to highly compressible. Fluent predictions for the pressure profiles on the disk were compared to test data so that the lift and drag forces and aerodynamic torque could be determined responsibly. Acceptable comparisons were noted.*

[DOI: 10.1115/1.2236129]

*Keywords:* butterfly valve, compressible flow, aerodynamic torque, bearing force, CFD

## Introduction

The objective of this study is to investigate the use of computational fluid dynamics (CFD) methods as applied to the flow of a compressible fluid past a butterfly valve. Fluent 6.0 has been selected as the CFD package to perform these calculations. The flow field of a compressible fluid in a butterfly valve is quite complex and can be rather challenging for any CFD code. To quantify the numerical error associated with CFD predictions, it is necessary to perform a proper validation, which requires that the grid, turbulence model, and solution technique be compared to actual test data over the full range of possible flow phenomena. The primary equation-solving technique that Fluent employs is the finite volume method. Fluent provides several options such as the choice of a coupled or segregated solver, as well as the use of implicit or explicit equations. Because the compressible flow field of a butterfly valve is complex and, since the butterfly valve geometry is also complex, the use of the coupled solver with implicit equations was chosen along with a second-order time and flow discretization.

The disk geometry chosen was a symmetric 0.18 aspect ratio biconvex circular-arc disk (BiCAD). The BiCAD was studied by Morris [1], who reported the dimensionless pressure profile on the upstream and downstream disk faces for various disk angles and pressure ratios. Morris used a duct of rectangular cross-section with an aspect ratio (height/depth) of 2.67.

## Background

Butterfly valves owe much of their popularity to their low production cost and their relatively small contribution to the total piping system resistance when the valve disk is in the full open

position. However, the same streamlined features of the valve disk that minimize the flow resistance also make predicting the aerodynamic torque difficult. Butterfly valve discs behave similarly to airfoils in that the angle of attack influences the flow field characteristics. Changing the angle of attack can generate or change points of separation and reattachment, size and location of recirculation regions, shock position, and in some cases can produce shock-induced separation. These phenomena influence the pressure profile on the disk, which in turn affects the lift and drag forces and the resulting aerodynamic torque (the flow-induced torque on the disk).

The magnitude of the lift and drag forces as well as the magnitude and direction of the aerodynamic torque are all influenced by the disk geometry, position, orientation, operating pressure ratio ( $P_b/P_o$ ), and piping configuration. Disk geometries are often divided into two classes: symmetric and asymmetric. The BiCAD disk studied here is a symmetric disk.

The required torque needed to control and operate a butterfly valve safely is strongly dependent on the aerodynamic torque and bearing torque. The resultant force acting on the disk governs both the bearing torque and is the dominant source of the aerodynamic torque. The aerodynamic torque results from the resultant force acting on the moment arm. The bearing torque results from the frictional force acting between the valve shaft and bearings when the disk experiences the resultant force. Therefore, to predict the required torque needed to control the valve disk position properly, a detailed knowledge of the dependency and influence of the previously mentioned independent variables on the resulting force is necessary. The geometry of the disk and the pressure ratio alone have a significant effect on the torque coefficient, and therefore require that each disk geometry be tested over a range of pressure ratios, disk positions, and disk orientations. The time and cost of testing could potentially be reduced if CFD were found to accurately predict the pertinent flow characteristics, forces, and torque acting on the valve disk. Then CFD could be used to assist in valve performance prediction. The potential use of CFD could

<sup>1</sup>Currently with Kalsi Engineering Inc., Sugar Land, TX.

Contributed by the Fluids Engineering Division of ASME for publication in the JOURNAL OF FLUIDS ENGINEERING. Manuscript received April 22, 2005; final manuscript received February 11, 2006. Assoc. Editor: Surya P. Vanka. Paper presented at the 2004 ASME Heat Transfer/Fluids Engineering Summer Conference (HT-FED2004), July 11–15, 2004, Charlotte, North Carolina, USA.



limit the need for expensive testing of all of the possible combinations of disk geometries, orientations, and positions.

Several investigators have studied the hydrodynamic torque (the torque induced by a nearly incompressible fluid such as water) and have developed accurate hydrodynamic torque and flow resistance coefficients ( $C_t$  and  $K_v$ , respectively) for various popular disk geometries, orientations, and piping configurations. The hydrodynamic/aerodynamic torque coefficient  $C_t$  is given for both 2-D and 3-D discs respectively by

$$C_{t,2-D} = \frac{T_{hydro}}{\Delta P_v A_c C} \quad (1a)$$

and

$$C_{t,3-D} = \frac{T_{hydro}}{\Delta P_v D^3}. \quad (1b)$$

The coefficients  $K_v$  and  $C_v$  (discussion of  $K_v$  and  $C_v$  can be found in [2]) are defined by

$$K_v = \frac{891 d^4}{C_v^2} \quad (2)$$

and

$$C_v = Q \sqrt{\frac{\rho}{\Delta P(62.4)}}, \quad (3)$$

where  $d$  is the internal diameter pipe in inches,  $Q$  is the flow rate in gallons per minute (GPM), and  $\Delta P_v$  is the valve pressure drop in psi.

It should be noted that  $K_v$  is dimensionless while  $C_v$  is not. The dimensions of  $C_v$  will depend on the selection of  $Q$ ,  $\rho$ , and  $\Delta P_v$ . However, the units for  $C_v$  in Eq. (3) are GPM (of water at 60°F) per psi drop across the valve, which gives rise to the value of 891 in Eq. (2). Kalsi Engineering [3], working both with Electrical Power Research Institute and on their own, has performed numerous flow tests that included several disk geometries, disk orientations, and piping configurations to better understand and predict the hydrodynamic and aerodynamic torque (contact Kalsi Engineering [3] for a complete listing of published papers and tests performed).

Coefficients for an incompressible flow, obtained through model testing, cannot be blindly applied to all butterfly valves, especially those with unique geometries, yet they do provide the means to accurately predict the valve pressure drop, the flow rate, the hydrodynamic and bearing torques, and other important valve performance values for many popular butterfly valve models operating in an incompressible medium or at very low flow velocities for a compressible fluid.

The effects of compressibility and the high dependency of the coefficients on the valve and piping configuration make it difficult to use incompressible coefficients when doing a compressible flow analysis. The torque coefficient,  $C_t$ , for a compressible flow depends on many flow and pipe parameters and frequently differs not only in magnitude but also in sign compared to coefficients for an incompressible flow. A universally accepted definition for the torque coefficient is not available; however a suggested alternative definition, labeled  $C_{t,c}$ , is given for both 2-D and 3-D discs, respectively, by

$$C_{t,c,2-D} = \frac{T_{aero}}{P_t A_c C} \quad (4a)$$

and

$$C_{t,c,3-D} = \frac{T_{aero}}{P_t D^3}. \quad (4b)$$

The coefficient  $C_{t,c}$  has an inherent weakness in that it is made dimensionless based on a static relationship and not a dynamic flow parameter such as the pressure drop or the dynamic pressure.

If the inlet static pressure is held constant but the mass flow rate is changed (say, by a downstream valve),  $C_{t,c}$  may result in different values even for the same disk geometry, orientation, and angle.

Many asymmetric discs, oriented with the shaft upstream, are largely self-closing for both incompressible and compressible flows; however, the magnitude of the torque may be different, even for the same operating pressures. An asymmetric disk oriented with the shaft downstream in an incompressible fluid has a self-closing torque over most of the stroke; however, the torque is almost entirely self-opening for a compressible fluid in the absence of a significant downstream resistance.

Valve-performance predictions are more difficult for butterfly valves operating in a compressible fluid. Silvester [4] developed a simplistic analytical model for predicting the aerodynamic torque and performed experimental tests on two disk geometries. The model results were then compared to the experimental results and the comparison showed moderate agreement. The experimental tests were conducted to investigate the effect on the aerodynamic torque by disk geometry, position, orientation, and pressure ratio. Steele and Watkins [5] performed experimental tests, which included various disk orientations, positions, upstream elbow orientations, and pressure ratios, for three similarly scaled disk geometries.

Additional investigators of particular interest are Morris and Dutton [6] who studied the effect of a 90 deg mitered elbow, Morris and Dutton [7] who studied the torque of two valves mounted in series, Danbon and Sollicc [8] who also studied the effects of an upstream elbow on both the instantaneous and time-mean aerodynamic torque, and Sollicc and Danbon [9] who discussed the choice of a coefficient for aerodynamic torque.

Morris's data [1] for the BiCAD at 30, 45, and 60 deg are used to validate our computational results. Morris [1] measured the static pressure distribution on two different disk geometries over a range of pressure ratios using a 2-D rectangular disk and wind tunnel. The flow field of the BiCAD was studied over a range of angles from the full open position, 90 deg, to nearly closed, 30 deg (Morris presented the data with an opening angle of 0 deg instead of 90 deg as used here). The pressure ratio,  $P_b/P_o$ , ranged from approximately 0.7 to 0.2. The experimental facility consisted of an upstream tank, which discharged directly into the inlet of the test section. The test section consisted of an upstream rectangular duct (four disk lengths long), the 2-D disk (projected in the third dimension), and a downstream rectangular duct. The test section was rectangular with an aspect ratio of 2.67.

The validation will include a comparison of the packaged turbulence models with select enhancement options, a comparison of grid structures, a spatial and temporal convergence/stability analysis, and a comparison of results for the pressure profile on the disk leading and trailing faces.

Fluent is used to help understand the flow field of a compressible fluid around the BiCAD and the aerodynamic torque acting on the BiCAD. This investigation is limited to a straight piping configuration with no additional piping components that will affect the approach velocity profile or provide an additional resistance except for four disk lengths of duct upstream and 15 disk lengths of straight duct downstream of the valve. This verification serves to form the foundation of future computational work in butterfly valve research that could include different disk geometries, orientations, and piping configurations. The work can be expanded further to include 3-D numerical models of circular discs.

## Torque Behavior and Flow Field Details

Developing a suitable test matrix requires an in-depth knowledge of the characteristic pressure ratios, disk positions, and other valve and piping parameters that have a significant effect on the valve performance and flow field. A comprehensive matrix should include pressure profile predictions, turbulence model comparisons, and a spatial and temporal convergence/stability analysis for

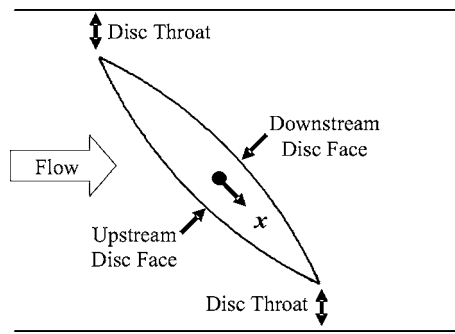


**Fig. 1** Illustrates the biconvex circular-arc disk (BiCAD) with a 0.18 aspect ratio (ASR), which was modeled after the test disk of Morris [1]. The coordinate  $x$  measures from the shaft center line along the disk chord.

all of the possible flow phenomena that can occur over the range of pressure ratios. As such, it is important to be knowledgeable of the flow field phenomena unique to each of the four characteristic pressure ratios (ChPRs).

These ChPRs are presented in the order in which they occur, starting with a pressure ratio of unity with the upstream stagnation pressure held constant and the downstream pressure lowered. The pressure ratios are defined as  $P_2/P_1$  and are based on the following phenomena:

- $P_{r1}$  — The first characteristic pressure ratio is reached when the torque coefficient deviates from the incompressible coefficient by a certain percentage, say 10%.
- $P_{r2}$  — The second occurs when the Mach number at the throats (or vena contracta) is unity (see Fig. 1).
- $P_{r3}$  — The third occurs when the supersonic flow formed by the expanding area on the downstream face of the disk reattaches to the trailing face as seen in Figs. 2–4.
- $P_{r4}$  — The fourth occurs when a further reduction in the downstream pressure no longer affects the flow field in the local vicinity of the disk so that the time-average torque remains constant.

These characteristic pressure ratios are of further importance for predicting the torque and flow field behavior. The characteristic pressure ratios are largely dependent on the disk position and moderately dependent on the disk geometry and orientation. Other factors, such as the presence of an upstream elbow or a downstream valve, may also affect these values.

The flow field corresponding to  $P_{r1}$ , for mid-stroke disk angles, will be similar to that of an incompressible flow. The flow remains subsonic. The upstream face of the disk and the wind tunnel wall will act similar to a C-D nozzle and accelerate the flow. Because of the steep diverging angle of the trailing face, the flow may separate from the leading edge of the downstream face of the disk. This is especially true for disk positions less than 70 deg. The flow downstream of the disk is dominated by vortex formations. The downstream pressure will fluctuate due to the shedding of vortices, which will cause force and torque fluctuations. A slight increase over the incompressible flow pressure loss will occur as a result of compressibility.

The flow field associated with  $P_{r2}$  is similar to that of  $P_{r1}$  with the exception of a higher pressure loss due to the sonic flow at the throat and a more complex recirculation region. The expanded high speed flow and the effects of compressibility help to shrink the recirculation region and reduce the size of the shed vortices. Although the sizes of the shed vortices decrease, they may be in closer proximity to the disk, which can cause large, high-frequency fluctuations in the pressure and aerodynamic torque acting on the disk.

As the downstream pressure is further reduced, the flow passing through the throat (the flow area formed by the disk edge and wind tunnel wall (see Fig. 5)) expands and accelerates to a supersonic speed. As the flow returns to subsonic speed downstream, it must pass through a shock wave, which results in a nonrecoverable pressure loss. The expanding gas further reduces the recirculation region until the flow reattaches to the trailing face and  $P_{r3}$  is reached. As the recirculation region is decreased, the pressure downstream is also decreased. For some disk angles near the closed position, this pressure ratio may not exist for realistic operating conditions; however, as the disk angle is increased, and the valve is opened, the pressure ratio at which the flow reattaches also increases. This is important because the reattached supersonic flow causes a drop in the pressure on the downstream face, which results in an amplified pressure differential across the disk and increases the resultant force and the aerodynamic torque.

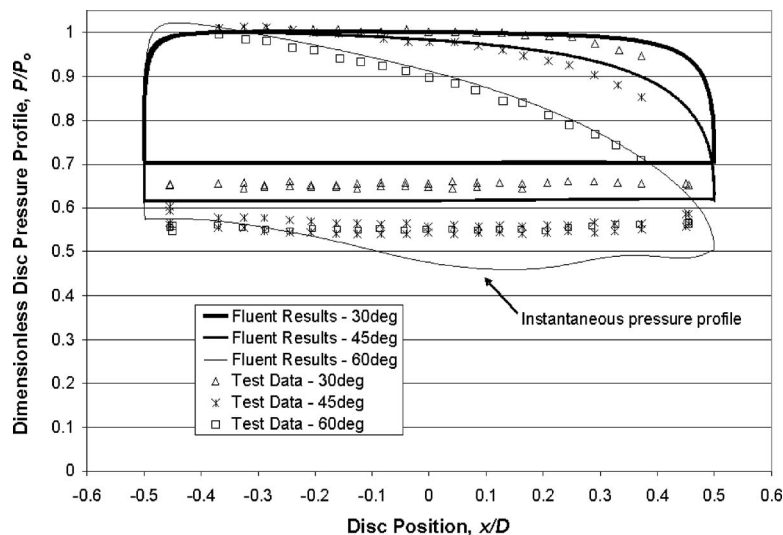


**Fig. 2** Comparison of Fluent results with test data [1] for case 1 for disk angles of 30, 45, and 60 deg

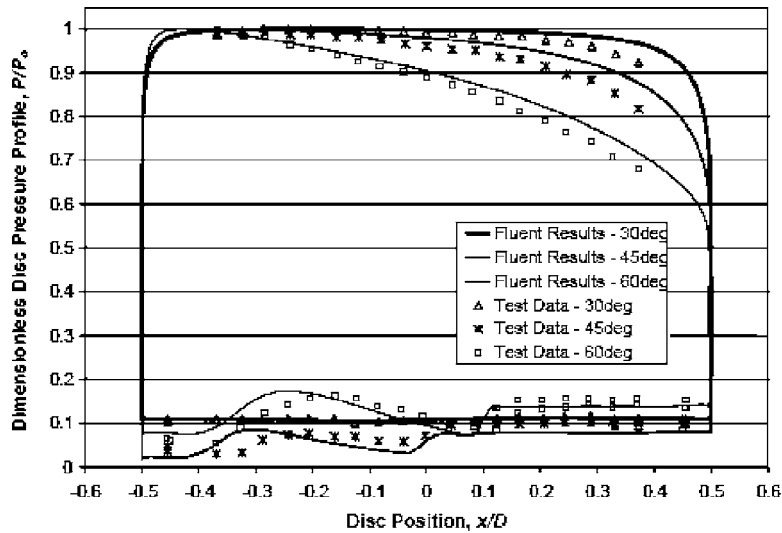


Fig. 3 Comparison of Fluent results with test data [1] for case 6 for disk angles of 30, 45, and 60 deg

The flow fields of  $P_{r3}$  and  $P_{r4}$  are very similar, the only differences being the location of the separation point on the trailing face and the presence of reflecting shocks for  $P_{r4}$ . For some disk geometries and positions,  $P_{r3}$  may be skipped and the transition from  $P_{r2}$  to  $P_{r4}$  may be immediate.

### Turbulence Model Comparison

The disk-pressure profile was predicted and compared to results for an operating pressure ratio,  $P_b/P_o$ , of 0.23 with the disk at 45 deg (see Fig. 5) using the Spalart-Allmaras,  $k-\epsilon$ , and  $k-\omega$  turbulence models, including a few turbulence model variants. The Spalart-Allmaras model is a one-equation model, while the  $k-\epsilon$  and  $k-\omega$  turbulence models are both two-equation models. The  $k-\epsilon$  models include the standard, the RNG (renormalization group theory), and the realizable models. The  $k-\omega$  models include the standard and the SST (shear stress transport) model.

Solutions for the best models are given in Fig. 5. Two of the models in Fig. 5 are part of the  $k-\epsilon$  family, one model from the  $k-\omega$  family and the fourth is the Spalart-Allmaras model. Of the  $k-\epsilon$  models, the RNG and realizable models, both with enhanced

wall treatment, produced the best results. In fact, the RNG and realizable models almost entirely overlap along the downstream face. Of the  $k-\omega$  models, the SST model with the compressibility option produced the best results. The Spalart-Allmaras model also provides good agreement compared with the other turbulence models. A discussion of and additional comparison of some of the above turbulence models for various flows can be found in Wilcox [10].

All three turbulence models are available as part of Fluent 6.0 and only a brief description of the base models and possible variants is given (see the Fluent User's Guide [11] for a complete description of all turbulence models and variants). The  $k-\epsilon$  RNG model with enhanced wall functions was chosen as the preferred model. However, the Spalart-Allmaras model might be the model of choice if a tradeoff between accuracy and computational time is needed [12]. The reasoning behind choosing the RNG model may not be entirely obvious from Fig. 5 since all four models seem to overpredict the pressure on the trailing half of the upstream disk face and fail to capture the pressure profile on the downstream

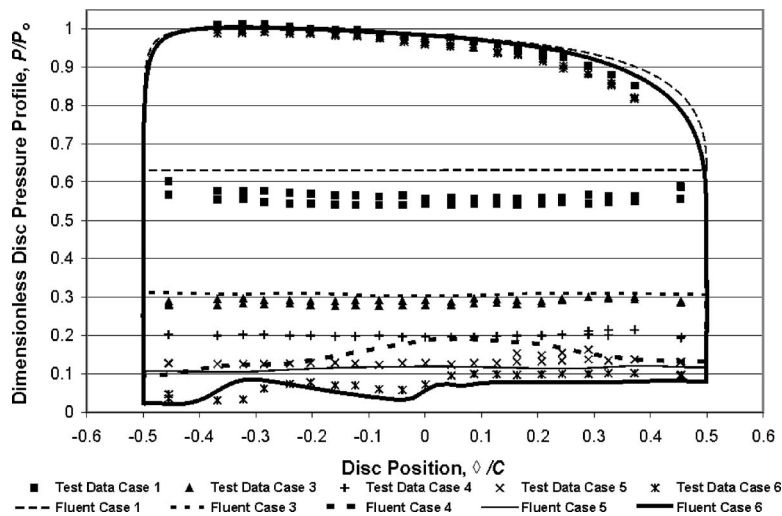
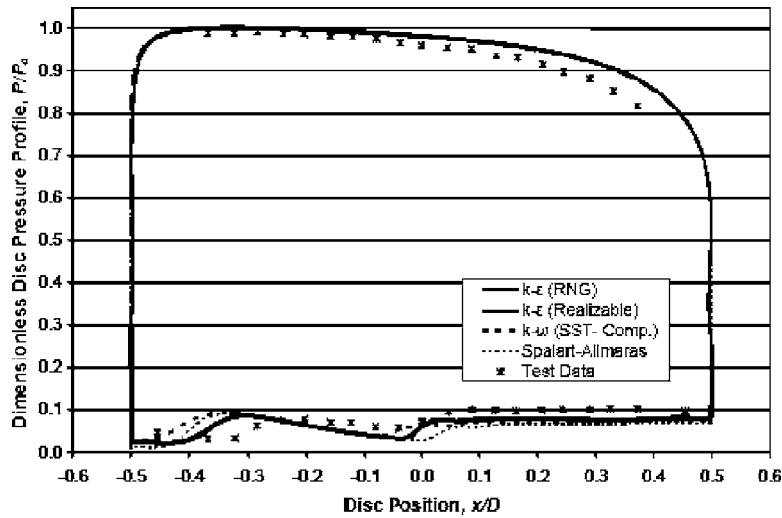


Fig. 4 Evolution of pressure field for the disk at 45 deg for cases 1, 3, 4, 5, and 6



**Fig. 5 Comparison of the dimensionless pressure profiles of the numerical results for the  $k-\epsilon$  RNG,  $k-\epsilon$  realizable,  $k-\omega$  SST, and the Spalart-Allmaras turbulence models. The test data corresponds to a disk at 45 deg and a pressure ratio of 0.24 [1].**

face. Possible explanations for the apparent shared weakness in the turbulence models will be discussed later in greater depth.

### Grid Validation

Different grids were developed using either solely quadrilateral elements (resulting in a structured grid) or a combination of quadrilateral and triangular elements (often called a hybrid or unstructured grid). These grids were used to test the grid spacing, determine the effect of structured versus hybrid grids, test the use of grid adaptation for both structured and unstructured grids, and determine the required downstream duct length to avoid outflow error due to a constant pressure boundary condition. The grid used to perform the numerical analysis for the disk angle of 45 deg is shown in Fig. 6.

Quadrilateral elements were used in the upstream and downstream sections of the computational wind tunnel away from the section of the grid in close proximity to the disk. Triangular elements were used near the disk, except for the elements on the disk face as seen in Fig. 6. The near wall elements on the wind tunnel walls appear as thick dark lines due to their close proximity to each other. Similarly constructed grids were used for the BiCAD at 30, 45, and 60 deg. The node count, for the grid shown in Fig. 6, is given in Table 1. Further discussion on Table 1 is found later in this section.

The grid structure has a strong influence on the quality of the numerical results and computational time required. It is expedient to develop a high-quality mesh that produces both accurate and computationally inexpensive solutions. However, it is usually not possible to have a mesh that accomplishes both. Solutions for structured grids are generally faster than those for unstructured

grids, but require more time to properly construct. Unstructured grids require a higher grid density to reduce numerical diffusion and can be computationally more expensive. Grid adaptation helps to bridge the gap between the two. The benefits and disadvantages of both structured and unstructured grid are discussed in [13]. Grid adaptation is discussed in *Fluent User's Guide* [11] and again in [13].

To illustrate the adaptation process, four adaptations were made based on the pressure and velocity gradients. The values of time-averaged lift, drag, and moment coefficients are shown in Table 1. Meshes 1–5 are hybrid grids, and meshes 6a–6d are adapted structured grids. Meshes 2–4 have been omitted for presentation purposes.

The coefficients  $C_D$  and  $C_L$  are made dimensionless using  $\Delta P_v$  as opposed to the dynamic pressure as was used by Leutwyler and Dalton [14] and are given as

$$C_D = \frac{F_D}{A_c C \Delta P_v} \quad (5)$$

and

$$C_L = \frac{F_L}{A_c C \Delta P_v} \quad (6)$$

A study was conducted using 5, 10, 15, and 30 disk lengths of downstream duct to determine the sensitivity of the placement of the constant pressure outflow boundary on the computation. In general, ten disk lengths were sufficient to achieve reliable results; however, when large fluctuations are present due to vortex shed-

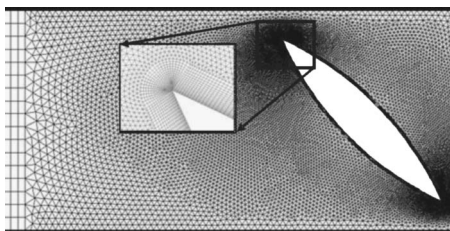


**Fig. 6 The computational grid, mesh 1, used to obtain results for the BiCAD at 45 deg**

**Table 1 The time-averaged coefficients for case 1 with the disk at 45 deg. Higher node count corresponds to a higher level of grid refinement.**

Mesh	$C_L$	$C_D$	$C_M$	Mass flowrate (lbm/s)	Node count
1	0.876	0.942	0.046	0.62	71,926
5	0.876	0.942	0.046	0.63	175,422
6a	0.886	0.924	0.038	0.61	12,333
6b	0.886	0.926	0.040	0.61	13,395
6c	0.880	0.931	0.043	0.62	24,505
6d	0.875	0.921	0.043	0.62	41,315

**Table 2 Pressure ratio matrix used by Morris [1]. Case numbers relate the pressure ratio and disk angle used in this report. Results for the italicized pressure ratios are included herein.**

Case	Disk position		
	30 deg	45 deg	60 deg
1	<i>0.74</i>	<i>0.73</i>	<i>0.72</i>
2	0.58	0.58	0.58
3	0.49	<i>0.48</i>	0.47
4	0.42	<i>0.41</i>	0.41
5	0.33	<i>0.32</i>	0.31
6	<i>0.24</i>	<i>0.24</i>	<i>0.23</i>

ding, as were present for cases 3–5, additional downstream length was needed. The time-averaged torque coefficient for case 4 was nearly identical for 10, 15, and 30 disk lengths; however, the additional duct length resulted in a slight reduction in the fluctuation intensity about the time-averaged value.

## Numerical Results

The numerical results presented here were obtained using a coupled implicit solver, second-order implicit time and second-order in space. The inlet boundary condition was a constant total (or stagnation) pressure inlet, which required specifying the total pressure, the static pressure (used to initialize the flow field), the total (stagnation) temperature, and two flow properties used for the  $k-\epsilon$  turbulence model. A pressure outlet boundary was used for the outflow boundary condition. The outlet boundary requires the exit pressure to be set. In the experimental test section used by Morris, the inlet boundary is four diameters upstream of the disk and the outlet is 15 disk lengths downstream. The backflow stagnation temperature and turbulence values must also be set; however, they are not used unless backflow exists at the exit. The computational wind tunnel wall required setting the wall thermal conditions, roughness height, and roughness constant. The wall thermal boundary condition was modeled using a zero heat-flux boundary. The effect of the roughness height and roughness constant were assumed to be negligible and set to 0 and 0.5, respectively (Fluent default values).

The stagnation pressures ranged from 440 kPa (63.9 psia) to 136 kPa (19.9 psia). The exit pressure was 101 kPa (14.7 psia). The stagnation temperature was 300 K (540 R). Different options were available for the turbulence model. The hydraulic diameter and turbulence intensity options were used and set to 5.15 cm (2.03 in.) and 1%, respectively. The hydraulic diameter was based on the 3-D rectangular wind tunnel of Morris [1]. The density was determined using the ideal gas law, and the viscosity was calculated using the Sutherland viscosity law.

A notable difference between the experimental data and the numerical results occurs along the upstream face as seen in Figs. 3 and 4. The pressure profile along the upstream face has a higher rate of decrease in the positive  $x$  direction for the experimental result than predicted numerically.

Several possibilities may exist to account for the difference between numerical predictions and experimental results. For this computation, there is no sidewall boundary layer and these 2-D calculations, when compared to Morris's data, show a slight difference which can be attributed to the lack of sidewall boundary layer. The discrepancy may also be due to a simple shortcoming in CFD or one of the modeling assumptions, for example, the inexactness of the ideal gas law or the effects of the imposed zero heat flux pipe boundary condition.

The pressure ratios used in the numerical investigation were based on the pressure ratios of Morris [1]. Table 2 relates the case number, disk position, and pressure ratio,  $P_b/P_o$ , that were used in this work and in Morris's research.

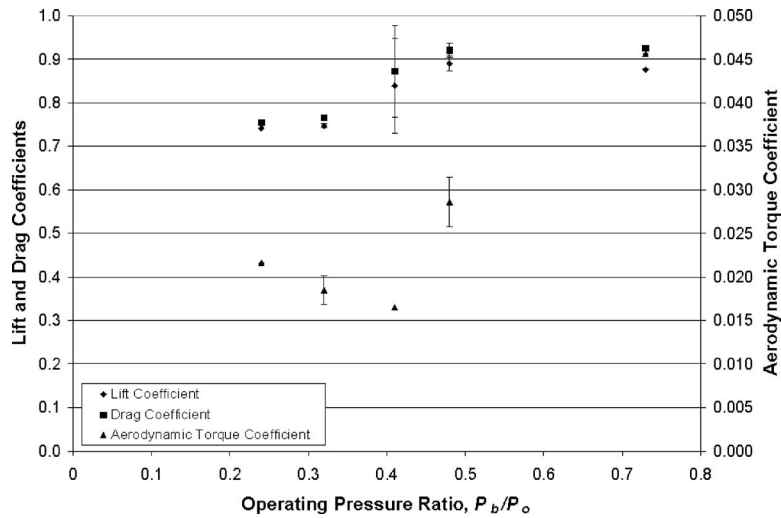
The effect of the disk angle on the pressure profile can be seen in Figs. 2 and 3. Figure 2 shows the pressure profile for case 1 at disk positions of 30, 45, and 60 deg. The numerical predictions for the downstream disk face pressure profiles are higher than reported by Morris [1]. Possible explanations for the difference are similar to those previously stated. Pressure fluctuations for the 60 deg pressure profile due to vortex formations in close proximity to the disk are noticeable. The absence of noticeable fluctuations for the 30 and 45 deg positions indicate that the location of the vortex structures is far enough downstream that they have only a minor influence on the downstream disk pressure profile. The absence of pressure fluctuations in the experimental results is likely due to the use of the scanning valve used to record the pressure measurements.

Figure 3 shows the pressure profiles for case 6 at disk positions of 30, 45, and 60 deg. Reattachment and shock-induced separation are present for the 45 and 60 deg profiles, while the uniform pressure profile for the 30 deg disk suggests that the flow remains unattached. For the disk at 45 and 60 deg, the location of the shock-induced separation point is clearly visible and can be identified as an increase in pressure near the shaft center line ( $x/D \sim 0$ ) along the downstream face followed by a nearly uniform pressure in the positive  $x$  direction. The uniform pressure results from a small recirculation region on the trailing half of the downstream face.

From Figs. 2 and 3, it is clear that, while the disk is in the nearly closed position, the stagnation point remains close to the pipe centerline, and the low flow velocity allows for a nearly uniform pressure profile to exist along the upstream face. As the disk opens toward 60 deg, the stagnation point moves toward the leading edge, away from the shaft centerline, and the profile begins to decrease along the upstream face. The location of the stagnation point has a strong influence on the location of the resultant force and thus affects the aerodynamic torque. Although the resultant force for a nearly closed disk may be large, if the location of the resultant force is near the shaft centerline, which is generally the case, the aerodynamic torque will be minimal. Likewise, a small resultant force acting near the disk edge, away from the shaft center line, may produce a significant aerodynamic torque. Since the bearing torque is dependent on the magnitude of the resultant force alone, there is no direct relationship between the aerodynamic torque and the bearing torque. To calculate the bearing and aerodynamic torque requires knowledge of both the magnitude and location of the resultant force. It should be noted that the geometry of the disk will influence the manner in which the stagnation point moves. For example, the stagnation point on a concave leading face will be different from that of the BiCAD disk which has a convex face. Also the curvature of the downstream face will influence reattachment and separation.

Figures 2–4 show the downstream pressure profiles are not only affected by the pressure ratio, but also by the disk position. Figure 4 illustrates how the pressure profiles change as the pressure ratio is decreased. As the pressure ratio is decreased from 1 to 0.73 (case 1 for the disk at 45°), the flow field begins to deviate from that of an incompressible fluid. The Mach number in the throat is just less than unity and the flow everywhere else is subsonic. The pressure profile for case 1 will be nearly identical to that of an incompressible flow field. As the pressure ratio is further reduced, case 3 is reached and the effect of the pressure reduction is evident. The pressure ratio corresponding to case 3 is between  $P_{r2}$  and  $P_{r3}$ . Cases 4–6 show the transition between  $P_{r2}$  and  $P_{r3}$  and  $P_{r3}$  and  $P_{r4}$ . As the pressure ratio approaches  $P_{r3}$  and finally  $P_{r4}$ , the pressure profile reaches a terminal form (see Fig. 4). A sharp increase in magnitude of the lift, drag, and torque coefficients occurs as the supersonic flow reattaches to the trailing face (Fig. 7).

Pressure fluctuations are noticeable in cases 4 and 5 (Fig. 4) and result in fluctuations in the aerodynamic torque (Fig. 7). The pressure fluctuations impact the instantaneous torque and forces acting



**Fig. 7 Time-averaged lift, drag, and aerodynamic torque coefficients for the disk at 45 deg as a function of the operating pressure ratio**

on the disk. The unsteadiness in the pressure, torque, and forces increases slightly from case 1 to case 3, then sharply from case 3 to 4, and then decrease again from case 5–6. The relatively intense fluctuations in case 4 are due to the formation of vortex structures in close proximity to the downstream face (Fig. 8). The location of the vortex structures differs compared to other pressure ratios. The location of these structures for case 4 is influenced by the expanding gas corresponding to the Mach number in the vena contracta. The expanding gas allows for vortex structures to influence the pressure field as seen in Fig. 10. The sonic flow at the throat accelerates to supersonic as it expands. The effect of the expanding air on the disk pressure profiles can be clearly seen by comparing Figs. 8 and 9 with Figs. 10 and 11. Shown in Figs. 10 and

11 are the Mach number vector field and pressure contours for case 1, respectively.

The effects of the pressure fluctuations are seen on the instantaneous aerodynamic torque coefficients for cases 1, 3, and 5 given in Fig. 12. The fluctuations were strongest for cases 3 and 4 (case 4 is not shown in Fig. 12 due to the high fluctuations) and noticeably less for case 5. The coefficients for case 6 were nearly constant in time due to the reattached flow, which suppressed the vortex formation near the disk face. Intense fluctuations in the torque (such as those present in cases 3 and 4) may cause severe vibration and possibly valve damage. The time-averaged lift and drag coefficients with fluctuation intensity are given in Table 3 as percent of the time-averaged value.

As the pressure ratio is reduced through  $P_{r,3}$ , the attached supersonic flow extends into the downstream region. The distance

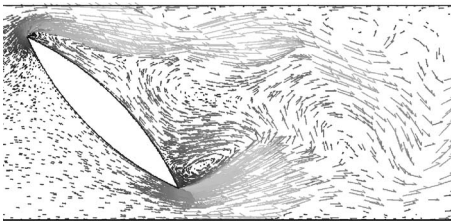


**Fig. 8 The Mach number vector plot for case 4 clearly shows the vortex formations caused by the expanding supersonic flow**

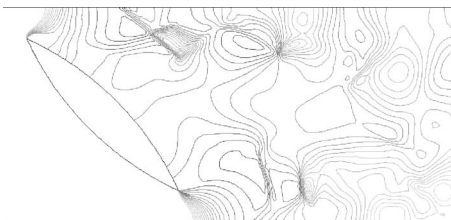


**Fig. 9 The pressure contours for case 4 downstream of the BiCAD due to the vortex formations and oblique shockwaves. The range of pressure values was set to capture the pressure field downstream of the disk and to omit the higher pressure upstream of the disk. The pressure contours range from 13.8 kPa (2 psia) to 124 kPa (18 psia). Low pressures are represented by dark lines and high pressures represented by lighter lines.**

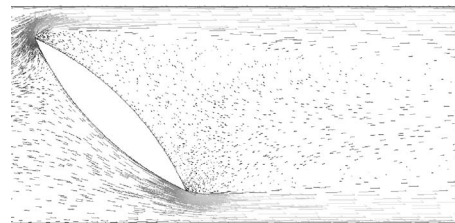


**Fig. 10 The Mach number vector plot for case 1 clearly shows the absence of vortex formations immediately downstream of the disk. The maximum Mach number is 0.85.**

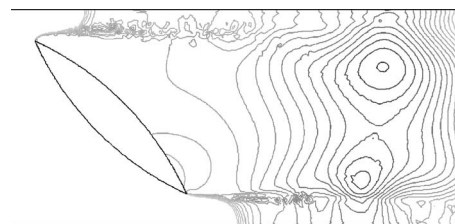


**Fig. 11 The pressure contours for case 1 downstream of the BiCAD. The pressure contours range from 86.5 kPa (12.55 psia) to 87.5 kPa (12.7 psia). The pressure field is nearly uniform in the local vicinity downstream of the disk due to the absence of vortex formations. Low pressures are represented by dark lines and high pressures represented by lighter lines.**

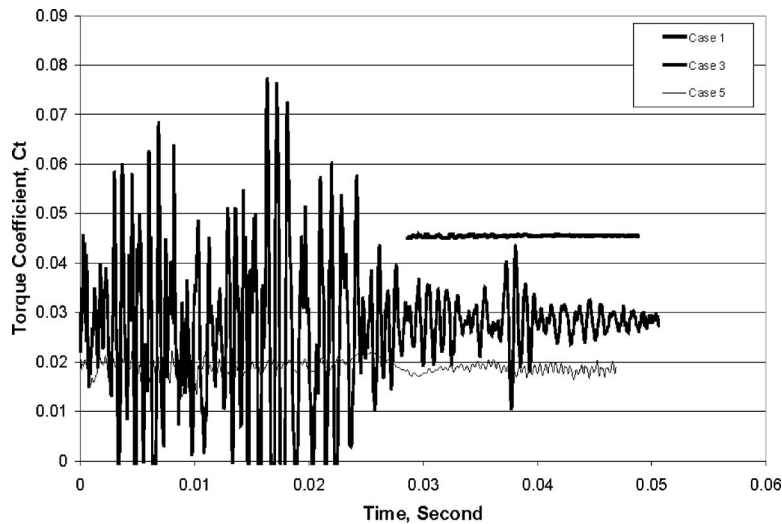


**Fig. 12 Time-dependent coefficients for cases 1, 3, and 5 with the disk at 45 deg**

into the downstream depends on the disk angle and the pressure ratio. However, once  $P_{r4}$  is reached, further decreases in the operating pressure ratio no longer influence the pressure acting on the disk, only the state of the flow in the downstream duct, as such the torque coefficient remains constant. For the BiCAD at 45 deg, the torque coefficient is only a function of the pressure ratio for values greater than  $\sim 0.24$ . The value of  $P_{r4}$  will change based on the disk angle and disk geometry.

The transition between the incompressible and compressible torque coefficients may be useful in developing a model used in predicting torque. It may be possible to predict intermediate values of the coefficients as functions of  $P_b/P_o$  or some other flow parameter.

Preliminary 3-D numerical studies using a rectangular duct for case 1 suggest that the actual physical flow field can be adequately modeled using a 2-D computational grid. An exception would be when strong 3-D effects are present. Strong 3-D effects would obviously include vortex formations that shed periodically and interact with other fluid structures.

## Conclusions

CFD has the potential to be a useful tool in analyzing compressible flow through butterfly valves. Standard turbulence models provide the means for predicting the pressure profiles on the disk surfaces. Furthermore, complex geometries can be modeled using hybrid grids.

Two-dimensional numerical results compare well to the rectangular duct (AR=2.67) experimental data [1], and provide the means for studying complex phenomena such as the effect of the pressure ratio on the downstream flow field and the resulting forces and torque acting on the disk. CFD can also reveal many important features of the flow field that might remain unnoticed

**Table 3 The time-averaged lift and drag coefficient for the BiCAD at 45 deg with the fluctuations about the mean**

Case	$C_L$	$C_D$
1	$0.876 \pm 0.18\%$	$0.925 \pm 0.17\%$
3	$0.880 \pm 2.1\%$	$0.910 \pm 1.8\%$
4	$0.839 \pm 13.0\%$	$0.872 \pm 12.0\%$
5	$0.747 \pm 0.57\%$	$0.765 \pm 0.59\%$
6	$0.741 \pm 0.12\%$	$0.755 \pm 0.11\%$

from experimental results such as vortex proximity, pressure fluctuations, and flow attachment/separation from the pipe walls and disk face.

The behaviors of the pressure profiles were consistent with the experimental data. The flow field is highly dependent on the pressure ratio acting across the valve. The numerical results show that for certain operating pressure ratios, pressure fluctuations were felt by the disk due to the close proximity of vortex structures to the downstream disk face. The vortex location was found to be dependent on the disk angle and the expansion of the fluid. The numerical results also show that the pressure fluctuations cause torque fluctuations. Torque fluctuations may cause severe vibrations to be present in the piping system.

The flow field and torque behavior are strongly dependent on the disk angle and pressure ratio until the pressure ratio is reduced below the fourth characteristic pressure ratio, at which point the flow field in the vicinity of the disk is unaffected by a further decrease of the pressure ratio.

This study can be expanded to include other disk geometries, piping configurations, and disk positions. It can be further expanded to include 3-D geometries as well, which include manufactured disk geometries in more complex piping systems.

## Acknowledgment

The authors would like to thank Kalsi Engineering for the financial and moral support that has made this work possible.

## Nomenclature

- $A_c$  = disk cross-sectional area
- $C$  = disk chord length
- $C_D$  = drag coefficient
- $C_L$  = lift coefficient
- $C_t$  = hydrodynamic torque coefficient
- $C_{tc}$  = aerodynamic torque coefficient
- $C_M$  = moment coefficient
- $C_v$  = flow coefficient
- $d$  = internal pipe diameter
- $D$  = disk diameter
- $F_D$  = drag force
- $F_L$  = lift force
- $K_v$  = valve resistance coefficient
- $P$  = pressure, absolute
- $Q$  = volumetric flow rate
- $T_{aero}$  = aerodynamic torque

$T_{hyd}$  = hydrodynamic torque  
 $V$  = average inlet velocity  
 $\Delta P_v$  = valve pressure drop  
 $\rho$  = fluid density

### Subscripts

$b$  = back pressure  
 $e$  = exit  
 $i$  = inlet  
 $o$  = stagnation  
 $v$  = valve

### References

- [1] Morris, M. J., 1987, "An Investigation of Compressible Flow Through Butterfly Valves," Ph.D. dissertation, University of Illinois, Urbana, IL.
- [2] Crane Co., 1988, "Flow through Valves, Fittings, and Pipes," Technical Paper No. 410, Signal Hill, CA.
- [3] Kalsi Engineering, 745 Park Two Drive, Sugar Land, TX, 77478-2885, 281-240-6500, www.kalsi.com
- [4] Silvester, R. S., 1980, "Torque Induced by Compressible Flow Through a Butterfly Valve with an Asymmetric Disc Design," BHRA Fluid Engineering, RR1602, Project No. R. P. 21373.
- [5] Steele, R., Jr., and Watkins, J. C., 1985, "Containment Purge and Vent Valve Test Program Final Report," EG&G Idaho, Inc., Idaho National Laboratory, NUREG/CR-4141 EG-2374.
- [6] Morris, M. J., and Dutton, J. C., 1991, "An Experimental Investigation of Butterfly-Valve Performance Downstream of an Elbow" ASME J. Fluids Eng., **113**, pp. 81–85.
- [7] Morris, M. J., and Dutton, J. C., 1991, "The Performance of Two Butterfly Valves Mounted in Series," ASME J. Fluids Eng., **113**, pp. 419–423.
- [8] Danbon, F., and Sollic, C., 2000, "Aerodynamic Torque of a Butterfly Valve-Influence of an Elbow on the Time-Mean and Instantaneous Aerodynamic Torque," ASME J. Fluids Eng., **122**, pp. 337–344.
- [9] Sollic, C., and Danbon, F., 1999, "Aerodynamic Torque Acting on a Butterfly Valve. Comparison and Choice of Torque Coefficient," ASME J. Fluids Eng., **121**, pp. 914–919.
- [10] Wilcox, D., 1993, *Turbulence Modeling for CFD*, Griffin Printing, Glendale, CA.
- [11] Fluent, 2001, "Fluent User's Guide," Ver. 6.0.20, Fluent Inc.
- [12] Bernard, P. W., and Wallace, J. M., 2002, *Turbulent Flow*, Wiley, New York.
- [13] Ferziger, J. H., and Peric, M., 2002, *Computational Methods for Fluid Dynamics*, Springer, Berlin.
- [14] Leutwyler, Z., and Dalton, C., 2004, "A CFD Study to Analyze the Aerodynamic Torque, Lift, and Drag Forces for a Butterfly Valve in the Mid-stroke Position," presented at the ASME HT-FED Summer 2004 Conference, Charlotte, NC.



# RANS Simulations of a Simplified Tractor/Trailer Geometry

**Christopher J. Roy**

Aerospace Engineering Department,  
Auburn University,  
211 Aerospace Engineering Building,  
Auburn, AL 36849-5338  
e-mail: cjroy@eng.auburn.edu

**Jeffrey Payne**

Aerosciences and Compressible Fluid Mechanics  
Department,  
Sandia National Laboratories,  
Albuquerque, NM 87185

**Mary McWherter-Payne**

Applied Aerospace Engineering and Advanced  
Concepts Department,  
Sandia National Laboratories,  
Albuquerque, NM 87185

*Steady-state Reynolds-averaged Navier-Stokes (RANS) simulations are presented for the three-dimensional flow over a simplified tractor/trailer geometry at zero degrees yaw angle. The simulations are conducted using a multi-block, structured computational fluid dynamics (CFD) code. The turbulence closure model employed is the two-equation Menter  $k-\omega$  model. The discretization error is estimated by employing two grid levels: a fine mesh of 20 million cells and a coarser mesh of 2.5 million cells. Simulation results are compared to experimental data obtained at the NASA-Ames  $7 \times 10$  ft wind tunnel. Quantities compared include vehicle drag, surface pressures, and time-averaged velocities in the trailer near wake. The results indicate that the RANS approach is able to accurately predict the surface pressure on the vehicle, with the exception of the base region. The pressure predictions in the base region are poor due to the inability of the RANS model to accurately capture the near-wake vortical structure. However, the gross pressure levels in the base region are in reasonable agreement with experiment, and thus the overall vehicle drag is well predicted. [DOI: 10.1115/1.2236133]*

## Introduction

In a typical class 8 tractor/trailer, power required to overcome rolling resistance and accessories increases linearly with vehicle speed, while energy losses due to aerodynamic drag increase with the cube of the speed. At a typical highway speed of 70 mph, aerodynamic drag accounts for approximately 65% of the energy output of the engine [1]. Due to the large number of tractor/trailers on the US highways, even modest reductions in aerodynamic drag can significantly reduce domestic fuel consumption. Lower fuel consumption will result in a reduction in pollution emissions, and, more importantly, a reduced dependence on fossil fuels.

The most common turbulence modeling approach for engineering applications involves solving the Reynolds-averaged Navier-Stokes (RANS) equations [2]. With this approach, the effects of the inherently three-dimensional and time-varying turbulent eddies on the mean flow are modeled and not simulated. These effects of the turbulence, namely increased transport of momentum and energy, are incorporated via the eddy viscosity and eddy conductivity, respectively. In general, it is desirable to obtain steady-state solutions to the RANS equations; the simulation of unsteady RANS flows may only be valid when there is a clear separation between the unsteady scales and the turbulent scales.

At moderate Reynolds numbers, the near wake behind a bluff body is dominated by large-scale vortex shedding. It appears that steady-state RANS is unable to accurately predict such nonstationary flows which are dominated by large-scale shedding. For example, at a Reynolds number of 22,000, steady-state RANS greatly overpredicts the length of the wake recirculation zone [3,4], thereby underpredicting the drag coefficient by nearly 25%. Unsteady RANS for this case performs much better [4,5], even though the separation of scales requirement appears to be violated. At much higher Reynolds numbers, the coherency of the large scale shedding is decreased. Recent work at a Reynolds number of 2 million indicates that steady-state RANS is capable of predicting drag accurately; however, the details of the near-wake flow differ significantly from experiment [6,7].

RANS turbulence models were generally developed to solve simple, zero pressure gradient attached flows. These models often

fail in the presence of large pressure gradients and/or separated flow regions. While the flow over the major part of a tractor/trailer is attached and therefore amenable to RANS modeling, the flow in the base region involves massive separation off of the rear end of the trailer. This separation zone is generally unsteady, with large-scale turbulent structures shedding from the edges. Accurate prediction of the flow in the base region is important since it determines the pressure on the trailer base. The pressure drag is the primary component of the overall aerodynamic drag for tractor/trailer configurations, and small errors in the predicted base pressures can significantly affect the drag calculations. Furthermore, since base drag is a major contributor to the overall aerodynamic drag [8], the details of the near-wake flow may be very important for the accurate simulation of drag reduction devices. The goal of this study is to assess the ability of steady-state RANS turbulence models to accurately predict the wake structure and aerodynamic drag for high Reynolds number tractor/trailer configurations.

## Problem Formulation

The configuration to be examined is the ground transportation system (GTS) studied experimentally at the NASA Ames research center [9]. The GTS geometry is a simplified tractor/trailer configuration that is mounted on four posts in the wind tunnel. A photograph of the GTS in the NASA Ames  $7 \times 10$  ft wind tunnel is shown in Fig. 1. The GTS model is an approximately 1/8 scale class 8 tractor/trailer configuration. The Reynolds number based on the trailer width ( $W=0.3238$  m) is 2 million, approximately one-half of full scale.

The GTS geometry, including the wind tunnel walls, is discretized using two mesh levels: a coarser mesh using 2.5 million cells and a fine mesh using 20 million cells. The grids are generated such that the wall  $y^+$  values on the truck surface, supports, and lower wind tunnel wall are everywhere less than unity on the fine mesh. The side and top wind tunnel walls employ slip flow (i.e., flow tangency) conditions. Structured meshes are employed using point-to-point match up at the block boundaries. The coarse mesh is domain decomposed into 125 zones and is shown in Fig. 2. The fine mesh is decomposed into 1149 zones. Both the coarse and fine meshes are run in parallel using a processor for each zone. The axes employed in the current effort are also shown in Fig. 2, with the  $x$  axis starting at the front of the tractor and running downstream, the  $y$  axis in the vertical direction, and the  $z$  axis starting at the GTS symmetry plane and running spanwise towards the side wall.

Contributed by the Fluids Engineering Division of ASME for publication in the JOURNAL OF FLUIDS ENGINEERING. Manuscript received July 14, 2005; final manuscript received February 16, 2006. Assoc. Editor: Malcolm J. Andrews. Paper presented at The Aerodynamics of Heavy Vehicles: Trucks, Buses and Trains, United Engineering Foundation, December 2–6, 2002.



Fig. 1 GTS model in the NASA Ames 7×10 ft wind tunnel (courtesy of Storms et al. [9])

In order to ensure that the simulated flow matches closely with the flow in the wind tunnel, a number of freestream conditions are matched. First, the inflow plane is set with the appropriate stagnation conditions of the tunnel shown in Table 1. The back pressure at the simulated outflow plane is then adjusted until the reference pressure located at ( $x/W=4.47$ ,  $y/W=2.59$ , and  $z/W=-4.7$ ) on the tunnel side wall reaches the wall reference pressure given in the table. The pressure coefficient is defined as

$$C_p = \frac{p - p_\infty}{\frac{1}{2} \rho_\infty u_\infty^2}$$

where  $p_\infty$  is the reference pressure given in Table 1 and the freestream density and velocity are found by assuming isentropic

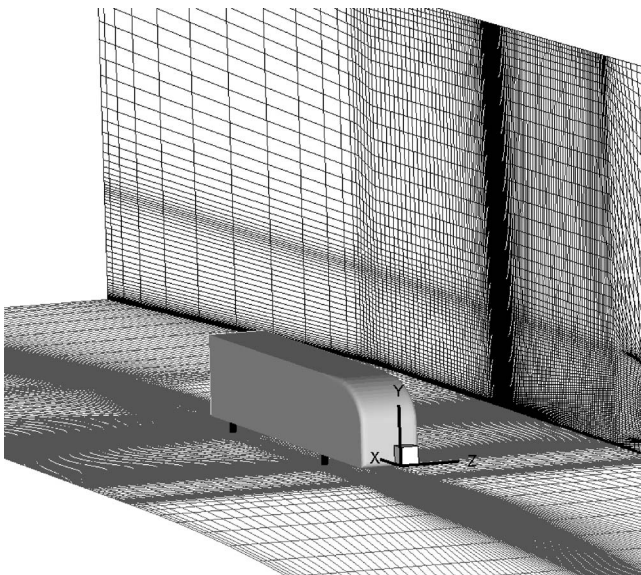


Fig. 2 Coarse grid computational mesh for the GTS geometry

Table 1 Freestream conditions used in the simulations

Tunnel condition	Value
Stagnation pressure	102,653.2 N/m <sup>2</sup>
Stagnation temperature	282 K
Wall reference pressure	97,582 N/m <sup>2</sup>
Reference Mach number	0.27
Back pressure	100,136.0 N/m <sup>2</sup>
Tunnel floor BL thickness	0.053 m
Wall temperature BC	adiabatic

flow from the plenum at the reference Mach number. The pressure coefficient on the wind tunnel side-wall from the fine grid simulation is compared to experimental values at two vertical stations in Fig. 3. Excellent agreement is shown for the tunnel wall pressure (note the expanded scale for  $C_p$ ). The boundary layer on the bottom wall was measured in a tunnel-empty configuration (i.e., without the GTS model inserted into the tunnel). Sample boundary layer profiles upstream of the GTS model from the simulation using the fine mesh are compared to the tunnel empty-profile from the experiment in Fig. 4. The simulation predicts a profile similar to the experiment; at least until the presence of the GTS model is seen approximately 0.3 m upstream.

### Numerical Formulation

**CFD Code.** The CFD code is SACCARA, the Sandia Advanced Code for Compressible Aerothermodynamics Research and Analysis, and was developed from a parallel distributed memory version [10] of the INCA code, originally written by Amtec Engineering. This code is used to solve the Navier-Stokes equations for conservation of mass, momentum, energy, and turbulence transport in three-dimensional form. The governing equations are discretized using a cell-centered finite-volume approach. A finite-volume form of Yee's symmetric TVD scheme [11] is employed. This flux scheme is second-order accurate and reduces to a first-order Roe-type flux [12] in regions of large gradients based on a *minmod* limiter. The viscous terms are discretized using central differences. The SACCARA code employs a massively parallel distributed memory architecture based on multi-block structured grids. The solver is a lower-upper symmetric Gauss-Seidel scheme [13], which provides for excellent scalability up to thousands of processors. A number of code verification studies

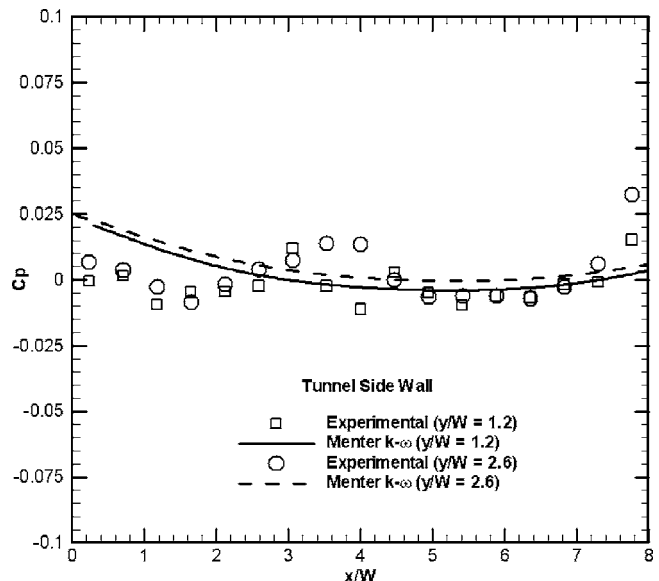


Fig. 3 Wind tunnel side-wall pressure

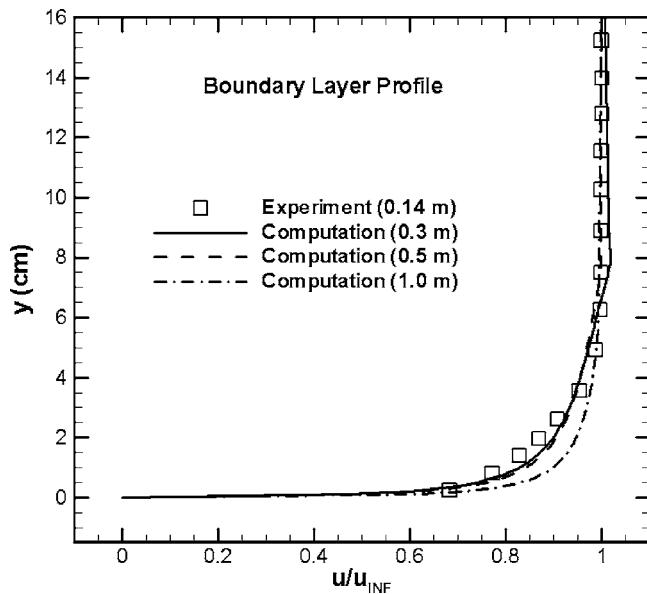


Fig. 4 Wind tunnel floor boundary layer profiles

have been performed that give confidence that the code is free from coding mistakes including comparison to established numerical benchmark solutions and code to code comparisons [14].

**Turbulence Model.** The turbulence model examined in the current work is the baseline (BSL) version of Menter's  $k-\omega$  turbulence model [15]. This is a hybrid model that uses a blending function to combine the best aspects of the  $k-\omega$  and the  $k-\epsilon$  turbulence models. Near solid walls, a  $k-\omega$  formulation is used that allows integration to the wall without any special damping or wall functions. Near the outer edge of the boundary layer and in shear layers, the model blends into a transformed version of the  $k-\omega$  formulation, thus providing good predictions for free shear flows. This model also shows less sensitivity to freestream turbulence quantities than other  $k-\omega$  formulations. The turbulence model was integrated to the wall in order to avoid model validation issues associated with wall functions.

### Numerical Accuracy

Before the simulation results can be compared to experimental data, the numerical accuracy of the solutions must be assessed. For the steady-state computations examined herein, the solution accuracy will be judged by examining the iterative convergence of the solutions to steady state as well as the discretization error.

**Iterative Convergence.** The solutions are marched (iterated) in pseudo-time until a steady-state answer is obtained. Iterative convergence is assessed by examining the steady-state residuals of the momentum equations. The steady-state residual is defined by plugging the solution at the current iteration into the discretized form of the steady-state governing equations (omitting the time derivative). For the SACCARA code, the iterative error in the solution tends to drop in a similar fashion as the residuals [16]. The coarse grid residuals were converged by approximately seven orders of magnitude, while the fine grid residuals were converged by approximately six orders of magnitude. This level of residual convergence is sufficient to ensure that the iterative error is small relative to the discretization error to be discussed below.

**Discretization Error.** The discretization error is estimated by generating solutions on two mesh levels. Since the coarse mesh is determined by eliminating every other gridline from the fine mesh, the grid is consistently refined throughout the entire domain, and Richardson extrapolation can be used to estimate the

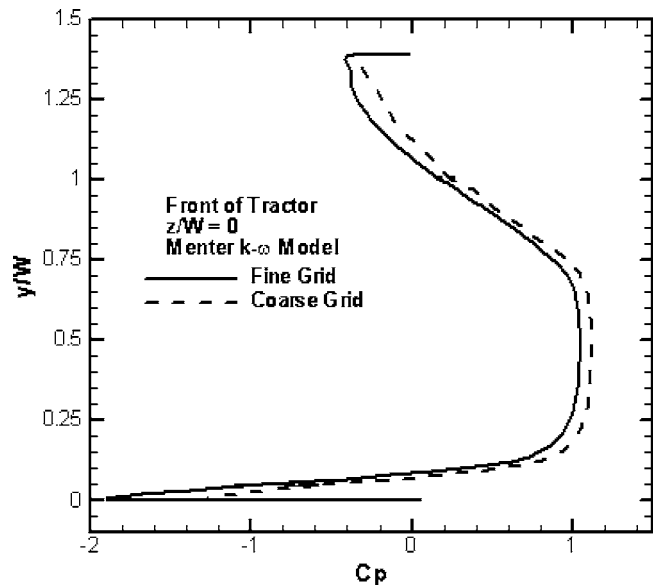


Fig. 5 Centerline pressure on the front of the GTS model (coarse and fine meshes)

exact solution. This extrapolated solution is then used to judge the error in the fine grid solution. The coarse and fine grid results for surface pressure on the front of the tractor along the vertical centerline are presented in Fig. 5. While the results do show some sensitivity to grid refinement, the estimated error in the fine grid solution found from Richardson extrapolation is approximately  $\pm 0.05$  in terms of  $C_p$ . Coarse and fine grid results for the centerline base of the trailer are shown in Fig. 6, with the maximum error estimated to be less than  $\pm 0.01$  in terms of  $C_p$  (note the expanded scale for  $C_p$  in this figure). These findings indicate that the fine grid simulation is sufficiently accurate to allow meaningful comparisons to the experimental data. While coarser grids are typically used for engineering studies where trends are of interest, extremely fine grids are employed here to allow a true assessment of the Menter BSL turbulence model in the limit as the cell size approaches zero (i.e., the solution to the continuous partial differential equations).

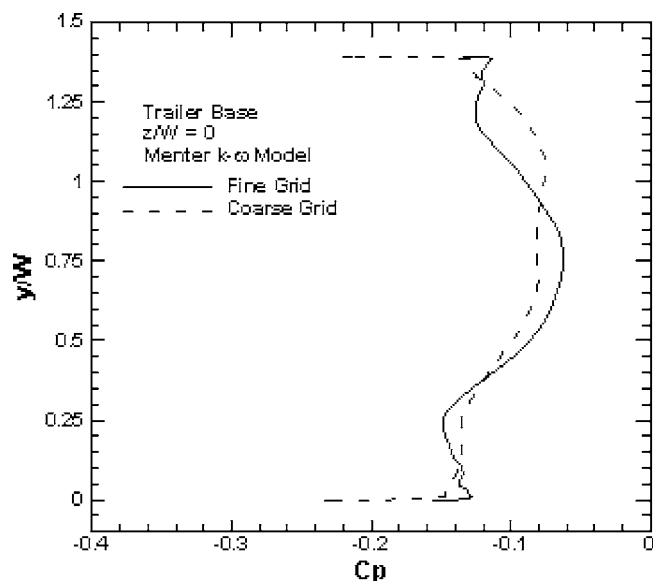


Fig. 6 Centerline pressure on the base of the trailer (coarse and fine meshes)

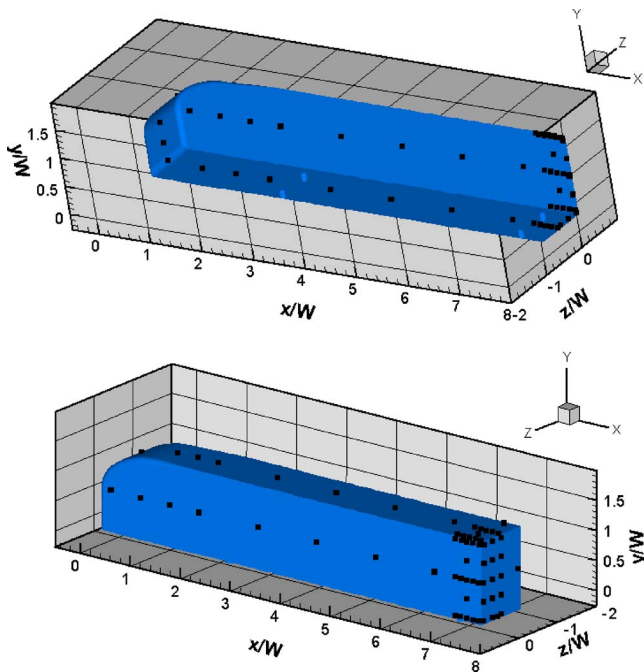


Fig. 7 Location of experimental pressure taps [9]

### Surface Comparisons

**Surface Pressure.** The experimental data obtained by Storms et al. [9] include numerous static pressure ports on all sides of the GTS geometry as illustrated in Fig. 7. The surface pressure for the Menter  $k-\omega$  turbulence model using the fine mesh is compared to experimental data on the top and bottom of the GTS geometry in Fig. 8. The scale shown for the pressure coefficient is enlarged to show the details of the pressure variations along the body. The pressure predictions along the top of the GTS are in good agreement with the experimental data with maximum differences within  $\pm 0.015 \Delta C_p$ . The pressure is also well predicted along the bottom of the model, with the exception of the area behind the rear posts. Flow separation occurs behind the cylindrical posts.

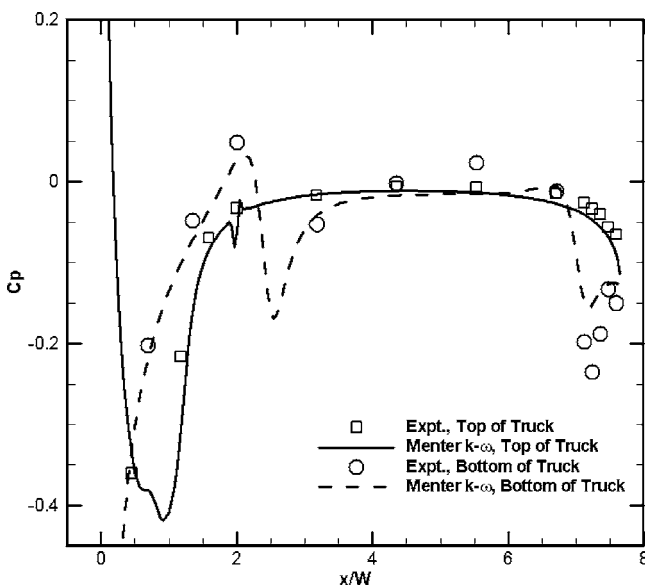


Fig. 8 Centerline surface pressures on the top and bottom of the GTS model

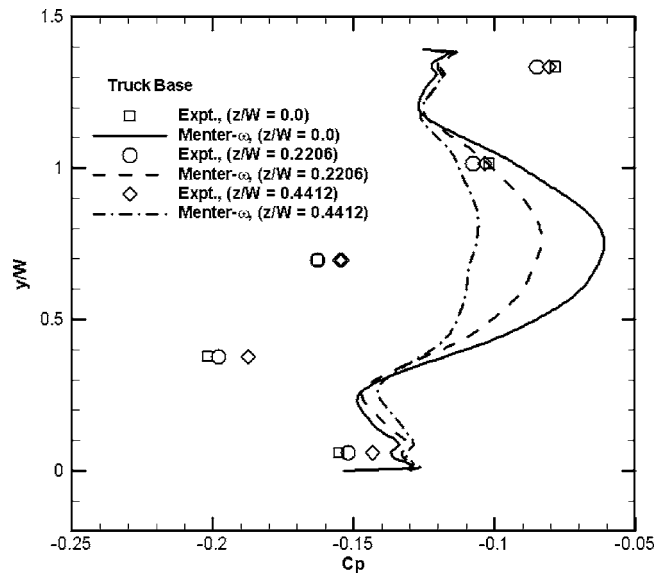


Fig. 9 Surface pressure on the trailer base for various spanwise locations

Due to the presence of the tunnel floor and GTS model lower surface boundary layers, the local Reynolds number based on the post diameter is on the order of 100,000. There is strong evidence that the steady-state RANS models perform poorly for Reynolds numbers near 22,000 [3]. Therefore, the fact that the current simulations overpredict the pressure in the wake of the post is not surprising.

Vertical pressure distributions are presented for the base of the trailer at three different spanwise locations in Fig. 9. The Menter  $k-\omega$  model does a reasonable job of matching the experimentally measured pressure levels; however, the details of the pressure variations are not well predicted. The simulations show a much more symmetric pressure profile from top to bottom at all three spanwise locations, while the experimental data show a steady increase in the pressure moving from  $y/W=0.4$  to the top of the base. The inability of the RANS model to accurately predict the details of the base pressure suggests that the details of the time-averaged, near-wake structure are probably not captured accurately.

**Aerodynamic Drag.** The aerodynamic drag prediction using the Menter  $k-\omega$  turbulence model is presented in Table 2 along with the experimentally measured value. Also shown in the table is the drag predicted with the Spalart-Allmaras one-equation turbulence model [17] using the same 20 million cell grid [6]. These drag results (both predicted and experimental) are for the GTS model only and do not include the support posts. The Menter  $k-\omega$  results are approximately 7.5% higher than the experimental value, while the Spalart-Allmaras results are nearly 50% higher. The overprediction of the drag with the Spalart-Allmaras model is due to the poor prediction of the base pressure and corresponding underpredictions of the extent of the near wake [6]. Also shown in the table is the estimated uncertainty in the experimental drag coefficient [9], and the estimated numerical error for the fine grid

Table 2 Drag coefficients

	Drag coefficient, $C_D$	Estimated uncertainty/error
Experiment [9]	0.25	$\pm 0.01$
Menter $k-\omega$	0.298	$\pm 0.06$
Spalart-Allmaras [6]	0.413	...

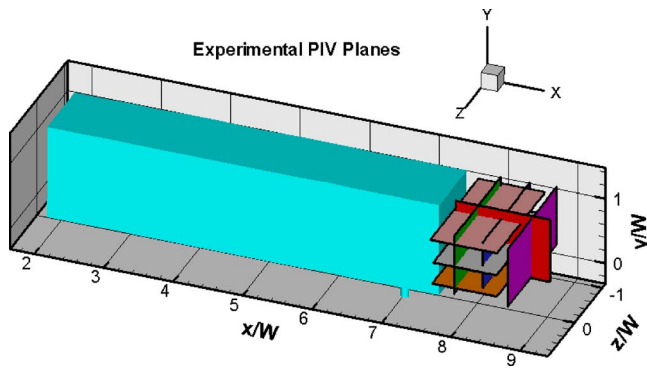


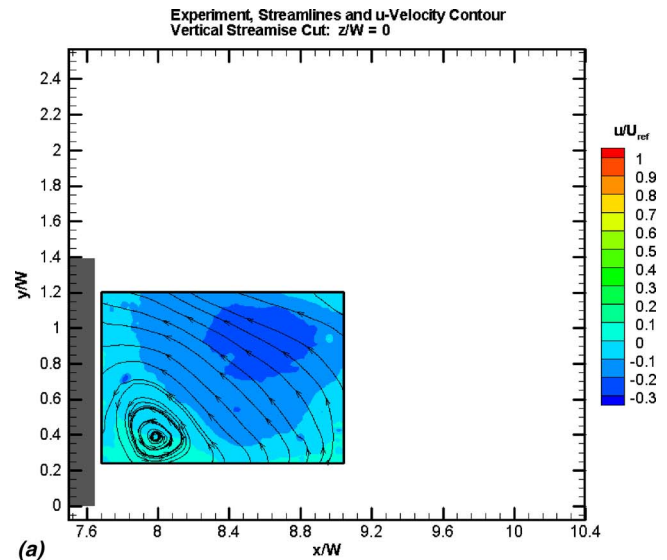
Fig. 10 Locations of experimental PIV planes [9]

Menter  $k-\omega$  simulation. This numerical error estimate is determined by performing Richardson extrapolation using the coarse and fine grid drag coefficients of 0.474 and 0.298, respectively. The resulting third-order accurate extrapolated value for the drag coefficient using the Menter  $k-\omega$  model is 0.239, which is very close to the experimentally measured value. These results suggest that while RANS does not accurately predict the pressure distributions in the base region, the pressure levels are close enough to provide good estimates of the vehicle drag. This conclusion is further supported by the work of Salari et al. [7]. It is unclear whether these findings will extend to drag reduction devices that operate by modifying the wake structure (e.g., boat tails), which as we shall see is not predicted correctly by the RANS approach.

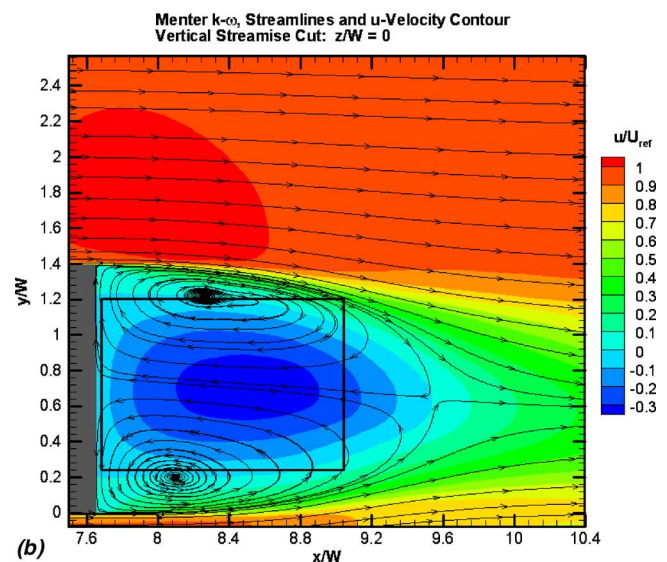
**Field Comparisons.** Velocity data are available from PIV measurements performed at the NASA Ames  $7 \times 10$  ft wind tunnel [9]. These PIV data represent a time-averaged picture of the flow in the wake regions immediately behind the trailer base, and the various planes with available experimental data are shown in Fig. 10. Two of these planes will be examined in this paper: the streamwise vertical cut located at the GTS centerline (side view) and a horizontal streamwise cut located at  $y/W=0.7$  (top view).

**Vertical Streamwise Cut (Side View).** Two-dimensional streamlines (using the  $x$  and  $y$  components of velocity only) based on the experimental PIV data are shown in a vertical streamwise cut through the wake centerline ( $z/W=0$ ) in Fig. 11(a). The flow is from left to right, with the base of the trailer shown on the left. The figure also gives contour plots of the axial component of velocity normalized by a reference velocity outside of the GTS near wake (i.e., a local freestream velocity) [9]. A large, counter-clockwise-rotating vortex is centered at approximately  $x/W=8$ ,  $y/W=0.4$ . Also, the presence of a clockwise-rotating vortex is suggested somewhere near the top right corner of the PIV window by the vertical nature of the streamlines at this location. A similar view of the 2D streamlines from the fine grid computations using the Menter  $k-\omega$  model is shown in Fig. 11(b), with the PIV window also given for reference. The RANS computations predict a much more symmetric pair of vortices than is indicated from the experimental data. The wake structure evident in this figure is consistent with the base pressure predictions given in Fig. 9, where low pressures correspond to large vertical velocity magnitudes along the base, and high pressures correspond to stagnation points.

The same pair of streamlines are given in Figs. 12(a) and 12(b), but the contour variable is now the vertical ( $y$ ) component of velocity. The experimental PIV data show a region of high vertical velocity centered about  $x/W=8.7$ ,  $y/W=0.6$  (Fig. 12(a)), while the RANS computations predict lower vertical velocities centered lower and farther downstream (Fig. 12(b)). Also shown in Fig. 12(a) are three streamwise locations ( $x/W=8.0, 8.4,$  and  $8.9$ ) where detailed comparisons between the computations and the



(a)

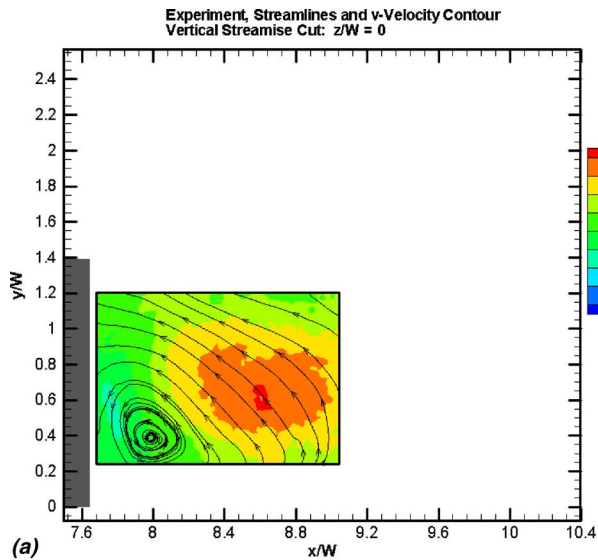


(b)

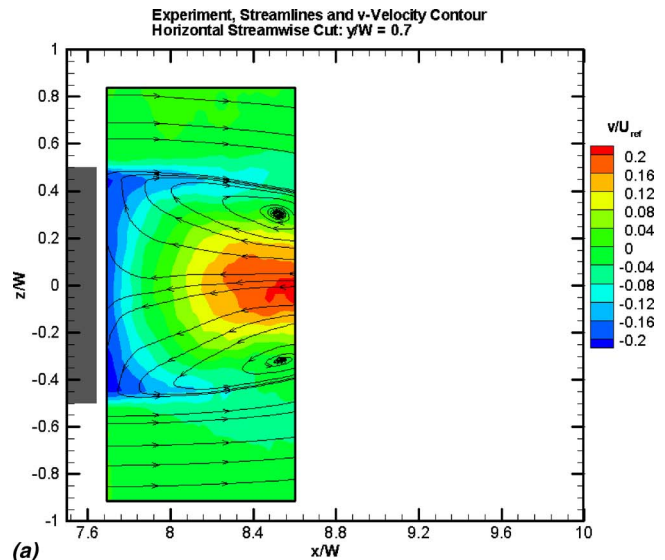
Fig. 11 2D streamlines and contours of streamwise velocity in (a) experiment and (b) computations: vertical streamwise cut ( $z/W=0$ )

data will be performed. These profiles of vertical velocity are presented in Fig. 13 and highlight again the symmetric nature of the computational predictions and the asymmetric nature of the experimental data. Due to the downstream location of the upper, clockwise-rotating vortex in the experiment, a positive, upwards-moving vertical velocity is shown at all three streamwise locations.

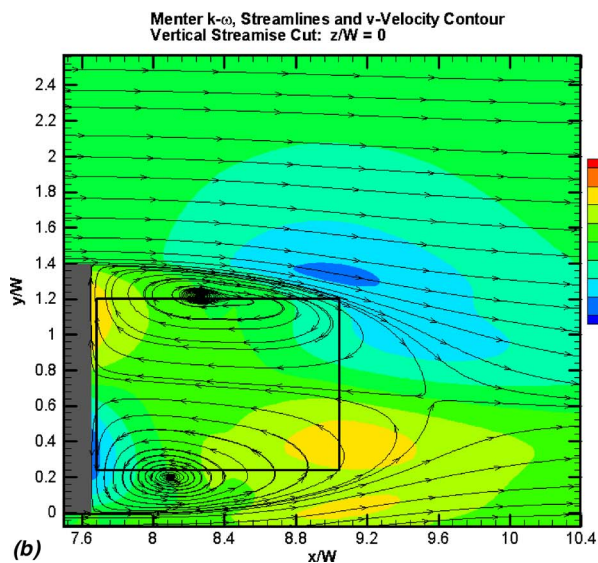
**Horizontal Streamwise Cut (Top View).** Experimental PIV results for 2D streamlines in a horizontal streamwise cut through the wake at  $y/W=0.7$  are shown in Fig. 14(a), along with contours of the vertical (out of plane) velocity component. Two counter-rotating, symmetric vortices are evident at  $x/W=8.5$ . The corresponding computational streamlines using the Menter  $k-\omega$  model are given in Fig. 14(b). In this case, the location of the vortices is accurately predicted by the RANS model, suggesting that the  $x$  and  $z$  components of velocity are predicted accurately (although not shown, this is indeed the case). However, the vertical velocity component in the experiment shows strong upward motion between the vortices and strong downward motion near the base, while the computations predict vertical velocities near zero for the entire plane. This result is consistent with the incor-



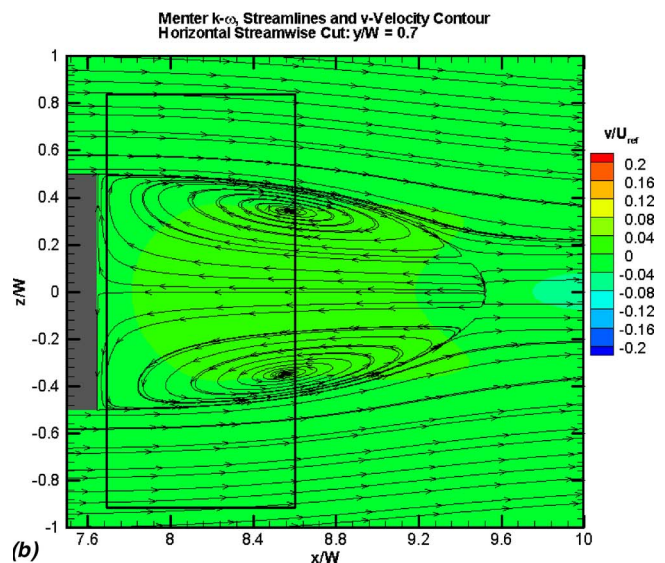
(a)



(a)



(b)



(b)

Fig. 12 2D streamlines and contours of vertical velocity in (a) experiment and (b) computations: vertical streamwise cut ( $z/W=0$ )

Fig. 14 2D streamlines and contours of vertical velocity in (a) experiment and (b) computations: horizontal streamwise cut ( $y/W=0.7$ )

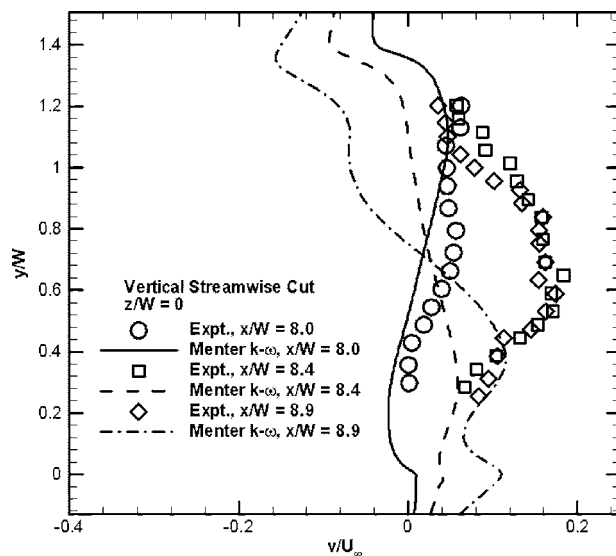


Fig. 13 Profiles of vertical velocity extracted from the vertical streamwise cut ( $z/W=0$ )

rectly predicted, symmetric nature of the vortices from top to bottom shown in Fig. 12(b), where the  $y/W=0.7$  location occurs along the stagnation streamline. The vertical velocity is extracted from the three axial locations indicated in Fig. 14(b), and the resulting comparisons are presented in Fig. 15. As expected, the computations predict vertical velocities near zero at all three locations, while the experimental data indicates downward flow near the base ( $x/W=7.8$ ) and upwards flow farther downstream ( $x/W=8.2$  and  $8.5$ ).

## Conclusions

Steady-state RANS simulations were conducted for the flow over the GTS geometry at a Reynolds number of 2 million. The numerical accuracy of the computed flowfields was assessed by performing the simulations on multiple grids. Steady-state RANS results using the Menter  $k-\omega$  turbulence model gave good agreement with the experimental data for surface pressure everywhere except in the base region, as well as good drag predictions. In the base region, the gross pressure levels were captured, but the predicted pressure distributions were symmetric in the vertical direction, contrary to the experimental data. The symmetry of the wake

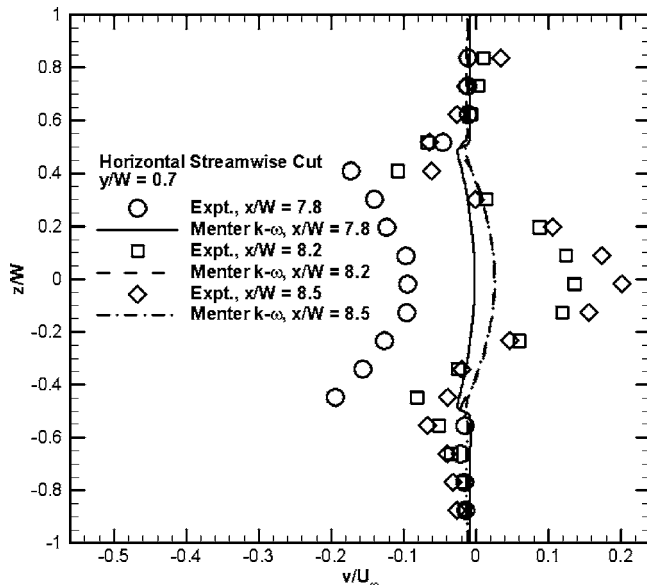


Fig. 15 Profiles of vertical velocity extracted from the horizontal streamwise cut ( $y/W=0.7$ )

structure for this case has also been observed with other turbulence models [6,7]. Similarly, the RANS approach was unable to accurately predict the details of the flow in the near-wake region, predicting a symmetric pair of counter-rotating vortices in the vertical centerline plane. The experimental PIV data gave a much more asymmetric flow structure in this plane, with the upper, clockwise-rotating vortex apparently centered at least a trailer-width downstream of the predicted location (outside of the PIV window).

While the steady-state Menter BSL turbulence model was shown to provide good drag estimates for this case at Reynolds number of 2 million, it has been demonstrated to give poor drag predictions at a lower Reynolds number of 22,000 due to the fact that large-scale nonturbulent shedding events are not modeled accurately [3]. Further study is required to identify the Reynolds number range where the Menter BSL model is valid. Furthermore, the current findings suggest that while RANS models may be able to accurately predict vehicle drag for baseline configurations, they will likely be unable to accurately predict the effects of drag reduction devices, which are designed to alter the near-wake structure. Accurate predictions of the near-wake structure will require more advanced turbulence modeling approaches such as large eddy simulation where the larger turbulent scales are resolved and the smaller scales are modeled.

## Acknowledgment

The authors would like to thank Kambiz Salari of Lawrence Livermore National Laboratory for his contributions in the area of mesh generation. We would also like to thank J. Chad Brown for his aid in preparing the figures. This work was supported by Sandia National Laboratories and the Department of Energy Office of Heavy Vehicles Technologies under the direction of Sidney Diamond and Jules Routbort. Sandia is a multiprogram laboratory operated by Sandia Corporation, a Lockheed Martin Company, for the United States Department of Energy's National Nuclear Security Administration under Contract No. DE-AC04-94AL85000.

## References

- [1] McCallen, R., Couch, R., Hsu, J., Browand, F., Hammache, M., Leonard, A., Brady, M., Salari, K., Rutledge, W., Ross, J., Storms, B., Heineck, J. T., Driver, D., Bell, J., and Zilliac, G., 1999, "Progress in Reducing Aerodynamic Drag for Higher Efficiency of Heavy Duty Trucks (Class 7-8)," SAE Paper No. 1999-01-2238.
- [2] Wilcox, D. C., 1998, *Turbulence Modeling for CFD*, 2nd ed., DCW Industries, Inc., La Canada, CA.
- [3] Roy, C. J., DeChant, L. J., Payne, J. L., and Blotner, F. G., 2003, "Bluff-Body Flow Simulations Using Hybrid RANS/LES," AIAA Paper No. 2003-3889.
- [4] Iaccarino, G., Ooi, A., Durbin, P. A., and Behnia, M., 2003, "Reynolds Averaged Simulation of Unsteady Separated Flow," *Int. J. Heat Fluid Flow*, **24**, pp. 147-156.
- [5] Rodi, W., 1997, "Comparison of LES and RANS Calculations of the Flow Around Bluff Bodies," *J. Wind. Eng. Ind. Aerodyn.*, **69-71**, pp. 55-75.
- [6] Roy, C. J., Payne, J. L., McWherter-Payne, M. A., and Salari, K., 2004, "RANS Simulations of a Simplified Tractor/Trailer Geometry," *Lecture Notes in Applied and Computational Mechanics, Vol. 19: The Aerodynamics of Heavy Vehicles: Trucks, Buses, and Trains*, R. McCallen, F. Browand, and J. Ross, Eds., Springer, Berlin, Germany, pp. 207-218.
- [7] Salari, K., Ortega, J. M., and Castellucci, P. J., 2004, "Computational Prediction of Aerodynamic Forces for a Simplified Integrated Tractor-Trailer Geometry," AIAA Paper No. 2004-2253.
- [8] Cooper, K. R., 2003, "Truck Aerodynamics Reborn—Lessons from the Past," SAE Paper No. 2003-01-3376.
- [9] Storms, B. L., Ross, J. C., Heineck, J. T., Walker, S. M., Driver, D. M., and Zilliac, G. G., 2001, "An Experimental Study of the Ground Transportation System (GTS) Model in the NASA Ames 7-by 10-ft Wind Tunnel," NASA TM-2001-209621.
- [10] Wong, C. C., Soetrisno, M., Blotner, F. G., Imlay, S. T., and Payne, J. L., 1995, "PINCA: a Scalable Parallel Program for Compressible Gas Dynamics With Nonequilibrium Chemistry," Sandia National Laboratories Report SAND 94-2436, Albuquerque, NM.
- [11] Yee, H. C., 1987, "Implicit and Symmetric Shock Capturing Schemes," NASA-TM-89464.
- [12] Roe, P. L., 1981, "Approximate Riemann Solvers, Parameter Vectors, and Difference Schemes," *J. Comput. Phys.*, **43**, pp. 357-372.
- [13] Yoon, S., and Jameson, A., 1988, "An LU-SSOR Scheme for the Euler and Navier-Stokes Equations," AIAA Paper No. 87-0600.
- [14] Roy, C. J., McWherter-Payne, M. A., and Oberkampf, W. L., 2003, "Verification and Validation for Laminar Hypersonic Flowfields Part I: Verification," *AIAA J.*, **41**(10), pp. 1934-1943.
- [15] Menter, F. R., 1994, "Two-Equation Eddy-Viscosity Turbulence Models for Engineering Applications," *AIAA J.*, **32**, pp. 1598-1605.
- [16] Roy, C. J., and Blotner, F. G., 2003, "Methodology for Turbulence Model Validation: Application to Hypersonic Transitional Flows," *J. Spacecr. Rockets*, **40**(3), pp. 313-325.
- [17] Spalart, P. R., and Allmaras, S. R., 1994, "A One-Equation Turbulence Model for Aerodynamic Flows," *Rech. Aerosp.*, **1**, pp. 5-21.

# Experimental Study of the Flow in a Simulated Hard Disk Drive

Charlotte Barbier

Joseph A. C. Humphrey<sup>1</sup>  
e-mail: jach@virginia.edu

Eric Maslen

Department of Mechanical and Aerospace  
Engineering,  
School of Engineering and Applied Science,  
University of Virginia,  
Charlottesville, VA 22904

*Instantaneous circumferential and radial velocity components of the air flowing past a symmetrical pair of suspension/slider-units (SSUs) attached to an E-Block/arm were measured in a specially designed corotating disk apparatus simulating a hard disk drive (HDD) using the particle image velocimetry technique. The geometrical dimensions of the components in the apparatus test section were scaled up by a factor of two, approximately, relative to those of a nominal 3½ inch HDD. Most of the measurements were obtained on the interdisk midplane for two angular orientations of the arm/SSUs: (a) One with the tip of the SSUs near the hub supporting the disks; (b) another with the tip of the SSUs near the rims of the disks. Data obtained for disk rotational speeds ranging from 250 to 3000 rpm (corresponding to 1250 to 15,000 rpm, approximately, in a 3½ inch HDD) were post-processed to yield mean and rms values of the two velocity components and of the associated shear stress, the mean axial vorticity, and the turbulence intensity (based on the two velocity components). At the locations investigated near the arm/SSUs, and for disk rotational speeds larger than 1500 rpm, the mean velocity components are found to be asymptotically independent of disk speed of rotation but their rms values appear to still be changing. At two locations 90 and 29 deg, respectively, upstream of the arm/SSUs, the flow approaching this obstruction displays features that can be attributed to the three-dimensional wake generated by the obstruction. Also, between these two locations and depending on the angular orientation of the arm/SSUs, the effect of the obstruction is to induce a three-dimensional region of flow reversal adjacent to the hub. Notwithstanding, the characteristics of the flow immediately upstream and downstream of the arm/SSUs appear to be determined by local flow-structure interactions. Aside from their intrinsic fundamental value, the data serve to guide and test the development of turbulence models and numerical calculation procedures for predicting this complex class of confined rotating flows, and to inform the improved design of HDDs.*  
[DOI: 10.1115/1.2236135]

## The Problem of Interest

**Background and Prior Work.** The trend in the computer disk drive industry is to manufacture smaller HDDs. The trend is driven by the desire to miniaturize drives for hand-held devices and other small-scale applications while maintaining high rates of electronic information transfer. It has been facilitated by major advances made in the area of electromagnetic recording materials and by the development of technologies that allow very high data storage densities and transfer rates [1]. The disks in current nominal 3½ in drives typically have information densities of 100 K tracks per inch (TPI) and rotate between 4200 and 15,000 rpm. Future 1 in drives are expected to have track densities upwards of 100 kTPI and to rotate between 3600 and 4500 rpm. The combination of high track densities with relatively high disk speeds of rotation contributes to the problem of magnetic head positioning error and associated track misregistration due to flow-induced vibrations of the arm/SSUs supporting the magnetic heads. As a consequence, there is a need to better understand and render predictable the flow-structure interactions arising in these devices.

The unobstructed flow in the space between a pair of disks corotating in a cylindrical enclosure has been the subject of considerable research. Measurements [2,3] and calculations [4,5] reveal a pair of toroidally shaped counter-rotating vortices in the interdisk space that are induced by the centrifugally driven flow arising in the thin Ekman layers next to the rotating disk surfaces. A circumferential instability corrugates these vortices to create

circumferentially distributed foci with axial component of vorticity that rotate at about 75–80% of the disk angular velocity. Nearer the hub clamping the disks, the interdisk flow approaches solid body rotation. In contrast, because of the shearing action by the enclosure wall, the flow near the rims of the disks transitions to the turbulent regime with increasing disk angular velocity and is convected radially inwards along the interdisk midplane by the pressure-induced force opposing the centrifugal force.

Relative to the unobstructed flow case, much less information exists in the archival literature pertaining to the obstructed flow between a pair of disks corotating in an enclosure. (Figs. 2 and 3, discussed further below, illustrate this flow configuration and define the geometrical meanings of “E-block,” “arm,” and “SSU” in the context of the present investigation.) Exceptions are the experimental studies of [6–10] and the analytical and numerical investigations of [11–18]. The experimental studies are mainly focused on the effects of a single, relatively large obstruction in the space between the disks that is meant to simulate the effects of an actuator arm on the flow. Such a geometry alone fails to capture the effects of the SSUs attached to it, or of the flow-mediated interactions that arise between the SSUs and the arm. Notwithstanding, these studies show that, depending on its size and relative angular orientation: (i) The flow approaching a simulated actuator arm can accelerate significantly, and in a direction parallel to the arm, as a consequence of the blockage the obstruction creates in the interdisk space; (ii) the flow at the tip of the arm where the suspensions attach is strongly sheared, with the possible formation of highly vortical layers; (iii) if the blockage presented by the arm is large enough, it can induce a three-dimensional region of flow reversal adjacent to the hub and upstream of the obstruction.

The numerical studies present more detailed impressions of the

<sup>1</sup>Corresponding author.

Contributed by the Fluids Engineering Division of ASME for publication in the JOURNAL OF FLUIDS ENGINEERING. Manuscript received October 13, 2005; final manuscript received March 13, 2006. Assoc. Editor: James A. Liburdy.



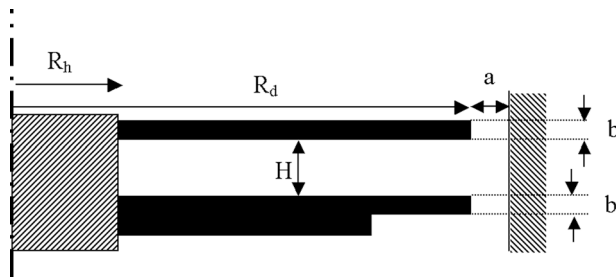


**Fig. 1** Side view of an unobstructed portion of the experimental test section with relevant geometrical variables defined. The top disk is made of glass and the bottom one of anodized aluminum. They are both clamped to a hub of radius  $R_h$  and the unit rotates about its central axis. The extra thickness of the bottom disk minimizes any tendency to wobble. The enclosure walls are made of Plexiglass. In this study:  $R_h=28.6$  mm,  $R_d=100$  mm,  $a=3$  mm,  $b=2$  mm,  $H=4.8$  mm.

three-dimensional, unsteady flow around an actuator arm and the SSUs attached to it. The low Reynolds number calculations performed by [11] for an arm-like obstruction reveal a three-dimensional region of flow reversal adjacent to the hub and upstream of the obstruction that result from the blocking effect on the flow approaching it. Large-eddy scale (LES) flow calculations by [12,13] suggest that SSU vibrations can be caused by pressure fluctuations in the space between a pair of suspensions and in the flow that is ingested from the enclosure surroundings back into the interdisk space downstream of the arm/SSUs. For suspensions of U-shaped cross section they also find: (a) Discrete-mode high-frequency vortex shedding from the suspension flange for an inner tracking arm/SSUs orientation; (b) multimode low-frequency vortex shedding from the arm for an outer tracking orientation. Direct numerical simulations (DNS) of the flow past an actuator arm with and without a weight-saving hole in it have been performed by [15]. For both cases, a three-dimensional spiral vortex arises downstream of the arm that affects arm vibrations. The characteristics of the spiral flow and of the associated arm vibrations appear to be affected by the flow generated in and spilling from the hole when present. Limited laser-Doppler velocimetry and vibrometry data are presented in support of these numerical findings. While very valuable, the computational time and storage requirements of current DNS- and LES-based calculation approaches limit numerical studies to relatively specific geometrical and dynamical conditions, thus precluding a systematic investigation of the effects of the relevant parameters on the flow past an arm/SSUs assembly and of the attendant flow-induced SSU vibrations. This is especially the case when the calculation domain encompasses the entire interdisk space.

Because of the major challenges associated with measuring and calculating this class of unsteady three-dimensional flows and the arm/SSUs vibrations they induce, the problem has been investigated numerically by reference to simpler (but much more computationally affordable) 2D approximations of the unsteady flow fields; see [19] and the references therein. This approach allows an improved qualitative understanding of the physics underpinning flow-induced arm/SSUs vibrations. However, because the component of motion tangent to the arm and the SSUs attached to it is significantly larger than the normal component [16–18], and because of the variations in geometry, including weight-saving holes, that can arise in the circumferential and radial directions, the 2D flow approach is limited in its capacity to guide design improvements essential for minimizing arm/SSUs vibrations.

**Relevant Considerations.** We are concerned with measuring the characteristics of the flow of air in a simulated HDD with focus on fluid motion in the vicinity of the E-block/arm/SSUs assembly. With reference to Fig. 1, a characteristic Reynolds num-

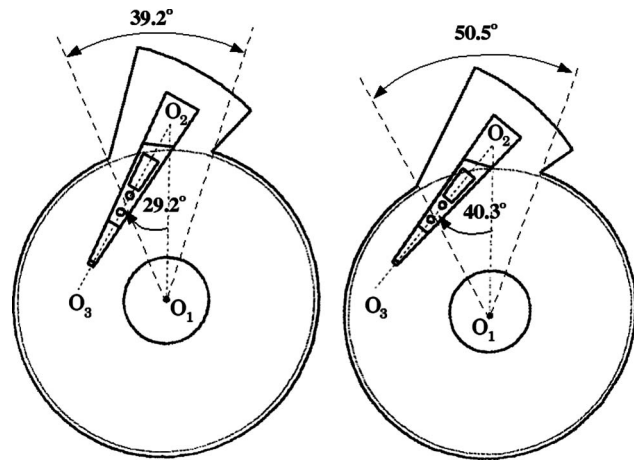


**Fig. 2** Plan view of the experimental test section as seen through the flat top of the Plexiglass enclosure and the top glass disk. The sketch shows to the left the inner (IC) and to the right the outer (OC) E-block/arm/SSUs configurations investigated. The arm/SSUs is located between the two disks. The E-block fits into a cavity extending from the side wall of the enclosure. The cavity is constructed such that its back curved inner surface is an arc of a circle centered at  $O_3$  of radius 170 mm and its opening spans 39.2 deg for the IC and 50.5 deg for the OC. For both orientations  $O_2O_3=128.4$  mm and  $O_1O_2=116$  mm. The hub and disks corotate counter-clockwise in this view.

ber for the flow between a pair of disks corotating in a HDD may be defined as  $Re_H = \Omega R_d H / \nu$ ; where  $\Omega$  (rad/s) is the angular velocity of the disks,  $R_d$  (m) is the radius of the disks,  $H$  (m) is the spacing between the disks, and  $\nu$  ( $m^2/s$ ) is the kinematic viscosity of air. For current  $3\frac{1}{2}$  inch drives with  $H \approx 2$  mm, the range in  $Re_H$  is 2250–9500, while for 1 in drives with  $H \approx 0.6$  mm it is likely to be 180–230, approximately. At these Reynolds numbers, especially for the  $3\frac{1}{2}$  inch drives, the flow in the vicinity of the disk rims and past the arm/SSUs is turbulent-like (highly vortical, three-dimensional and unsteady), while that nearer the hub is much less so. However, because of the range in geometrical scales of the various objects in the path of the flow,  $Re_H$  alone does not inform unambiguously on the nature of the fluid motion and, at a minimum, it is necessary to also consider the geometry and angular orientation of the E-block/arm/SSUs assembly in the interdisk space.

The suspension of a SSU is generally tapered in whole or in part, being wide at its base where it connects to the supporting arm, and narrow at its tip where the slider supporting the read/write magnetic head is located. The cross section of a suspension can be rectangular or U-shaped. Like the arm, the suspension may have weight-saving holes. Combined, the E-block, arm and SSUs block and redirect a significant part of the interdisk flow approaching these units. As a consequence, significant flow-structure interactions are expected to arise, partly as the result of highly vortical motions in the wakes of the arm, the suspensions, and the sliders attached to the suspension tips. The extent of these interactions depends on the relative angular orientation of these objects with respect to the approaching flow. With reference to Fig. 2, for one case, the “inner configuration” (IC), the tips of the SSUs are located close to the hub clamping the disks. For the other case, the “outer configuration” (OC), the tips are located close to the rims of the rotating disks. In the IC case, the arm and SSUs present the largest blockage to the approaching flow, favoring strong flow-structure interactions in spite of the solid body rotation nature of the flow near the hub. In the OC case, even though the arm/SSUs assembly is more closely aligned with the direction of the approaching flow, the slider at the tip of the SSU is in a region of

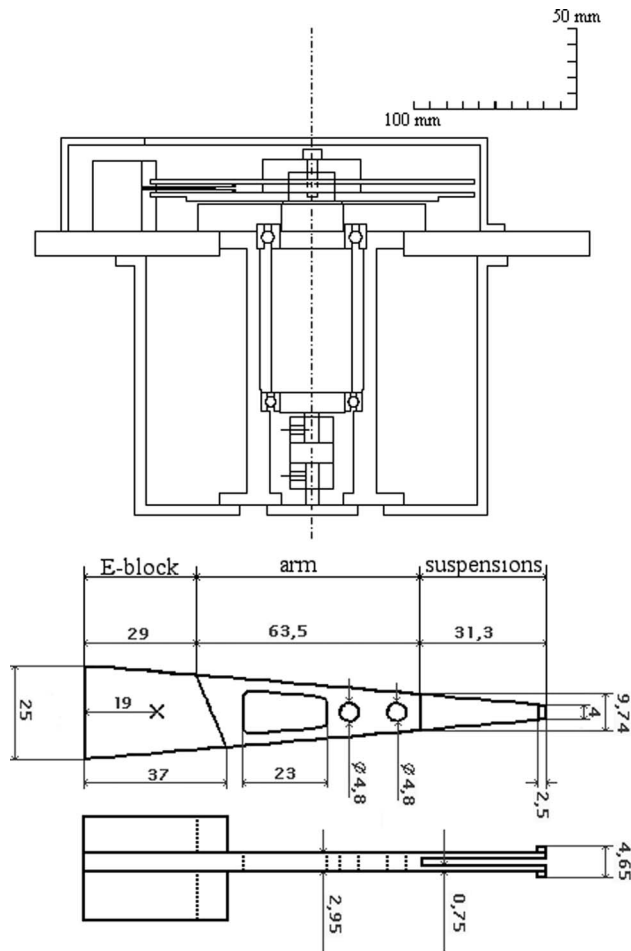


**Fig. 3** Sketches and dimensions in mm of the corotating disks flow apparatus (top: Side view) and of the E-block, arm and SSUs (bottom: Top and side views). The E-block/arm/SSUs assembly is also shown to the left of the test section in the top figure. Three weight-saving holes are cut into the arm. The two angular orientations investigated for the E-block/arm/SSUs assembly are shown in Fig. 2.

higher rotational velocity and nearer the fixed enclosure wall where shear-generated turbulence can be intense.

## The Experiment

**Apparatus.** Dimensional sketches of the corotating disks flow apparatus and of the E-block/arm/SSUs assembly investigated are provided in Fig. 3. To facilitate optical accessibility to the flow, the geometrical dimensions in the test section were scaled up by a factor of two, approximately, relative to the main features of a nominal  $3\frac{1}{2}$  inch Western Digital Caviar 38400 HDD. Two cylindrically shaped enclosures were built of Plexiglass, one for the IC and another for the OC configurations investigated. The E-block/arm/SSUs assembly was made of anodized aluminum. The E-block fits into a cavity extending from the side wall of the enclosure, and the arm/SSUs penetrate the interdisk space symmetrically with respect to the interdisk midplane. The suspensions are tapered so that their rectangular cross sections vary along their length. The surfaces of the arm and of the suspension facing a disk are parallel to the surface of the disk. A parallelepiped made of Teflon was attached to the tip of each suspension to simulate the sliders. The spacing between a slider and its facing disk was  $75\ \mu\text{m}$ , approximately. In so far as the flow is concerned, the E-block/arm/SSUs assembly was essentially motionless.

The bottom disk in the test section was made of anodized alu-

minum and the top of glass. Both disks have a radius of 100 mm and a thickness of 2 mm. The disk surfaces are flat ( $<6.4\ \mu\text{m}$ ) and optically smooth. The disks are spaced 4.8 mm apart by a solid anodized aluminum ring of outer radius 28.6 mm, and the spacing between the rims of the disks and the inner wall of the enclosure is 3 mm. Disk wobble was estimated to be less than  $\pm 65\ \mu\text{m}$  and is believed to be of no consequence to the flow established in the interdisk space. (As implied in Fig. 1, the bottom aluminum disk has a thickness of 6.35 mm up to a radius of 75 mm to minimize any tendency to wobble.) The disks are clamped down about a spindle that is driven by a brushless dc electric motor with a speed range of 10–5000 rpm. In order to ensure smooth rotation, the rotor axis spins within two ball bearings that are mounted in a solid inner casing. The inner casing is itself fixed to an outer casing consisting of a massive hollow metal cylinder such that the apparatus is essentially vibration-free for the range of rotational speeds investigated. A shaft encoder for feedback control of the rotor speed is mounted to the motor and its signal is provided to a GALIL DMC 1417 motion control board.

**Equipment.** A TSI Power View system was used to perform the particle image velocimeter (PIV) measurements. This system employs a pair of New Wave Solo Dual Nd:YAG lasers (50 mJ/pulse, 532 nm wavelength). An articulated arm with an optical head attached, consisting of a 200 mm spherical lens combined with a  $-15\ \text{mm}$  cylindrical lens, was used to produce a laser light sheet 46 mm wide and 0.04 mm at the waist with a divergence angle of 0.017 rad (1.75 mm/100 mm).

The duration of a single laser pulse was 3–5 ns and the time between pulses ranged between  $80\ \mu\text{s}$  at low fluid velocities and  $10\ \mu\text{s}$  at high velocities. A Power View 4M CCD camera with an AF Nikkor (Nikon) 60 mm f2.8 lens set at about 180 mm from the enclosure was used to capture the PIV images. The camera has  $2\ \text{K} \times 2\ \text{K}$  pixel resolution (12-bit digital output) at 17 frames per second. The system is controlled by a Laser Pulse Computer Controller Synchronizer interfaced to a Dual Processor Intel Xeon 2.0 GHz PC computer with 1 GB RAM and with a total storage of 400 GB. TSI Insight 4 software was used for image acquisition and subsequent post-processing. Two-frame cross-correlations were performed on image pairs by means of FFT using a Gaussian peak search algorithm. In a single acquisition of two consecutive images, a procedure utilizing velocity cutoff limits and a local mean filter is applied for removing spurious data. Flow statistics including mean and rms values of the circumferential and radial velocity components, mean axial vorticity, and the turbulence intensity and turbulent kinetic energy (based on the two velocity components) were derived from the ensemble of image pairs obtained for each measurement case. A Dell 530 workstation was used to control apparatus motor rotation and the PIV velocity measurements, and to conduct post-processing of the image pairs from which the final flow field data were obtained.

To guarantee high quality PIV measurements, the particle seeding agent must be sufficiently dense and homogeneously distributed to have at least 15 particles per interrogation spot [20]. This was achieved by using an interrogation window of 32 pixels. For a  $2048 \times 2048$  pixel image, processed with 50% subregion overlap, a  $128 \times 128$  grid of vectors was obtained with a resolution of  $0.428 \times 0.428\ \text{mm}^2$ . This image characterizes the flow in a square  $54.78 \times 54.78\ \text{mm}^2$ , which is only a subsection of the total area of interest. The flow field of the entire area of interest was obtained from a composite of 6 to 7 subsections patched together.

Sharper definitions of fluid motion near the hub and the E-block/arm/SSUs were obtained by applying fluorescent paint to their surfaces. The fluorescent paint works to shift the wavelength of the background light reflected from these surfaces so that, using an appropriate filter, only the light scattered from the seeding agent is detected by the camera. In this way measurements were obtained to within 1 to 2 mm from these surfaces.

**Methodology and Validation.** Prior to taking a series of PIV measurements, the rotational speed of the disks was fixed. The cavity on the side wall of the enclosure (Fig. 2) was then flooded with droplets composed of 10% by volume of glycerol in water ( $\rho_p \approx 1.021 \text{ g/cm}^3$ ,  $d_p \approx 1 \text{ }\mu\text{m}$ ) generated by a TSI jet atomizer. Within about 5 s, after which the measurements were made, the seeding agent had fully dispersed and any flow perturbations associated with particle injection were assumed to be negligible. (In 5 s at 250 rpm the disks have rotated 21 times, and at 3000 rpm they have rotated 250 times.) All the PIV velocity measurements presented here were obtained on the interdisk midplane, which passes midway between the two suspensions attached to the arm. For this, 300 image pairs were taken in groups of 30 image pairs to guarantee statistically independent data, with the fresh injection of particles taking place between groups. In this way a series of runs was performed, with each run in the series corresponding to a larger disk rpm than the preceding run.

The apparatus and measurement procedure were validated in a test section consisting of a perfectly circular Plexiglass enclosure without an obstruction between the pair of corotating disks. This is the configuration investigated in [4] for  $Re_H \approx 2000$ . Measurements of the mean and rms circumferential velocity component were obtained at 1000 rpm, corresponding to  $Re_H \approx 3220$ . Good quantitative agreement was found with respect to the mean circumferential velocity component measured by [4], and good qualitative agreement was found for the rms [17]. The rms values measured in [4] are generally larger, most probably due to the much larger disk spacing in [4] ( $H/Rd=0.091$  versus 0.048 in the present experiment).

**Uncertainties.** All linear and angular dimensions in the test section were known to better than  $\pm 0.1 \text{ mm}$  and  $\pm 1^\circ$ , respectively. The uncertainty in disk angular velocity was estimated to be less than  $\pm 0.5\%$ . Sources and magnitudes of uncertainties affecting PIV measurements are well documented in the literature [21]. Here attention is focused on those relevant to this work. Although a minimum number of 250 image pairs was found to be large enough to minimize sample size uncertainties of the mean and rms values of the velocity components, all velocity measurements are based on 300 image pairs. Checks on the sufficiency of a 300 picture pair ensemble size were performed by increasing the ensemble size to 900 picture pairs. However, no significant improvements in the mean and rms values of velocity were observed (difference less than 0.2% of the disk rim velocity,  $R_d\Omega$ ). The theoretical (Stokes drag-based) relaxation time of the seeding agent particles ( $\tau_p = \rho_p d_p^2 / 18\mu$ ) in air at  $23^\circ\text{C}$  is  $\tau_p < 3.1 \text{ }\mu\text{s}$ . Since this time scale is much smaller than the time scale associated with the most energetic eddies in the flow (about  $75 \text{ }\mu\text{s}$  at 3000 rpm, based on a length scale  $l_S = H$  and a velocity scale  $v_S$  corresponding to 10% turbulence intensity,  $v_S = 0.10 R_d\Omega$ ), particle lag was assumed to be negligible. Although there were no significant optical uncertainties due to the curvature of the enclosure wall penetrated by the pulsed laser light sheet, it was critical to align the sheet to illuminate the interdisk midplane. Uncertainties due to out-of-plane particle displacement in an interrogation subregion, or to the time between laser pulses, were negligible. Assuming a normal distribution for the dimensionless mean velocity components yielded a statistical uncertainty for these quantities ranging from  $\pm 1$  to  $\pm 4\%$  with 95% confidence. Likewise, assuming a chi-square distribution for the dimensionless variances yielded an uncertainty less than  $\pm 9\%$  for the dimensionless rms velocity components and less than  $\pm 18\%$  for the dimensionless shear stress  $\langle u_r u_\theta \rangle^*$ , also with 95% confidence.

## Results and Discussion

**Asymptotic Invariance of the Flow.** Measurements of the circumferential and radial velocity components were obtained for 250, 500, 1000, 1500, 2000, and 3000 rpm corresponding to a

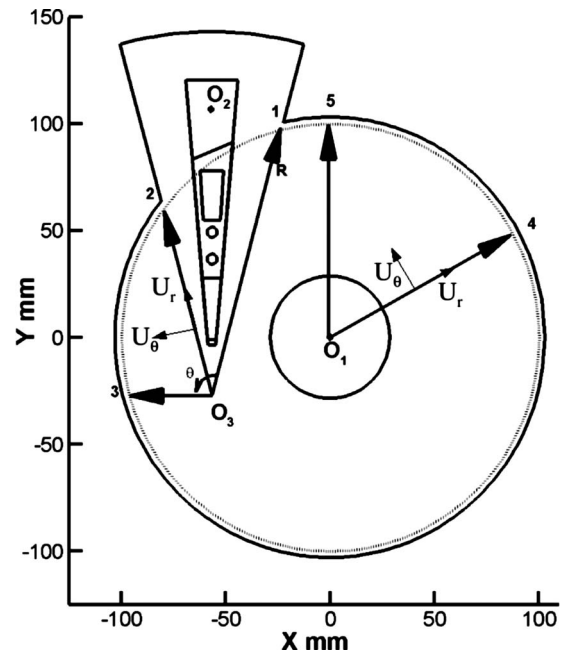


**Fig. 4 Sketch defining the circumferential and radial velocity components with respect to cylindrical coordinate systems centered at  $O_1$  and  $O_3$ , respectively. The asymptotic invariance of the flow is checked by reference to mean and rms velocity profiles of these two velocity components obtained at locations 1, 2, 3, 4, and 5 on the interdisk midplane.**

range in  $Re_H$  of 800–9700. (Note that 3000 rpm in the experimental apparatus corresponds to about 15,000 rpm in a nominal  $3\frac{1}{2}$  HDD.) The data for all the cases investigated are plotted in [17] and the original data can be obtained from the authors upon request.

The asymptotic invariance of the flow with increasing disk speed of rotation was checked by reference to mean and rms velocity component profiles obtained from the PIV measurements at the five locations shown in Fig. 4, upstream and downstream of the E-block/arm/SSUs for both the IC and OC orientations. Results obtained for these two orientations are, respectively, shown in Figs. 5 and 6. In this regard note that: (i) In all figures, mean and rms velocities, and the shear stress, are normalized by the rim speed of the disks,  $\Omega R_d$ ; (ii) The velocity components in Figs. 5 and 6 are plotted relative to an  $(r, \theta)$  cylindrical coordinate system centered at point  $O_3$  in Fig. 4; (iii) the data in Figs. 7–12 are plotted relative to an  $(r, \theta)$  cylindrical coordinate system centered at point  $O_1$  in Fig. 4.

It is clear from the profiles in Figs. 5 and 6 that for both the IC and OC orientations the means of both velocity components tend to asymptotic limits with increasing disk speed of rotation, but the rms values are still changing. Notwithstanding, for both orientations the rms profiles at different rpm tend towards similar shapes.

Immediately upstream of the arm/SSUs (location 1 in Fig. 4) for both the OC (Fig. 5(a)) and IC (Fig. 6(a)) orientations, the mean circumferential velocity component shows relatively large values near the rims of the disks where their rotational velocity is largest. As a consequence, because of the shearing action of the fixed enclosure wall, this is also a region of relatively high rms velocities. For both orientations at this location, relatively low absolute values of the mean velocity components and high values of their rms are observed for small values of the radius ( $R < 30\text{--}40 \text{ mm}$ ) near the tips of the SSUs.

For the OC case upstream of the arm/SSUs (Fig. 5(a)), two peaks are observed at  $R \approx 18 \text{ mm}$  and  $R \approx 30 \text{ mm}$  for the mean and rms values of both velocity components. The peaks at  $R$

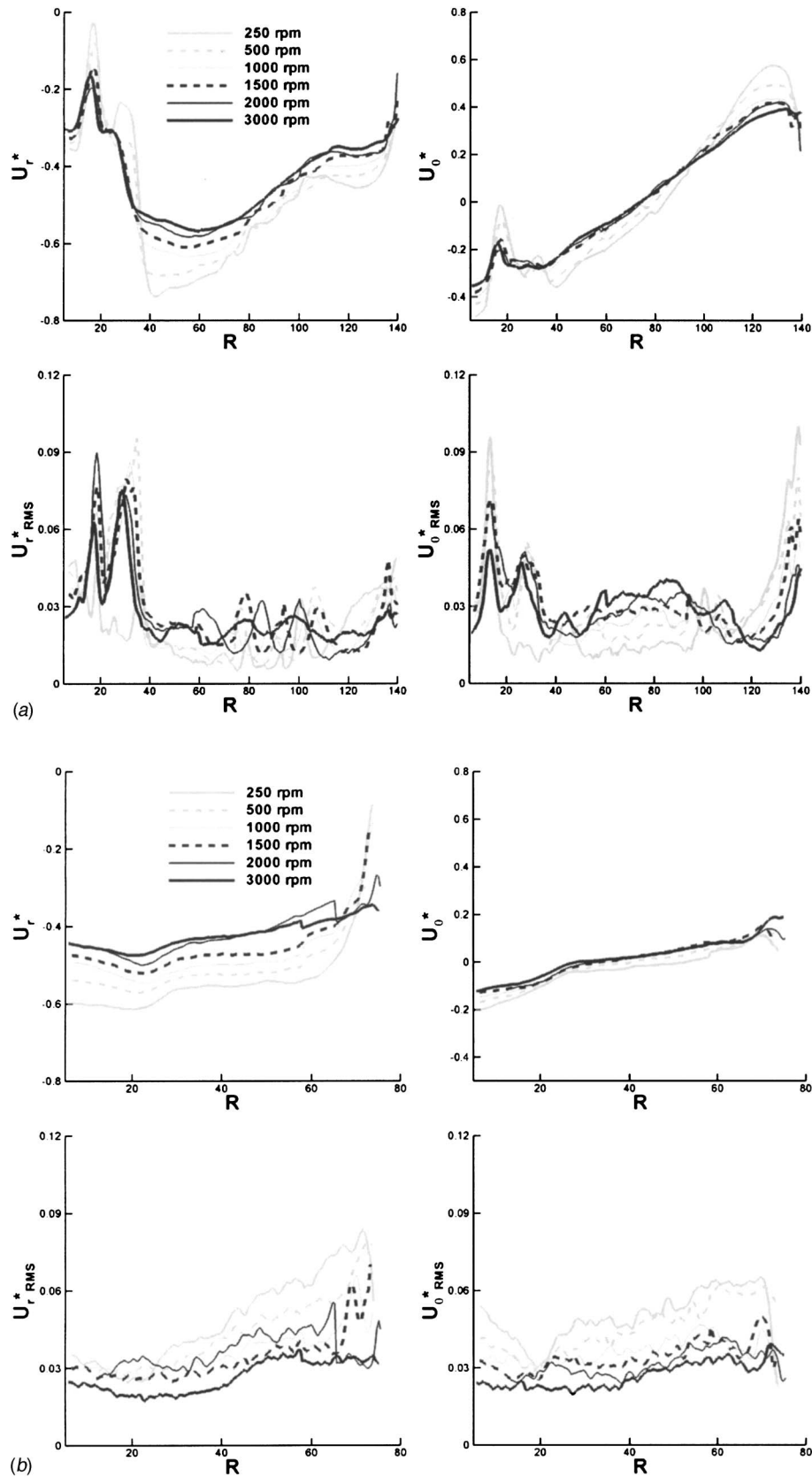
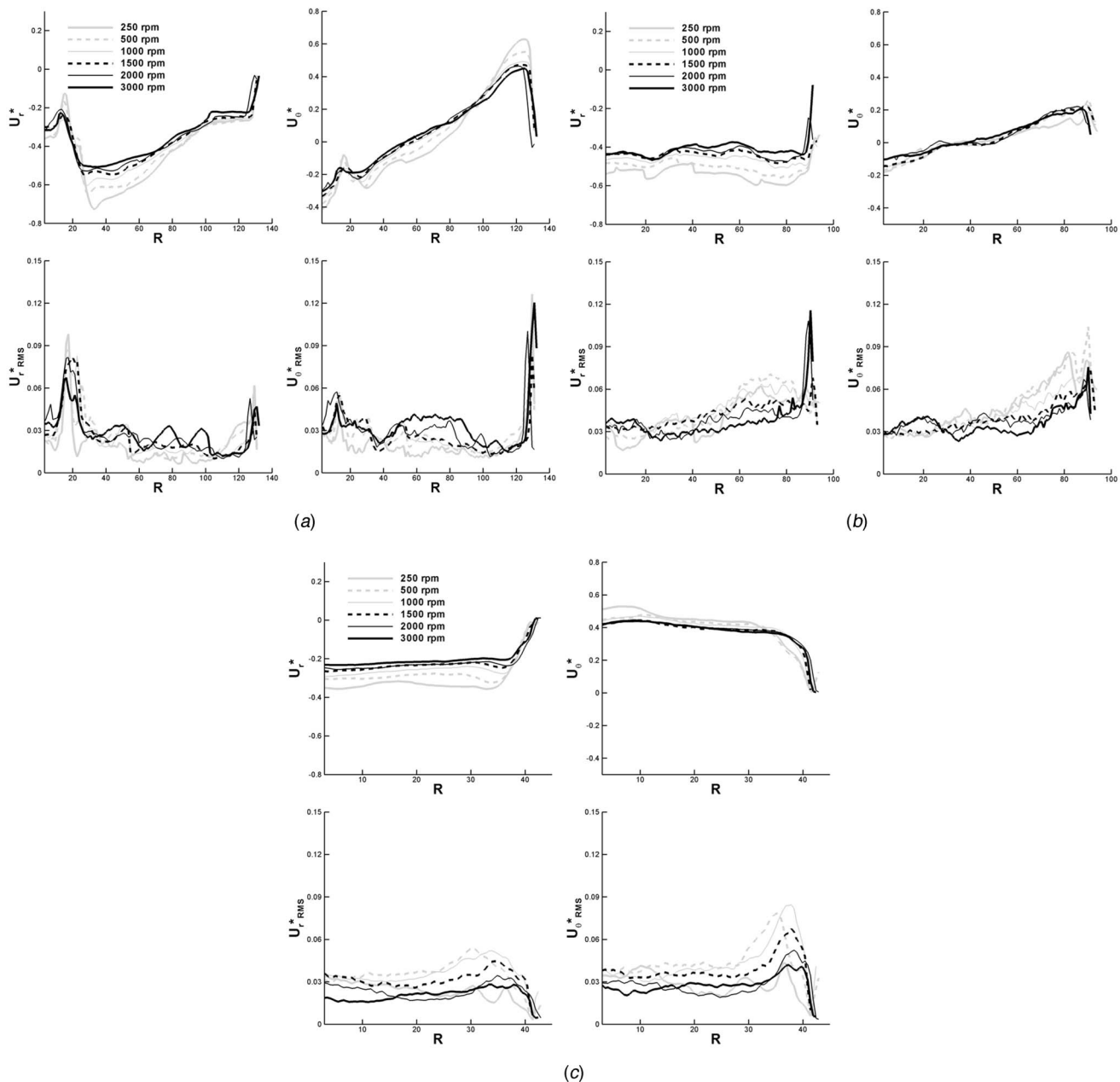


Fig. 5 (a) Mean and rms values of the radial and circumferential velocity components as a function of radial position and disk rpm at location 1 in Fig. 4 for the outer configuration in Fig. 2. Radius  $R$  is given in mm. (b) Mean and rms values of the radial and circumferential velocity components as a function of radial position and disk rpm at location 2 in Fig. 4 for the outer configuration in Fig. 2. Radius  $R$  is given in mm.



**Fig. 6** (a) Mean and rms values of the radial and circumferential velocity components as a function of radial position and disk rpm at location 1 in Fig. 4 for the inner configuration in Fig. 2. Radius  $R$  is given in mm. (b) Mean and rms values of the radial and circumferential velocity components as a function of radial position and disk rpm at location 2 in Fig. 4 for the inner configuration in Fig. 2. Radius  $R$  is given in mm. (c) Mean and rms values of the radial and circumferential velocity components as a function of radial position and disk rpm at location 3 in Fig. 4 for the inner configuration in Fig. 2. Radius  $R$  is given in mm.

$\approx 18$  mm correspond to the effects on the flow due to the wakes of the sliders; the sliders work to locally reduce both mean velocity components while significantly increasing their rms. The peaks at  $R \approx 30$  mm correspond to a second wake induced by the arm. This wake originates at the tip of the arm where the suspensions attach. It is characterized by two shear layers that form on either side of the tip of the arm. Figures 8 and 9, discussed below, and DNS calculations by [17], clearly show the presence of these two wakes. Between  $R=40$  and 80 mm, the mean radial velocity component increases substantially in absolute value as the bulk flow changes direction to accelerate through the space between the arm/SSUs and the hub. In contrast to location 1, the mean and rms velocity component profiles downstream of the arm/SSUs in Fig.

5(b) (location 2 in Fig. 4) are relatively flat and featureless. However, the rms values of both velocity components generally increase with increased proximity to the downstream corner of the cavity containing the E-block.

The general shapes of the mean and rms velocity profiles for the IC case at location 1 (Fig. 6(a)) are similar to those for the OC case at the same location (Fig. 5(a)). However, the effects due to the wake induced by the arm are less noticeable. As for the OC case, near the sliders ( $R < 20$  mm) the rms velocity components are large compared to their local means, indicating that the flow in the vicinity of the sliders is very unsteady and possibly turbulent. Location 2 (Fig. 4) is immediately behind the arm. Here the absolute value of the mean circumferential velocity component is ev-

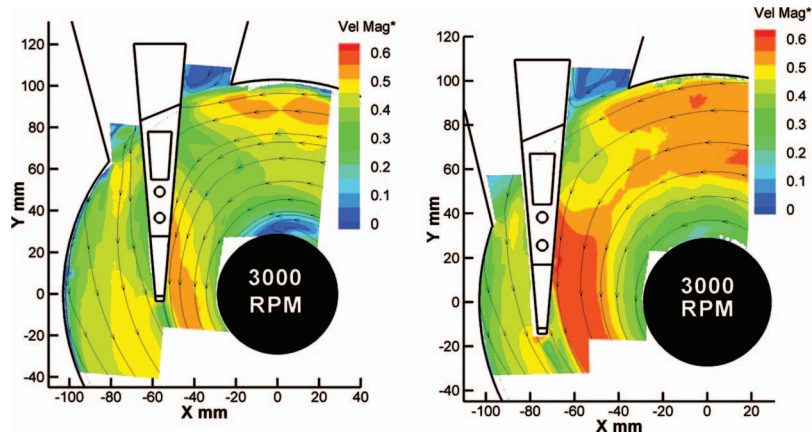


Fig. 7 Contours of mean velocity magnitude with streamlines superimposed for the inner configuration (left) and outer configuration (right) at 3000 rpm

everywhere relatively small (Fig. 6(b)) and the corresponding mean radial velocity component is fairly uniform and featureless. As for the OC case, the rms values of both velocity components increase with increased proximity to the downstream corner of the cavity.

At location 3 (Fig. 6(c)) relatively uniform mean velocity component profiles are observed but their corresponding rms values increase with increasing proximity to the enclosure wall.

The ensemble averaged data discussed above does not provide

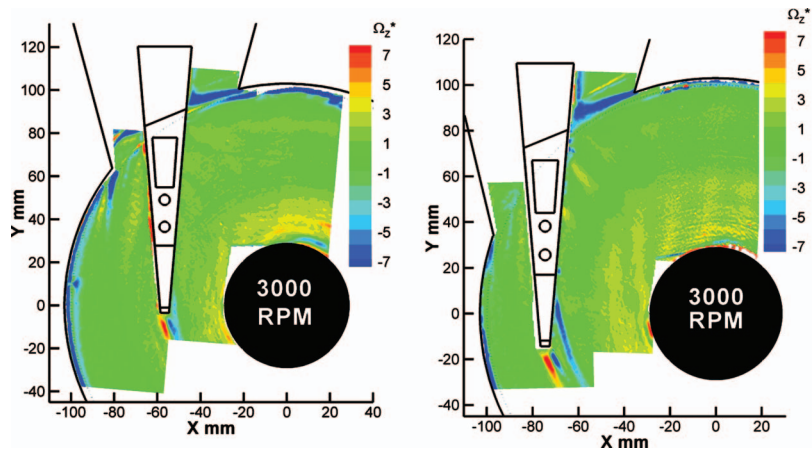


Fig. 8 Contours of the mean axial component of vorticity (normal to disk surface) for the inner configuration (left) and outer configuration (right) at 3000 rpm

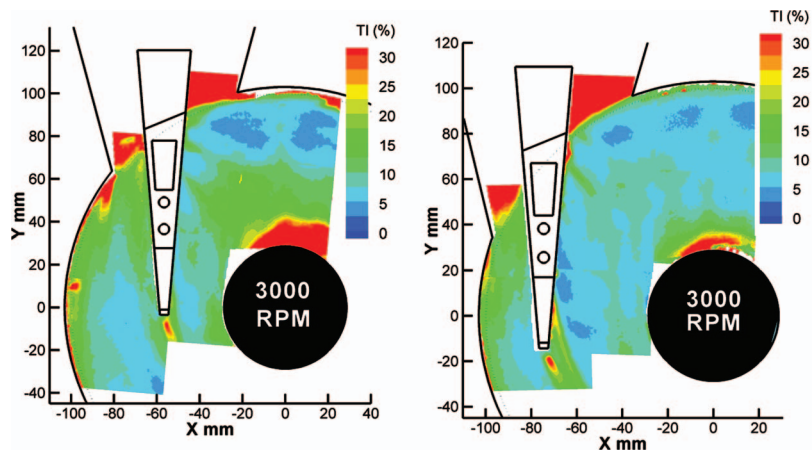


Fig. 9 Contours of the turbulence intensity (based on two velocity components) for the inner configuration (left) and outer configuration (right) at 3000 rpm

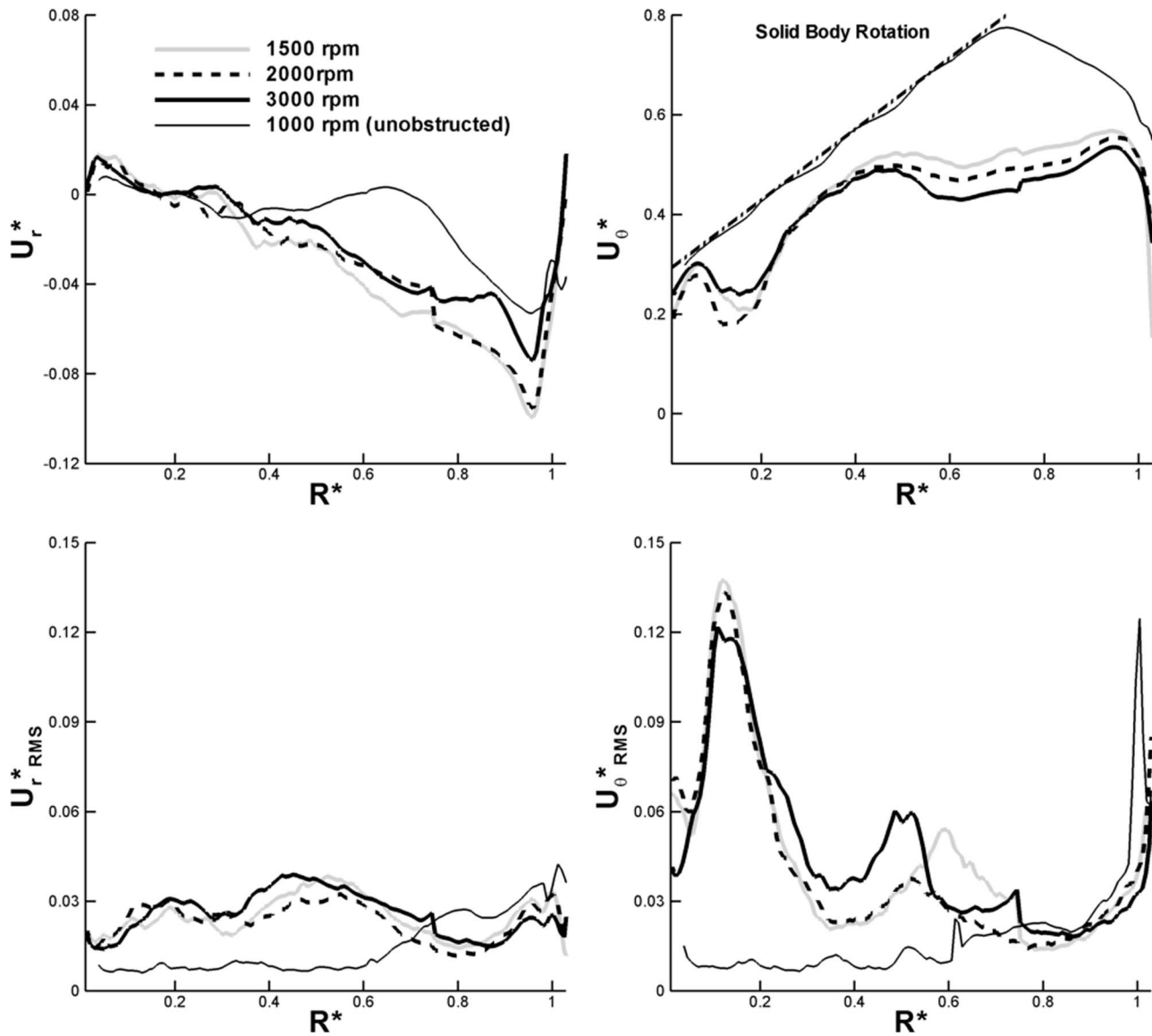


Fig. 10 Mean and rms values of the radial and circumferential velocity components as a function of radial position and disk rpm at location 4 in Fig. 4 for the inner configuration in Fig. 2. In this figure  $R^* = (r - R_h) / (R_d - R_h)$ ; see Fig. 1. The dash-dot line in the plot for  $U_\theta^*$  denotes solid body rotation.

clear cut evidence of the effects on the flow due to the weight-saving holes cut into the arm. In contrast, instantaneous PIV snapshots and DNS calculations by [17] reveal that at any instant in time the distribution of vorticity in the flow, downstream of the arm where the largest (trapezoidal-shaped) hole is located, is streaky and grainy due to intense shearing by the rotating disks of highly vortical fluid ejected from this hole.

**Velocity Magnitude and Streamlines, Vorticity and Turbulence Intensity.** The dimensionless mean velocity magnitude,  $V_{\text{mag}}^*$ , mean vorticity,  $\Omega_z^*$ , and turbulence intensity TI (%) are defined as follows in terms of the mean ( $U_r$ ,  $U_\theta$ ) and rms ( $U_{r \text{ rms}}$ ,  $U_{\theta \text{ rms}}$ ) velocity components derived from the PIV measurements of the flow field:

$$V_{\text{mag}}^* = \frac{\sqrt{U_r^2 + U_\theta^2}}{R_d \Omega}$$

$$\Omega_z^* = \frac{1}{\Omega r} \left( \frac{\partial(rU_\theta)}{\partial r} - \frac{\partial U_r}{\partial \theta} \right)$$

$$\text{TI}(\%) = 100 \frac{\sqrt{U_{r \text{ rms}}^2 + U_{\theta \text{ rms}}^2}}{\sqrt{U_r^2 + U_\theta^2}}$$

Contours of  $V_{\text{mag}}^*$  with streamlines superimposed are shown in Fig. 7 for the IC and OC orientations. For both cases the contours and streamlines are found to be very similar at all the rotational speeds investigated. Therefore, attention is restricted here to the data obtained for the highest rotational speed, 3000 rpm. For both arm/SSUs orientations the streamlines show that the bulk of the flow approaching the E-block/arm is deflected radially inwards and accelerated in the space between the obstruction and the hub. (The lower acceleration observed for the inner configuration case is attributed to larger momentum losses induced by the arm/SSUs in this configuration.) In principle, this accelerating turning flow should form a highly sheared boundary layer along the length of the upstream surface of the arm. However, a portion of the flow in this boundary layer is removed by the disks which, in rotating past the arm surfaces facing them, suck fluid from the boundary layer into the passages formed by the disks and the facing arm surfaces. It is suggested that the sucking action contributes to a combined

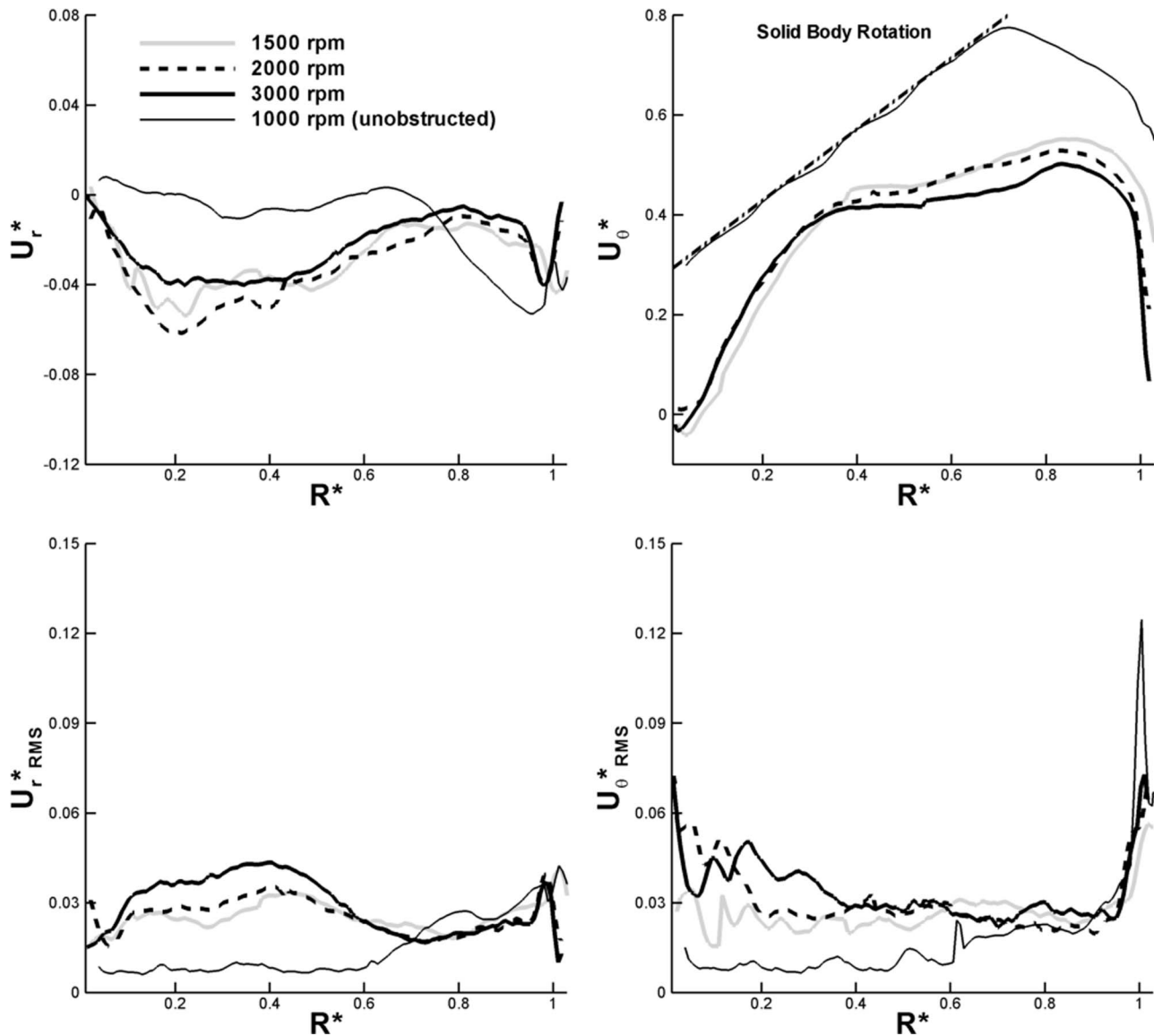


Fig. 11 Mean and rms values of the radial and circumferential velocity components as a function of radial position and disk rpm at location 5 in Fig. 4 for the inner configuration in Fig. 2. In this figure  $R^* = (r - R_h) / (R_d - R_h)$ ; see Fig. 1. The dash-dot line in the plot for  $U_\theta^*$  denotes solid body rotation.

thinning and laminarizing of the flow immediately along the upstream arm surface. In the region between the arm/SSUs and the hub, the direction of the fluid velocity virtually coincides with that of the disks but is of higher magnitude than the local disk velocity. The sliders on the SSUs significantly decelerate the flow going past them creating a wake of relatively high turbulence intensity. The wake does not arise immediately next to the tip of the suspensions, but about two millimeters further downstream on the midplane.

For the IC case, a region of three-dimensional flow reversal (Fig. 7) and high turbulence intensity (Fig. 9) is observed near the hub. While the flow reversal is absent for the OC case, the turbulence intensity in this region is also relatively high. The reversal of fluid motion is due to the larger blockage of the flow in the IC case (56%) relative to the OC (48%) and was observed at all the rotational speeds explored. It has also been calculated numerically by Suzuki and Humphrey (1997) for a radially aligned, arm-like blockage in the space between a pair of disks corotating in a cylindrical enclosure at 300 rpm.

For both the IC and OC orientations, contours of the axial vor-

ticity (Fig. 8) and turbulence intensity (Fig. 9) reveal a strongly vortical and energetic shear layer detaching from the upstream corner of the cavity containing the E-block. This layer impinges on the E-block, near to the location where it connects to the arm, and then appears to wrap around the back of the E-block in the cavity. For both orientations, a second shear layer is formed at the downstream corner of the cavity. Also for both orientations, a pair of vortical shear layers appears in the wake of the sliders on the SSUs. A single curved shear layer (especially noticeable for the OC case) appears on the upstream side of the suspensions. As mentioned previously, it is one of a pair originating at the tip of the arm where the suspensions attach, and is due to the wake induced by the arm on the flow. The second shear layer, of opposite sign of vorticity, cannot be measured using the PIV technique due to the optical interference of the top suspension. However, DNS calculations by [17] show that both shear layers originate at the tip of the arm, between the suspensions. These calculations also confirm that the shear layer detaching from the upstream corner of the cavity does, indeed, wrap around the back of the E-block.



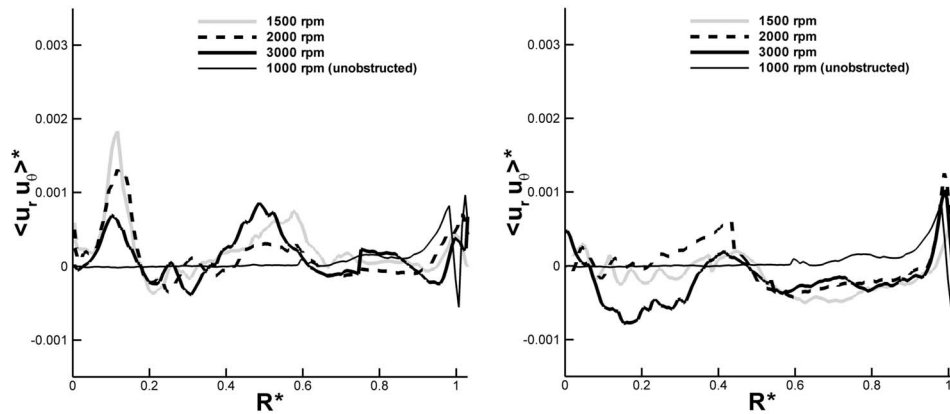


**Fig. 12**  $\langle u_r u_\theta \rangle^*$  shear stress as a function of radial position and disk rpm at locations 4 (left) and 5 (right) in Fig. 4 for the inner configuration in Fig. 2. In this figure  $R^* = (r - R_h) / (R_d - R_h)$ ; see Fig. 1.

### Characteristics of the Flow Upstream of the Arm/SSUs.

Limited measurements were also made for the mean and rms values of the circumferential and radial velocity components and for the  $\langle u_r u_\theta \rangle$  shear stress, along locations 4 and 5 in Fig. 4 for the arm/SSUs in the IC orientation. The lines denoting locations 4 and 5 are, respectively, oriented at 90 and 29 deg relative to a line connecting points  $O_1$  and  $O_2$  in Fig. 4. The results are plotted in Figs. 10–12 relative to an  $(r, \theta)$  cylindrical coordinate system centered at point  $O_1$ . Also shown in the figures are data corresponding to measurements obtained for this study in the absence of the E-block/arm/SSUs in the interdisk space. Note that in these figures the radial coordinate is  $R^* = (r - R_h) / (R_d - R_h)$ .

Three points are especially worthy of mention. The first concerns the large differences in all the quantities plotted between the obstructed and unobstructed flow cases. It is clear that at these two upstream locations the general effect of the obstruction is to significantly decrease the local values of the mean velocity components while increasing their corresponding rms. The second point concerns the shapes of the rms and shear stress profiles at location 4 which reveal a pair of maxima for  $R^* < 0.7$ . The maxima spanning  $0.05 \leq R^* \leq 0.20$  are attributed to the highly unsteady nature of the reversed three-dimensional flow induced near the hub by the presence of the obstruction (see Figs. 7 and 9). The maxima spanning  $0.40 \leq R^* \leq 0.70$  are attributed to the unsteady vortical wake imprinted by the arm/SSUs on the flow downstream of it. Relative to the unobstructed flow case the mean circumferential velocity component profiles at both upstream locations (4 and 5) show significantly reduced velocities. The third point concerns the high levels of turbulence intensity observed between locations 4 and 5 on the interdisk midplane near the hub, plotted in Fig. 9 for 3000 rpm and discussed above. Analysis of the experimental data shows that the production of turbulent kinetic energy on the interdisk midplane between these two locations is dominated by the term  $-\langle u_r u_\theta \rangle (\partial U_\theta / \partial r)$ . This is because of geometrical symmetry and because of the dominance of the circumferential component of motion between these two locations. When considered in combination, the profiles for  $U_\theta$  in Figs. 10 and 11 and the profiles for  $\langle u_r u_\theta \rangle$  in Fig. 12 show that at 3000 rpm (the most turbulent flow condition examined) the largest positive values of  $-\langle u_r u_\theta \rangle (\partial U_\theta / \partial r)$  between locations 4 and 5 arise at radial locations falling in the range  $0.1 \leq R^* \leq 0.4$ .

Notwithstanding these noteworthy findings, a comparison with the mean and rms velocity profiles corresponding to location 1 (Fig. 6(a)), immediately upstream of the arm/SSUs, shows that the flow changes completely in the course of a 90 deg degree turn, suggesting that it is primarily determined by local flow-structure interactions.

### Conclusions

Velocity measurements have been made for the flow in a simulated HDD that retains the essential physics of a real device. PIV data for two velocity components are presented for a geometrical configuration scaled up by a factor of two, approximately, relative to a nominal 31/2 inch HDD. The results presented here were obtained on the interdisk midplane in the presence of an E-block/arm/SSUs assembly at two orientation angles. The highest disk speed of rotation investigated was 3000 rpm, corresponding approximately to 15,000 rpm in a nominal 31/2 inch HDD. At 3000 rpm in the experiment, the velocity component means have essentially attained an asymptotically invariant state but the rms velocities and the shear stress appear to still be evolving.

The data reveal strong influences of the arm/SSUs on the flow that depend on the relative orientation angle of this obstruction in the interdisk space. The blockage presented by the obstruction redirects a large portion of the flow tangentially along the upstream surfaces of the arm/SSUs. A pair of highly vortical shear layers arises in the wake originating at the tip of the arm, where the suspensions attach, and a second pair arises downstream of the sliders attached to the suspensions. Shear layers also originate at the upstream and downstream corners of the cavity extending from the side of the enclosure.

About 90 deg upstream of the arm/SSUs and near the hub surface, the blockage induces a region of highly unsteady turbulent motion which, for the IC configuration, results in a three-dimensional flow reversal. Also for the IC configuration, the flow 90 and 29 deg upstream of the arm/SSUs reveals the imprint of the wake induced by the obstruction in the flow. However, by the time the flow arrives at the arm/SSUs it has evolved to reflect, primarily, the dominant effects of more local flow structure interactions. In this regard, the bulk of the flow arriving at the arm/SSUs is strongly deflected in a direction parallel to the upstream arm surface impinged, forming a boundary layer on this surface. Simultaneously, the flow is accelerated tangentially to this surface by the effect of the area contraction in the space between the arm/SSUs and the hub. However, it is likely that the upstream arm surface boundary layer is thinned and laminarized by the suction action of the disks which remove fluid from it. This would result in a protective layer of high speed fluid that essentially “washes” the upstream surfaces of the arm/SSUs from the effects of the approaching flow. As a consequence, local flow-structure interactions appear to be primarily responsible for the relatively large levels of rms velocities and vorticity observed downstream of the arm/SSUs.

The results presented here point to a number of sources potentially capable of driving flow-induced arm/SSUs vibrations, as

well as potentially capable of damping them, which should be carefully considered in developing improved HDD designs. In particular, to reduce flow-driven SSU vibrations, every effort should be made to remove or minimize sharp edges capable of generating energetic shear layers in this high speed flow.

### Acknowledgment

The authors gratefully acknowledge financial support provided by the INSIC EHDR Program, San Diego, CA, for this study, and helpful technical discussions held with R. Evans, A. H. Sacks, and M. Kazemi. Excellent technical support was provided by S. Pothos of TSI incorporated for the PIV measurements. Our thanks go to E. Spenceley, L. Steva, B. Thiede, and C. Pfister for their help in designing and constructing the apparatus. C. Barbier is the recipient of the 2005 AAM Founders Prize provided in support of her research by the Robert M. and Mary Haythornthwaite Foundation.

### References

- [1] INSIC (Information Storage Industry Consortium), 2004, "The Future of Storage Applications, Information Continuity From Backup to Archive," July 18–22, 2004, Monterey, CA.
- [2] Abrahamson, S. D., Eaton, J. E., and Koga, D., 1989, "The Flow Between Shrouded Corotating Disks," *Phys. Fluids A*, **1**, pp. 241–251.
- [3] Humphrey, J. A. C., and Gor, D., 1993, "Experimental Observation of an Unsteady Detached Shear Layer in Enclosed Corotating Disk Flow," *Phys. Fluids A*, **5**, pp. 2438–2442.
- [4] Schuler, C., Ustry, W., Weber, B., Humphrey, J. A. C., and Greif, R., 1990, "On the Flow in the Unobstructed Space Between Shrouded Corotating Disks," *Phys. Fluids A*, **2**, pp. 1760–1770.
- [5] Humphrey, J. A. C., Schuler, C. A., and Webster, D. R., 1995, "Unsteady Laminar Flow Between a Pair of Disks Corotating in a Fixed Cylindrical Enclosure," *Phys. Fluids*, **7**, pp. 1225–1240.
- [6] Abrahamson, S. D., Chiang, C., and Eaton, J. K., 1991, "Flow Structure in Head-Disk Assemblies and Implications for Design," *Adv. Inf. Storage Syst.*, **1**, pp. 79–110.
- [7] Tzeng, H., and Humphrey, J. A. C., 1991, "Corotating Disk Flow in an Axisymmetric Enclosure With and Without a Bluff Body," *Int. J. Heat Fluid Flow*, **12**, pp. 194–201.
- [8] Humphrey, J. A. C., Schuler, C. A., and Iglesias, I., 1992, "Analysis of Viscous Dissipation in Disk Storage Systems and Similar Flow Configurations," *Phys. Fluids A*, **4**, pp. 1415–1427.
- [9] Ustry, W., Humphrey, J. A. C., and Greif, R., 1993, "Unsteady Flow in the Obstructed Space Between Disks Corotating in a Cylindrical Enclosure," *J. Fluids Eng.*, **115**, pp. 620–626.
- [10] Gross, H. M., 2003, "Off-Track Vibrations of the Read-Write Heads in Hard Disk Drives," Ph.D. thesis, University of California.
- [11] Suzuki, H., and Humphrey, J. A. C., 1997, "Flow Past Large Obstructions Between Corotating Disks in Fixed Cylindrical Enclosures," *J. Fluids Eng.*, **119**, pp. 499–505.
- [12] Shimizu, H., Tokuyama, M., Imai, M., Nakamura, S., and Sakai, K., 2001, "Study of Aerodynamic Characteristics in Hard Disk Drives by Numerical Simulation," *IEEE Trans. Magn.*, **37**, pp. 831–836.
- [13] Shimizu, H., Shimizu, T., Tokuyama, M., Masuda, H., and Nakamura, S., 2003, "Numerical Simulation of Positioning Error Caused by Air-Flow-Induced Vibration of Head Gimbals Assembly in Hard Disk Drive," *IEEE Trans. Magn.*, **39**, pp. 806–811.
- [14] Kubotera, H., Tsuda, N., Tatewaki, M., and Maruyama, T., 2002, "Aerodynamic Vibration Mechanism of HDD Arms Predicted by Unsteady Numerical Simulations," *IEEE Trans. Magn.*, **38**, pp. 2201–2203.
- [15] Tsuda, N., Kubotera, H., Tatewaki, M., Noda, S., Hashiguchi, M., and Maruyama, T., 2003, "Unsteady Analysis and Experimental Verification of the Aerodynamic Vibration Mechanism of HDD Arms," *IEEE Trans. Magn.*, **39**, pp. 819–825.
- [16] Humphrey, J. A. C., Kazemi, M., and Herrero, J., 2003, "Method for Calculating the Velocity of Air Flowing Past a Pair of Suspensions in a Disk Drive," *Microsyst. Technol.*, **9**, pp. 534–540.
- [17] Barbier, C., 2005, "Experimental and Numerical Study of the Flow in a Simulated Hard Disk Drive," Ph. D. thesis, University of Virginia. See, also, an *errata* filed with the thesis.
- [18] Kazemi, M. R., 2005, "Numerical Modeling of Magnetic Head Positioning Error Due to Flow-Suspension Interactions in Disk Drives," Ph. D. thesis, University of Virginia.
- [19] Humphrey, J. A. C., Haj-Hariri, H., Iwasaki, T., Kazemi, M., and Rosales, L., 2002, "Modeling and Controlling Flow-Induced Suspension-Head Unit Vibrations in Hard Disk Drives," *Microsyst. Technol.*, **8**, pp. 375–382.
- [20] Keane, R. D., and Adrian, R. J., 1990, "Optimization of Particle Image Velocimeters. Part I: Double Pulsed Systems," *Meas. Sci. Technol.*, **1**, pp. 1202–1215.
- [21] Raffel, M., Willert, C., and Kompenhans, J., 1998, *Particle Image Velocimetry — A Practical Guide*, Springer-Verlag, Berlin.

# Onset of Vortex Shedding in a Periodic Array of Circular Cylinders

L. Zhang

S. Balachandar

e-mail: s-bala@uiuc.edu

Department of Theoretical and Applied Mechanics,  
University of Illinois,  
Urbana, IL 61801

*Hopf bifurcation of steady base flow and onset of vortex shedding over a transverse periodic array of circular cylinders is considered. The influence of transverse spacing on critical Reynolds number is investigated by systematically varying the gap between the cylinders from a small value to large separations. The critical Reynolds number behavior for the periodic array of circular cylinders is compared with the corresponding result for a periodic array of long rectangular cylinders considered in [Balachandar, S., and Parker, S. J., 2002, "Onset of Vortex Shedding in an Inline and Staggered Array of Rectangular Cylinders," Phys. Fluids, 14, pp. 3714–3732]. The differences between the two cases are interpreted in terms of differences between their wake profiles.*

[DOI: 10.1115/1.2201630]

## 1 Introduction

Flow over a periodic array of bluff bodies appears in many engineering applications. The onset of vortex shedding in such flows has a strong influence on the mean and fluctuating forces and heat transfer. It is of interest then to study the influence of spacing between the cylinders within the periodic array on the onset of vortex shedding. In particular, if the critical Reynolds number ( $Re_{cr}$ ) for an isolated cylinder is known, what can be said about the critical Reynolds number for the onset of vortex shedding in a periodic array of such cylinders?

Owing to its technological significance, several investigations have considered flow over a periodic array of circular cylinders. These investigations, however, either have been in low  $Re$  regime [1,2] or have focused attention on wake vortex interaction and drag computation at significantly higher  $Re$  [3–5]. Of particular relevance to the present work is the investigation of onset of vortex shedding past a periodic array of long rectangular cylinders [6]. They observed transverse spacing between the cylinders to be the only critical parameter in deciding the onset of vortex shedding and the streamwise spacing between the cylinders, provided larger than two diameters, not to be important. With increasing transverse spacing between adjacent cylinders  $Re_{cr}$  first decreases and this behavior was shown to be well predicted by a simple one-dimensional stability theory. After reaching a minimum  $Re_{cr}$  will increase with increasing transverse spacing and approach that of an isolated long rectangular cylinder in cross flow.

Here we consider the canonical geometry of circular cross section and investigate onset of vortex shedding for flow past a transverse array of circular cylinders. Instead of a two-dimensional array of cylinders, we only consider a transverse array (see Fig. 1). Based on the results of [3,6], we do not expect the presence of additional columns of cylinders downstream or upstream to influence the stability, provided the streamwise spacing between columns is sufficiently large. The key issue to be explored is how generic is the dependence of  $Re_{cr}$  on transverse spacing. Interestingly, we observe the onset of vortex shedding for the array of circular cylinders to be quite different from that of long rectangular cylinders of large aspect ratio. The difference in behavior can be explained in terms of subtle differences in the structure of the steady base flow.

## 2 Methodology

A uniform ambient flow of velocity,  $U_\infty^*$ , past a periodic array of circular cylinders with a transverse pitch of  $L_y^*$ , as shown in Fig. 1(a), is studied. Here superscript  $*$  denotes a dimensional quantity. Otherwise all quantities presented are nondimensional, with cylinder diameter,  $d^*$ , as the length scale,  $U_\infty^*$  as the velocity scale and  $\rho U_\infty^{*2}$  as the pressure scale, where  $\rho$  is the fluid density. At low Reynolds numbers to be considered here, when the flow is steady or just undergoing Hopf bifurcation, the flow field can be considered to be periodic as well along the transverse,  $y$ , direction with wavelength  $L_y$ . The computational domain is thus restricted to a single unit of the periodic array and shown in Fig. 1(a) as the rectangular region.  $L_{x1}$  and  $L_{x2}$  are the horizontal distances from the center of the cylinder to the inflow and outflow boundaries, upstream and downstream of the cylinder. The cylinders are taken to be long along their axis without end effects and thus the steady base flow and its instability to periodic vortex shedding will be considered to be two dimensional. The governing continuity and incompressible Navier-Stokes equations are solved and the only nondimensional parameter is the Reynolds number defined as  $Re = U_\infty^* d^* / \nu$ .

A uniform velocity of unit magnitude is applied at the inlet and periodic boundary conditions are employed along the transverse direction. Since the outflow boundary is placed sufficiently far away from the cylinder, a simple condition of zero streamwise gradient is applied there. The spatial discretization of the computational domain is based on the spectral element technique [7]. The temporal discretization is based upon an operator splitting approach in which the nonlinear convective, viscous and pressure gradient effects are decoupled via an operator-integration-factor method [7]. A second order accurate time advancement scheme is used in our simulation.

For any chosen combination of  $L_y$  and  $Re$ , the first step of the stability analysis is to obtain a steady base flow. At supercritical Reynolds numbers a steady base flow is obtained with the present time-accurate code by enforcing symmetry about the centerline of the cylinder wake as follows

$$u(x, y_c + y', t) = u(x, y_c - y', t), \quad v(x, y_c + y', t) = -v(x, y_c - y', t) \quad (1)$$

where  $y_c$  is the coordinate of the body centerline and  $y'$  is the distance from the centerline. This enforced symmetry prevents the existence of any antisymmetric disturbance, and therefore a steady flow can be established even at supercritical Reynolds numbers.

Contributed by the Fluids Engineering Division of ASME for publication in the JOURNAL OF FLUIDS ENGINEERING. Manuscript received November 9, 2004; final manuscript received February 15, 2006. Review conducted by Joseph Katz.

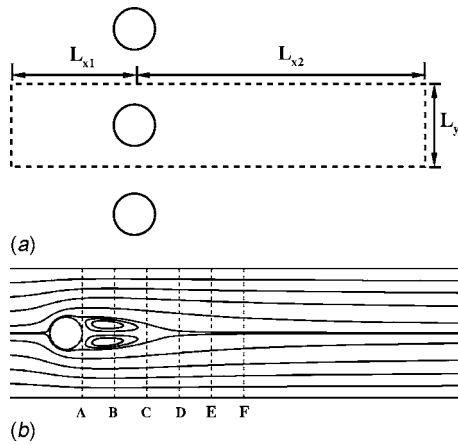


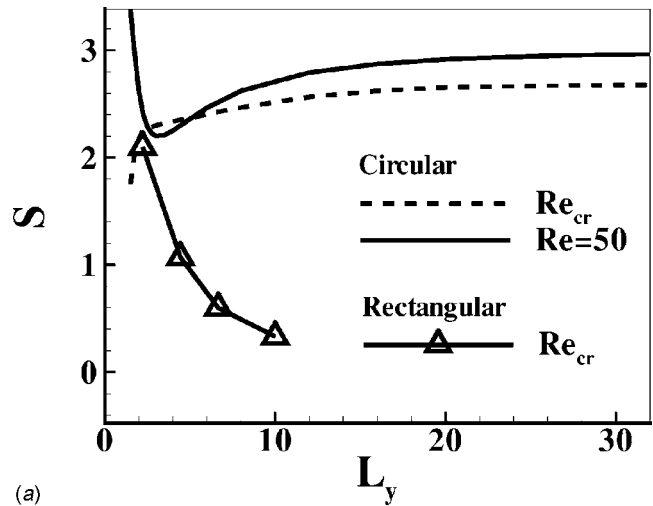
**Fig. 1** (a) The geometric arrangement for uniform flow past a transverse array of cylinders of circular cross section and (b) streamlines of the steady symmetric base flow at  $Re=50$  for  $L_y=4$

The stability of the fully developed base flow is investigated by introducing an antisymmetric disturbance into the flow and carefully monitoring its time evolution. In the present simulations the disturbance is introduced for a short period  $T$  in the form of inflow variation:  $u(x=-L_{x1}, y') = 1.0 + a * y' * \sin(2\pi t/T)$ . The disturbance was introduced for one complete period and after which a uniform flow was maintained at the inlet. Thus no net circulation is added into the flow. Following the introduction of the small disturbance, the flow is allowed to evolve in time, with the disturbance growing in case of instability and decaying otherwise. We have verified that the computed growth rate is not dependent on either the disturbance amplitude (a) or the disturbance period (T) over a wide range of their value. The growth of the disturbance is measured by calculating the norm of the difference between the disturbed,  $\mathbf{u}$ , and the base,  $\mathbf{u}_b$ , velocity fields

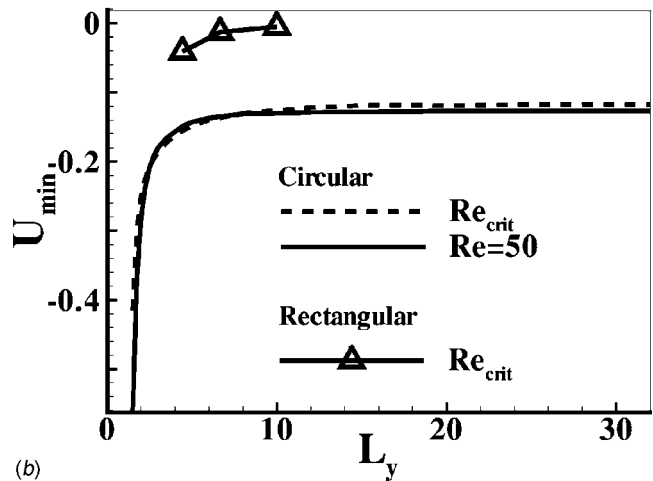
$$\|\mathbf{u}'\| = \|\mathbf{u} - \mathbf{u}_b\| = \left\{ \sum_{e=1}^{N_e} \sum_{i=1}^{N_x} \sum_{j=1}^{N_y} [((u_{i,j} - u_{b,i,j})^2 + (v_{i,j} - v_{b,i,j})^2) w_i w_j J(i,j,e)] \right\}^{1/2}$$

where the sum is over all the  $N_x \times N_y$  grid points within all the  $N_e$  spectral elements. The sum includes the quadrature weights  $w_i$  and  $w_j$ , and the Jacobian matrix  $J(i,j,e)$  in order to account for the nonuniform grid distribution and accurately represent the volume integral. Based on the above global measure of disturbance, the growth or decay rate of disturbance as a function of Reynolds number can be obtained and thereby the critical Reynolds number can be evaluated.

The simulations to be reported have been performed with a sufficiently large domain of  $L_{x1}=10$  and  $L_{x2}=28$ . Up to 2592 spectral elements are used to resolve the computational domain with  $9 \times 9$  Gauss-Lobatto Legendre collocation points within each element. By varying  $L_{x2}$  from 28 to 50 and the polynomial order of the spectral element ( $N_x$  and  $N_y$ ) from 5 to 10 we have verified that the results on mean flow and disturbance growth rate to be presented are well converged in terms of placement of the downstream boundary and in terms of spatial and temporal resolution. As shown in other studies [8] for flow past a circular cylinder, provided the inflow and outflow boundaries are placed at least about 8 and 14 diameters away from the center of the cylinder, their influence on flow development can be neglected. The present choice of computational domain size adequately satisfies this requirement.



(a)



(b)

**Fig. 2** (a) Wake length and (b) minimum streamwise velocity along the wake centerline. Results are shown for both the circular cylinder investigated here and for the long rectangular cylinder considered by [6]. For the circular cylinder results are presented for varying  $L_y$  at both  $Re=50$  (results at other  $Re$  are qualitatively similar) and  $Re=Re_{cr}$ .

### 3 Results

Here we systematically investigate the stability of 19 different periodic cylinder arrays with the transverse spacing between adjacent cylinders varied from  $L_y=1.5$  to  $L_y=32$ . The steady base flow at  $Re=50$  and  $L_y=4$  is shown in Fig. 1(b) as an example. A pair of recirculation eddies can be seen in the wake and the steady flow at other Reynolds numbers and other transverse spacings qualitatively remain the same.

The absolute instability of the steady base flow that initiates the onset of periodic vortex shedding can be gauged in terms of the reverse flow in the wake region. As a measure of the extent of reverse flow region, in Fig. 2(a) we plot its length, measured in terms of distance between the downstream end of the cylinder ( $x=0.5$ ) and the end of the separation region along the wake centerline. The strength of the reverse flow measured in terms of maximum negative velocity is also plotted in Fig. 2(b) and both these results are plotted as a function of transverse spacing at a fixed Reynolds number of  $Re=50$ . The maximum reverse flow magnitude decreases with increasing  $L_y$  and reaches a near constant value of about  $-0.13$  for  $L_y > 10$ . The size of the recirculation region, however, shows an interesting trend. For small  $L_y$  the recirculation region shrinks with increasing  $L_y$ , reaches a mini-

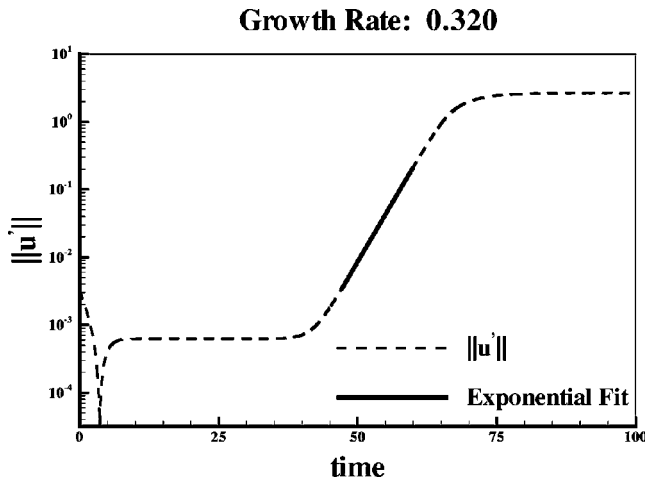


Fig. 3 Log-linear plot of  $\|u'\|$  versus time for  $L_y=1.5$  and  $Re=38$ ; the growth rate obtained is 0.320

imum length of about 2.3 at  $L_y \approx 3$ , and with further increase in transverse spacing the wake length increases slowly and approaches a value of about 2.7 corresponding to that of an isolated cylinder in cross flow. As we will see below, this behavior of the reverse flow region has an inverse relation to the behavior of critical Reynolds number for the onset of unsteadiness.

The above characterizations of the recirculation region are also plotted as a function of  $L_y$  at  $Re_{cr}$ . As will be seen below, over a narrow range of  $2.5 < L_y < 5$ , the critical Reynolds number becomes larger than 50 and outside this range  $Re_{cr} < 50$ . The behavior of the steady base flow for all  $L_y$  is such that with increasing  $Re$  both the wake length and the intensity of reverse flow increases. This Reynolds number dependence accounts for the difference between the results for  $Re=50$  and  $Re_{cr}$  seen in Fig. 2. For comparison the wake length and maximum reverse flow for the rectangular cylinder array considered in [6] are also plotted in Fig. 2, at the critical Reynolds number. The substantial difference between the circular cross section and the long rectangular cross section considered in [6] is clearly evident in the wake behavior. For the periodic array of long rectangular cylinders the recirculation region is considerably small and the reverse flow is significantly weaker.

By monitoring the global measure of perturbation, the growth rate is extracted from the slope of the exponential growth region

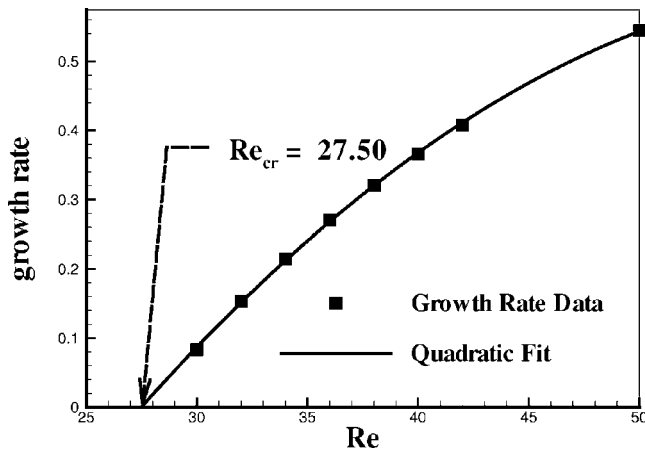


Fig. 4 Quadratic fit of growth rate versus  $Re$  for  $L_y=1.5$  case.  $Re_{cr}$  is the critical  $Re$  at which the growth rate is zero. Extrapolation of the plot gives a  $Re_{cr}$  of 27.5. For  $L_y=1.5$ , Reynolds numbers greater than 27.5 will result in vortex shedding.

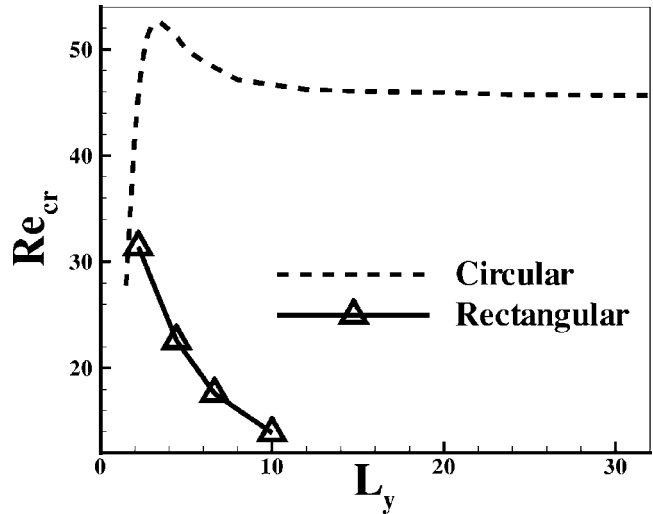


Fig. 5 Critical Reynolds number versus transverse separation for both the circular and the long rectangular cylinder geometries. The results for the long rectangular cylinder are from [6].

of the log-linear plot of  $\log\|u'\|$  versus time. For illustration, the plot for  $L_y=1.5$  at  $Re=38$  is shown in Fig. 3, which yields a growth rate of about 0.320. For Reynolds numbers above criticality the growth rate is positive and by extrapolating the growth rate obtained for several Reynolds numbers the critical Reynolds number corresponding to zero growth rate can be obtained. The growth rate thus obtained at several supercritical Reynolds numbers for  $L_y=1.5$  is shown in Fig. 4. A quadratic fit that well captures the growth rate versus  $Re$  is also shown. Extrapolating the computed results, a critical Reynolds number of  $Re_{cr}=27.50$  is obtained.  $Re_{cr}$  thus obtained for varying transverse spacings is shown in Fig. 5. For large transverse spacing as  $L_y \rightarrow \infty$  the critical Reynolds number approaches a value of about 46, corresponding to that of an isolated cylinder in uniform cross flow [9,10].

The structure of the unstable mode is extracted in terms of the growing disturbance. Figure 6 shows the streamwise and transverse velocity contours of the growing disturbance for the case of  $L_y=2$  and  $Re=50$ . Also shown in Fig. 6 is the vortical structure of the wake extracted in terms of swirling strength, defined as the imaginary part of the complex conjugate eigenpair of the velocity gradient tensor [11]. The structure of the unstable mode is qualitatively the same as that seen for rectangular cylinder array (see [6]) and is characteristic of wake instability. The onset of unsteadiness is clearly associated with a periodic evolution of the disturbance superposed over its exponential growth. Figure 6 shows the structure of the unstable mode at one instance in time and the eigenmode at other time instances corresponds to a downstream propagation of the vortical disturbance. For all transverse spacings the structure of the growing disturbance is very similar to that shown in Fig. 6.

#### 4 Discussion

The variation in  $Re_{cr}$  with transverse spacing for the case of circular cylinder array is distinctly different from that obtained in [6] for long rectangular cylinders (see Fig. 5). For the rectangular cylinder as  $L_y$  is increased from about 2 to 10,  $Re_{cr}$  decreased from about 31.4 to 13.9. Stability analysis of a one-dimensional sinusoidal profile of transverse wavelength equal to  $L_y$  was performed to explain the above behavior.

In [6] it was argued that the critical Reynolds number for a periodic array, provided the wake profile is nearly sinusoidal in shape, can be expressed as

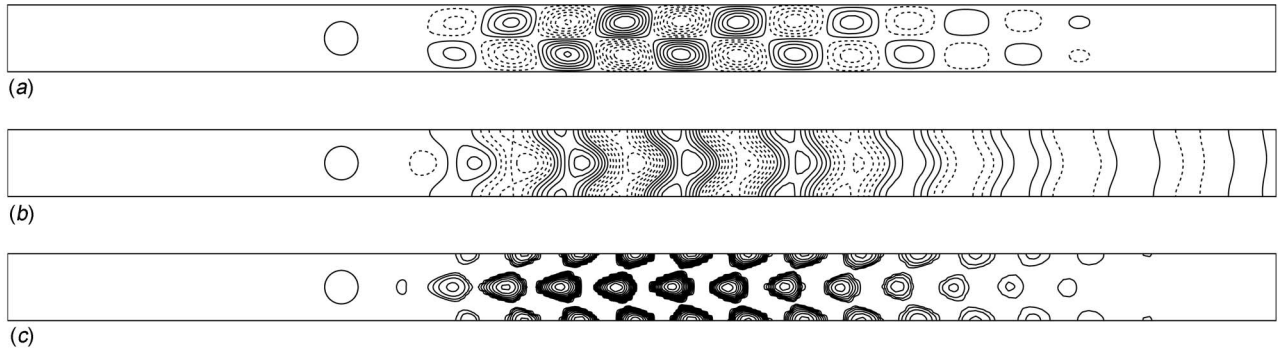


**Fig. 6** The eigenvector of the unstable mode at  $Re=50$  and  $L_y=2$ . Plotted are contours of (a) streamwise velocity, (b) transverse velocity, and (c) swirling strength [11].

$$Re_{cr} = \frac{c(L_y - 1)^\gamma}{L_y} \quad (2)$$

Here the factor  $L_y$  in the denominator accounts for the fact that for a sinusoidal wake profile the appropriate length scale is not the thickness (or diameter) of the cylinder, but the transverse spacing between the cylinders. The factor  $(L_y - 1)^\gamma$  in the numerator accounts for the decrease in the strength of reverse flow with increasing  $L_y$ . In the case of long rectangular cylinders, it was observed that for  $L_y$  in the range 2–10, the wake profiles are nearly sinusoidal. As a result, in accordance to the one-dimensional stability theory, a near perfect collapse of  $Re_{cr}$  can be obtained with  $\gamma=0.344$ . The scaled critical Reynolds number was given by  $c = Re_{cr} L_y / (L_y - 1)^{0.344} \approx 65$ .

For the periodic array of rectangular cylinders, as transverse spacing increases above ten the velocity profile in the wake is expected to deviate from sinusoidal shape. In response,  $Re_{cr}$  will increase after reaching a minimum and approach a value of about 112, corresponding to that of an isolated rectangular cylinder. In contrast for the case of an array of circular cylinders, a critical Reynolds number of about 46 for an isolated cylinder is approached from above. Thus the asymptotic behavior as  $L_y \rightarrow \infty$  is quite different for the two cases.

Specifically, while the dependence of  $Re_{cr}$  on  $L_y$  for the case of long rectangular cylinders can be accurately described in terms of the one-dimensional stability theory of sinusoidal base profile, the  $Re_{cr}$  versus  $L_y$  trend for the circular cylinder exhibits a complex dependence. A close examination of the steady base flow profiles for both the array of rectangular and circular cylinders reveals that the fundamental difference between their stability is in how their streamwise velocity profiles in the wake region depart from a pure sinusoid. In case of periodic array of long rectangular cylinders, the channel region between the rectangles, for at least  $L_y$  less than 10, was long enough to establish nearly developed flow between them, which subsequently developed into a near sinusoidal profile in the immediate wake region. On the other hand, the wake profiles for the case of circular cylinder array shown in Fig. 7, for  $L_y=4$  and  $Re=50$ , clearly show substantial departure from a pure sinusoidal shape. The velocity profiles are shown at several streamwise locations starting from the trailing edge of the cylinder and spaced one nondimensional unit apart in the  $x$  direction, whose locations are shown as the dashed lines in Fig. 1(b).

As may be expected at  $x=0.5$ , where the trailing end of the cylinders is located, the velocity profile (Profile A) deviates substantially from a pure sinusoid. However, unlike in the case of long rectangular cylinders, the velocity profiles do not quickly relax to a sinusoidal shape. A quantitative estimate of this departure can be obtained with a cosine series expansion of the nondimensional streamwise velocity profile of the form

$$u(y') = c_0 + \sum_{k=1}^{\infty} c_k \cos\left(k \left[ \pi + \frac{2\pi y'}{L_y} \right]\right), \quad (3)$$

where  $c_1$  is the amplitude of primary sinusoidal variation and  $c_2$  is the amplitude of first harmonic and so on. Table 1 presents the first few cosine coefficients for the different profiles, marked A, B, C, etc., in Fig. 7. The first and higher harmonics are not entirely negligible either in the recirculation regions or downstream of it. In contrast, for the rectangular cylinders,  $c_2$  was about an order on magnitude lower and the higher coefficients are virtually zero, indicating a near pure sinusoidal profile.

Stability of the one-dimensional periodic base flow profile given in Eq. (3) was analyzed by [6]. In the limit of  $\epsilon=c_2/c_1 \rightarrow 0$  the critical Reynolds number for the onset of absolute instability in the wake was obtained as

$$Re_{cr} = 9 \frac{(c_1 - 0.945)^{0.95}}{L_y}. \quad (4)$$

Note that  $c_1$  greater than 1 results in a region of negative streamwise velocity and corresponds to the presence of reversed flow. According to the above formula absolute instability sets in as long as  $c_1 > 0.945$  and thus there is no need for a reversed flow region in case of purely sinusoidal base flow. For the case of rectangular cylinder array the wake profiles were close to being pure sinusoidal and as a result the onset of vortex shedding occurred at fairly small values of reversed flow.

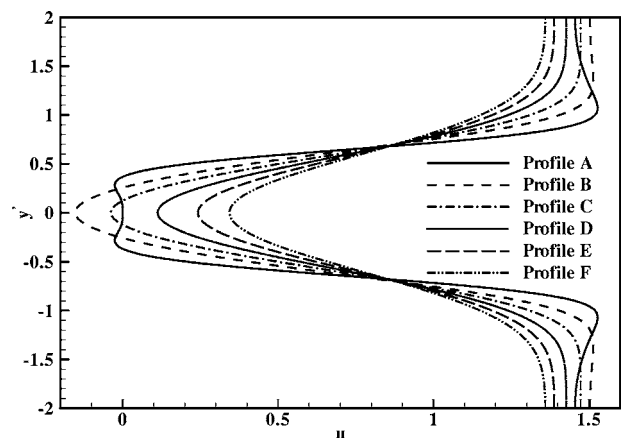


**Fig. 7** Streamwise velocity profiles at six different streamwise locations in the cylinder wake for  $Re=50$  and  $L_y=4$ . The  $x$  locations are shown in Fig. 1(b).

**Table 1 The first few Fourier cosine expansion coefficients for the six velocity profiles shown in Fig. 7**

Coefficient	Profile A	Profile B	Profile C	Profile D	Profile E	Profile F
0	1.000	1.000	1.000	1.000	1.000	1.000
1	0.786	0.801	0.720	0.628	0.552	0.494
2	-0.408	-0.360	-0.294	-0.234	-0.187	-0.149
3	0.009	0.037	0.038	0.030	0.021	0.014
4	0.141	0.040	0.014	0.005	0.002	0.001

According to stability the theory presented in [6] positive values of  $\epsilon$  accelerate the onset of instability, while negative values of  $\epsilon$  delay the onset. The broad freestream velocity between the circular cylinders and a narrow focused deficit region behind the cylinders seen in Fig. 7 correspond to negative values of  $\epsilon$  (also see Table 1). Thus the effect of higher harmonics in the case of circular cylinder array is to slow down the onset of wake instability. This observation is consistent with the fact that a relatively strong reverse flow in the wake region is required in the case of circular cylinder (see Fig. 2(b)).

For small transverse separation ( $L_y < 3$ ) the wake profile behind the circular cylinder array does develop into a near sinusoidal shape. However, in this range of separation, with increasing  $L_y$ , the magnitude of reverse flow rapidly decreases (see Fig. 2(a)). This decrease more than compensates for the increase in length scale and thus results in an increasing  $Re_{cr}$  with increasing  $L_y$ . For  $L_y > 3$  the magnitude of reverse flow remains nearly uniform, however, as was discussed above, the wake profile begins to depart from pure sinusoid and the net effect is a slow decrease in  $Re_{cr}$  with  $L_y$ . Thus for a circular cylinder array the observed dependence of critical Reynolds number on transverse spacing, although more complex, is consistent with one-dimensional stability theory presented in [6].

In a bluff body wake the velocity profile continuously changes along the flow direction. Immediately downstream of the tail end of the body a region of reverse flow begins. As we progress downstream, a point of maximum reverse flow is first reached, from then on the magnitude of reverse flow decreases. At the reattachment point, the reverse flow is identically zero and further downstream the wake profile remains entirely positive. Which of these profiles controls the critical behavior at the onset of instability is an open question [12–14]. This issue has been discussed in the literature in the context of mode selection. In the case of long rectangular cylinders the variation in critical Reynolds number with  $L_y$  to some extent appears to depend on the level of maximum reverse flow. In the present case of an array of circular cylinders it is interesting to note that  $Re_{cr}$  versus  $L_y$  appears to be dependent on the extent of reverse flow, rather than the magnitude of maximum reverse flow.

## 5 Conclusion

A numerical investigation of the stability of steady base flow over a transverse periodic array of circular cylinders is considered. Particular attention is paid to the effect of transverse spacing on the critical Reynolds number for the onset of vortex shedding. For very large values of transverse spacing, a critical Reynolds number of about 46 corresponding to that of an isolated circular cylinder is recovered. As the transverse spacing between adjacent circular cylinders is decreased,  $Re_{cr}$  first increases reaching a maximum of about 52.5 at  $L_y \approx 3$  and then with further decrease in  $L_y$ , the critical Reynolds number rapidly decreases. The above result is expected to be valid even for a two-dimensional array of

inline and staggered cylinders, provided the streamwise spacing between adjacent transverse columns is greater than few cylinder diameters [3,6].

The dependence of  $Re_{cr}$  on  $L_y$  obtained for the canonical circular cylinder geometry is quite different from that observed in [6] for the case of a periodic array of long rectangular cylinders. The difference in the stability of steady base flow for these two geometries can be traced back to sinusoidal versus nonsinusoidal nature of streamwise velocity profiles in the wake region. The long channel region between the cylinders in case of long rectangular cross section allows for the development of a near sinusoidal profile and as a result the dependence of  $Re_{cr}$  versus  $L_y$  follows the predictions of a one-dimensional stability theory. For the case of circular cylinder array the departure from a pure sinusoidal profile in the wake is quite significant and as a result the onset of vortex shedding exhibits quite a different trend. Of importance is the fact that  $Re_{cr}$  appears to be dependent more on the size of the recirculation region, than on the intensity of the maximum reverse flow.

## Acknowledgment

The computations presented here were performed at the National Center for Supercomputing Applications. The authors acknowledge the Computational Science and Engineering Fellowship that supported L.Z. The authors also express their sincere thanks to Dr. Paul Fischer for his help with the spectral element code.

## References

- [1] Sangani, A. S., and Acrivos, A., 1982, "Slow Flow Past Periodic Arrays of Cylinders With Application to Heat Transfer," *Int. J. Multiphase Flow*, **8**, pp. 193–206.
- [2] Wang, C. Y., 2001, "Stokes Flow Through a Rectangular Array of Circular Cylinders," *Fluid Dyn. Res.*, **29**(2), pp. 65–80.
- [3] Chen, Y. N., 1968, "Flow Induced Vibration and Noise in Tube-Bank Heat Exchangers Due to Von Karman Streets," *J. Eng. Ind.*, **90**, pp. 134–146.
- [4] Koch, D. L., and Ladd, A. J. C., 1997, "Moderate Reynolds Number Flows Through Periodic and Random Arrays of Aligned Cylinders," *J. Fluid Mech.*, **349**, pp. 31–66.
- [5] Lee, S. L., and Yang, J. H., 1997, "Modeling of Darcy-Forchheimer Drag for Fluid Flow Across a Bank of Circular Cylinders," *Int. J. Heat Mass Transfer*, **40**, pp. 3149–3155.
- [6] Balachandar, S., and Parker, S. J., 2002, "Onset of Vortex Shedding in an Inline and Staggered Array of Rectangular Cylinders," *Phys. Fluids*, **14**, pp. 3714–3732.
- [7] Deville, M. O., Fischer, P. F., and Mund, E. H., 2002, *High-Order Methods for Incompressible Fluid Flow*, Cambridge University Press, Cambridge.
- [8] Tezduyar, T. E., and Shih, R., 1991, "Numerical Experiments on Downstream Boundary of Flow Past Cylinder," *J. Eng. Mech.*, **117**, pp. 854–871.
- [9] Zebib, A., 1987, "Stability of Viscous Flow Past a Circular Cylinder," *J. Eng. Math.*, **21**, pp. 155–165.
- [10] Jackson, P., 1987, "A Finite Element Study of the Onset of Vortex Shedding in Flow Past Various Shaped Bodies," *J. Fluid Mech.*, **182**, pp. 23–45.
- [11] Zhou, J., Adrian, R. J., Balachandar, S., and Kendall, T. M., 1999, "Mechanisms for Generating Coherent Packets of Hairpin Vortices in Near-Wall Turbulence," *J. Fluid Mech.*, **387**, pp. 353–396.
- [12] Pierrehumbert, R. T., 1984, "Local and Global Baroclinic Instability of Zonally Varying Flow," *J. Atmos. Sci.*, **41**, pp. 2141–2162.
- [13] Koch, W., 1985, "Local Instability Characteristics and Frequency Determination of Self-Excited Wake Flows," *J. Sound Vib.*, **99**, pp. 53–83.
- [14] Monkewitz, P. A., and Nguyen, L. N., 1987, "Absolute Instability in the Near-Wake of Two-Dimensional Bluff Bodies," *J. Fluids Struct.*, **1**, pp. 165–184.

## Pranab K. Mohapatra

Assistant Professor  
Department of Civil Engineering,  
Indian Institute of Technology  
Kanpur, India, 208016  
e-mail: pranab@iitk.ac.in

## M. Hanif Chaudhry

Mr. and Mrs. Irwin B. Kahn Professor and Chair  
e-mail: Chaudhry@sc.edu

## Ahmed Kassem

Research Assistant Professor  
e-mail: kassem@enr.sc.edu

Department of Civil and Env. Engineering,  
University of South Carolina,  
300 South Main Street,  
Columbia, SC 29208

## Jamaluddin Moloo

Assistant Professor  
Department of Internal Medicine,  
University of South Carolina,  
Columbia, SC 29208  
e-mail: moloo@gw.mp.sc.edu

# Detection of Partial Blockages in a Branched Piping System by the Frequency Response Method

*Steady oscillatory flow in a branched piping system with partial blockages is studied by using the frequency response method. The peak pressure frequency diagrams at the downstream end are developed with the partial blockage at different locations in the system by using the transfer matrix method. A systematic procedure is presented to estimate the size and the location of a single partial blockage in the system. For more than one partial blockage, it is observed that there is a definite relationship between the frequency responses of the individual and combined partial blockages. [DOI: 10.1115/1.2238880]*

*Keywords: branched piping system, partial blockage, steady-oscillatory flow, frequency domain, transfer matrix method, peak pressure frequency diagram*

## Introduction

Both natural and man-made flow systems generally have a branch line, e.g., water supply systems, sewer networks, and cardiovascular system. Partial or full blockages, though unwanted, may occur due to solid waste deposition in a sewer line, due to freezing in water supply pipes, and due to plaque deposition in a cardiovascular system. Blockage at any location, in the main line or in a branch, may cause problems and information about the size and location of the blockage helps in taking remedial action. Presently available methods to detect the location of a blockage in a fluid system require inspections and/or measurements throughout the system. These methods are time consuming and costly. Scott and Satterwhite [1] used the backpressure technique for monitoring the development of blockages in gas flow lines. The technique works by comparing production data to a base line performance curve (the relationship between pressure drop and flow rate) to quantify partial blockages. Scott and Yi [2] developed an analysis method that allows generalized application of the friction-loss technique to partial blockages of any length. Adewumi et al. [3] presented the interaction of pipeline transients with blockages in pipes. They demonstrated that detection of blockage could be achieved by generating an appropriate transient pulse at the inlet. A pipeline may be scanned by using radio-isotope technology to detect blockages [4]. Typical areas of application include: Scale thickness in well flow lines and associated manifolds; ice blockage in flare gas lines; hydrate blockage in gas lines; halon levels in fire fighting spheres and cylinders; and, oil carry over into exit gas lines of offshore separators. The Senaco AS100 is an acoustic sensor used for detection of blockages in pipes [5]. It reacts instantly to changes in flow of pellets, powders, or most bulk solids in pipes, chutes, vibratory feeders, pneumatic conveyors, and

gravity flow systems. Any sudden blockage that prevents product flow or any rupture that increases flow as product escapes from a pipe or bag is immediately detected by the AS100. A semi-autonomous surveillance method has been used for sewer maintenance [6]. The Doppler guide wire for detecting stenosis in human cardiovascular systems [7] measures pressure gradients across a stenosis. Recently, Wang [8] developed a technology for blockage detection in water distribution systems. His research work is focused on the dynamic effects of blockage on pipeline transients. Analytical solutions expressed in a Fourier series for the transients in a pipeline have led to the development of a new detection technique that utilizes the damping of a transient event by a blockage.

The flow transients may be analyzed either in the time domain or in the frequency domain. In the time domain, the method of characteristics (MOC) is used to solve the governing partial differential equations [9,10]. Two methods are available for analysis in the frequency domain: the impedance method [9] and the transfer matrix method [10]. The concept of impedance was introduced by Rocard [11] and was applied later by Waller [12]. Streeter and Wylie [9] used this method to analyze complex systems. The transfer matrix method has been used for analyzing structural and mechanical vibrations [13,14] and for analyzing the electrical systems [15]. Chaudhry [10] presented this method for the analysis of hydraulic systems. The impedance method produces lengthy algebraic equations whereas the transfer matrix method is simple and systematic. Mpesha et al. [16,17] presented a methodology to detect leaks in piping system by using the transfer matrix method. This procedure is extended herein to detect blockages in a branched piping system.

In this paper, frequency responses due to partial blockages in a branched piping system are analyzed. The methodology is described first and some typical examples are presented to demonstrate the application of the method.

Contributed by the Fluids Engineering Division of ASME for publication in the JOURNAL OF FLUIDS ENGINEERING. Manuscript received July 21, 2003; final manuscript received January 15, 2006. Review conducted by Joseph Katz.



## Methodology

Unsteady flow in a piping system is described by the continuity and momentum equations. These equations in the time domain are converted into the frequency domain by assuming a sinusoidal variation of pressure and flow and by linearizing the nonlinear functions. The transfer matrix method is used herein and a short description of the method is presented in the following section; for details, refer to Chaudhry [10].

**Frequency Analysis by Transfer Matrix Method.** A hydraulic system consists of several components, and a transfer matrix may be used to describe each component. Transfer matrices are classified into three types: A field matrix,  $F$ , relating state vectors at two adjacent sections of a pipe; a point matrix,  $P$ , relating state vectors just to the left and to the right of a discontinuity; and an overall transfer matrix,  $U$ , relating state vectors at one end of the system to those at the other end. The state vector is defined as  $[q \ h \ 1]^T$ . By using the equations governing unsteady flow in pipes, the field matrix relating the state vectors at sections  $i$  and  $i+1$  of the  $i$ th pipe of length  $L_i$  may be obtained as

$$F_i = \begin{bmatrix} \cosh \mu_i L_i & -\frac{1}{Z_c} \sinh \mu_i L_i & 0 \\ -Z_c \sinh \mu_i L_i & \cosh \mu_i L_i & 0 \\ 0 & 0 & 1 \end{bmatrix} \quad (1)$$

where  $\mu = \sqrt{-w^2/a^2 + jgAwR/a^2}$ ;  $R = fQ_0/gD_0A^2$  (for turbulent flow);  $R = 64\vartheta/gAD_0^2$  (for laminar flow);  $g$ =acceleration due to gravity;  $A$ =cross-sectional area of the pipe;  $D_0$ =inside diameter of the pipe;  $f$ = Darcy-Weisbach friction factor;  $a$ =wave velocity;  $j = \sqrt{-1}$ ;  $w$ =frequency;  $\nu$ =kinematic viscosity of the fluid;  $Q_0$ =mean discharge; and  $Z_c$ =characteristic impedance of the pipe  $= \mu_i a_i^2 / jwgA_i$ . A point matrix is derived for each of the discontinuities, such as a valve, branch, or series junction. For example, the point matrix for an oscillating valve with sinusoidal valve motion is

$$P_{ov} = \begin{bmatrix} 1 & 0 & 0 \\ -\frac{2H_0}{Q_0} & 1 & \frac{2H_0k}{\tau_0} \\ 0 & 0 & 1 \end{bmatrix} \quad (2)$$

where  $H_0$ =mean pressure head;  $k$ =amplitude of the valve motion; and  $r_0$ =mean relative valve opening. Similarly, point matrix for a partial blockage,  $P_{pb}$ , is given by

$$P_{pb} = \begin{bmatrix} 1 & 0 & 0 \\ -\frac{2\Delta H_0}{Q_0} & 1 & 0 \\ 0 & 0 & 1 \end{bmatrix} \quad (3)$$

where  $\Delta H_0$ =the mean head loss across the partial blockage corresponding to the mean discharge,  $Q_0$ .

In the present study, the branch pipe has a dead end and the point matrix for this case is given by

$$P_{bd} = \begin{bmatrix} 1 & u_{b12} & 0 \\ u_{b11} & 0 & 0 \\ 0 & 1 & 0 \\ 0 & 0 & 1 \end{bmatrix} \quad (4)$$

where  $u_{b11}$  and  $u_{b12}$  are the elements of the overall matrix for the branch pipe. It may be noted that the overall transfer matrix for the branch,  $U_b$ , may be computed from the respective field and point matrices, considering the branch as a single pipe. In addition, point matrix for a partial blockage has to be considered in the calculation of  $U_b$ , if there is a partial blockage present in the

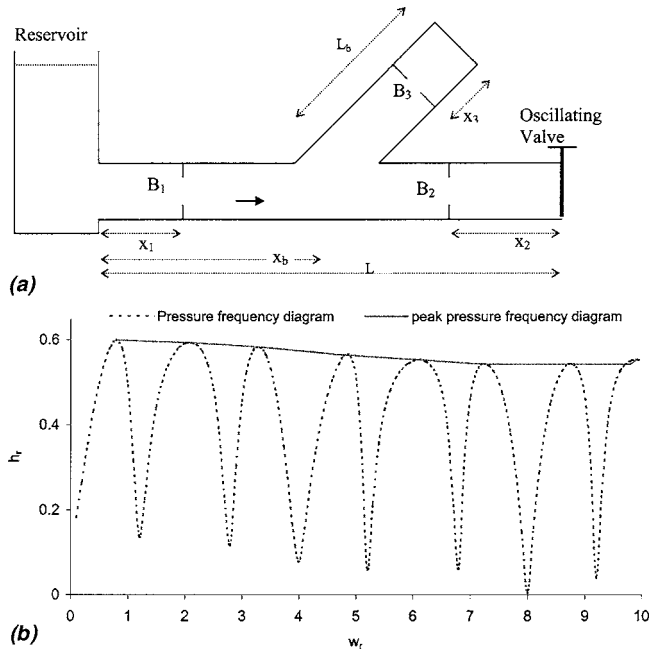


**Fig. 1 (a) Definition sketch fro branched piping system with partial blockages; (b) pressure frequency diagram and peak pressure frequency diagram at the valve**

branch pipe.

The overall transfer matrix  $U$  is obtained by an ordered multiplication of individual field and point matrices as

$$U = F_n P_n \dots F_3 P_3 F_2 P_2 F_1 \quad (5)$$

where  $n$ =number of components in the system.

The frequency response of fluid systems with different types of forcing functions may be determined systematically. In this paper, an oscillating valve at the downstream end of the piping system is considered as the forcing function. By using the point matrix for an oscillating valve and the boundary condition at the valve, the following expressions are obtained

$$q_{n+1}^L = u_{11} q_1^R + u_{13} \quad (6)$$

and

$$h_{n+1}^L = u_{21} q_1^R + u_{23} \quad (7)$$

where

$$q_1^R = \frac{u_{23} - \frac{2H_0}{Q_0} u_{13} + \frac{2H_0k}{\tau_0} u_{33}}{u_{21} - \frac{2H_0}{Q_0} u_{11} + \frac{2H_0k}{\tau_0} u_{31}} \quad (8)$$

and  $u_{11}, u_{12}, \dots, u_{13}$ =elements of the overall transfer matrix  $U$ . The absolute values of  $h_{n+1}^L$  and  $q_{n+1}^L$  are the amplitudes of pressure head and discharge fluctuations at the valve, respectively. The overall transfer matrix is obtained by using Eq. (5) and the frequency response is determined by using Eqs. (6)–(8).

**Peak Pressure Frequency Diagram.** By repeating the preceding procedure, amplitude of pressure fluctuation,  $h_{n+1}^L$  is calculated for different values of frequencies,  $w$ . The pressure frequency diagram is developed between  $h_r$  and  $w_r$ , where  $h_r = h_{n+1}^L / H_0$  is the amplitude of nondimensional pressure fluctuation and  $w_r = w / w_{th}$  is the frequency ratio (dotted curve in Fig. 1(b)). It may be noted that the theoretical frequency is given by  $w_{th} = 2\pi / T_{th}$ , where the theoretical period of the pipeline  $T_{th}$  is the sum of the period of each of the pipes with lengths  $L_1, L_2, \dots, L_n$ . A peak pressure fre-

**Table 1 Different scenarios for partial blockages in branch-pipe**

Case	Scenario
1	Partial blockage in the main line upstream of the branching junction (only $B_1$ )
2	Partial blockage in the main line downstream of the branching junction (only $B_2$ )
3	Partial blockage in the branch (only $B_3$ )
4	Partial blockages in the main line at both sides of branching junction ( $B_1$ and $B_2$ )
5	Partial blockages in the main line upstream of the branching junction and in the branch ( $B_1$ and $B_3$ )
6	Partial blockages in the main line downstream of the branching junction and in the branch ( $B_2$ and $B_3$ )
7	Three partial blockages ( $B_1$ , $B_2$ , and $B_3$ )

quency diagram is obtained from the pressure frequency diagram by joining the peaks of the nondimensional pressure amplitudes (solid line in Fig. 1(b)). Similarly, discharge frequency and peak discharge frequency diagrams are obtained from the nondimensional discharge,  $q_r = q_{r+1}^L / Q_0$ , and nondimensional frequency,  $w_r$ .

### Partial Blockage in Branched Piping System

Definition sketch for partial blockages in a branched piping system is shown in Fig. 1. The main line has a constant-level reservoir at the upstream end and an oscillating valve at the downstream end produces the steady-oscillatory flow. The branch has a dead end. The length of the main line is  $L$  and the length of the branch pipe is  $L_b$ . The branching junction is located at a distance of  $x_b$  from the upstream end of the main line. Partial blockages ( $B_1, B_2, B_3$ ) at three different locations are shown in this figure. The location of the blockage,  $x$ , is defined by the distance from the respective ends. The size of the blockage is defined as  $z = 1 - D/D_0$ , where  $D$  is the diameter of the opening at the partial blockage and  $D_0$  is the diameter of the pipe. The value of  $z$  lies between 0.0 and 1.0. A larger value of  $z$  indicates less opening and it is associated with a larger value of head loss. The size and the location of a partial blockage affect the frequency response of the system. Depending on the combination of the partial blockages, seven different cases are considered for a detailed analysis (Table 1). The common parameters used in these cases are: length of main pipe,  $L = 1600$  m; mean discharge,  $Q_0 = 0.1$  m<sup>3</sup>/s; mean pressure head,  $H_0 = 50$  m; internal diameter of the main pipe as well as of the branch pipe,  $D_0 = 0.3046$  m; wave velocity in the main and branch pipes,  $a = 1200$  m/s; friction coefficient for the pipe wall,  $f = 0.0$ ; and,  $k$  value for the oscillating valve = 0.3.

**Case 1: Partial Blockage in Main Line Upstream of Branching Junction ( $B_1$ ).** Three different cases for the location of the partial blockage from the reservoir ( $x_1 = 200, 400$  and  $600$  m) are considered and the size of the partial blockage in all these cases is assumed to be  $z_1 = 0.55$ , which causes a mean pressure head loss of 15 m for a flow of  $0.1$  m<sup>3</sup>/s. The peak pressure frequency diagrams at the downstream end of the main line are presented in Figs. 2(a)–2(c). In all these curves, the peak comes first and the number of prominent troughs (troughs having values  $\geq 90\%$  of the maximum amplitude) in these curves indicates the location of the blockage. For example, the number of prominent troughs are 6, 12 and 18 which indicate values of  $x_1 = 200, 400$ , and  $600$  m, respec-

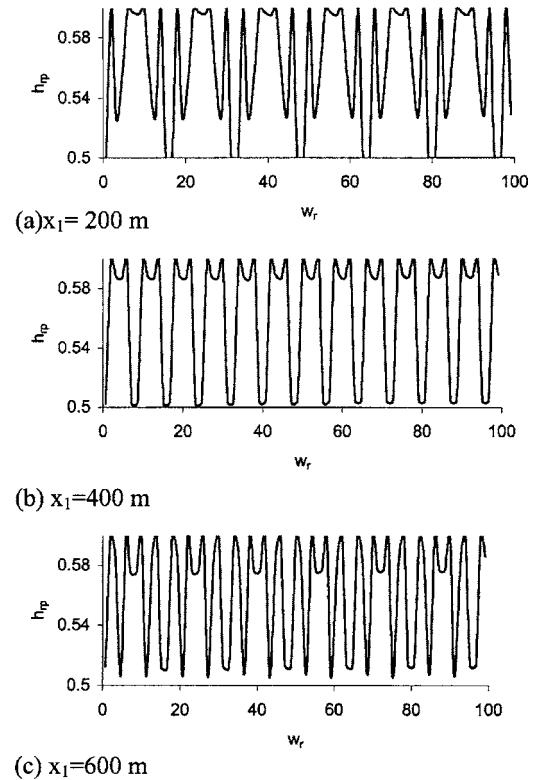


**Fig. 2 Peak pressure frequency diagram for partial blockage  $B_1$  ( $z=0.55$ ) upstream of branching junction**

tively. The average value in the peak pressure frequency diagrams is constant, (i.e.,  $\bar{h}_{rp} = 0.563$ ) in Figs. 2(a)–2(c). This indicates the size of the blockage. Average value of nondimensional pressure fluctuation is defined as  $\bar{h}_{rp} = (1/N) \sum_1^N h_{rpi}$ ; where,  $h_{rpi}$  is the ordinate corresponding to  $i$ th frequency ratio (refer Fig. 2).

**Case 2: Partial Blockage in Main Line Downstream of Branching Junction ( $B_2$ ).** As in the previous case, three different locations of the partial blockage are considered ( $x_2 = 200, 400$ , and  $600$  m). The size of the partial blockage,  $z_2 = 0.55$ . The peak pressure frequency diagrams at the downstream end of the main line are presented in Figs. 3(a)–3(c). The trough comes first in all these curves. A constant average peak pressure in these curves ( $\bar{h}_{rp} = 0.572$ ) indicates the size of the partial blockage and the number of peaks indicates the location of the partial blockage from the valve. As the distance from the valve end increases, the number of peaks in the peak pressure frequency diagram becomes larger. Comparing Figs. 2 and 3, the frequency responses are more clear (well defined peaks or troughs) when the blockage is located downstream of the branching junction. It is probably due to the proximity of the partial blockage to the valve, where the frequency responses are computed.

The effect of the size of the blockage ( $z = 0.40, 0.50$ , and  $0.55$ ) on the peak pressure frequency diagram is presented in Fig. 4. As the blockage size increases the amplitude and the average value ( $\bar{h}_{rp}$ ) in the peak pressure frequency diagram increase. It may be noted that the upper limit of the curves remain same where as the lower limit decreases with increase in the blockage size.

**Case 3: Partial Blockage in the Branch Pipe ( $B_3$ ).** Three different locations of the partial blockage ( $x_3 = 200, 400$ , and  $600$  m) are considered and the size of the partial blockage is  $z_3 = 0.55$ . This size of the blockage in the branch pipe is assumed to have a head loss of 15 m for a discharge of  $0.1$  m<sup>3</sup>/s. The peak

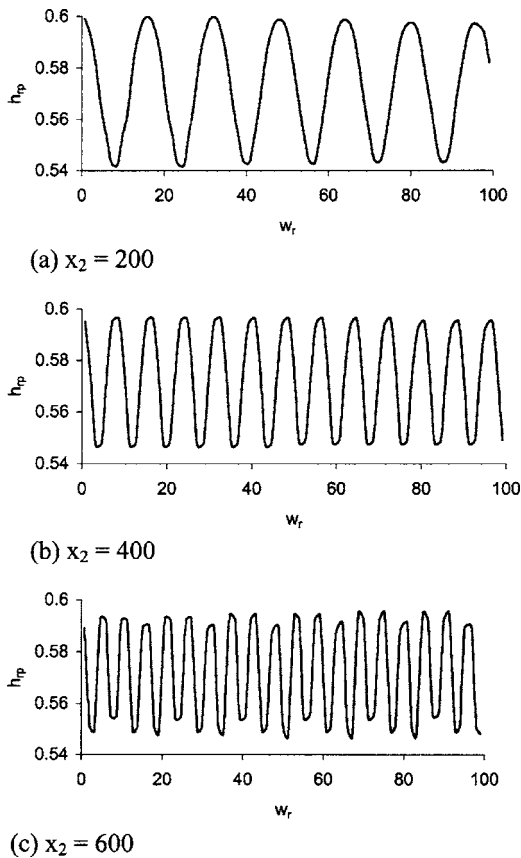


**Fig. 3 Peak pressure frequency diagram for partial blockage  $B_2$  ( $z=0.55$ ) downstream of branching junction**

pressure frequency diagrams are presented in Figs. 5(a)–5(c). As usual, a constant value of average peak pressure ( $\bar{h}_{pp}=0.573$ ) indicates the size of the partial blockage and different numbers of peaks in the peak pressure frequency diagram indicate the position of the partial blockage from the dead end. It is interesting to note that for a single partial blockage downstream of the branch (case 2) and in the branch (case 3) the number of peaks and the average peak pressure are similar. For example, Figs. 3(b) and 5(b) are similar and it is very difficult to distinguish one from the other. Therefore, the peak discharge frequency diagram may be utilized to differentiate between Cases 2 and 3. The peak discharge frequency diagram for  $x_2=x_3=200$  m is shown in Fig. 6. The numbers of troughs are equal in the peak pressure frequency and peak discharge frequency diagrams when the partial blockage is located in the main line. However, when the blockage is in the branch pipe, the number of troughs is more in the peak discharge frequency diagram. In addition, the average value of the peak discharge is less (0.255 versus 0.263) when the partial blockage is in the branch pipe. A summary of the results derived from various numerical experiments indicating the effect of the size of a partial blockage on the average and lower limits in the peak pressure frequency diagram is presented in Table 2.

**Case 4: Partial Blockages at Both Sides of Branch ( $B_1$  and  $B_2$ ).** As a test case, the size and location of the partial blockages considered are:  $z_1=0.55$ ,  $z_2=0.50$ ,  $x_1=200$  m, and  $x_2=300$  m. The partial blockage sizes correspond to head losses of  $\Delta H_{01}=15$  m,  $\Delta H_{02}=10$  m, respectively, for a discharge of  $0.1$  m<sup>3</sup>/s. Other parameters are the same as those used in the previous cases. The peak pressure frequency diagram for the individual and combined partial blockages is presented in Fig. 7. It is difficult to know the

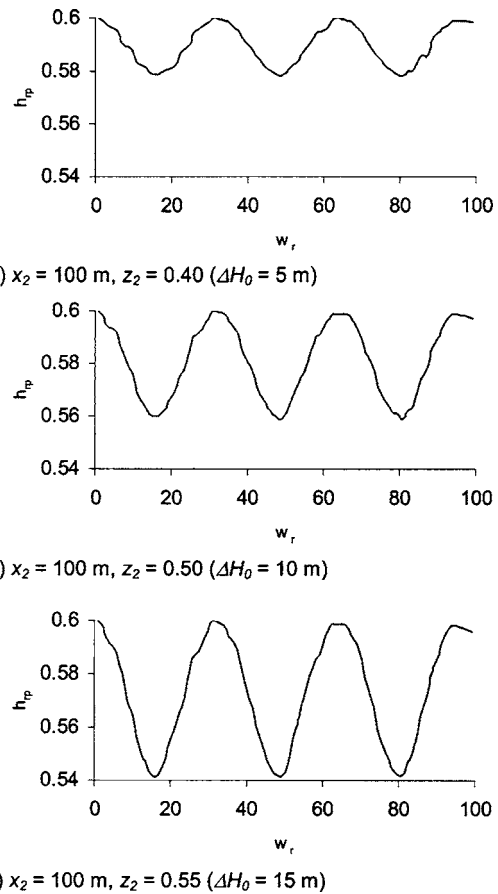


**Fig. 4 Effect of blockage size on peak pressure frequency response**

individual responses from the combined response. However, there is a definite relationship between the individual and combined responses

$$c_1 + c_2 - c_{1-2} = c_0 \quad (9)$$

In Eq. (9),  $c_1$  is the ordinate for any nondimensional frequency,  $w_r$ , in Fig. 7(a);  $c_2$  and  $c_{1-2}$  are the corresponding ordinates in Figs. 7(b) and 7(c), respectively, for the same  $w_r$  value; and,  $c_0$  is the peak pressure when there is no blockage in the system (0.6 in the present case). Equation (9) is true for any combination of  $x_1$ ,  $x_2$ ,  $z_1$ , and  $z_2$ . Thus, it can be used to predict the development of an extra partial blockage in the main line if the frequency response of an existing blockage is known. For example, if the response for  $B_2$  is known and with time the new response becomes  $c_{1-2}$  due to the development of an additional partial blockage,  $B_1$ , then,  $c_1$  can be predicted by using Eq. (9). A comparison of predicted  $c_1$  using Eq. (9) and actual  $c_1$  is shown in Fig. 8.

**Case 5: Partial Blockages in and Upstream of Branch ( $B_1$  and  $B_3$ ).** Similar to that of case 5, a test is considered:  $z_1=0.55$ ,  $z_3=0.50$ ,  $x_1=200$  m, and  $x_3=300$  m. Other parameters are the same as those used in the previous cases. The frequency response for the peak pressure due to the individual and combined partial blockages is presented in Fig. 9. It is difficult to isolate the individual responses from the combined response. However, there is a relationship between the responses, i.e.,

$$c_1 + c_3 - c_{1-3} = c_0 \quad (10)$$

**Case 6: Partial Blockages in and Downstream of Branch ( $B_2$  and  $B_3$ ).** The following test case is analyzed:  $z_1=0.55$ ,  $z_3=0.50$ ,  $x_2=200$  m, and  $x_3=300$  m. The frequency response for the peak

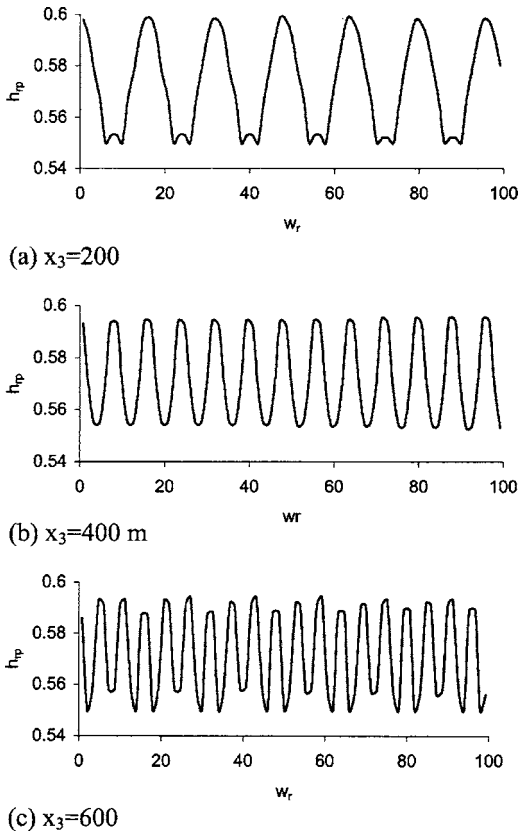


Fig. 5 Peak pressure frequency diagram for partial blockage  $B_3$  ( $z=0.55$ ) in the branch

pressure due to the individual and combined partial blockages is presented in Fig. 10. Similar to cases 5 and 6, there is a relationship between the responses

$$c_2 + c_3 - c_{2-3} = c_0 \quad (11)$$

It may be noted that Eqs. (9)–(11) are similar and can be used to predict the development of an extra partial blockage if the frequency response of an existing blockage is known. These equations may also be used to predict any change in the size of an existing blockage.

**Case 7: Three Partial Blockages Present ( $B_1$ ,  $B_2$ , and  $B_3$ ).** Consider the size and location of these partial blockages as  $z_1 = 0.55$ ,  $z_2 = 0.50$ ,  $z_3 = 0.50$ ,  $x_1 = 400$  m,  $x_2 = 200$  m, and  $x_3 = 300$  m. Other parameters are the same as those used in the previous cases. The peak pressure frequency diagrams for the individual and combined partial blockages are presented in Fig. 11. The derivation of the individual responses from the combined response is difficult and the following relationship between the responses exists

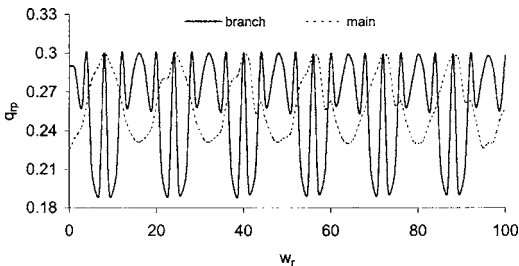


Fig. 6 Peak discharge frequency diagram for partial blockages in the main and branch pipes

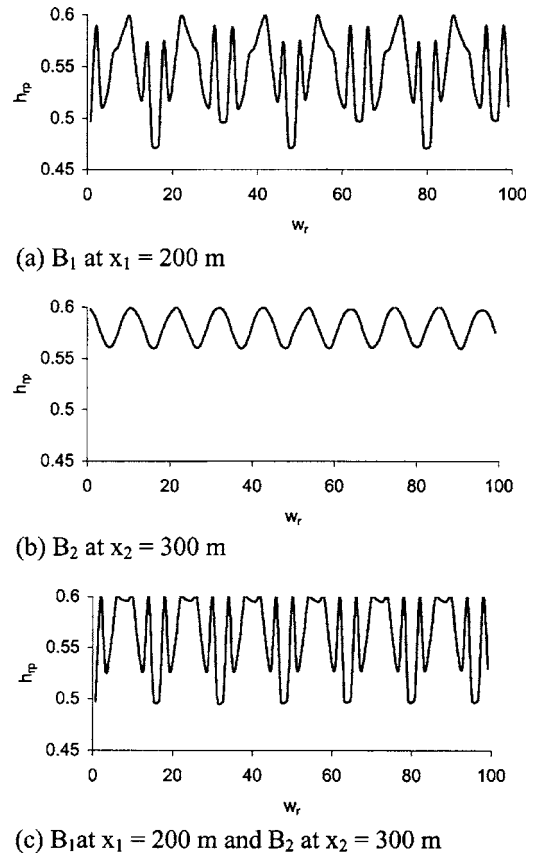


Fig. 7 Peak pressure frequency diagram for partial blockages in main line on both sides branching junction

$$c_1 + c_2 + c_3 - c_{1-2-3} = 2c_0 \quad (12)$$

### Effect of Branching Junction Location and Branch Length

All the results presented above are based on the values,  $x_b = 800$  m and  $L_b = 800$  m. The effects of the variation of these parameters are investigated by considering some examples. In case 2, the partial blockage is located in the main line and downstream of the branching junction. The peak pressure frequency diagram for  $x_b = 1200$  m is presented in Fig. 12(a) while all the other parameters are the same as those used in case 2 and  $x_2 = 200$  m. A comparison of Figs. 3(a) and 12(a) shows that the number of peaks, the lower and upper limits and the average values are the same in both the figures. However, there is a slight change in the shape. Similar results (not presented here) are obtained for the partial blockage at other locations in the main line or in the branch

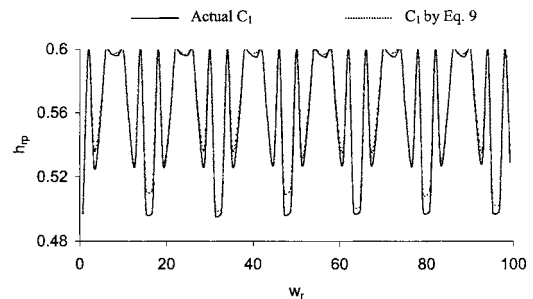
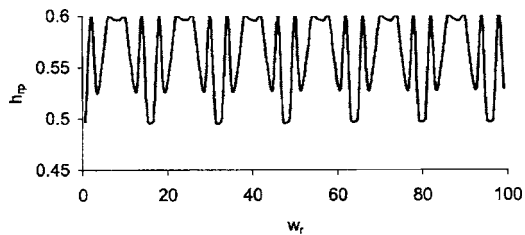
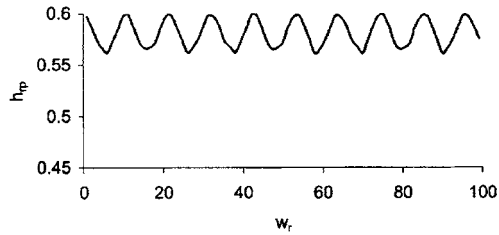


Fig. 8 Frequency response of  $B_1$  from frequency responses of  $B_2$  and combination of  $B_1$  and  $B_2$



(a) B<sub>1</sub> at x<sub>1</sub> = 200 m



(b) B<sub>3</sub> at x<sub>3</sub> = 300 m

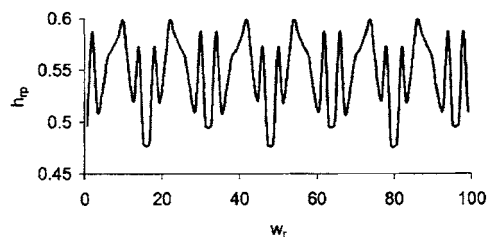


**Fig. 9 Peak pressure frequency diagram for partial blockages in branch and main line upstream of branching junction**

pipe. The peak pressure frequency diagram for the same case (case 2) is presented in Fig. 12(b) for a different branch length ( $L_b=1600$  m). This also indicates that when the partial blockage is in the main line, the effect of the branch length on the peak pressure frequency diagram is insignificant. However, the branch length affects the results if the partial blockage is in the branch pipe (Fig. 12(c)). A comparison of Figs. 5(a) and 12(c) shows that the lower limit decreases for a longer branch length. In addition, a longer branch pipe results in extra intermediate peaks in the peak pressure frequency diagram. However, it is important to note that the number of prominent peaks and the average value remain the same.

### Detection of Single Partial Blockage

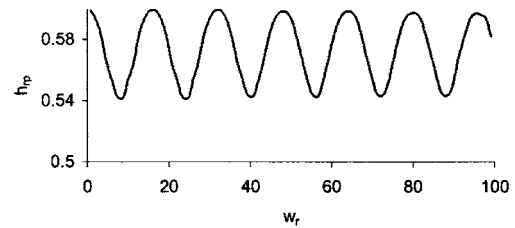
Based on the results of cases 1–3 presented above, the following procedure is proposed to detect a single partial blockage in a branched piping system.

1. Prepare the peak pressure frequency diagram for a range of nondimensional frequency ( $0-w_{rm}$ ) at the downstream end of the main line. There is no blockage if the diagram shows a horizontal line.

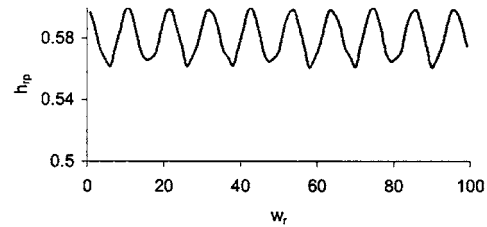
2. Count the number of prominent peaks,  $N_p$ , prominent troughs,  $N_r$ , (prominent values are those with more than 90% of the maximum amplitude) and calculate the average value ( $\bar{h}_{rp}$ ). Check whether a peak or a trough is first in this diagram.

(a) If the peak is first, then the partial blockage is located in the main line and upstream of the branching junction. Go to step 4.

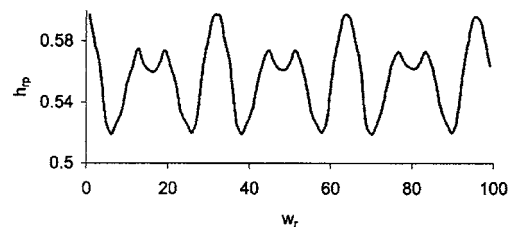
(b) If the trough is first, then the partial blockage is located either in the branch pipe or in the main line and downstream of branching junction.



(a) B<sub>2</sub> at x<sub>2</sub> = 200 m



(b) B<sub>3</sub> at x<sub>3</sub> = 300 m



(c) B<sub>2</sub> at x<sub>2</sub> = 200 m and B<sub>3</sub> at x<sub>3</sub> = 300 m

**Fig. 10 Peak pressure frequency diagram for partial blockages in branch and main line downstream of branching junction**

3. If 2(b) is true, then prepare the peak discharge frequency diagram at the downstream end of the main line for the same range of nondimensional frequency.

(a) If the numbers of troughs are equal in the peak discharge and peak pressure frequency diagrams, then the blockage is located in the main line and downstream of the branching junction.

(b) If the number of troughs is more in the peak discharge frequency diagram than that in the peak pressure frequency diagram, then the blockage is located in the branch pipe.

4. From the average value ( $\bar{h}_{rp}$ ) obtained in the peak pressure diagram, find the size of the partial blockage,  $z$ , by using Table 2 and selecting the appropriate case.

5. Use the formula  $x=(25/12)(LN/w_{rm})$  to estimate the location of the partial blockage. If 2(a) is true, then  $x=x_1$ , and  $N=N_r$ ; if 3(a) is true, then  $x=x_2$  and  $N=N_p$ , and if 3(b) is true, then  $x=x_3$  and  $N=N_p$ .  $L$  is the length of the main pipe.

### Results

Results presented in this work are for simplified cases (one branch pipe, friction factor is zero, etc.) and therefore, these should not be used directly to real life piping systems. The following limitations of the present study should be kept in mind before applying the method to real life situations. Real systems have uncertainties about friction values, diameters, demands, pipe properties, and system topologies. Decision on the range of frequencies should take into account the practical aspects such as friction of pipe, wave speed, and constraints in valve operation. Filtering may be required for the pressure signals recorded at the downstream valve. Valve operation (continuous opening and closing) may require specialized instrumentation. Maximum fluctuation in the head loss due to the partial blockage should be very

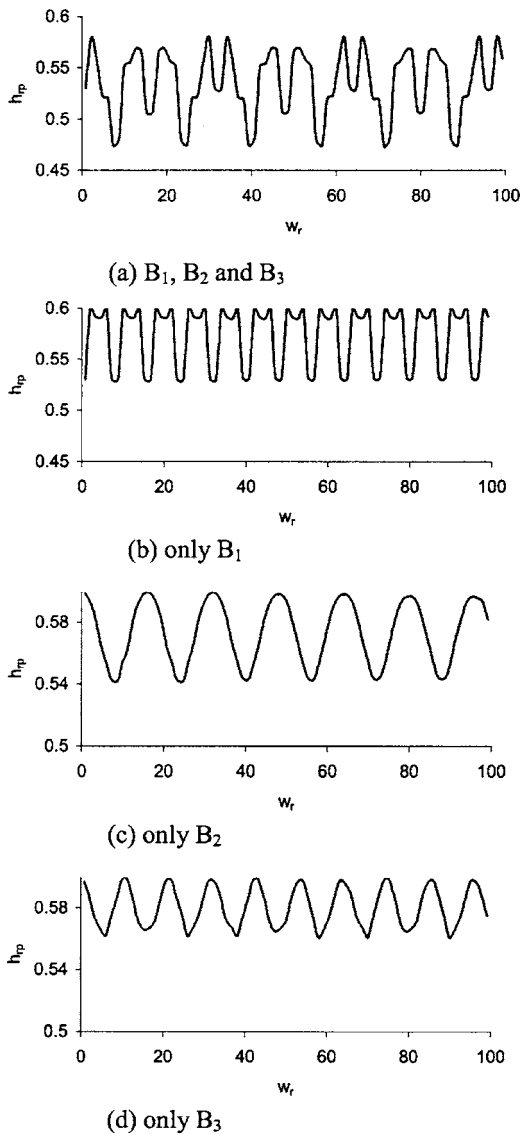


Fig. 11 Peak pressure frequency diagram for three partial blockages

less compared to the equilibrium pressure head of the system. In addition, the proposed methodology assumes a single phase liquid flow with constant temperature.

Effect of pipe friction on peak pressure frequency diagram for the following data is presented in Fig. 13. Main pipe:  $L=800$  m,  $D_0=0.050$  m,  $f=0.01$ ,  $a=1000$  m/s; branch pipe:  $L=200$  m,  $D_0=0.025$  m,  $a=1000$  m/s,  $x_b=300$  m; partial blockage:  $z_1=z_3=0.00$ ,  $z_2=0.40$ ,  $x_2=50$  m. Other data are the same as those used in the earlier examples. It may be noted that the pressure fluctuation is decreased due to effect of pipe friction. However, the characteristics of the peak pressure frequency diagram (number of peaks/troughs) remains same, i.e., the detection procedure will still be valid.

In the absence of experimental data, the methodology has been validated against the results obtained by the MOC, for detection of blockage in a single pipeline. The peak pressure frequency diagram at the downstream valve is computed both by MOC and present method (Fig. 13). The peak pressure fluctuations by MOC are underpredicted as compared to that by the present method. However, the overall matching is satisfactory because of the non-linearities, the amplitude of the positive swings in pressure oscillations is larger than the negative swings in the MOC simulations

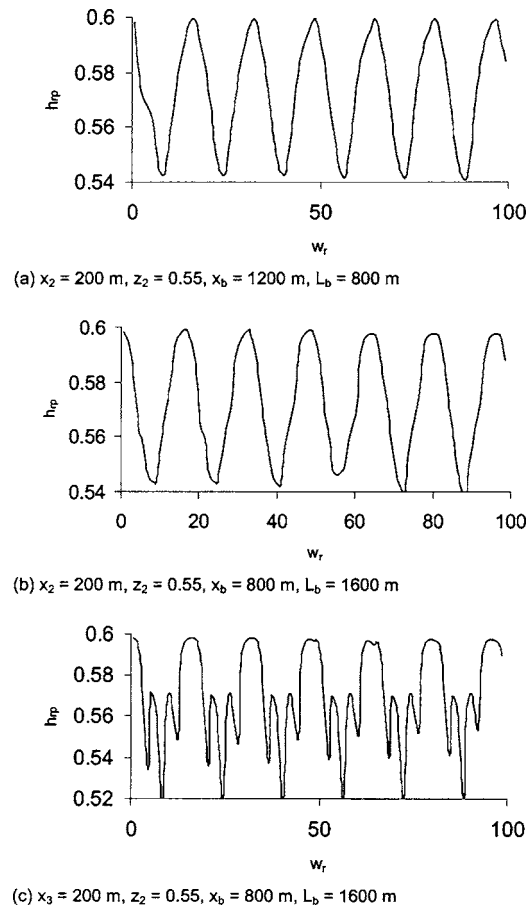


Fig. 12 Effect of branching junction and branch length on peak pressure frequency diagram

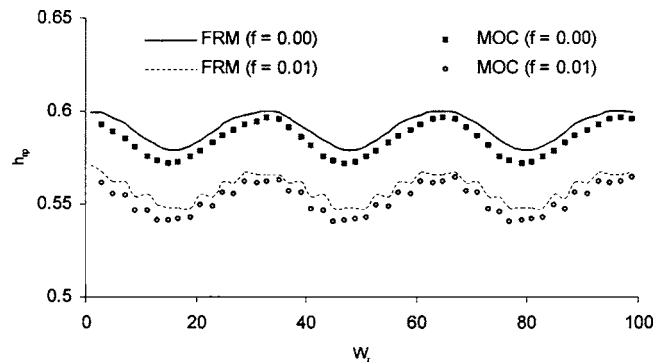


Fig. 13 Peak pressure frequency diagram with and without pipe friction

[18]. In the transfer matrix method, however, the amplitudes of the positive and negative swings are equal. Thus, the amplitudes from the trough to peak are approximately the same in both methods indicating a very good comparison.

The methodology presented herein has potential for applications to real life piping systems. A valve at the downstream end is periodically opened and closed. The operation time of the valve depends on the length of the main pipeline and wave velocity and it should not be less than the theoretical time period,  $T_{th}$  for each frequency. At the location of the oscillating valve, the amplitudes of the pressure fluctuations are recorded. This procedure is repeated for a range of frequencies by varying the period of valve

**Table 2 Effect of blockage size on peak pressure frequency diagram**

Relative head Loss, $\Delta H_0/H_0$	Blockage size, $z$	Main line, upstream of branching junction		Main line, downstream of branching junction		Branch pipe	
		Average peak pressure	Lower limit of peak pressure	Average peak pressure	Lower limit of peak pressure	Average peak pressure	Lower limit of peak pressure
0.10	0.40	0.586	0.56	0.589	0.58	0.589	0.58
0.20	0.55	0.563	0.50	0.572	0.55	0.573	0.55
0.30	0.60	0.544	0.45	0.558	0.52	0.559	0.52

oscillations. As the method uses the peak pressure fluctuations, only odd values of  $w_r$  are used. The peak pressure frequency diagram is obtained from the recorded values of peak pressure fluctuation and the corresponding frequency (valve oscillation) and it is used to estimate the location and the size of the blockage.

**Summary and Conclusions**

In this study, the flow in a branched piping system with partial blockages was analyzed in the frequency domain by using the transfer matrix method. There is a constant-head reservoir at the upstream end and an oscillating valve at the downstream end of the main line produces steady oscillatory flow in the system. The peak pressure frequency diagrams at the oscillating valve were presented for partial blockages in the branched piping system. The following important conclusions were derived.

1. A systematic procedure has been developed to detect a single partial blockage in the branched piping system. The pattern of the peak pressure frequency diagram indicates the broad area of location of the partial blockage, i.e., upstream or downstream of branching junction or in the branch pipe. The number of prominent peaks (or troughs) in this diagram indicates the location of the blockage and the average value in this diagram indicates the size.

2. The location of the branching junction and the length of the branch pipe have insignificant effect on the peak pressure frequency diagram when the blockage is located in the main line. However, the branch length has an effect on the peak pressure frequency diagram if the blockage is in the branch pipe.

3. For more than one partial blockage in the system, there is a definite relationship between the frequency responses of the individual and combined partial blockages. The development of an extra partial blockage can be detected by using this relationship, if the frequency response of the existing blockage(s) is known. This relationship may also be used to predict a change in the size of an existing blockage.

**Acknowledgment**

Funding provided by the School of Medicine and College of Engineering Joint Research Development Fund (RDF), University of South Carolina is acknowledged. Partial support from the Office of the Vice-President for Research of the University of South Carolina is also acknowledged.

**Nomenclature**

- $A$  = cross-sectional area of the pipe
- $a$  = wave velocity
- $B_1$  = partial blockage of size  $z_1$  located in the main line and upstream of the branching junction, at a distance of  $x_1$  from the reservoir end

- $B_2$  = partial blockage of size  $z_2$  located in the main line and downstream of the branching junction, at a distance of  $x_2$  from the valve end
- $B_3$  = partial blockage of size  $z_3$  located in the branch pipe, at a distance of  $x_3$  from the dead end
- $c_i$  = coordinates of the peak pressure frequency response at the valve
- $D$  = diameter of the opening at partial blockage
- $D_0$  = inside diameter of the pipe
- $F$  = field matrix
- $f$  = Darcy-Weisbach friction factor
- $g$  = acceleration due to gravity
- $H_0$  = mean pressure head
- $h_{n+1}^L$  = amplitude of pressure head fluctuation
- $h_r$  = nondimensional pressure amplitude
- $h_{rp}$  = nondimensional peak pressure amplitude
- $\bar{h}_{rp}$  = average value of nondimensional peak pressure amplitude
- $i$  = subscript  $i$  denotes the  $i$ th pipe in the system
- $j = \sqrt{-1}$
- $k$  = amplitude of the valve motion
- $L$  = length of the main line
- $L_b$  = length of the branch pipe
- $N$  = number of peaks (or troughs) in the peak pressure frequency diagram
- $n$  = number of components in the system
- $P$  = point matrix
- $P_{bd}$  = point matrix for a branch pipe with a dead end
- $P_{pb}$  = point matrix for partial blockage
- $P_{ov}$  = point matrix for oscillating valve
- $Q_0$  = mean discharge
- $q_{n+1}^L$  = amplitude of discharge fluctuation
- $q_r$  = nondimensional discharge amplitude
- $q_{rp}$  = nondimensional peak discharge amplitude
- $T_{th}$  = theoretical period
- $U$  = overall transfer matrix for main line
- $U_b$  = transfer matrix for the branch
- $u_{11}, u_{12}, \dots, u_{13}$  = elements of the overall extended transfer matrix  $U'$
- $U_{b11}, u_{b12}$  = elements of the transfer matrix  $U_b$
- $w$  = frequency
- $w_r = w/w_{th}$  = nondimensional frequency
- $w_{rm}$  = maximum value of the nondimensional frequency in the peak pressure frequency diagram
- $w_{th} = 2\pi/T_{th}$  = theoretical frequency
- $x_1$  = location of a partial blockage in the main line and upstream of the branching junction, from the reservoir end

$x_2$  = location of a partial blockage in the main line and downstream of the branching junction, from the valve end  
 $x_3$  = location of a partial blockage in the branch pipe, from the dead end  
 $x_b$  = location of the branching junction from the reservoir end  
 $Z_c$  = characteristic impedance of the pipe =  $\mu_i a_i^1 / j \omega g A_i$   
 $z$  = size of partial blockage  
 $\Delta H_0$  = head loss across the partial blockage  
 $\tau_0$  = mean relative valve opening  
 $\nu$  = kinematic viscosity of the fluid

## References

- [1] Scott, S. L., and Satterwhite, L. A., 1998, "Evaluation of the Back Pressure Technique for Blockage Detection in Gas Flow Lines," *ASME J. Energy Resour. Technol.*, ASME, **120**, pp. 27–31.
- [2] Scott, S. L., and Yi, J., 1999, "Flow Testing Methods to Detect and Characterize Partial Blockages in Looped Subsea Flow Lines," *ASME J. Energy Resour. Technol.*, ASME, **121**, pp. 154–160.
- [3] Adewumi, M. A., Eltohami, E. S., and Ahmed, W. H., 2000, "Pressure Transients Across Constrictions," *ASME J. Energy Resour. Technol.*, ASME, **122**, pp. 34–41.
- [4] [www.synetix.com/methanol/services-pipescan.htm](http://www.synetix.com/methanol/services-pipescan.htm).
- [5] [www.lesman.com](http://www.lesman.com).
- [6] Gooch, R. M., Clarke, T. A., and Ellis, T. J., 1996, "A Semi-Autonomous Sewer Surveillance and Inspection Vehicle," *Proc. IEEE Intelligent Vehicles, Japan*, pp. 64–69.
- [7] Bach, R. G., and Kern, M. J., 1997, "Practical Coronary Physiology: Clinical Applications of the Flow Velocity Guidewire," W. B. Saunders, ed., Davidson, C.J., *Cardiol. Clin.: Intravascular Imaging and Doppler*, 15(1), 79–99.
- [8] Wang, X. J., 2002, "Development of Advanced Leak and Blockage Detection Techniques in Water Distribution Systems," [www.civeng.adelaide.edu.au/postgrads/wang\\_xj.html](http://www.civeng.adelaide.edu.au/postgrads/wang_xj.html).
- [9] Wylie, E. B., and Streeter, V. L., 1993, *Fluid Transients in Systems*, Prentice-Hall, Englewood Cliffs, NJ.
- [10] Chaudhry, M. H., 1987, *Applied Hydraulic Transients*, 2nd ed., Van Nostrand Reinhold, New York.
- [11] Rocard, Y., 1937, *Les phenomenes d'auto-oscillation dans les installations hydrauliques*, Paris.
- [12] Waller, E. J., 1958, "Prediction of Pressure Surges in Pipelines by Theoretical and Experimental Methods," Publication No. 101, Oklahoma State University, Still Water, OK.
- [13] Pestel, E. C., and Lackie, F. A., 1963, *Matrix Methods in Elastomechanics*, McGraw-Hill, New York.
- [14] Molloy, C. T., 1957, "Use of Four Pole Parameters in Vibration Calculations," *J. Acoust. Soc. Am.*, **29**(7), pp. 842–853.
- [15] Reed, M. B., 1955, *Electrical Network Synthesis*, Prentice-Hall, New York, Chap. 2.
- [16] Mpesha, W., Gassman, S. L., and Chaudhry, M. H., 2001, "Leak Detection in Pipes by Frequency Response Method," *J. Hydraul. Eng.*, **127**(2), pp. 134–147.
- [17] Mpesha, W., Gassman, S. L., and Chaudhry, M. H., 2002, "Leak Detection in Pipes by Frequency Response Method Using a Step Excitation," *J. Hydraul. Res.*, **40**(1), pp. 55–62.
- [18] Chaudhry, M. H., 1970, "Resonance in Pressurized Piping Systems," Doctoral thesis, University of British Columbia, Vancouver, Canada, p. 79.



## The Classical Plane Couette-Poiseuille Flow With Variable Fluid Properties

Asterios Pantokratoras

School of Engineering,  
Democritus University of Thrace,  
67100 Xanthi, Greece  
e-mail: apantokr@civil.duth.gr

*A theoretical study of the effect of variable viscosity and variable thermal conductivity on the classical plane Couette-Poiseuille flow is presented in this brief communication. The investigation concerns engine oil, air, and water taking into account the variation of these quantities with temperature. The results are obtained with the numerical simulation of the governing equations and cover large temperature differences. Velocity and temperature profiles are presented as well as the volume flow rate and the heat flux between the plates. It is found that temperature profiles are close to the straight line for oil and water and depart significantly from the straight line for air due to nonlinear thermal conductivity. Dynamic viscosity plays an important role on the results which depart significantly from those of a fluid with constant properties. [DOI: 10.1115/1.2238878]*

*Keywords:* Couette-Poiseuille flow, variable properties, forced convection

### 1 Introduction

One of the simplest flows in fluid mechanics is the flow between two parallel plates one of them being stationary and the other moving with constant velocity. This flow is called the Couette flow in honor of Couette [1] who performed experiments on the flow between a fixed and moving concentric cylinder (White [2]). Another simple flow between two parallel plates is the Poiseuille flow which is due to pressure gradient along the plates. This is named after Poiseuille [3] a French physician who experimented with low-speed flow in tubes. These two flows and the combination of them, called the Couette-Poiseuille flow, are included in almost all fluid mechanics books as an introductory step to fluid mechanics. Usually these flows concern fluids with constant physical properties. The literature on the classical Couette-Poiseuille flow concerning fluids with variable physical properties is scarce. After conducting an extensive investigation the only

relevant work found is that by Barletta and Zanchini [4] who, among others, treated the problem of the Poiseuille flow of a Newtonian fluid with temperature dependent viscosity in a channel with constant but different wall temperatures. The working fluids were engine oil, ethylene glycol, and water, with maximum temperature difference between the plates equal to 100 K. In the present work we treat in a systematic way the problem of the Couette-Poiseuille flow for engine oil, air, and water, taking into account the variation of both viscosity and thermal conductivity with temperature for large temperature differences. The temperature range is 273–430 K for engine oil, 150–3000 K for air, and 273–373 K for water.

### 2 The Mathematical Model

The momentum and energy equation for the plane Couette-Poiseuille flow with variable properties are

$$\text{momentum equation} \quad \frac{\partial}{\partial y} \left( \mu \frac{\partial u}{\partial y} \right) - \frac{dp}{dx} = 0 \quad (1)$$

$$\text{energy equation} \quad \frac{\partial}{\partial y} \left( k \frac{\partial T}{\partial y} \right) = 0 \quad (2)$$

where  $x$  is the horizontal coordinate,  $y$  is the vertical coordinate,  $u$  is the velocity along the plates,  $dp/dx$  is the pressure gradient,  $\mu$  is the fluid dynamic viscosity,  $k$  is the thermal conductivity, and  $T$  the fluid temperature.

The boundary conditions at the two plates are

$$y = 0 \quad u = 0, \quad T = T_1 \quad (3)$$

$$y = b \quad u = u_2, \quad T = T_2 \quad (4)$$

where  $T_1$  is the temperature of the lower plate,  $T_2$  is the temperature of the upper plate,  $u_2$  is the velocity of the upper plate, and  $b$  is the distance between the plates.

Normal air is a transparent, nonparticipating fluid and the boundary conditions in the present problem are prescribed temperature at the plates. This means that the standard equations of motion and energy are valid (Ozisk [5]) and for that reason radiation has not been included in our analysis.

In some cases of the present work large temperature differences exist between the plates and the question arises if buoyancy should be taken into account. The flow between two very long and wide, nonmoving, horizontal plates with constant but unequal temperatures with  $T_1 > T_2$  is known in the literature as the Rayleigh-Benard problem and has been studied extensively. It is generally accepted that there is a critical Rayleigh number for the onset of convection and its value is 1708 (Bejan [6], page 252). The Rayleigh number is defined as

$$\text{Ra} = \frac{g\beta_f(T_1 - T_2)b^3}{\alpha_f\nu_f} = 0 \quad (5)$$

where  $\beta$  is the coefficient of thermal expansion,  $\alpha$  is the thermal diffusivity, and  $\nu$  is the kinematic viscosity all calculated at film temperature  $(T_1 + T_2)/2$ . When the Rayleigh number is lower than

Contributed by the Fluids Engineering Division of ASME for publication in the JOURNAL OF FLUIDS ENGINEERING. Manuscript received January 9, 2006; final manuscript received May 3, 2006. Assoc. Editor: Dimitris Drikakis.

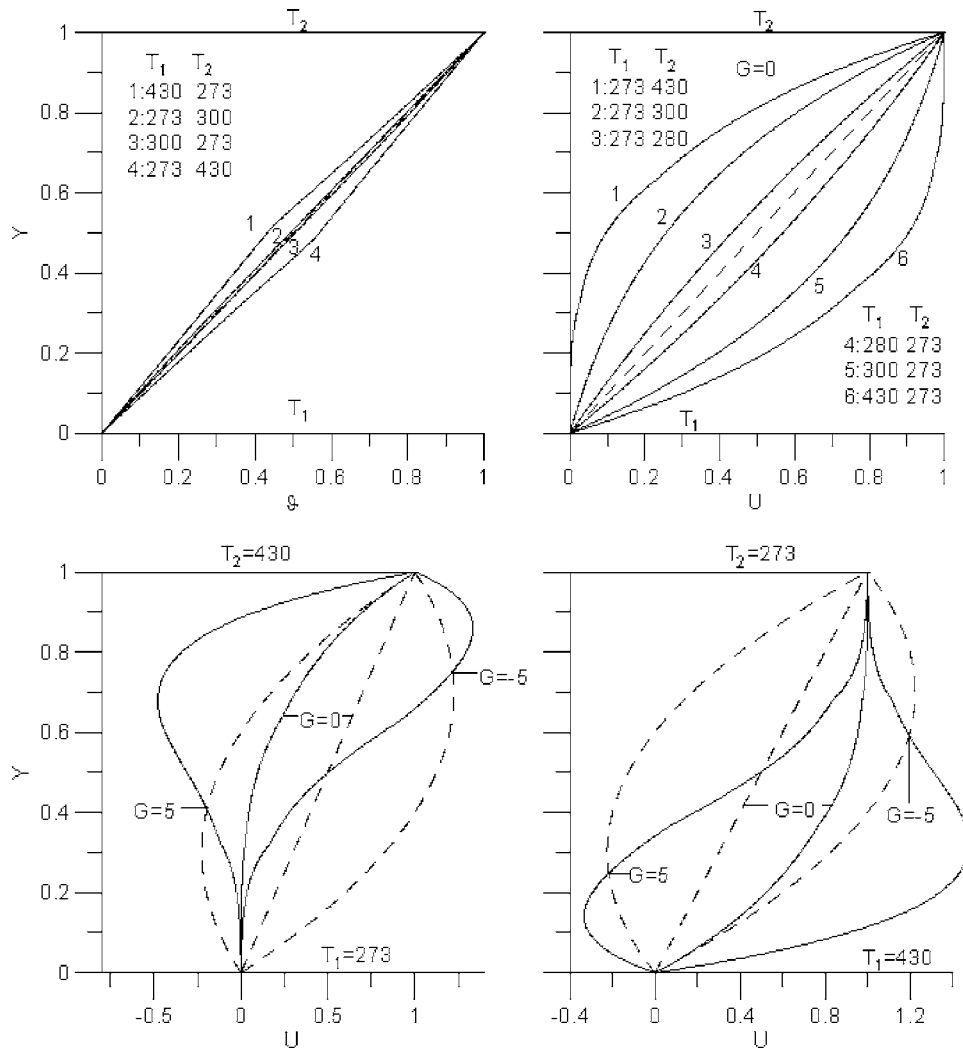


**Fig. 1 Temperature and velocity distribution for oil: Solid line, present work with variable properties; Dashed line solution for a fluid with constant properties**

1708 no motion occurs whereas immediately above 1708 the flow consists of counterrotating two-dimensional rolls named as Bernard cells. Our results are valid only for Rayleigh numbers lower than 1708 where buoyancy is negligible. For the cases with  $T_1 < T_2$  we have stable density stratification and our results are valid without the above limit.

In some special cases Eqs. (1) and (2) may accept analytical solutions. In the present work we solved these equations directly, without any transformation, using the finite difference method of Patankar [7]. The solution procedure starts with a known distribution of velocity and temperature at the channel entrance ( $x=0$ ) and marches along the plates. These profiles were used only to start the computations and their shape had no influence on the results which were taken far downstream. At the channel entrance the temperature and velocity were taken uniform with a very small value. At each downstream position the discretized Eqs. (1) and (2) are solved using the tridiagonal matrix algorithm (TDMA). As  $x$  increases the successive velocity profiles become more and more similar and the same happens with temperature profiles. The solution procedure stops at the point where the successive velocity and successive temperature profiles become identical (fully developed flow both hydrodynamically and thermally). The forward step size  $\Delta x$  was 0.01 mm and the lateral grid cells 500. The

results are grid independent. The parabolic solution procedure is a well known solution method and has been used extensively in the literature. It appeared for the first time in 1970 (Patankar and Spalding [8]) and has been included in classical fluid mechanics textbooks (see page 275 in White [2]). In the numerical simulation  $\mu$  and  $k$  have been considered as functions of temperature. A detailed description of the solution procedure, with variable thermophysical properties, may be found in Pantokratoras [9].

It should be noted here that the energy equation (2) is completely independent from the momentum equation (1) but the momentum equation is dependent on the energy equation because viscosity is a function of temperature. The temperature dependent thermal conductivity changes the temperature and this change is transferred to the momentum equation through viscosity.

### 3 Results and Discussion

Two important quantities for this problem are the nondimensional volume flow rate between the plates and the nondimensional heat flux defined by the following equations:

$$M = \int_0^1 U dY \quad (6)$$

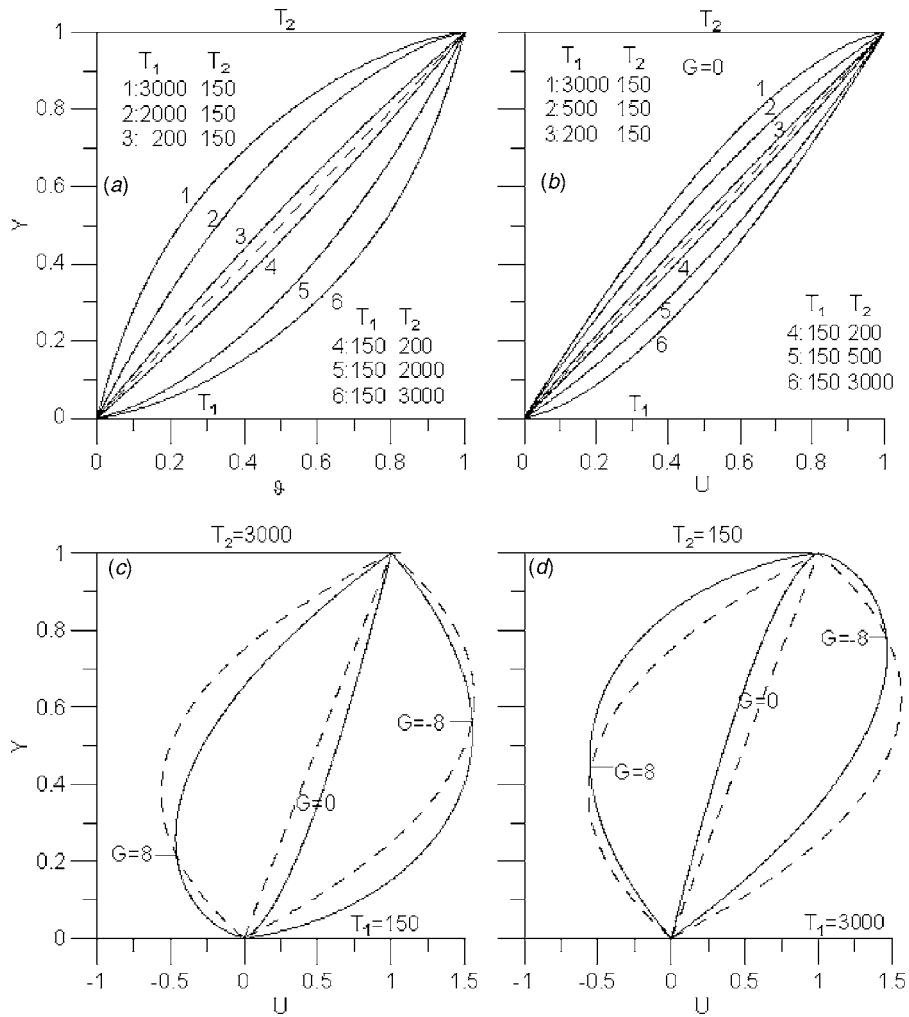


**Fig. 2 Temperature and velocity distribution for air: Solid line, present work with variable properties: Dashed line solution for a fluid with constant properties**

$$Q = \int_0^1 U \vartheta dY \quad (7)$$

The dimensionless velocity  $U$ , the dimensionless temperature  $\vartheta$ , and the dimensionless distance  $Y$  are given by the following equations:

$$U = \frac{u}{u_2} \quad (8)$$

$$\vartheta = \frac{T - T_1}{T_2 - T_1} \quad (9)$$

$$Y = \frac{y}{b} \quad (10)$$

Another useful quantity for this problem is the dimensionless pressure gradient defined as (Hashemabadi et al. [10])

$$G = \frac{b^2}{\mu_f \mu_2} \frac{dp}{dx} \quad (11)$$

where  $\mu_f$  is the fluid viscosity at film temperature  $(T_1 + T_2)/2$ . The Brinkman number is (White [2], page 108)

$$Br = \frac{\mu_f}{k_f} \frac{u_m^2}{(T_2 - T_1)} \quad (12)$$

where  $k_f$  is the fluid thermal conductivity at film temperature  $(T_1 + T_2)/2$  and  $u_m$  is the mean velocity given by the following equation:

$$u_m = 1/b \int_0^b u dy \quad (13)$$

The Brinkman number represents the ratio of heat generation (viscous dissipation) due to friction to fluid conduction effects. When the Brinkman number is high the heat produced, due to friction between the fluid particles, is high and should be taken into account whereas when the Brinkman is low the frictional heating is negligible. In a fluid with constant thermal conductivity the linear temperature profile changes to parabolic if the Brinkman number is high and the heat produced due to friction is high (White [2], page 107). For low speed flows, like those treated in the present paper, the Brinkman number is very small, even for oil, and for that reason the viscous dissipation term in the energy equation has been ignored (White [2], page 108). However, the temperature profiles presented in the following paragraphs depart from the linear form but this is caused by the nonlinear (temperature-dependent) thermal conductivity and not due to viscous dissipation.

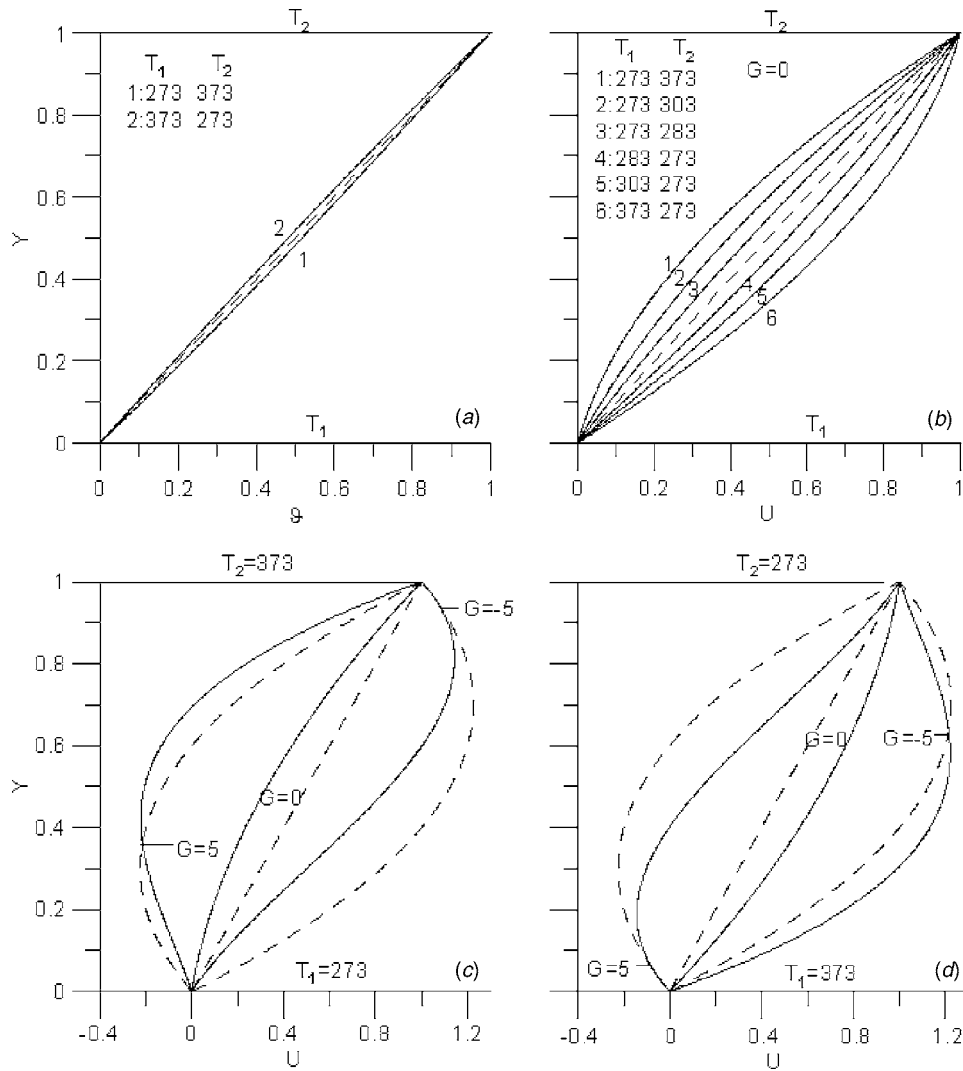


**Fig. 3 Temperature and velocity distribution for water: Solid line, present work with variable properties: Dashed line solution for a fluid with constant properties**

For Couette flows and constant fluid properties the flow is laminar when the Reynolds number is lower than 1500 (White [2], page 113). This Reynolds number is based on the velocity of the moving plate. For the present Couette-Poiseuille flow with variable fluid properties we calculated the Reynolds number from the following equation:

$$Re = \frac{\rho_f u_m b}{\mu_f} \quad (14)$$

where  $\rho_f$  is the fluid density at film temperature  $(T_1 + T_2)/2$ . We used as characteristic velocity the mean velocity, calculated with variable fluid properties, instead of the moving plate velocity because this mean velocity is more representative. The mean velocity is a result of the numerical simulation. The Reynolds number of the present work is lower than 1500 and the flow is laminar.

The forward step size  $\Delta x$  was 0.01 mm and the lateral grid cell is 500. For a fixed value of lateral grid points the results are independent of  $\Delta x$ . The only thing that changes is the distance from the channel entrance until the results take their final value. However, the results are dependent on the number of lateral grid points. We tried different numbers of lateral grid points and we found that usually 300 lateral grid points are sufficient. The  $\Delta x = 0.01$  mm and 500 lateral grid points cover all the cases treated and thus the results of the present work are grid independent.

**3.1 Results for Engine Oil.** For engine oil the density, dynamic viscosity, and thermal conductivity are given by the following equations for  $273 \text{ K} \leq T \leq 430 \text{ K}$  (Zografos et al. [11]):

$$\rho(\text{kg/m}^3) = -0.59212T + 1061.3 \quad (15)$$

$$\mu(\text{Ns/m}^2) = 3.0865 \exp(-20.306(T/260 - 1.0605)) \quad (16)$$

$$\mu(\text{Ns/m}^2) = 0.08254 \exp(-13.321(T/330 - 0.99988)) \quad (17)$$

$$\mu(\text{Ns/m}^2) = 0.01396 \exp(-8.6352(T/380 - 0.99994)) \quad (18)$$

$$k(\text{W/mK}) = -4.29 \times 10^{-4}T + 0.264 \quad 273 \text{ K} \leq T < 280 \text{ K} \quad (19)$$

$$k(\text{W/mK}) = -2.3810 \times 10^{-6}T^2 + 1.3976 \times 10^{-3}T - 6.6025 \times 10^{-2} \quad 280 \text{ K} \leq T \leq 350 \text{ K} \quad (20)$$

$$k(\text{W/mK}) = 0.138 \quad 350 \text{ K} < T < 360 \text{ K} \quad (21)$$

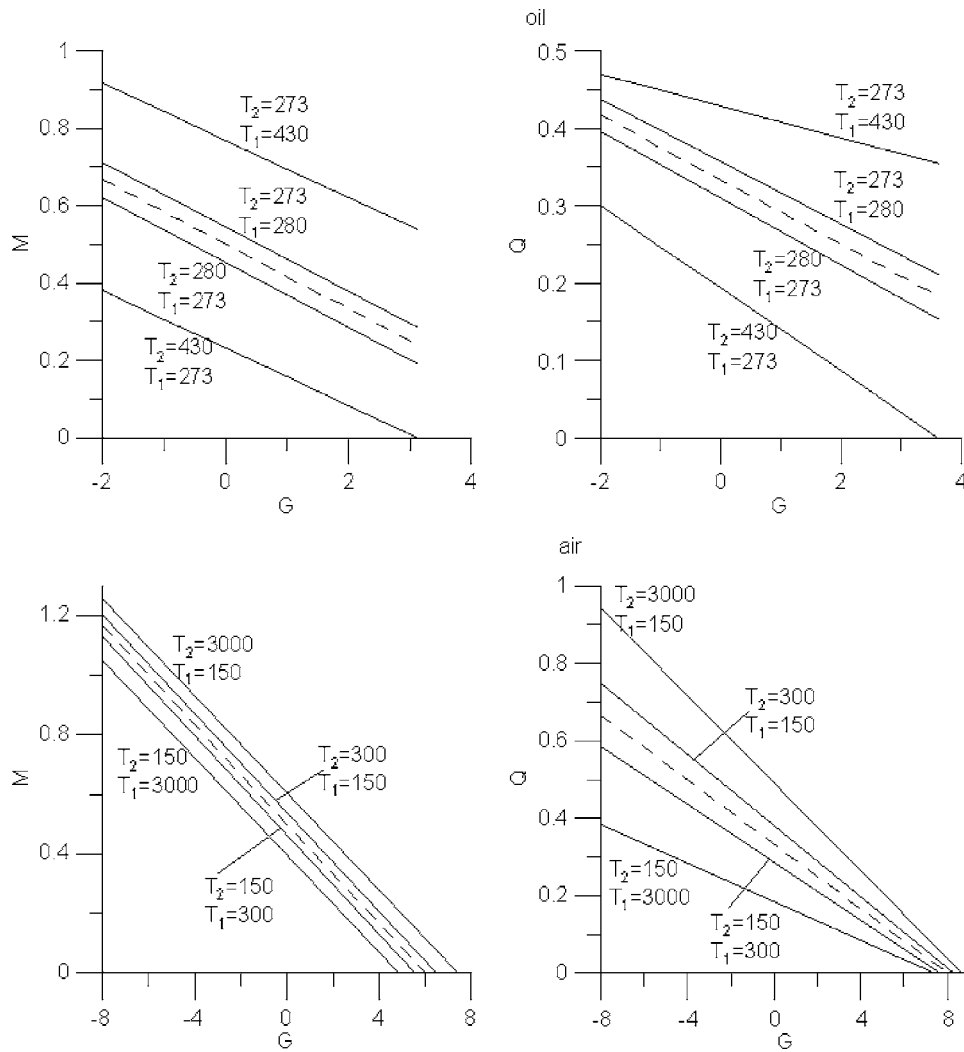


**Fig. 4 Variation of flow rate  $M$  and heat flux  $Q$  for oil and air: Solid line, present work with variable properties; Dashed line solution for a fluid with constant properties**

$$k(\text{W/mK}) = 4.881 \times 10^{-9}T^3 - 5.0844 \times 10^{-6}T^2 + 1.6475 \times 10^{-3}T + 2.4042 \times 10^{-2} \quad 360 \text{ K} \leq T \leq 430 \text{ K} \quad (22)$$

The nondimensional temperature distribution between the plates is shown in Fig. 1(a) for different plate temperatures. We see that the temperature profiles diverge from the straight line due to temperature dependent thermal conductivity. As the temperature difference between the plates decreases the temperature profiles approach the straight line which is valid for a fluid with constant thermal conductivity and this is proof that our solution procedure gives correct results. The energy equation is independent from the momentum equation, the temperature profiles are valid for both Couette and Poiseuille flow and are independent of  $G$ . In Fig. 1(b) velocity profiles are shown for Couette flow ( $G=0$ ) and different temperatures of the plates. In some velocity profiles there are points where velocity shows a small jump (discontinuity). Taking into account Eqs. (16)–(18) we see that viscosity is given by three different functions for  $273 \text{ K} \leq T \leq 430 \text{ K}$ . These small jumps appear at the temperatures where the viscosity function changes its form. Here some details are given of the method used to treat the variation of viscosity and thermal conductivity with temperature (the treatment is described analytically in pages 526–529 by White [2]). The finite difference form of the momentum equation is the following:

$$\mu_{m,n}(T_{m,n}) \frac{u_{m,n+1} - 2u_{m,n} + u_{m,n-1}}{\Delta y^2} - \frac{dp}{dx} = 0 \quad (23)$$

We denote the  $(x, y)$  location of a mesh point by subscripts  $(m, n)$ . The neighboring mesh points along  $y$  are  $(m, n+1)$  and  $(m, n-1)$ . If the temperature lies in the range  $273 \text{ K} \leq T \leq 330 \text{ K}$  we use Eq. (16) to calculate viscosity  $\mu_{m,n}(T_{m,n})$ . Let us suppose that the temperature in the next mesh point lies in the range  $330 \text{ K} \leq T \leq 380 \text{ K}$ . In that case we use Eq. (17) to calculate viscosity and so on. The same procedure is used for the calculation of thermal conductivity. It is obvious that, although the expressions (16)–(22) are not continuously differentiable, this is not a problem for the numerical method used.

Now turning back to Fig. 1 we see that as  $\Delta T$  decreases the velocity profiles approach the straight line which is valid for a fluid with constant properties, which again proves that our solution procedure gives correct results. From Fig. 1(b) it is seen that the variation of viscosity with temperature has a strong influence on velocity. The oil viscosity is a strong function of temperature. For case 1 oil viscosity is large near the lower plate (cold plate). The high viscosity hinders the oil velocity and for that reason we see almost zero velocity near the lower plate. In case 6 oil viscosity is low near the lower plate (hot plate) and for that reason velocities are greater than those of case 1 at the lower plate. In the

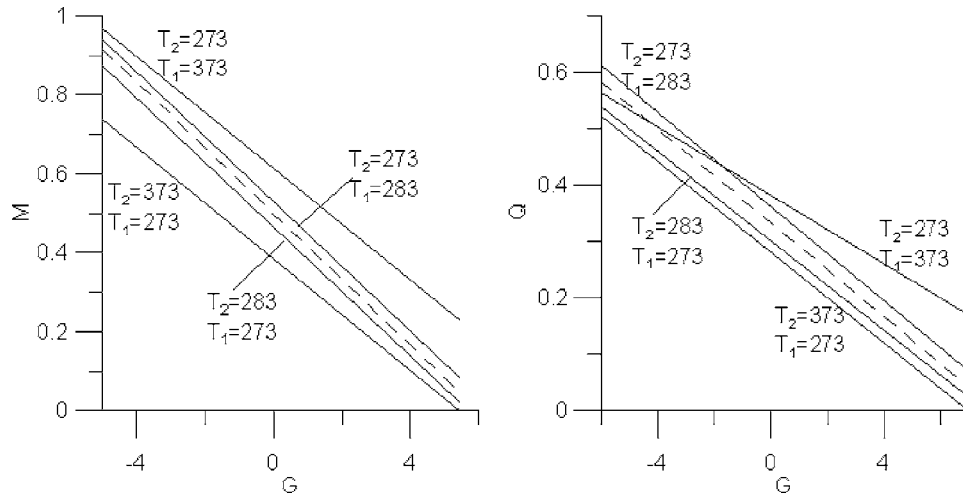


**Fig. 5 Variation of flow rate  $M$  and heat flux  $Q$  for water: Solid line, present work with variable properties; Dashed line solution for a fluid with constant properties**

lower plate of case 1 and in the upper plate of case 6 the wall shear stress is almost zero. In Figs. 1(c) and 1(d) velocity profiles are shown for the Couette-Poiseuille flow. We observe again large departures from the analytical solutions which correspond to a fluid with constant properties. The analytical solution for velocity is

$$U = -\frac{G}{2}Y(1-Y) + Y \quad (24)$$

The velocities near the cold plate are very small due to high oil viscosity.

Another point that must be mentioned here is the existence of some symmetry in the above figures for reverse plate temperatures (for example, 273–430, 430–273). Let us consider cases 1 and 6 in Fig. 1(b) and let the velocity of case 1 at a fixed distance from the lower plate is  $U_1$  while the velocity of case 6 at the same distance from the upper plate is  $U_6$ . The relation between these velocities is always  $U_1 + U_6 = 1$ . The same relation is valid for the temperatures in Fig. 1(a). The symmetry in Figs. 1(c) and 1(d) exists for reverse plate temperatures and opposite  $G$  values. A correspondence example is 273–430,  $G = +5$  and 430–273,  $G = -5$ . In this case the sum of the two velocities, which correspond to the same distance from the lower plate and upper plate, is constant but not equal to 1 as shown in Fig. 1(b). All the above kinds of symmetry exist also in the results for air and water that are presented in the following pages.

**3.2 Results for Air.** For air the density, dynamic viscosity and thermal conductivity are given by the following equations for  $150 \text{ K} \leq T \leq 3000 \text{ K}$  (Zografos et al. [11])

$$\rho(\text{kg/m}^3) = 345.57(T - 2.6884)^{-1} \quad (25)$$

$$\begin{aligned} \mu(\text{Ns/m}^2) &= 2.5914 \times 10^{-15}T^3 - 1.4346 \times 10^{-11}T^2 + 5.0523 \\ &\times 10^{-8}T + 4.1130 \times 10^{-6} \end{aligned} \quad (26)$$

$$\begin{aligned} k(\text{W/mK}) &= 1.5797 \times 10^{-17}T^5 - 9.4600 \times 10^{-14}T^4 + 2.2012 \\ &\times 10^{-10}T^3 - 2.3758 \times 10^{-7}T^2 + 1.7082 \times 10^{-4}T \\ &- 7.488 \times 10^{-3} \end{aligned} \quad (27)$$

In Fig. 2(a) the temperature distribution is presented for different plate temperatures. We see that the temperature profiles diverge from the straight line due to temperature dependent thermal conductivity and this divergence is quite significant. In Fig. 2(b) velocity profiles are shown for the Couette flow ( $G=0$ ) and different temperatures of the plates. Viscosity of air increases with increas-

ing temperature and decreases as temperature decreases. Near the lower plate air viscosity is large for case 1 (hot plate) and small for case 6 (cold plate) and for that reason velocities of case 6 are greater than those of case 1. In Figs. 2(c) and 2(d) velocity profiles are shown for the Couette-Poiseuille flow. We observe again departures from the analytical solutions which correspond to a fluid with constant properties.

**3.3 Results for Water.** For water the density, dynamic viscosity, and thermal conductivity are given by the following equations for  $273 \text{ K} \leq T \leq 600 \text{ K}$  (Zografos et al. [11])

$$\begin{aligned} \rho(\text{kg/m}^3) &= -3.0115 \times 10^{-6}T^3 + 9.6272 \times 10^{-4}T^2 - 0.11052T \\ &+ 1022.4 \end{aligned} \quad (28)$$

$$\mu(\text{Ns/m}^2) = 3.8208 \times 10^{-2}(T - 252.33)^{-1} \quad (29)$$

$$\begin{aligned} k(\text{W/mK}) &= 4.2365 \times 10^{-9}T^3 - 1.1440 \times 10^{-5}T^2 + 7.1959 \\ &\times 10^{-3}T - 0.63262 \end{aligned} \quad (30)$$

Figure 3(a) shows the temperature distribution between the plates. The thermal conductivity of water is a weak function of temperature and for that reason the divergence from the straight line is small. In Fig. 3(b) velocity profiles are shown for the Couette flow ( $G=0$ ) and different temperatures of the plates. Viscosity of water decreases with increasing temperature and increases as temperature decreases. This behavior is similar to that of oil and for that reason this figure is qualitatively similar to Fig. 1(b). Figures 3(c) and 3(d) present velocity profiles for Couette-Poiseuille flow and are similar to Figs. 1(c) and 3(d) which correspond to oil.

Figures 4 and 5 present the variation of dimensionless flow rate  $M$  and dimensionless heat flux  $Q$  as a function of the pressure gradient  $G$ . We observe departures from the constant properties values. It should be noted here that the quantities  $M$  and  $Q$  for a fluid with constant properties are given by the following equations:

$$M = \frac{1}{2} - \frac{1}{12}G \quad (31)$$

$$Q = -\frac{G}{6} + \frac{G}{8} + \frac{1}{3} \quad (32)$$

Except of the possible scientific value the results of the present work may have an educational value if they are included in the introductory chapters of fluid mechanics books where the usual

practice is to analyze the Couette and Poiseuille flow assuming constant fluid properties. The inclusion of fluids with variable properties will provide another view to fluid mechanics students.

## References

- [1] Couette, M., 1890, "Etudes sur le Frottement des Liquides," *Ann. Chim. Phys.*, **21**, pp. 433–510.
- [2] White, F., 1991, *Viscous Fluid Flow*, 2nd ed., McGraw-Hill, New York.
- [3] Poiseuille, J. L. M., 1840, "Recherches Experimentelles sur le Mouvement des Liquides dans les Tubes de tres Petits Diametres," *Compt. Rend.*, **11**, pp. 961–967.
- [4] Barletta, A., and Zanchini, E., 2001, "Mixed Convection With Variable Viscosity in an Inclined Channel With Prescribed Wall Temperatures," *Int. Commun. Heat Mass Transfer*, **28**, pp. 1043–1052.
- [5] Ozisik, M. N., 1987, "Interaction of Radiation With Convection," in *Handbook of Single-Phase Convective Heat Transfer*, Wiley, New York.
- [6] Bejan, A., 1995, *Convection Heat Transfer*, 2nd ed., Wiley, New York.
- [7] Patankar, S. V., 1980, *Numerical Heat Transfer and Fluid Flow*, McGraw-Hill, New York.
- [8] Patankar, S. V., and Spalding, D. B., 1970, *Heat and Mass Transfer in Boundary Layers*, Intertext, London.
- [9] Pantokratoras, A., 2002, "Laminar Free-convection Over a Vertical Isothermal Plate With Uniform Blowing or Suction in Water With Variable Physical Properties," *Int. J. Heat Mass Transfer*, **45**, pp. 963–977.
- [10] Hashemabadi, S. H., Etemad, S. Gh., and Thibault, J., 2004, "Forced Convection Heat Transfer of Couette-Poiseuille Flow of Nonlinear Viscoelastic Fluids Between Parallel Plates," *Int. J. Heat Mass Transfer*, **47**, pp. 3985–3991.
- [11] Zografos, A. I., Martin, W. A., and Sunderland, J. E., 1987, "Equations of Properties as a Function of Temperature for Seven Fluids," *Comput. Methods Appl. Mech. Eng.*, **61**, pp. 177–187.

# Moderately and Widely Spaced Circular Cylinders in Crossflow and a Universal Wake Number

D. Sumner<sup>1</sup>

e-mail: david.sumner@usask.ca

A. J. Schenstead

Department of Mechanical Engineering,  
University of Saskatchewan,  
57 Campus Drive,  
Saskatoon, Saskatchewan, S7N 5A9, Canada

*The universal wake number concept was examined for the flow around two circular cylinders of equal diameter arranged in moderately and widely spaced staggered configurations. The experiments were conducted in the subcritical Reynolds number regime for  $P/D=1.5-4.0$ . The results establish new limits for the validity of the universal wake number concept for moderately and widely spaced staggered cylinders in crossflow, and extend the results of an earlier study that focused only on closely spaced staggered cylinders. [DOI: 10.1115/1.2238879]*

## 1 Introduction

The wakes of many two-dimensional bluff bodies are characterized by a Kármán vortex street for a wide range of Reynolds number,  $Re$ . The vortex shedding frequency,  $f$ , is expressed as the Strouhal number,  $St$  ( $=fD/U$  for the case of a circular cylinder, where  $D$  is the diameter and  $U$  is the freestream velocity). Given that similar vortex wakes develop behind dissimilar two-dimensional bluff bodies, universal wake numbers have been proposed which are independent of the cross-sectional geometry of the body and the freestream conditions, and depend instead on length and velocity scales associated with the vortex wake. The universal Strouhal number,  $St^*$ , is based on the wake width and the velocity just outside the shear layer near the point of boundary layer separation [1–3]. Using an approximate, semi-empirical expression for the wake width [4],  $St^*$  can be expressed in terms of the mean drag force coefficient,  $C_D$ , the mean base pressure coefficient,  $C_{PB}$ , and the base pressure parameter,  $K(=(1-C_{PB})^{1/2})$ :

$$St^* = -\frac{St C_D}{K C_{PB}} \quad (1)$$

The universal wake number of Griffin [4] is the product of the universal Strouhal number,  $St^*$ , and a modified drag force coefficient,  $C_D^*$  ( $=-C_{PB}/K^2$ ). The product  $St^* C_D^*$  remains almost constant for a wide range of two-dimensional bluff-bodies and flow conditions, and is now known as the Griffin number,  $G$  [5,6]:

$$G = St^* C_D^* = \frac{St C_D}{K^3} \quad (2)$$

These two universal wake numbers,  $St^*$  and  $G$ , are suited to a variety of isolated, two-dimensional bluff bodies [4], and collapse of the data is seen for bodies with both moveable and fixed separation points, with smooth and rough surfaces, with splitter plates and base bleed, in steady and confined flow, undergoing forced

and free vibration, at an angle to the freestream, and through the subcritical, supercritical, and postcritical regimes [1–8].

Previously [9], it was shown that the universal wake number concept could be extended to two closely spaced staggered circular cylinders in crossflow, where two equal-diameter cylinders (Fig. 1(a)) are spaced at a center-to-center distance,  $P$ , and at an incidence angle,  $\alpha$ , to the freestream. When the cylinders are closely spaced, i.e., when  $P/D < 1.5$  (where  $P/D$  is the pitch ratio), the flow pattern is similar to a single bluff body, and a single vortex street is found in the wake. By considering the cylinders as a single body, using the total drag force acting on the cylinders and the average base pressure coefficient of the two cylinders, the Griffin number was found to be an effective universal wake number, with average values of  $G=0.073$  (standard deviation of 10%) for  $P/D=1.125$  and  $G=0.077$  (standard deviation of 15%) for  $P/D=1.25$  [9]. These values were within 31% of the single-cylinder value of  $G=0.062$  measured in the same wind tunnel, suggesting that the vortex wake developing behind the closely spaced cylinders is only to some extent similar to that of a single bluff body.

Some moderately spaced ( $1.5 \leq P/D < 3.0$ ) and widely spaced staggered cylinders ( $P/D \geq 3.0$ ) exhibit single-bluff-body behavior at small  $\alpha$ . Most moderately and widely spaced configurations, however, have vortex shedding occurring at different frequencies from both cylinders [10–12], with a complex interaction between the two vortex streets [11]. Of interest in the present study is whether the universal wake number concept can also be applied to the individual cylinders for moderately and widely spaced staggered configurations.

## 2 Experimental Approach

Experiments were conducted in a low-speed, closed-return wind tunnel. The experimental setup was similar to Ref. [9,12]. Two circular cylinders of  $D=0.032$  m were mounted between end plates and arranged in a staggered configuration, with  $P/D=1.5, 1.75, 2.0, 2.5, 3.0, \text{ or } 4.0$ ,  $\alpha=0-90$  deg, and  $Re=3 \times 10^4-7 \times 10^4$ . One cylinder, mounted vertically from a force balance and instrumented with base static pressure taps along its span, was centrally located in the test section. The second cylinder could be rotated in  $\alpha$  about the central cylinder using a computer-controlled turntable. In this way, the central cylinder could represent either an upstream or downstream cylinder over the full range of incidence angle,  $\alpha=0-90$  deg. The uncertainty in angular position was estimated at  $\pm 0.25^\circ$ . The cylinder length was  $L=0.768$  m, giving an aspect ratio of  $AR=L/D=24$ .

Flow conditions were measured with a Pitot-static probe and Datametrics Barocell absolute and differential pressure transducers. The base pressure was measured with a Validyne differential pressure transducer. Data were acquired with a Pentium II computer, a National Instruments AT-MIO-64F-5 12-bit multifunction board and LabVIEW software. The power spectra were obtained with a TSI 1210-T1.5 single-component hot-wire probe, a TSI IFA-100 anemometer, a National Instruments PCI-6024E 12-bit data acquisition board, and the National Instruments virtual bench digital signal analyzer. The probe was typically positioned at  $x/D=3.0$  and  $y/D=1.0$  from either cylinder (Fig. 1(b)). The measurement uncertainty in  $St$ ,  $St^*$ , and  $G$ , was estimated at  $\pm 4\%$  at  $Re=5 \times 10^4$ .

## 3 Results

The universal wake number data (Figs. 2 and 3, Table 1) were independent of  $Re$ . Separate universal wake numbers,  $St^*$  and  $G$ , for the upstream and downstream cylinders were calculated from Eqs. (1) and (2), respectively, using each cylinder's individual data for  $C_D$ ,  $C_{PB}$ , and  $St$ . For each  $P/D$ , average values of  $St^*$  and  $G$  were calculated. The standard deviation was used to judge whether a universal wake number was obtained. The standard error was used to assess the closeness to the single-cylinder values

<sup>1</sup>Corresponding author.

Contributed by the Fluids Engineering Division of ASME for publication in the JOURNAL OF FLUIDS ENGINEERING. Manuscript received July 8, 2005; final manuscript received March 13, 2006. Review conducted by Joseph Katz.



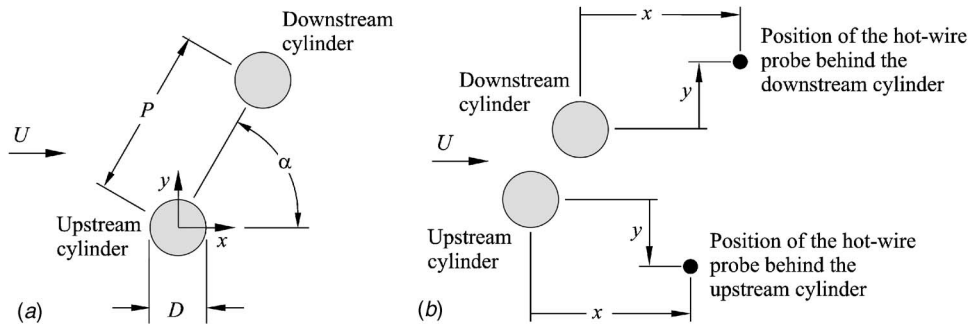


**Fig. 1 Two staggered circular cylinders in cross flow: (a) nomenclature and (b) location of the hot-wire probe behind each cylinder**

of the universal wake numbers, which were found to be  $St^* = 0.104$  and  $G = 0.062$  for the present experimental conditions.

**3.1 Moderately Spaced Cylinders.** The data for two moderately spaced staggered cylinders (Fig. 2, Table 1) are mostly similar for  $P/D = 1.5, 1.75, 2.0,$  and  $2.5$ . The behavior of the  $St$  data is more complex than for closely spaced cylinders [9–12], and for a wide range of  $\alpha$  two distinct Strouhal numbers are measured (Fig. 2). Based on the measurement location, the higher  $St$  corresponds to vortex shedding from the upstream cylinder and the lower  $St$  corresponds to vortex shedding from the downstream cylinder. As  $\alpha$  is increased to  $90$  deg, and as  $P/D$  is increased from  $1.5$  to  $2.5$ , the difference between these two Strouhal numbers becomes progressively smaller, and their values become closer to the single-cylinder value. For  $P/D = 1.5$  and  $1.75$  (Figs. 2(a) and 2(b)), two different Strouhal numbers are measured when the cylinders are side-by-side,  $\alpha = 90$  deg. This is the result of the biased flow pattern, where the flow through the gap between the cylinders is deflected towards one of the cylinders. Each cylinder has a different size of near-wake region and a different vortex shedding frequency [11,12]. The biased flow pattern is not found at  $P/D = 2.0$  and  $2.5$  (Figs. 2(c) and 2(d)), and therefore only one  $St$  value is measured at  $\alpha = 90$  deg. At lower incidence angles,  $\alpha < 30$  deg, there is some scatter in the  $St$  data, particularly for the downstream cylinder. A very high Strouhal number is found at the critical incidence angle,  $\alpha \approx 7$ – $11$  deg, corresponding to the inner

lift peak and its associated minimum  $C_D$  [12].

For both the upstream and downstream cylinders in moderately staggered configurations, the best collapse of the universal wake number data occurs when  $\alpha \geq 30$  deg and at the higher pitch ratios ( $P/D = 2.0$  and  $2.5$ , Figs. 2(c) and 2(d), Table 1). When  $\alpha < 30$  deg, there is more scatter in  $St^*$  and  $G$  (Fig. 2), particularly at the location of the inner lift peak; the amount of scatter reduces as  $P/D$  increases.

At smaller pitch ratios,  $P/D = 1.5$  and  $1.75$  (Figs. 2(a) and 2(b), Table 1), the universal wake numbers for the upstream cylinder agree poorly with the single-cylinder values for nearly all  $\alpha$ . The agreement improves (i.e., the standard error decreases, Table 1) with increasing  $P/D$ , to within 19% of the single-cylinder value of  $St^*$  and within 14% of the single-cylinder value of  $G$  at  $P/D = 2.5$ .

The universal wake number data for the downstream cylinder show better overall agreement than the upstream cylinder. When  $\alpha \geq 30$  deg, there is good agreement for both  $St^*$  and  $G$  for all  $P/D$  (Fig. 2, Table 1), the standard error decreasing with increasing  $P/D$  to within 6% of the single-cylinder value of  $St^*$  and 8% of the single-cylinder value of  $G$  at  $P/D = 2.5$ . When  $\alpha < 30$  deg, there are complex changes in the flow patterns, mean aerodynamic forces,  $C_{PB}$ , and  $St$ . Both  $St^*$  and  $G$  for the downstream cylinder become negative near the location of the inner lift peak,  $\alpha \approx 7$ – $11$  deg [12].

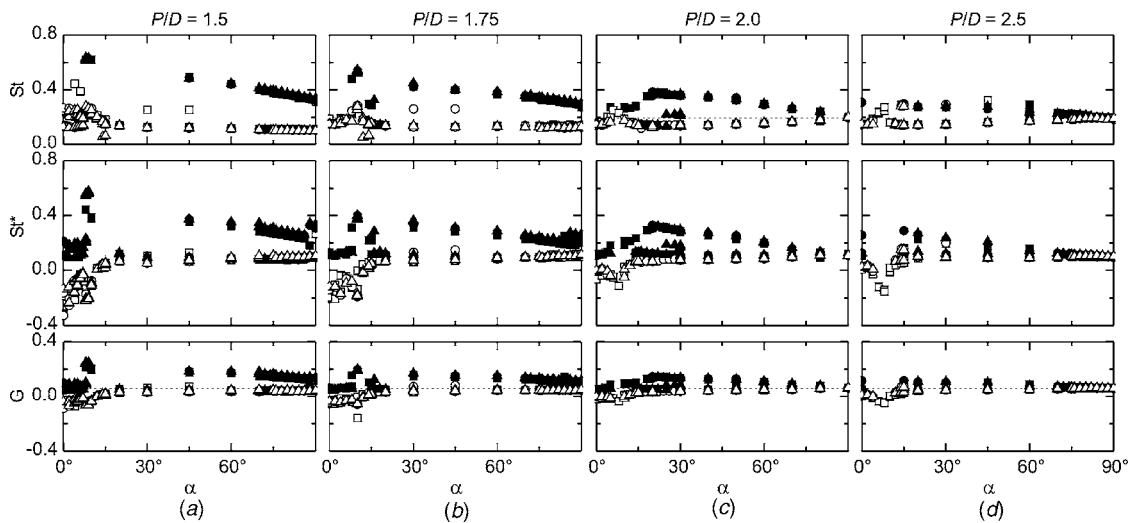


**Fig. 2 Vortex shedding data for moderately spaced staggered cylinders: (a)  $P/D = 1.5$ ; (b)  $P/D = 1.75$ ; (c)  $P/D = 2.0$ ; (d)  $P/D = 2.5$ . ■ or □,  $Re = 3.2 \times 10^4$ ; ● or ○,  $Re = 5.6 \times 10^4$ ; ▲ or △,  $Re = 7.2 \times 10^4$ . Solid symbols: upstream cylinder. Open symbols: downstream cylinder. Dashed line: single cylinder.**

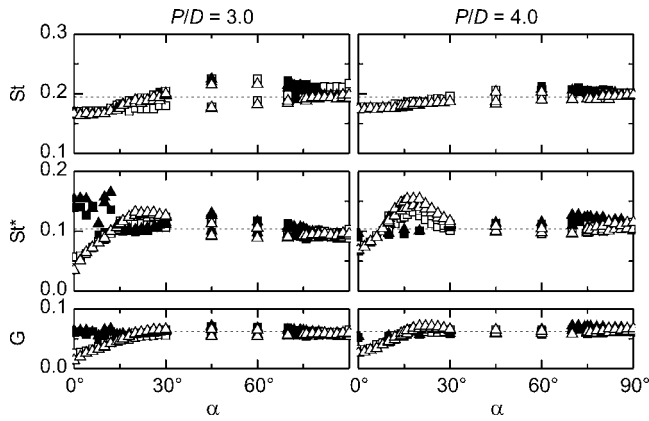


Fig. 3 Vortex shedding data for widely spaced staggered cylinders: (a)  $P/D=3.0$ ; (b)  $P/D=4.0$ . Symbols as in Fig. 2.

**3.2 Widely Spaced Cylinders.** The data for two widely spaced staggered cylinders (Fig. 3, Table 1) are mostly similar for  $P/D=3.0$  and  $4.0$ . The same  $St$  is measured behind both cylinders for most  $\alpha$ , and therefore both cylinders undergo vortex shedding at the same frequency. This Strouhal number remains close to single-cylinder value, indicating the reduced effects of interference between the cylinders. Two distinct Strouhal numbers are measured at intermediate and high  $\alpha$ , but the difference between them is very small, particularly for  $P/D=4.0$ , Fig. 3(b). This less complex behavior contrasts with the behavior of the mean aerodynamic force and base pressure coefficients for the downstream cylinder at smaller  $\alpha$ , where the outer lift peak occurs at  $\alpha \approx 18$  deg and the minimum  $C_D$  occurs at  $\alpha=0$  deg [12].

Universal wake numbers (Fig. 3, Table 1) consistent with the single-cylinder values from the present experiments are obtained for widely spaced staggered cylinders over most  $\alpha$ , for both the upstream and downstream cylinders. For the upstream cylinder, universal values of  $St^*$  (16% standard deviation for  $P/D=3.0$ ) and  $G$  (8% standard deviation for  $P/D=4.0$ ) are obtained over the entire range of incidence angle. Both  $St^*$  and  $G$  for the upstream cylinder show good agreement with the single-cylinder values,

which indicates that alternate vortex formation and shedding from the upstream cylinder occurs in a similar manner to that of a single cylinder.

For the downstream cylinder, universal values of  $St^*$  (11% standard deviation for  $P/D=3.0$ ) and  $G$  (7% standard deviation for  $P/D=3.0$ ) are obtained when  $\alpha > 30$  deg (Fig. 3, Table 1). Within this range of  $\alpha$ , the  $St^*$  data are within 12% and the  $G$  data are within 8% of the single-cylinder values. When  $\alpha < 30$  deg (Fig. 3), proximity interference and vortex impingement from the upstream cylinder cause the downstream cylinder to experience a large inward-directed lift force (the outer lift peak), a reduction in drag force, and an increase in base pressure. Vortex formation and shedding from the downstream cylinder is accordingly altered such that there is poor agreement for the universal wake numbers. Overall, the agreement with the single-cylinder values is best for the Griffin number,  $G$ , suggesting that this is the more appropriate choice of universal wake number for widely spaced staggered cylinders.

## 4 Conclusions

In the present study, the universal wake number concept was examined for the flow around two circular cylinders of equal diameter arranged in moderately and widely spaced staggered configurations. The experiments were conducted in the subcritical Reynolds number regime for  $P/D=1.5-4.0$ . The results establish new limits for the validity of the universal wake number concept for moderately and widely spaced staggered cylinders in cross-flow, and extend the results of an earlier study that focused only on closely spaced staggered cylinders [9].

For moderately spaced staggered cylinders, from  $P/D=1.5-2.5$ , vortex shedding occurs from both cylinders at most  $\alpha$ , but there are complex interactions between the two individual vortex wakes. The universal wake number concept is suitable for vortex shedding from the downstream cylinder when  $\alpha \geq 30$  deg. The Griffin number was more universal and was in better agreement with the established single-bluff-body value. Best agreement for the downstream cylinder was obtained at the largest pitch ratio,  $P/D=2.5$ , with an average value of  $G=0.059$  (standard deviation of 7%) which is within 8% of the single-body value.

Table 1 Average universal wake numbers (from the data in Figs. 2 and 3)

Upstream Cylinder	Range	$St^*$	Std. Dev.	Std. Error	$G$	Std. Dev.	Std. Error
$P/D = 1.5$	$\alpha \geq 30$ deg	0.298	11%	189%	0.154	10%	150%
$P/D = 1.75$	$\alpha \geq 30$ deg	0.238	16%	134%	0.126	12%	106%
$P/D = 2.0$	$\alpha \geq 30$ deg	0.197	32%	108%	0.104	24%	78%
$P/D = 2.5$	$\alpha \geq 30$ deg	0.115	14%	19%	0.068	10%	14%
$P/D = 3.0$	all $\alpha$	0.108	16%	17%	0.060	7%	7%
$P/D = 4.0$	all $\alpha$	0.111	8%	11%	0.064	8%	9%
Downstream Cylinder	Range	$St^*$	Std. Dev.	Std. Error	$G$	Std. Dev.	Std. Error
$P/D = 1.5$	$\alpha \geq 30$ deg	0.087	16%	21%	0.041	8%	35%
$P/D = 1.75$	$\alpha \geq 30$ deg	0.096	13%	14%	0.047	9%	25%
$P/D = 2.0$	$\alpha \geq 30$ deg	0.091	16%	18%	0.051	17%	22%
$P/D = 2.5$	$\alpha \geq 30$ deg	0.101	5%	6%	0.059	7%	8%
$P/D = 3.0$	$\alpha \geq 30$ deg	0.098	11%	12%	0.059	7%	8%
$P/D = 4.0$	$\alpha \geq 30$ deg	0.105	5%	5%	0.062	4%	4%

For widely spaced staggered cylinders,  $P/D=3.0$  and  $4.0$ , both the upstream and downstream cylinders undergo vortex shedding at nearly all  $\alpha$ , and the cylinders behave very similar to individual bluff bodies, particularly when  $\alpha \geq 30$  deg. The Griffin number was more universal and was in better agreement with the single-cylinder value; this result was consistent with the previous study for closely spaced cylinders [9]. For the upstream cylinder, average values of  $G=0.060$  (standard deviation of 7%) and  $G=0.064$  (standard deviation of 8%) were obtained over all  $\alpha$ , these values being within 9% of the single-body value. For the downstream cylinder, good agreement was obtained for  $\alpha \geq 30$  deg, with average values of  $G=0.059$  (standard deviation of 7%) and  $G=0.062$  (standard deviation of 4%) over all  $\alpha$ , these values being within 4% of the single-cylinder value in the present experiments and of the same order of the measurement uncertainty ( $\pm 4\%$ ).

The reason  $St^*$  is less successful may be attributed to the semi-empirical wake width assumption, which is based on Roshko's "notched hodograph theory" [1]. There are several reasons why this wake width-base pressure relationship may be invalid for staggered cylinders at small  $\alpha$  and moderate  $P/D$ . First, wake interference from the downstream cylinder significantly reduces the size and width of the near-wake region behind the upstream cylinder [11]. As Nakamura [8] noted, the after-body shape of a bluff body strongly influences the vortex formation behavior and the near-wake flow field, leading to poor behavior of  $St^*$  for bluff bodies with after-bodies. In the case of staggered cylinders, the downstream cylinder behaves similarly to an after-body at small  $\alpha$  and moderate  $P/D$ . Second, proximity interference from the upstream cylinder, the strong gap flow between the cylinders, and the nonuniform flow approaching the downstream cylinder [11], alter the pressure distribution on the downstream cylinder compared to the single cylinder. As Buresti [5] noted, Roshko's "notched hodograph theory" requires separation to occur at an angle less than 90 deg from the front of the cylinder. For this reason,  $St^*$  is unsuccessful for isolated circular cylinders at supercritical and postcritical  $Re$  [5], where separation is delayed. In some staggered configurations, the pressure distributions on either of the two cylinders may be influenced sufficiently, by wake and proximity interference, to invalidate the semi-empirical wake

width-base pressure relationship. A reason why the Griffin number is more successful is that by being a product of  $St^*$  and  $C_{D^*}$  (Eq. (2)), it becomes a function only of the wake velocity scale and independent of the wake length scale [5]. Improved collapse of the data may be obtained by using the gap flow velocity (which was not measured in the present experiments) or a more representative base pressure (which was measured at 180 deg from the front of the cylinder).

### Acknowledgment

The support of the Natural Sciences and Engineering Research Council (NSERC) and the University of Saskatchewan USTEP program is gratefully acknowledged.

### References

- [1] Roshko, A., 1955, "On the Wake and Drag of Bluff Bodies," *J. Aeronaut. Sci.*, **22**, pp. 124–132.
- [2] Bearman, P. W., 1967, "On Vortex Street Wakes," *J. Fluid Mech.*, **28**, pp. 625–641.
- [3] Griffin, O. M., 1978, "A Universal Strouhal Number for the 'Locking-On' of Vortex Shedding to the Vibrations of Bluff Cylinders," *J. Fluid Mech.*, **85**, pp. 591–606.
- [4] Griffin, O. M., 1981, "Universal Similarity in the Wakes of Stationary and Vibrating Bluff Structures," *ASME J. Fluids Eng.*, **103**, pp. 52–58.
- [5] Buresti, G., 1983, "Appraisal of Universal Wake Numbers From Data for Roughened Circular Cylinders," *ASME J. Fluids Eng.*, **105**, pp. 464–468.
- [6] Adachi, T., 1997, "Effects of Surface Roughness on the Universal Strouhal Number Over the Wide Reynolds Number Range," *J. Wind. Eng. Ind. Aerodyn.*, **69-71**, pp. 399–412.
- [7] Chen, J. M., and Fang, Y.-C., 1996, "Strouhal Numbers of Inclined Flat Plates," *J. Wind. Eng. Ind. Aerodyn.*, **61**, pp. 99–112.
- [8] Nakamura, Y., 1996, "Vortex Shedding From Bluff Bodies and a Universal Strouhal Number," *J. Fluids Struct.*, **10**, pp. 159–171.
- [9] Sumner, D., 2004, "Closely Spaced Circular Cylinders in Cross-Flow and a Universal Wake Number," *ASME J. Fluids Eng.*, **126**, pp. 245–249.
- [10] Kiya, M., Arie, M., Tamura, H., and Mori, H., 1980, "Vortex Shedding From Two Circular Cylinders in Staggered Arrangement," *ASME J. Fluids Eng.*, **102**, pp. 166–173.
- [11] Sumner, D., Price, S. J., and Paidoussis, M. P., 2000, "Flow-Pattern Identification for Two Staggered Circular Cylinders in Cross-Flow," *J. Fluid Mech.*, **411**, pp. 263–303.
- [12] Sumner, D., Richards, M. D., and Akosile, 2005, "Two Staggered Circular Cylinders of Equal Diameter in Cross-Flow," *J. Fluids Struct.*, **20**, pp. 255–276.

# 3-D Simulation of Dividing Flows in 90 deg Rectangular Closed Conduits

A. S. Ramamurthy

e-mail: ram@civil.concordia.ca

Junying Qu

Diep Vo

Chao Zhai

Department of Civil Engineering,  
Concordia University,  
1455 de Maisonneuve West,  
Montreal, Quebec H3G 1M8, Canada

[DOI: 10.1115/1.2243301]

## Introduction

Dividing flows in closed conduits (Fig. 1) are encountered often in environmental engineering and hydraulic engineering, while dealing with water and wastewater treatment plants, water distribution networks, and irrigation systems. There are many variables that influence the performance of these systems. In the past, the study of dividing flows has been restricted to physical models, one-dimensional theoretical analysis or one-dimensional numerical solutions. Several studies [1–5] have provided the various energy loss coefficients for flow past junctions of circular closed conduits. Popp and Sallet [6] used LDV to obtain the velocity field data for dividing flow past a rectangular tee junction for which the area ratio  $L/B=1$  (Fig. 1). Ramamurthy and Zhu [7] provided experimental data for dividing flows in 90 deg junctions of rectangular closed conduits. Very recently, Weber et al. [8] performed an extensive experimental study of 90 deg open channel junction flows for the purpose of providing comprehensive data needed for numerical code validation [9]. Fu [10] studied the flows in manifolds using the  $k-\epsilon$  model and verified the predictions using data of tests in which laser Doppler anemometry (LDA) was used.

In the present study, the Reynolds averaged Navier-Stokes (RANS) equations are applied to dividing flows in 90 deg rectangular conduit junctions. The three-dimensional  $k-\omega$  turbulence model of Wilcox [11] is adopted for numerical simulation to obtain the dividing flow characteristics. These characteristics include the energy loss coefficients, pressure profiles, velocity profiles, and the mean flow pattern. The results are validated using the experimental data of Ramamurthy and Zhu [7]. Following validation, it is easy to extend the range of simulated design data to suit the specific needs of other engineering devices that involve dividing closed conduit flows. The numerical model can be used without too much effort to obtain results such as energy loss coefficients for different area ratios and discharge ratios.

## Experimental Data

The experimental data for dividing flows in 90 deg closed conduit junctions are presented by Ramamurthy and Zhu [8] involv-

ing a range of area ratios and discharge ratios. Their test conduits consisted of a main conduit 6.3 m long and a branch conduit 1.25 m long. The inner dimensions of the main conduit were  $91.5 \times 41.2 \text{ mm}^2$ . The flow depth in the main conduit and the branch conduit were the same. For the rectangular branch conduits, three different cross sections were used to get the area ratios  $L/B$  of 1.0, 0.77, and 0.22. Here,  $L$  and  $B$  respectively denote the widths of the branch and main conduits (Fig. 1). The Dantec Laser Doppler Anemometry (LDA) unit was used to measure velocities in the test section. Very closely spaced 1.5 mm diameter wall taps were used to measure the wall pressure [7].

The experimental data related to mean velocities and pressure were mainly collected along the central line of the conduits, as the flow was assumed to be two-dimensional in the test program [7]. Details of the experimental data are available in related publications [12].

## Numerical Model

This proposed model solves the standard three-dimensional Reynolds averaged continuity and Navier-Stokes equations for turbulent steady-state flow based on the two-equation  $k-\omega$  model of Wilcox [11]. A finite volume method is used to discretize the model equations. The model employs the collocated-grid approach. The approximation of the convection term is handled by the deferred correction scheme (DCS), which combines the advantages of both the upwind difference scheme (UDS) and the central difference scheme (CDS). The pressure-velocity coupling is achieved using the SIMPLE algorithm. The discretized equations are solved with a Stone-based tridiagonal solver.

## Boundary Conditions

At the conduit boundary, the wall-function approach proposed by Launder and Spalding [13] is used. The universal logarithmic law of the wall, which is applicable to the fully turbulent region outside the viscous sublayer, is expressed as

$$\frac{u}{u_\tau} = \frac{1}{\kappa} \ln \frac{u_\tau y}{\nu} + C \quad (1)$$

Here,  $u$ =resultant velocity parallel to the wall at the first cell,  $u_\tau$ =resultant friction velocity,  $k=0.41$ ,  $y$ =normal distance to the wall,  $\nu$ =kinematic viscosity and  $C=5.0$  for smooth surfaces.

The near wall values of turbulent kinetic energy  $k$  and the specific dissipation rate are specified by assuming local equilibrium of turbulence [11]:

$$k = \frac{u_\tau^2}{\sqrt{\beta_0^*}}, \quad \omega = \frac{u_\tau}{\sqrt{\beta_0^*} \kappa y} \quad \text{where } \beta_0^* = \frac{9}{100} \quad (2)$$

For the main conduit, at the inlet, known flow velocities and turbulent quantities for fully developed conduit flow are prescribed. At the outlet of the main conduit, the pressure is specified as zero. Further, for mean flow velocities and turbulence quantities, the zero-gradient along the conduit flow direction is applied. At the

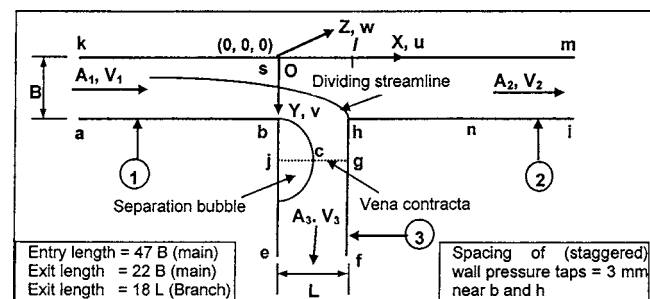


Fig. 1 Dividing rectangular conduit flow junction (O denotes the origin)

Contributed by the Fluids Engineering Division of ASME for publication in the JOURNAL OF FLUIDS ENGINEERING. Manuscript received February 27, 2003; final manuscript received June 27, 2005. Assoc. Editor: Fernando F. Grinstein.

**Table 1 Summary of grid cells**

No.	B (m)	L (m)	L/B	Z (m)	No. of grid cells					
					X <sub>upstream</sub>	X <sub>downstream</sub>	X <sub>branch</sub>	Y <sub>main conduit</sub>	Y <sub>branch</sub>	Z
SM2	0.0915	0.0705	0.77	0.0412	120	100	16	20	30	12

outlet of the branch conduit, the flow parameters are obtained using the extrapolation method.

**Solution Procedure**

Body fitted coordinates are used in the Cartesian frame. Mesh SM1 is generated for the chosen area ratio  $L/B=0.77$  (Table 1). The flow domain is meshed with a power law function, which generates a fine mesh in the vicinity of the conduit boundary. The grid cells adjacent to the boundary region are constructed within the fully turbulent region.

The solution procedure is continued until convergence is achieved. To this end, the error reduction in successive steps has to be at least three orders of magnitude. The results of numerical modeling are also checked for grid independence, while keeping the first grid cells within the fully turbulent region.

**Results and Discussions**

The model developed presently also includes the two-dimensional version of the numerical simulation. The two-dimensional model is able to predict the velocity data of the experiments [7] reasonably well. However, it slightly under predicts the pressure loss along the length of the conduit. Consequently,

the available test data are compared with the three-dimensional model. The three-dimensional simulation includes the frictional losses occurring at all sides of the conduits. As such, it agrees better with the experimental data, where frictional losses do occur on all sides of the conduits. Although test data are available for three area ratios, for brevity, only the data for one typical area ratio ( $L/B=0.77$ ) are used for validation.

**Energy Loss Coefficients.** The coefficients  $K_{12}$  and  $K_{13}$ , denoting the loss of energy from section 1 to 2 and from section 1 to 3, respectively (Fig. 1), are presented below. Thus,

$$E_1 = \frac{p_1}{\rho g} + \frac{V_1^2}{2g}, \quad E_2 = \frac{p_2}{\rho g} + \frac{V_2^2}{2g}, \quad E_3 = \frac{p_3}{\rho g} + \frac{V_3^2}{2g} \quad (3)$$

$$K_{12} = \frac{E_1 - E_2}{V_1^2/2g}, \quad K_{13} = \frac{E_1 - E_3}{V_1^2/2g} \quad (4)$$

Here,  $\rho$ =density of water and  $g$ =acceleration due to gravity. The total energy, pressure, discharge, and velocity of flow are, respectively,  $E$ ,  $p$ ,  $Q$ , and  $V$ . Suffixes 1, 2, and 3 refer to sections 1, 2, and 3 in Fig. 1.

For validation, test data [7] related to  $L/B=0.77$  are used. The

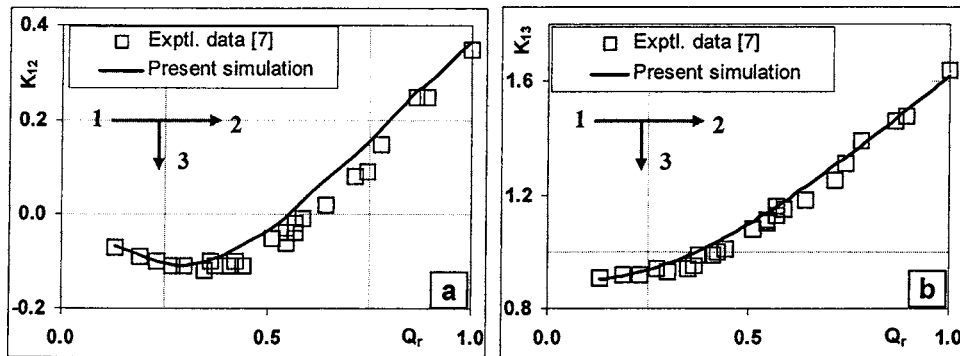


**Fig. 2 Comparison of energy loss coefficients ( $L/B=0.77$ ). (a)  $K_{12}$ , (b)  $K_{13}$ .**

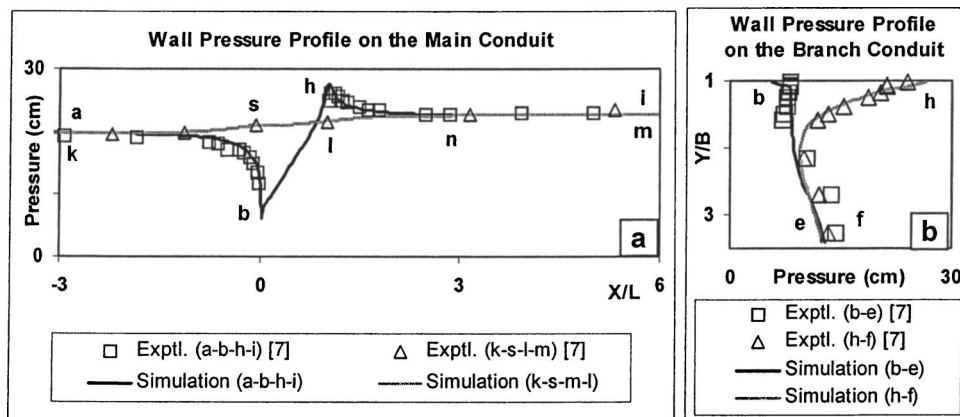


**Fig. 3 Pressure profile for  $L/B=0.77$  and  $Q_3/Q_2=0.57$**

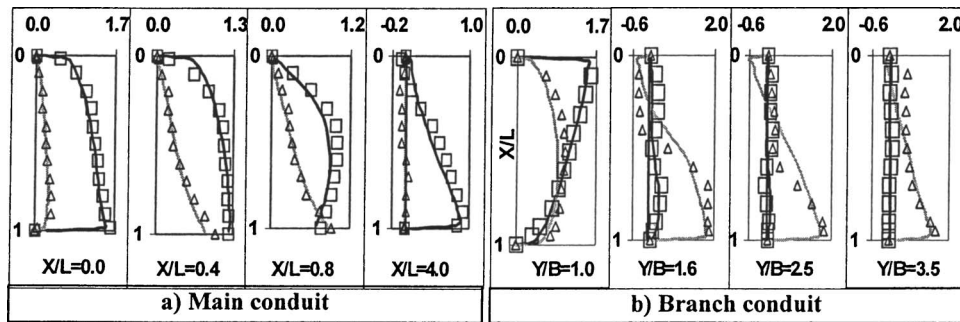


Fig. 4 Velocity distribution at sections of the main and the branch conduits:  $\square$ : experimental data  $u/U_0$  [12],  $\Delta$ : experimental data  $v/U_0$  [12], —simulation  $u/U_0$ , and —simulation  $v/U_0$ .

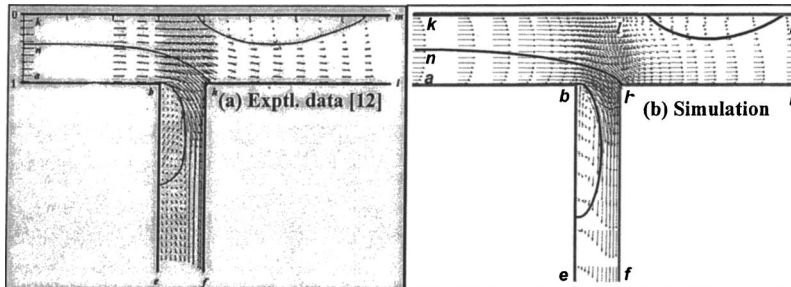


Fig. 5 Comparison of mean flow pattern for  $L/B=0.77$  and  $Q_3/Q_1=0.57$

agreement between predicted data and test data is similar for other  $L/B$  ratios. For the rectangular conduit ( $L/B=0.77$ ), Figs. 2(a) and 2(b) show the variation of the energy loss coefficients  $K_{12}$  and  $K_{13}$  with  $Q_r=Q_3/Q_1$ . They indicate that the predicted values of  $K_{12}$  and  $K_{13}$  agree with the experiment data [7].

**Pressure Distribution.** As stated earlier, the test data [7] were mainly obtained along the central line of the conduits, as the flow was assumed to be two-dimensional in the test program. Figures 3–5 present the comparison of test data with the predicted data for dividing conduit flows ( $L/B=0.77$  and  $Q_r=0.57$ ).

The measured wall pressure profiles along the main conduit and the branch conduit agree reasonably well with the predicted wall pressure profiles (Figs. 3(a) and 3(b)). Due to the acceleration of the flow entering the lateral, the pressure along the near wall  $ab$  (Fig. 1) of the main conduit drops drastically at the corner  $b$ . Along the main conduit wall, the stagnation pressure near the corner  $h$  of the near wall decreases to the value of the pressure along the far wall  $lm$  in a short distance  $hn$  (Fig. 3(a)). In general, the simulation also faithfully predicts the pressures along the walls of the branch conduit (Fig. 3(b)). The recovery of pressure in the branch is slightly lower than the measured pressure (Fig. 3(b)). The predicted and the experimental wall pressure data agree well for other area ratios and discharge ratios. These data are not shown for brevity.

**Velocity Profiles.** Figure 4(a) indicates that the simulation can predict the profiles of the velocity components  $u$  and  $v$  reasonably well in the main conduit. Outside the junction section, the  $v$  component is relatively weak compared to the  $u$  component. Again in Fig. 4(b), there is a reasonable agreement between the predicted and experimental values of the velocity components in the branch including the existence of reverse flow. However, the simulation indicates a reverse flow in the branch up to  $Y/B=3.5$ , while the test data show a reverse flow only up to  $Y/B=2.5$ .

**Mean Flow Pattern.** Flow separation occurs when there is an abrupt change in the wall alignment away from the direction of

the flow as at point  $b$  or when the flow encounters the adverse pressure gradient due to flow expansion as in the main conduit region  $lm$ , downstream of the junction (Fig. 5). The shape of the simulated zone of separation compares qualitatively with the separation zone of the experiment data. The simulation clearly predicts the very low velocities along the far wall region  $lm$  of the main conduit. The reattachment appears to be somewhat longer in the simulation.

## Conclusions

The three-dimensional two-equation turbulence model faithfully reproduces the mean flow characteristics of dividing flows of 90 deg junctions of rectangular closed conduits. These characteristics include the energy loss coefficients, pressure profiles, velocity profiles, and the mean flow pattern. The numerical results predict the experimental data related to pressure and velocity fields very well. The zone of flow separation predicted by the model also qualitatively agrees with the experimental data. Numerical models can be used to obtain results such as energy loss coefficients for different area ratios and discharge ratios without too much effort.

## References

- [1] McNowen, J. S., 1954, "Mechanics of Manifold Flow," *Trans. Am. Soc. Civ. Eng.*, **110**, pp. 1103–1142.
- [2] Gardel, A., 1957, "Les Pertes de Charge Dans Les Ecoulements au Travers de Branchements en Te" ("Pressure Drops in Flows Through T-Shaped Pipe Fittings"), *Bull. Tech. Suisse Romande*, **83**(9), pp. 123–130 and **83**(10), pp. 143–148.
- [3] Blaisdell, F. W., and Manson, P. W., 1963, "Loss of Energy at Sharp-Edge Pipe Junction in Water Conveyance Systems," *Tech. Bull. 1283*, U.S. Department of Agriculture, Washington DC.
- [4] Bajura, R. A., 1971, "A Model for Flow Distribution in Manifolds," *ASME J. Eng. Power*, pp. 7–12.
- [5] Ito, H., and Imai, K., 1973, "Energy Losses at 90 Degree Pipe Junctions," *J. Hydr. Div.*, **99**(9), pp. 1353–1368.
- [6] Popp, M., and Sallet, D. W., 1983, "Experimental Investigation of One- and Two-Phase Flow," *Intl. Conf. On the Physical Modeling of Multi-Phase Flow*, BHRA Fluid Engineering, pp. 67–90.

- [7] Ramamurthy, A. S., and Zhu, W., 1996, "Dividing Flows in 90° Junctions of Rectangular Closed Conduits," *J. Hydraul. Eng.*, **122**(12), pp. 687–691.
- [8] Weber, L. J., 2001, "Experiments on Flow at a 90° Open-channel Junction," *J. Hydraul. Eng.*, **127**(5), pp. 268–280.
- [9] Huang, J., 2002, "Three-Dimensional Numerical Study of Flows in Open-Channel Junctions," *J. Hydraul. Eng.*, **128**(3), pp. 268–280.
- [10] Fu, H., 1992, "Computation of Three-Dimensional Turbulent Flows in a Pipe Junction With Reference to Engine Inlet Manifolds," *Proc. Inst. Mech. Eng.* 206(6), pp. 285–295.
- [11] Wilcox, D. C., 2000, *Turbulence Modeling for CFD*, DCW Industries, Inc.
- [12] Zhu, W., 1995, "Characteristics of Dividing and Combining Flows," Ph.D. thesis, Concordia University, Montreal, Canada.
- [13] Lander, B. E., and Spalding, D. B., 1974, "The Numerical Computation of Turbulent Flows," *Comput. Methods Appl. Mech. Eng.*, **3**, pp. 269–289.

# Announcement

Dear Department Chair:

Would you like to honor your most outstanding faculty members in the fluids area? Please consider nominating them for the:

## **2007 FLUIDS ENGINEERING AWARD**

The Fluids Engineering Award is the most prestigious award conferred by ASME upon an individual in the field. It recognizes an individual for his/her outstanding contributions, over a period of years, to the engineering profession, and in particular to the field of fluids engineering through research, practice, or teaching.

**Award:** \$1000, Bronze Medal Certificate

**Deadline for nominations: September 30, 2006**

**Email your nomination to:**

Dr. A. Guinzburg, Chair  
Honors and Awards Committee  
ASME Fluids Engineering Division  
310-429-3665  
adiel@alumni.caltech.edu

### **Past Recipients of the Fluids Engineering Award are:**

2004: Joseph Katz	2005: Andrea Prosperetti
2002: Paul Cooper	2003: Marvin Goldstein
2000: Fazle Hussain	2001: Ramesh Agarwal
1998: Mike Roco	1999: Michael P. Païdoussis
1996: Budugur Lakshminarayana	1997: Virendra C. Patel
1994: Graham B. Wallis	1995: Clayton T. Crowe
1992: Christopher E. Brennen	1993: Roger E. A. Arndt
1990: Turgut Sarpkaya	1991: Frank M. White
1988: Allan J. Acosta	1989: William C. Reynolds
1986: Milton S. Plesset	1987: Mark V. Morkovin
1984: Hans W. Liepmann	1985: Apollo M. O. Smith
1981: Ascher H. Shapiro	1983: George Rudinger
1974: Steven J. Kline	1979: Robert C. Dean, Jr.
1968: George F. Wislicenus	1972: Howard W. Emmons

For additional information regarding the Fluids Engineering Award, please check:

**<http://divisions.asme.org/fed/awards/fea.html>**

For the nomination procedure and forms, please check:

**<http://www.asme.org/honors/>**